Direct Method of Generating Floor Response Spectra for Structures Considering Soil-Structure Interaction

by

Yue Li

A thesis
presented to the University of Waterloo
in fulfilment of the
thesis requirement for the degree of
Doctor of Philosophy
in
Civil Engineering

Waterloo, Ontario, Canada, 2024

© Yue Li 2024

Examining Committee Membership

The following served on the Examining Committee for this thesis. The decision of the Examining Committee is by majority vote.

External Examiner	Dr. Wenxing Zhou Professor
Supervisor	Dr. Wei-Chau Xie Professor
Internal Member	Dr. Mahesh Pandey Professor
Internal Member	Dr. Shunde Yin Professor
Internal-external Member	Dr. Jun Liu Professor

Author's Declaration

I hereby declare that I am the sole author of this thesis. This is a true copy of the thesis, including any required final revisions, as accepted by my examiners.

I understand that my thesis may be made electronically available to the public.

Abstract

Floor Response Spectra (FRS) are crucial for the seismic design and safety assessment of structures, systems, and components (SSCs) in nuclear power facilities. Generating accurate FRS requires considering soil-structure interaction (SSI) effects, especially for structures with flexible foundations and spatially varying ground motions. This thesis presents a comprehensive approach to address these challenges in the context of nuclear power plant (NPP) structures, with a specific focus on the applicability of this method to Small Modular Reactors (SMRs). The main contributions are as follows:

(1). A novel direct spectra-to-spectra method is extended for efficient FRS generation in multi-supported structures, incorporating SSI effects through a substructure approach. This method converts Foundation Input Response Spectra (FIRS) into Foundation Level Input Response Spectra (FLIRS) using analytically derived transfer matrices based on soil stiffness and structural modal information. It accommodates both flexible and rigid foundations under varying seismic inputs, eliminating intermediate spectrum-compatible time history generations and full system reanalysis when properties change. (**Chapter 2**)

(2). A numerical example of a 3-DOF structure with two structural nodes and one foundation node supported by a generalized soil spring is presented to verify the proposed method. Both theoretical formulation and numerical simulation verified and solidified the equivalence of seismic responses between the coupled soil-structure system under FIRS excitations and the decoupled structure under FLIRS inputs. This validation confirms the theoretical rigor of replacing FIRS with FLIRS in the analysis. (**Chapter 3**)

(3). A comprehensive methodology for evaluating dynamic soil stiffness matrices is presented, utilizing the relationship between dynamic flexibility and stiffness matrices. The method applies sinusoidal excitations to calculate steady-state response amplitudes and phase lags, deriving real and imaginary parts of the dynamic response. A progressive validation strategy is employed, systematically validating the method from simple lumped-mass systems to continuous-mass systems, then to complex 3D half-space soil models, ensuring its reliability across various scenarios. This approach

provides a robust and versatile tool for characterizing dynamic soil stiffness properties across various structural complexities. The method can significantly reduces dependence on specialized software running in "blackbox", such as ACS SASSI, thus enhance the accessibility and efficiency of seismic analysis for nuclear facilities. (**Chapter 4**)

(4). The proposed direct method was applied to the multiple supported structure with SSI taken into account. The FRS from the proposed method shows excellent agreement with "benchmark" time history results, particularly in horizontal directions, with errors consistently below 5%. Two seismic input scenarios, fully correlated and fully independent excitations at multiple supports, are explored, showcasing the method's versatility. Some discrepancies in vertical direction are attributed to limitations in vertical tRS, indicating areas for future refinement including the need to refine tRS. (**Chapter 5**)

(5). Parametric studies investigate the influence of site conditions and internal-external structure coupling element stiffness on FRS. Evaluated across various site classes per ASCE 7-10 standard, the method demonstrates robust performance for most site types. The study reveals optimal stiffness ranges affecting FRS peaks. It also identifies energy transfer patterns between structural components as the stiffness in the connecting elements changes, offering insights for nuclear facility design. (**Chapter 5**)

The methodologies developed in this thesis advance the state-of-the-art in seismic analysis and design of nuclear structures, particularly SMRs. By addressing the complex challenges posed by multi-support excitations and SSI, this research provides a foundation for safer and more economical designs of nuclear facilities.

Acknowledgements

I express my deepest gratitude to my supervisor, Professor Wei-Chau Xie, who has been the keystone in the arch of my doctoral journey. His profound knowledge, rigorous academic attitude, and unwavering support have stabilized the base of both my research and personal growth. I am equally grateful to Mrs. Cong-Rong Xie for her kindness and care. Their support has given me a sense of belonging in Canada, creating a stable foundation that made me feel as if I have found another family here.

My sincere appreciation extends to the thesis committee members: Professors Wenxing Zhou, Mahesh Pandey, Shunde Yin, and Jun Liu. Their insights have significantly enhanced the reliability of my work and broadened my academic perspectives.

Heartfelt thanks go to my colleagues, particularly Dr. Rui Wang, Dr. Wei Jiang, Dr. Yang Zhou, Dr. Bo Li, Dr. Lanlan Yang, for sharing their insights and codes, substantially impacting this research's load-bearing capacity. The intellectual stimulation from all my friends has created a positive moment in this journey.

I bear the ultimate load of gratitude to my family. To my parents, parents-in-law, and sister: thank you for being my deep foundation. To my wife, Rui Liu: your love and sacrifices have been the seismic-resistant bedrock of my pursuits. To Julie and Jayden: your smiles have been a constant source of excitation against daily fatigue.

To all who have contributed to the design, construction, and maintenance of my academic structure, I am eternally grateful. Your collective support has created a resilient framework that will stand the test of time.

Dedication

TO

My Family

Table of Contents

List of Figures . . . . . **xiii**

List of Tables . . . . . **xxv**

Nomenclature . . . . . **xxvi**

1 Introduction **1**

1.1 SMR: New Alternative to Nuclear Power 1

1.2 Advantages and Current Status of SMR 2

1.2.1 Advantages of SMR Technology 2

1.2.2 Development Status of SMR 4

1.3 Structural Features of SMR 5

1.4 Challenges in Developing SMR 7

1.5 Previous Research on Floor Response Spectra (FRS) 9

1.5.1 Seismic Response Analysis Methods 9

1.5.2 Generating Floor Response Spectra (FRS) 10

1.6 Soil-Structure Interactions (SSI) 15

1.7 Dynamic Soil Stiffness Matrix 21

1.8 Objectives of Proposed Research 23

1.9 Organization of This Thesis 23

2 Direct Method for Generating FRS **25**

2.1 Generating FRS of Structures under Multiple Excitations 25

2.1.1 Responses of Multi-Supported Structures 26

2.1.2 Floor Response Spectra 33

2.1.3 Direct Method for Generating FRS for Structures under Excitations at Multiple Supports 34

2.1.3.1 FRSMS-CQC Combination Rule 34
2.1.3.2 Determination of $\rho_{k0}^{m\hat{m},i}$, $\rho_{k\kappa}^{m\hat{m},i}$, and $\rho_{0}^{m\hat{m},i}$ 37
2.1.3.3 FRSMS-SRSS Combination Rule 43
2.2 Generating FRS for Structures under Multiple Excitations Considering SSI 43
2.2.1 Substructure Method 44
2.2.1.1 Dynamic Stiffness Matrix 44
2.2.1.2 Substructure Model for Flexible Foundation 44
2.2.1.3 Free-Field Soil Model 45
2.2.1.4 Structure with Multiple Support Excitations 47
2.2.2 Foundation Level Input Response Spectra (FLIRS) 48
2.2.3 Generating FRS of Multi-Supported Structures under Seismic Excitations Considering SSI 53
2.2.4 Procedure of Generating FRS Considering SSI 54
2.3 Summary 57

3 Validation of the General Formulation for Generating FRS Considering SSI . . . 58
3.1 Introduction 58
3.2 Classification of the Sites 60
3.3 Theoretical Validation 61
3.3.1 Coupled Soil-Structure Model 62
3.3.2 Fixed-Base Model 63
3.3.3 Model Comparison 64
3.4 Numerical Validation 64
3.4.1 Fundamental Parameters 65
3.4.2 Developing FLIRS 66
3.5 Developing FRS from General Formulation 69
3.6 Effect of SSI on the FRS of Structure 72
3.7 Summary 74

4 Dynamic Soil Stiffness Matrices **75**
4.1 Dynamic Stiffness Matrix and Dynamic Flexibility Matrix 75
4.2 Verification for Lumped-Mass System -- A 3-DOF Structure 78
4.2.1 Theoretical Derivation 79
4.2.2 Analytical Calculation 84
4.2.3 Numerical Calculation 86
4.2.4 Comparison of Analytical and Numerical Results 98
4.3 Verification for Consistent-Mass System -- A Simply Supported Beam 98
4.3.1 Problem Description 99
4.3.2 Theoretical Derivation 100
4.3.3 Comparison of Frequencies 103
4.3.4 Comparison of Deflection in The Simply Supported Beam 103
4.3.5 Dynamic Flexibility Matrix of The Simply Supported Beam 104
4.4 Verification for 3-Dimensional Half-Space Soil 106
4.4.1 Harmonic Excitation on An Elastic Soil 106
4.4.2 Generic Derivation in 3D Soil 112
4.4.3 Numerical Simulation for Elastodynamic 3D Half-Space Soil 117
4.4.4 Validation Against Classical Solutions ($\omega = 0$) 129
4.4.5 Validation Against Analytical Solutions ($\omega \neq 0$) 131
4.5 Dynamic Soil Stiffness for A Three-Layer Soil Foundation 131
4.6 Summary 135

5 Generating FRS of Structures under Multi-support Excitations Considering SSI 137
5.1 Model of Structure 137
5.2 Model of Soil 141
5.3 Foundation Input Response Spectra (FIRS) 143
5.4 Development of Floor Response Spectra (FRS) 156
5.4.1 Dynamic Influence Matrix 156

5.4.2 Case of Fully Correlated Excitation 156
5.4.3 Discussion for the FRS with fully correlated excitation 159
5.4.4 Case of Fully Independent Excitation 170
5.4.5 Discussion for the FRS with Fully Independent Excitation 171
5.5 FRS Differences Between Fully Correlated and Independent Cases 182
5.6 Influence of Site Conditions on FRS 185
5.6.1 Key Soil Parameters in This Study 186
5.6.2 FRS for Soil in Different Sites 187
5.6.3 Discussion 190
5.7 Influence of Coupling Element Stiffness on FRS 190
5.7.1 Stiffness Variation of Coupling Elements 190
5.7.2 FRS Results and Analysis 191
5.7.3 Discussion 195
5.8 Summary 196

6 Conclusions and Future Research 200
6.1 Direct Spectra-to-Spectra Method for Generating Floor Response Spectra 200
6.2 Generating FRS Considering Soil-Structure Interaction 201
6.3 Evaluation of Dynamic Soil Stiffness Matrices 203
6.4 Application to Multi-Support Excitations and SSI Effects 204
6.5 Future Research 205

Bibliography 206

Appendix A Classification of Soil Sites 212

Appendix B Results of FLIRS and FRS 214

Appendix C Response of Amplitudes and Phase Lags for Nodes on Soil Cake 221

Appendix D FRS for Different Site Classes 234

List of Figures

1.1	Model of a small modular reactor (SMR).	6
1.2	Distinct embedment depths of conventional NPP and SMR.	8
1.3	Rigid and flexible foundation for structures.	8
1.4	Two methods of generating floor response spectrum.	11
1.5	Effect of SSI on FRS.	18
1.6	Soil-structure interaction.	18
1.7	Finite element model for SSI complete method.	20
2.1	Multiple DOF primary structure under excitations at multiple supports.	27
2.2	Substructural model for flexible foundation.	46
2.3	SSI using FLIRS for flexible foundation.	47
2.4	Procedure for generating FRS for multiply supported structures considering SSI.	56
3.1	Simplified model for validation and demonstration of the general formulation	59
3.2	Ground response spectra of compatible time histories	68
3.3	Modification factor $\mathcal{R}$ in different soil cases	68
3.4	Comparison of FLIRS and the corresponding FRS from time history analyses (k_s=8 $\times$ 10^4 kN/m)	70
3.5	FLIRS for different soil cases	70
3.6	tRS in direct method for different soil cases	71
3.7	Comparison of FRS for Node 1 (k_s=8 $\times$ 10^4 kN/m)	73

3.8 Soil-structure interaction effect on FRS 73

4.1 Relationship between real part and imaginary part for steady state 79

4.2 3DOF Model for Theoretical Verification 80

4.3 Response of DOF 1 under cosinusoidal loading applied at DOF 1 88

4.4 Response of DOF 2 under cosinusoidal loading applied at DOF 1 88

4.5 Response of DOF 3 under cosinusoidal loading applied at DOF 1 89

4.6 Steady-state response of DOF 1 under loading at DOF 1 89

4.7 Steady-state response of DOF 2 under loading at DOF 1 90

4.8 Steady-state response of DOF 3 under loading at DOF 1 90

4.9 Response of DOF 1 under cosinusoidal loading applied at DOF 2 92

4.10 Response of DOF 2 under cosinusoidal loading applied at DOF 2 92

4.11 Response of DOF 3 under cosinusoidal loading applied at DOF 2 93

4.12 Steady-state response of DOF 1 under loading at DOF 2 93

4.13 Steady-state response of DOF 2 under loading at DOF 2 94

4.14 Steady-state response of DOF 3 under loading at DOF 2 94

4.15 Response of DOF 1 under cosinusoidal loading applied at DOF 3 95

4.16 Response of DOF 2 under cosinusoidal loading applied at DOF 3 95

4.17 Response of DOF 3 under cosinusoidal loading applied at DOF 3 96

4.18 Steady-state response of DOF 1 under loading at DOF 3 96

4.19 Steady-state response of DOF 2 under loading at DOF 3 97

4.20 Steady-state response of DOF 3 under loading at DOF 3 97

4.21 Harmonic Loading on A Simply Supported Beam 100

4.22 First Three Dominant Modes of A Simply Supported Beam 105

4.23 Frequency-dependent deflection of A_{22} and A_{42} 107

4.24 Frequency-dependent phase lags of φ_{22} and φ_{42} 107

4.25 Frequency-dependent deflection of A_{24} and A_{44} 108

4.26 Frequency-dependent phase lags of φ_{24} and φ_{44} 108

4.27 Real part of elements F_{24} and F_{44} for the dynamic flexibility matrix 109

4.28 Imaginary part of elements F_{24} and F_{44} for the dynamic flexibility matrix 109

4.29 Definition of dynamic soil stiffness 111

4.30 Infinitesimal cubes in harmonic motion 111

4.31 Model of soil in 3D half-space 119

4.32 Normal and horizontal loads on the ground of 3D half-space 119

4.33 X Amplitude in 1-1' under dynamic normal load 121

4.34 Y Amplitude in 1-1' under dynamic normal load 121

4.35 Z Amplitude in 1-1' under dynamic normal load 121

4.36 Phase lag in X direction in 1-1' under dynamic normal load 121

4.37 Phase lag in Y direction in 1-1' under dynamic normal load 121

4.38 Phase lag in Z direction in 1-1' under dynamic normal load 121

4.39 X Amplitude in 2-2' under dynamic normal load 122

4.40 Y Amplitude in 2-2' under dynamic normal load 122

4.41 Z Amplitude in 2-2' under dynamic normal load 122

4.42 Phase lag in X direction in 2-2' under dynamic normal load 122

4.43 Phase lag in Y direction in 2-2' under dynamic normal load 122

4.44 Phase lag in Z direction in 2-2' under dynamic normal load 122

4.45 Real part in X direction in 1-1' under dynamic normal load 123

4.46 Real part in Y direction in 1-1' under dynamic normal load 123

4.47 Real part in Y direction in 1-1' under dynamic normal load 123

4.48 Imaginary part in X direction in 1-1' under dynamic normal load 123

4.49 Imaginary part in Y direction in 1-1' under dynamic normal load 123

4.50 Imaginary part in Z direction in 1-1' under dynamic normal load 123

4.51 Real part in X direction in 2-2' under dynamic normal load 124

4.52 Real part in Y direction in 2-2' under dynamic normal load 124

4.53 Real part in Z direction in 2-2' under dynamic normal load 124

4.54 Imaginary part in X direction in 2-2' under dynamic normal load 124

4.55 Imaginary part in Y direction in 2-2' under dynamic normal load 124

4.56 Imaginary part in Z direction in 2-2' under dynamic normal load 124

4.57 X Amplitude in 1-1' under dynamic horizontal load 125

4.58 Y Amplitude in 1-1' under dynamic horizontal load 125

4.59 Z Amplitude in 1-1' under dynamic horizontal load 125

4.60 Phase lag in X direction in 1-1' under dynamic horizontal load 125

4.61 Phase lag in Y direction in 1-1' under dynamic horizontal load 125

4.62 Phase lag in Z direction in 1-1' under dynamic horizontal load 125

4.63 X Amplitude in 2-2' under dynamic horizontal load 126

4.64 Y Amplitude in 2-2' under dynamic horizontal load 126

4.65 Z Amplitude in 2-2' under dynamic horizontal load 126

4.66 Phase lag in X direction in 2-2' under dynamic horizontal load 126

4.67 Phase lag in Y direction in 2-2' under dynamic horizontal load 126

4.68 Phase lag in Z direction in 2-2' under dynamic horizontal load 126

4.69 Real part in X direction in 1-1' under dynamic horizontal load 127

4.70 Real part in Y direction in 1-1' under dynamic horizontal load 127

4.71 Real part in Z direction in 1-1' under dynamic horizontal load 127

4.72 Imaginary part in X direction in 1-1' under dynamic horizontal load 127

4.73 Imaginary part in Y direction in 1-1' under dynamic horizontal load 127

4.74 Imaginary part in Z direction in 1-1' under dynamic horizontal load 127

4.75 Real part in X direction in 2-2' under dynamic horizontal load 128

4.76 Real part in Y direction in 2-2' under dynamic horizontal load 128

4.77 Real part in Z direction in 2-2' under dynamic horizontal load 128

4.78 Imaginary part in X direction in 2-2' under dynamic horizontal load 128

4.79 Imaginary part in Y direction in 2-2' under dynamic horizontal load 128

4.80 Imaginary part in Z direction in 2-2' under dynamic horizontal load 128

4.81 Comparison of vertical displacement in 1-1' under dynamic normal load with $\omega = 0$ 130

4.82 Comparison of horizontal displacement in 1-1' under dynamic normal load with $\omega = 0$ 130

4.83 Comparison of vertical displacement in 1-1' under dynamic horizontal load with $\omega = 0$ 132

4.84 Comparison of horizontal displacement in 1-1' under dynamic horizontal load with $\omega = 0$ 132

4.85 Dynamic soil stiffness of the half-space soil 133

4.86 The three-layered soils and their properties 133

4.87 Comparison of the dynamic soil stiffness matrices by different approach 134

5.1 Sketch of structure and soil model for generating FRS 138

5.2 Numerical model for generating dynamic soil stiffness matrix 142

5.3 Real part in X direction under harmonic load at Node 1 in X direction 144

5.4 Real part in Y direction under harmonic load at Node 1 in X direction 144

5.5 Real part in Z direction under harmonic load at Node 1 in X direction 144

5.6 Imaginary part in X direction under harmonic load at Node 1 in X direction 145

5.7 Imaginary part in Y direction under harmonic load at Node 1 in X direction 145

5.8 Imaginary part in Z direction under harmonic load at Node 1 in X direction 145

5.9 Real part in X direction under harmonic load at Node 1 in Y direction 146

5.10 Real part in Y direction under harmonic load at Node 1 in Y direction 146

5.11 Real part in Z direction under harmonic load at Node 1 in Y direction 146

5.12 Imaginary part in X direction under harmonic load at Node 1 in Y direction 147

5.13 Imaginary part in Y direction under harmonic load at Node 1 in Y direction 147

5.14 Imaginary part in Z direction under harmonic load at Node 1 in Y direction 147

5.15 Real part in X direction under harmonic load at Node 1 in Z direction 148

5.16 Real part in Y direction under harmonic load at Node 1 in Z direction 148

5.17 Real part in Z direction under harmonic load at Node 1 in Z direction 148

5.18 Imaginary part in X direction under harmonic load at Node 1 in Z direction 149

5.19 Imaginary part in Y direction under harmonic load at Node 1 in Z direction 149

5.20 Imaginary part in Z direction under harmonic load at Node 1 in Z direction 149

5.21 Real part in X direction under harmonic load at Node 4 in X direction 150

5.22 Real part in Y direction under harmonic load at Node 4 in X direction 150

5.23 Real part in Z direction under harmonic load at Node 4 in X direction 150

5.24 Imaginary part in X direction under harmonic load at Node 4 in X direction 151

5.25 Imaginary part in Y direction under harmonic load at Node 4 in X direction 151

5.26 Imaginary part in Z direction under harmonic load at Node 4 in X direction 151

5.27 Real part in X direction under harmonic load at Node 4 in Y direction 152

5.28 Real part in Y direction under harmonic load at Node 4 in Y direction 152

5.29 Real part in Z direction under harmonic load at Node 4 in Y direction 152

5.30 Imaginary part in X direction under harmonic load at Node 4 in Y direction 153

5.31 Imaginary part in Y direction under harmonic load at Node 4 in Y direction 153

5.32 Imaginary part in Z direction under harmonic load at Node 4 in Y direction 153

5.33 Real part in X direction under harmonic load at Node 4 in Z direction 154

5.34 Real part in Y direction under harmonic load at Node 4 in Z direction 154

5.35 Real part in Z direction under harmonic load at Node 4 in Z direction 154

5.36 Imaginary part in X direction under harmonic load at Node 4 in Z direction 155

5.37 Imaginary part in Y direction under harmonic load at Node 4 in Z direction 155

5.38 Imaginary part in Z direction under harmonic load at Node 4 in Z direction 155

5.39 Seismic excitation cases of fully correlated and independent 157

5.40 Modulus of the dynamic influence matrix for superstructure nodes. 157

5.41 Modulus of FLIRS transfer matrix. 160

5.42 FLIRS modification factor for fully correlated case. 160

5.43 FLIRS by direct method in the fully correlated excitation case. 161

5.44 FRS in H1 direction at Node 5 in the fully correlated excitation case. 161

5.45 FRS in H2 direction at Node 5 in the fully correlated excitation case. 162

5.46 FRS in V direction at Node 5 in the fully correlated excitation case. 162

5.47 FRS in H1 direction at Node 6 in the fully correlated excitation case. 163

5.48 FRS in H2 direction at Node 6 in the fully correlated excitation case. 163

5.49 FRS in V direction at Node 6 in the fully correlated excitation case. 164

5.50 FRS in H1 direction at Node 7 in the fully correlated excitation case. 164

5.51 FRS in H2 direction at Node 7 in the fully correlated excitation case. 165

5.52 FRS in V direction at Node 7 in the fully correlated excitation case. 165

5.53 FRS in H1 direction at Node 2 in the fully correlated excitation case. 166

5.54 FRS in H2 direction at Node 2 in the fully correlated excitation case. 166

5.55 FRS in V direction at Node 2 in the fully correlated excitation case. 167

5.56 FRS in H1 direction at Node 3 in the fully correlated excitation case. 167

5.57 FRS in H2 direction at Node 3 in the fully correlated excitation case. 168

5.58 FRS in V direction at Node 3 in the fully correlated excitation case. 168

5.59 FLIRS modification factor for fully independent case. 172

5.60 FLIRS by direct method in the fully independent excitation case. 172

5.61 FRS in H1 direction at Node 5 in the fully independent excitation case. 173

5.62 FRS in H2 direction at Node 5 in the fully independent excitation case. 173

5.63 FRS in V direction at Node 5 in the fully independent excitation case. 174

5.64 FRS in H1 direction at Node 6 in the fully independent excitation case. 174

5.65 FRS in H2 direction at Node 6 in the fully independent excitation case. 175

5.66 FRS in V direction at Node 6 in the fully independent excitation case. 175

5.67 FRS in H1 direction at Node 7 in the fully independent excitation case. 176

5.68 FRS in H2 direction at Node 7 in the fully independent excitation case. 176

5.69 FRS in V direction at Node 7 in the fully independent excitation case. 177

5.70 FRS in H1 direction at Node 2 in the fully independent excitation case. 177

5.71 FRS in H2 direction at Node 2 in the fully independent excitation case. 178

5.72 FRS in V direction at Node 2 in the fully independent excitation case. 178

5.73 FRS in H1 direction at Node 3 in the fully independent excitation case. 179

5.74 FRS in H2 direction at Node 3 in the fully independent excitation case. 179

5.75 FRS in the V direction at Node 3 in the fully independent excitation case. 180

5.76 FRS-DM at Node 2 in fully correlated and independent excitation cases. 183

5.77 FRS-DM at Node 3 in fully correlated and independent excitation cases. 183

5.78 FRS-DM at Node 5 in fully correlated and independent excitation cases. 184

5.79 FRS-DM at Node 6 in fully correlated and independent excitation cases. 184

5.80 FRS-DM at Node 7 in fully correlated and independent excitation cases. 185

5.81 FRS in H1 direction at Node 7 for soil case A (correlated). 188

5.82 FRS in H1 direction at Node 7 for soil case B (correlated). 188

5.83 FRS in H1 direction at Node 7 for soil case C (correlated). 189

5.84 FRS in H1 direction at Node 7 for soil case D (correlated). 189

5.85 FRS for internal node in H1 direction for fully correlated case (Node 2). 193

5.86 FRS for internal node in H1 direction for fully correlated case (Node 3). 193

5.87 FRS for containment node in H1 direction for fully correlated case (Node 5). 194

5.88 FRS for containment node in H1 direction for fully correlated case (Node 6). 194

5.89 FRS for containment node in H1 direction for fully correlated case (Node 7). 195

5.90 FRS for internal node 2 in H1 direction for fully independent case. 197

5.91 FRS for internal node 3 in H1 direction for fully independent case. 197

5.92 FRS for containment node 5 in H1 direction for fully independent case. 198

5.93 FRS for containment node 6 in H1 direction for fully independent case. 198

5.94 FRS for containment node 7 in H1 direction for fully correlated case. 199

B.1 Comparison of FLIRS and the corresponding FRS from time history analyses (site D, k_s=1 $\times$ 10^5 kN/m) 214

B.2 Comparison of FLIRS and the corresponding FRS from time history analyses (site C) 215

B.3 Comparison of FLIRS and the corresponding FRS from time history analyses (site B) 216

B.4 Comparison of FRS for Node 1 (site D) 216

B.5 Comparison of FRS for Node 1 (site C) 217

B.6 Comparison of FRS for Node 1 (site B) 218

B.7 Comparison of FRS for Node 2 (medium soil of site D) 218

B.8 Comparison of FRS for Node 2 (harder soil of site D, stiff soil of site C) 219

B.9 Comparison of FRS for Node 2 (soft rock of site C, hard rock of site B) 220

C.1 Amplitude in X direction under harmonic load at Node 1 in X direction 221

C.2 Amplitude in Y direction under harmonic load at Node 1 in X direction 221

C.3 Amplitude in Z direction under harmonic load at Node 1 in X direction 222

C.4 Phase Angle in X direction under harmonic load at Node 1 in X direction 222

C.5 Phase Angle in Y direction under harmonic load at Node 1 in X direction 222

C.6 Phase Angle in Z direction under harmonic load at Node 1 in X direction 223

C.7 Amplitude in X direction under harmonic load at Node 1 in Y direction 223

C.8 Amplitude in Y direction under harmonic load at Node 1 in Y direction 223

C.9 Amplitude in Z direction under harmonic load at Node 1 in Y direction 224

C.10 Phase Angle in X direction under harmonic load at Node 1 in Y direction 224

C.11 Phase Angle in Y direction under harmonic load at Node 1 in Y direction 224

C.12 Phase Angle in Z direction under harmonic load at Node 1 in Y direction 225

C.13 Amplitude in X direction under harmonic load at Node 1 in Z direction 225

C.14 Amplitude in Y direction under harmonic load at Node 1 in Z direction 225

C.15 Amplitude in Z direction under harmonic load at Node 1 in Z direction 226

C.16 Phase Angle in X direction under harmonic load at Node 1 in Z direction 226

C.17 Phase Angle in Y direction under harmonic load at Node 1 in Z direction 226

C.18 Phase Angle in Z direction under harmonic load at Node 1 in Z direction 227

C.19 Amplitude in X direction under harmonic load at Node 4 in X direction 227

C.20 Amplitude in Y direction under harmonic load at Node 4 in X direction 227

C.21 Amplitude in Z direction under harmonic load at Node 4 in X direction 228

C.22 Phase Angle in X direction under harmonic load at Node 4 in X direction 228

C.23 Phase Angle in Y direction under harmonic load at Node 4 in X direction 228

C.24 Phase Angle in Z direction under harmonic load at Node 4 in X direction 229

C.25 Amplitude in X direction under harmonic load at Node 4 in Y direction 229

C.26 Amplitude in Y direction under harmonic load at Node 4 in Y direction 229

C.27 Amplitude in Z direction under harmonic load at Node 4 in Y direction 230

C.28 Phase Angle in X direction under harmonic load at Node 4 in Y direction 230

C.29 Phase Angle in Y direction under harmonic load at Node 4 in Y direction 230

C.30 Phase Angle in Z direction under harmonic load at Node 4 in Y direction 231

C.31 Amplitude in X direction under harmonic load at Node 4 in Z direction 231

C.32 Amplitude in Y direction under harmonic load at Node 4 in Z direction 231

C.33 Amplitude in Z direction under harmonic load at Node 4 in Z direction 232

C.34 Phase Angle in X direction under harmonic load at Node 4 in Z direction 232

C.35 Phase Angle in Y direction under harmonic load at Node 4 in Z direction 232

C.36 Phase Angle in Z direction under harmonic load at Node 4 in Z direction 233

D.1 FRS in H1 direction at Node 2 for soil case A (correlated). 234

D.2 FRS in H1 direction at Node 3 for soil case A (correlated). 235

D.3 FRS in H1 direction at Node 5 for soil case A (correlated). 235

D.4 FRS in H1 direction at Node 6 for soil case A (correlated). 236

D.5 FRS in H1 direction at Node 2 for soil case B (correlated). 236

D.6 FRS in H1 direction at Node 3 for soil case B (correlated). 237

D.7 FRS in H1 direction at Node 5 for soil case B (correlated). 237

D.8 FRS in H1 direction at Node 6 for soil case B (correlated). 238

D.9 FRS in H1 direction at Node 2 for soil case C (correlated). 238

D.10 FRS in H1 direction at Node 3 for soil case C (correlated). 239

D.11 FRS in H1 direction at Node 5 for soil case C (correlated). 239

D.12 FRS in H1 direction at Node 6 for soil case C (correlated). 240

D.13 FRS in H1 direction at Node 2 for soil case D (correlated). 240

D.14 FRS in H1 direction at Node 3 for soil case D (correlated). 241

D.15 FRS in H1 direction at Node 5 for soil case D (correlated). 241

D.16 FRS in H1 direction at Node 6 for soil case D (correlated). 242

List of Tables

3.1	Ranges of soil spring stiffness for different sites	61
3.2	Soil spring stiffnesses in the numerical calculation	65
3.3	Modal information of fixed-base model	66
4.1	Amplitude and phase lag for different DOFs under corresponding dynamic loadings	91
4.2	Real and imaginary parts of dynamic flexibility matrix elements for the 3-DOF structure	99
4.3	Real and imaginary parts of dynamic flexibility matrix elements for the 3-DOF structure	99
5.1	Nodal information of reactor building model	139
5.2	Beam Element Properties of reactor building model	139
5.3	Natural frequencies of reactor building model	140
5.4	Properties of soils for each layer	141
5.5	FRS differences between time history and direct method for the fully correlated case	169
5.6	FRS differences between time history and direct method for the fully independent case	181
5.7	Selected soil parameters for different sites	187
5.8	Stiffness variation cases for coupling elements	191
A.1	Evaluation of soil stiffnesses for different site classes	213
A.2	Estimated lower and upper bound of soil stiffnesses for different site classes	213

Nomenclature

AR	Amplification Ratio
ASCE	American Society of Civil Engineersε
CENA	Central and Eastern North America
CQC	Complete Quadratic Combination
CSA	Canadian Standard Association
DOF	Degree(s)-of-Freedom
FEM	Finite Element Method
FIRS	Foundation Input Response Spectrum
FITH	Foundation Input Time History
FLIRS	Foundation Level Input Response Spectrum
FLITH	Foundation Level Input Time History
FRS	Floor Response Spectrum
FRS-CQC	Complete Quadratic Combination for FRS
FRSMS-CQC	Complete Quadratic Combination for FRS of Multiple Supports
FRSMS-SRSS	Square Root of Sum of Squares for FRS of Multiple Supports
F-tRS	t-Response Spectrum of Floor Response Spectrum
GRS	Ground Response Spectrum
GWe	Gigawatt of electric
LB	Lower Bound
MDOF	Multiple Degrees-of-Freedom
MWe	Megawatt of electric
NEP	Non-Exceedance Probability

NPP	Nuclear Power Plant(s)
PEER	Pacific Earthquake Engineering Research
PGA	Peak Ground Acceleration
PSD	Power Spectral Density
PSDF	Power Spectral Density Function
SDOF	Single Degree-of-Freedom
SMR	Small Modular Reactor(s)
SRSS	Square-Root-of-Sum-of-Squares
SSCs	Structures, Systems and Components
SSI	Soil-Structure Interaction
tRS	*t*-Response Spectrum
ttRS	*t*-Response Spectrum for Tertiary Response Spectrum
UB	Upper Bound
UHS	Uniform Hazard Spectrum
USNRC	U.S.Nuclear Regulatory Commission

C H A P T E R 1

Introduction

1.1 SMR: New Alternative to Nuclear Power

Nuclear power is one of the largest sources of clean energy. As of 2019, it occupies about 30% of global low-carbon power. World Nuclear Association (2021) predicted that nuclear energy would double within 20 years despite some phase-outs planned in some countries, and is anticipated to triple by the mid-21st century, and increase more than tenfold by the end of this century (Pedraza, 2017) in the carbon-constrained world.

Although the presence of carbon-free energy brought by nuclear power plants continues to change the global energy supply and consumption patterns, potential crises harbour the superficial scenery of this miracle. The highly sophisticated and complex way of generating electricity has attracted broad attention, not only in the substantial initial capital investment, but in the hidden threat to public safety if not dedicated to it with great care. The Fukushima Daiichi Disaster in 2011 Japan has notably spotlighted a worldwide interest in reducing operation and maintenance expenses of conventional nuclear power plants (NPPs) while improving their safety performance. This circumstance led to an extensive focus and the flourishing of Small Modular Reactors (SMR) in recent years.

SMR are a novel class of nuclear power plants characterized by their reduced physical size, modular design, and advanced reactor technology. An SMR is defined as, by the International Atomic Energy Agency (IAEA), reactors producing less than 300 MWe of

electrical power. The consensus among experts, engineers, and technicians is that the SMR are a new generation of nuclear reactors that are considerably smaller in dimensions and energy output than conventional nuclear power reactors. The SMR are

- **S**mall. SMR are significantly smaller in comparison to traditional large-scale nuclear reactors. SMR offer a more compact and cost-effective design and a reduction in the fuel required for power generation.
- **M**odular. SMR are factory customizable, transportable as integration, and scalable in manufacturing. The modular design allows for the easy addition or replacement of modules, thereby increasing the flexibility and scalability of the power plant.
- **R**eactors. The technology utilizes nuclear fission, a process by which the nucleus of an atom is split into smaller nuclei, to release energy in the form of heat. This heat is then harnessed to generate steam, driving turbines to produce electricity. SMR can adopt various fuel types, such as low-enriched uranium or thorium, and can also feature different types of reactors, such as pressurized water or gas-cooled reactors.

Most importantly, SMR are considered to be enhanced in safety features compared with traditional NPPs. It is widely regarded as a promising new alternative to leverage nuclear power, which can provide more resilient support for remote regions and undeveloped areas.

1.2 Advantages and Current Status of SMR

1.2.1 Advantages of SMR Technology

The development and implementation of SMR represent a significant advancement in nuclear power generation. It has several advantages over traditional large-scale NPPs, including affordability, flexibility, and reliability, making SMR an attractive option for a wide range of applications. As such, proposals for implementing SMR technology have remarkably increased in several countries. The advantages of SMR over conventional NPPs have been widely acknowledged and have garnered significant attention in both academic and industry circles.

- **Affordability**

SMR offer an affordable alternative to traditional large-scale NPPs due to their reduced size and more compact design, which results in lower fuel requirements and reduced construction and operation costs. For instance, the construction, operation, and maintenance of a conventional NPP require large-scale complex facilities and infrastructures, as well as over 6000 skilled workers, which can result in a cost of up to US $9 billion for a 1000 MWe nuclear power reactor and a construction period of 10 to 15 years in some cases. An SMR, on the other hand, is significantly reduced in size, requiring lower up-front capital investment and shorter construction time. Furthermore, the techniques in modular construction, such as factory-based manufacturing and assembly, can further reduce costs and increase standardization and quality control, making SMR a more cost-effective option for providing energy, especially to remote or underdeveloped areas.

- **Flexibility**

  The modular design of SMR affords a great degree of flexibility in construction and operation. Modularization allows for the factory fabrication of structures, systems, and components (SSCs), which can be transported to designated sites and assembled on-site. This technology has several benefits, including improved standardization, quality control, and increased flexibility and scalability, making SMR an attractive option for powering remote and rural communities and various applications. The modular design also allows for the easy addition or replacement of modules, increasing the scalability and adaptability of reactors. Furthermore, individual modules can be replaced or upgraded without shutting down the entire power plant, manifesting the flexibility of SMR from a maintenance perspective.

- **Reliability**

  SMR also offer increased reliability. Advanced reactor technology and passive safety systems, such as natural circulation and gravity-driven cooling, can help reduce the likelihood of accidents and improve the safety of nuclear plants. The safety radius of an existing large-scale nuclear reactor is approximately 10 miles, whereas an SMR is estimated at about 1/4 miles. SMR can be installed underground, preventing the

release of radioactive materials in case of an accident, thus significantly improving containment and security. Therefore, it is an energy source with minimal risk to the public, making SMR a more reliable option than traditional NPPs.

The affordability, flexibility, and reliability of SMR allow for a notable reduction in the construction period and capital investment, highlighting the potential for versatile and prosperous applications in the future.

1.2.2 Development Status of SMR

Research and development of SMR have been ongoing for several years, with various proposed designs and concepts. However, most designing of SMR have yet to be commercialized, and only a few projects have progressed beyond the demonstration phase. Despite the lack of standardization and a clear regulatory framework, some developments in SMR recently occurred. There are more than 70 SMR designs under development for different applications all around the world.

In Canada, the government has taken the SMR as a potential solution to the challenges of traditional large-scale nuclear reactors. The Canadian Nuclear Safety Commission (CNSC), the regulatory body responsible for the oversight of nuclear energy in Canada, announced the development of a regulatory framework for the deployment of SMR in Canada in 2016, which includes the development of a licensing process for SMR, as well as guidelines for the design, construction, and operation of these reactors. The Canadian Nuclear Laboratories (CNL) has been working on the development of SMR technology, aiming to commercialize SMR in Canada by the early 2030s. Ultra Safe Nuclear Corporation (USNC) has developed a small modular reactor design that utilizes thorium fuel, which can potentially reduce the risk of proliferation and improve the safety of reactors. Several provinces, for example, Saskatchewan, Ontario, New Brunswick and Alberta, are actively pursuing SMR. To advance New Brunswick's position as a leader in SMR technology, a $10 million investment was made to establish an SMR research cluster, with an additional $10 million in funding matched by industry partners. Furthermore, Ontario Power Generation (OPG) recently announced its plans to construct the first SMR in North America at the Darlington New Nuclear Project site (Darlington B project) in December 2022. The project is anticipated to

receive a construction license in 2024, with completion expected in 2028 and commercial operation set to commence in 2029.

The United States government has initiated a program to promote the advancement of SMR technology, with a total of $755 million in funding allocated since 2012, including a significant portion of $336 million granted to a single developer. The distribution of funds has occurred gradually over time, with additional funding expected in the future. The United States Department of Energy (DoE) has increased its budget for nuclear energy by 20% indicating the current Administration's support for this form of energy. NuScale Power has already received approval from the Nuclear Regulatory Commission (NRC) for its SMR design and is now working on commercial deployment. Furthermore, TerraPower and Westinghouse Electric Company are progressing in developing their own SMR designs.

The government of the United Kingdom has announced that the development of SMR will be invested in as part of its plan to reduce carbon emissions. A consortium led by Rolls-Royce has unveiled a small modular reactor design in the UK.

In Russia, Rosatom, the state-owned nuclear energy corporation, has developed several designs of SMR and has also announced plans to build several SMR plants in the Arctic region. Similarly, China has also expressed interest in developing SMR technology, with the Chinese National Nuclear Corporation (CNNC) working on several designs of SMR.

1.3 Structural Features of SMR

The design philosophy in structures of SMR differs significantly from that of conventional nuclear reactors due to their functionality and characteristics. The differences are reflected in various aspects, such as the size of buildings, type of foundations, burial depth of structures, and so on. Understanding the structural characteristics of SMR is essential to properly design and construct to ensure all safety and functional requirements can be satisfied while still being cost-effective and efficient. In this section, the structural differences of buildings between SMR and conventional nuclear reactors will be discussed.

Figure 1.1 displays a typical structural model of an SMR, mainly comprised of reinforced concrete walls and slabs, containment pools, and reactor modules. The reactor modules are

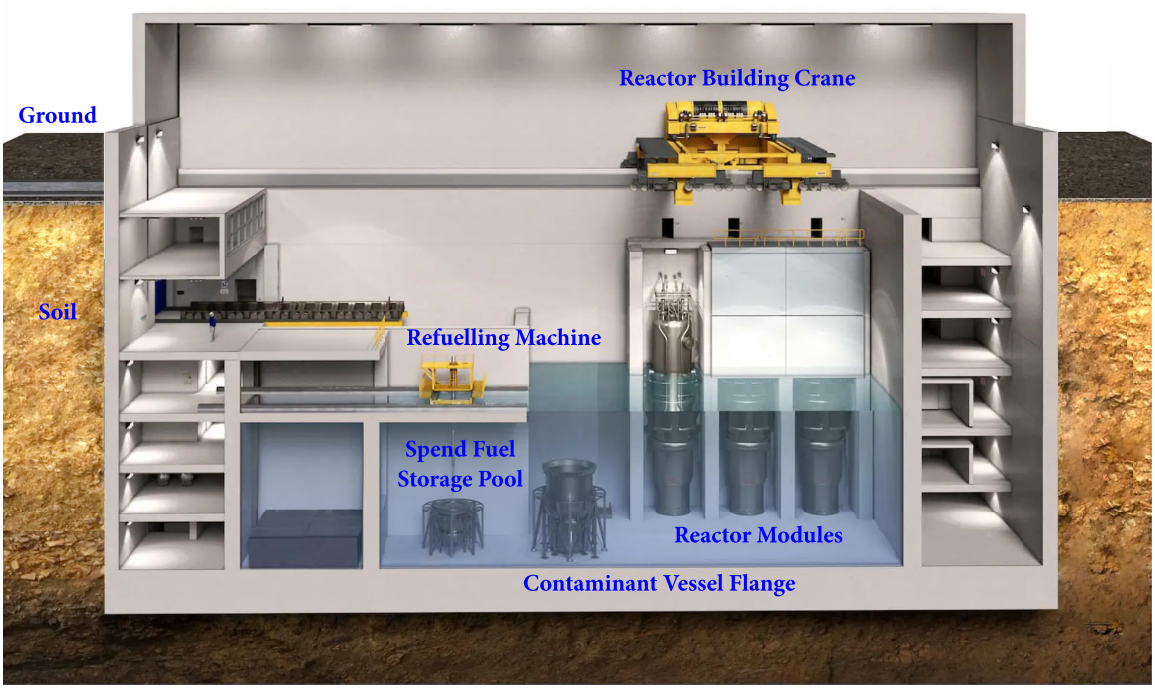


Figure 1.1 Model of a small modular reactor (SMR).

self-contained and placed in a common large water pool, known as the reactor pool, while a smaller water pool called spent fuel storage pool is incorporated to facilitate the cooling of used fuel. The building of SMR has a significantly smaller total height than traditional nuclear reactors. Specifically, the total height of an SMR is around 30 meters (Guner *et al.*, 2022), which is approximately half the containment height of CANDU® 6.

It is also observed that the major part of the SMR structure is deeply or even fully embedded underground, while the structures in traditional reactors, such as CANDU® 6, are built above the ground. This embedment feature can enhance the containment and security of the reactor by providing additional layers of protection against natural disasters and man-made threats, such as terrorist attacks. In contrast, the superstructure of traditional reactors, such as CANDU® 6, is installed above ground, making it more vulnerable to external hazards and attacks.

In addition, the containment structure in SMR is designed to be sealed. It can prevent the release of radioactive materials in case of an accident, minimizing the risk of exposure to the public. On the contrary, the contaminant in CANDU® 6 is not sealed, indicating that radioactive materials can be released into the environment if an accident occurs.

The distinction in structures between SMR and traditional nuclear reactors, saying CANDU® 6, demonstrates the superiority of SMR structures in improving safety performance. By using a modular design, factory production, and passive safety systems in SMR, along with a smaller total height, the standardization, efficiency, and protection against accidents of SMR are uplifted. Therefore, structural safety during operation and maintenance are increased, enhancing public safety.

1.4 Challenges in Developing SMR

The safety of nuclear facilities during operation and maintenance is of paramount importance. In light of several devastating earthquakes in recent decades, seismic risk analysis of critical engineering structures has become a crucial and widely studied topic in earthquake engineering. This topic has received global attention, especially after the Fukushima disaster, the global nuclear energy industry has launched an extensive re-evaluation of seismic hazards and risks to NPP systems. Regulators are closely examining existing methods for estimating the seismic risk of SSCs in NPPs. As per existing design guidelines, the SSCs must be designed to withstand the effects of the Safe Shutdown Earthquake ground motion.

The same issue exists in SMR. One of the critical safety goals of SMR is to have a multi-layered defence that is highly robust against all significant threats and events. As depicted in Figure 1.2, SMR are designed partially or fully embedded below the ground. The design of these deeply buried structures has not yet been established in Canadian and American codes and standards for nuclear facilities (ASCE, 1998; ASCE, 2005; CSA, 2020), posting new technical challenges concerning the seismic analysis and design of structures in SMR. It is crucial to develop an accurate and reliable method to address those unique challenges.

This circumstance posts new technical challenges with respect to the seismic analysis and design of structures in SMR. To address these unique challenges, it is crucial to develop accurate and reliable analysis methods for SMR structures.

- **Flexible Foundation**

  Traditional NPPs are usually constructed on solid bedrock foundations in ideal geological conditions, such as the Darlington Nuclear Generating Station located on the

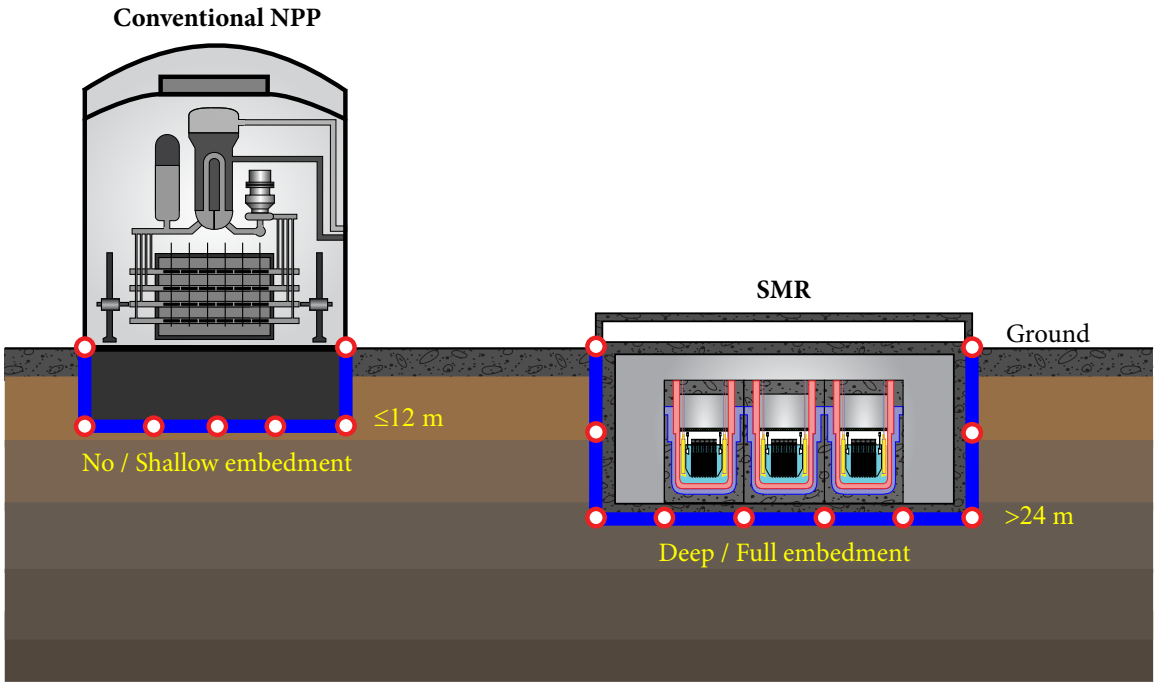


Figure 1.2 Distinct embedment depths of conventional NPP and SMR.

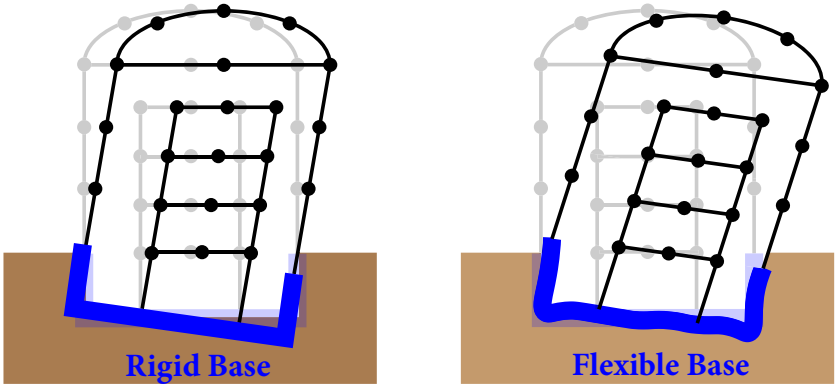


Figure 1.3 Rigid and flexible foundation for structures.

Canadian Shield. In contrast, SMR are designed to be flexible in site selection and can be built on relatively soft ground. This condition presents a new challenge for analyzing SMR structures since the foundation can no longer be treated as rigid. It is illustrated in Figure 1.3 that difference in foundation rigidity has a significant impact on the deformation and response of the superstructure. Therefore, it is essential to consider flexible foundation conditions in the analysis.

- **Seismic Excitations at Multiple Supports**

  Considering seismic excitations at multiple supports is crucial for structures in SMR due to the deeply or fully embedded characteristics. Both sidewalls and the base support the structure for the deeply buried foundation. When subjected to the earthquake, the foundation and the structure act as a structure-foundation system, undergoing seismic excitations at multiple points. This consideration is particularly critical when the surrounding soil is relatively soft, which is a common occurrence in SMR due to their flexibility and versatility in site selection. Therefore, the seismic response of the structure cannot be evaluated based on the response at a single point.

- **Soil-Structure Interaction (SSI)**

  When a structure is founded on soil and subjected to an earthquake ground motion, the responses of the structure and soil are interdependent, which is known as the soil-structure interaction (SSI) effect. This is a critical concern in a large heavy structure which is founded on firm soil; for a light structure on stiff soil, the SSI effect is minimal. Thus, the SSI effects can be significant for a heavy structure of nuclear facilities on relatively soft soil.

Consequently, implementing a reliable and efficient approach that accounts for soil-structure interaction (SSI) effects with seismic excitations at multiple supports is essential for the seismic analysis and design of deeply or fully embedded structures in SMR.

1.5 Previous Research on Floor Response Spectra (FRS)

1.5.1 Seismic Response Analysis Methods

Practically, seismic response of secondary systems can be determined by two approaches: floor response spectrum approach and combined primary-secondary system approach.

Floor Response Spectrum Method

The floor response spectrum (FRS) approach is a decoupled analysis method involving analyzing the primary and secondary systems individually, which allows for a more efficient and accurate analysis of the structure.

The first step in the FRS approach is to perform a dynamic analysis of the primary structure without considering the effect of the secondary system. This can be done using a set of time histories that are compatible with prescribed ground motion spectra. The response of the primary structure at the locations where the secondary systems are attached is obtained. This information is used as the input for a single-degree-of-freedom (SDOF) oscillator to generate FRS. The FRS can be utilized to estimate the maximum response of the secondary system, such as a floor or a wall, quickly and accurately. As it allows engineers to identify potential areas of concern, this method can be extended to analyze SMR structures, which is essential for the safety and performance of SMR.

Combined Primary-Secondary System Method

The combined primary-secondary system approach is a method in which the primary and secondary systems are modelled as an integral part. Both time history analysis and response spectrum analysis can be applied for determining the responses of the secondary systems. There is no doubt that this approach can give theoretically accurate responses of secondary systems, however, some challenges and difficulties exist.

Large differences between the characteristics of primary systems and that of secondary systems, such as mass and stiffness, may cause serious numerical problems in a modal analysis or time history analysis, thus give inaccurate solutions. Also, there are usually excessive degrees-of-freedom in a combined primary-secondary system, dynamic analysis of the entire system is not efficient since only seismic responses of secondary systems are of interest. Moreover, although a combined primary-secondary system analysis can give seismic responses for a secondary system at a certain location. There may be a large number of secondary systems and the locations of secondary system may be varied, the calculation of each case is not feasible or desirable from a practical point of view. Consequently, the combined primary-secondary system approach is not widely used in practice.

1.5.2 Generating Floor Response Spectra (FRS)

ASCE (1998) proposes that floor response spectra shall be generated by time history analyses or a direct spectra-to-spectra method, as shown in Figure 1.4.

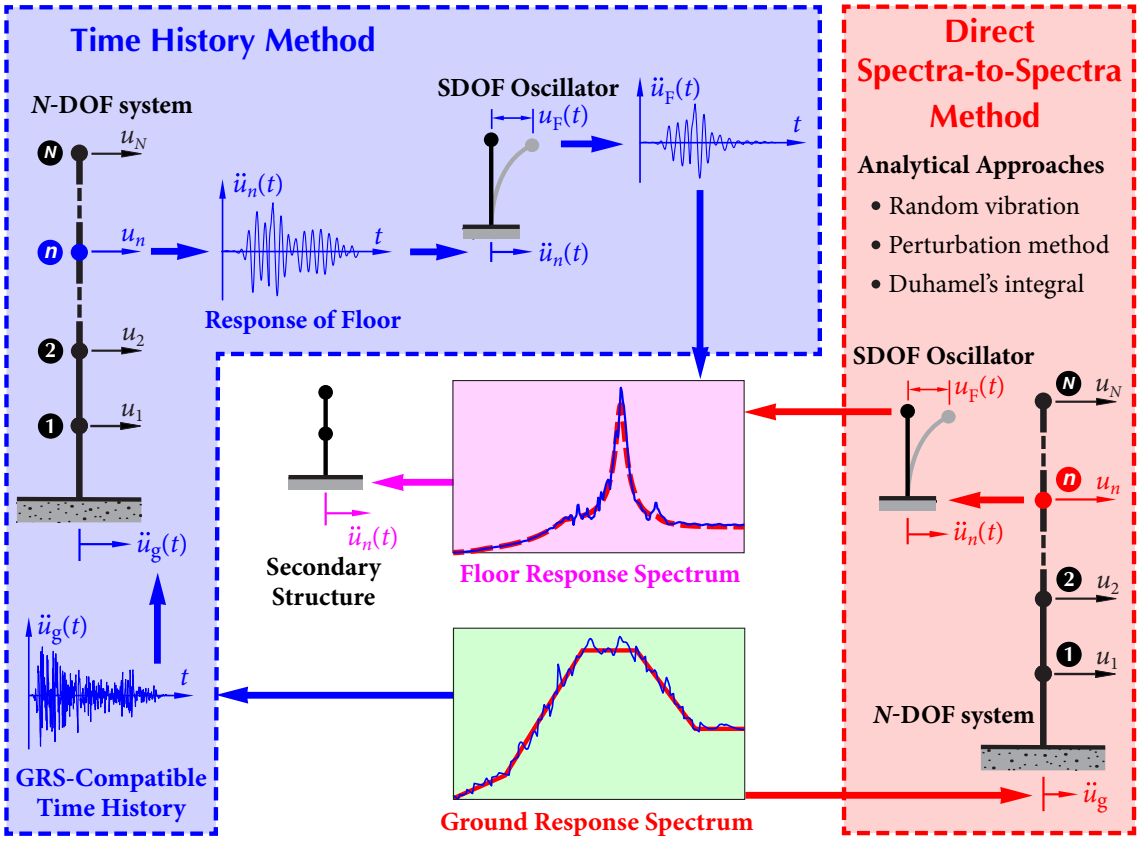


Figure 1.4 Two methods of generating floor response spectrum.

Time History Method

For time history method, a dynamic analysis for primary structure is conduct by using modal superposition or direct time integration method. The time histories at the locations to which secondary systems are attached are obtained and sequently are used to generate floor response spectra. Conceptually, a time history analysis can give accurate responses for a given ground motion record. However, recorded ground motion time histories representative of the site of interest are generally not available, therefore, artificial time histories compatible with a target ground response spectrum are usually generated as intermediate input to the primary structure. However, it has been recognized that there are significant variabilities in FRS generated by the time history method (Chen and Soong, 1988; Singh, 1988; Villaverde, 1997), in the sense that two spectrum-compatible time histories may give

significantly different FRS. Hence, if only a single set of tri-directional earthquake time histories, or even a small number of sets of tri-directional earthquake time histories, is used in the time history analysis to calculate FRS, the FRS obtained is not reliable. Consequently, a large number of sets of tri-directional earthquake time histories may be required to obtain an reliable probabilistic description of FRS; but this procedure is not only cumbersome but also computationally expensive.

Direct Spectra-to-Spectra Method

Various direct spectra-to-spectra methods have been developed to avoid the deficiencies of time history methods. The "direct" means that ground response spectrum is used at input directly without generating any intermediate input such as spectrum-compatible time histories or spectrum-compatible power spectral density functions. In the direct methods, floor response spectra are analytically expressed in terms of ground motion spectra and some basic modal information of the primary structure, including modal frequencies and damping ratios, mode shapes, and modal participation factors, which can be obtained from a modal analysis.

Some research work on developing direct spectra-to-spectra method for generation of floor response spectra has been conducted during the past decades.

Traditional Direct Method

Biggs and Roesset (1970) first proposed a simple semi-empirical method to generate floor response spectra without performing time history analyses. Seismic response of secondary systems is considered as a combination of amplification of ground motion and amplification of structure motion. Amplification curves for the two types of amplification were developed empirically based on an analysis for a model subjected to four actual earthquake records. Maximum response of secondary system is calculated by combining the responses of all structural modes through the square root of the sum of the squares (SRSS) rule. Similar approaches were carried out later by Kapur and Shao (1970), Duff (1975).

Singh (1975) develop a method to generate floor response spectra based on random vibration theory which incorporates a probabilistic concept. This approach is further extended by Singh (1980) considering resonance cases when the frequency of secondary systems is

closed to one of the natural frequencies of the primary structure. In this method, the primary structure is assumed to be subject to a stochastic ground excitation characterized by power spectral density function (PSDF). The PSDF of structural responses, which are associated with the mean squared responses of secondary system, are obtained in terms of modal information of primary structure, complex frequency response functions, and PSDF of the prescribed ground motion. The mean square responses of secondary systems is then connected to its maximum response by multiplied with a peak factor. A similar method on the basis random vibration principles in conjunction with mode acceleration formulation was also presented by Singh and Sharma (1985).

Some direct approaches of generating FRS involving frequency domain analyses were developed. Scanlan (1974), Jeanpierre and Livolant (1977) present direct calculation methods of floor response spectra by taking the Fourier transform of ground motion. Peters *et al.* (1977) conducted a modal analysis for a structure with interaction-free, a single degree-of-freedom system attached, to produce approximate modal information of the structure-equipment system. An analytical expression of equipment response in non-resonance cases was derived and an approximation for secondary system response in a resonance case was recommended. The total responses of secondary system are determined through the SRSS modal combination rule.

In current practice, FRS is generally generated without considering the effect of SSI interaction. For the tuning cases, one of the terms becomes the first-order derivative of the relative velocity with respect to damping, which cannot be determined analytically in terms of the input GRS. Singh (1980), Kiureghian *et al.* (1983), Igusa and Kiureghian (1985) studied the response of a tuned primary-secondary system under a wide-band stochastic input which can be approximated as white noise in this case. Yasui *et al.* (1993), An *et al.* (2013) considered the phase differences between the primary and secondary systems in the time domain to obtain an approximate value of this tuning term.

Although there have been a number of direct spectra-to-spectra methods available for generating FRS since 1970s, they have not been widely used in nuclear industry. Some methods give conservative results in some frequency ranges but unconservative results in other frequency ranges due to the various approximations used. Furthermore, it is

unknown when and by how much the FRS obtained is conservative or unconservative. If the results are scaled so that the resulting FRS are conservative over the entire frequency range, FRS in some frequency ranges become excessively conservative. The results of FRS should be conservative but not too conservative; otherwise, the cost of seismic qualification of systems, structures, and components (SSC) of nuclear power plants will be significantly increased. Some methods are derived based on pronounced theories, the implementation of these methods are, however, not free of complication and difficulties. For instance, the direct method developed by Singh (1975, 1980) is recommended in standard ASCE (1998). Although FRS is defined analytically in terms of the modal information of the primary structure and ground response spectra, some coefficients are not given explicitly. These coefficients which lack for physical meaning to engineers have to be obtained by solving systems of equations. Moreover, numerical difficulties may be encountered in solving the equations, particularly, for large complex structure.

A Novel Direct Method

Recently, a new direct spectra-to-spectra method for generating FRS was proposed by Jiang *et al*. (2015). It can give accurate FRS conveniently for complex structures with closely-spaced modes. In this method, the seismic response of an SDOF oscillator supported by an SDOF primary structure is derived at first, and *t*-response spectrum (tRS) is then employed for the tuning case (Li *et al*., 2015). Based on Random Vibration Theory (RVT), a new modal combination method for generating FRS, i.e., FRS-CQC, is proposed to represent the correlation of responses between SSCs and the associated primary structure with closely-spaced modes, by which an SDOF oscillator supported by a multiple DOF (MDOF) primary structure is considered. As a result, FRS can be obtained from input GRS and the modal information of primary structures, which is calculated by the typical modal analysis.

Jiang, Zhou, and Xie (2022) incorporated the substructure technique and introduced a modified input response spectrum, referred to as Foundation Level Input Response Spectrum (FLIRS), to account for the effect of soil-structure interaction. In this approach, the foundation is considered to be rigid, which is a simplification of the real-world scenario. Additionally, the seismic excitations are input at only one point, known as excitations at single

support. Wang and Xie (2022a, 2022b) further developed this method to account for excitations at multiple supports. This method is crucial to ensure the safety and performance of deeply or fully embedded structures.

The analysis of FRS of structures has undergone an evolution in methodology, from initially considering seismic excitations at single support on the rigid foundation, to incorporating the effect of soil-structure interaction on the rigid foundation, and finally accounting for excitations at multiple supports. The direct method has improved in precision, aligning more closely with engineering practice and increasing the reliability of FRS analysis.

However, these methods still have limitations. For example, the foundations of deeply embedded structures in SMR cannot be considered rigid if founded on relatively soft soil. The method has to be further improved to account for flexible foundations, excitations at multiple supports, and soil-structure interactions. To address these limitations, further research and development are necessary to provide an even more accurate evaluation of FRS for these deeply or fully embedded structures in SMR. This will help ensure the safety and performance of the structures under seismic excitations.

1.6 Soil-Structure Interactions (SSI)

In seismic analysis, the input ground motion at the base level is commonly assumed to be the same as the free field ground motion, which is the motion of the site in the absence of the structure and of any excavation. This assumption has been justified for structures sitting on rigid rock or very stiff soil because the large stiffness of the surrounding medium can constrain the motion of foundation to be approximately the free-field motion (Zhou, 2019). However, it has been demonstrated that the soil-structure interaction (SSI) cannot be neglected when the supporting soil is relatively soft or the superstructure is massive due to (Wolf, 1985a; 1987):

- Seismic responses at the foundation of the structure are different from the free-field responses at the site due to the influence of superstructure.

- The interaction between structure and its surrounding soil leads to a further change of the seismic input at the base.

It is conventionally believed that taking SSI effect into account will reduce the overall seismic responses of structure because the fundamental period of the building is elongated whereas the spectral value of ground response spectrum at lower frequencies is relatively low. Furthermore, the effective damping of a combined soil-structure system, which depends on not only structural damping but also soil material damping and soil radiation damping, is significantly higher than that of the structure itself. This larger damping causes more energy dissipation and further reduction of the responses of primary structure. For example, Kennedy *et al*. (1981) found that the soil-structure interaction tends to cause lower shear forces and moments and to higher compressive axial forces in the concrete walls, which increases the stability of the structure under strong earthquakes.

Although numerous effort has been made in studying the influence of SSI effect on the seismic performance of primary structure, only a few research investigated the effect of SSI on the floor acceleration demands. Chaudhuri and Gupta (2003) proposed a mode acceleration approach based on substructure method for generating FRS considering the effect of SSI. A numerical study of a 15-story shear building was conducted and the results indicate that soil-structure interaction should not be ignored when generating FRS unless the soil is very stiff relative to the superstructure. The extent of SSI effect is found to be highly dependent on the soil properties and the natural frequency, damping coefficient and the location of the oscillator.

The seismic response and FRS of a 4-story steel frame supported by a relative stiff soil were investigated by Raychowdhury and Ray-Chaudhuri (2015). It was found that the consideration of SSI always reduces the response of secondary components around the fundamental period of the building. It was also concluded that the maximum value of FRS tend to decrease when SSI is taken into account; however, the second or the third peak of FRS including SSI effect might be higher than that of fixed-base structure.

Zhang and Jiang (2017) studied the effect of SSI on the structural response as well as equipment response by comparing the results from experiment and finite element analysis using ANSYS. In the experiment, the equipment was modelled as a SDOF oscillator mounted

on the top of the 4-story steel frame structure, which was placed on a shaking table to simulate earthquake events. The soil was modelled as a three-layer half-space medium using eight-node solid element in ANSYS. They concluded that the peak response of both main structure and secondary equipment are reduced due to the presence of soil, while the amount of reduction highly depends on the type of the ground motion and its intensity.

The typical myth about the effect of SSI on FRS is that considering SSI will benefit the seismic design of secondary components as the maximum spectral value of FRS usually decreases with the account of SSI effect. However, it is well investigated that FRS peaks occur at the frequencies of the structure dominant modes. The presence of soil results in the change of structural natural frequencies, and thus leads to shifting of FRS peaks, which could possibly approach to the resonant frequencies of equipment and its supporting building. Consequently, the seismic input to equipment could be significantly increased. It has been pointed out by Jiang (2016) that while the maximum spectral value of FRS decreases when SSI effect is considered, the seismic input of secondary structure can be increased by 40% at certain frequencies, as shown in Figure 1.5.

Therefore, seismic input and structural analysis should not be considered independently when the structure is founded on relatively soft soil. The seismic analysis of structures considering SSI effect can be conducted through two major steps (Jiang, 2016):

1. A site response analysis is performed first to determine the foundation input response spectra (FIRS) from the GRS or response spectra prescribed at the bedrock base on the theory of wave propagation. The free-field can be generally modelled as a series of soil layers sitting on the bedrock, which is usually regarded as an elastic homogeneous half-space as shown in Figure 1.6. This step is usually conducted by earthquake professionals which is out of the scope of this study.
2. With a known FIRS, a dynamic analysis is then implemented to the structure together with the surrounding soil, considering the interaction between the structure and the surrounding soil.

The rapid progress of SSI studies after 1970s has been stimulated by the needs of the nuclear power industry. It is well understood that SSI effect should be included as one of the essential dynamic properties of NPP reactor buildings (Lou *et al.*, 2011). The methods

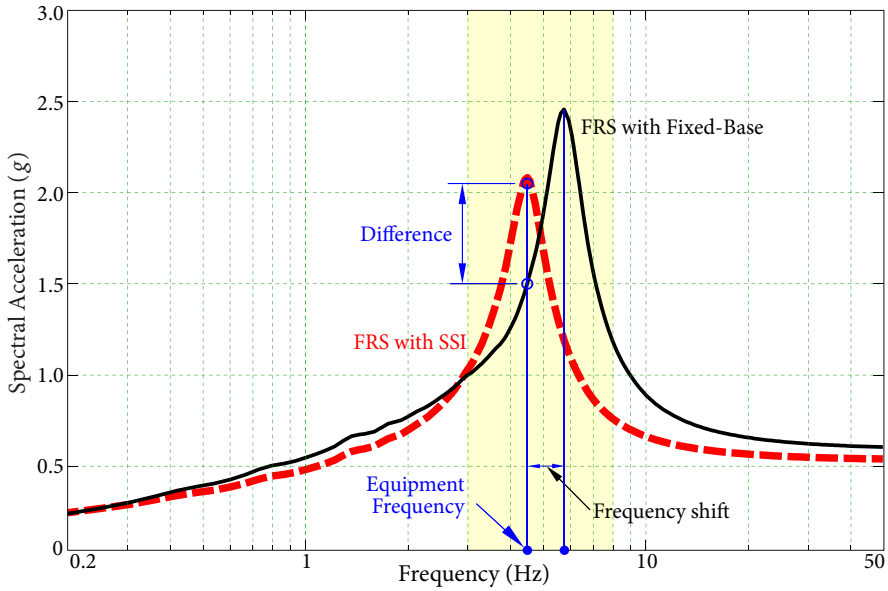


Figure 1.5 Effect of SSI on FRS.

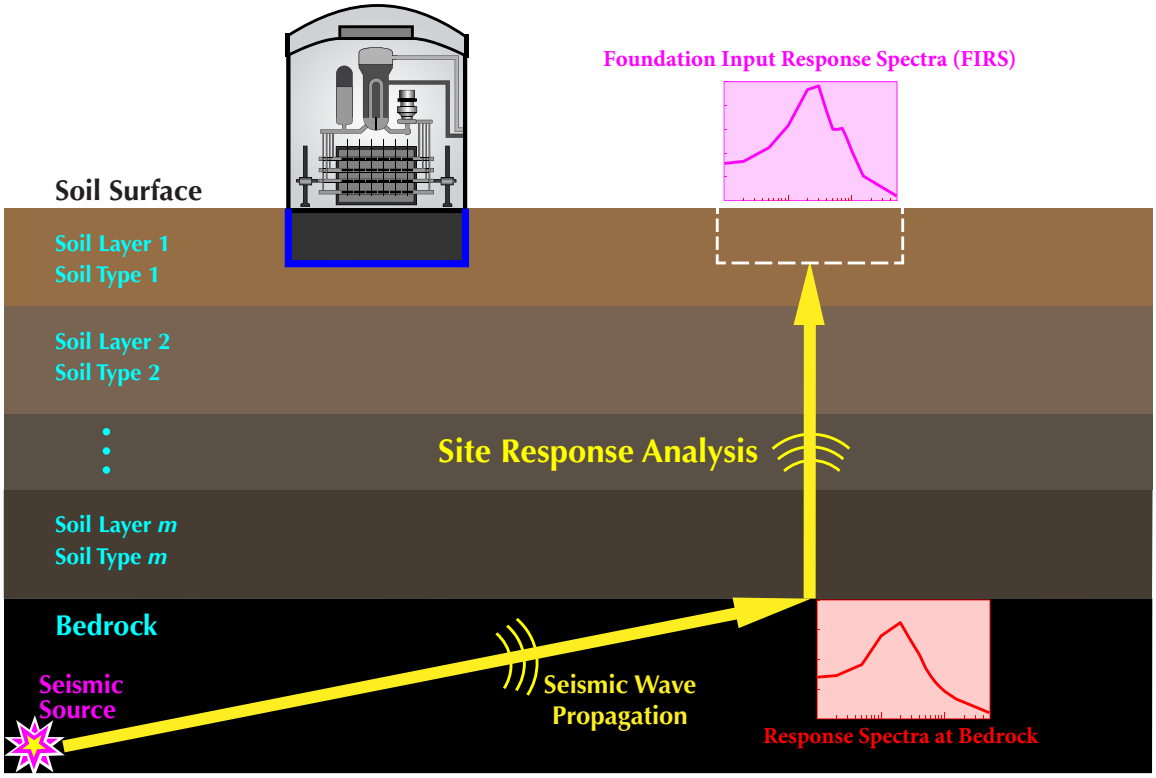


Figure 1.6 Soil-structure interaction.

of the investigation of SSI effect can be mainly classified into the complete method and the substructure method.

Complete Method

In the complete method or the coupled soil-structure method, the structure and a part of the surrounding soil deposit, which is denoted as near field soil, are modelled as the combined soil-structure system. Then the seismic analysis is performed to the integrated system as shown in Figure 1.7 (Wolf, 1985B; Bielak and Christiano, 1984). This model is always based on the Finite Element Method (FEM), and the system is discretized into finite elements. Since the soil deposit is actually an unbounded continuous solid and cannot be modelled by finite elements, an artificial boundary is required to model the near field soil. Furthermore, to simulate the radiation damping of semi-infinite space, the scale of the soil deposit should be large enough (Lou *et al.*, 2011). This requirement, however, causes a tremendous consumption of time and computer resource. As a result, a number of artificial boundaries have been proposed to reduce the scale of the FEM model (Lysmer *et al.*, 1983; Higdon, 1991; Collino, 1993; Liao and Wong, 1984; Wang, 2005).

Although many transmitting boundaries were proposed to increase the efficiency of the numerical simulation, the application of the complete method still requires relatively significant time as well as computational memories because a large system of coupled equations need to solved. In addition, the use of these artificial transmitting boundaries and the necessity that the bedrock has to be located at relative shallow depth may also lead to inaccuracy by FEM. Furthermore, the entire analysis procedure has to be repeated when one of the properties of the superstructure or soil is changed, while only the responses of the structure are of interest. Therefore, the complete method is not widely used in the nuclear power industry due to the limitations above.

Substructure Method

The other method for SSI analysis is called the substructure method (Gutierrez and Chopra, 1978). This method, which is theoretically equivalent to the complete method, permits the whole system to be divided into more manageable parts and to analyze these parts separately.

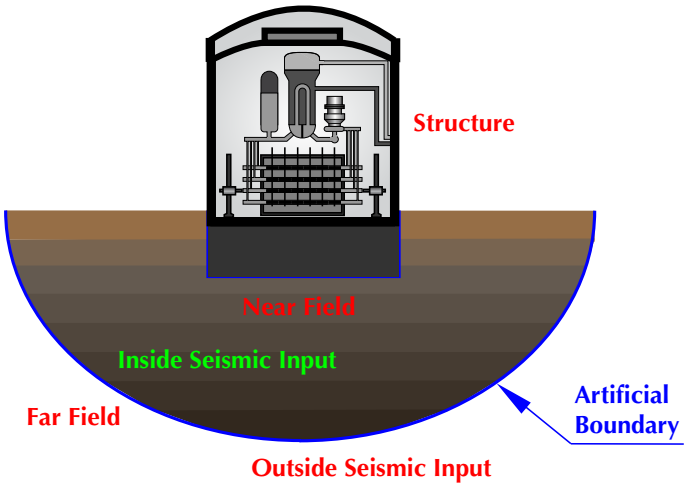


Figure 1.7 Finite element model for SSI complete method.

Some commercial finite element analysis software packages, such as SASSI (Lysmer *et al.*, 1983), ACS SASSI (Ghiocel, 2015), were developed on the basis of the substructure method, and are currently employed in practice to analyze the seismic response of a soil-structure system. It should be noted that the entire analysis in ACS SASSI is performed in frequency domain using the complex response method and finite element techniques. The transient analysis is handled by Fast Fourier Transform techniques in which the dynamic response at each frequency can be obtained. Lastly, the vibrational behavior in time domain can be evaluated by inverse Fourier Transform. However, the dynamic analysis in frequency domain requires the seismic inputs to be spectrum-compatible time histories, which means that the deficiencies of time history analysis as discussed in Section 1.5.2, are inevitable.

Thus, it is desirable to develop an efficient and accurate method for generating FRS taking into account the SSI effect. Several studies on the generation of FRS using the direct method considering the effect of SSI have been carried out. Jiang (2016) performed a seismic analysis for structures with rigid foundation. Rigid foundation means that there is no deformation of the foundation so that the foundation can be simplified to a single point. The direct method for generating FRS proposed by the author becomes applicable in this case once the equivalent input, i.e., Foundation Level Input Response Spectra (FLIRS), is determined. This method is modified by Zhou (2019) to include the flexibilities of foundations. Although the method proposed by Zhou (2019) can deal with the situation of

multiple excitations, it condenses all the deformations to a single point, which might has theoretical defect for structures undergo seismic excitation at different supports. Wang and Xie (2022b) further extended this method by dividing structural responses into dynamic and quasi-static parts, rather than referring them to a single point. This allows for the application of the method to structures with earthquake excitations from multiple supports without the need for condensation.

In the proposed method, the SSI effect is further incorporated in generating FRS for the structures, ensuring the applicability of the direct method to deeply or fully embedded structures. This approach is crucial for ensuring the safety and performance of such structures in SMRs under seismic conditions.

1.7 Dynamic Soil Stiffness Matrix

The dynamic soil stiffness matrix is a fundamental component in SSI analysis, especially for structures subject to seismic excitations. This matrix encapsulates the soil's resistance to deformation under dynamic loading, representing the relationship between applied forces and resulting displacements at the soil-structure interface (Gazetas, 1991). Derived from soil properties such as shear modulus, Poisson's ratio, and density, along with the geometric configuration of the soil-structure system, it accounts for the frequency-dependent nature of soil behaviour under dynamic conditions (Wolf, 1994).

The evolution of dynamic soil stiffness analysis spans over two centuries, marked by a transition from simple analytical solutions to sophisticated numerical methods: The foundational work in this field began with Winkler (Molina-Villegas *et al.*, 2022) and Boussinesq (Verruijt, 2017), who provided analytical solutions for simple, symmetric structures on homogeneous soil. While these methods were fast and often accurate for their intended applications, they were limited in their ability to model complex structural geometries.

Gazetas (1991) made a significant contribution by proposing simplified formulas for computing dynamic impedances of surface and embedded rigid foundations. These formulas, covering a wide range of foundation shapes and embedment conditions, remain widely used due to their simplicity and reasonable accuracy. Wolf (1994) introduced a hybrid

approach combining analytical and numerical methods for computing dynamic stiffness of embedded foundations, aiming to balance computational efficiency with accuracy for practical engineering applications.

The advent of powerful computational tools enabled the development of more advanced numerical methods. Dominguez (1993) provided a comprehensive treatment of Boundary Element Method (BEM) applications in SSI analysis, demonstrating its effectiveness in calculating dynamic stiffness matrices for various foundation types. More recently, Zhou (2019) applied BEM to evaluate dynamic soil stiffness for nuclear power plant structures. For the scenarios of more specialized studies addressing complex aspects of SSI, Waas (1985) explored displacement solutions for dynamic loads in stratified media. Kim (2000) conducted dynamic analysis of grouped pile foundations in layered soils. Ceballos (2012) proposed new wave propagation models for half-space to improve response analysis of soil profiles. Morici (2019) presented simple formulas to estimate parameters of lumped systems reproducing the dynamic stiffness of end-bearing pile foundations.

In contemporary practice in nuclear engineering, specialized software like ACS SASSI has become a standard tool in the nuclear industry for SSI analysis. Despite its widespread adoption, several challenges persist:

(1). The accurate computation of dynamic stiffness matrices for geologically complex sites, particularly those with unstratified complex strata, continues to pose technical difficulties.

(2). The limited availability and high cost of specialized software restrict widespread access, potentially impeding comprehensive analyses by a broader range of practitioners.

(3). The inherent "blackbox" nature of commercial software raises concerns about the transparency and verifiability of results, potentially compromising the reliability of critical analyses in nuclear facility design.

These challenges highlight the urgent need for more accessible, efficient, and transparent methods in SSI analysis for nuclear structures, especially for SMRs with deep embedment and complex foundation systems. The pronounced SSI effects in these structures necessitate precise evaluation of dynamic soil stiffness to ensure robust performance under diverse dynamic loading scenarios. Future research must focus on developing methods that optimally

balance accuracy and computational efficiency, while being accessible to a broader range of practitioners.

1.8 Objectives of Proposed Research

The primary objective of this study is to enhance the existing direct method for floor response spectra (FRS) making it applicable to deeply embedded small modular reactors (SMR) by incorporating the effects of (a) flexible foundation; (b) excitations at multiple supports; and (c) soil-structure interaction (SSI) of SMR.

The specific objectives of this study include:

- Extend the method proposed by Wang (2023) to multi-supported structures, integrating SSI effects.
- Develop practice-orientated methods for evaluating dynamic soil stiffness matrix for SSI analysis, reducing dependence on specialized commercial software.
- Verify the adaptability and efficiency of the proposed method through comprehensive case studies and comparisons with traditional approaches.

1.9 Organization of This Thesis

This thesis is organized into six chapters, structured to present a logical progression of the research from theoretical foundations to practical applications. The organization of this Thesis are summarized as follows:

- Chapter 1 introduces the background, motivation, and objectives of the research, highlighting the challenges of FRS generation in nuclear facility design, especially for emerging SMRs.
- Chapter 2 presents the development of the direct spectra-to-spectra method for generating FRS of multi-supported structures with soil-structure interaction taken into account. It details the theoretical formulation and demonstrates the procedure for proceeding with the proposed approach.

- Chapter 3 focuses on the incorporation of SSI effects in FRS generation. It introduces the concept of FLIRS and presents mathematical and numerical examples to verify the proposed method. Parametric studies investigating the influence of soil conditions on FRS are also presented.
- Chapter 4 provides a comprehensive exploration of dynamic soil stiffness matrix evaluation. It presents the theoretical foundation, validation using lumped-mass and continuous-mass systems, and extension to 3D half-space soil models, validating the effectiveness of the proposed method.
- Chapter 5 demonstrates the application of the developed methodologies to generate FRS for nuclear structures under multi-support excitations and SSI effects. It presents comparative analyses with time history methods and examines the impact of site classification and the stiffness of coupling element on FRS.
- Chapter 6 summarizes the key contributions and findings of the research, discusses their implications for seismic analysis and design of nuclear facilities, and outlines directions for future research.

C H A P T E R 2

Direct Method for Generating FRS

This chapter addresses the critical challenges in the seismic analysis of nuclear power plant structures: generating Floor Response Spectra (FRS) while accounting for both multiple support excitations and Soil-Structure Interaction (SSI). This methodology is particularly crucial for critical structures in the nuclear power industry, such as SMRs and other nuclear facilities, where accurate seismic assessment is paramount for safety analysis and design.

2.1 Generating FRS of Structures under Multiple Excitations

For a deeply-embedded structure, such as Small Modular Reactors, the structure is subjected to earthquake excitations not only at the foundation, but also at the side walls. Hence, an SMR is subjected to seismic excitations at multiple points. Furthermore, the seismic inputs could be different at different input points because the depth of structures can not be neglected and soil properties could vary significantly with the depth. Therefore, it is necessary to extend the direct method for generating FRS developed by Jiang *et al.* (2015), which is applicable to a structure with fixed base, to structures under multiple seismic excitation inputs. Wang has developed the direct method for generating FRS for structures with multiple seismic excitations. To ensure the coherence of the dissertation, this section is also presented, but was primarily conducted by Wang (2023).

2.1.1 Responses of Multi-Supported Structures

Equations of Motion of the Primary Structure

Consider a general three-dimensional multiple degrees-of-freedom (MDOF) structure under multiple tridirectional seismic excitation inputs as shown in Figure 2.1. There are M seismic input nodes or supports, which are directly subjected to seismic excitations. For a typical input node m, it is subjected to tridirectional seismic excitations $\ddot{u}_g^{m,i}(t)$, $i=1,2,3$, in which $i=1$ and 2 represent the two orthogonal horizontal directions, and $i=3$ represents the vertical direction. The structure has N response nodes, or non-input nodes, which are not directly subjected to earthquake excitations. For a typical response node n, it has six DOF, including three translational DOF $u_{n,1}^{\mathrm{R}}$, $u_{n,2}^{\mathrm{R}}$, $u_{n,3}^{\mathrm{R}}$, and three rotational DOF $u_{n,4}^{\mathrm{R}}$, $u_{n,5}^{\mathrm{R}}$, $u_{n,6}^{\mathrm{R}}$. The superscript R stands for "RESPONSE". The displacement vector of the structure consists of two parts:

1. $\mathbf{u}^{\mathrm{I}}=\left\{u_{1,1}^{\mathrm{I}},\ u_{1,2}^{\mathrm{I}},\ u_{1,3}^{\mathrm{I}};\cdots;u_{m,1}^{\mathrm{I}},\ u_{m,2}^{\mathrm{I}},\ u_{m,3}^{\mathrm{I}};\cdots;u_{M,1}^{\mathrm{I}},\ u_{M,2}^{\mathrm{I}},\ u_{M,3}^{\mathrm{I}}\right\}^T$, in which there are $3M$ components of the displacements of the input or support nodes. The superscript I stands for "INPUT".
2. $\mathbf{u}^{\mathrm{R}}=\left\{u_{1,1}^{\mathrm{R}},\ u_{1,2}^{\mathrm{R}},\ldots,\ u_{1,6}^{\mathrm{R}};\cdots;u_{n,1}^{\mathrm{R}},\ u_{n,2}^{\mathrm{R}},\ldots,\ u_{n,6}^{\mathrm{R}};\cdots;u_{N,1}^{\mathrm{R}},\ u_{N,2}^{\mathrm{R}},\ldots,\ u_{N,6}^{\mathrm{R}}\right\}^T$, where there are $6N$ components of the displacements of the response or non-input nodes.

The equation of dynamic equilibrium of the structure can be written in partitioned matrix form as

$$\begin{bmatrix}\mathbf{M}_{\mathrm{II}} & \mathbf{M}_{\mathrm{IR}}\\ \mathbf{M}_{\mathrm{RI}} & \mathbf{M}_{\mathrm{RR}}\end{bmatrix}\begin{Bmatrix}\ddot{\mathbf{u}}^{\mathrm{I}}\\ \ddot{\mathbf{u}}^{\mathrm{R}}\end{Bmatrix}+\begin{bmatrix}\mathbf{C}_{\mathrm{II}} & \mathbf{C}_{\mathrm{IR}}\\ \mathbf{C}_{\mathrm{RI}} & \mathbf{C}_{\mathrm{RR}}\end{bmatrix}\begin{Bmatrix}\dot{\mathbf{u}}^{\mathrm{I}}\\ \dot{\mathbf{u}}^{\mathrm{R}}\end{Bmatrix}+\begin{bmatrix}\mathbf{K}_{\mathrm{II}} & \mathbf{K}_{\mathrm{IR}}\\ \mathbf{K}_{\mathrm{RI}} & \mathbf{K}_{\mathrm{RR}}\end{bmatrix}\begin{Bmatrix}\mathbf{u}^{\mathrm{I}}\\ \mathbf{u}^{\mathrm{R}}\end{Bmatrix}=\begin{Bmatrix}\mathbf{F}^{\mathrm{I}}\\ \mathbf{F}^{\mathrm{R}}\end{Bmatrix}=\begin{Bmatrix}\mathbf{F}^{\mathrm{I}}\\ \mathbf{0}\end{Bmatrix},\quad(2.1.1)$$

where $\mathbf{M}_{\mathrm{II}}$, $\mathbf{C}_{\mathrm{II}}$ and $\mathbf{K}_{\mathrm{II}}$ are the mass, damping and stiffness matrices associated with the input nodes (supports), respectively; $\mathbf{M}_{\mathrm{RR}}$, $\mathbf{C}_{\mathrm{RR}}$ and $\mathbf{K}_{\mathrm{RR}}$, respectively, are the mass, damping and stiffness matrices associated with the response nodes, while the other matrices in equation (2.1.1) describe the coupling effect between the response nodes and supports. These matrices can be determined from the properties of the structure using a finite element method, while it is desirable to determine the displacement vector $\mathbf{u}^{\mathrm{R}}$ of the response nodes

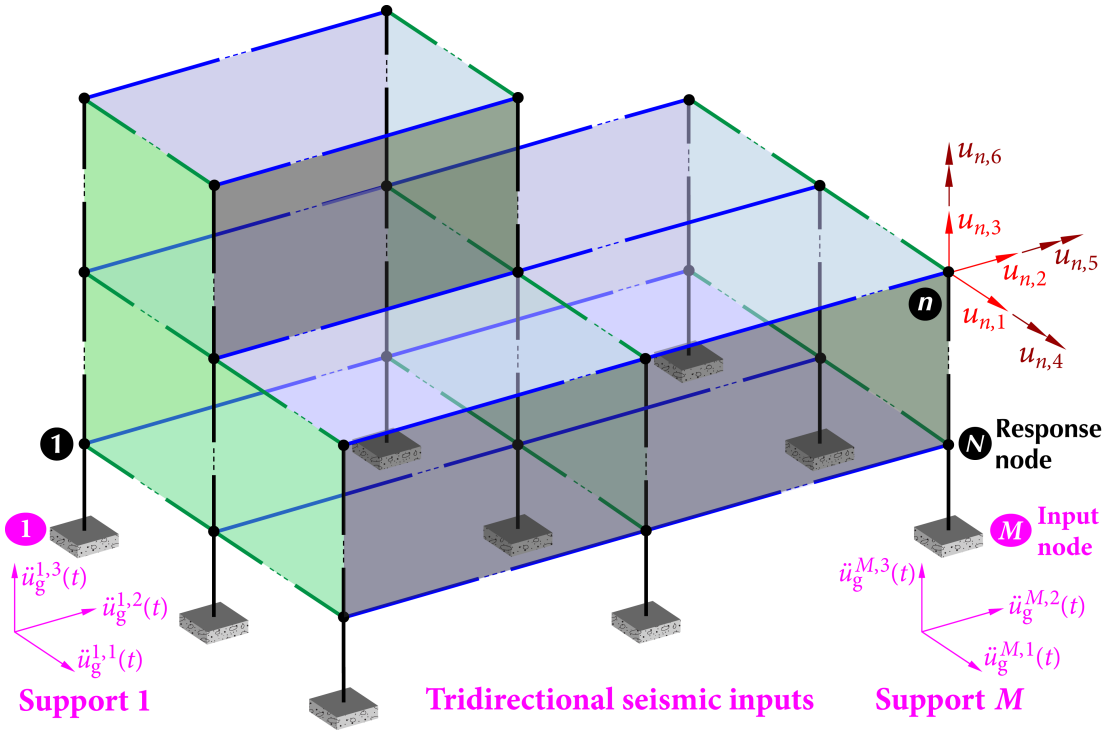


Figure 2.1 Multiple DOF primary structure under excitations at multiple supports.

by giving the support excitations $\mathbf{F}^{\mathrm{I}}$. Note that there are no external loading directly applied on the response nodes of the structure, i.e., $\mathbf{F}^{\mathrm{R}}=\mathbf{0}$.

Separate the displacements in two parts as

$$\begin{Bmatrix}\mathbf{u}^{\mathrm{R}}\\ \mathbf{u}^{\mathrm{I}}\end{Bmatrix}=\begin{Bmatrix}\mathbf{u}^{\mathrm{RS}}\\ \mathbf{u}^{\mathrm{I}}\end{Bmatrix}+\begin{Bmatrix}\mathbf{x}\\ \mathbf{0}\end{Bmatrix}, \tag{2.1.2}$$

In equation (2.1.2), $\mathbf{u}^{\mathrm{RS}}$ is the vector of displacements of the response nodes due to static load of the prescribed support displacements $\mathbf{u}^{\mathrm{I}}$ at each time instant, which is called the *quasi-static* displacement vector. The vector $\mathbf{x}$ is called the *dynamic* displacement vector, because a dynamic analysis is needed to evaluate it. This partitioning of the response was firstly proposed by Burdisso and Singh (1987) and was also utilized by Chopra (2012).

$\mathbf{u}^{\mathrm{RS}}$ and $\mathbf{u}^{\mathrm{I}}$ are related through

$$\begin{bmatrix}\mathbf{K}_{\mathrm{II}} & \mathbf{K}_{\mathrm{IR}}\\ \mathbf{K}_{\mathrm{RI}} & \mathbf{K}_{\mathrm{RR}}\end{bmatrix}\begin{Bmatrix}\mathbf{u}^{\mathrm{I}}\\ \mathbf{u}^{\mathrm{RS}}\end{Bmatrix}=\begin{Bmatrix}\mathbf{F}^{\mathrm{IS}}\\ \mathbf{0}\end{Bmatrix}, \tag{2.1.3}$$

where $\mathbf{F}^{IS}$ is the vector of forces at the input nodes necessary to statically impose displacement $\mathbf{u}^{I}$. If the structure is statically determinate or if the support system undergoes rigid-body motion, then $\mathbf{F}^{IS} = \mathbf{0}$.

The second block-row of equation (2.1.3) gives the relationship between quasi-static displacements and the motions of supports, i.e., $\mathbf{K}_{RI}\mathbf{u}^{I} + \mathbf{K}_{RR}\mathbf{u}^{RS} = \mathbf{0}$, which leads to

$$\mathbf{u}^{RS} = -\boldsymbol{\mathcal{I}}\mathbf{u}^{I}, \qquad \boldsymbol{\mathcal{I}} = (\mathbf{K}_{RR})^{-1}\mathbf{K}_{RI}, \tag{2.1.4}$$

in which $\boldsymbol{\mathcal{I}}$ is called the *influence vector* because it describes the influence of support motions on the displacements of structures.

The second block-row of equation (2.1.1) can be written as

$$\mathbf{M}_{RI}\ddot{\mathbf{u}}^{I} + \mathbf{M}_{RR}\ddot{\mathbf{u}}^{R} + \mathbf{C}_{RI}\dot{\mathbf{u}}^{I} + \mathbf{C}_{RR}\dot{\mathbf{u}}^{R} + \mathbf{K}_{RI}\mathbf{u}^{I} + \mathbf{K}_{RR}\mathbf{u}^{R} = \mathbf{F}^{R} = \mathbf{0}.$$

Substituting equation (2.1.2) into the above equation yields

$$\mathbf{M}_{RR}\ddot{\mathbf{x}} + \mathbf{C}_{RR}\dot{\mathbf{x}} + \mathbf{K}_{RR}\mathbf{x} = \mathbf{p}_{e}(t), \tag{2.1.5}$$

where $\mathbf{p}_{e}(t)$ is the vector of effective earthquake forces given by

$$\mathbf{p}_{e}(t) = -(\mathbf{M}_{RI}\ddot{\mathbf{u}}^{I} + \mathbf{M}_{RR}\ddot{\mathbf{u}}^{RS}) - (\mathbf{C}_{RI}\dot{\mathbf{u}}^{I} + \mathbf{C}_{RR}\dot{\mathbf{u}}^{RS}) - (\mathbf{K}_{RI}\mathbf{u}^{I} + \mathbf{K}_{RR}\mathbf{u}^{RS}). \tag{2.1.6}$$

The last term of equation (2.1.6) can be dropped due to the relationship given by equation (2.1.3). Then using the simplification proposed by Burdisso and Singh (1987), i.e., the damping terms can be neglected because their magnitudes are relatively small compared to the other terms, while $\mathbf{M}_{RI}$ is a null matrix for structures with lumped masses, equation (2.1.6) can be simplified to

$$\mathbf{p}_{e}(t) = -\mathbf{M}_{RR}\ddot{\mathbf{u}}^{RS}. \tag{2.1.7}$$

Substituting equation (2.1.4) into equation (2.1.7), the vector of effective earthquake forces becomes

$$\mathbf{p}_{e}(t) = \mathbf{M}_{RR}\boldsymbol{\mathcal{I}}\ddot{\mathbf{u}}^{I}. \tag{2.1.8}$$

The above procedure for setting up the equation of the motion of response nodes is similar to Burdisso and Singh (1987) and Chopra (2012). Because the seismic excitations are

tridirectional earthquake ground motions at the M input nodes, equation (2.1.8) can be written as

$$\mathbf{p}_{\mathrm{e}}(t) = \mathbf{M}_{\mathrm{RR}} \sum_{m=1}^{M} \sum_{i=1}^{3} \boldsymbol{\mathcal{I}}^{m,i} \ddot{u}_{\mathrm{g}}^{m,i}(t). \tag{2.1.9}$$

Hence, equation (2.1.5) becomes

$$\mathbf{M}_{\mathrm{RR}} \ddot{\mathbf{x}} + \mathbf{C}_{\mathrm{RR}} \dot{\mathbf{x}} + \mathbf{K}_{\mathrm{RR}} \mathbf{x} = \mathbf{M}_{\mathrm{RR}} \sum_{m=1}^{M} \sum_{i=1}^{3} \boldsymbol{\mathcal{I}}^{m,i} \ddot{u}_{\mathrm{g}}^{m,i}(t). \tag{2.1.10}$$

In equation (2.1.10), $\boldsymbol{\mathcal{I}}^{m,i}$ represents the $[3(m-1)+i]$-th column of the influence vector $\boldsymbol{\mathcal{I}}$, which reflects the influence of seismic input in direction i at node m on the response nodes of the structure. In equation (2.1.4), because $\mathbf{K}_{\mathrm{RR}}$ is the stiffness matrix for the response nodes of the structure, its inverse is the flexibility matrix $\mathbf{F}_{\mathrm{RR}}$. The influence vector can be written as $\boldsymbol{\mathcal{I}} = (\mathbf{K}_{\mathrm{RR}})^{-1}\mathbf{K}_{\mathrm{RI}} = \mathbf{F}_{\mathrm{RR}}\mathbf{K}_{\mathrm{RI}}$. Therefore, $\boldsymbol{\mathcal{I}}^{m,i}$ is given by

$$\boldsymbol{\mathcal{I}}^{m,i} = \begin{Bmatrix} \sum_{\tilde{n}=1}^{N} \sum_{\tilde{j}=1}^{6} F_{1,1}^{\tilde{n},\tilde{j}} K_{\tilde{n},\tilde{j}}^{m,i} \\ \vdots \\ \sum_{\tilde{n}=1}^{N} \sum_{\tilde{j}=1}^{6} F_{1,6}^{\tilde{n},\tilde{j}} K_{\tilde{n},\tilde{j}}^{m,i} \\ \vdots \\ \vdots \\ \sum_{\tilde{n}=1}^{N} \sum_{\tilde{j}=1}^{6} F_{N,1}^{\tilde{n},\tilde{j}} K_{\tilde{n},\tilde{j}}^{m,i} \\ \vdots \\ \sum_{\tilde{n}=1}^{N} \sum_{\tilde{j}=1}^{6} F_{N,6}^{\tilde{n},\tilde{j}} K_{\tilde{n},\tilde{j}}^{m,i} \end{Bmatrix}_{6N\times 1} = \begin{Bmatrix} \vdots \\ \sum_{\tilde{n}=1}^{N} \sum_{\tilde{j}=1}^{6} F_{n,j}^{\tilde{n},\tilde{j}} K_{\tilde{n},\tilde{j}}^{m,i} \\ \vdots \end{Bmatrix}_{6N\times 1}, \tag{2.1.11}$$

in which the $[6(n-1)+j]$-th row of the vector is $\sum_{\tilde{n}=1}^{N} \sum_{\tilde{j}=1}^{6} F_{n,j}^{\tilde{n},\tilde{j}} K_{\tilde{n},\tilde{j}}^{m,i}$, which represents the influence of seismic excitation in direction i of input node m on the dynamic response in direction j of response node n of the structure. Note that in equation (2.1.11) and the remainder of this paper, for simplicity of notations, $F_{n,j}^{\tilde{n},\tilde{j}}$ refers to the element of the flexibility matrix $\mathbf{F}_{\mathrm{RR}}$ and $K_{\tilde{n},\tilde{j}}^{m,i}$ refers to the element of the stiffness matrix $\mathbf{K}_{\mathrm{RI}}$ by dropping the subscripts "RR" and "RI".

The influence vector can also be expressed in terms of the number of DOF as

$$\boldsymbol{\tau}^{m,i} = \begin{Bmatrix} \sum_{\kappa=1}^{6N} F_1^{\kappa} K_{\kappa}^{m,i} \\ \sum_{\kappa=1}^{6N} F_2^{\kappa} K_{\kappa}^{m,i} \\ \vdots \\ \sum_{\kappa=1}^{6N} F_{6N}^{\kappa} K_{\kappa}^{m,i} \end{Bmatrix}_{6N\times 1} = \begin{Bmatrix} \vdots \\ \sum_{\kappa=1}^{6N} F_k^{\kappa} K_{\kappa}^{m,i} \\ \vdots \end{Bmatrix}_{6N\times 1}, \tag{2.1.12}$$

where the kth row in the influence vector is $\sum_{\kappa=1}^{6N} F_k^{\kappa} K_{\kappa}^{m,i}$, which reflects the influence of seismic input in direction i of node m on the kth DOF of the structure. For ease of presentation, the two-subscript-notation n, j (node, direction) and the one-subscript-notation $k = 6(n-1)+j$ are used interchangeably; the former is advantageous in describing the quantity in terms of node and direction, while the latter gives the position of the quantity in the corresponding vector.

Denoting $\mathbf{M} = \mathbf{M}_{\mathrm{RR}}$, $\mathbf{C} = \mathbf{C}_{\mathrm{RR}}$, and $\mathbf{K} = \mathbf{K}_{\mathrm{RR}}$, equation (2.1.10) can be written as

$$\mathbf{M}\ddot{\mathbf{x}} + \mathbf{C}\dot{\mathbf{x}} + \mathbf{K}\mathbf{x} = \mathbf{M} \sum_{m=1}^{M} \sum_{i=1}^{3} \boldsymbol{\tau}^{m,i} \ddot{u}_{\mathrm{g}}^{m,i}(t), \tag{2.1.13}$$

where

$$\mathbf{x} = \begin{Bmatrix} \mathbf{x}_1 \\ \mathbf{x}_2 \\ \vdots \\ \mathbf{x}_N \end{Bmatrix}, \qquad \mathbf{x}_n = \begin{Bmatrix} x_{n,1} \\ x_{n,2} \\ \vdots \\ x_{n,6} \end{Bmatrix}, \quad n = 1, 2, \ldots, N,$$

$\mathbf{M}$, $\mathbf{C}$, and $\mathbf{K}$ are, respectively, the mass, damping, and stiffness matrices of dimension $6N \times 6N$, and $\mathbf{x}_n$ is the vector of dynamic displacements of response node n.

Free Vibration

Consider undamped free vibration of the structure $\mathbf{M}\ddot{\mathbf{x}}(t) + \mathbf{K}\mathbf{x}(t) = \mathbf{0}$. Let $\omega_1, \omega_2, \ldots, \omega_{6N}$ be the $6N$ natural frequencies, $\boldsymbol{\Omega} = \mathrm{diag}\{\omega_1, \omega_2, \ldots, \omega_{6N}\}^T$, and $\boldsymbol{\Phi} = [\boldsymbol{\varphi}_1, \boldsymbol{\varphi}_2, \ldots, \boldsymbol{\varphi}_{6N}]$ be the modal matrix, where $\boldsymbol{\varphi}_k = \{\boldsymbol{\varphi}_{1,k}^T, \boldsymbol{\varphi}_{2,k}^T, \ldots, \boldsymbol{\varphi}_{N,k}^T\}^T$ is the kth mode shape, with $\boldsymbol{\varphi}_{n,k} = \{\varphi_{n,1;k}, \varphi_{n,2;k}, \ldots, \varphi_{n,6;k}\}^T$. In element $\varphi_{n,j;k}$, the first subscript n refers to the node

number, the second subscript j indicates the direction of response, and the third subscript k is the mode number.

The modal matrix $\mathbf{\Phi}$ has the following orthogonal properties

$$\begin{aligned}\mathbf{\Phi}^T\mathbf{M}\mathbf{\Phi} &= \operatorname{diag}\left\{\bar{m}_1,\ \bar{m}_2,\ \ldots,\ \bar{m}_{6N}\right\}^T = \bar{\mathbf{m}},\\ \mathbf{\Phi}^T\mathbf{K}\mathbf{\Phi} &= \bar{\mathbf{m}}\mathbf{\Omega}^2 = \operatorname{diag}\left\{\bar{m}_1\omega_1^2,\ \bar{m}_2\omega_2^2,\ \ldots,\ \bar{m}_{6N}\omega_{6N}^2\right\}^T,\end{aligned} \tag{2.1.14}$$

where $\bar{m}_1,\ \bar{m}_2, \ldots,\ \bar{m}_{6N}$ are the modal masses. Assume that the structure has classical damping so that the modal matrix $\mathbf{\Phi}$ can also diagonalize the damping matrix, i.e.,

$$\mathbf{\Phi}^T\mathbf{C}\mathbf{\Phi} = \operatorname{diag}\left\{\bar{c}_1, \bar{c}_2, \ldots, \bar{c}_{6N}\right\}^T, \qquad \bar{c}_k = \bar{m}_k \cdot 2\zeta_k\omega_k. \tag{2.1.15}$$

Forced Vibration

Let

$$\mathbf{x} = \sum_{m=1}^{M}\sum_{i=1}^{3}\mathbf{x}^{m,i}(t). \tag{2.1.16}$$

From equation (2.1.13), one has

$$\mathbf{M}\ddot{\mathbf{x}}^{m,i} + \mathbf{C}\dot{\mathbf{x}}^{m,i} + \mathbf{K}\mathbf{x}^{m,i} = \mathbf{M}\,\boldsymbol{\iota}^{m,i}\,\ddot{u}_{\mathrm{g}}^{m,i}(t). \tag{2.1.17}$$

Apply the transformation

$$\mathbf{x}^{m,i}(t) = \mathbf{\Phi}\mathbf{Q}^{m,i}(t), \quad m = 1, 2, \ldots, M, \quad i = 1, 2, 3, \tag{2.1.18}$$

where

$$\mathbf{Q}^{m,i} = \begin{Bmatrix}\mathbf{Q}_1^{m,i}\\ \mathbf{Q}_2^{m,i}\\ \vdots\\ \mathbf{Q}_N^{m,i}\end{Bmatrix} = \begin{Bmatrix}\Gamma_1^{m,i}q_1^{m,i}\\ \Gamma_2^{m,i}q_2^{m,i}\\ \vdots\\ \Gamma_{6N}^{m,i}q_{6N}^{m,i}\end{Bmatrix},\quad \mathbf{Q}_n^{m,i} = \begin{Bmatrix}\Gamma_{n,1}^{m,i}q_{n,1}^{m,i}\\ \Gamma_{n,2}^{m,i}q_{n,2}^{m,i}\\ \vdots\\ \Gamma_{n,6}^{m,i}q_{n,6}^{m,i}\end{Bmatrix},\quad \mathbf{x}^{m,i} = \begin{Bmatrix}\mathbf{x}_1^{m,i}\\ \mathbf{x}_2^{m,i}\\ \vdots\\ \mathbf{x}_N^{m,i}\end{Bmatrix}, \mathbf{x}_n^{m,i} = \begin{Bmatrix}x_{n,1}^{m,i}\\ x_{n,2}^{m,i}\\ \vdots\\ x_{n,6}^{m,i}\end{Bmatrix},$$

$$x_{n,j}^{m,i} = \sum_{\nu=1}^{N}\sum_{\delta=1}^{6}\varphi_{n,j;6(\nu-1)+\delta}\,\Gamma_{\nu,\delta}^{m,i}\,q_{\nu,\delta}^{m,i} = \sum_{k=1}^{6N}\varphi_{n,j;k}\,\Gamma_k^{m,i}\,q_k^{m,i}, \tag{2.1.19}$$

$$\mathcal{L}_{n,j}^{m,i} = \boldsymbol{\varphi}_{6(n-1)+j}^T\mathbf{M}\boldsymbol{\iota}^{m,i}, \quad \text{or} \quad \mathcal{L}_k^{m,i} = \boldsymbol{\varphi}_k^T\mathbf{M}\boldsymbol{\iota}^{m,i}, \tag{2.1.20}$$

$$\Gamma_{n,j}^{m,i} = \frac{\mathcal{L}_{n,j}^{m,i}}{\bar{m}_{6(n-1)+j}}, \quad \text{or} \quad \Gamma_k^{m,i} = \frac{\mathcal{L}_k^{m,i}}{\bar{m}_k} = \frac{\boldsymbol{\varphi}_k^T\mathbf{M}\boldsymbol{\iota}^{m,i}}{\boldsymbol{\varphi}_k^T\mathbf{M}\boldsymbol{\varphi}_k}. \tag{2.1.21}$$

$\mathcal{L}_{n,j}^{m,i}$ is the *earthquake excitation factor*, quantifying the contribution of earthquake excitation in the ith direction of node m to the modal response $q_{n,j}^{m,i}$. $\Gamma_k^{m,i}$ is the *modal participation factor*; if $\Gamma_k^{m,i}$ is small, then the contribution of mode $\boldsymbol{\varphi}_k$ to the structural response due to excitation in the ith direction of node m is small.

Substituting equation (2.1.18) into (2.1.17) and multiplying $\boldsymbol{\Phi}^T$ from the left yields

$$(\boldsymbol{\Phi}^T\mathbf{M}\boldsymbol{\Phi})\ddot{\mathbf{Q}}^{m,i}(t) + (\boldsymbol{\Phi}^T\mathbf{C}\boldsymbol{\Phi})\dot{\mathbf{Q}}^{m,i}(t) + (\boldsymbol{\Phi}^T\mathbf{K}\boldsymbol{\Phi})\mathbf{Q}^{m,i}(t) = \boldsymbol{\Phi}^T\mathbf{M}\boldsymbol{\mathcal{I}}^{m,i}\ddot{u}_{\mathrm{g}}^{m,i}(t).$$

Using relations (2.1.14), (2.1.15), (2.1.20), and (2.1.21) gives

$$\ddot{q}_k^{m,i}(t) + 2\zeta_k\omega_k\dot{q}_k^{m,i}(t) + \omega_k^2 q_k^{m,i}(t) = \ddot{u}_{\mathrm{g}}^{m,i}(t), \tag{2.1.22}$$

where $k = 1, 2, \ldots, 6N$, $m = 1, 2, \ldots, M$, $i = 1, 2, 3$.

The absolute acceleration of the nth node in direction j due to earthquake excitation in direction i at node m can be obtained using equation (2.1.2)

$$\begin{aligned}
\ddot{u}_{n,j}^{\mathrm{R},m,i}(t) &= \ddot{x}_{n,j}^{m,i}(t) + \ddot{u}_{n,j}^{\mathrm{RS},m,i}(t) = \sum_{k=1}^{6N}\varphi_{n,j;k}\Gamma_k^{m,i}\ddot{q}_k^{m,i}(t) - \mathcal{I}_{n,j}^{m,i}\ddot{u}_{\mathrm{g}}^{m,i}(t) \\
&= \sum_{k=1}^{6N}\varphi_{n,j;k}\Gamma_k^{m,i}\ddot{q}_k^{m,i} - \sum_{\tilde{n}=1}^{N}\sum_{\tilde{j}=1}^{6}F_{n,j}^{\tilde{n},\tilde{j}}K_{\tilde{n},\tilde{j}}^{m,i}\ddot{u}_{\mathrm{g}}^{m,i} \\
&= \sum_{k=1}^{6N}\varphi_{n,j;k}\Gamma_k^{m,i}\ddot{q}_k^{m,i} - \sum_{k=1}^{6N}F_{n,j}^{k}\,K_k^{m,i}\ddot{u}_{\mathrm{g}}^{m,i} \\
&= \sum_{k=1}^{6N}\varphi_{n,j;k}\Gamma_k^{m,i}\left(\ddot{u}_{\mathrm{g}}^{m,i} - 2\zeta_k\omega_k\dot{q}_k^{m,i} - \omega_k^2 q_k^{m,i}\right) - \sum_{k=1}^{6N}F_{n,j}^{k}\,K_k^{m,i}\ddot{u}_{\mathrm{g}}^{m,i} \\
&= -\sum_{k=1}^{6N}\varphi_{n,j;k}\Gamma_k^{m,i}\left(2\zeta_k\omega_k\dot{q}_k^{m,i} + \omega_k^2 q_k^{m,i}\right) - \left[\sum_{k=1}^{6N}\left(F_{n,j}^{k}\,K_k^{m,i} - \varphi_{n,j;k}\Gamma_k^{m,i}\right)\right]\ddot{u}_{\mathrm{g}}^{m,i} \\
&= -\sum_{k=1}^{6N}\varphi_{n,j;k}\Gamma_k^{m,i}\ddot{u}_k^{m,i} - \mathcal{J}_{n,j}^{m,i}\ddot{u}_{\mathrm{g}}^{m,i},
\end{aligned} \tag{2.1.23}$$

in which $\ddot{u}_k^{m,i}$ is the absolute acceleration response of the kth mode given by

$$\ddot{u}_k^{m,i} = 2\zeta_k\omega_k\dot{q}_k^{m,i} + \omega_k^2 q_k^{m,i},$$

and

$$\mathcal{J}_{n,j}^{m,i} = \sum_{k=1}^{6N}\left(F_{n,j}^{k}\,K_k^{m,i} - \varphi_{n,j;k}\Gamma_k^{m,i}\right)$$

represents the influence of ground input in direction i at node m to the acceleration response of the structure in direction j at node n. The similar derivation of the absolute response can also be seen in Asfura and Kiureghian (1986).

In earthquake engineering, negative sign has no real significance with regard to earthquake excitation and can be dropped; hence, equation (2.1.23) can be written as

$$\ddot{u}_{n,j}^{\mathrm{R},m,i}(t) = \sum_{k=1}^{6N} \varphi_{n,j;k}\, \Gamma_k^{m,i}\, \ddot{u}_k^{m,i} + \mathcal{I}_{n,j}^{m,i}\, \ddot{u}_{\mathrm{g}}^{m,i}. \tag{2.1.24}$$

The absolute acceleration of the structure due to excitation in direction i from all supports can be obtained as

$$\ddot{u}_{n,j}^{\mathrm{R},i}(t) = \sum_{m=1}^{M} \ddot{u}_{n,j}^{\mathrm{R},m,i}(t) = \sum_{m=1}^{M}\sum_{k=1}^{6N} \varphi_{n,j;k}\, \Gamma_k^{m,i}\, \ddot{u}_k^{m,i} + \sum_{m=1}^{M} \mathcal{I}_{n,j}^{m,i}\, \ddot{u}_{\mathrm{g}}^{m,i}. \tag{2.1.25}$$

Then the absolute acceleration of the nth node in direction j can be evaluated by

$$\ddot{u}_{n,j}^{\mathrm{R}}(t) = \sum_{i=1}^{3} \ddot{u}_{n,j}^{\mathrm{R},i}(t). \tag{2.1.26}$$

2.1.2 Floor Response Spectra

If the absolute response $u_{n,j}^{\mathrm{R},i}(t)$ of node n in direction j due to earthquake excitations at multiple supports in direction i is input to an SDOF oscillator (ω_0, ζ_0), the governing equations of motion are

$$\ddot{x}_{n,j}^{\mathrm{F},i}(t) + 2\zeta_0\omega_0\, \dot{x}_{n,j}^{\mathrm{F},i}(t) + \omega_0^2\, x_{n,j}^{\mathrm{F},i}(t) = -\ddot{u}_{n,j}^{\mathrm{R},i}(t), \tag{2.1.27}$$

$$\ddot{u}_{n,j}^{\mathrm{F},i}(t) = \ddot{x}_{n,j}^{\mathrm{F},i}(t) + \ddot{u}_{n,j}^{\mathrm{R},i}(t) = -2\zeta_0\omega_0\, \dot{x}_{n,j}^{\mathrm{F},i}(t) - \omega_0^2\, x_{n,j}^{\mathrm{F},i}(t), \tag{2.1.28}$$

where $x_{n,j}^{\mathrm{F},i}(t) = u_{n,j}^{\mathrm{F},i}(t) - u_{n,j}^{\mathrm{R},i}(t)$ is the displacement of the oscillator relative to node n in direction j, and $u_{n,j}^{\mathrm{F},i}(t)$ is the absolute displacement of the oscillator. The superscript "F" denotes that the oscillator is mounted on a floor. The maximum absolute acceleration of the oscillator

$$\mathcal{S}_{\mathrm{A};n,j}^{i}(\omega_0, \zeta_0) = \left|\ddot{u}_{n,j}^{\mathrm{F},i}(t)\right|_{\max} \tag{2.1.29}$$

is the floor (acceleration) response spectrum (FRS) of response node (floor) n in direction j subjected to earthquake excitations at multiple supports in direction i.

It is specified in ASCE Standard 4-98 (ASCE, 1998) that, for direct spectra-to-spectra methods, when the response spectrum of a given direction at a given location has contributions from more than one spatial component of earthquakes, these contributions shall be combined by the SRSS (Square Root of the Sum of the Squares) rule. Hence, combining contributions from tridirectional earthquake excitations, FRS of node n in direction j is given by

$$\mathcal{S}_{\mathrm{A};n,j}(\omega_0,\zeta_0)=\sqrt{\sum_{i=1}^{3}\Big[\mathcal{S}^{i}_{\mathrm{A};n,j}(\omega_0,\zeta_0)\Big]^2}. \tag{2.1.30}$$

2.1.3 Direct Method for Generating FRS for Structures under Excitations at Multiple Supports

In equation (2.1.25), the first term $\sum_{m=1}^{M}\sum_{k=1}^{6N}\ddot{u}^{m,i}_{n,j;k}$ is the response due to the interaction between the structure nodes and input nodes, which is regarded as dynamic part; whereas the second term $\sum_{m=1}^{M}\mathcal{I}^{m,i}_{n,j}\ddot{u}^{m,i}_{\mathrm{g}}$ is the response due to the ground motion, which can be treated as quasi-static part. Corresponding to these two terms, the absolute acceleration response of the oscillator (ω_0,ζ_0) under the excitation $\ddot{u}^{\mathrm{R},i}_{n,j}(t)$ can be written as

$$z^{\mathrm{R},i}_{n,j}(t)=\sum_{m=1}^{M}\sum_{k=1}^{6N}z^{m,i}_{n,j;k}(t)+\sum_{m=1}^{M}\mathcal{I}^{m,i}_{n,j}z^{m,i}_{\mathrm{g}}(t), \tag{2.1.31}$$

in which $z^{m,i}_{n,j;k}(t)$ is the absolute response of the oscillator due to $\ddot{u}^{m,i}_{n,j;k}(t)$, and $z^{m,i}_{\mathrm{g}}(t)$ is the absolute response of the oscillator due to $\ddot{u}^{m,i}_{\mathrm{g}}(t)$. It should be emphasized that it is important to separate the two terms in equation (2.1.31) so that the various correlations can be properly accounted, which is one of the novel contributions of this research.

Because the maximum values of $z^{m,i}_{n,j;k}(t)$ and $z^{m,i}_{\mathrm{g}}(t)$ do not occur at the same time, they have to be combined appropriately. In this section, a new combination rule for generating FRS of multiply supported structures is developed based on the theory of random vibration.

2.1.3.1 FRSMS-CQC Combination Rule

In this section, a new combination rule, called FRSMS-CQC, which can account for the correlation between FRS from any pairs of two different vibration modes, the correlation between FRS from a vibration mode and FRS due to ground input at a support, and the

correlation between FRS due to ground inputs at two different supports, is developed. FRSMS-CQC stands for a Complete Quadratic Combination (CQC) rule for obtaining FRS of structures with earthquake excitations at multiple supports (MS).

Squaring both sides of equation (2.1.31) gives

$$\begin{aligned}\left\{z_{n,j}^{\mathrm{R},i}(t)\right\}^2 &= \left\{\sum_{m=1}^{M}\sum_{k=1}^{6N} z_{n,j;k}^{m,i}(t) + \sum_{m=1}^{M}\mathcal{I}_{n,j}^{m,i} z_{\mathrm{g}}^{m,i}(t)\right\}\times\left\{\sum_{\hat{m}=1}^{M}\sum_{\kappa=1}^{6N} z_{n,j;\kappa}^{\hat{m},i}(t) + \sum_{\hat{m}=1}^{M}\mathcal{I}_{n,j}^{\hat{m},i} z_{\mathrm{g}}^{\hat{m},i}(t)\right\}\\ &= \sum_{m=1}^{M}\sum_{\hat{m}=1}^{M}\sum_{k=1}^{6N}\sum_{\kappa=1}^{6N} z_{n,j;k}^{m,i}(t)\, z_{n,j;\kappa}^{\hat{m},i}(t) + 2\sum_{m=1}^{M}\sum_{\hat{m}=1}^{M}\sum_{k=1}^{6N}\mathcal{I}_{n,j}^{\hat{m},i} z_{n,j;k}^{m,i}(t)\, z_{\mathrm{g}}^{\hat{m},i}(t)\\ &\quad + \sum_{m=1}^{M}\sum_{\hat{m}=1}^{M}\mathcal{I}_{n,j}^{m,i}\,\mathcal{I}_{n,j}^{\hat{m},i} z_{\mathrm{g}}^{m,i}(t)\, z_{\mathrm{g}}^{\hat{m},i}(t).\end{aligned}$$

Taking the expected value of both sides results in the mean-square response

$$\begin{aligned}\mathrm{E}\left[\left\{z_{n,j}^{\mathrm{R},i}(t)\right\}^2\right] &= \sum_{m=1}^{M}\sum_{\hat{m}=1}^{M}\sum_{k=1}^{6N}\sum_{\kappa=1}^{6N}\mathrm{E}\left[z_{n,j;k}^{m,i}(t)\, z_{n,j;\kappa}^{\hat{m},i}(t)\right] + 2\sum_{m=1}^{M}\sum_{\hat{m}=1}^{M}\sum_{k=1}^{6N}\mathcal{I}_{n,j}^{\hat{m},i}\,\mathrm{E}\left[z_{n,j;k}^{m,i}(t)\, z_{\mathrm{g}}^{\hat{m},i}(t)\right]\\ &\quad + \sum_{m=1}^{M}\sum_{\hat{m}=1}^{M}\mathcal{I}_{n,j}^{m,i}\,\mathcal{I}_{n,j}^{\hat{m},i}\,\mathrm{E}\left[z_{\mathrm{g}}^{m,i}(t)\, z_{\mathrm{g}}^{\hat{m},i}(t)\right]\\ &= \sum_{m=1}^{M}\sum_{\hat{m}=1}^{M}\sum_{k=1}^{6N}\sum_{\kappa=1}^{6N}\rho_{k\kappa}^{m\hat{m},i}\sqrt{\mathrm{E}\left[\left\{z_{n,j;k}^{m,i}(t)\right\}^2\right]}\sqrt{\mathrm{E}\left[\left\{z_{n,j;\kappa}^{\hat{m},i}(t)\right\}^2\right]}\\ &\quad + 2\sum_{m=1}^{M}\sum_{\hat{m}=1}^{M}\sum_{k=1}^{6N}\mathcal{I}_{n,j}^{\hat{m},i}\,\rho_{k0}^{m\hat{m},i}\sqrt{\mathrm{E}\left[\left\{z_{n,j;k}^{m,i}(t)\right\}^2\right]}\sqrt{\mathrm{E}\left[\left\{z_{\mathrm{g}}^{\hat{m},i}(t)\right\}^2\right]}\\ &\quad + \sum_{m=1}^{M}\sum_{\hat{m}=1}^{M}\rho_{0}^{m\hat{m},i}\,\mathcal{I}_{n,j}^{m,i}\,\mathcal{I}_{n,j}^{\hat{m},i}\sqrt{\mathrm{E}\left[\left\{z_{\mathrm{g}}^{m,i}(t)\right\}^2\right]}\sqrt{\mathrm{E}\left[\left\{z_{\mathrm{g}}^{\hat{m},i}(t)\right\}^2\right]},\end{aligned} \tag{2.1.32}$$

in which $\rho_{k\kappa}^{m\hat{m},i}$ is the correlation coefficient between the contribution from the kth mode due to the input at support m in direction i and the contribution from the κth mode due to the input at support $\hat{m}$ in direction i; $\rho_{k0}^{m\hat{m},i}$ is the correlation coefficient between the contribution from kth mode due to the input at support m in direction i and the contribution of an oscillator (ω_0, ζ_0) due to the input at support $\hat{m}$ in direction i; $\rho_{0}^{m\hat{m},i}$ is the correlation coefficient between the contribution of an oscillator (ω_0, ζ_0) due to the input at support m

in direction i and the contribution of an oscillator (ω_0, ζ_0) due to the input at support $\hat{m}$ in direction i.

In the theory of random processes, the maximum values of $z_{n,j;k}^{m,i}$, $z_{\mathrm{g}}^{m,i}$, and $z_{n,j}^{\mathrm{R},i}$ are related to the corresponding mean-square values by peak factors. In earthquake engineering, it is reasonable to assume that the peak factors are the same, i.e.,

$$\begin{aligned}
\left| z_{n,j;k}^{m,i}(t) \right|_{\max} &= R_{n,j;k}^{m,i} = \mathcal{PF} \sqrt{\mathrm{E}\left[\left\{ z_{n,j;k}^{m,i}(t) \right\}^2 \right]}, \\
\left| z_{\mathrm{g}}^{m,i}(t) \right|_{\max} &= \mathcal{S}_{\mathrm{A}}^{m,i}(\omega_0, \zeta_0) = \mathcal{PF} \sqrt{\mathrm{E}\left[\left\{ z_{\mathrm{g}}^{m,i}(t) \right\}^2 \right]}, \\
\left| z_{n,j}^{\mathrm{R},i}(t) \right|_{\max} &= \mathcal{S}_{\mathrm{A};n,j}^{i}(\omega_0, \zeta_0) = \mathcal{PF} \sqrt{\mathrm{E}\left[\left\{ z_{n,j}^{\mathrm{R},i}(t) \right\}^2 \right]},
\end{aligned} \tag{2.1.33}$$

in which $R_{n,j;k}^{m,i}$ is the maximum absolute value of $z_{n,j;k}^{m,i}$ given by Jiang *et al.* (2015), the maximum absolute value of $z_{\mathrm{g}}^{m,i}$ is the corresponding GRS $\mathcal{S}_{\mathrm{A}}^{m,i}(\omega_0, \zeta_0)$ of an oscillator (ω_0, ζ_0), and $\mathcal{S}_{\mathrm{A};n,j}^{i}(\omega_0, \zeta_0)$ is the maximum absolute value of $z_{n,j}^{\mathrm{R},i}$.

Substituting equations (2.1.33) into equation (2.1.32) gives

$$\begin{aligned}
\left\{ \frac{\mathcal{S}_{\mathrm{A};n,j}^{i}(\omega_0, \zeta_0)}{\mathcal{PF}} \right\}^2 = & \sum_{m=1}^{M} \sum_{\hat{m}=1}^{M} \sum_{k=1}^{6N} \sum_{\kappa=1}^{6N} \rho_{k\kappa}^{m\hat{m},i} \left\{ \frac{R_{n,j;k}^{m,i}}{\mathcal{PF}} \right\} \left\{ \frac{R_{n,j;\kappa}^{\hat{m},i}}{\mathcal{PF}} \right\} \\
& + 2 \sum_{m=1}^{M} \sum_{\hat{m}=1}^{M} \sum_{k=1}^{6N} \mathcal{J}_{n,j}^{\hat{m},i} \, \rho_{k0}^{m\hat{m},i} \left\{ \frac{R_{n,j;k}^{m,i}}{\mathcal{PF}} \right\} \left\{ \frac{\mathcal{S}_{\mathrm{A}}^{\hat{m},i}(\omega_0, \zeta_0)}{\mathcal{PF}} \right\} \\
& + \sum_{m=1}^{M} \sum_{\hat{m}=1}^{M} \rho_{0}^{m\hat{m},i} \, \mathcal{J}_{n,j}^{m,i} \, \mathcal{J}_{n,j}^{\hat{m},i} \left\{ \frac{\mathcal{S}_{\mathrm{A}}^{m,i}(\omega_0, \zeta_0)}{\mathcal{PF}} \right\} \left\{ \frac{\mathcal{S}_{\mathrm{A}}^{\hat{m},i}(\omega_0, \zeta_0)}{\mathcal{PF}} \right\}.
\end{aligned} \tag{2.1.34}$$

Multiplying $\mathcal{PF}^2$ to both sides of equation (2.1.34) yields

$$\begin{aligned}
\left[\mathcal{S}_{\mathrm{A};n,j}^{i}(\omega_0, \zeta_0) \right]^2 = & \sum_{m=1}^{M} \sum_{\hat{m}=1}^{M} \sum_{k=1}^{6N} \sum_{\kappa=1}^{6N} \rho_{k\kappa}^{m\hat{m},i} \, R_{n,j;k}^{m,i} \, R_{n,j;\kappa}^{\hat{m},i} \\
& + 2 \sum_{m=1}^{M} \sum_{\hat{m}=1}^{M} \sum_{k=1}^{6N} \mathcal{J}_{n,j}^{\hat{m},i} \, \rho_{k0}^{m\hat{m},i} \, R_{n,j;k}^{m,i} \, \mathcal{S}_{\mathrm{A}}^{\hat{m},i}(\omega_0, \zeta_0) \\
& + \sum_{m=1}^{M} \sum_{\hat{m}=1}^{M} \rho_{0}^{m\hat{m},i} \, \mathcal{J}_{n,j}^{m,i} \, \mathcal{J}_{n,j}^{\hat{m},i} \, \mathcal{S}_{\mathrm{A}}^{m,i}(\omega_0, \zeta_0) \, \mathcal{S}_{\mathrm{A}}^{\hat{m},i}(\omega_0, \zeta_0).
\end{aligned} \tag{2.1.35}$$

Finally, similar to equation (2.1.30), the total FRS of node n in direction j under tridirectional earthquake excitations at multiple inputs can be determined by combining $\mathcal{S}^{i}_{\mathrm{A};n,j}(\omega_0,\zeta_0)$ using the SRSS rule

$$\mathcal{S}_{\mathrm{A};n,j}(\omega_0,\zeta_0)=\sqrt{\sum_{i=1}^{3}\Big[\mathcal{S}^{i}_{\mathrm{A};n,j}(\omega_0,\zeta_0)\Big]^2}. \tag{2.1.36}$$

2.1.3.2 Determination of $\rho_{k0}^{m\hat{m},i}$, $\rho_{k\kappa}^{m\hat{m},i}$, and $\rho_{0}^{m\hat{m},i}$

The correlation coefficient between the contribution from kth mode due to the input $\ddot{u}^{m,i}_{n,j;k}(t)$ and the contribution of an oscillator (ω_0,ζ_0) due to the input $\ddot{u}_{\mathrm{g}}^{\hat{m},i}(t)$, i.e., $\rho_{k0}^{m\hat{m},i}$ in equations (2.1.32) and (2.1.35), can be obtained as follows.

The contribution from the kth mode to the response of the oscillator (ω_0,ζ_0) mounted on the MDOF structure under earthquake excitation in direction i at support m, i.e., $z_k^{m,i}$, is given by (see, e.g., Xie *et al.*, 2019)

$$z_k^{m,i}(t)=\omega_0^2\,\omega_k^2\cdot C_k(t)*\ddot{u}_{\mathrm{g}}^{m,i}(t),\quad C_k(t)=h_0(t)*h_k(t), \tag{2.1.37}$$

where "$*$" denotes the operation of convolution, while

$$h_k(t)=\mathrm{e}^{-\zeta_k\omega_k t}\,\frac{\sin\omega_{k,\mathrm{d}}t}{\omega_{k,\mathrm{d}}},\quad \omega_{k,\mathrm{d}}=\omega_k\sqrt{1-\zeta_k^2}, \tag{2.1.38}$$

and its Fourier transform is

$$\mathcal{H}_k(\omega)=\int_{-\infty}^{\infty}h_k(\tau)\,\mathrm{e}^{-\mathrm{i}\omega\tau}\,\mathrm{d}\tau=\frac{1}{(\omega_k^2-\omega^2)+\mathrm{i}2\zeta_k\omega_k\omega}. \tag{2.1.39}$$

The contribution to the oscillator (ω_0,ζ_0) under earthquake excitation in direction i at support $\hat{m}$ is

$$z_{\mathrm{g}}^{\hat{m},i}(t)=\omega_0^2\,h_0(t)*\ddot{u}_{\mathrm{g}}^{\hat{m},i}(t). \tag{2.1.40}$$

The covariance between $z_k^{m,i}(t)$ and $z_{\mathrm{g}}^{\hat{m},i}(t)$ is given by

$$\begin{aligned}
&\mathrm{E}\Big[z_k^{m,i}(t)\;z_{\mathrm{g}}^{\hat{m},i}(t+\tau)\Big]\\
&\quad=\mathrm{E}\Big[\Big\{\omega_0^2\,\omega_k^2\cdot C_k(t)*\ddot{u}_{\mathrm{g}}^{m,i}(t)\Big\}\cdot\Big\{\omega_0^2\,h_0(t+\tau)*\ddot{u}_{\mathrm{g}}^{\hat{m},i}(t+\tau)\Big\}\Big]\\
&\quad=\mathrm{E}\Big[\omega_0^4\,\omega_k^2\int_{-\infty}^{\infty}C_k(\tau_1)\,\ddot{u}_{\mathrm{g}}^{m,i}(t-\tau_1)\,\mathrm{d}\tau_1\int_{-\infty}^{\infty}h_0(\tau_2)\,\ddot{u}_{\mathrm{g}}^{\hat{m},i}(t+\tau-\tau_2)\,\mathrm{d}\tau_2\Big]
\end{aligned}$$

$$= \omega_0^4\,\omega_k^2 \int_{-\infty}^{\infty}\int_{-\infty}^{\infty} C_k(\tau_1)\,h_0(\tau_2)\,\mathrm{E}\Big[\,\ddot{u}_{\mathrm{g}}^{m,i}(t-\tau_1)\,\ddot{u}_{\mathrm{g}}^{\hat{m},i}(t+\tau-\tau_2)\Big]\,\mathrm{d}\tau_1\,\mathrm{d}\tau_2. \quad (2.1.41)$$

Taking Fourier transform of both sides of equation (2.1.41) yields

$$\begin{aligned}\mathcal{S}_{z_k^{m,i}\,z_{\mathrm{g}}^{\hat{m},i}}(\omega) &= \int_{-\infty}^{\infty} \mathrm{E}\big[z_k^{m,i}(t)\;z_{\mathrm{g}}^{\hat{m},i}(t+\tau)\big]\cdot \mathrm{e}^{-\mathrm{i}\omega\tau}\,\mathrm{d}\tau \\ &= \omega_0^4\,\omega_k^2 \int_{-\infty}^{\infty}\int_{-\infty}^{\infty}\int_{-\infty}^{\infty} C_k(\tau_1)\,h_0(\tau_2)\,R_{\ddot{u}_{\mathrm{g}}^{m,i}\,\ddot{u}_{\mathrm{g}}^{\hat{m},i}}(\tau+\tau_1-\tau_2)\cdot \mathrm{e}^{-\mathrm{i}\omega\tau}\,\mathrm{d}\tau_1\,\mathrm{d}\tau_2\,\mathrm{d}\tau.\end{aligned} \quad (2.1.42)$$

Setting $\tau_3 = \tau+\tau_1-\tau_2$, equation (2.1.42) can be written as

$$\begin{aligned}\mathcal{S}_{z_k^{m,i}\,z_{\mathrm{g}}^{\hat{m},i}}(\omega) &= \omega_0^4\,\omega_k^2 \int_{-\infty}^{\infty} C_k(\tau_1)\,\mathrm{e}^{\mathrm{i}\omega\tau_1}\,\mathrm{d}\tau_1 \int_{-\infty}^{\infty} h_0(\tau_2)\,\mathrm{e}^{-\mathrm{i}\omega\tau_2}\,\mathrm{d}\tau_2 \int_{-\infty}^{\infty} R_{\ddot{u}_{\mathrm{g}}^{m,i}\,\ddot{u}_{\mathrm{g}}^{\hat{m},i}}(\tau_3)\,\mathrm{e}^{-\mathrm{i}\omega\tau_3}\,\mathrm{d}\tau \\ &= \omega_0^4\,\omega_k^2\cdot \mathcal{C}_k^*(\omega)\cdot \mathcal{H}_0(\omega)\cdot \mathcal{S}_{\ddot{u}_{\mathrm{g}}^{m,i}\,\ddot{u}_{\mathrm{g}}^{\hat{m},i}}(\omega),\end{aligned} \quad (2.1.43)$$

where $\mathcal{C}_k(\omega) = \mathcal{H}_0(\omega)\,\mathcal{H}_k(\omega)$ is the Fourier transform of the convolution $C_k(t)$, $\mathcal{C}_k^*(\omega)$ is the complex conjugate of $\mathcal{C}_k(\omega)$. Taking the inverse Fourier transform of equation (2.1.43) yields

$$\mathrm{E}\big[z_k^{m,i}(t)\,z_{\mathrm{g}}^{\hat{m},i}(t+\tau)\big] = \frac{\omega_0^4\,\omega_k^2}{2\pi}\int_{-\infty}^{\infty} \mathcal{C}_k^*(\omega)\cdot \mathcal{H}_0(\omega)\cdot \mathcal{S}_{\ddot{u}_{\mathrm{g}}^{m,i}\,\ddot{u}_{\mathrm{g}}^{\hat{m},i}}(\omega)\,\mathrm{e}^{\mathrm{i}\omega\tau}\,\mathrm{d}\omega. \quad (2.1.44)$$

Setting $\tau = 0$ gives

$$\mathrm{E}\big[z_k^{m,i}(t)\,z_{\mathrm{g}}^{\hat{m},i}(t)\big] = \frac{\omega_0^4\,\omega_k^2}{2\pi}\int_{-\infty}^{\infty} \mathcal{C}_k^*(\omega)\cdot \mathcal{H}_0(\omega)\cdot \mathcal{S}_{\ddot{u}_{\mathrm{g}}^{m,i}\,\ddot{u}_{\mathrm{g}}^{\hat{m},i}}(\omega)\,\mathrm{d}\omega. \quad (2.1.45)$$

$\mathcal{S}_{\ddot{u}_{\mathrm{g}}^{m,i}\,\ddot{u}_{\mathrm{g}}^{\hat{m},i}}(\omega)$ is the cross-power spectral density function of ground accelerations $\ddot{u}_{\mathrm{g}}^{m,i}(t)$ and $\ddot{u}_{\mathrm{g}}^{\hat{m},i}(t)$, which is usually expressed as

$$\mathcal{S}_{\ddot{u}_{\mathrm{g}}^{m,i}\,\ddot{u}_{\mathrm{g}}^{\hat{m},i}}(\omega) = \gamma^{\,m\hat{m},i}(\omega)\,\sqrt{\mathcal{S}_{\ddot{u}_{\mathrm{g}}^{m,i}\,\ddot{u}_{\mathrm{g}}^{m,i}}(\omega)\;\mathcal{S}_{\ddot{u}_{\mathrm{g}}^{\hat{m},i}\,\ddot{u}_{\mathrm{g}}^{\hat{m},i}}(\omega)}\,. \quad (2.1.46)$$

where $\mathcal{S}_{\ddot{u}_{\mathrm{g}}^{m,i}\,\ddot{u}_{\mathrm{g}}^{m,i}}(\omega)$ and $\mathcal{S}_{\ddot{u}_{\mathrm{g}}^{\hat{m},i}\,\ddot{u}_{\mathrm{g}}^{\hat{m},i}}(\omega)$ are the power density functions of ground excitations $\ddot{u}_{\mathrm{g}}^{m,i}(t)$ and $\ddot{u}_{\mathrm{g}}^{\hat{m},i}(t)$, respectively, $\gamma^{\,m\hat{m},i}(\omega)$ is the coherency function characterizing the spatial variation of seismic ground motions. Various theoretical and empirical models of the coherency function have been developed (Luco and Wong, 1986; Abrahamson *et al.*, 1991). Furthermore, for a site of interest, the spatial coherency function $\gamma^{\,m\hat{m},i}(\omega)$ may

also be available or postulated, such as those proposed by Der Kiureghian (1996) and Zhang *et al.* (2012). For each support m, $m=1,2,\ldots,M$, the power spectral density function $\mathcal{S}_{\ddot{u}_g^{m,i}\ddot{u}_g^{m,i}}(\omega)$ may be available or postulated, such as the Kanai-Tajimi power spectral density function (Villaverde, 2009). Then equations (2.1.46) and (2.1.45) can be evaluated easily.

In the following, two important special cases, which have applications in nuclear facilities, are considered.

Case 1: Seismic Excitations $\ddot{u}_g^{m,i}(t)$ and $\ddot{u}_g^{\hat{m},i}(t)$ Identical

This case is applicable to structures of small sizes, such as SMR, which is modelled as deeply-embedded structures with flexible foundations. For these structures, earthquake excitations in a direction do not change much at different supports, which means that the input in direction i at support m and the input in direction i at support $\hat{m}$, i.e., $\ddot{u}_g^{m,i}(t)$ and $\ddot{u}_g^{\hat{m},i}(t)$, are approximately the same. As a result, it can be reasonably assumed that $\ddot{u}_g^{m,i}(t)=\ddot{u}_g^{\hat{m},i}(t)=\ddot{u}_g^{i}(t)$, $i=1,2,3$. Equation (2.1.44) becomes

$$\mathrm{E}\big[z_k^{m,i}(t)\, z_g^{\hat{m},i}(t)\big]=\frac{\omega_0^4\,\omega_k^2}{2\pi}\int_{-\infty}^{\infty}\mathcal{H}_0^*(\omega)\cdot\mathcal{H}_0(\omega)\cdot\mathcal{H}_k^*(\omega)\cdot\mathcal{S}_{\ddot{u}_g^i\ddot{u}_g^i}(\omega)\,\mathrm{d}\omega. \tag{2.1.47}$$

Because ground motions can be generally modelled as wide-band noises, it is reasonable to assume the seismic input $\ddot{u}_g^i(t)$ as a white noise by letting the power spectral density function $\mathcal{S}_{\ddot{u}_g^i\ddot{u}_g^i}(\omega)=\mathcal{S}_A^i$. Therefore, equation (2.1.47) can be written as

$$\mathrm{E}\big[z_k^{m,i}(t)\, z_g^{\hat{m},i}(t)\big]=\frac{\omega_0^4\,\omega_k^2}{2\pi}\,\mathcal{S}_A^i\int_{-\infty}^{\infty}\mathcal{H}_0^*(\omega)\,\mathcal{H}_0(\omega)\,\mathcal{H}_k^*(\omega)\,\mathrm{d}\omega=\frac{\omega_0^4\,\omega_k^2}{2\pi}\,\mathcal{S}_A^i\cdot I_{0k}^*, \tag{2.1.48}$$

where

$$\begin{aligned}
I_{0k}^* &= \int_{-\infty}^{\infty}\mathcal{H}_0^*(\omega)\,\mathcal{H}_0(\omega)\,\mathcal{H}_k^*(\omega)\,\mathrm{d}\omega\\
&= \int_{-\infty}^{\infty}\frac{1}{(\omega_0^2-\omega^2)^2+(2\zeta_0\omega_0\omega)^2}\cdot\frac{1}{(\omega_k^2-\omega^2)-\mathrm{i}2\zeta_k\omega_k\omega}\,\mathrm{d}\omega\\
&= \int_{-\infty}^{\infty}\frac{\omega_k^2-\omega^2}{\Delta_{0k}}\,\mathrm{d}\omega+\mathrm{i}\int_{-\infty}^{\infty}\frac{2\zeta_k\omega_k\omega}{\Delta_{0k}}\,\mathrm{d}\omega=\mathcal{R}e(I_{0k})+\mathrm{i}\,\mathcal{I}m(I_{0k}),\\
\Delta_{0k} &= \big[(\omega_0^2-\omega^2)^2+(2\zeta_0\omega_0\omega)^2\big]\cdot\big[(\omega_k^2-\omega^2)+(2\zeta_k\omega_k\omega)^2\big],
\end{aligned}$$

$\mathcal{R}e(I_{0k})$ and $\mathcal{I}m(I_{0k})$ are the real and imaginary parts of I_{0k}, respectively, and can be evaluated by the method of residue to yield (see, e.g., Xie *et al.*, 2019)

$$\mathcal{R}e(I_{0k}) = \int_{-\infty}^{\infty} \frac{\omega_k^2 - \omega^2}{\Delta_{0k}} \,\mathrm{d}\omega = \frac{\pi\,\alpha_{0k}}{2\zeta_0\omega_0^5}, \qquad \mathcal{I}m(I_{0k}) = \int_{-\infty}^{\infty} \frac{2\zeta_k\,\omega_k\,\omega}{\Delta_{0k}} \,\mathrm{d}\omega = 0, \tag{2.1.49}$$

in which

$$\alpha_{0k} = \frac{(4\zeta_0^2 - 1)^2 + 4\zeta_0\zeta_k r_k + r_k^2}{4\zeta_0\zeta_k r_k(r_k^2+1) + 4(\zeta_0^2 + \zeta_k^2)\,r_k^2 + (1-r_k^2)^2}, \quad r_k = \frac{\omega_k}{\omega_0}. \tag{2.1.50}$$

Substituting equations (2.1.49) and (2.1.50) into equation (2.1.48) gives

$$\mathrm{E}\big[z_k^{m,i}(t)\, z_{\mathrm{g}}^{\hat{m},i}(t)\big] = \frac{\omega_0^4\,\omega_k^2}{2\pi}\,\mathcal{S}_{\mathrm{A}}^i \cdot \mathcal{R}e(I_{0k}) = \frac{\omega_k^2\;\mathcal{S}_{\mathrm{A}}^i}{4\zeta_0\,\omega_0}\,\alpha_{0k} = \frac{\omega_0\,\mathcal{S}_{\mathrm{A}}^i}{4\zeta_0}\,r_k^2\,\alpha_{0k}. \tag{2.1.51}$$

The expected value of the mean-square response of $z_{\mathrm{g}}^{\hat{m},i}$, i.e., $\mathrm{E}\Big[\big\{z_{\mathrm{g}}^{\hat{m},i}(t)\big\}^2\Big]$, can be determined using the same approach. The autocorrelation function is given by

$$\mathrm{E}\big[z_{\mathrm{g}}^{\hat{m},i}(t)\, z_{\mathrm{g}}^{\hat{m},i}(t+\tau)\big] = \omega_0^4 \int_{-\infty}^{\infty}\int_{-\infty}^{\infty} h_0(\tau_1)\,h_0(\tau_2)\,\mathrm{E}\Big[\ddot{u}_{\mathrm{g}}^{\hat{m},i}(t-\tau_1)\,\ddot{u}_{\mathrm{g}}^{\hat{m},i}(t+\tau-\tau_2)\Big]\,\mathrm{d}\tau_1\,\mathrm{d}\tau_2. \tag{2.1.52}$$

Taking Fourier transform of both sides and setting $\tau_3 = \tau + \tau_1 - \tau_2$ yields

$$\mathcal{S}_{z_{\mathrm{g}}^{\hat{m},i} z_{\mathrm{g}}^{\hat{m},i}}(\omega) = \omega_0^4 \cdot \mathcal{H}_0^*(\omega) \cdot \mathcal{H}_0(\omega) \cdot \mathcal{S}_{\ddot{u}_{\mathrm{g}}^{\hat{m},i}\,\ddot{u}_{\mathrm{g}}^{\hat{m},i}}(\omega). \tag{2.1.53}$$

Taking the inverse Fourier transform of equation (2.1.53) yields

$$\mathrm{E}\big[z_{\mathrm{g}}^{\hat{m},i}(t)\, z_{\mathrm{g}}^{\hat{m},i}(t+\tau)\big] = \frac{\omega_0^4}{2\pi}\int_{-\infty}^{\infty} \mathcal{H}_0^*(\omega) \cdot \mathcal{H}_0(\omega) \cdot \mathcal{S}_{\ddot{u}_{\mathrm{g}}^i\,\ddot{u}_{\mathrm{g}}^i}(\omega)\,\mathrm{e}^{\mathrm{i}\omega\tau}\,\mathrm{d}\omega. \tag{2.1.54}$$

Setting $\tau = 0$ results in

$$\mathrm{E}\Big[\big\{z_{\mathrm{g}}^{\hat{m},i}(t)\big\}^2\Big] = \frac{\omega_0^4}{2\pi}\,\mathcal{S}_{\mathrm{A}}^i \int_{-\infty}^{\infty} \mathcal{H}_0^*(\omega)\,\mathcal{H}_0(\omega)\,\mathrm{d}\omega = \frac{\omega_0^4}{2\pi}\,\mathcal{S}_{\mathrm{A}}^i \cdot \frac{\pi}{2}\,\frac{1}{\zeta_0\omega_0^3} = \frac{\omega_0\,\mathcal{S}_{\mathrm{A}}^i}{4\zeta_0}. \tag{2.1.55}$$

From equation (8.4.43) in Xie *et al.* (2019), one has

$$\mathrm{E}\Big[\big\{z_k^{m,i}(t)\big\}^2\Big] = \frac{\omega_0\,\mathcal{S}_{\mathrm{A}}^i}{4\zeta_0}\,\beta_k \cdot r_k^4, \tag{2.1.56}$$

in which

$$\beta_k = \frac{\zeta_0 + 4\zeta_0^2\zeta_k r_k + 4\zeta_0\zeta_k^2 r_k^2 + \zeta_k r_k^3}{\zeta_k r_k^3\left(1 - 2r_k^2 + r_k^4 + 4\zeta_0\zeta_k r_k + 4\zeta_k^2 r_k^2 + 4\zeta_0^2 r_k^2 + 4\zeta_0\zeta_k r_k^3\right)}. \tag{2.1.57}$$

Using equations (2.1.48), (2.1.55), and (2.1.56), $\rho_{k0}^{m\hat{m},i}$ in equation (2.1.32) is given by

$$\rho_{k0}^{m\hat{m},i} = \frac{\mathrm{E}\left[z_k^{m,i}(t)\, z_{\mathrm{g}}^{\hat{m},i}(t)\right]}{\sqrt{\mathrm{E}\left[\left\{z_k^{m,i}(t)\right\}^2\right]\cdot \mathrm{E}\left[\left\{z_{\mathrm{g}}^{\hat{m},i}(t)\right\}^2\right]}} = \frac{\dfrac{\omega_0\, \mathcal{S}_{\mathrm{A}}^i}{4\zeta_0}\cdot r_k^2 \cdot \alpha_{0k}}{\sqrt{\dfrac{\omega_0\, \mathcal{S}_{\mathrm{A}}^i}{4\zeta_0}\,\beta_k \cdot r_k^4 \cdot \dfrac{\omega_0\, \mathcal{S}_{\mathrm{A}}^i}{4\zeta_0}}} = \frac{\alpha_{0k}}{\sqrt{\beta_k}}. \tag{2.1.58}$$

Note that $\rho_{k\kappa}^{m\hat{m},i}$ in equation (2.1.35) can be obtained from Jiang *et al.* (2015) by letting $\ddot{u}_{\mathrm{g}}^{m,i}(t) = \ddot{u}_{\mathrm{g}}^{\hat{m},i}(t) = \ddot{u}_{\mathrm{g}}^{i}(t)$, from which $\rho_{k\kappa}^{m\hat{m},i}$ can be written as

$$\rho_{k\kappa}^{m\hat{m},i} = \frac{\alpha_{k\kappa}}{\sqrt{\beta_k\beta_\kappa}}, \tag{2.1.59}$$

where $\alpha_{k\kappa}$ can be obtained using equation (2.1.60) derived by Jiang *et al.* (2015), and β_k is given by equation (2.1.57). Finally, by the assumption of Case 1, $\ddot{u}_{\mathrm{g}}^{m,i}$ and $\ddot{u}_{\mathrm{g}}^{\hat{m},i}$ are identical, which means $\rho_0^{m\hat{m},i} = 1$.

$$\alpha_{k\kappa} = \prod_{l=1}^{3} D_{k\kappa,l}^{-1} \cdot \sum_{l=0}^{4} C_{k\kappa,l}\,\zeta_0^l, \tag{2.1.60}$$

in which $C_{k\kappa,l}$ and $D_{k\kappa,l}$ are constants in terms of ζ_0, ζ_k, ζ_κ, $r_k = \omega_k/\omega_0$, and $r_\kappa = \omega_\kappa/\omega_0$, given by

$$D_{k\kappa,1} = 1 - 2r_\kappa^2 + r_\kappa^4 + 4\zeta_0\zeta_\kappa r_\kappa + 4\zeta_0\zeta_\kappa r_\kappa^3 + 4\zeta_0^2 r_\kappa^2 + 4\zeta_\kappa^2 r_\kappa^2,$$

$$D_{k\kappa,2} = 1 - 2r_k^2 + r_k^4 + 4\zeta_0\zeta_k r_k + 4\zeta_0\zeta_k r_k^3 + 4\zeta_0^2 r_k^2 + 4\zeta_k^2 r_k^2,$$

$$D_{k\kappa,3} = (r_k^2 - r_\kappa^2)^2 + 4\zeta_k\zeta_\kappa r_k r_\kappa (r_k^2 + r_\kappa^2) + 4r_k^2 r_\kappa^2(\zeta_k^2 + \zeta_\kappa^2),$$

$$C_{k\kappa,0} = (1 - r_k^2 - r_\kappa^2 + r_k^2 r_\kappa^2 + 4\zeta_k\zeta_\kappa r_k r_\kappa)\cdot D_{k\kappa,3},$$

$$\begin{aligned} C_{k\kappa,1}/4 = {} & 2\zeta_k r_k + 2\zeta_\kappa r_\kappa + 8\zeta_k\zeta_\kappa r_k r_\kappa(\zeta_k r_k + \zeta_\kappa r_\kappa) - 4(\zeta_k r_k^3 + \zeta_\kappa r_\kappa^3) + 8\zeta_k^3 r_k^3 + 8\zeta_\kappa^3 r_\kappa^3 \\ & - 2r_k r_\kappa(\zeta_k r_\kappa^3 + \zeta_\kappa r_k^3) + 8\zeta_k\zeta_\kappa r_k r_\kappa(\zeta_k r_k^3 + \zeta_\kappa r_\kappa^3) + 4r_k^2 r_\kappa^2(\zeta_k r_k + \zeta_\kappa r_\kappa) \\ & - 8r_k^2 r_\kappa^2(\zeta_k^3 r_k + \zeta_\kappa^3 r_\kappa) - 8\zeta_k\zeta_\kappa r_k^2 r_\kappa^2(\zeta_k r_\kappa + \zeta_\kappa r_k) + 32\zeta_k^2\zeta_\kappa^2 r_k^2 r_\kappa^2(\zeta_k r_k + \zeta_\kappa r_\kappa) \end{aligned}$$

$$
\begin{aligned}
&+ r_k r_\kappa(\zeta_k r_\kappa^5 + \zeta_\kappa r_k^5) + r_k^2 r_\kappa^2(\zeta_k r_k^3 + \zeta_\kappa r_\kappa^3) + 4\zeta_k\zeta_\kappa r_k^2 r_\kappa^2(\zeta_k r_\kappa^3 + \zeta_\kappa r_k^3) \\
&- 2r_k^3 r_\kappa^3(\zeta_k r_\kappa + \zeta_\kappa r_k) + 4r_k^3 r_\kappa^3(\zeta_k^3 r_\kappa + \zeta_\kappa^3 r_k) + 8\zeta_k\zeta_\kappa r_k^3 r_\kappa^3(\zeta_k r_k + \zeta_\kappa r_\kappa), \\
C_{k\kappa,2}/4 &= 8\zeta_k^2 r_k^2 + 8\zeta_\kappa^2 r_\kappa^2 + 16\zeta_k\zeta_\kappa r_k r_\kappa + 64\zeta_k^2\zeta_\kappa^2 r_k^2 r_\kappa^2 - 4\zeta_k\zeta_\kappa r_k r_\kappa(r_k^2 + r_\kappa^2) \\
&+ 32\zeta_k\zeta_\kappa r_k r_\kappa(\zeta_k^2 r_k^2 + \zeta_\kappa^2 r_\kappa^2) + 6r_k^2 r_\kappa^2 - 12r_k^2 r_\kappa^2(\zeta_k^2 + \zeta_\kappa^2) - 3(r_k^4 + r_\kappa^4) \\
&+ 8\zeta_k\zeta_\kappa r_k r_\kappa(r_k^4 + r_\kappa^4) - r_k^2 r_\kappa^2(r_k^2 + r_\kappa^2) + 8\zeta_k^2 r_k^4 + 8\zeta_\kappa^2 r_\kappa^4 + 4r_k^2 r_\kappa^2(\zeta_k^2 + \zeta_\kappa^2)(r_k^2 + r_\kappa^2) \\
&+ 16\zeta_k^2\zeta_\kappa^2 r_k^2 r_\kappa^2(r_k^2 + r_\kappa^2) + 16\zeta_k\zeta_\kappa r_k^3 r_\kappa^3(\zeta_k^2 + \zeta_\kappa^2) + r_k^6 + r_\kappa^6, \\
C_{k\kappa,3}/16 &= 8\zeta_k\zeta_\kappa r_k r_\kappa(\zeta_k r_k + \zeta_\kappa r_\kappa) + 2\zeta_k r_k^3 + 2\zeta_\kappa r_\kappa^3 + r_k r_\kappa(\zeta_k r_\kappa^3 + \zeta_\kappa r_k^3) \\
&+ 4\zeta_k\zeta_\kappa r_k r_\kappa(\zeta_k r_k^3 + \zeta_\kappa r_\kappa^3) - 2r_k^2 r_\kappa^2(\zeta_k r_k + \zeta_\kappa r_\kappa) + 4r_k^2 r_\kappa^2(\zeta_k^3 r_k + \zeta_\kappa^3 r_\kappa) \\
&+ 8\zeta_k\zeta_\kappa r_k^2 r_\kappa^2(\zeta_k r_\kappa + \zeta_\kappa r_k) + \zeta_k r_k^5 + \zeta_\kappa r_\kappa^5, \\
C_{k\kappa,4}/16 &= D_{k\kappa,3}.
\end{aligned}
$$

Case 2: Independent Seismic Excitations

This case also has important applications in nuclear power plants. For example, consider the main steam line that has some supports on the reactor building and some supports on the service building. The support excitations of the anchors on the reactor building and those on the service building can be considered as approximately independent. The coefficient of correlation is denoted as $\bar{\rho}$ for this case.

The expectation term in equation (2.1.41) becomes zero when $m \neq \hat{m}$, which leads to $\bar{\rho}_{k0}^{m\hat{m},i} = 0$. Therefore, the correlation coefficient $\bar{\rho}_{k0}^{m\hat{m},i}$ can be written as

$$\bar{\rho}_{k0}^{m\hat{m},i} = \delta_{m\hat{m}}\, \rho_{k0}^{m\hat{m},i}, \tag{2.1.61}$$

in which $\rho_{k0}^{m\hat{m},i}$ in the right hand side is given by equation (2.1.58), and $\delta_{m\hat{m}}$ denotes the Kronecker delta function, i.e., $\delta_{m\hat{m}} = 0$ if $m \neq \hat{m}$, and $\delta_{m\hat{m}} = 1$ if $m = \hat{m}$. Similarly, $\bar{\rho}_{k\kappa}^{m\hat{m},i}$ and $\bar{\rho}_{0}^{m\hat{m},i}$ can be written as

$$\bar{\rho}_{k\kappa}^{m\hat{m},i} = \delta_{m\hat{m}}\, \rho_{k\kappa}^{m\hat{m},i}, \qquad \bar{\rho}_{0}^{m\hat{m},i} = \delta_{m\hat{m}}. \tag{2.1.62}$$

As can be seen from equations (2.1.61) and (2.1.62), the correlation coefficients are zero when the earthquake excitations are from different supports.

2.1.3.3 FRSMS-SRSS Combination Rule

To verify the superiority of the proposed FRSMS-CQC combination rule, the SRSS (Square Root of Sum of Squares) combination rule is also applied to combine the FRS and the results are then compared with FRS by FRSMS-CQC combination. In FRSMS-SRSS combination rule, the correlation between FRS due to vibrational mode and ground inputs, as well as the correlation between the responses of oscillators due to ground inputs at different supports are neglected, which means that the inputs at different supports are considered as independent.

FRS in direction j at node n due to earthquake excitations in direction i can be written as

$$\left[\mathcal{S}^{i}_{\mathrm{A};n,j}(\omega_0,\zeta_0)\right]^2 = \sum_{m=1}^{M}\sum_{k=1}^{6N}\sum_{\kappa=1}^{6N}\rho^{mm,i}_{k\kappa}\,R^{m,i}_{n,j;k}\,R^{m,i}_{n,j;\kappa} + \sum_{m=1}^{M}\left[\mathcal{I}^{m,i}_{n,j}\,\mathcal{S}^{m,i}_{\mathrm{A}}(\omega_0,\zeta_0)\right]^2, \quad (2.1.63)$$

and total FRS in direction j at node n can be obtained by equation (2.1.36). Equation (2.1.63) is expressed in the form of SRSS because no correlation term between FRS due to vibrational mode and ground input is considered, and is herein referred as FRSMS-SRSS. It should be mentioned that although FRSMS-SRSS neglects some correlation parts, the correlation between the responses of oscillators excited by any two vibration modes is still considered. Thus, the main advantages of the FRS-CQC method proposed by Jiang *et al.* (2015) are still applicable. As a result, FRSMS-SRSS, although cannot provide result as accurate as FRSMS-CQC, can still give much more reliable FRS than the conventional SRSS combination rule.

2.2 Generating FRS for Structures under Multiple Excitations Considering SSI

A general formulation is derived based on the substructure method in this chapter. The substructure method is an analytical technique that converts the Foundation Input Response Spectra (FIRS) obtained from site response analyses, represented by the tri-directional free-field motion, into Foundation Level Input Response Spectra (FLIRS). In this method, the interface between foundation and structure is simplified as a set of generalized soil springs to consider the effect of SSI. These FLIRS can subsequently be input as seismic excitations

in the direct spectra-to-spectra method for generating floor response spectra (FRS). The necessary inputs for this approach are the geometry of the structure, the dynamic soil stiffness, and basic modal information, such as natural frequencies and modal shapes.

2.2.1 Substructure Method

2.2.1.1 Dynamic Stiffness Matrix

For an MDOF linear system, the equation of motion is of the form

$$\mathbf{M}\ddot{\mathbf{x}}(t) + \mathbf{C}\dot{\mathbf{x}}(t) + \mathbf{K}\mathbf{x}(t) = \mathbf{p}(t), \tag{2.2.1}$$

where $\mathbf{M}$, $\mathbf{C}$, $\mathbf{K}$ are the mass, damping, and stiffness matrices, respectively, $\mathbf{p}(t)$ is the load vector, and $\mathbf{x}(t)$ is the response vector. Under harmonic excitation $\mathbf{p}(t) = \mathbf{P}e^{i\omega t}$, the response $\mathbf{x}(t)$ can be expressed as $\mathbf{x}(t) = \mathbf{X}e^{i\omega t}$, and equation (2.2.1) becomes

$$\mathbf{S}\mathbf{X} = \mathbf{P}, \qquad \mathbf{S} = -\omega^2\mathbf{M} + i\omega\mathbf{C} + \mathbf{K}, \tag{2.2.2}$$

where $\mathbf{S}$ is the frequency-dependent *dynamic stiffness matrix*. In terms of the dynamic stiffness matrix, equation of motion (2.2.1) can be expressed as an equation of dynamic equilibrium (2.2.2).

2.2.1.2 Substructure Model for Flexible Foundation

A coupled soil–structure model is shown in Figure 2.2. Let $\mathbf{U}_{\mathrm{R}}$ and $\mathbf{U}_{\mathrm{B}}$ be amplitudes of the absolute displacement vectors of the structure and foundation, respectively, where the subscript "R" stands for the "Response" DOF (nodes), which are not in contact with the soil, the subscript "B" stands for the "Boundary" DOF (nodes), which are on the boundary of soil–structure interface, and the superscript "S" stands for "Structure". The equation of dynamic equilibrium of the structure is given by

$$\begin{bmatrix} \mathbf{S}^{\mathrm{S}}_{\mathrm{RR}} & \mathbf{S}^{\mathrm{S}}_{\mathrm{RB}} \\ \mathbf{S}^{\mathrm{S}}_{\mathrm{BR}} & \mathbf{S}^{\mathrm{S}}_{\mathrm{BB}} \end{bmatrix} \begin{Bmatrix} \mathbf{U}_{\mathrm{R}} \\ \mathbf{U}_{\mathrm{B}} \end{Bmatrix} = \begin{Bmatrix} \mathbf{P}_{\mathrm{R}} \\ \mathbf{P}_{\mathrm{B}} \end{Bmatrix}, \tag{2.2.3}$$

where $\mathbf{P}_{\mathrm{R}}$ is the amplitude vector of the loads applied on the response nodes of the structure, and $\mathbf{P}_{\mathrm{B}}$ is the amplitude vector of the interaction forces between the structure and soil. For earthquake excitation, the nodes of the structure not in contact with the soil are not loaded, i.e., $\mathbf{P}_{\mathrm{R}} = \mathbf{0}$.

Let $\mathbf{S}_{BB}^{G}$ be the dynamic stiffness matrix of the soil with excavation, and $\mathbf{U}_{B}^{G}$ be the amplitudes of absolute displacement vector of the soil with excavation under the earthquake excitation. The superscript "G" stands for "Ground" or the soil with excavation. The interaction forces of the soil depend on the relative motion between the foundation (base) and the soil at the interface, i.e.,

$$\mathbf{P}_{B} = \mathbf{S}_{BB}^{G}\,(\mathbf{U}_{B}^{G} - \mathbf{U}_{B}). \tag{2.2.4}$$

Equation (2.2.3) becomes

$$\begin{bmatrix} \mathbf{S}_{RR}^{S} & \mathbf{S}_{RB}^{S} \\ \mathbf{S}_{BR}^{S} & \mathbf{S}_{BB}^{S} + \mathbf{S}_{BB}^{G} \end{bmatrix} \begin{Bmatrix} \mathbf{U}_{R} \\ \mathbf{U}_{B} \end{Bmatrix} = \begin{Bmatrix} \mathbf{0} \\ \mathbf{S}_{BB}^{G}\,\mathbf{U}_{B}^{G} \end{Bmatrix}. \tag{2.2.5}$$

The earthquake excitation is characterized by $\mathbf{U}_{B}^{G}$, which is the motion of the nodes on the soil–structure interface of the soil with excavation. It is desirable to replace $\mathbf{U}_{B}^{G}$ by the free-field motion $\mathbf{U}_{B}^{F}$ that does not depend on the excavation.

2.2.1.3 Free-Field Soil Model

The free-field soil can be divided into the excavated soil and the soil with excavation as shown in Figure 2.2. Regarding the excavated soil as a "structure" and referring to equation (2.2.5), one has $\tilde{\mathbf{U}}_{B} = \mathbf{U}_{B}^{F}$, $\tilde{\mathbf{S}}_{BR}^{S} = \mathbf{0}$, and hence $\tilde{\mathbf{S}}_{BB}^{S} = \mathbf{S}_{BB}^{E}$, which is the dynamic stiffness matrix of the excavated soil. The superscript "E" stands for "Excavated soil". The second block-row of equation (2.2.5) gives

$$\begin{bmatrix} \tilde{\mathbf{S}}_{BR}^{S} & \tilde{\mathbf{S}}_{BB} + \mathbf{S}_{BB}^{G} \end{bmatrix} \begin{Bmatrix} \times \\ \mathbf{U}_{B}^{F} \end{Bmatrix} = \left\{ \mathbf{S}_{BB}^{G}\,\mathbf{U}_{B}^{G} \right\} \implies (\mathbf{S}_{BB}^{E} + \mathbf{S}_{BB}^{G})\mathbf{U}_{B}^{F} = \mathbf{S}_{BB}^{G}\,\mathbf{U}_{B}^{G}. \tag{2.2.6}$$

Adding the excavated soil to the soil with excavation leads to the free-field system, i.e.,

$$\mathbf{S}_{BB}^{E} + \mathbf{S}_{BB}^{G} = \mathbf{S}_{BB}^{F}, \quad \text{or} \quad \mathbf{S}_{BB}^{G} = \mathbf{S}_{BB}^{F} - \mathbf{S}_{BB}^{E}. \tag{2.2.7}$$

Hence, equation (2.2.6) can be written as

$$\mathbf{S}_{BB}^{F}\,\mathbf{U}_{B}^{F} = \mathbf{S}_{BB}^{G}\,\mathbf{U}_{B}^{G}, \tag{2.2.8}$$

in which $\mathbf{S}_{BB}^{F}$ is the dynamic stiffness matrix of the free-field discretized at the nodes where the structure is inserted, and $\mathbf{U}_{B}^{F}$ is the free-field motion at the nodes of the soil–structure

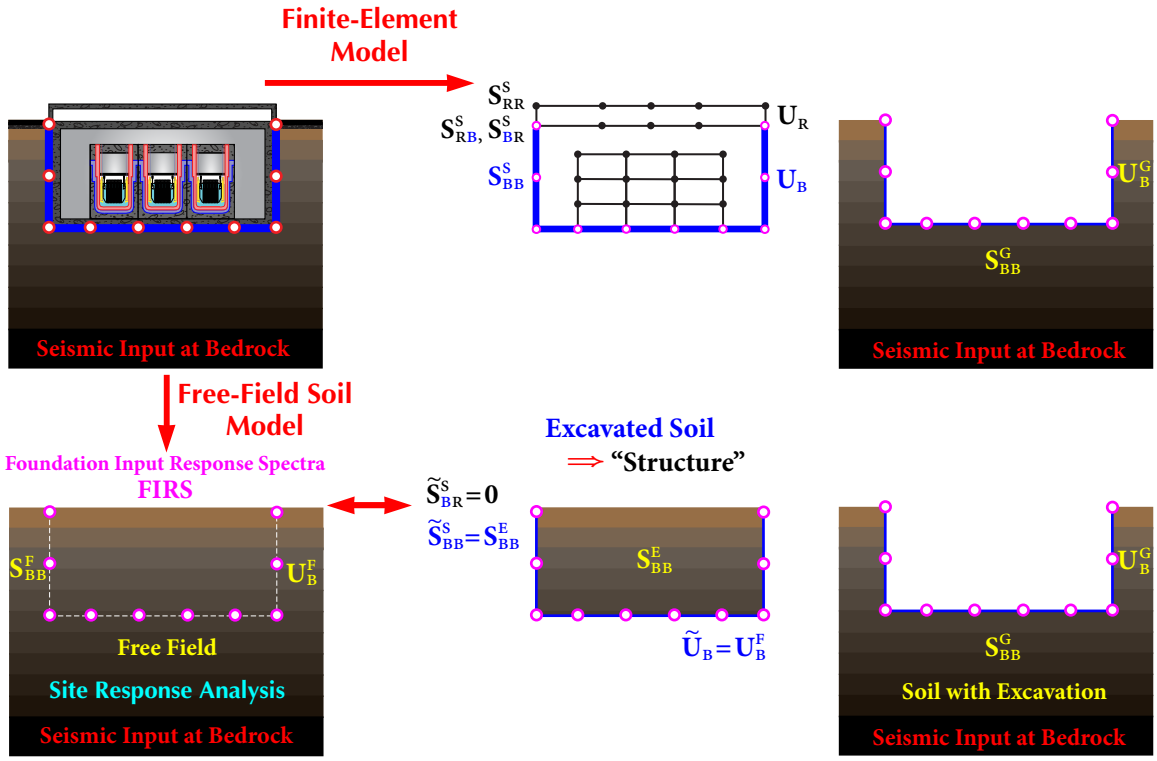


Figure 2.2 Substructural model for flexible foundation.

interface. Hence, $\mathbf{U}_B^F$ is the free-field response of the soil at the foundation level; the acceleration response spectra of $\ddot{\mathbf{u}}_B^F$ are the FIRS, which can be obtained from a site response analysis of the free-field.

Using (2.2.8), equation (2.2.5) becomes

$$\begin{bmatrix} \mathbf{S}_{RR}^S & \mathbf{S}_{RB}^S \\ \mathbf{S}_{BR}^S & \mathbf{S}_{BB}^S + \mathbf{S}_{BB}^G \end{bmatrix} \begin{Bmatrix} \mathbf{U}_R \\ \mathbf{U}_B \end{Bmatrix} = \begin{Bmatrix} \mathbf{0} \\ \mathbf{S}_{BB}^F \mathbf{U}_B^F \end{Bmatrix}. \tag{2.2.9}$$

This is the equation of motion of the structure supported on a *generalized soil spring* characterized by the dynamic stiffness matrix $\mathbf{S}_{BB}^G$, and the other end of the spring is subjected to earthquake excitation $\mathbf{U}_B^F$, which is free-field response at the foundation level. Using (2.2.7), equation (2.2.9) can also be written as

$$\begin{bmatrix} \mathbf{S}_{RR}^S & \mathbf{S}_{RB}^S \\ \mathbf{S}_{BR}^S & (\mathbf{S}_{BB}^S - \mathbf{S}_{BB}^E) + \mathbf{S}_{BB}^F \end{bmatrix} \begin{Bmatrix} \mathbf{U}_R \\ \mathbf{U}_B \end{Bmatrix} = \begin{Bmatrix} \mathbf{0} \\ \mathbf{S}_{BB}^F \mathbf{U}_B^F \end{Bmatrix}. \tag{2.2.10}$$

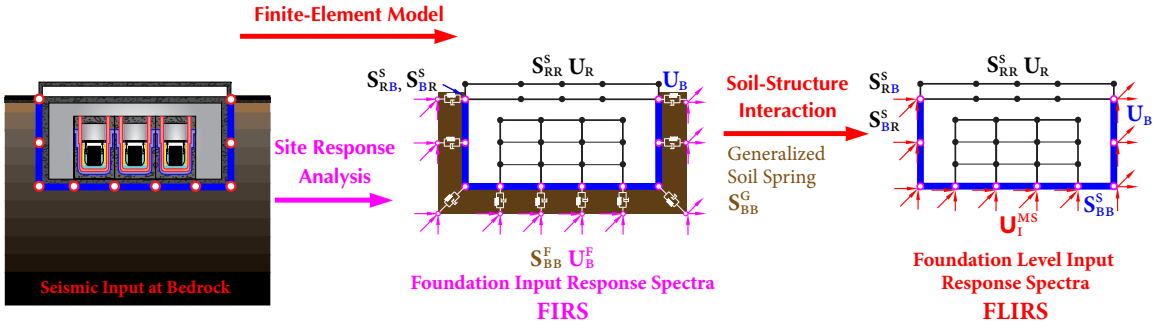


Figure 2.3 SSI using FLIRS for flexible foundation.

☞ A generalized soil spring, characterized by the dynamic stiffness matrix $\mathbf{S}_{BB}^{G}$, is not an elastic spring in the ordinary sense characterized by spring constant k.

2.2.1.4 *Structure with Multiple Support Excitations*

With $\mathbf{P}_R = \mathbf{0}$, the first block-row of equation (2.2.3) becomes

$$\mathbf{S}_{RR}^{S}\mathbf{U}_R + \mathbf{S}_{RB}^{S}\mathbf{U}_B = \mathbf{0} \implies \mathbf{U}_R = \mathbf{s}^{MS}\mathbf{U}_B, \quad \mathbf{s}^{MS} = -\left(\mathbf{S}_{RR}^{S}\right)^{-1}\mathbf{S}_{RB}^{S}, \tag{2.2.11}$$

where $\mathbf{s}^{MS}$ is the dynamic stiffness matrix for analysis of the structure with multiple support excitations, with the superscript "MS" standing for "Multiple Supports".

In seismic analysis and design, only translational ground motions are considered, while rotational ground motions are not considered. Reorganize vector $\mathbf{U}_R$ and rewrite $\mathbf{U}_B$ as

$$\mathbf{U}_R = \begin{Bmatrix} \mathbf{U}_{R,T} \\ \mathbf{U}_{R,R} \end{Bmatrix}_{6N\times 1}, \qquad \mathbf{U}_B = \begin{Bmatrix} \mathbf{U}_I^{MS} \\ \mathbf{0} \end{Bmatrix}_{6\times 1}, \tag{2.2.12}$$

where the subscripts "T" and "R" stand for "Translational" and "Rotational" DOF, respectively. $\mathbf{U}_I^{MS}$ is the vector of seismic excitations in the three orthogonal translational directions at the multiple input nodes. Note that each "boundary" node "B" has six DOF; when seismic excitations at the soil–structure are considered, they are referred as "Input" nodes "I" with seismic excitations in the three orthogonal translational directions.

Rearranging and partitioning $\mathbf{s}^{MS}$ accordingly, one has

$$\mathbf{s}^{MS} = \begin{bmatrix} \mathbf{S}_{TT}^{MS} & \mathbf{S}_{TR}^{MS} \\ \mathbf{S}_{RT}^{MS} & \mathbf{S}_{RR}^{MS} \end{bmatrix}_{6N\times 6}, \tag{2.2.13}$$

in which each submatrix is of dimension $3N\times 3M$. Equation (2.2.11) can be written as

$$\begin{Bmatrix} \mathbf{U}_{\mathrm{R,T}} \\ \mathbf{U}_{\mathrm{R,R}} \end{Bmatrix} = \begin{bmatrix} \mathbf{S}_{\mathrm{TT}}^{\mathrm{MS}} & \mathbf{S}_{\mathrm{TR}}^{\mathrm{MS}} \\ \mathbf{S}_{\mathrm{RT}}^{\mathrm{MS}} & \mathbf{S}_{\mathrm{RR}}^{\mathrm{MS}} \end{bmatrix} \begin{Bmatrix} \mathbf{U}_{\mathrm{I}}^{\mathrm{MS}} \\ \mathbf{0} \end{Bmatrix} = \begin{Bmatrix} \mathbf{S}_{\mathrm{TT}}^{\mathrm{MS}}\mathbf{U}_{\mathrm{I}}^{\mathrm{MS}} \\ \mathbf{S}_{\mathrm{RT}}^{\mathrm{MS}}\mathbf{U}_{\mathrm{I}}^{\mathrm{MS}} \end{Bmatrix}. \tag{2.2.14}$$

Multiplying the first block-row of equation (2.2.14) by $\left(\mathbf{S}_{\mathrm{TT}}^{\mathrm{MS}}\right)^T$ yields

$$\left(\mathbf{S}_{\mathrm{TT}}^{\mathrm{MS}}\right)^T \mathbf{U}_{\mathrm{R,T}} = \left[\left(\mathbf{S}_{\mathrm{TT}}^{\mathrm{MS}}\right)^T \mathbf{S}_{\mathrm{TT}}^{\mathrm{MS}}\right] \mathbf{U}_{\mathrm{I}}^{\mathrm{MS}}. \tag{2.2.15}$$

The reason for performing this manipulation is to make $\left[\left(\mathbf{S}_{\mathrm{TT}}^{\mathrm{MS}}\right)^T \mathbf{S}_{\mathrm{TT}}^{\mathrm{MS}}\right]$ a square matrix of dimension $3M\times 3M$, the purpose of which will be clear in Section 3.2.

The tridirectional (translational) acceleration response spectra $\mathbf{U}_{\mathrm{I}}^{\mathrm{MS}}$ applied at multiple supports (nodes) of the flexible foundation of a structure are called *Foundation Level Input Response Spectra* (FLIRS), as illustrated in Figure 2.3. It is important to note that FLIRS are different from the *Foundation Input Response Spectra* (FIRS), which are the acceleration response spectra at the elevation of the foundation of the *free-field*, as shown in Figure 2.3.

2.2.2 Foundation Level Input Response Spectra (FLIRS)

It is desirable to determine the equivalent FLIRS for a structure with seismic excitations at multiple supports in seismic design and assessment. In SSI analysis, a seismic analysis of structures with multiple supports can be performed using the equivalent FLIRS as the seismic input, instead of a coupled soil–structure analysis using FIRS as the seismic input.

From the first block-row of equation (2.2.10), one obtains

$$\mathbf{U}_{\mathrm{R}} = -\left(\mathbf{S}_{\mathrm{RR}}^{\mathrm{S}}\right)^{-1}\mathbf{S}_{\mathrm{RB}}^{\mathrm{S}}\,\mathbf{U}_{\mathrm{B}} = \mathbf{S}^{\mathrm{MS}}\mathbf{U}_{\mathrm{B}}. \tag{2.2.16}$$

From the second block-row of equation (2.2.10), one has

$$\mathbf{S}_{\mathrm{BR}}^{\mathrm{S}}\,\mathbf{U}_{\mathrm{R}} + \left[\left(\mathbf{S}_{\mathrm{BB}}^{\mathrm{S}} - \mathbf{S}_{\mathrm{BB}}^{\mathrm{E}}\right) + \mathbf{S}_{\mathrm{BB}}^{\mathrm{F}}\right]\mathbf{U}_{\mathrm{B}} = \mathbf{S}_{\mathrm{BB}}^{\mathrm{F}}\,\mathbf{U}_{\mathrm{B}}^{\mathrm{F}}. \tag{2.2.17}$$

Substituting equation (2.2.16) into (2.2.17) yields

$$\mathbf{S}_{\mathrm{BR}}^{\mathrm{S}}\,\mathbf{S}^{\mathrm{MS}}\mathbf{U}_{\mathrm{B}} + \left[\left(\mathbf{S}_{\mathrm{BB}}^{\mathrm{S}} - \mathbf{S}_{\mathrm{BB}}^{\mathrm{E}}\right) + \mathbf{S}_{\mathrm{BB}}^{\mathrm{F}}\right]\mathbf{U}_{\mathrm{B}} = \mathbf{S}_{\mathrm{BB}}^{\mathrm{F}}\,\mathbf{U}_{\mathrm{B}}^{\mathrm{F}},$$

which gives

$$\underbrace{\mathbf{U}_{\mathrm{B}}}_{6M\times 1} = \underbrace{\mathbf{S}^{-1}}_{6M\times 6M}\ \underbrace{\mathbf{S}^{\mathrm{F}}_{\mathrm{BB}}}_{6M\times 6M}\ \underbrace{\mathbf{U}^{\mathrm{F}}_{\mathrm{B}}}_{6M\times 1}, \qquad \mathbf{S} = \underbrace{\mathbf{S}^{\mathrm{S}}_{\mathrm{BR}}}_{6M\times 6N}\ \underbrace{\mathbf{S}^{\mathrm{MS}}}_{6N\times 6M} + \underbrace{\left(\mathbf{S}^{\mathrm{S}}_{\mathrm{BB}} - \mathbf{S}^{\mathrm{E}}_{\mathrm{BB}}\right) + \mathbf{S}^{\mathrm{F}}_{\mathrm{BB}}}_{6M\times 6M}. \tag{2.2.18}$$

Note that $\mathbf{S}^{-1}\mathbf{S}^{\mathrm{F}}_{\mathrm{BB}}$ is a square matrix of dimension $6M\times 6M$; partition it as follows:

$$\mathbf{S}^{-1}\mathbf{S}^{\mathrm{F}}_{\mathrm{BB}} = \mathbf{T} = \begin{bmatrix} \mathbf{T}_{\mathrm{TT}} & \mathbf{T}_{\mathrm{TR}} \\ \mathbf{T}_{\mathrm{RT}} & \mathbf{T}_{\mathrm{RR}} \end{bmatrix}_{6M\times 6M}, \tag{2.2.19}$$

in which each submatrix is of dimension $3M\times 3M$.

In a site response analysis, the soil medium is modelled as a series of infinite layers on a half-space, and the rotational responses of free-field should be very small under the translational excitation at bedrock. Hence, the rotational input at foundation level is negligible compared to the translational input; the rotational input is usually not given by a site response analysis and is taken as 0.

From equations (2.2.16) and (2.2.18), one has

$$\mathbf{U}_{\mathrm{R}} = \mathbf{S}^{\mathrm{MS}}\,\mathbf{T}\,\mathbf{U}^{\mathrm{F}}_{\mathrm{B}}, \tag{2.2.20}$$

i.e.,

$$\begin{aligned} \begin{Bmatrix} \mathbf{U}_{\mathrm{R,T}} \\ \mathbf{U}_{\mathrm{R,R}} \end{Bmatrix}_{6N\times 1} &= \begin{bmatrix} \mathbf{S}^{\mathrm{MS}}_{\mathrm{TT}} & \mathbf{S}^{\mathrm{MS}}_{\mathrm{TR}} \\ \mathbf{S}^{\mathrm{MS}}_{\mathrm{RT}} & \mathbf{S}^{\mathrm{MS}}_{\mathrm{RR}} \end{bmatrix}_{6N\times 6M} \begin{bmatrix} \mathbf{T}_{\mathrm{TT}} & \mathbf{T}_{\mathrm{TR}} \\ \mathbf{T}_{\mathrm{RT}} & \mathbf{T}_{\mathrm{RR}} \end{bmatrix}_{6M\times 6M} \begin{Bmatrix} \mathbf{U}^{\mathrm{F}}_{\mathrm{B,T}} \\ \mathbf{0} \end{Bmatrix}_{6M\times 1}, \qquad \mathbf{U}^{\mathrm{F}}_{\mathrm{B,T}} = \mathbf{U}^{\mathrm{F}}_{\mathrm{I}}, \\ &= \begin{bmatrix} \mathbf{S}^{\mathrm{MS}}_{\mathrm{TT}} & \mathbf{S}^{\mathrm{MS}}_{\mathrm{TR}} \\ \mathbf{S}^{\mathrm{MS}}_{\mathrm{RT}} & \mathbf{S}^{\mathrm{MS}}_{\mathrm{RR}} \end{bmatrix} \begin{bmatrix} \mathbf{T}_{\mathrm{TT}}\,\mathbf{U}^{\mathrm{F}}_{\mathrm{I}} \\ \mathbf{T}_{\mathrm{RT}}\,\mathbf{U}^{\mathrm{F}}_{\mathrm{I}} \end{bmatrix} = \begin{Bmatrix} \mathbf{S}^{\mathrm{MS}}_{\mathrm{TT}}\mathbf{T}_{\mathrm{TT}}\,\mathbf{U}^{\mathrm{F}}_{\mathrm{I}} + \mathbf{S}^{\mathrm{MS}}_{\mathrm{TR}}\mathbf{T}_{\mathrm{RT}}\,\mathbf{U}^{\mathrm{F}}_{\mathrm{I}} \\ \mathbf{S}^{\mathrm{MS}}_{\mathrm{RT}}\mathbf{T}_{\mathrm{TT}}\,\mathbf{U}^{\mathrm{F}}_{\mathrm{I}} + \mathbf{S}^{\mathrm{MS}}_{\mathrm{RR}}\mathbf{T}_{\mathrm{RT}}\,\mathbf{U}^{\mathrm{F}}_{\mathrm{I}} \end{Bmatrix}. \end{aligned} \tag{2.2.21}$$

Note that it is not possible to have a single set of tridirectional translational FLIRS in a dynamic analysis of a structure under seismic excitations at multiple supports to give both correct translational responses $\mathbf{U}_{\mathrm{R,T}}$ and rotational responses $\mathbf{U}_{\mathrm{R,R}}$. In generating FRS, only translational responses are needed; hence, from the first block-row of equation (2.2.21), one has

$$\mathbf{U}_{\mathrm{R,T}} = \mathbf{S}^{\mathrm{MS}}_{\mathrm{TT}}\mathbf{T}_{\mathrm{TT}}\,\mathbf{U}^{\mathrm{F}}_{\mathrm{I}} + \mathbf{S}^{\mathrm{MS}}_{\mathrm{TR}}\mathbf{T}_{\mathrm{RT}}\,\mathbf{U}^{\mathrm{F}}_{\mathrm{I}}. \tag{2.2.22}$$

Multiplying $\left(\mathbf{S}_{TT}^{MS}\right)^T$ from the left yields

$$\begin{aligned}\left(\mathbf{S}_{TT}^{MS}\right)^T \mathbf{U}_{R,T} &= \left\{\left(\mathbf{S}_{TT}^{MS}\right)^T \mathbf{S}_{TT}^{MS} \mathbf{T}_{TT} + \left(\mathbf{S}_{TT}^{MS}\right)^T \mathbf{S}_{TR}^{MS} \mathbf{T}_{RT}\right\} \mathbf{U}_I^F \\ &= \left[\left(\mathbf{S}_{TT}^{MS}\right)^T \mathbf{S}_{TT}^{MS}\right] \left\{\mathbf{T}_{TT} + \left[\left(\mathbf{S}_{TT}^{MS}\right)^T \mathbf{S}_{TT}^{MS}\right]^{-1} \left(\mathbf{S}_{TT}^{MS}\right)^T \mathbf{S}_{TR}^{MS} \mathbf{T}_{RT}\right\} \mathbf{U}_I^F . \\ &= \left[\left(\mathbf{S}_{TT}^{MS}\right)^T \mathbf{S}_{TT}^{MS}\right] \boldsymbol{\mathcal{T}} \mathbf{U}_I^F , \end{aligned} \tag{2.2.23}$$

where

$$\underbrace{\boldsymbol{\mathcal{T}}}_{3M\times 3M} = \underbrace{\mathbf{T}_{TT}}_{3M\times 3M} + \underbrace{\left[\left(\mathbf{S}_{TT}^{MS}\right)^T \mathbf{S}_{TT}^{MS}\right]^{-1}}_{(3M\times 3N)\times(3N\times 3M)} \underbrace{\left(\mathbf{S}_{TT}^{MS}\right)^T}_{3M\times 3N} \underbrace{\mathbf{S}_{TR}^{MS}}_{3N\times 3M} \underbrace{\mathbf{T}_{RT}}_{3M\times 3M} . \tag{2.2.24}$$

The first and second terms of $\boldsymbol{\mathcal{T}}$ denote the contributions from the translational and rotational motions of the foundation in the soil–structure system, respectively. Because $\left[\left(\mathbf{S}_{TT}^{MS}\right)^T \mathbf{S}_{TT}^{MS}\right]$ is a square matrix of dimension $3M\times 3M$, it is relative easy to determine its inverse because M is much smaller than N. Thus, the purpose of the transformation in equation (2.2.15) becomes evident.

Comparing equations (2.2.23) and (2.2.15), one obtains the equivalent FLIRS as

$$\mathbf{U}_I^{MS} = \boldsymbol{\mathcal{T}} \mathbf{U}_I^F . \tag{2.2.25}$$

It is important to emphasize that, although the FLIRS $\mathbf{U}_I^{MS}$ would not give correct rotational responses $\mathbf{U}_{R,R}$ of a structure, it gives exact translational responses $\mathbf{U}_{R,T}$ and hence exact FRS because only translational responses are required to generate FRS. Therefore, a dynamic analysis of the structure under the seismic excitations of FLIRS $\mathbf{U}_I^{MS}$ at multiple supports gives exactly the same FRS as a full coupled soil–structure analysis under the seismic excitations of FIRS $\mathbf{U}_I^F$.

Based on the theory of random vibration, the relationship between the PSD functions of $\mathbf{U}_I^{MS}$ and $\mathbf{U}_I^F$ can be determined by (Lin, 1967)

$$\boldsymbol{\mathcal{S}}_{\ddot{U}\ddot{U}}^{MS}(\omega) = \boldsymbol{\mathcal{T}}(\omega)\, \boldsymbol{\mathcal{S}}_{\ddot{U}\ddot{U}}^{F}(\omega)\, \tilde{\boldsymbol{\mathcal{T}}}(\omega), \tag{2.2.26}$$

where $\boldsymbol{\mathcal{S}}_{\ddot{U}\ddot{U}}^{MS}(\omega)$ and $\boldsymbol{\mathcal{S}}_{\ddot{U}\ddot{U}}^{F}(\omega)$ are $3M\times 3M$ matrices of the cross PSD functions of $\ddot{\mathbf{U}}_I^{MS}$ and $\ddot{\mathbf{U}}_I^F$, respectively. $\tilde{\boldsymbol{\mathcal{T}}}(\omega)$ denotes the complex conjugate and transpose of the transfer

function $\boldsymbol{\mathcal{T}}(\omega)$. The terms in the main diagonals of $\boldsymbol{\mathcal{S}}_{\ddot{U}\ddot{U}}^{\mathrm{MS}}(\omega)$ and $\boldsymbol{\mathcal{S}}_{\ddot{U}\ddot{U}}^{\mathrm{F}}(\omega)$ represent the auto-PSD functions of FLIRS and FIRS, respectively, while the other terms indicate the cross-PSD functions of FLIRS and FIRS, respectively. Let $\mathcal{S}_{\ddot{U}\ddot{U};\,m,i}^{\mathrm{MS};\hat{m},\hat{i}}(\omega)$ denotes the element of the (m,i)-th row, $(\hat{m},\hat{i})$-th column or $[3(m-1)+i]$-th row, $[3(\hat{m}-1)+\hat{i}]$-th column of $\boldsymbol{\mathcal{S}}_{\ddot{U}\ddot{U}}^{\mathrm{MS}}(\omega)$. From equation (2.2.26), the elements in the cross-PSD functions can be written as

$$\mathcal{S}_{\ddot{U}\ddot{U};\,m,i}^{\mathrm{MS};\hat{m},\hat{i}}(\omega) = \boldsymbol{\mathcal{T}}_{m,i}(\omega)\,\boldsymbol{\mathcal{S}}_{\ddot{U}\ddot{U}}^{\mathrm{F}}(\omega)\,\tilde{\boldsymbol{\mathcal{T}}}^{\hat{m},\hat{i}}(\omega) = \sum_{p=1}^{3M}\sum_{q=1}^{3M}\mathcal{T}_{m,i}^{p}(\omega)\,\mathcal{S}_{\ddot{U}\ddot{U};\,p}^{\mathrm{F};\,q}(\omega)\,\tilde{\mathcal{T}}_{q}^{\hat{m},\hat{i}}(\omega), \quad (2.2.27)$$

where $\mathcal{T}_{m,i}^{p}(\omega)$ and $\tilde{\mathcal{T}}_{q}^{\hat{m},\hat{i}}(\omega)$ are the (m,i)-th row, p-th column of $\boldsymbol{\mathcal{T}}(\omega)$ and q-th row, $(\hat{m},\hat{i})$-th column of $\tilde{\boldsymbol{\mathcal{T}}}(\omega)$, respectively. When $m=\hat{m}$ and $i=\hat{i}$, the term $\mathcal{S}_{\ddot{U}\ddot{U};\,m,i}^{\mathrm{MS};\hat{m},\hat{i}}(\omega)$ becomes $\mathcal{S}_{\ddot{U}\ddot{U};\,m,i}^{\mathrm{MS};m,i}(\omega)$, i.e., the auto-PSD of FLIRS at support m in direction i, denoted as $\mathcal{S}_{\ddot{U}\ddot{U}}^{\mathrm{MS};m,i}(\omega)$ for convenience.

The mean-square response of an SDOF oscillator $(\omega_0,\,\zeta_0)$ under a base excitation $\ddot{U}_{m,i}^{\mathrm{F}}$ can be obtained by

$$\mathrm{E}\Big[\Big\{\ddot{R}_0^{\mathrm{F};m,i}(t)\Big\}^2\Big] = \frac{1}{2\pi}\int_{-\infty}^{\infty}\left|\omega_0^2\,\mathcal{H}(\omega)\right|^2\mathcal{S}_{\ddot{U}\ddot{U}}^{\mathrm{F};m,i}(\omega)\,\mathrm{d}\omega, \quad (2.2.28)$$

where

$$\mathcal{H}(\omega) = \frac{1}{(\omega_0^2-\omega^2)+\mathrm{i}2\zeta_0\omega_0\omega} \quad (2.2.29)$$

is the complex frequency response function of the SDOF oscillator $(\omega_0,\,\zeta_0)$ with respect to base excitation. Similarly, the mean-square response of an SDOF oscillator $(\omega_0,\,\zeta_0)$ under a base excitation $\ddot{U}_{m,i}^{\mathrm{MS}}$ can be obtained by

$$\begin{aligned}\mathrm{E}\Big[\Big\{\ddot{R}_0^{\mathrm{MS};m,i}(t)\Big\}^2\Big] &= \frac{1}{2\pi}\int_{-\infty}^{\infty}\left|\omega_0^2\,\mathcal{H}(\omega)\right|^2\mathcal{S}_{\ddot{U}\ddot{U}}^{\mathrm{MS};m,i}(\omega)\,\mathrm{d}\omega \\ &= \frac{1}{2\pi}\int_{-\infty}^{\infty}\left|\omega_0^2\,\mathcal{H}(\omega)\right|^2\sum_{p=1}^{3M}\sum_{q=1}^{3M}\mathcal{T}_{m,i}^{p}(\omega)\,\mathcal{S}_{\ddot{U}\ddot{U};\,p}^{\mathrm{F};\,q}(\omega)\,\tilde{\mathcal{T}}_{q}^{m,i}(\omega)\;\mathrm{d}\omega. \quad (2.2.30)\end{aligned}$$

The ratio between the mean square response of an SDOF oscillator under base excitation $\ddot{U}_{m,i}^{\mathrm{F}}$ and that under base excitation $\ddot{U}_{m,i}^{\mathrm{MS}}$ can be determined by

$$\left[\mathcal{R}^{m,i}(\omega_0,\zeta_0)\right]^2 = \frac{\mathrm{E}\Big[\Big\{\ddot{R}_0^{\mathrm{MS};m,i}(t)\Big\}^2\Big]}{\mathrm{E}\Big[\Big\{\ddot{R}_0^{\mathrm{F};m,i}(t)\Big\}^2\Big]}$$

$$= \frac{\dfrac{1}{2\pi}\displaystyle\int_{-\infty}^{\infty} \left|\omega_0^2\,\mathcal{H}(\omega)\right|^2 \sum_{p=1}^{3M}\sum_{q=1}^{3M} \mathcal{T}_{m,i}^{p}(\omega)\,\mathcal{S}_{\ddot{U}\ddot{U};\,p}^{\mathrm{F};\,q}(\omega)\,\tilde{\mathcal{T}}_{q}^{m,i}(\omega)\;\mathrm{d}\omega}{\dfrac{1}{2\pi}\displaystyle\int_{-\infty}^{\infty} \left|\omega_0^2\,\mathcal{H}(\omega)\right|^2 \mathcal{S}_{\ddot{U}\ddot{U}}^{\mathrm{F};m,i}(\omega)\,\mathrm{d}\omega}$$

$$= \frac{\displaystyle\int_{-\infty}^{\infty} \left|\mathcal{H}(\omega)\right|^2 \sum_{p=1}^{3M}\sum_{q=1}^{3M} \mathcal{T}_{m,i}^{p}(\omega)\,\mathcal{S}_{\ddot{U}\ddot{U};\,p}^{\mathrm{F};\,q}(\omega)\,\tilde{\mathcal{T}}_{q}^{m,i}(\omega)\;\mathrm{d}\omega}{\displaystyle\int_{-\infty}^{\infty} \left|\mathcal{H}(\omega)\right|^2 \mathcal{S}_{\ddot{U}\ddot{U}}^{\mathrm{F};m,i}(\omega)\,\mathrm{d}\omega}. \tag{2.2.31}$$

The maximum response of an SDOF oscillator, which is by the definition of the response spectrum, is usually related to its root-mean-square response through a peak factor as

$$\mathcal{S}_{\mathrm{A}}(\omega_0,\zeta_0) = \left|\ddot{R}_0(t)\right|_{\max} = \mathcal{P}\!\mathit{f} \cdot \sqrt{\mathrm{E}\left[\ddot{R}_0^2(t)\right]}. \tag{2.2.32}$$

Combining equations (2.2.31) and (2.2.32) yields the tridirectional FLIRS in direction i of input node m for a structure with multiple supports

$$\mathcal{S}_{\mathrm{A}}^{\mathrm{MS};m,i}(\omega_0,\zeta_0) = \frac{\mathcal{P}\!\mathit{f}^{\mathrm{MS}}}{\mathcal{P}\!\mathit{f}^{\mathrm{F}}}\;\mathcal{R}^{m,i}(\omega_0,\zeta_0)\;\mathcal{S}_{\mathrm{A}}^{\mathrm{F};m,i}(\omega_0,\zeta_0). \tag{2.2.33}$$

For responses in earthquake engineering, the values of peak factors $\mathcal{P}\!\mathit{f}^{\mathrm{MS}}$ and $\mathcal{P}\!\mathit{f}^{\mathrm{F}}$ do not differ significantly, i.e., $\mathcal{P}\!\mathit{f}^{\mathrm{MS}} \approx \mathcal{P}\!\mathit{f}^{\mathrm{F}}$. Hence

$$\mathcal{S}_{\mathrm{A}}^{\mathrm{MS};m,i}(\omega_0,\zeta_0) = \mathcal{R}^{m,i}(\omega_0,\zeta_0)\;\mathcal{S}_{\mathrm{A}}^{\mathrm{F};m,i}(\omega_0,\zeta_0), \tag{2.2.34}$$

in which $\mathcal{R}^{m,i}(\omega_0,\zeta_0)$ can be interpreted as the response spectrum modification factor from FIRS to FLIRS.

If the structure is only excited by tri-directional seismic input at a single support while the ground motions in different directions are generally regarded as independent, equation (2.2.26) is reduced to

$$\boldsymbol{\mathcal{S}}_{\ddot{U}\ddot{U}}^{\mathrm{SS}}(\omega) = \left[\left|\boldsymbol{\mathcal{T}}(\omega)\right|^2\right] \boldsymbol{\mathcal{S}}_{\ddot{U}\ddot{U}}^{\mathrm{F}}(\omega), \tag{2.2.35}$$

where the superscript "ss" stands for single support and $\left[\left|\boldsymbol{\mathcal{T}}(\omega)\right|^2\right]$ denotes a matrix in which each element is equal to the squared modulus of the corresponding element in $\boldsymbol{\mathcal{T}}$. For a complex number $a+\mathrm{i}\,b$, its modulus is defined as $\left|a+\mathrm{i}\,b\right| = \sqrt{a^2+b^2}$.

As a result, the FLIRS modification factor can be written as

$$\left[\mathcal{R}^{i}(\omega_0,\zeta_0)\right]^2=\frac{\dfrac{1}{2\pi}\displaystyle\int_{-\infty}^{\infty}\left|\omega_0^2\,\mathcal{H}(\omega)\right|^2\left[\left|\boldsymbol{\mathcal{T}}_i(\omega)\right|^2\right]\mathcal{S}_{\ddot{U}\ddot{U}}^{\mathrm{F};i}(\omega)\,\mathrm{d}\omega}{\dfrac{1}{2\pi}\displaystyle\int_{-\infty}^{\infty}\left|\omega_0^2\,\mathcal{H}(\omega)\right|^2\mathcal{S}_{\ddot{U}\ddot{U}}^{\mathrm{F};i}(\omega)\,\mathrm{d}\omega},\tag{2.2.36}$$

in which $\boldsymbol{\mathcal{T}}_i(\omega)$ is the i-th row of $\boldsymbol{\mathcal{T}}(\omega)$. For excitations with wide-band power spectral densities, $\mathcal{S}_{\ddot{U}\ddot{U}}^{\mathrm{F};m,i}(\omega)$ can be approximated by constant $\mathcal{S}_{\ddot{U}\ddot{U}}^{\mathrm{F};m,i}$. Therefore, equation (2.2.36) can be simplified to

$$\left[\mathcal{R}^{i}(\omega_0,\zeta_0)\right]^2=\frac{\dfrac{1}{2\pi}\displaystyle\int_{-\infty}^{\infty}\left|\mathcal{H}(\omega)\right|^2\left[\left|\boldsymbol{\mathcal{T}}_i(\omega)\right|^2\right]\mathbf{1}\,\mathrm{d}\omega}{\dfrac{1}{2\pi}\displaystyle\int_{-\infty}^{\infty}\left|\mathcal{H}(\omega)\right|^2\,\mathrm{d}\omega},\tag{2.2.37}$$

where $\mathbf{1}$ is the 3×1 vector with all elements being 1. Equation (2.2.37) is the same as equation (4.3.14) in Jiang (2016).

Comparing equation (2.2.31) with equation (2.2.37), it is observed that for the situation of multiple excitations, the modification factor in direction i at support m not only depends on the ground motion at that support, but is also influenced by the ground motions at other supports.

2.2.3 Generating FRS of Multi-Supported Structures under Seismic Excitations Considering SSI

As mentioned before, the decoupled model with FLIRS as input is equivalent to the combined soil-structure model under the excitation FIRS. Therefore, the FLIRS obtained by the proposed method in Section 2.2.2 can be directly input to the decoupled model to generate FRS in conjunction with the direct method.

However, it should be noted that the explicit form of the combination coefficients in FRSMS-CQC combination rule developed in Section 2.1.3.1 is not available when considering SSI. As can be seen in equation (2.1.46), for the generation of FRS of structures with excitations at multiple supports, the coherence function of the ground inputs (i.e., FIRS) at different supports is involved. This is changed to the coherence function of FLIRS with the presence of soil. From the view of practice, it is reasonable to simplify the coherence

function of ground motions, such as by assuming fully-correlated or independent cases discussed previously, so that the explicit form of the coefficients in FRSMS-CQC combination rule can be obtained. However, it is not proper to deal with FLIRS in a similar way, because the correlation between FLIRS is highly related to the properties of soil and the superstructure, as can be seen from equation (2.2.26). For example, the motions of supports may be correlated to some extent even if the corresponding FIRS are independent.

Therefore, the significant difference between the case of the excitations at multiple supports and at a single support is that the correlations of the generated FLIRS in the former case need to be considered. Neglecting this correlation of FLIRS at different supports will result in a significant error in the generation of FRS using FLIRS.

To consider the correlation of FLIRS at different supports, the cross-power density function of FLIRS specified by equation (2.2.26) must be considered. As a result, the integrals in equations (2.1.45) need to be evaluated numerically for multi-supported structures with SSI effect. This indicates that the direct method for the generation of FRS of multi-supported structures considering SSI effect involves more computational cost than singly supported structures. However, it is still much more efficient than a set of time history analyses. Furthermore, significant variabilities in the time history method can be eliminated with the implementation of the proposed method.

2.2.4 Procedure of Generating FRS Considering SSI

For a structure in an SMR with its flexible foundation embedded in layered soil, a procedure for generating FRS considering SSI is illustrated in Figure 2.4 and is summarized as follows:

1. Consider the layered soil as a free-field. With seismic input applied at the bedrock, a site response analysis is performed to obtain the FIRS $\mathbf{U}_{\mathrm{I}}^{\mathrm{F}}$, at the elevation of the foundation.
2. Establish a model of the layered soil. Determine the dynamic stiffness matrices of the excavated soil $\mathbf{S}_{\mathrm{BB}}^{\mathrm{E}}$ and the soil with excavation $\mathbf{S}_{\mathrm{BB}}^{\mathrm{G}}$. The dynamic stiffness matrix of the free-field is $\mathbf{S}_{\mathrm{BB}}^{\mathrm{F}} = \mathbf{S}_{\mathrm{BB}}^{\mathrm{G}} + \mathbf{S}_{\mathrm{BB}}^{\mathrm{E}}$.
3. Set up a finite element model of the structure. Determine the dynamic stiffness matrices $\mathbf{S}_{\mathrm{RR}}^{\mathrm{S}}, \mathbf{S}_{\mathrm{RB}}^{\mathrm{S}}, \mathbf{S}_{\mathrm{BR}}^{\mathrm{S}}, \mathbf{S}_{\mathrm{BB}}^{\mathrm{S}}$.

4. Determine the FLIRS:

   - Partition matrix $\mathbf{S}^{\mathrm{MS}} = -\left(\mathbf{S}^{\mathrm{S}}_{\mathrm{RR}}\right)^{-1}\mathbf{S}^{\mathrm{S}}_{\mathrm{RB}} = \begin{bmatrix} \mathbf{S}^{\mathrm{MS}}_{\mathrm{TT}} & \mathbf{S}^{\mathrm{MS}}_{\mathrm{TR}} \\ \mathbf{S}^{\mathrm{MS}}_{\mathrm{RT}} & \mathbf{S}^{\mathrm{MS}}_{\mathrm{RR}} \end{bmatrix}_{6N\times 6M}$
   - $\mathbf{S} = \mathbf{S}^{\mathrm{S}}_{\mathrm{BR}}\,\mathbf{S}^{\mathrm{MS}} + \left(\mathbf{S}^{\mathrm{S}}_{\mathrm{BB}} - \mathbf{S}^{\mathrm{E}}_{\mathrm{BB}}\right) + \mathbf{S}^{\mathrm{F}}_{\mathrm{BB}}$, dimension $6M\times 6M$

     Determine the inverse $\mathbf{S}^{-1}$
   - Partition matrix $\mathbf{S}^{-1}\mathbf{S}^{\mathrm{F}}_{\mathrm{BB}} = \begin{bmatrix} \mathbf{T}_{\mathrm{TT}} & \mathbf{T}_{\mathrm{TR}} \\ \mathbf{T}_{\mathrm{RT}} & \mathbf{T}_{\mathrm{RR}} \end{bmatrix}_{6M\times 6M}$
   - Transfer matrix: $\boldsymbol{\mathcal{T}} = \mathbf{T}_{\mathrm{TT}} + \left[\left(\mathbf{S}^{\mathrm{MS}}_{\mathrm{TT}}\right)^{T}\mathbf{S}^{\mathrm{MS}}_{\mathrm{TT}}\right]^{-1}\left(\mathbf{S}^{\mathrm{MS}}_{\mathrm{TT}}\right)^{T}\mathbf{S}^{\mathrm{MS}}_{\mathrm{TR}}\,\mathbf{T}_{\mathrm{RT}}$
   - FLIRS modification factor:

     $$\left[\mathcal{R}^{m,i}(\omega_0,\zeta_0)\right]^2 = \frac{\displaystyle\int_{-\infty}^{\infty}\left|\mathcal{H}(\omega)\right|^2 \sum_{p=1}^{3M}\sum_{q=1}^{3M}\mathcal{T}^{p}_{m,i}(\omega)\,\mathcal{S}^{\mathrm{F};\,q}_{\ddot{U}\ddot{U};\,p}(\omega)\,\tilde{\mathcal{T}}^{m,i}_{q}(\omega)\,\mathrm{d}\omega}{\displaystyle\int_{-\infty}^{\infty}\left|\mathcal{H}(\omega)\right|^2 \mathcal{S}^{\mathrm{F};m,i}_{\ddot{U}\ddot{U}}(\omega)\,\mathrm{d}\omega}$$
   - FLIRS: $\mathcal{S}^{\mathrm{MS};m,i}_{\mathrm{A}}(\omega_0,\zeta_0) = \mathcal{R}^{m,i}(\omega_0,\zeta_0)\;\mathcal{S}^{\mathrm{F};m,i}_{\mathrm{A}}(\omega_0,\zeta_0)$
   - Cross-power density function of FLIRS: $\boldsymbol{\mathcal{S}}^{\mathrm{MS}}_{\ddot{U}\ddot{U}}(\omega) = \boldsymbol{\mathcal{T}}(\omega)\;\boldsymbol{\mathcal{S}}^{\mathrm{F}}_{\ddot{U}\ddot{U}}(\omega)\,\tilde{\boldsymbol{\mathcal{T}}}(\omega)$

5. The FLIRS $\mathcal{S}^{\mathrm{MS};m,i}_{\mathrm{A}}(\omega_0,\zeta_0)$ together with the cross-power density function $\boldsymbol{\mathcal{S}}^{\mathrm{MS}}_{\ddot{U}\ddot{U}}(\omega)$ are input to the decoupled finite element model of the structure to generate the required FRS, which are exactly the same as the FRS obtained from a fully coupled soil–structure analysis under the excitation of FIRS.

Therefore, when the direct spectra-to-spectra method presented in Section 2.1 is applied to structures with flexible foundation under the excitation of FLIRS $\mathcal{S}^{\mathrm{MS};m,i}_{\mathrm{A}}(\omega_0,\zeta_0)$, FRS with complete probabilistic descriptions of FRS peaks (FRS with any desired level of NEP p) can be obtained. If the time history method is applied, such a result could only be obtained from a large number of coupled soil–structure analyses using a commercial finite element software, such as ACS SASSI, with a large number of generated time-histories compatible with the FIRS.

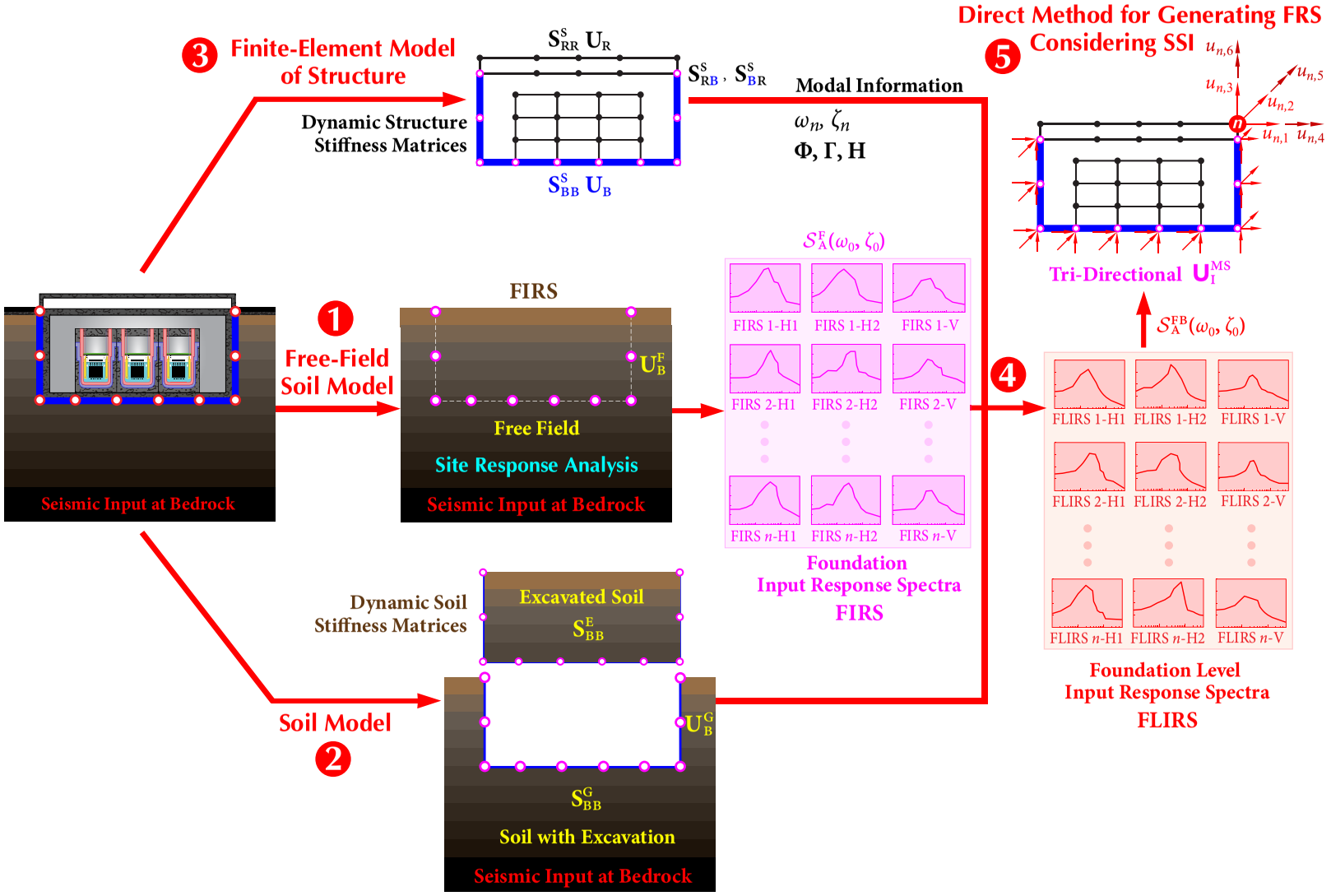


Figure 2.4 Procedure for generating FRS for multiply supported structures considering SSI.

2.3 Summary

This chapter introduces a method for generating FRS considering multiple support excitations and SSI, with a focus on nuclear power plant structures like SMRs. By integrating these factors, the chapter aims to improve the accuracy and reliability of seismic analysis in nuclear facility design, addressing critical challenges in the field. The method utilizes a transfer function, which is derived in frequency domain, to establish the relationship between FIRS and FLIRS. The FLIRS modification factor, which is the ratio between FLIRS and the corresponding FIRS, is derived based on the transfer function. The modification factor is given implicitly because it depends on the structural information and the soil properties, which can be easily evaluated numerically once the information is given. Using FLIRS modification factor, FLIRS can be generated directly, which are then input to the decoupled model to generate FRS using the direct method. It has been proved that FRS of the decoupled structure using FLIRS is theoretically equivalent to that generated by the combined soil-structure system using FIRS.

CHAPTER 3

Validation of the General Formulation for Generating FRS Considering SSI

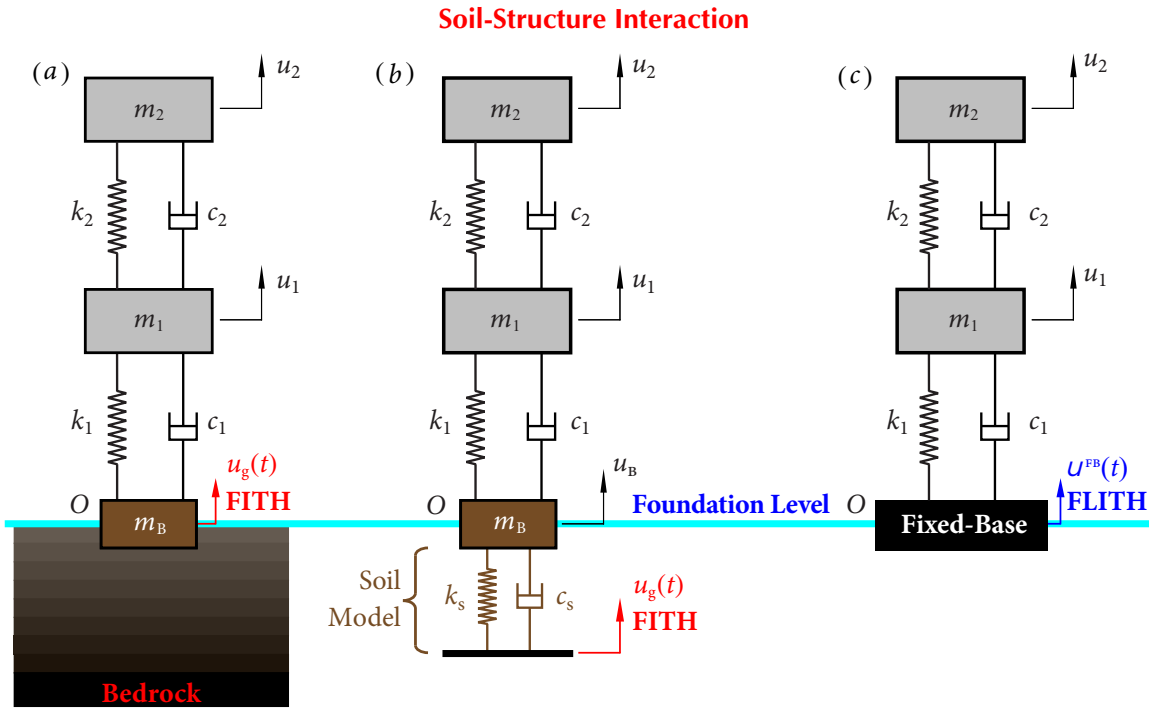
3.1 Introduction

The primary objective of this chapter is to evaluate the effectiveness and accuracy of the general formulation presented in Section 2.2 for generating FRS considering SSI for structures with flexible foundations. While the principal purpose of this research is to study structures with multiple supports, it is essential to start with a singly supported structure to validate the proposed method from both theoretical and numerical perspectives.

To ensure the simplicity and convenience of the expressions, a 2-DOF system is considered as an illustration. This guarantees that the system is an MDOF system, which is more typical and representative than an SDOF system in practice, and is possible to obtain an exact mathematical solution for validation.

The structure system consists of two structural masses m_1, m_2 and one foundation or base mass m_B founded on the top of soil above the bedrock, as shown in Figure 3.1 (a), and can move vertically under the excitation of earthquake. The stiffnesses and dampings for the connected springs and dampers components are k_1, c_1, and k_2, c_2.

To perform seismic response analysis for the structure system, site response analysis is firstly performed based on the prescribed free field seismic wave; then the *Foundation Input Response Spectrum* (FIRS) based on wave propagation theory can be applied at the bottom



FITH: Foundation Input Time History (Free-field time history at foundation) $\ddot{u}_g(t)$

FIRS: Foundation Input Response Spectrum (Free-field response spectrum at foundation) $\mathcal{RS}\{\ddot{u}_g(t)\}$

FLITH: Foundation Level Input Time History
(Fixed-base time history at foundation level considering SSI) $\ddot{u}^{FB}(t)$

FLIRS: Foundation Level Input Response Spectrum
(Fixed-base response spectrum at foundation level considering SSI) $\mathcal{RS}\{\ddot{u}^{FB}(t)\}$

Figure 3.1 Simplified model for validation and demonstration of the general formulation

of the structure foundation. FIRS-compatible time history is called *Foundation Input Time History* (FITH). The induced response spectrum at the foundation level would be different from FIRS because of the consideration of interaction between structure and soil. It is called *Foundation Level Input Response Spectrum* (FLIRS). FLIRS-compatible time history is called *Foundation Level Input Time History* (FLITH). FLIRS despite being input at the same foundation level as FIRS, differs from the latter due to the consideration of SSI effects. It can be used as a direct input into fixed-base model for conducting seismic analysis that takes SSI effects into account.

The structural system in Figure 3.1 (a) can be modelled as a fully coupled soil-structure model, as shown in Figure 3.1 (b). The coupled model simplifies the underlying soil at the

interface as a set of generalized soil springs, with the stiffness and damping being k_s and c_s, respectively. Then the interdependent response can be represented in terms of masses, stiffnesses and dampings of structure and soil. The generalized soil springs are considered to have a length approaching zero. Consequently, the response spectrum at the upper structure nodes should be identical whether FIRS input at the "bottom" end of foundation level without SSI, or the FLIRS input at the "top" end while considering SSI. Therefore, the FLIRS input at the fixed-base in Figure 3.1 (c) would induce the same response spectra as Figure 3.1 (b).

To be more quantitative in verifying the approach, the proposed general formulation will be numerically compared with time history analysis. The general formulation will be deemed effective and accurate if the results obtained from the general formulation and time history analysis are highly consistent. The variability inherent in time history analysis, manifested in the rugged spectral shapes of FRS, will be taken into account through statistical measures such as mean FRS, median FRS, or FRS with 84.1% non-exceedance probability (NEP). These statistical results, obtained from a large number of time history analyses, will be used as “benchmarks” for evaluating the accuracy of the proposed direct method. To ensure meaningful comparison between results from the two methods, the input response spectrum (FIRS) must closely relate to the input time history (FITH).

3.2 Classification of the Sites

Site classification determines the properties and characteristics of the soil in a specific location, which affects the responses of structures. As stated previously, site selection of SMR can vary significantly due to their flexibility, and is pivotal to determine properties of soils for the safety performance of SMR. The prevailing provisions and guidelines, related to the design and construction of nuclear facilities, categorize sites into different classes based on their seismic hazard potential.

The sites are generally classified based on the soil and rock characteristics in an area. As per ASCE/SEI 7-10 (2010), the site is classified into 6 categories, i.e., Class A, B, C, D, E, and F, in which Class A to E represent the stiffness of the soil from hard rock to highly variable

soil, while Class F refers to the soil that requires site response analysis in accordance with Section 21.1(ASCE, 2010).

When the underlying soil is uniform to a depth equal to the largest foundation dimension, the soil stiffness can be considered a simplified frequency-independent soil spring. The frequency-dependent impedance functions can be calculated for the specific foundation shape and site condition, or obtained from impedance tables, which are available for regular shapes, such as circular or rectangular square disks. The equivalent horizontal and vertical spring stiffness can be calculated accordingly, as demonstrated in Appendix A. The approximated ranges of soil stiffness for different site classes are summarized in Table 3.1. The different soil stiffnesses in the distinct classes of sites are then used for numerical analysis in the verification.

Given that site Class E is characterized by soft clay soil with an average shear wave velocity below 600 ft/s or an average standard penetration value of less than 15, it is a notable soft underlying mat, on which it is unsuitable for constructing any heavy structures. While encountering such soft base may be inevitable in some cases, it is crucial to implement proper treatment to ensure that the site meets the minimum standard in construction. Therefore, the lower bound of soil stiffness herein is set as Class D.

Table 3.1 Ranges of soil spring stiffness for different sites

Bound	site A	site B	site C	site D	site E
LB k_s (kN/m)	5×10^8	5×10^7	1×10^7	3×10^6	2×10^5
UB k_s (kN/m)	2×10^{12}	9×10^9	1×10^9	2×10^8	6×10^7

3.3 Theoretical Validation

In this section, formulations are derived for the example illustrated in Figure 3.1. The relationship between FIRS and FLIRS can then be substantiated by examining the response of nodes in the superstructure of coupled soil-structure and fixed-base model. To simplify the presentation, the derivation uses time history as the input; the corresponding response spectra can be obtained readily from the time histories.

3.3.1 Coupled Soil-Structure Model

Denote $u_1(t)$, $u_2(t)$, and $u_B(t)$ as the absolute displacements of m_B, m_1, and m_2 in the coupled model, respectively. $u_g(t)$ is the displacement of ground motion, the first and second derivatives of $\mathbf{u}(t)$ are then represent as velocity and accelerations. Due to the earthquake excitation at the "bottom" end of the soil spring, the equation of motion can be derived using D'Alambert's principle and given the following matrix form

$$\begin{bmatrix} m_1 & & \\ & m_2 & \\ & & m_B \end{bmatrix} \begin{Bmatrix} \ddot{u}_1(t) \\ \ddot{u}_2(t) \\ \ddot{u}_B(t) \end{Bmatrix} + \begin{bmatrix} c_1+c_2 & -c_2 & -c_1 \\ -c_2 & c_2 & 0 \\ -c_1 & 0 & c_1+c_s \end{bmatrix} \begin{Bmatrix} \dot{u}_1(t) \\ \dot{u}_2(t) \\ \dot{u}_B(t) \end{Bmatrix} + \begin{bmatrix} k_1+k_2 & -k_2 & -k_1 \\ -k_2 & k_2 & 0 \\ -k_1 & 0 & k_1+k_s \end{bmatrix} \begin{Bmatrix} u_1(t) \\ u_2(t) \\ u_B(t) \end{Bmatrix} = \begin{Bmatrix} 0 \\ 0 \\ c_s\,\dot{u}_g(t)+k_s\,u_g(t) \end{Bmatrix}. \tag{3.3.1}$$

The response displacement vector $[u_1(t), u_2(t), u_B(t)]^T$ can be expressed as $\mathbf{u}(t)=\mathbf{U}\,e^{i\omega t}$, thus, $\dot{\mathbf{u}}(t)=(i\omega)\mathbf{U}\,e^{i\omega t}$, $\ddot{\mathbf{u}}(t)=-\omega^2\mathbf{U}\,e^{i\omega t}$. Similarly, $\mathbf{U}_g(t)=\mathbf{U}_g\,e^{i\omega t}$, $\dot{\mathbf{u}}_g(t)=(i\omega)\,\mathbf{U}_g\,e^{i\omega t}$. Equation (3.3.1) can be rearranged as

$$\begin{bmatrix} \mathbf{S}^S_{RR} & \mathbf{S}^S_{RB} \\ \mathbf{S}^S_{BR} & \mathbf{S}_{BB} \end{bmatrix} \begin{Bmatrix} \mathbf{U}_R \\ \mathbf{U}_B \end{Bmatrix} = \begin{Bmatrix} \mathbf{0} \\ \mathbf{S}^G_{BB}\,\mathbf{U}_g \end{Bmatrix}, \tag{3.3.2}$$

in which,

$$\begin{aligned} \mathbf{S}^S_{RR} &= \begin{bmatrix} -\omega^2 m_1+i\omega(c_1+c_2)+(k_1+k_2) & -i\omega c_2-k_2 \\ -i\omega c_2-k_2 & -\omega^2 m_2+i\omega c_2+k_2 \end{bmatrix}, \\ \mathbf{S}_{BB} &= (-\omega^2 m_B+i\omega c_1+k_1)+(i\omega c_s+k_s) = \mathbf{S}^S_{BB}+\mathbf{S}^G_{BB}, \\ \mathbf{S}^S_{BR} &= \begin{bmatrix} -i\omega c_1-k_1 & 0 \end{bmatrix},\ \mathbf{S}^S_{RB} = (\mathbf{S}^S_{BR})^T, \end{aligned}$$

are the frequency dependent dynamic stiffness matrices, which have the same physical meaning with those in Section 3.2. $\mathbf{U}=[\mathbf{U}_R,\ \mathbf{U}_B]^T$, in which $\mathbf{U}_R$ is the response displacement vector of the structure, $\mathbf{U}_R=[\mathbf{U}_1,\ \mathbf{U}_2]^T$, $\mathbf{U}_B$ is the displacement vector at boundary considering SSI.

From the first row of equation (3.3.2), the relationship between the dynamic response of structure nodes and the foundation nodes can be determined as

$$\mathbf{U}_{\mathrm{R}} = -(\mathbf{S}^{\mathrm{S}}_{\mathrm{RR}})^{-1}\mathbf{S}^{\mathrm{S}}_{\mathrm{RB}}\,\mathbf{U}_{\mathrm{B}} = \mathbf{S}^{\mathrm{MS}}\,\mathbf{U}_{\mathrm{B}}, \tag{3.3.3}$$

where $\mathbf{S}^{\mathrm{MS}}$ has the same definition as in equation (2.2.11). The second row of equation (3.3.2) gives,

$$\mathbf{S}_{\mathrm{BB}}\,\mathbf{U}_{\mathrm{B}} + \mathbf{S}^{\mathrm{S}}_{\mathrm{BR}}\,\mathbf{U}_{\mathrm{R}} = \mathbf{S}^{\mathrm{G}}_{\mathrm{BB}}\,\mathbf{U}_{\mathrm{g}} \implies \mathbf{U}_{\mathrm{B}} = (\mathbf{S}_{\mathrm{BB}})^{-1}(\mathbf{S}^{\mathrm{G}}_{\mathrm{BB}}\,\mathbf{U}_{\mathrm{g}} - \mathbf{S}^{\mathrm{S}}_{\mathrm{BR}}\,\mathbf{U}_{\mathrm{R}}). \tag{3.3.4}$$

Substituting equation (3.3.4) into equation (3.3.3) yields

$$\mathbf{U}_{\mathrm{R}} = -(\mathbf{S}^{\mathrm{S}}_{\mathrm{RR}})^{-1}\mathbf{S}^{\mathrm{S}}_{\mathrm{RB}}\,(\mathbf{S}_{\mathrm{BB}})^{-1}(\mathbf{S}^{\mathrm{G}}_{\mathrm{BB}}\,\mathbf{U}_{\mathrm{g}} - \mathbf{S}^{\mathrm{S}}_{\mathrm{BR}}\,\mathbf{U}_{\mathrm{R}}), \tag{3.3.5}$$

$$\implies \left[\mathbf{S}_{\mathrm{BB}}(\mathbf{S}^{\mathrm{S}}_{\mathrm{BR}}\,\mathbf{S}^{\mathrm{S}}_{\mathrm{RB}})^{-1}\mathbf{S}^{\mathrm{S}}_{\mathrm{BR}}\,\mathbf{S}^{\mathrm{S}}_{\mathrm{RR}} - \mathbf{S}^{\mathrm{S}}_{\mathrm{BR}}\right]\mathbf{U}_{\mathrm{R}} = -\mathbf{S}^{\mathrm{G}}_{\mathrm{BB}}\,\mathbf{U}_{\mathrm{g}}. \tag{3.3.6}$$

3.3.2 Fixed-Base Model

A coupled soil-structure model that utilizes FIRS as an input can be replaced by a fixed-base model with a modified input of FLIRS. The equation of motion for the fixed-base model is

$$\begin{bmatrix} m_1 & \\ & m_2 \end{bmatrix}\begin{Bmatrix} \ddot{u}_1(t) \\ \ddot{u}_2(t) \end{Bmatrix} + \begin{bmatrix} c_1+c_2 & -c_2 \\ -c_2 & c_2 \end{bmatrix}\begin{Bmatrix} \dot{u}_1(t) \\ \dot{u}_2(t) \end{Bmatrix} + \begin{bmatrix} k_1+k_2 & -k_2 \\ -k_2 & k_2 \end{bmatrix}\begin{Bmatrix} u_1(t) \\ u_2(t) \end{Bmatrix} = \begin{Bmatrix} c_1\dot{u}^{\mathrm{FB}}(t)+k_{\mathrm{s}}u^{\mathrm{FB}}(t) \\ 0 \end{Bmatrix}. \tag{3.3.7}$$

in which, superscript $^{\mathrm{FB}}$ stands for *fixed-base*. Analogous to the coupled model, equation (3.3.7) in the frequency domain can be rewritten as,

$$\begin{bmatrix} -\omega^2 m_1+\mathrm{i}\omega(c_1+c_2)+(k_1+k_2) & -\mathrm{i}\omega c_2-k_2 \\ -\mathrm{i}\omega c_2-k_2 & -\omega^2 m_2+\mathrm{i}\omega c_2+k_2 \end{bmatrix}\begin{Bmatrix} u_1 \\ u_2 \end{Bmatrix} = \begin{Bmatrix} \mathrm{i}\omega c_1+k_1 \\ 0 \end{Bmatrix}\mathbf{U}^{\mathrm{FB}}, \tag{3.3.8}$$

in which $\mathbf{U}^{\mathrm{FB}}$ is the amplitude of $\mathbf{u}^{\mathrm{FB}}(t)$. The matrix form of equation (3.3.8) is

$$\mathbf{S}^{\mathrm{S}}_{\mathrm{RR}}\,\mathbf{U}_{\mathrm{R}} = -\mathbf{S}^{\mathrm{S}}_{\mathrm{RB}}\,\mathbf{U}^{\mathrm{FB}}, \tag{3.3.9}$$

where $\mathbf{S}^{\mathrm{S}}_{\mathrm{RR}}$, $\mathbf{U}_{\mathrm{R}}$, and $\mathbf{S}^{\mathrm{S}}_{\mathrm{RB}}$ are defined in equation (3.3.2). Equation (3.3.9) gives,

$$\mathbf{U}_{\mathrm{R}} = -(\mathbf{S}^{\mathrm{S}}_{\mathrm{RR}})^{-1}\mathbf{S}^{\mathrm{S}}_{\mathrm{RB}}\,\mathbf{U}^{\mathrm{FB}} = \mathbf{S}^{\mathrm{MS}}\mathbf{U}^{\mathrm{FB}} \tag{3.3.10}$$

3.3.3 Model Comparison

From equations (3.3.3) and (3.3.10), it can be concluded that the displacement vector $\mathbf{U}_B$ including effect of SSI in the coupled soil-structure model and the displacement vector $\mathbf{U}^{FB}$ in the fixed-base model are identical, i.e.,

$$\mathbf{U}_B = \mathbf{U}^{FB}. \tag{3.3.11}$$

It is evident that the input earthquake excitation $\ddot{\mathbf{u}}(t)$ in the coupled soil-structure model is equivalent to the input $\ddot{\mathbf{u}}^{FB}(t)$ in the fixed-base model, demonstrating the theoretical validity of replacing the coupled model with the fixed-base model by changing the input from the acceleration of $\ddot{\mathbf{u}}(t)$ to the input of $\ddot{\mathbf{u}}^{FB}(t)$, known as FITH and FLITH, respectively.

To further investigate the relationship between the amplitude of input of $\mathbf{U}^{FB}(t)$ in the fixed-base model and the input of $\mathbf{U}_g(t)$ in the coupled model. Substituting equation (3.3.10) into equation (3.3.6) yields

$$\begin{aligned}
\left[\mathbf{S}_{BB}(\mathbf{S}^S_{BR}\mathbf{S}^S_{RB})^{-1}\mathbf{S}^S_{BR}\mathbf{S}^S_{RR} - \mathbf{S}^S_{BR}\right](\mathbf{S}^S_{RR})^{-1}\mathbf{S}^S_{RB}\mathbf{U}^{FB} &= \mathbf{S}^G_{BB}\mathbf{U}_g, \\
\Longrightarrow \quad \left[\mathbf{S}_{BB} - \mathbf{S}^S_{BR}(\mathbf{S}^S_{RR})^{-1}\mathbf{S}^S_{RB}\right]\mathbf{U}^{FB} &= \mathbf{S}^G_{BB}\mathbf{U}_g.
\end{aligned}$$

$$\therefore \quad \underbrace{\mathbf{U}^{FB}}_{\text{Amplitude of FLITH}} = \underbrace{\left[\mathbf{S}_{BB} - \mathbf{S}^S_{BR}(\mathbf{S}^S_{RR})^{-1}\mathbf{S}^S_{RB}\right]^{-1}\mathbf{S}^G_{BB}}_{\text{Modification factor}} \underbrace{\mathbf{U}_g}_{\text{Amplitude of FITH}} \tag{3.3.12}$$

The amplitude $\mathbf{U}_g$ of FITH is thus transformed to the amplitude $\mathbf{U}^{FB}$ of FLITH by considering SSI. This is clearly a special case of equation (2.2.18). The main difference is that equation (2.2.18) is more generic because it includes rotational DOFs. Although the case presented is relatively simple, it provides insight into how the SSI effect influences the response of structures, and the physical meaning of FLIRS.

3.4 Numerical Validation

To verify the accuracy and demonstrate the efficiency of the general formulation for generating FRS of structures, a numerical example is presented for the 3-DOF system problem shown in Figure 3.1.

3.4.1 Fundamental Parameters

The process of generating FRS by general formulation from a prescribed ground motion is applied to the 3-DOF system in Figure 3.1. With a focus on the nuclear facilities, the dominant frequencies of around 5.0 Hz and 12.0 Hz and a uniform damping ratio of $\zeta_0 = 5\%$ are chosen accordingly. Thus the essential parameters are determined as follows: masses $m_1 = 3000\,\text{kg}$, $m_2 = 1500\,\text{kg}$; stiffnesses $k_1 = 6000\,\text{kN/m}$, $k_2 = 5000\,\text{kN/m}$; damping coefficients, $c_1 = 4.0\,\text{kN·s/m}$, $c_2 = 4.5\,\text{kN·s/m}$. The mass of foundation is $m_\text{B} = 3000\,\text{kg}$, damping is $c_\text{s} = 550\,\text{kN·s/m}$.

It should be mentioned that the diagonalizability of the coupled soil-structure system is not required for generating FLIRS, but it is necessary to apply the direct method to evaluate FRS, which relies on modal responses. Air damping coefficients $c_{1A} = 8.46\,\text{kN·s/m}$ and $c_{2A} = 3.51\,\text{kN·s/m}$ are added on the masses m_1 and m_2 to account for air resistance. Therefore, only the diagonal elements in the damping matrix of Equation (3.3.1) are affected by c_{1A} and c_{2A}, while the non-diagonal elements are not influenced. Equation (3.3.1) becomes

$$\begin{bmatrix} m_1 & & \\ & m_2 & \\ & & m_\text{B} \end{bmatrix} \begin{Bmatrix} \ddot{u}_1(t) \\ \ddot{u}_2(t) \\ \ddot{u}_\text{B}(t) \end{Bmatrix} + \begin{bmatrix} c_1 + c_{1A} + c_2 + c_{2A} & -c_2 & -c_1 \\ -c_2 & c_2 + c_{2A} & 0 \\ -c_1 & 0 & c_1 + c_{1A} + c_\text{s} \end{bmatrix} \begin{Bmatrix} \dot{u}_1(t) \\ \dot{u}_2(t) \\ \dot{u}_\text{B}(t) \end{Bmatrix} + \begin{bmatrix} k_1 + k_2 & -k_2 & -k_1 \\ -k_2 & k_2 & 0 \\ -k_1 & 0 & k_1 + k_\text{s} \end{bmatrix} \begin{Bmatrix} u_1(t) \\ u_2(t) \\ u_\text{B}(t) \end{Bmatrix} = \begin{Bmatrix} 0 \\ 0 \\ c_\text{s}\,\dot{u}_\text{g}(t) + k_\text{s}\,u_\text{g}(t) \end{Bmatrix}.$$

A range of underlying soil stiffness k_s values, as listed in Table 3.2, is used for evaluating the general formulation method for different classes of sites.

Table 3.2 Soil spring stiffnesses in the numerical calculation

Site class	D		C		B
Case number	1	2	3	4	5
Soil type	Medium soil	Harder Soil	Stiff soil	Soft rock	Medium hard rock
Stiffness k_s (kN/m)	8×10^4	1×10^5	5×10^5	1×10^6	5×10^6

Input Ground Response Spectra (GRS)

The 5% horizontal design spectrum in USNRC R.G. 1.60 (1973) is taken as FIRS. The peak ground acceleration (PGA) is anchored at $0.3g$. 30 sets of time histories as FITH compatible with FIRS are generated by the Hilbert-Huang Transform method (Ni *et al.*, 2011; 2013), and will be used for performing time history analysis to provide the benchmark for FRS. The 30 sets of input ground response spectra are shown in Figure 3.2.

Modal Information

Modal analysis is conducted to determine the modal frequencies, modal participation factors, and modal shapes of the structural model, which are then used to generate FRS in the direct method. Modal information of the fixed-base model are listed in Table 3.3.

The natural frequencies of the coupled system decrease when soil is considered. For instance, when the soil stiffness is low, such as $k_s = 8 \times 10^4$ kN/m, the natural frequencies are 5.20 Hz, 12.09 Hz, and 27.02 Hz, indicating that the structure becomes more flexible when the soil is taken into account; when $k_s = 5 \times 10^6$ kN/m, the first two dominant frequencies are 5.36 Hz and 12.19 Hz, respectively, which are close to those of the fixed-base model, suggesting that the system behaves approximately equivalent to the fixed-base model.

Table 3.3 Modal information of fixed-base model

Mode	Frequency (Hz)	Modal Shape
1	5.37	[0.659, 1.000]
2	12.19	[1.000, −12.186]

3.4.2 Developing FLIRS

FLIRS is the first requisite in generating FRS from the general formulation. For the various cases of soil, the dimensionless transfer matrix of the coupled soil-structure model $\mathbf{S}^{MS}$ is computed for different values of ω, varying from 0.002π to 200π with an increment of 0.02π; then the modification factor $\mathcal{R}$ can be determined frequency by frequency. $\mathcal{R}$ is then used to evaluate the modification from FIRS to FLIRS. FLIRS are then input as GRS in the fixed model allowing for considering the SSI effects directly.

Modification Factor

Figure 3.3 illustrates the variation of $\mathcal{R}$ with respect to the frequency of the soil-structure system. The values at highest peak and lowest valley notably varies with the change of k_s. It is seen that the stiffer the soil is, the closer the $\mathcal{R}$ is to 1.

When the $k_s = 8 \times 10^4$ kN/m, values of $\mathcal{R}$ are observed at 1.13, 0.91, and 1.06, for the peak 1, valley, and peak 2, occurring at frequencies of 4.82 Hz, 5.70 Hz, and 11.38 Hz, respectively, indicating that the presence of soil modified the fundamental frequency of the structure significantly, while the second fundamental frequency is affected to a lesser degree.

For $k_s = 1 \times 10^5$ kN/m, peak 1 of $\mathcal{R}$ shifts to a higher frequency, while the frequency of the valley is vice versa. Both of the frequencies move toward the first frequency of the structure, which is 5.37 Hz.

For $k_s = 5 \times 10^6$ kN/m, peak 1 of $\mathcal{R}$ appears at 5.02 Hz, and the valley at 5.70 Hz, with corresponding $\mathcal{R}$ values of 1.002 and 0.998, suggesting that the two frequencies approach the fundamental frequency of 5.37 Hz and $\mathcal{R}$ approaches 1 as the soil becomes stiffer. Peak 2 of $\mathcal{R}$ falls significantly to a steady value of 1.

The observed frequency shifts and changes in $\mathcal{R}$ can be interpreted as resulting from the absorption of vibration by the soil in the coupled system. The soil acts as a vibration absorber, where the energy of excitation is absorbed at the natural frequencies of the fixed-base model. It can be observed that softer soil leads to greater modification of seismic excitations, indicating a more significant SSI effect.

Development of FLIRS

It is essential to use FLIRS in the direct method as it accounts for SSI. FLIRS includes dynamic stiffness matrices $\mathbf{S}$ in terms of foundation $\mathbf{S}^{s}_{BB}$, structure $\mathbf{S}^{s}_{RR}$, the influence of foundation on the structure $\mathbf{S}^{s}_{RB}$, and the influence of structure on the foundation $\mathbf{S}^{s}_{BR}$ under seismic excitation (FIRS). It can be input directly as GRS for a corresponding fixed-base model, as illustrated in Figure 3.1.

Generated FLIRS are compared with the results from time history analysis to validate their accuracy. Although there is no direct method to generate FLIRS in time history analysis, it has been demonstrated that FLIRS in fixed-base models are equivalent to the

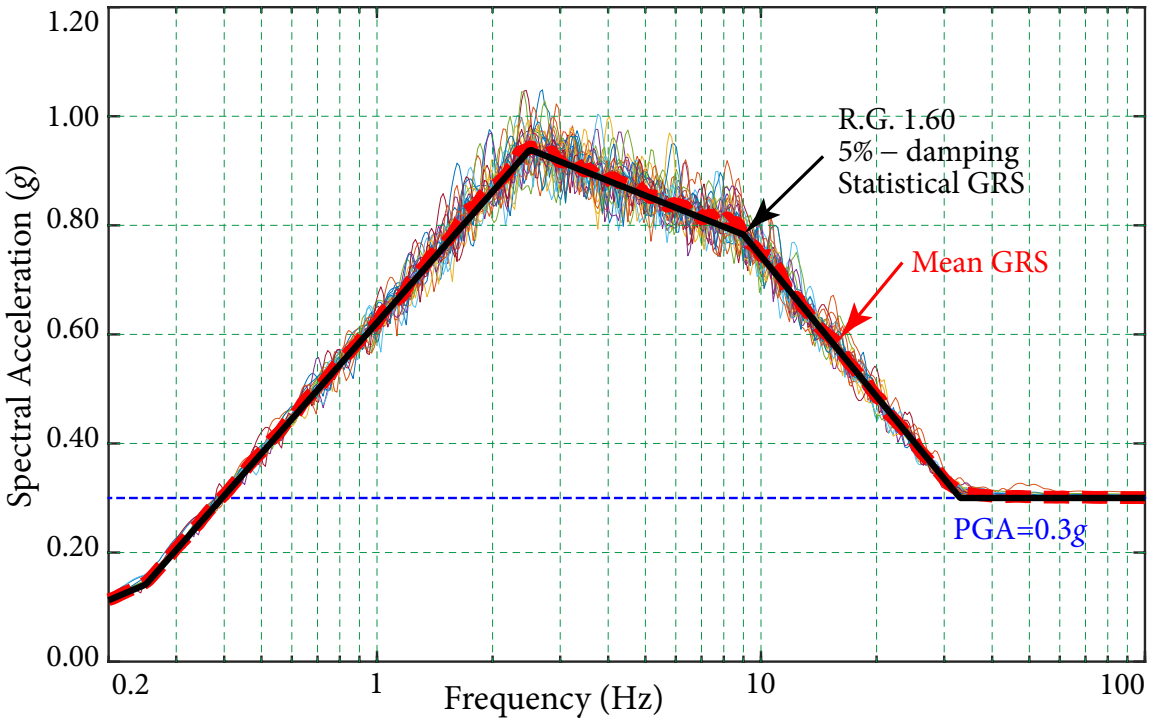


Figure 3.2 Ground response spectra of compatible time histories

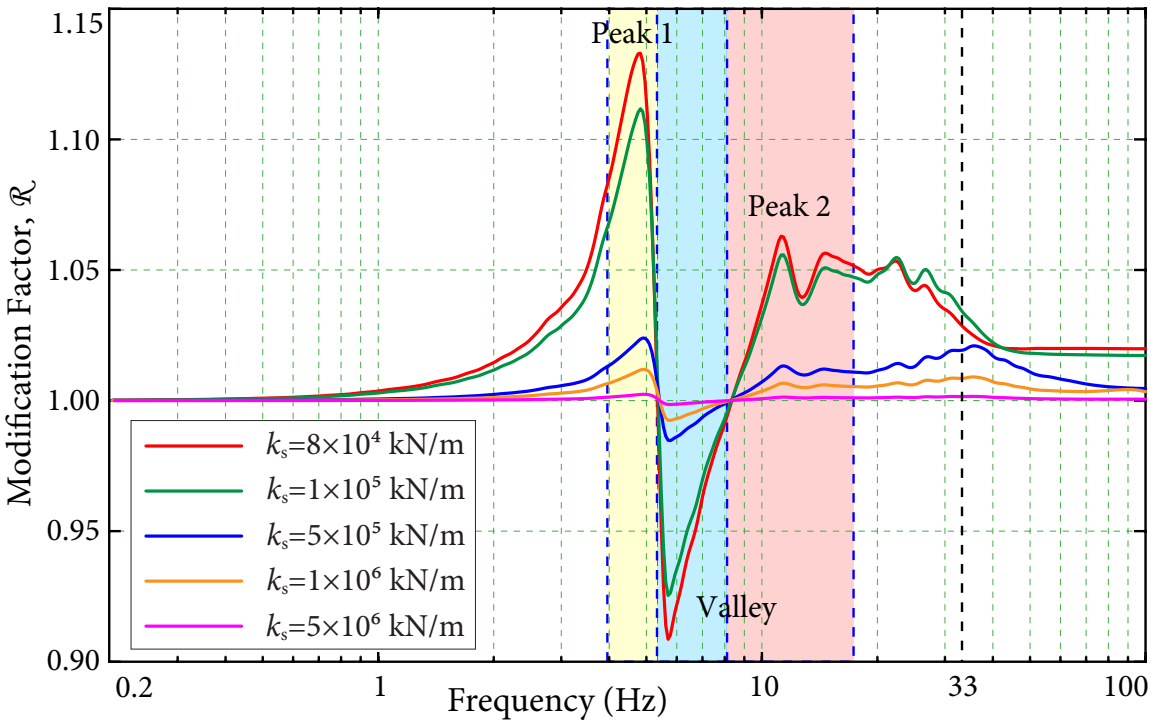


Figure 3.3 Modification factor $\mathcal{R}$ in different soil cases

FRS at the corresponding base nodes in coupled systems. Thus, FLIRS can be validated by comparing with the mean FRS at the foundation node m_{B} of the coupled system. To better demonstrate the effectiveness and accuracy of FLIRS in different sites, the FRS of node m_{B} and the corresponding FLIRS are plotted in Figure 3.4 for the softest soil case; other soil cases are presented in Appendix B. The black line is the FLIRS while the red dash line is the benchmark. The blue dash line is the FIRS, which is R.G. 1.60 design spectrum. It can be observed that the FLIRS and mean FRS agree extremely well, with all the relative errors smaller than 3.5% regardless of the type of soil. Meanwhile, FRS obtained by time history analyses exhibit significant fluctuations, varying from -15% to over $+25\%$ for different k_{s}.

Effect of Soil Stiffness on the FLIRS

A parametric study is conducted to investigate the effects of soil stiffness on the FLIRS. FLIRS for all the cases are presented in Figure 3.5. It is observed that FLIRS is significantly amplified when relatively soft soil is present. Peak 1 of FLIRS shifts to a higher frequency with increased soil stiffness. For example, the frequency shifts from 4.69 Hz to 4.96 Hz when k_{s} increases from 8×10^{4} kN/m to 1×10^{6} kN/m; and is very close to the fundamental frequency of 5.37 Hz when $k_{\mathrm{s}}=5\times10^{6}$ kN/m. Alteration of the valley demonstrates a comparable pattern. The frequency varies from 5.70 Hz to 5.37 Hz with the increase in soil stiffness, indicating that stiffer soil results in lower SSI. Conversely, softer soil cause frequency shifts to a lower value, demonstrating that the SSI effect is significant when the soil is soft.

3.5 Developing FRS from General Formulation

t-Response Spectrum (tRS)

It is crucial to determine FRS at various elevations or floors of the supporting structures where the critical SSCs are mounted. When the direct method is applied to generate FRS, the following quantity is required when the equipment and supporting structure are in resonance (tuning)

$$\mathcal{S}_{\mathrm{A}}^{\mathrm{t}}(\omega,\zeta)=\frac{1}{2}\left|-\omega^{2}t\mathrm{e}^{-\zeta\omega t}\cos\omega t*\ddot{u}_{\mathrm{g}}(t)+\omega\mathrm{e}^{-\zeta\omega t}\sin\omega t*\ddot{u}_{\mathrm{g}}(t)\right|_{\max}. \tag{3.5.1}$$

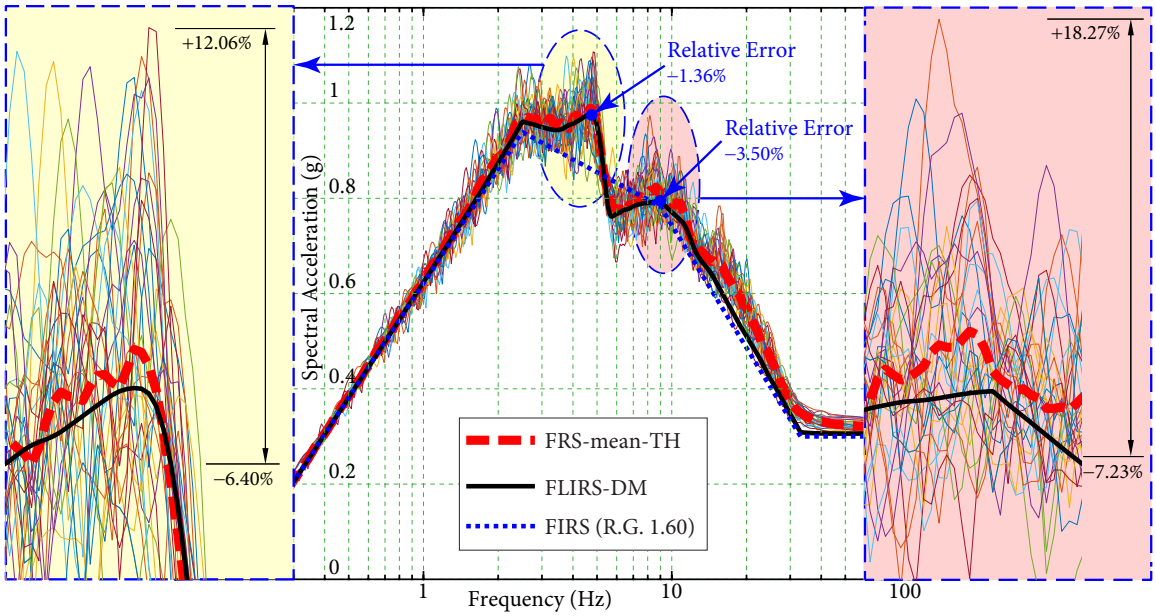


Figure 3.4 Comparison of FLIRS and the corresponding FRS from time history analyses (k_s=8 × 10^4 kN/m)

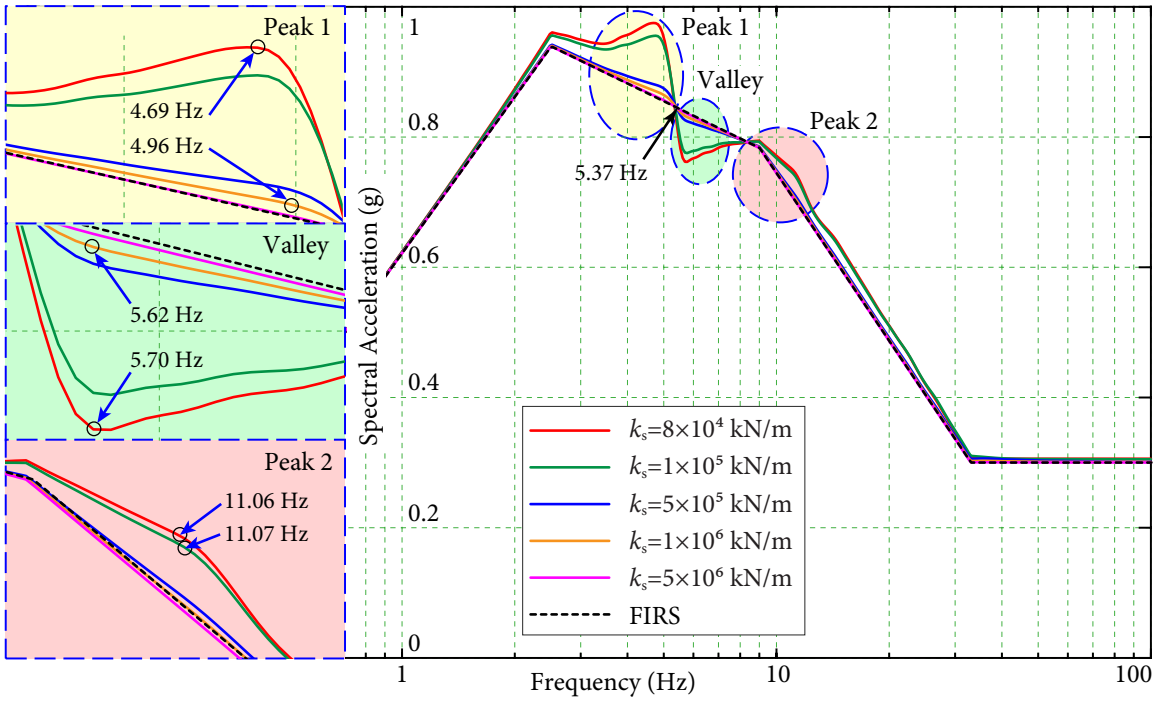


Figure 3.5 FLIRS for different soil cases

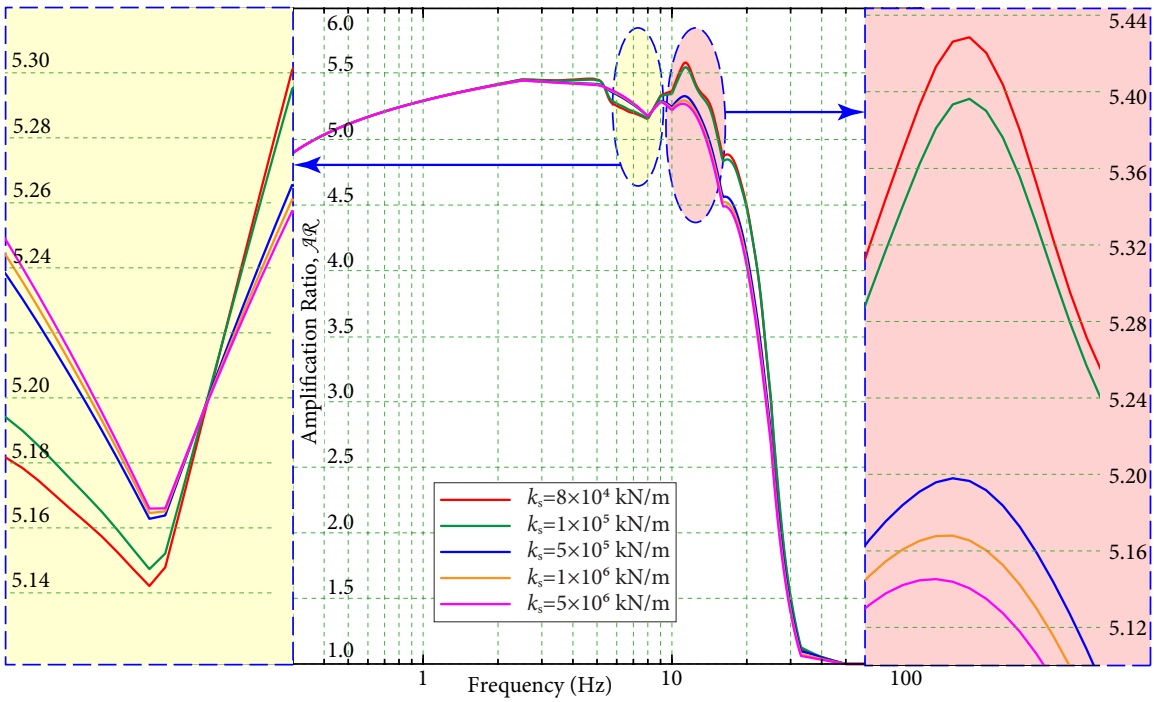


Figure 3.6 tRS in direct method for different soil cases

This equation is defined as t-Response Spectrum (tRS), in which "t" indicates "tuning" or the extra "t" variable in the first convolution term as compared to GRS. A comprehensive study on the statistical relationship between GRS and tRS was conducted by Li *et al.* (2015). The amplification ratio, $AR = \mathcal{S}_{\mathrm{A}}^{\mathrm{t}}(f,\zeta)/\mathcal{S}_{\mathrm{A}}(f,\zeta)$, was determined for various soil stiffness cases, where $\mathcal{S}_{\mathrm{A}}^{\mathrm{t}}(f,\zeta)$ is tRS, $\mathcal{S}_{\mathrm{A}}(f,\zeta)$ is the GRS. To generate FRS for the structure, FLIRS, which include the effect of SSI, are input as the GRS into fixed-base model. AR of all tRS are presented in Figure 3.6. It is evident that the change of peaks and valleys align with those of FLIRS, indicating that the presence of SSI affects the responses of structure. A significant dip is observed in the frequency range of 5.3 Hz to 10 Hz, which can be attributed to energy absorption of underlying soil at specific frequencies close to the fundamental frequencies of the structure.

Validation of FRS from General Formulation

FRS at various nodes are plotted along with the FRS generated by the 30 sets of time history analyses. The case of softest soil at Node 1 is presented in Figure 3.7, while other cases are

shown in Appendix B. FRS obtained by the direct method and the mean FRS of the time history analyses, which are regarded as the benchmark, are shown in black solid lines and red dash lines, respectively. It is seen that the FRS obtained by the general formulation are agree extremely well with the benchmark FRS over the entire frequency range, whereas results from time histories analyses exhibit large variability. Taken FRS at Node 1 in the softest soil as an example, the relative errors of FRS from general formulation and the benchmark are $+1.84\%$ and -3.08% for peak 1 and 2, respectively. As shown in Figures B.7 to B.9), the relative errors range from $+4.75\%$ to -1.87% for peak 1, and $+4.84\%$ to $+1.75\%$ for peak 2, when FRS at Node 2 is compared.

However, the results obtained from time history analyses exhibit significant variability, with an overall maximum overestimation and underestimation of 42.43% and 42.70%, and 40.80% and 47.42%, for Node 1 and Node 2, respectively, depending on the input of time histories. Nevertheless, the differences at the FRS peaks and valleys between general formulation and benchmarks are generally less than 5%, which are well within the range of acceptable errors, suggesting the reliability and accuracy of general formulation method in generating FRS of structures.

3.6 Effect of SSI on the FRS of Structure

The influence of SSI on FRS is initially examined by comparing the benchmarks of mean FRS for the fixed-base and the coupled models, as shown in Figure 3.8. The underlying soil reduces the peak value of FRS by -17.78% and -6.34% at peaks 1 and 2, respectively, indicating that SSI effect is significant while considering soil. However, the FRS of the soil-structure model is not always lower than that of the fixed-base model. There is an average increase of 6.24% in FRS between frequencies of 2 Hz and 5 Hz, which, if neglected, could lead to non-conservative results in structural design. Moreover, similar to FLIRS, the main peak of FRS shifts towards lower frequencies as the SSI increases, which may have implications for the design of structures. Therefore, SSI should be considered not only for changes in the FRS value but also for shifting FRS peaks.

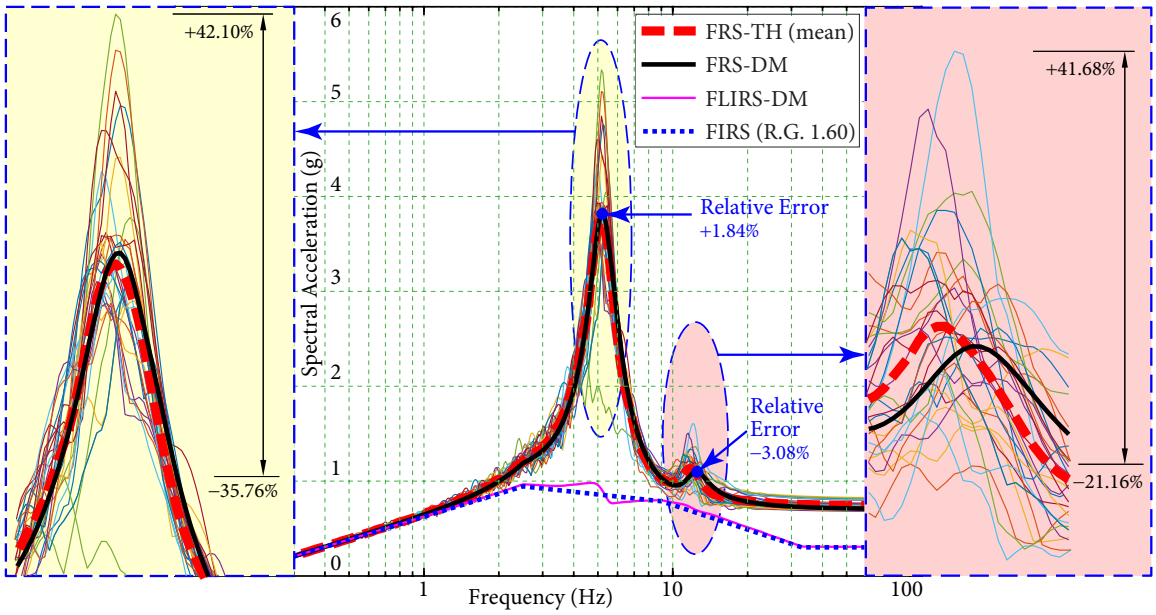


Figure 3.7 Comparison of FRS for Node 1 (k_s=8 × 10^4 kN/m)

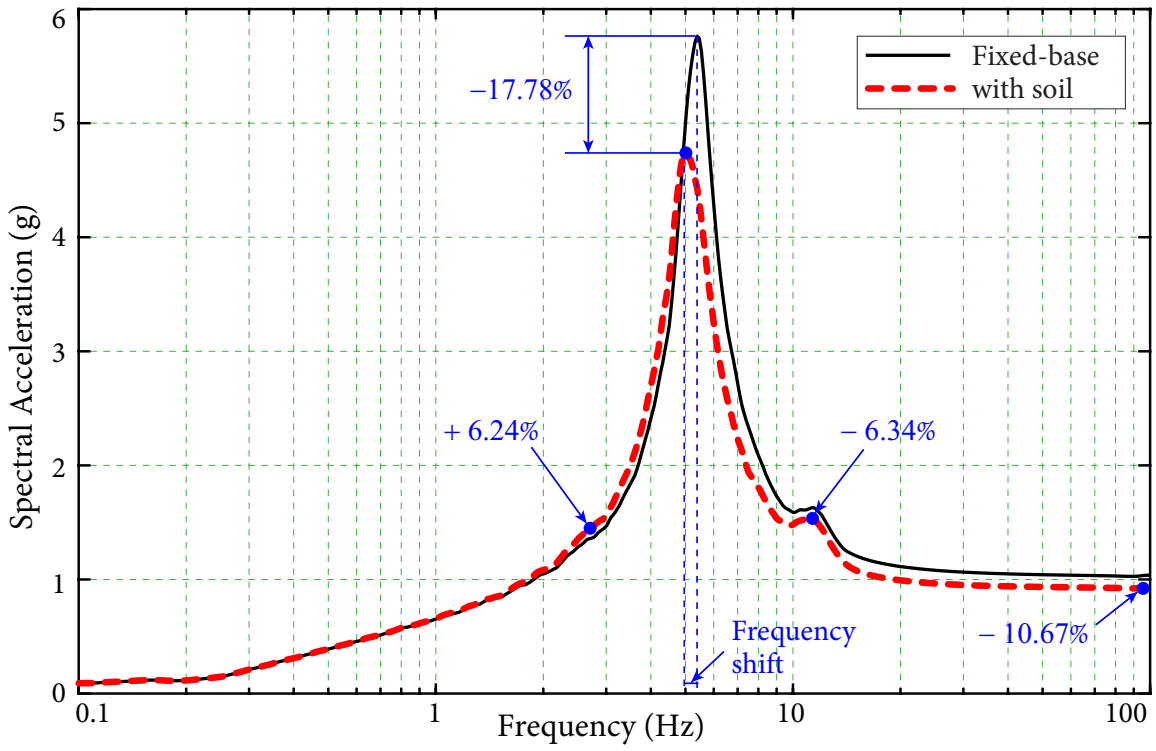


Figure 3.8 Soil-structure interaction effect on FRS

3.7 Summary

A numerical example is presented to verify the proposed method considering SSI. Although the structure in this chapter is not complicated, it allows the explicit expressions of the matrices in the formulation to be existed. A 3-DOF structure with two structure nodes and one foundation node supported by a generalized soil spring at a single support is studied. The theoretical formulation of FLIRS in this example demonstrates the seismic responses of the coupled soil-structure system under the excitations FIRS is equivalent to those of the decoupled structure under the modified inputs FLIRS. As a result, the replacement of FIRS with soil by FLIRS is theoretically rigorous. The numerical results of FRS indicate that the proposed method is of great accuracy in the generation of FRS considering the effect of SSI.

Parametric studies are also performed to investigate the influence of soil conditions on FRS. It is found that the consideration of soil might either increase or decrease the seismic responses of secondary structures. The effect of SSI could result in the shifting of FRS peaks. Hence, it is of great practical importance to consider SSI in the structural dynamic analysis.

In summary, the proposed method is validated accurate and efficient for the generation of FRS considering SSI for sites with soil classification of D or higher, which is generally the case in the nuclear power industry.

C H A P T E R 4

Dynamic Soil Stiffness Matrices

The accurate characterization of SSI plays a pivotal role in the seismic analysis and design of SMRs. At the heart of SSI lies the determination of the dynamic soil stiffness matrix, which acts as a crucial bridge between excitation forces and responses in soil-structure systems. This matrix encapsulates the intricate behaviour of soil under dynamic loading conditions and is a frequency-dependent property that accounts for mass, stiffness, and damping characteristics. However, deriving this matrix involves complex mathematical formulations, posing a significant challenge for researchers and potentially impeding progress in SSI analysis. This chapter presents a comprehensive exploration of dynamic soil stiffness matrices, covering their derivation, evaluation procedures, and progressive validation, thereby enhancing understanding and facilitating more accurate seismic analysis and design of SMRs and other critical nuclear facilities.

4.1 Dynamic Stiffness Matrix and Dynamic Flexibility Matrix

In the realm of structural dynamics analysis for nuclear power plants, particularly those involving deeply embedded SMRs, the dynamic stiffness matrix of the surrounding soil plays a pivotal role. The dynamic stiffness matrix, denoted as $\mathbf{S}(\omega)$, serves as a fundamental tool for characterizing the intricate excitation-response relationship between the underlying soil and super structure system in the frequency domain. It encapsulates the frequency-

dependent behaviour of the system, taking into account the inherent mass, stiffness, and damping properties, which effect the soil-structure interaction.

Consider the steady-state harmonic problem of a multiple degrees-of-freedom system, the equation of motion is

$$\mathbf{M}\ddot{\mathbf{x}}(t) + \mathbf{C}\dot{\mathbf{x}}(t) + \mathbf{K}\mathbf{x}(t) = \mathbf{p}(t) \tag{4.1.1}$$

Let $\mathbf{x}(t) = \mathbf{X}\,e^{i\omega t}, \mathbf{p}(t) = \mathbf{P}\,e^{i\omega t}$,

$$-\omega^2\,\mathbf{M}\,\mathbf{X}\,e^{i\omega t} + i\omega\mathbf{C}\,\mathbf{X}\,e^{i\omega t} + \mathbf{K}\mathbf{X}\,e^{i\omega t} = \mathbf{P}\,e^{i\omega t} \tag{4.1.2}$$

Let $\mathbf{S}(\omega) = -\omega^2\,\mathbf{M} + i\omega\,\mathbf{C} + \mathbf{K}$, then the equation (4.1.2) becomes

$$\mathbf{S}(\omega)\,\mathbf{X} = \mathbf{P} \tag{4.1.3}$$

in which $\mathbf{S}(\omega)$ is the frequency-dependent dynamic stiffness matrix, representing a complex frequency response function, $\mathbf{K} - \omega^2\,\mathbf{M}$ represents the real part of the dynamic stiffness matrix caused by static stiffness and the inertia effect, while $-i\,\omega\,\mathbf{C}$ is the imaginary part considering the damping effect. It is a square matrix with dimensions equal to the degrees of freedom of the structure. Multiply by the inverse matrix of $\mathbf{S}(\omega)$ yields,

$$\mathbf{X} = \mathbf{S}(\omega)^{-1}\mathbf{P} = \mathbf{F}(\omega)\,\mathbf{P} \tag{4.1.4}$$

where $\mathbf{F}(\omega) = \mathbf{S}(\omega)^{-1}$ is the dynamic flexibility matrix. It is a dynamic generalization of the static flexibility matrix. Consider the special case with $P_i = 1, P_1 = P_2 = \ldots = P_{i-1} = P_{i+1} = \ldots = P_n = 0$, then the dynamic flexibility matrix $X_{ij} = F_{ij}$, suggesting that F_{ij} is the displacement at point i due to a unit load applied at point j. It is notice that $\mathbf{F}(\omega = 0) = \mathbf{K}^{-1}$, multiplying both sides by eigenvector and its transpose yields

$$\mathbf{\Phi}^T\,\mathbf{F}^{-1}\mathbf{\Phi} = \mathbf{\Phi}^T\,\mathbf{K}\mathbf{\Phi}. \tag{4.1.5}$$

For a multiple degree-of-freedom structure, if the mode shape vector Φ_i is normalized, $\Phi_i^T\,\mathbf{M}\,\Phi_i = 1$, the flexibility matrix $\mathbf{F}$ can be determined in two ways: using either dynamic or static data. Measuring the static tests is more accurate than dynamic ones; however, the sensitivity of static methods to the change in the structural parameters is low. The static methods only require the stiffness properties, whereas the dynamic methods require the use of mass, stiffness and damping properties.

Flexibility Matrix

In the finite element method, apply a unit dynamic load in a specific DOF i, while loads in other DOF are 0, the steady-state dynamic displacement in any DOF j can be determined. This concept is fundamental to the evaluation of the dynamic flexibility matrix. The load vector $\mathbf{P}$ can be expressed as follows,

$$\mathbf{P} = \begin{Bmatrix} P_1 \\ P_2 \\ \vdots \\ P_i \\ \vdots \\ P_n \end{Bmatrix} = \begin{Bmatrix} 0 \\ 0 \\ \vdots \\ 1 \\ \vdots \\ 0 \end{Bmatrix} \quad \left(P_i = 1, \quad \text{other elements are } 0\right) \tag{4.1.6}$$

where $P_i = 1$ represents the unit dynamic load applied at DOF i, and all other elements of the load vector are 0.

Under this loading condition, the relationship between the steady-state dynamic displacement X_{ji} at DOF j and the corresponding element F_{ji} of the dynamic flexibility matrix can be expressed as:

$$X_{ji} = F_{ji} \tag{4.1.7}$$

where X_{ji} is the amplitude of dynamic steady-state displacement in DOF j when a unit dynamic load is applied at DOF i, while loads at other DOF are 0.

Considering a harmonic excitation, the relationship between the displacement and the dynamic flexibility in the complex form can be expressed as,

$$X_{ji}\, \mathrm{e}^{\mathrm{i}\omega t} = F_{ji}(\omega)\, \mathrm{e}^{\mathrm{i}\omega t}. \tag{4.1.8}$$

Using Euler's formula, $\mathrm{e}^{\mathrm{i}\omega t} = \cos\,\omega t + \mathrm{i}\sin\,\omega t$, equation (4.1.8) can be rewritten as,

$$\left(X_{ji}^{\mathcal{R}e} + \mathrm{i}\, X_{ji}^{\mathcal{I}m}\right)\left[\cos\,\omega t + \mathrm{i}\sin\,\omega t\right] = \left[F_{ji}^{\mathcal{R}e}(\omega) + \mathrm{i}\, F_{ji}^{\mathcal{I}m}(\omega)\right]\left[\cos\,\omega t + \mathrm{i}\sin\,\omega t\right]. \tag{4.1.9}$$

Expanding the above equation yields,

$$\begin{aligned} &\left[X_{ji}^{\mathcal{R}e}\,\cos\,\omega t - X_{ji}^{\mathcal{I}m}\,\sin\,\omega t\right] + \mathrm{i}\left[X_{ji}^{\mathcal{R}e}\,\sin\,\omega t - X_{ji}^{\mathcal{I}m}\,\cos\,\omega t\right] \\ = &\left[F_{ji}^{\mathcal{R}e}(\omega)\,\cos\,\omega t - F_{ji}^{\mathcal{I}m}(\omega)\,\sin\,\omega t\right] + \mathrm{i}\left[F_{ji}^{\mathcal{R}e}(\omega)\,\sin\,\omega t - F_{ji}^{\mathcal{I}m}(\omega)\,\cos\,\omega t\right] \end{aligned} \tag{4.1.10}$$

Note that if

- A dynamic load $\cos \omega t$ is applied, use the real parts;
- A dynamic load $\sin \omega t$ is applied, use the imaginary parts.

These relationships allow us to determine the real and imaginary parts of the dynamic flexibility matrix elements by applying the appropriate harmonic loads and evaluating the corresponding steady-state displacements. Therefore, the follow procedure can be adopted to evaluating the elements in the dynamic flexibility matrix.

Procedure

- Apply a unit dynamic load $\cos \omega t$ at DOF i, while loads at other DOF are 0.
- Determine the dynamic steady-state displacement at DOF j,

$$\begin{aligned} X_{ji}(t) &= X_{ji}^{\mathcal{R}e} \cos \omega t - X_{ji}^{\mathcal{I}m} \sin \omega t = A_{ji} \cos\left(\omega t + \varphi_{ji}\right) \\ \therefore \quad F_{ji}^{\mathcal{R}e}(\omega) &= X_{ji}^{\mathcal{R}e} = A_{ji} \cos \varphi_{ji}, \qquad F_{ji}^{\mathcal{I}m}(\omega) = X_{ji}^{\mathcal{I}m} = A_{ji} \sin \varphi_{ji}. \end{aligned} \tag{4.1.11}$$

Alternative Procedure

- Apply a unit dynamic load $\sin \omega t$ at DOF i, while loads at other DOF are 0.
- Determine the dynamic steady-state displacement at DOF j,

$$\begin{aligned} X_{ji}(t) &= X_{ji}^{\mathcal{R}e} \sin \omega t + X_{ji}^{\mathcal{I}m} \cos \omega t = A_{ji} \sin\left(\omega t + \varphi_{ji}\right) \\ \therefore \quad F_{ji}^{\mathcal{R}e}(\omega) &= X_{ji}^{\mathcal{R}e} = A_{ji} \cos \varphi_{ji}, \qquad F_{ji}^{\mathcal{I}m}(\omega) = X_{ji}^{\mathcal{I}m} = A_{ji} \sin \varphi_{ji}. \end{aligned} \tag{4.1.12}$$

Figure 4.1 demonstrates the relationship between real part and imaginary part of the steady-state response. The amplitude of the response, A_{ij}, can be evaluated by $A_{ji} = \sqrt{\left(F_{ji}^{\mathcal{R}e}\right)^2 + \left(F_{ji}^{\mathcal{I}m}\right)^2}$; the phase lag, $\varphi_{ji} = \arctan\left(F_{ji}^{\mathcal{R}e} / F_{ji}^{\mathcal{I}m}\right)$.

4.2 Verification for Lumped-Mass System – A 3-DOF Structure

In this section, an analytical analysis and numerical analysis are conducted on a 3-DOF structural system, as shown in Figure 4.2. The dynamic steady-state displacements are

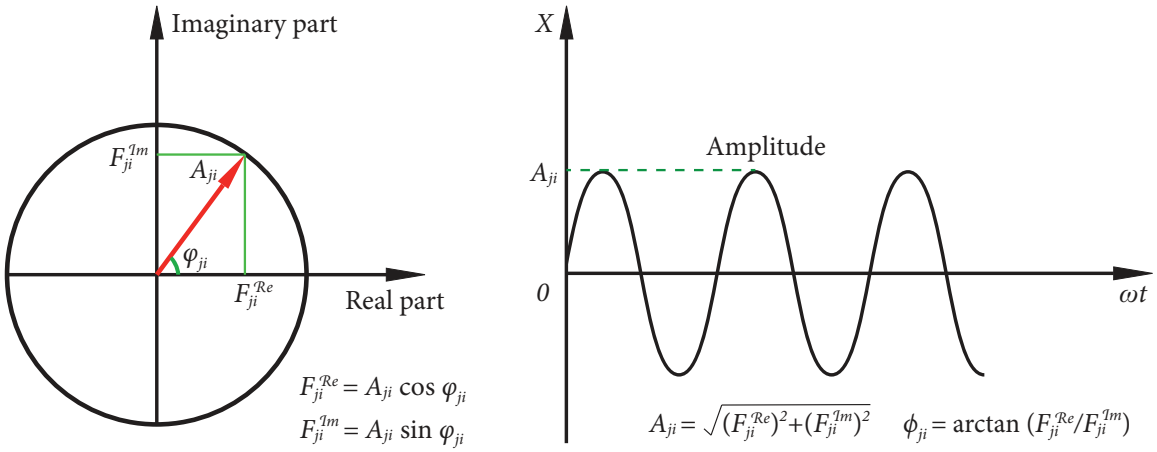


Figure 4.1 Relationship between real part and imaginary part for steady state

derived for each DOF under the corresponding dynamic sinusoidal loading. These displacements are then assembled to form the dynamic flexibility matrix. Meanwhile, the dynamic stiffness matrix for the 3-DOF system is computed. The multiplication of the dynamic flexibility matrix and the dynamic stiffness matrix is proven to result in an identity matrix, **I**, verifying that the dynamic stiffness matrix can be obtained by inversing the dynamic flexibility matrix. The comparison between the results obtained from the analytical and numerical analyses demonstrates that applying dynamic harmonic loading at the corresponding nodes allows for the determination of the associated displacements. These displacements can then be assembled into the dynamic flexibility matrix, from which the dynamic stiffness matrix can be derived. The results show excellent agreement between the two approaches, confirming the reliability of the method.

4.2.1 Theoretical Derivation

For the 3-DOF structure system as shown in Figure 4.2, the equation of motion can be written as,

$$\begin{bmatrix} m_1 & 0 & 0 \\ 0 & m_2 & 0 \\ 0 & 0 & m_3 \end{bmatrix} \begin{bmatrix} \ddot{x}_1 \\ \ddot{x}_2 \\ \ddot{x}_3 \end{bmatrix} + \begin{bmatrix} c_1 + c_2 & -c_2 & 0 \\ -c_2 & c_2 + c_3 & -c_3 \\ 0 & -c_3 & c_3 \end{bmatrix} \begin{bmatrix} \dot{x}_1 \\ \dot{x}_2 \\ \dot{x}_3 \end{bmatrix} + \begin{bmatrix} k_1 + k_2 & -k_2 & 0 \\ -k_2 & k_2 + k_3 & -k_3 \\ 0 & -k_3 & k_3 \end{bmatrix} \begin{bmatrix} x_1 \\ x_2 \\ x_3 \end{bmatrix} = \begin{bmatrix} P_1 \cos \omega t \\ P_2 \cos \omega t \\ P_3 \cos \omega t \end{bmatrix} \tag{4.2.1}$$

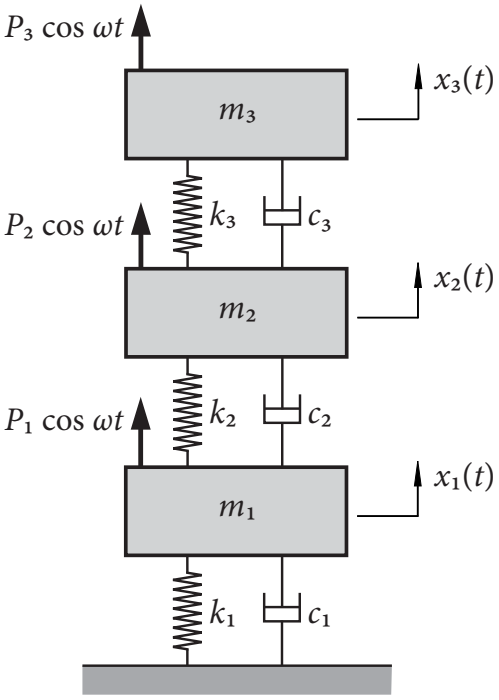


Figure 4.2 3DOF Model for Theoretical Verification

The equations of motion can be written using the $\mathcal{D}$-operator as

$$\begin{bmatrix} m_1\,\mathcal{D}^2+(c_1+c_2)\,\mathcal{D}+k_1+k_2 & -c_2\,\mathcal{D}-k_2 & 0 \\ -c_2\,\mathcal{D}-k_2 & m_2\,\mathcal{D}^2+(c_2+c_3)\,\mathcal{D}+k_2+k_3 & -c_3\,\mathcal{D}-k_3 \\ 0 & -c_3\,\mathcal{D}-k_3 & m_3\,\mathcal{D}^2+c_3\,\mathcal{D}+k_3 \end{bmatrix} \begin{bmatrix} x_1 \\ x_2 \\ x_3 \end{bmatrix} = \begin{bmatrix} P_1\cos\omega t \\ P_2\cos\omega t \\ P_3\cos\omega t \end{bmatrix} \tag{4.2.2}$$

Because of the existence of damping, the responses of free vibration (complementary solutions) decay exponentially and approach zero as time increases. Hence, it is practically more important and useful to study responses of forced vibration (particular solutions). The determinant of the coefficient matrices are

$$\varphi(\mathcal{D}) = \begin{vmatrix} m_1\,\mathcal{D}^2+(c_1+c_2)\,\mathcal{D}+k_1+k_2 & -c_2\,\mathcal{D}-k_2 & 0 \\ -c_2\,\mathcal{D}-k_2 & m_2\,\mathcal{D}^2+(c_2+c_3)\,\mathcal{D}+k_2+k_3 & -c_3\,\mathcal{D}-k_3 \\ 0 & -c_3\,\mathcal{D}-k_3 & m_3\,\mathcal{D}^2+c_3\,\mathcal{D}+k_3 \end{vmatrix} \tag{4.2.3}$$

and

$$\Delta_1 = \begin{vmatrix} P_1 \cos \omega t & -c_2\, \mathcal{D} - k_2 & 0 \\ P_2 \cos \omega t & m_2\, \mathcal{D}^2 + (c_2 + c_3)\, \mathcal{D} + k_2 + k_3 & -c_3\, \mathcal{D} - k_3 \\ P_3 \cos \omega t & -c_3\, \mathcal{D} - k_3 & m_3\, \mathcal{D}^2 + c_3\, \mathcal{D} + k_3 \end{vmatrix},$$

$$\Delta_2 = \begin{vmatrix} m_1\, \mathcal{D}^2 + (c_1 + c_2)\, \mathcal{D} + k_1 + k_2 & P_1 \cos \omega t & 0 \\ -c_2\, \mathcal{D} - k_2 & P_2 \cos \omega t & -c_3\, \mathcal{D} - k_3 \\ 0 & P_3 \cos \omega t & m_3\, \mathcal{D}^2 + c_3\, \mathcal{D} + k_3 \end{vmatrix},$$

$$\Delta_3 = \begin{vmatrix} m_1\, \mathcal{D}^2 + (c_1 + c_2)\, \mathcal{D} + k_1 + k_2 & -c_2\, \mathcal{D} - k_2 & P_1 \cos \omega t \\ -c_2\, \mathcal{D} - k_2 & m_2\, \mathcal{D}^2 + (c_2 + c_3)\, \mathcal{D} + k_2 + k_3 & P_2 \cos \omega t \\ 0 & -c_3\, \mathcal{D} - k_3 & P_3 \cos \omega t \end{vmatrix}. \tag{4.2.4}$$

Applying Cramer's Rule and replacing $\mathcal{D}^2$ with $-\omega^2$ (Xie, 2010) yields the particular solutions $x_{1P}(t), x_{2P}(t)$ and $x_{3P}(t)$ or response of forced vibration due to the excitation

$$\begin{aligned} x_{1P}(t) &= \frac{\Delta_1}{\Phi(\mathcal{D})} = \frac{(\alpha_1\, \mathcal{D} + \beta_1)\, \cos(\omega\, t)}{A_0\, \mathcal{D} + B_0} \\ x_{2P}(t) &= \frac{\Delta_2}{\Phi(\mathcal{D})} = \frac{(\alpha_2\, \mathcal{D} + \beta_2)\, \cos(\omega\, t)}{A_0\, \mathcal{D} + B_0} \\ x_{3P}(t) &= \frac{\Delta_3}{\Phi(\mathcal{D})} = \frac{(\alpha_3\, \mathcal{D} + \beta_3)\, \cos(\omega\, t)}{A_0\, \mathcal{D} + B_0} \end{aligned} \tag{4.2.5}$$

where

$A_0 = \{[m_1\, c_3 + (c_1 + c_2)\, m_2 + c_2\, m_1]\, m_3 + m_2\, c_3\, m_1\}\, \omega^4 + \{[(-k_1 - k_2)\, c_3 + (-c_1 - c_2)\, k_3 - c_1\, k_2 - k_1\, c_2]\, m_3 + [(-k_1 - k_2)\, m_2 - c_1\, c_2 - k_2\, m_1]\, c_3 - k_3\, [(c_1 + c_2)\, m_2 + c_2\, m_1]\}\, \omega^2 + c_3\, k_1\, k_2 + k_3\, (c_1\, k_2 + c_2\, k_1)$,

$B_0 = -\omega^6\, m_1\, m_2\, m_3 + (((c_1 + c_2)\, c_3 + m_1\, k_3 + (k_1 + k_2)\, m_2 + c_1\, c_2 + k_2\, m_1)\, m_3 + ((c_1 + c_2)\, m_2 + c_2\, m_1)\, c_3 + m_2\, k_3\, m_1)\, \omega^4 + (((-k_1 - k_2)\, k_3 - k_1\, k_2)\, m_3 + (-c_1\, k_2 - c_2\, k_1)\, c_3 - ((k_1 + k_2)\, m_2 + c_1\, c_2 + k_2\, m_1)\, k_3)\, \omega^2 + k_1\, k_2\, k_3$,

$\alpha_1 = ((-m_3\, c_2 - c_3\, (m_2 + m_3))\, P_1 - m_3\, P_2\, c_2)\, \omega^2 + (c_2\, k_3 + c_3\, k_2)\, (P_1 + P_2 + P_3)$,

$\beta_1 = \omega^4 P_1 m_2 m_3 + ((-c_3 c_2 - m_3 k_2 - k_3 (m_2 + m_3)) P_1 - c_3 (P_2 + P_3) c_2 - m_3 P_2 k_2) \omega^2 + k_3 k_2 (P_1 + P_2 + P_3)$,

$\alpha_2 = ((-m_1 c_3 - m_3 (c_1 + c_2)) P_2 - P_1 c_2 m_3 - P_3 c_3 m_1) \omega^2 + ((k_1 + k_2) c_3 + k_3 (c_1 + c_2)) P_2 + ((k_1 + k_2) P_3 + k_2 P_1) c_3 + k_3 ((c_1 + c_2) P_3 + P_1 c_2)$,

$\beta_2 = \omega^4 P_2 m_1 m_3 + (((-c_1 - c_2)c_3 - m_1 k_3 - m_3(k_1 + k_2))P_2 + ((-c_1 - c_2)P_3 - P_1 c_2)c_3 - k_2 m_3 P_1 - m_1 P_3 k_3)\omega^2 + k_3(k_1 + k_2)P_2 + k_3((k_1 + k_2)P_3 + k_2 P_1)$,

$\alpha_3 = ((-m_1 c_3 + (-m_1 - m_2) c_2 - m_2 c_1) \omega^2 + (k_1 + k_2) c_3 + k_3 (c_1 + c_2) + k_1 c_2 + c_1 k_2) P_3 - m_1 P_2 c_3 \omega^2 + ((k_1 + k_2) P_2 + k_2 P_1) c_3 + ((c_1 + c_2) P_2 + P_1 c_2) k_3$,

$\beta_3 = (m_1 m_2 \omega^4 + ((-c_1 - c_2) c_3 - m_1 k_3 - c_1 c_2 + (-m_1 - m_2) k_2 - m_2 k_1) \omega^2 + k_3 (k_1 + k_2) + k_1 k_2) P_3 + (((-c_1 - c_2) P_2 - P_1 c_2) c_3 - k_3 m_1 P_2) \omega^2 + k_3 ((k_1 + k_2) P_2 + k_2 P_1)$.

By eliminating $(A_0 \mathcal{D} + B_0)$ in the denominator in equation (4.2.5), the steady-state solution can be re-written as,

$$\begin{aligned} x_{1P}(t) &= x_{1C} \cos \omega t + x_{1S} \sin \omega t \\ x_{2P}(t) &= x_{2C} \cos \omega t + x_{2S} \sin \omega t \\ x_{3P}(t) &= x_{3C} \cos \omega t + x_{3S} \sin \omega t \end{aligned} \tag{4.2.6}$$

in which,

$$\begin{aligned} x_{1C}(t) &= \frac{A_0 \alpha_1 \omega^2 + B_0 \beta_1}{A_0^2 \omega^2 + B_0^2}, & x_{1S}(t) &= \frac{A_0 \beta_1 - \alpha_1 B_0}{A_0^2 \omega^2 + B_0^2}; \\ x_{2C}(t) &= \frac{A_0 \alpha_2 \omega^2 + B_0 \beta_2}{A_0^2 \omega^2 + B_0^2}, & x_{2S}(t) &= \frac{A_0 \beta_2 - \alpha_2 B_0}{A_0^2 \omega^2 + B_0^2}; \\ x_{3C}(t) &= \frac{A_0 \alpha_3 \omega^2 + B_0 \beta_3}{A_0^2 \omega^2 + B_0^2}, & x_{3S}(t) &= \frac{A_0 \beta_3 - \alpha_2 B_0}{A_0^2 \omega^2 + B_0^2}. \end{aligned} \tag{4.2.7}$$

According to the fundamental concept of the dynamic flexibility matrix in Section 4.1, the element f_{ji} $(i, j = 1, 2, 3)$ represents the displacement induced by the unit harmonic load $P_i = P \cos \omega t$ $(P = 1)$ which is applied in DOF i, while loadings in other DOF are 0. Dynamic flexibility matrix can be determined from the definition. Therefore, the elements are as follows,

(1). $P_1 = \cos\omega t, P_2 = 0, P_3 = 0$ are applied in DOF 1, 2, and 3, respectively. Substituting P_1, P_2, and P_3 into equation (4.2.7) gives

$$\begin{aligned} f_{11} &= (x_{1C} + \mathrm{i}\, x_{1S})\,|_{P_1=\cos\omega t,\, P_2=0,\, P_3=0}, \\ f_{21} &= (x_{2C} + \mathrm{i}\, x_{2S})\,|_{P_1=\cos\omega t,\, P_2=0,\, P_3=0}, \\ f_{31} &= (x_{3C} + \mathrm{i}\, x_{3S})\,|_{P_1=\cos\omega t,\, P_2=0,\, P_3=0}. \end{aligned} \tag{4.2.8}$$

(2). $P_1 = 0, P_2 = \cos\omega t, P_3 = 0$ are applied in DOF 1, 2, and 3, respectively.

$$\begin{aligned} f_{12} &= (x_{1C} + \mathrm{i}\, x_{1S})\,|_{P_1=0,\, P_2=\cos\omega t,\, P_3=0}, \\ f_{22} &= (x_{2C} + \mathrm{i}\, x_{2S})\,|_{P_1=0,\, P_2=\cos\omega t,\, P_3=0}, \\ f_{32} &= (x_{3C} + \mathrm{i}\, x_{3S})\,|_{P_1=0,\, P_2=\cos\omega t,\, P_3=0}. \end{aligned} \tag{4.2.9}$$

(3). $P_1 = 0, P_2 = 0, P_3 = \cos\omega t$ are applied in DOF 1, 2, and 3, respectively.

$$\begin{aligned} f_{13} &= (x_{1C} + \mathrm{i}\, x_{1S})\,|_{P_1=0,\, P_2=0,\, P_3=\cos\omega t}, \\ f_{23} &= (x_{2C} + \mathrm{i}\, x_{2S})\,|_{P_1=0,\, P_2=0,\, P_3=\cos\omega t}, \\ f_{33} &= (x_{3C} + \mathrm{i}\, x_{3S})\,|_{P_1=0,\, P_2=0,\, P_3=\cos\omega t}. \end{aligned} \tag{4.2.10}$$

Then the dynamic flexibility matrix **F** can be assembled as

$$\mathbf{F} = \begin{bmatrix} f_{11} & f_{12} & f_{13} \\ f_{21} & f_{22} & f_{23} \\ f_{31} & f_{32} & f_{33} \end{bmatrix} \tag{4.2.11}$$

From the definition of dynamic stiffness matrix, $\mathbf{S}(\omega)$ equals to

$$\mathbf{S}(\omega) = \begin{bmatrix} -\omega^2 m_1 + \mathrm{i}\,\omega\,(c_1 + c_2) + (k_1 + k_2) & -\mathrm{i}\,\omega\, c_2 - k_2 & 0 \\ -\mathrm{i}\,\omega\, c_2 - k_2 & -\omega^2 m_2 + i\,\omega\,(c_2 + c_3) + (k_2 + k_3) & -\mathrm{i}\,\omega\, c_3 - k_3 \\ 0 & -\mathrm{i}\,\omega\, c_3 - k_3 & -\omega^2 m_3 + \mathrm{i}\,\omega\, c_3 + k_3 \end{bmatrix} \tag{4.2.12}$$

Multiplying matrices **S** and **F** obtain

$$\mathbf{S}\,\mathbf{F} = \mathbf{I}, \tag{4.2.13}$$

suggesting that the dynamic stiffness matrix **S** is the inverse matrix of dynamic flexibility matrix **F**.

4.2.2 Analytical Calculation

In this section, an analytical calculation is presented to demonstrate the method for evaluating the dynamic stiffness matrix of the 3-DOF system shown in Figure 4.2. The purpose of this example is to validate the derivation and fundamental procedure for obtaining the dynamic stiffness matrix from the dynamic flexibility matrix, as described in the previous sections. The 3-DOF system is chosen for its simplicity and ability to illustrate the key steps involved in the evaluation process. The system parameters used in the analytical calculation are as follows:

- Masses: $m_1 = 6000\,\text{kg}, m_2 = 4000\,\text{kg}, m_3 = 3000\,\text{kg}$;
- Stiffnesses: $k_1 = 70000\,\text{N/m}, k_2 = 60000\,\text{N/m}, k_3 = 50000\,\text{N/m}$;
- Damping coefficients: $c_1 = 800\,\text{N·s/m}, c_2 = 600\,\text{N·s/m}, c_3 = 400\,\text{N·s/m}$.

The circular frequency considered in the calculation is $\omega = 5\,\text{rad/s}$. To minimize the computational error in calculating the dynamic flexibility matrix, it is advisable to introduce a sufficiently large amplitude for the dynamic load of $P_0 = 10000\,\text{N}$, to ensure the structure undergoes numerically significant displacement. The computed dynamic flexibility matrix can be then unitize by dividing P_0. This helps to reduce the data errors that may arise when dealing with tiny displacements.

In this analytical calculation, the dynamic loading is taken as a cosine function of $P = P_0 \cos\omega t$, the real part of Equation (4.1.10) is used to evaluate the dynamic flexibility matrix elements. The analytical calculation follows the procedure in Section 4.1.

Loading at DOF 1

Apply the unit cosinusoidal loading $P = P_0 \cos 5t$ at m_1, while loads at m_2 and m_3 are 0. In this case, the displacement are as follows,

$$f_{11}^{\text{Ana}} = x_{1C} + \mathrm{i}\, x_{1S} = \frac{25A_0\,\alpha_1 + B_0\,\beta_1}{25A_0^2 + B_0^2} + \mathrm{i}\,\frac{A_0\,\beta_1 - \alpha_1\,B_0}{25A_0^2 + B_0^2} = -0.18385 - \mathrm{i}\,0.03480$$

$$f_{21}^{\text{Ana}} = x_{2C} + \mathrm{i}\, x_{2S} = \frac{25A_0\,\alpha_2 + B_0\,\beta_2}{25A_0^2 + B_0^2} + \mathrm{i}\,\frac{A_0\,\beta_2 - \alpha_2\,B_0}{25A_0^2 + B_0^2} = -0.10156 - \mathrm{i}\,0.00477$$

$$f_{31}^{\text{Ana}} = x_{3C} + \mathrm{i}\, x_{3S} = \frac{25A_0\,\alpha_3 \;+ B_0\,\beta_3}{25A_0^2 \;+ B_0^2} + \mathrm{i}\,\frac{A_0\,\beta_3 - \alpha_3\,B_0}{25A_0^2 \;+ B_0^2} = 0.20005 + \mathrm{i}\,0.03367 \tag{4.2.14}$$

Loading at DOF 2

Apply the unit cosinusoidal loading $P = P_0 \cos 5t$ at m_2, while loads at m_1 and m_3 are 0. In this case, the displacement are as follows,

$$\begin{aligned} f_{12}^{\text{Ana}} &= -0.10156 - \mathrm{i}\,0.00477 \\ f_{22}^{\text{Ana}} &= 0.03381 - \mathrm{i}\,0.01195 \\ f_{32}^{\text{Ana}} &= -0.06983 + \mathrm{i}\,0.01561 \end{aligned} \tag{4.2.15}$$

Loading at DOF 3

Apply the unit cosinusoidal loading $P = P_0 \cos 5t$ at m_3, while loads at m_1 and m_2 are 0. In this case, the displacement are as follows,

$$\begin{aligned} f_{13}^{\text{Ana}} &= 0.20005 + \mathrm{i}\,0.03367 \\ f_{23}^{\text{Ana}} &= -0.06983 + \mathrm{i}\,0.01561 \\ f_{33}^{\text{Ana}} &= -0.25541 - \mathrm{i}\,0.04606 \end{aligned} \tag{4.2.16}$$

Assemble Matrices

The elements of the dynamic flexibility matrix $\bar{\mathbf{F}}^{\,\text{Ana}}$ are thus been evaluated, where the superscript $^{\text{Ana}}$ indicates that these values are obtained through analytical calculations. By assembling these elements according to Equation (4.2.11), the dynamic flexibility matrix $\mathbf{F}(\omega)|_{\omega=5}$ is obtained. To obtain the dynamic flexibility matrix $\bar{\mathbf{F}}^{\,\text{Ana}}$ under unit loading, each element of $\mathbf{F}^{\,\text{Ana}}$ is divided by the loading amplitude $P_0 = 10000\,\text{N}$. $\bar{\mathbf{F}}^{\,\text{Ana}}$ is

$$\begin{aligned} \bar{\mathbf{F}}^{\,\text{Ana}} &= \frac{\mathbf{F}^{\,\text{Ana}}}{P_0} \\ &= \begin{bmatrix} -1.83853 - \mathrm{i}\,0.34796 & -1.01562 - \mathrm{i}\,0.04773 & 2.00047 + \mathrm{i}\,0.33674 \\ -1.01562 - \mathrm{i}\,0.04773 & 0.33813 - \mathrm{i}\,0.11949 & -0.69831 + \mathrm{i}\,0.15606 \\ 2.00047 + \mathrm{i}\,0.33674 & -0.69831 + \mathrm{i}\,0.15606 & -2.55405 - \mathrm{i}\,0.46057 \end{bmatrix} \times 10^{-4} \end{aligned} \tag{4.2.17}$$

The dynamic stiffness matrix $\mathbf{S}(\omega)^{\text{Ana}}|_{\omega=5}$ is obtained by inverting the dynamic flexibility matrix in Equation 4.2.17. $\mathbf{S}^{\text{Ana}}$ is,

$$\begin{aligned}\mathbf{S}^{\text{Ana}} &= \left[\bar{\mathbf{F}}^{\text{Ana}}\right]^{-1} \\ &= \begin{bmatrix} -20000 + \mathrm{i}\,7000 & -60000 - \mathrm{i}\,3000 & 0 + \mathrm{i}\,0 \\ -60000 - \mathrm{i}\,3000 & 10000 + \mathrm{i}\,5000 & -50000 - \mathrm{i}\,2000 \\ 0 + \mathrm{i}\,0 & -50000 - \mathrm{i}\,2000 & -25000 + \mathrm{i}\,2000 \end{bmatrix}\end{aligned} \tag{4.2.18}$$

This dynamic stiffness matrix $\mathbf{S}^{\text{Ana}}$ is found to be identical to the analytically derived dynamic stiffness matrix given in Equation (4.2.12). This agreement confirms the validity of the relationship expressed in Equation (4.2.13), which states that the dynamic stiffness matrix is the inverse of the dynamic flexibility matrix.

4.2.3 Numerical Calculation

A numerical example is presented for the 3-DOF system problem shown in Figure 4.2. This example serves to validate the fundamental procedure for obtaining the dynamic stiffness matrix from the dynamic flexibility matrix, as elaborated in Section 4.2.1. The 3-DOF system is chosen for its simplicity and ability to illustrate the key steps involved in the evaluation process.

To validate the numerical method for evaluating the dynamic stiffness matrix of soil in the subsequent studies, it is essential to ensure the consistency between the numerical and analytical results. In this section, a numerical calculation is performed on the 3-DOF structure system shown in Figure 4.2, and the results are compared with the analytical solution derived in Section 4.2.1. This comparison aims to verify the accuracy and reliability of the numerical approach, such as the algorithm in extracting amplitude of steady-state response, and the phase lag between the response and loading. The numerical calculation follows the procedure outlined in Section 4.1.

By demonstrating the consistency between the numerical and analytical results for the 3-DOF system, confidence can be established in the numerical method's ability to accurately evaluate the dynamic stiffness matrix. This validation is crucial for extending the algorithm

in the numerical approach to more complex soil-structure interaction problems, where analytical solutions may not be readily available.

To evaluate the dynamic flexibility matrix of the 3-DOF system numerically, the following steps are performed:

(1). Apply a cosinusoidal load $P_0 \cos \omega t$ to each mass (m_1, m_2, and m_3) individually, while keeping the forces on the other masses zero. Calculate the steady-state responses for each mass under each loading condition using the numerical method. Denote the responses as f_{ji}^{Num}, where j represents the mass at which the response is measured, and i represents the mass at which the load is applied.

(2). Assemble the steady-state responses to form the dynamic flexibility matrix $\mathbf{F}^{\text{Num}}$ using Equation (4.2.11). This matrix represents the displacement response of the system to the applied harmonic loads.

(3). Unitized the dynamic flexibility matrix $\mathbf{F}^{\text{Num}}$. by dividing each element by the loading amplitude P_0 to obtain the unitized dynamic flexibility matrix $\bar{\mathbf{F}}^{\text{Num}}$.

(4). Invert the unitized dynamic flexibility matrix $\bar{\mathbf{F}}^{\text{Num}}$ to obtain the dynamic stiffness matrix $\mathbf{S}^{\text{Num}}$.

These steps provide a clear and concise procedure for numerically evaluating the dynamic flexibility matrix and subsequently obtaining the dynamic stiffness matrix for the 3-DOF system. By comparing the numerically obtained dynamic stiffness matrix with the analytical solution, the accuracy of the numerical method can be verified.

Loading at DOF 1

When a cosinusoidal load is applied at m_1, the responses of DOFs 1, 2, and 3 are shown in Figures 4.3 to 4.5. The responses exhibit an initial transient phase followed by a steady-state phase. The steady-state response is of interest for evaluating the dynamic characteristics of the system, such as the amplitude and phase of the displacement response, which are essential for studying the system's dynamic behaviour and validating the analytical model.

The portion of steady-state response are plotted along with the applied dynamic force in Figures 4.6 to 4.8. From these plots, the amplitudes and phase lags of the steady-state responses f_{11}^{Num}, f_{21}^{Num}, and f_{31}^{Num} can be computed. The results are presented in Table 4.1.

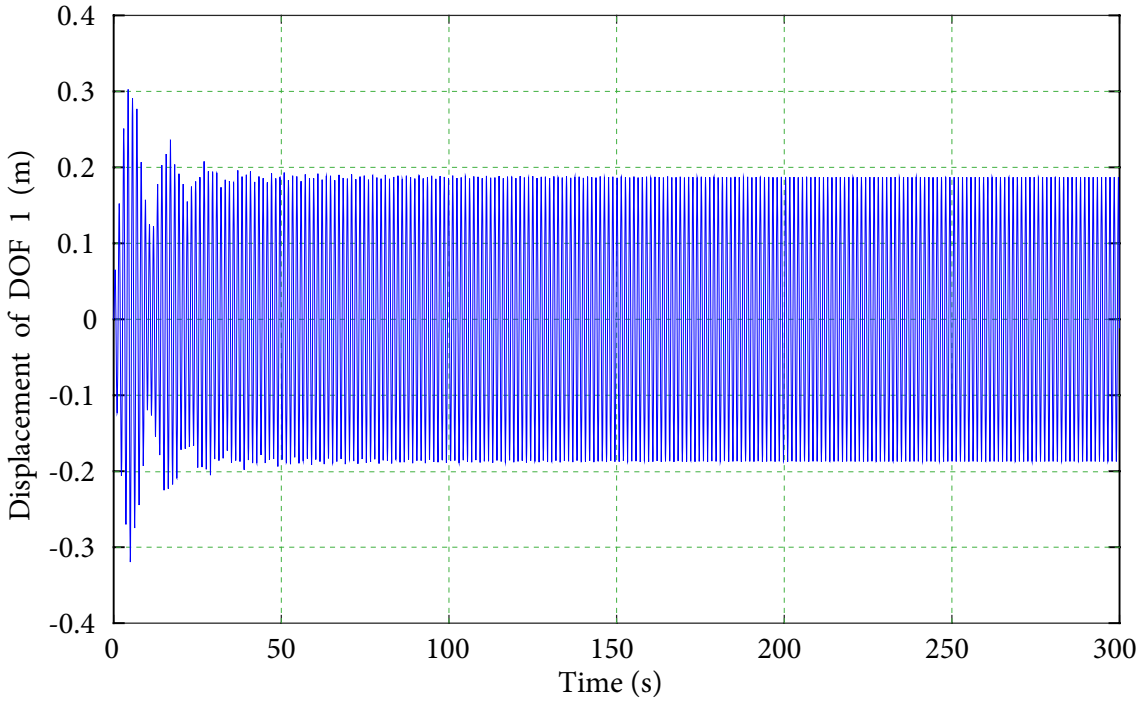


Figure 4.3 Response of DOF 1 under cosinusoidal loading applied at DOF 1

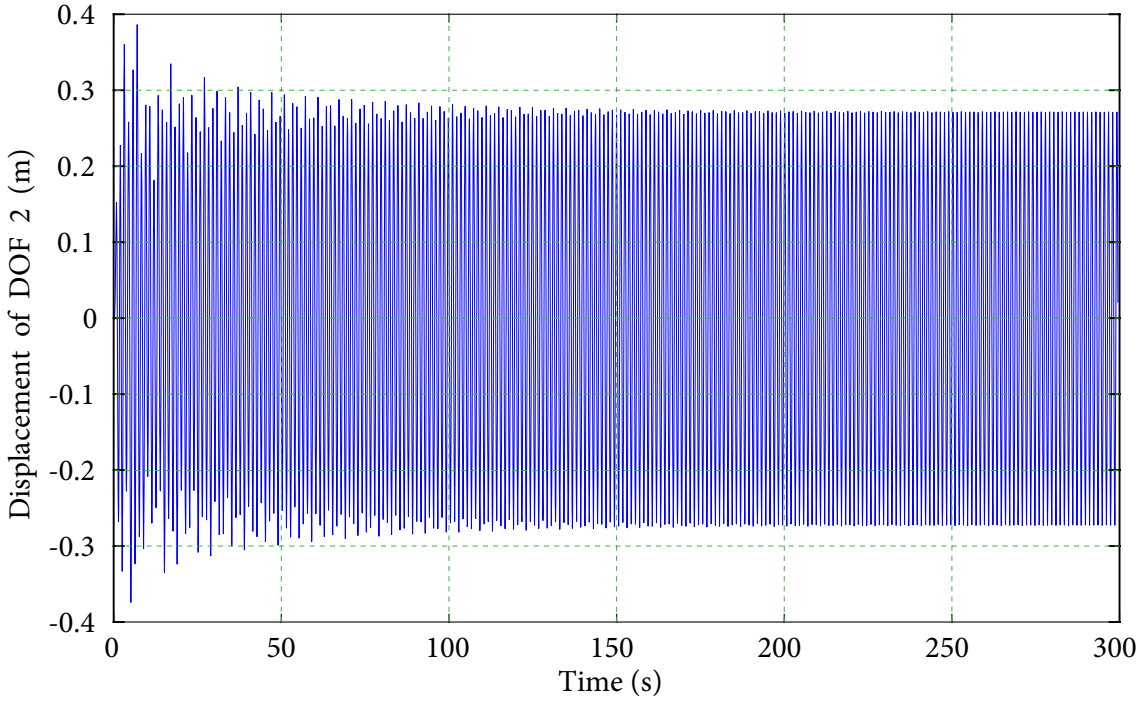


Figure 4.4 Response of DOF 2 under cosinusoidal loading applied at DOF 1

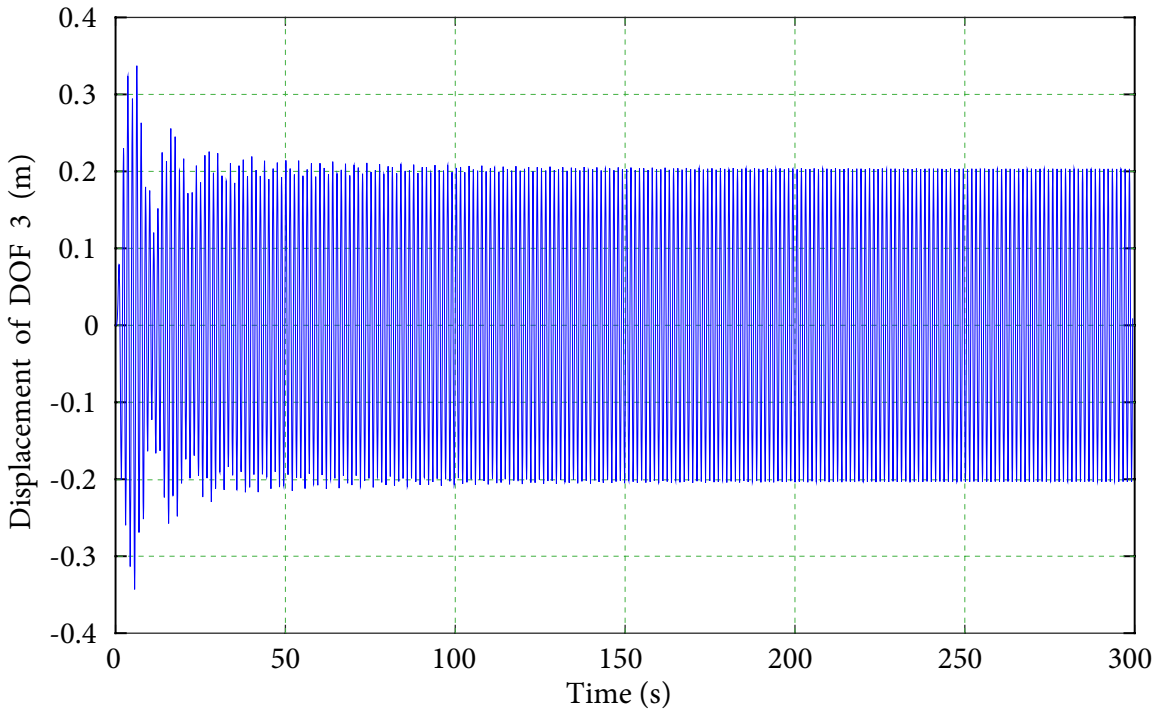


Figure 4.5 Response of DOF 3 under cosinusoidal loading applied at DOF 1

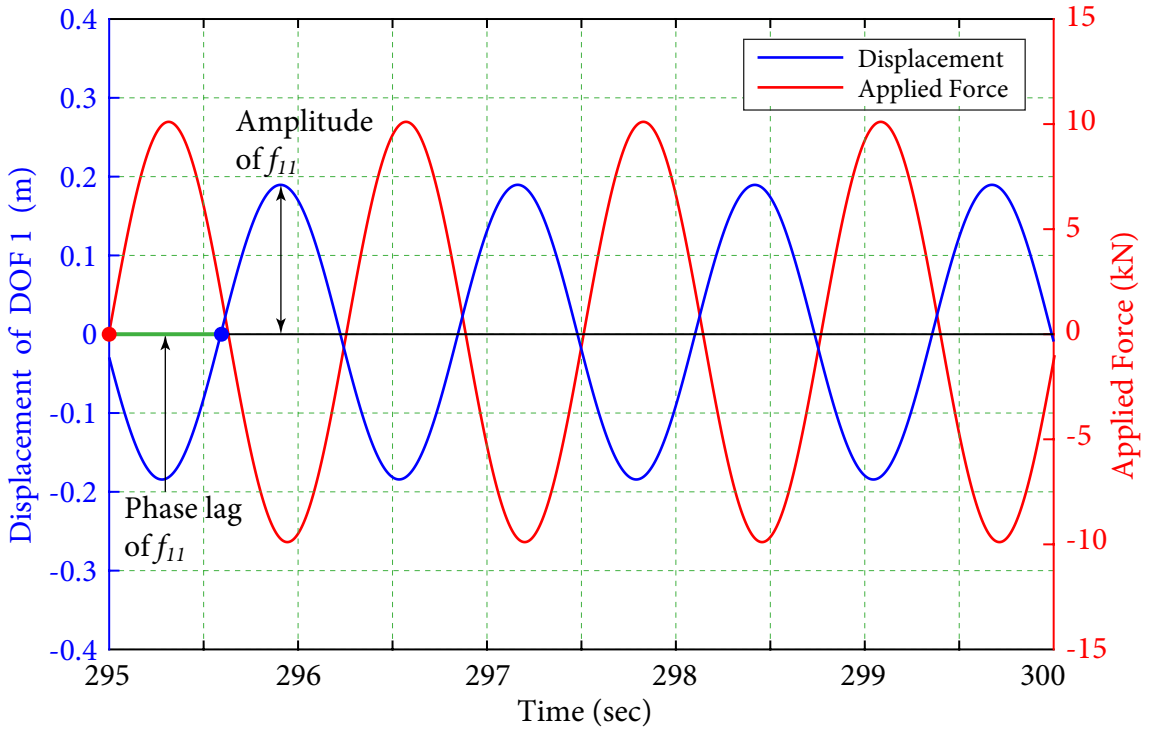


Figure 4.6 Steady-state response of DOF 1 under loading at DOF 1

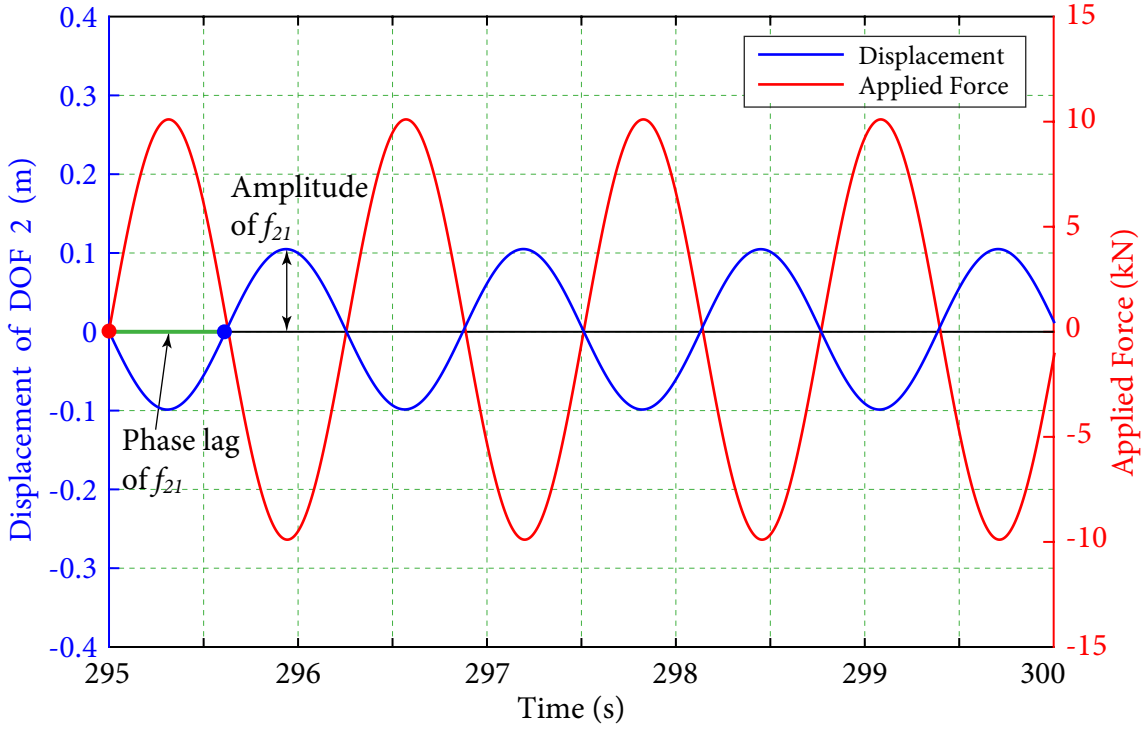


Figure 4.7 Steady-state response of DOF 2 under loading at DOF 1

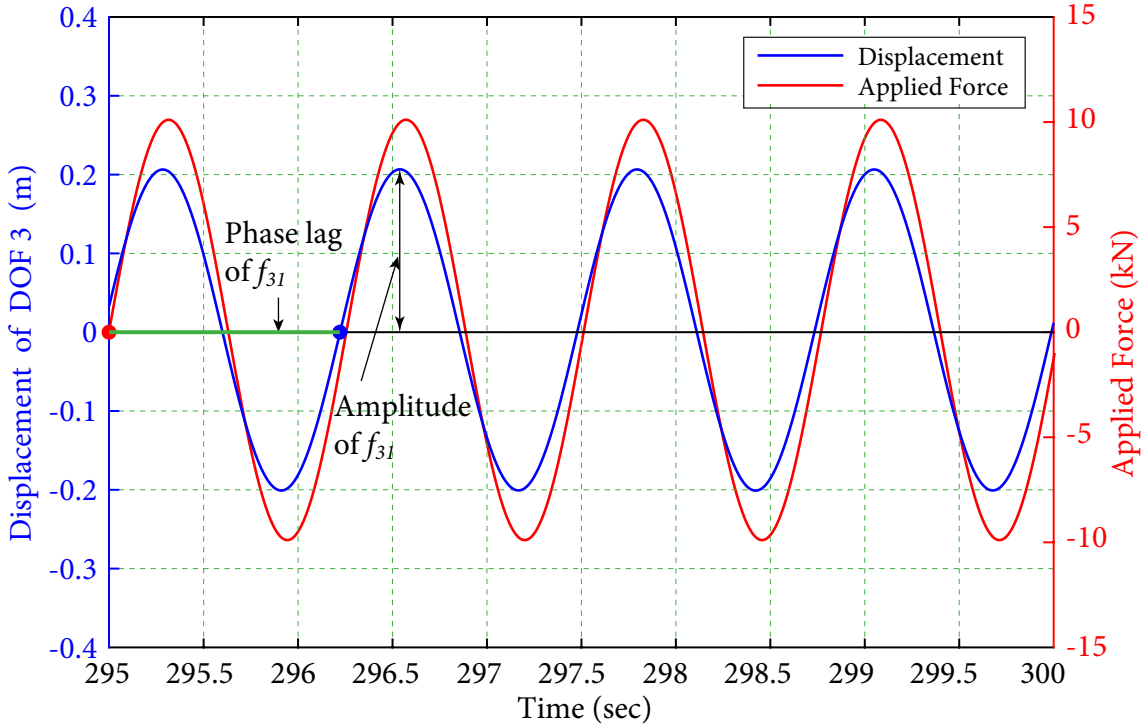


Figure 4.8 Steady-state response of DOF 3 under loading at DOF 1

Loading at DOF 2

When a cosinusoidal load is applied at m_2, the responses of DOFs 1, 2, and 3 are shown in Figures 4.9 to 4.11. The responses exhibit an initial transient phase followed by a steady-state phase. The steady-state response is of interest for evaluating the dynamic characteristics of the system, such as the amplitude and phase of the displacement response, which are essential for studying the system's dynamic behaviour and validating the analytical model.

The portion of steady-state response are plotted along with the applied dynamic force in Figures 4.12 to 4.14. From these plots, the amplitudes and phase lags of the steady-state responses f_{12}^{Num}, f_{22}^{Num}, and f_{32}^{Num} can be computed. The results are presented in Table 4.1.

Loading at DOF 3

When a cosinusoidal load is applied at m_3, the responses of DOFs 1, 2, and 3 are shown in Figures 4.15 to 4.17. The responses exhibit an initial transient phase followed by a steady-state phase. The steady-state response is of interest for evaluating the dynamic characteristics of the system, such as the amplitude and phase of the displacement response, which are essential for studying the system's dynamic behaviour and validating the analytical model.

The portion of steady-state response are plotted along with the applied dynamic force in Figures 4.18 to 4.20. From these plots, the amplitudes and phase lags of the steady-state responses f_{13}^{Num}, f_{23}^{Num}, and f_{33}^{Num} can be computed. The results are presented in Table 4.1.

The real and imaginary parts of the elements for dynamic flexibility matrix $\mathbf{F}^{\text{Num}}$ are calculated using Equation (4.1.11) and presented in Table 4.2. Assembling these parts yields

Table 4.1 Amplitude and phase lag for different DOFs under corresponding dynamic loadings

Force Applied at	Response at DOF 1		Response at DOF 2		Response at DOF 3	
	Amplitude	Phase lag	Amplitude	Phase lag	Amplitude	Phase lag
DOF 1	0.187	-2.955	0.102	3.189	0.203	0.166
DOF 2	0.102	3.189	0.036	-0.338	0.072	2.923
DOF 3	0.203	0.166	0.072	2.923	0.260	-2.964

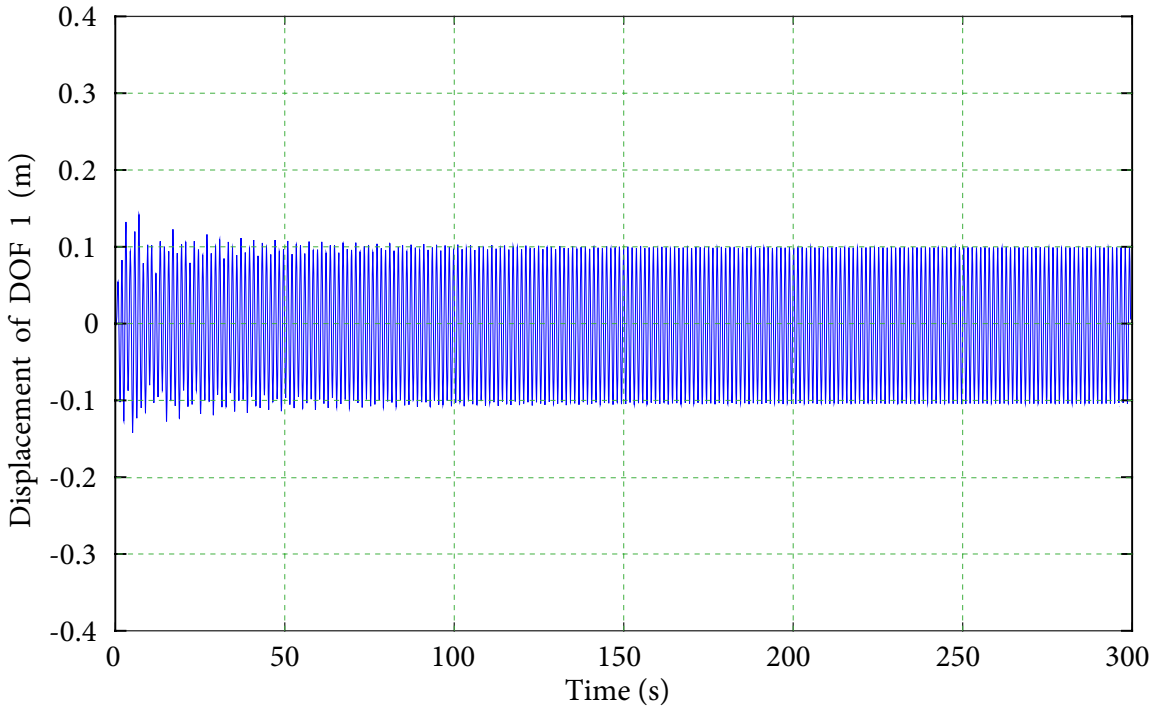


Figure 4.9 Response of DOF 1 under cosinusoidal loading applied at DOF 2

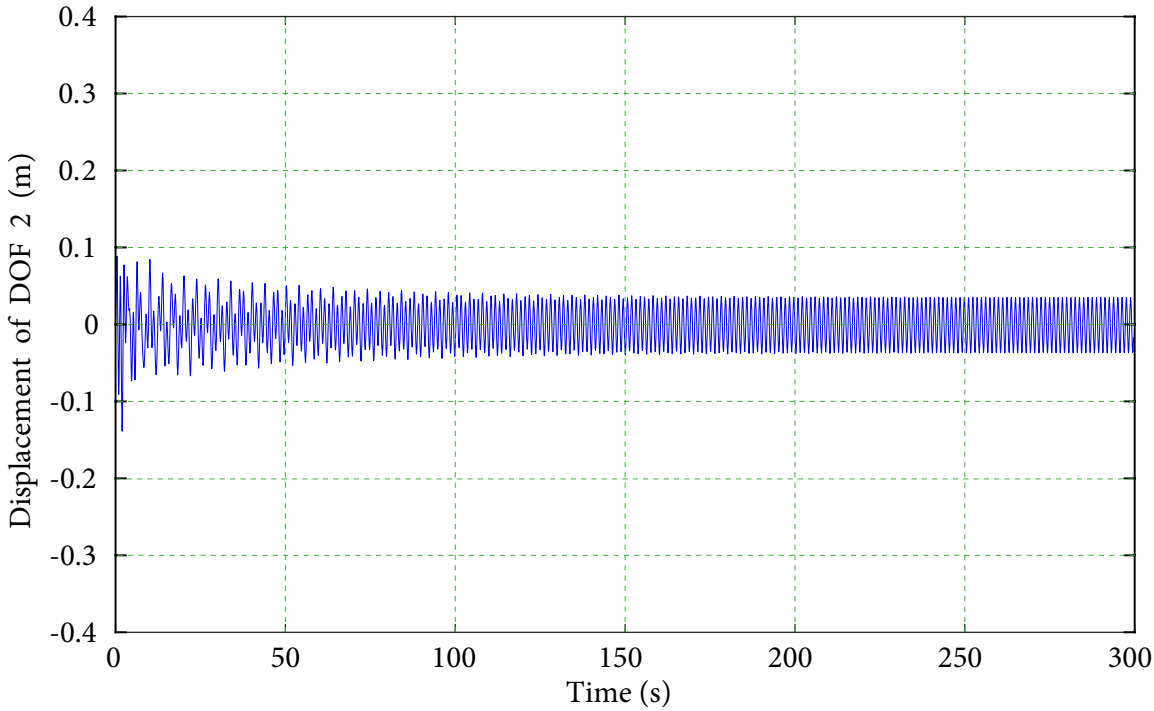


Figure 4.10 Response of DOF 2 under cosinusoidal loading applied at DOF 2

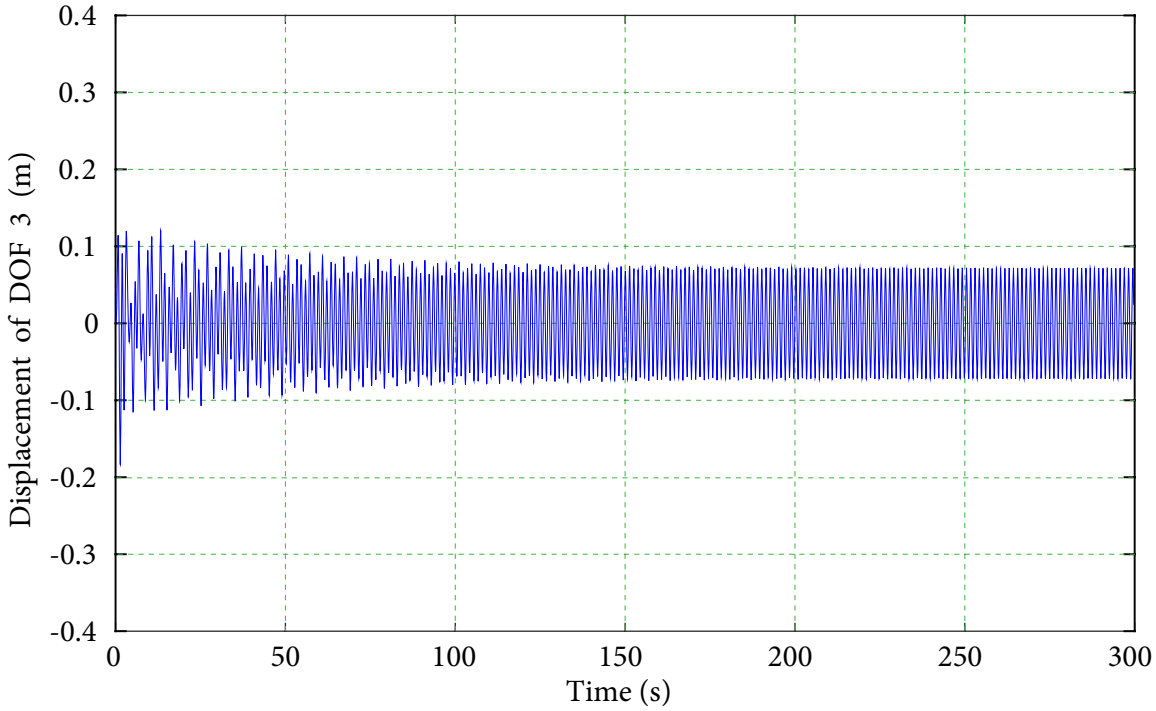


Figure 4.11 Response of DOF 3 under cosinusoidal loading applied at DOF 2

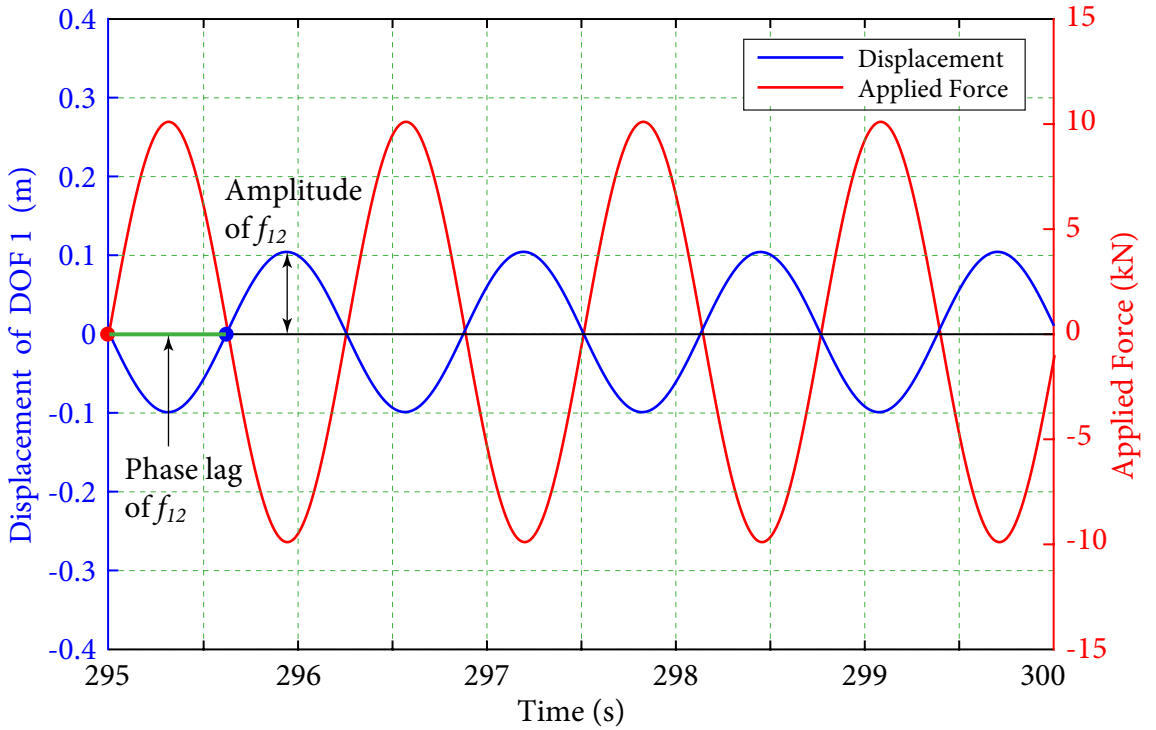


Figure 4.12 Steady-state response of DOF 1 under loading at DOF 2

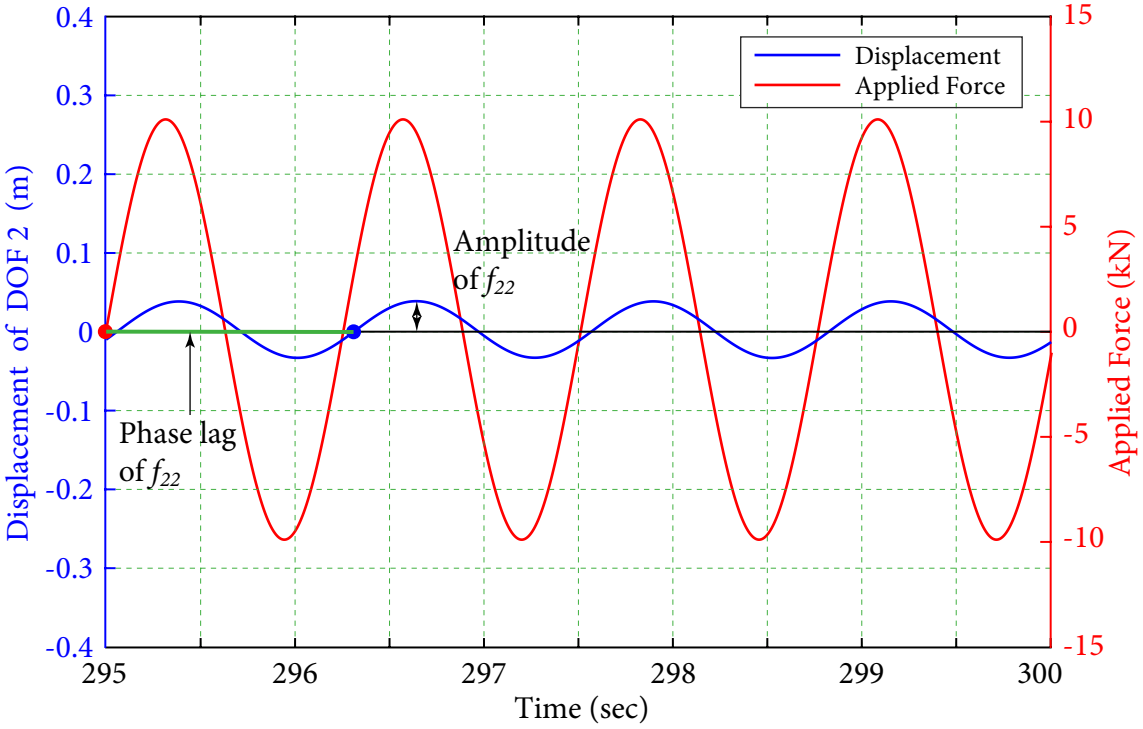


Figure 4.13 Steady-state response of DOF 2 under loading at DOF 2

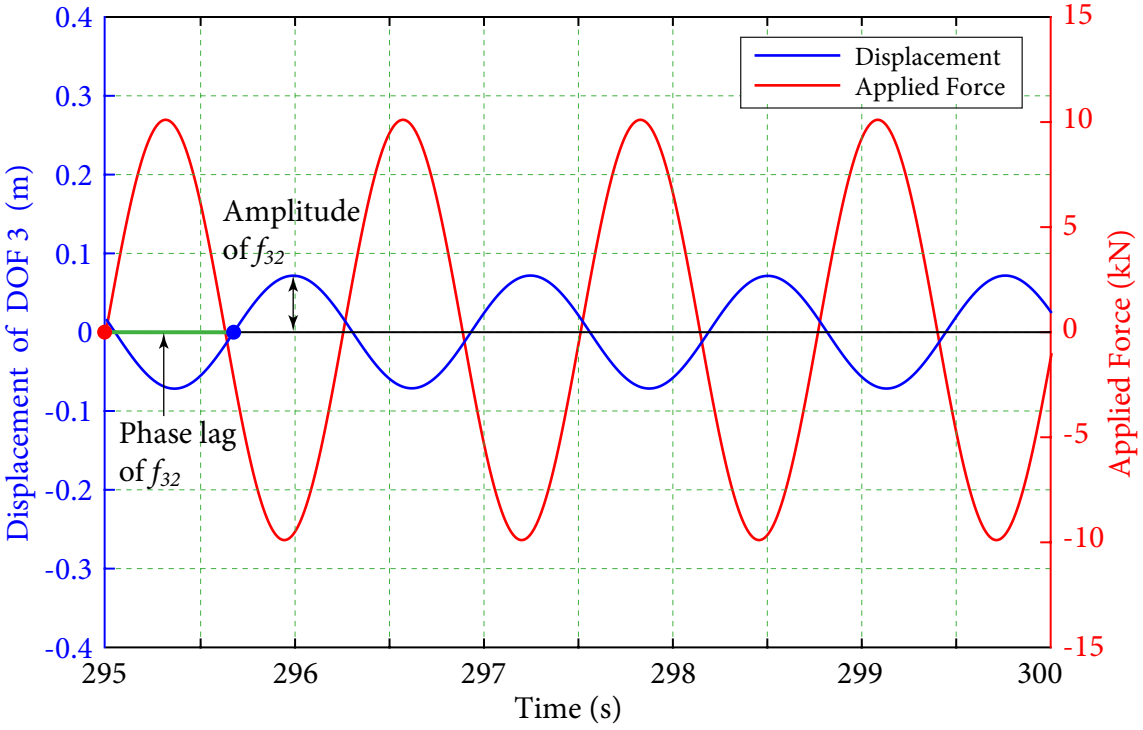


Figure 4.14 Steady-state response of DOF 3 under loading at DOF 2

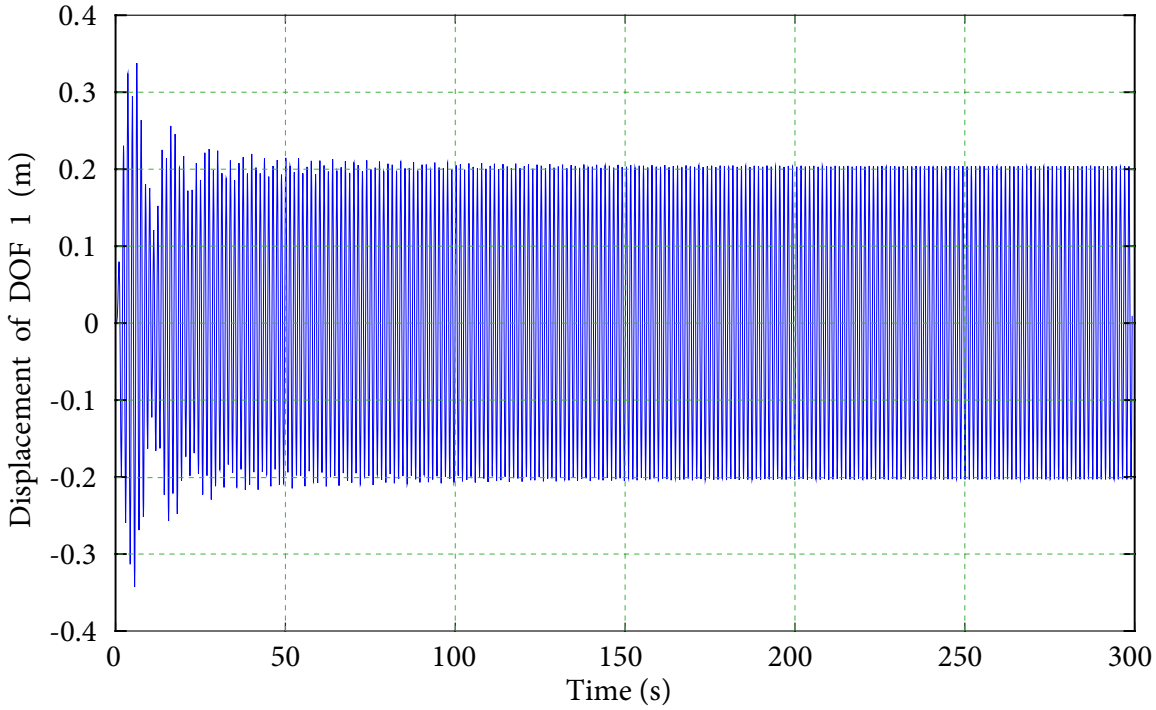


Figure 4.15 Response of DOF 1 under cosinusoidal loading applied at DOF 3

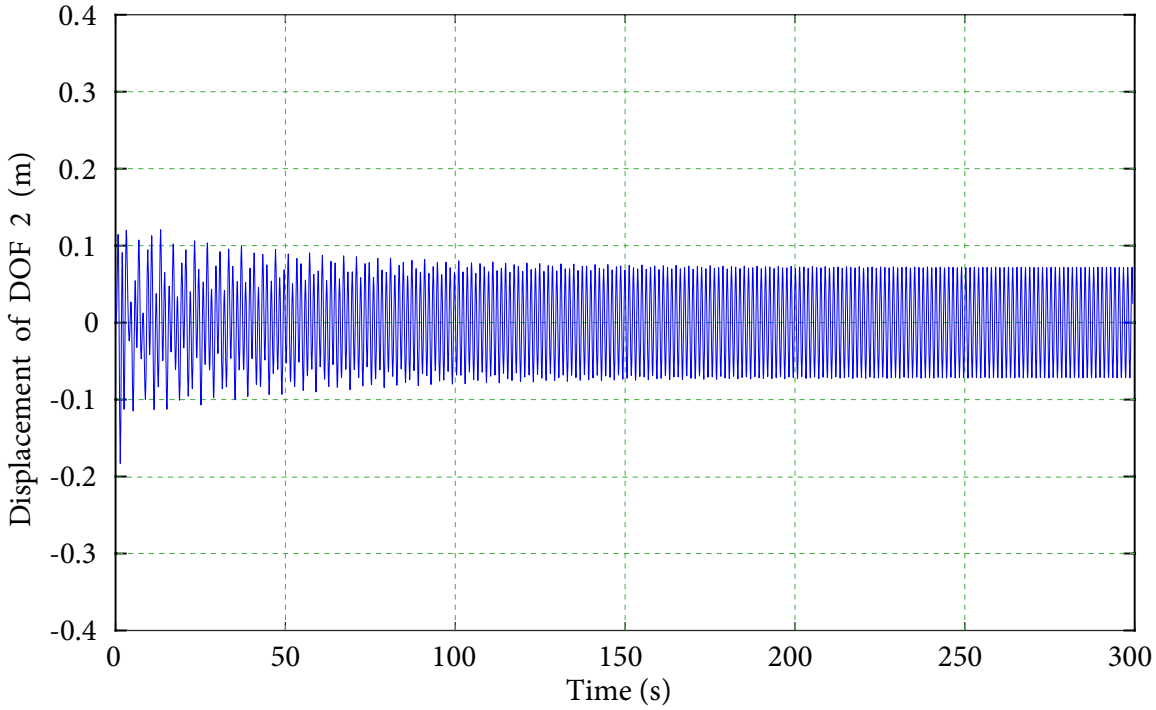


Figure 4.16 Response of DOF 2 under cosinusoidal loading applied at DOF 3

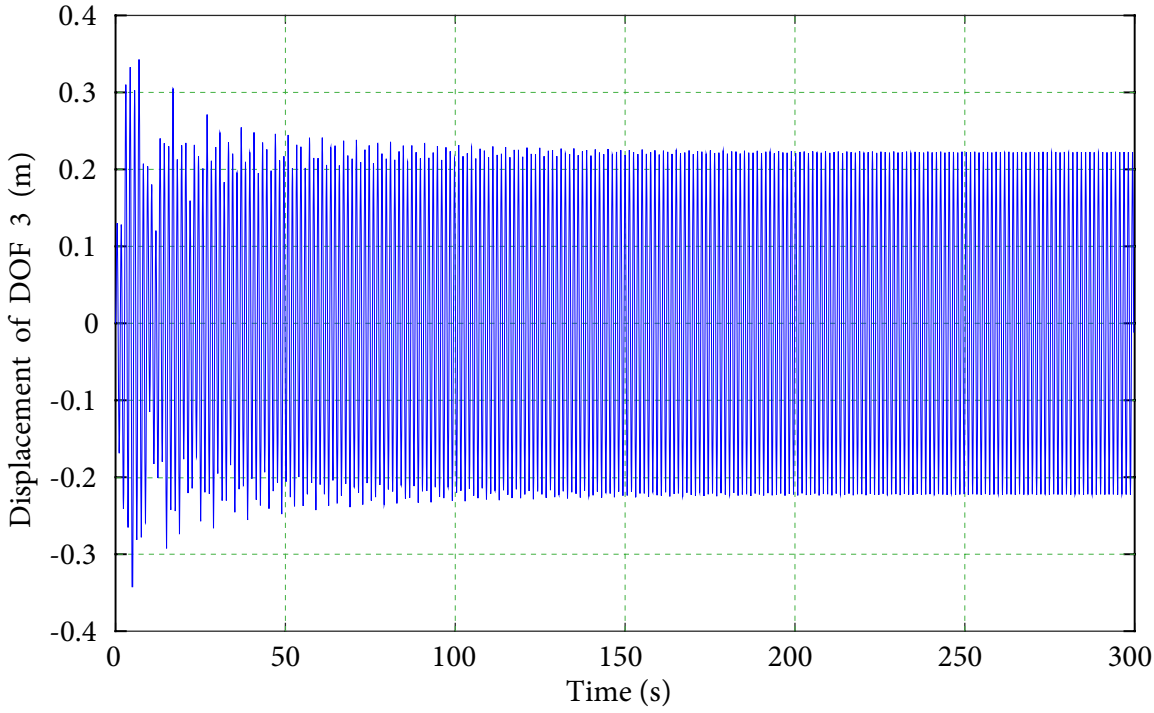


Figure 4.17 Response of DOF 3 under cosinusoidal loading applied at DOF 3

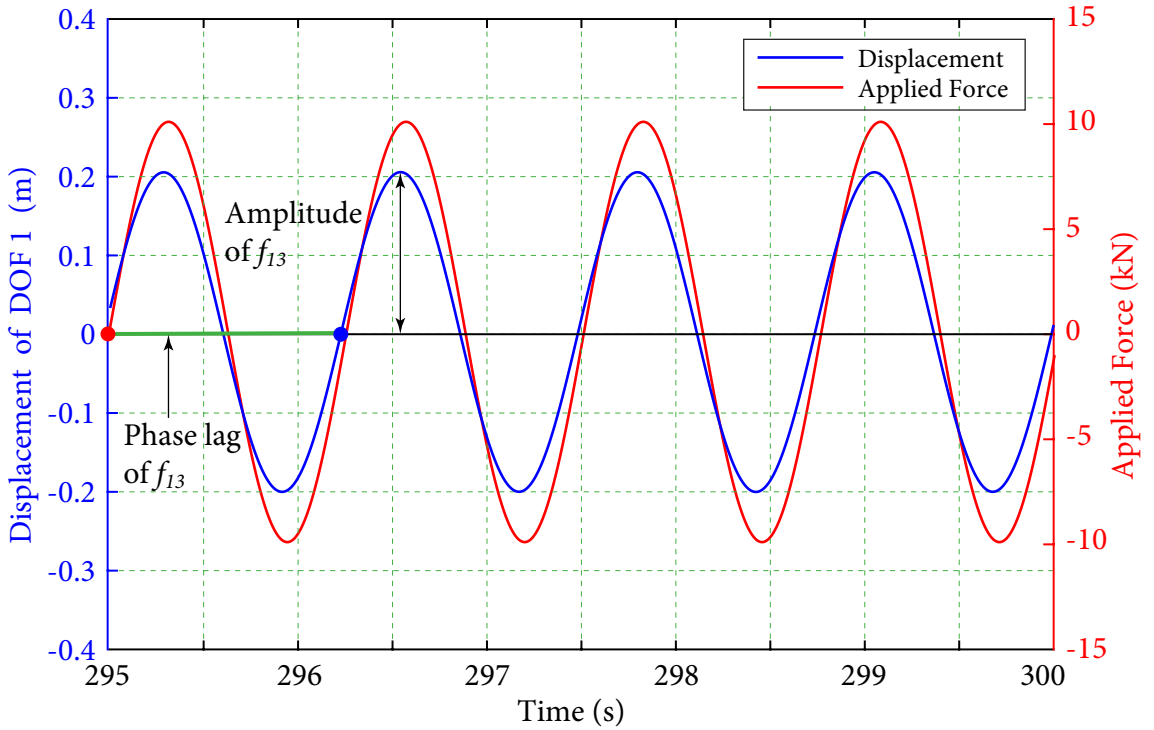


Figure 4.18 Steady-state response of DOF 1 under loading at DOF 3

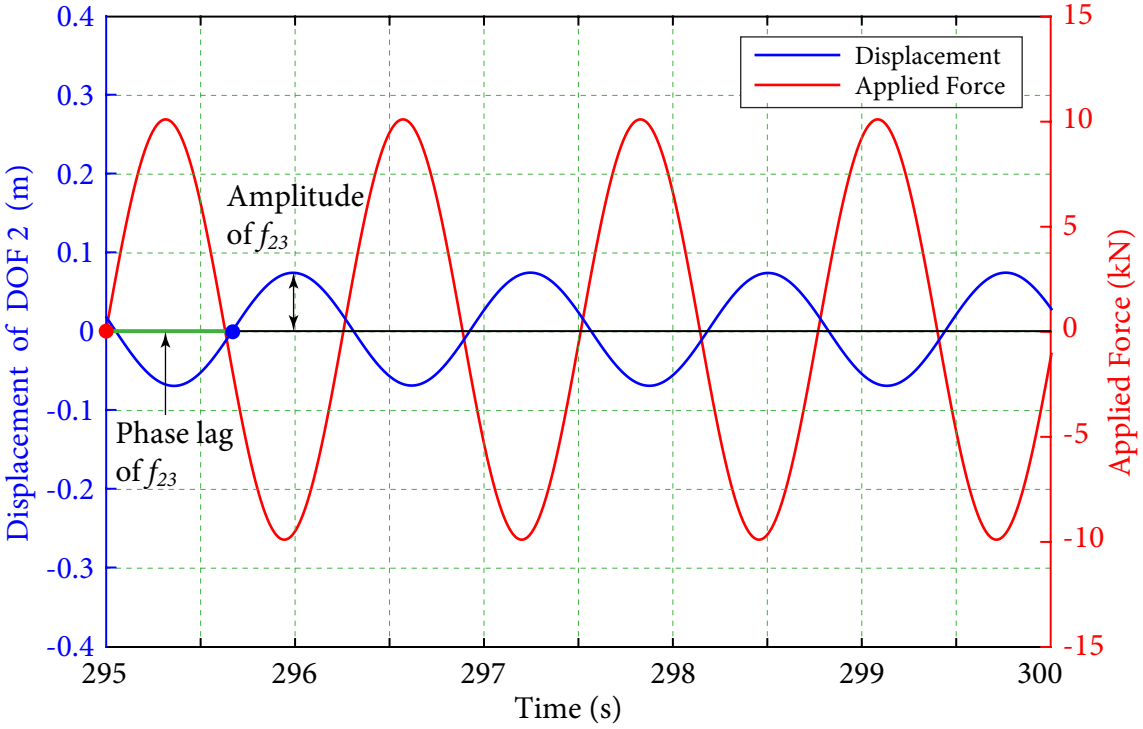


Figure 4.19 Steady-state response of DOF 2 under loading at DOF 3

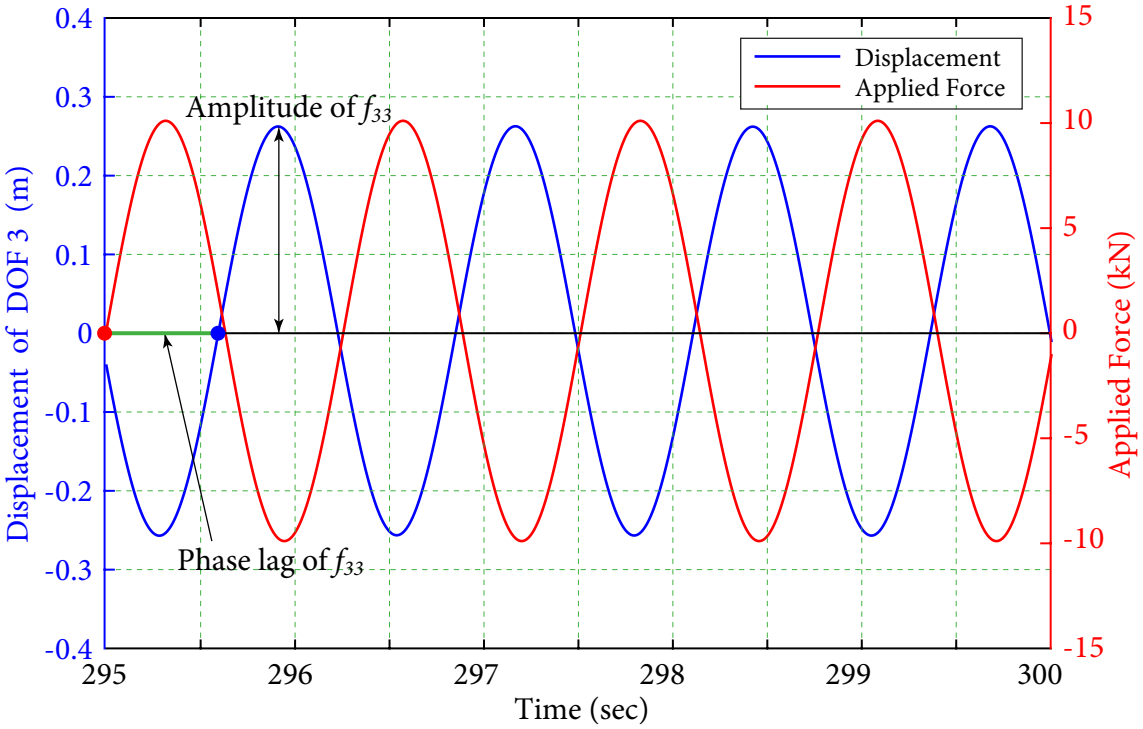


Figure 4.20 Steady-state response of DOF 3 under loading at DOF 3

the complete dynamic flexibility matrix $\mathbf{F}^{\text{Num}}$ corresponding to the loading amplitude of $P_0 = 10000\,\text{N}$. To obtain the unitized dynamic flexibility matrix $\bar{\mathbf{F}}^{\text{Num}}$ under unit loading, each element of $\mathbf{F}^{\text{Num}}$ is divided by P_0. The dynamic stiffness matrix $\mathbf{S}^{\text{Num}}$ can then be derived from $\bar{\mathbf{F}}^{\text{Num}}$.

4.2.4 Comparison of Analytical and Numerical Results

Table 4.3 presents the differences between the real and imaginary parts of the dynamic flexibility matrix elements obtained from the analytical and numerical methods. The comparison reveals that the differences are relatively small, with the largest differences being 0.52 % for the real part and -0.29 % for the imaginary part.

The discrepancies between the analytical and numerical results can be attributed to two main factors. First, the numerical method calculates the steady-state response based on a finite number of time steps, and the selected time points may not exactly coincide with the peak amplitudes of the response. Second, the phase lag between the applied force and the steady-state response may introduce additional errors in the numerical calculations. The differences between the results are within an acceptable range. The close agreement between the two methods demonstrates the accuracy and reliability of the numerical algorithm for evaluating the dynamic flexibility matrix and subsequently deriving the dynamic stiffness matrix.

4.3 Verification for Consistent-Mass System – A Simply Supported Beam

The previous problem is based on the structure with lumped-mass. It is more applicable in the scenarios of upper ground structure. Nevertheless, the exact treatment by analytical methods of wave motion in complex structural components, such as soil foundation, is extremely challenging, if not impossible. For that reason, several one- or two-dimensional models that provide approximate descriptions have been developed. These models are based on a priori assumptions with regard to the form of the displacements across the smaller dimension(s) of the component, generally in the cross-sectional area. For beams and rods, the assumptions simplify the kinematics description to such an extent that one-

Table 4.2 Real and imaginary parts of dynamic flexibility matrix elements for the 3-DOF structure

Force Applied at	Response at DOF 1		Response at DOF 2		Response at DOF 3	
	Real	Imaginary	Real	Imaginary	Real	Imaginary
DOF 1	-0.184	-0.035	-0.102	-0.005	0.200	0.034
DOF 2	-0.102	-0.005	0.034	-0.012	-0.070	0.016
DOF 3	0.200	0.034	-0.070	0.016	-0.256	-0.046

Table 4.3 Real and imaginary parts of dynamic flexibility matrix elements for the 3-DOF structure

Force Applied at	Response at DOF 1		Response at DOF 2		Response at DOF 3	
	Real	Imaginary	Real	Imaginary	Real	Imaginary
DOF 1	0.02 %	-0.17 %	0.08 %	-0.03 %	0.06 %	-0.23 %
DOF 2	0.08 %	-0.03 %	0.52 %	0.05 %	0.26 %	-0.29 %
DOF 3	0.06 %	-0.23 %	0.26 %	-0.29 %	0.10 %	-0.26 %

dimensional approximate theories can describe the wave motions. For the cases of time-harmonic excitation, it was found that the approximate theories can account adequately for the dispersive behaviour of at least the lowest mode of the exact solution over a limited but significant range of wave numbers and frequencies.

In this section, a simply supported beam is constructed. The exact formulation for the response of the beam is derived. Then a comparison of the dynamic stiffness matrices obtained from the theoretical and numerical method is performed. The approach to establish the dynamic stiffness matrix for the simply supported beam is essentially the same as the method to develop the elastic stiffness.

4.3.1 Problem Description

Consider the case of a simply supported beam subjected to a dynamic concentrated load $P\sin\omega t$ applied at $x = a$ as shown in Figure 4.21. Young's modulus E, mass density ρ, cross-sectional area A, second moment of inertial I, length L.

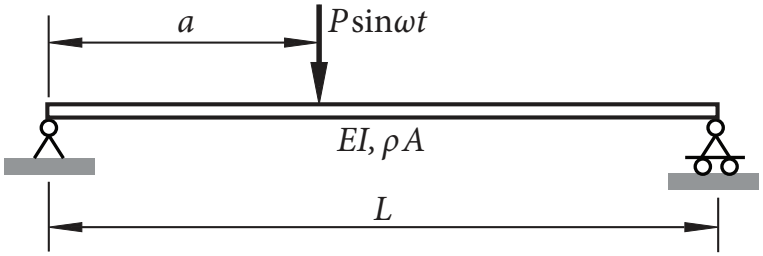


Figure 4.21 Harmonic Loading on A Simply Supported Beam

4.3.2 Theoretical Derivation

The dynamic concentrated load can be expressed as

$$w(x,t) = P\sin\,\omega\,t\,\delta(x-a). \tag{4.3.1}$$

where $\delta(x-a)$ is the Dirac delta function, $\delta(x-a)=0$, if $t \neq a, \delta(x-a) \to +\infty$, as $t \to a$. The partial differential equation of motion becomes

$$EI\frac{\partial^4 v}{\partial x^4} + c\frac{\partial v}{\partial t} + \rho A\frac{\partial^2 v}{\partial t^2} = P\sin\omega\,t\,\delta(x-a) \tag{4.3.2}$$

Applying the method of separation of variables and using the results obtained for free vibration, let

$$v(x,t) = \sum_{n=1}^{\infty} q_n(t)\sin\frac{n\pi x}{L} \tag{4.3.3}$$

Substituting into the equation of motion yields

$$\left[\rho A\sum_{n=1}^{\infty}\ddot{q}_n(t) + c\sum_{n=1}^{\infty}\dot{q}_n(t) + EI\sum_{n=1}^{\infty}q_n(t)\left(\frac{n\pi}{L}\right)^4\right]\sin\frac{n\pi x}{L} = P\sin\omega\,t\delta(x-a) \tag{4.3.4}$$

Multiplying the equation by $\sin\dfrac{k\pi x}{L}$ $(k=1,2,\ldots)$, and integrating with respect to x from 0 to L gives

$$\begin{aligned}\sum_{n=1}^{\infty}\left[\rho A\,\ddot{q}_n(t) + c\,\dot{q}_n(t) + EI\left(\frac{n\pi}{L}\right)^4 q_n(t)\right]\int_0^L \sin\frac{n\pi x}{L}\sin\frac{k\pi x}{L}dx \\ = P\sin\omega\,t\int_0^L \delta(x-a)\sin\frac{k\pi x}{L}dx\end{aligned} \tag{4.3.5}$$

Using the orthogonality of sine function and the property of Dirac delta function

$$\int_{a-\epsilon}^{a-\epsilon} f(x)\delta(x-a)dx = f(a),$$

one obtains, for $k = 1, 2, ...,$

$$\left[\rho\, A\, \ddot{q}_k(t) + c\, \dot{q}_k(t) + EI \left(\frac{k\pi}{L}\right)^4 q_k(t)\right] \cdot \frac{L}{2} = P \sin\omega\, t\, \sin\frac{k\pi\, a}{L}, \tag{4.3.6}$$

The above equation can be re-written as,

$$\ddot{q}_k(t) + 2\,\zeta_k\omega_k\,\dot{q}_k(t) + \omega_k^2 q_k(t) = p_k\, \sin\omega t \tag{4.3.7}$$

in which

$$\omega_k = \left(\frac{k\pi}{L}\right)^2 \sqrt{\frac{EI}{\rho A}}, \qquad 2\,\zeta_k\,\omega_k = \frac{c}{\rho\, A}, \qquad p_k = \frac{2P}{\rho AL}\, \sin\frac{k\pi\, a}{L} \tag{4.3.8}$$

This is a system of infinitely many uncoupled second-order linear ordinary differential equations. Each equation can be solved separately. The general solution is given by

$$q_k^C(t) = \mathrm{e}^{-\zeta_k\,\omega_k\, t}\, \left(A\cos\omega_d t + B\sin\omega_d t\right) \tag{4.3.9}$$

where $\omega_d = \omega_k\sqrt{1-\zeta_k^2}$ is the damped natural circular frequency, the coefficients A and B are determined from the initial conditions $v(0)$ and $v'(0)$. It is the transient response of free vibration. It decays exponentially and approaches zero as $t \to \infty$. As time increases, transient response diminishes and becomes negligible in practice. The particular solution to equation (4.3.7), which is associated with the right-hand side of the equation. represents the steady-state solution, It persists as time goes to infinity. The particular solution satisfies,

$$\begin{aligned} q_k^P(t) &= p_k\, \frac{1}{\mathcal{D}^2 + 2\,\zeta_k\omega_k\,\mathcal{D} + \omega_k^2}\, \sin\omega t \\ &= p_k\, \frac{1}{-\omega^2 + 2\,\zeta_k\omega_k\,\mathcal{D} + \omega_k^2}\, \sin\omega t \\ &= p_k\, \frac{(\omega_k^2 - \omega^2) - 2\,\zeta_k\omega_k\,\mathcal{D}}{[(\omega_k^2-\omega^2)^2 + (2\,\zeta_k\omega_k\omega)^2]}\, \sin\omega t \end{aligned}$$

$$
\begin{aligned}
&= p_k \left[\frac{(\omega_k^2 - \omega^2)}{(\omega_k^2 - \omega^2)^2 + (2\,\zeta_k\,\omega_k\,\omega)^2} \sin\,\omega t \;-\; \frac{2\,\zeta_k\,\omega_k\,\omega}{(\omega_k^2 - \omega^2)^2 + (2\,\zeta_k\,\omega_k\,\omega)^2} \cos\,\omega t \right] \\
&= \frac{p_k}{\sqrt{(\omega_k^2 - \omega^2)^2 + (2\,\zeta_k\,\omega_k\,\omega)^2}} \left(\cos\varphi_k t \sin\,\omega t \;-\; \sin\varphi t \sin_k \omega t \right) \\
&= \frac{p_k}{\sqrt{(\omega_k^2 - \omega^2)^2 + (2\,\zeta_k\,\omega_k\,\omega)^2}} \sin\left(\omega t - \varphi_k\right),
\end{aligned}
\tag{4.3.10}
$$

where

$$
\varphi_k = \arctan\frac{2\,\zeta_k\,\omega_k\,\omega}{\omega_k^2 - \omega^2} = \arctan\frac{2\,\zeta_k\,r_k}{1 - r_k^2}, \qquad r_k = \frac{\omega}{\omega_k}, \tag{4.3.11}
$$

φ_k is the k^{th} phase angle or phase lag. r_k is the k^{th} frequency ratio. The applied force $P\sin\,\omega\,t$ is maximum at $\omega\,t = \frac{1}{2}\,\pi, \frac{3}{2}\,\pi, ...,$ the response $q_k^P(t)$ is maximum at $\omega\,t - \varphi_k = \frac{1}{2}\,\pi, \frac{3}{2}\,\pi, \ldots.$ It lags behind the loading by a time $\frac{\varphi_k}{\omega}$. Therefore, the steady-state solution is the response of forced vibration due to the externally applied dynamic load given by

$$
q_{k,\,\text{steady-state}}(t) = \frac{p_k}{\sqrt{(\omega_k^2 - \omega^2)^2 + (2\,\zeta_k\,\omega_k\,\omega)^2}} \sin\left(\omega t - \varphi_k\right) \quad (k = 1, 2, ...). \tag{4.3.12}
$$

Therefore, the steady-state response of the beam is

$$
\begin{aligned}
v(x,t) &= \sum_{k=1}^{n} q_{k,\,\text{steady-state}}(t)\, \sin\frac{k\pi\,x}{L} \\
&= \sum_{k=1}^{n} \left[\frac{p_k}{\sqrt{\left(\omega_k^2 - \omega^2\right)^2 + (2\,\zeta_k\,\omega_k\,\omega)^2}} \sin\left(\omega t - \varphi_k\right) \right] \sin\tfrac{k\pi\,x}{L} \\
&= \sum_{k=1}^{n} \left[\frac{2P}{\rho A L} \frac{1}{\sqrt{\left(\omega_k^2 - \omega^2\right)^2 + (2\zeta_k\omega_k\omega)^2}} \sin\left(\omega t - \arctan\frac{2\zeta_k\omega_k\omega}{\omega_k^2 - \omega^2}\right) \sin\tfrac{k\pi\,a}{L} \right] \sin\tfrac{k\pi\,x}{L}
\end{aligned}
\tag{4.3.13}
$$

It is seen that, when $\omega = \omega_k$, the beam is in resonance in the k^{th} mode, leading to a large amplitude of vibration in the k^{th} mode. n is the total degrees-of-freedom of the system. The

amplitude of the response of forced vibration is

$$|v(x)|_{\text{Ampl}} = \sum_{k=1}^{n} \frac{p_k}{w_k^2} \frac{1}{\sqrt{\left(1-r^2\right)^2 + (2\,\zeta_k\, r)^2}} \sin\frac{k\pi x}{L} \tag{4.3.14}$$

4.3.3 Comparison of Frequencies

Parameters for the above beam are as follows: Young's modulus $E = 200\,MPa$, Poisson ratio $\nu = 0.30$, density of the material $\rho = 2500\,kg/m^3$, the cross-section dimension is $B \times H = 0.2\,m \times 0.2\,m$, length of the beam $L = 6\,m$. Damping coefficient $\zeta = 15\%$. Harmonic loading $p = 10 \sin\omega\, t$ kN is applied at $a = 2.0\,m$ from the left side. Considering the first 3 natural frequencies of the beam, the analytical frequencies given by Equation (4.3.8) are as follows,

$$\begin{aligned}
\omega_1 &= \left(\frac{1\pi}{L}\right)^2 \sqrt{\frac{EI}{\rho A}} = 4.4769 \qquad \Longrightarrow \qquad f_1^{\text{Ana}} = 0.71253\,\text{Hz};\\
\omega_2 &= \left(\frac{2\pi}{L}\right)^2 \sqrt{\frac{EI}{\rho A}} = 17.9078 \qquad \Longrightarrow \qquad f_2^{\text{Ana}} = 2.85011\,\text{Hz};\\
\omega_3 &= \left(\frac{3\pi}{L}\right)^2 \sqrt{\frac{EI}{\rho A}} = 40.2925 \qquad \Longrightarrow \qquad f_3^{\text{Ana}} = 6.41275\,\text{Hz}.
\end{aligned} \tag{4.3.15}$$

When performing modal analysis in ANSYS, the calculated frequencies are as follows, with the first three modes are shown in Figure 4.22.

$$f_1^{\text{Num}} = 0.71263\,\text{Hz}, \quad f_2^{\text{Num}} = 2.85171\,\text{Hz}, \quad f_3^{\text{Num}} = 6.42115\,\text{Hz}. \tag{4.3.16}$$

The discrepancies between the corresponding frequencies obtained from analytical and numerical calculations are smaller than 0.15% for all three cases investigated.

4.3.4 Comparison of Deflection in The Simply Supported Beam

As aforementioned, when the force P applied at $x = 2$m, the deflection at $x = 2$m and $x = 4$m are f_{22} and f_{42}. By analogous, when the force P applied at $x = 4$m, the deflection at $x = 2$m and $x = 4$m are f_{24} and f_{44}. Equation (4.3.14) suggests the formula for solving the

amplitude of the response under forced vibration. Thus, the deflection can be calculated by,

$$|v(x)| = \left| \frac{2P}{\rho AL} \sum_{k=1}^{n} \frac{\sin \frac{k\pi a}{L} \sin \frac{k\pi x}{L}}{w_k^2 \sqrt{(1-r_k^2)^2 + (2\zeta r_k)^2}} \right| . \tag{4.3.17}$$

The deflection matrix from analytical method can be written as,

$$\begin{bmatrix} f_{22}^{\text{Ana}} & f_{24}^{\text{Ana}} \\ f_{42}^{\text{Ana}} & f_{44}^{\text{Ana}} \end{bmatrix} = \begin{bmatrix} -1.3255 & -1.1695 \\ -1.1695 & -1.3255 \end{bmatrix} . \tag{4.3.18}$$

The deflection matrix from numerical method is,

$$\begin{bmatrix} f_{22}^{\text{Num}} & f_{24}^{\text{Num}} \\ f_{42}^{\text{Num}} & f_{44}^{\text{Num}} \end{bmatrix} = \begin{bmatrix} -1.3364 & -1.1682 \\ -1.1682 & -1.3364 \end{bmatrix} . \tag{4.3.19}$$

As can be seen from Equation (4.3.18) and (4.3.19), the discrepancies between the results obtained from the analytical and numerical methods are smaller than 1 % , which is considered negligible in the context of this study.

4.3.5 Dynamic Flexibility Matrix of The Simply Supported Beam

In the previous section, the dynamic stiffness matrix can be determined from the flexibility matrix. The element X_{ji} represents the dynamic steady-state displacement in DOF j when a unit dynamic load is applied at DOF i.

In Section 4.1, it was demonstrated that the dynamic stiffness matrix can be determined from the flexibility matrix. The element X_{ji} represents the dynamic steady-state displacement in DOF j when a unit dynamic load is applied at DOF i. In the previous section, the dynamic stiffness matrix for a specific angular frequency of $\omega = 5$ was determined and validated by comparing it with the analytical solution.

However, it is often necessary to obtain the dynamic stiffness matrix for a range of excitation frequencies in dynamic response analysis. This is because the dynamic behaviour of structures can vary significantly depending on the frequency of the applied loads. To accurately analyze the response of a structure under different excitation scenarios, it is essential to evaluate the "true dynamic" stiffness matrix for frequencies spanning a relevant range, such as 0 to 100 Hz. To achieve this goal, a harmonic analysis is performed. By

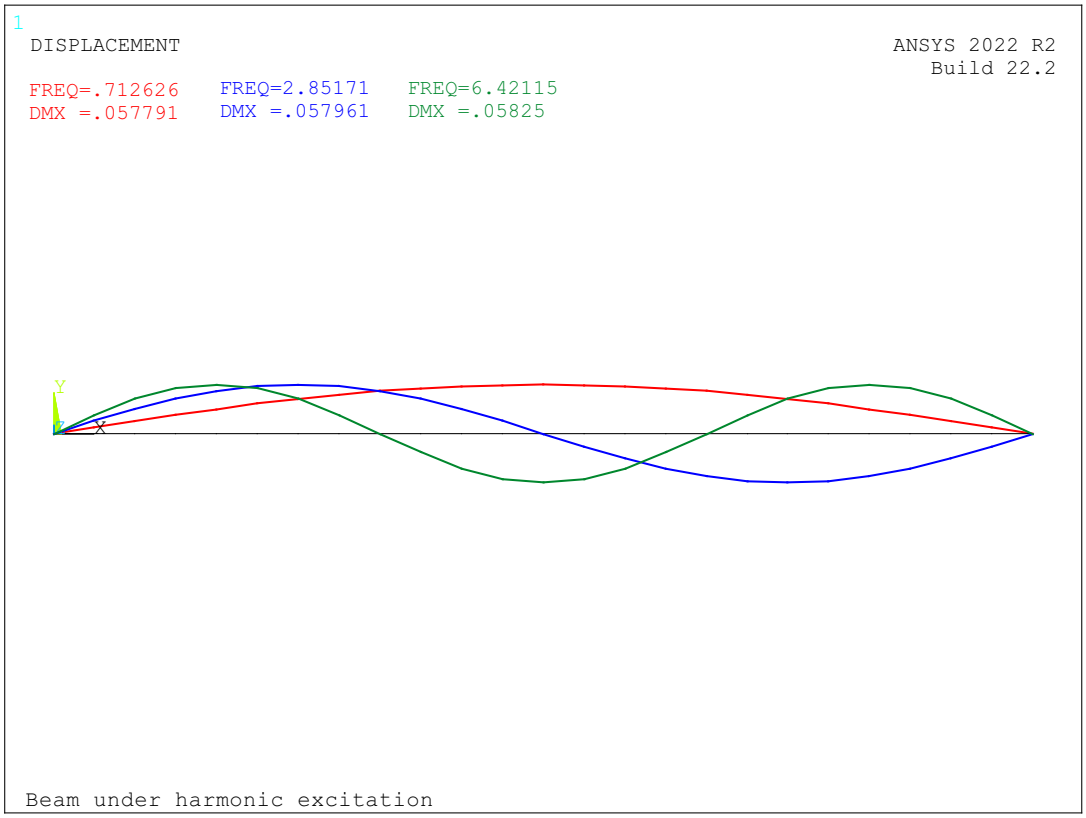


Figure 4.22 First Three Dominant Modes of A Simply Supported Beam

applying dynamic loads with varying frequencies and analyzing the corresponding steady-state responses, the dynamic flexibility matrix for each frequency can be constructed. The dynamic stiffness matrix can then be obtained by inverting the unitized dynamic flexibility matrix, as described in Section 4.2.

The procedure for performing harmonic analysis is as follows:

- Select a range of excitation frequencies, e.g., from 0 to 100 Hz, with an appropriate step of frequency.
- For each frequency, apply a dynamic load at each DOF individually, while keeping the other DOFs unloaded.
- Measure the steady-state displacement response at all DOFs for each loading case.
- Assemble the dynamic flexibility matrix using the obtained steady-state displacements.

- Unitized the flexibility matrix by dividing each element by the amplitude of the applied dynamic load.
- Invert the unitized flexibility matrix to obtain the dynamic stiffness matrix for the current frequency.
- Repeat steps 2-6 for all frequencies in the selected range.

By following this procedure, the frequency-dependent deflection of the beam is obtained. The amplitudes and phase lags at $x=2$ m and $x=4$ m are shown from Figure 4.23 to Figure 4.26. In the figures, A_{22} and A_{42} are the amplitudes at $x=2$ m and $x=4$ m when the dynamic force applied at $a=2$ m; φ_{22} and φ_{42} are the phase lags at $x=2$ m and $x=4$ m when the dynamic force applied at $a=2$ m. A_{24} , A_{44} and φ_{24} and φ_{44} are the corresponding amplitudes and phase lags when the dynamic force applied at $a=4$ m, respectively.

Then the real and imaginary parts under different frequencies are calculated by the amplitudes A_{ji} and phase lags φ_{ji} . The real parts of X_{22} and X_{42} are shown in Figure 4.27, the imaginary parts of X_{24} and X_{44} are shown in Figure 4.28. From the section 4.1, we know that $F_{22}=X_{22}$, $F_{42}=X_{42}$, and $F_{24}=X_{24}$, $F_{44}=X_{44}$. Thus the dynamic flexibility matrix is as follows,

$$F=\begin{bmatrix} F_{22} & F_{24} \\ F_{42} & F_{44} \end{bmatrix} \tag{4.3.20}$$

The real and imaginary parts of the elements in this matrix are shown in Figure 4.27 and Figure 4.28. In the consequence, the dynamic stiffness matrix can be evaluated by inversing the equation (4.3.20).

4.4 Verification for 3-Dimensional Half-Space Soil

4.4.1 Harmonic Excitation on An Elastic Soil

In Soil-Structure Interaction (SSI) analysis, the frequency-dependent dynamic soil stiffness plays a crucial role in determining the response of the underlying soil. It is an essential element in accurately modeling and predicting the behavior of soil-structure systems. This section aims to extend the previously discussed method to generate the dynamic soil stiffness matrix for a 3-dimensional soil space.

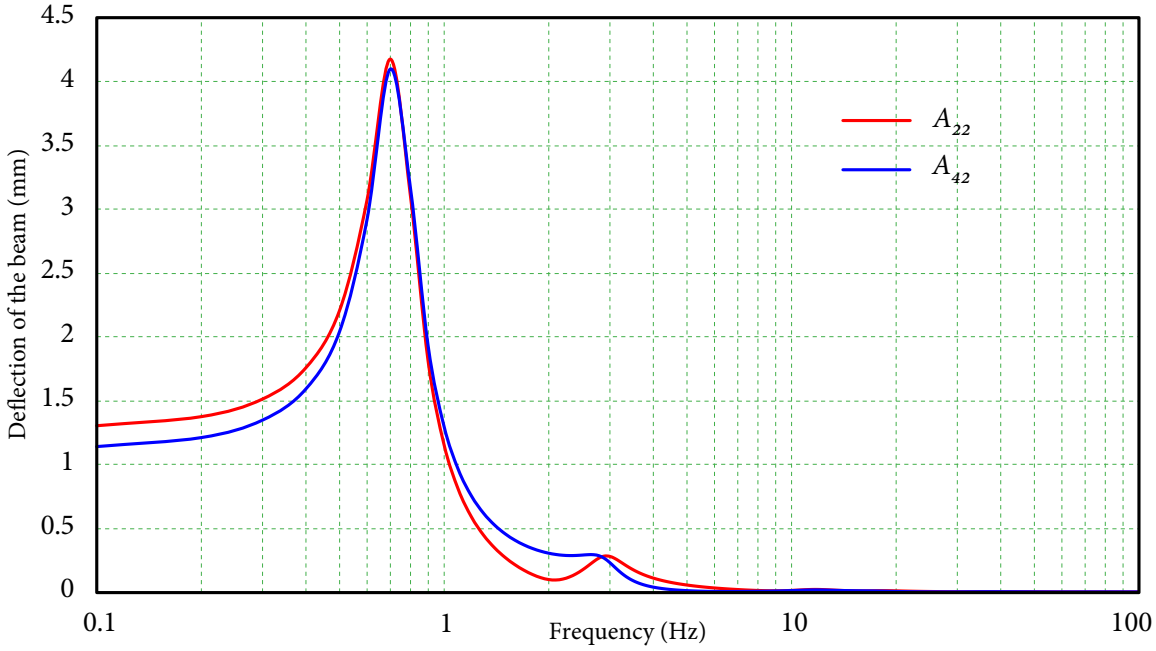


Figure 4.23 Frequency-dependent deflection of A_{22} and A_{42}

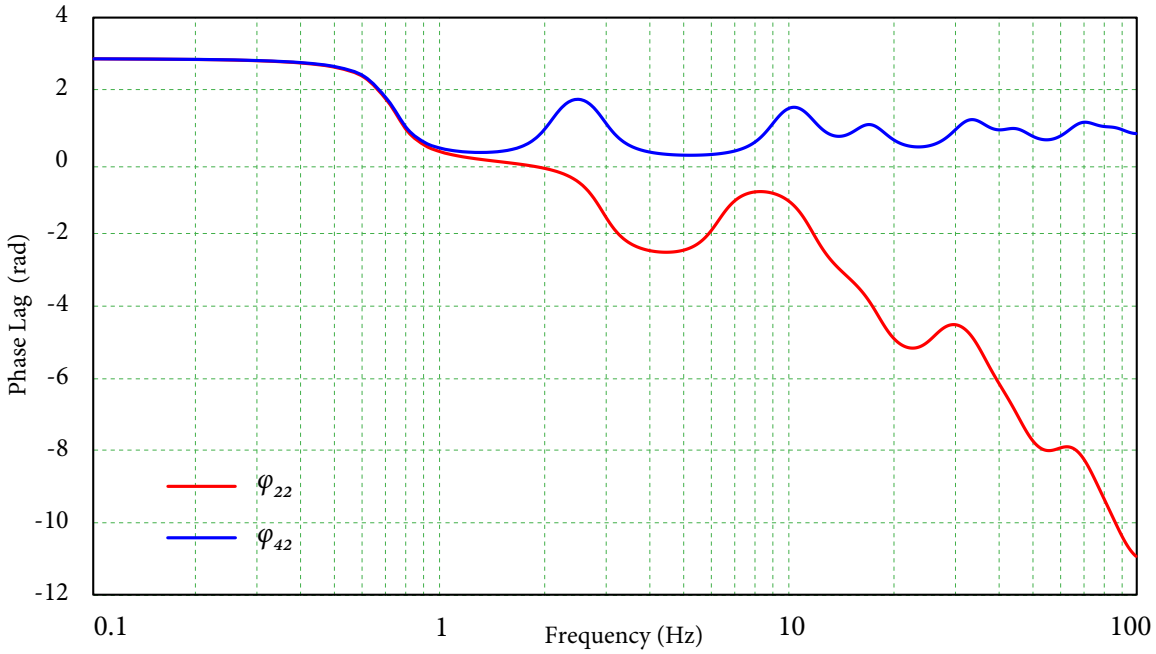


Figure 4.24 Frequency-dependent phase lags of φ_{22} and φ_{42}

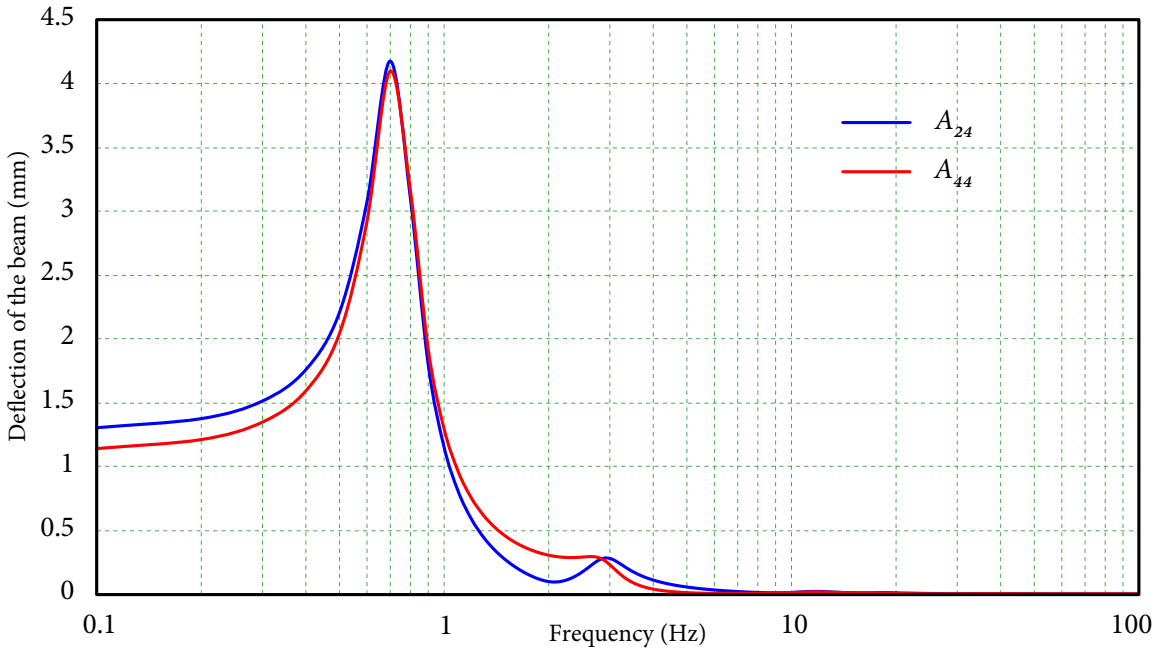


Figure 4.25 Frequency-dependent deflection of A_{24} and A_{44}

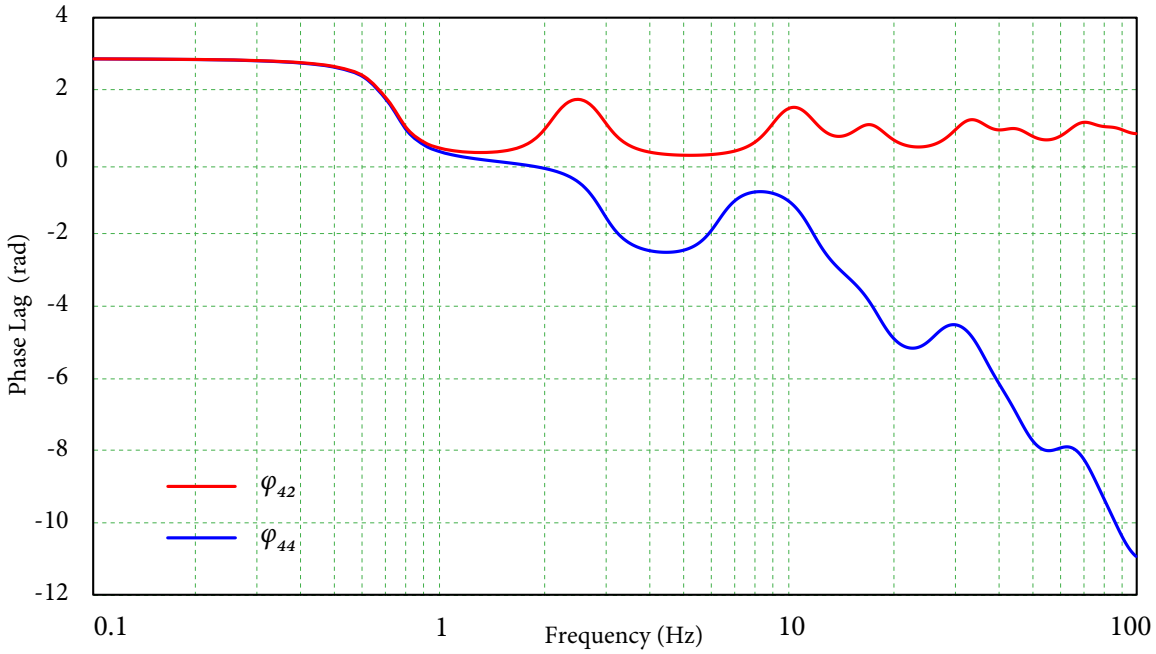


Figure 4.26 Frequency-dependent phase lags of φ_{24} and φ_{44}

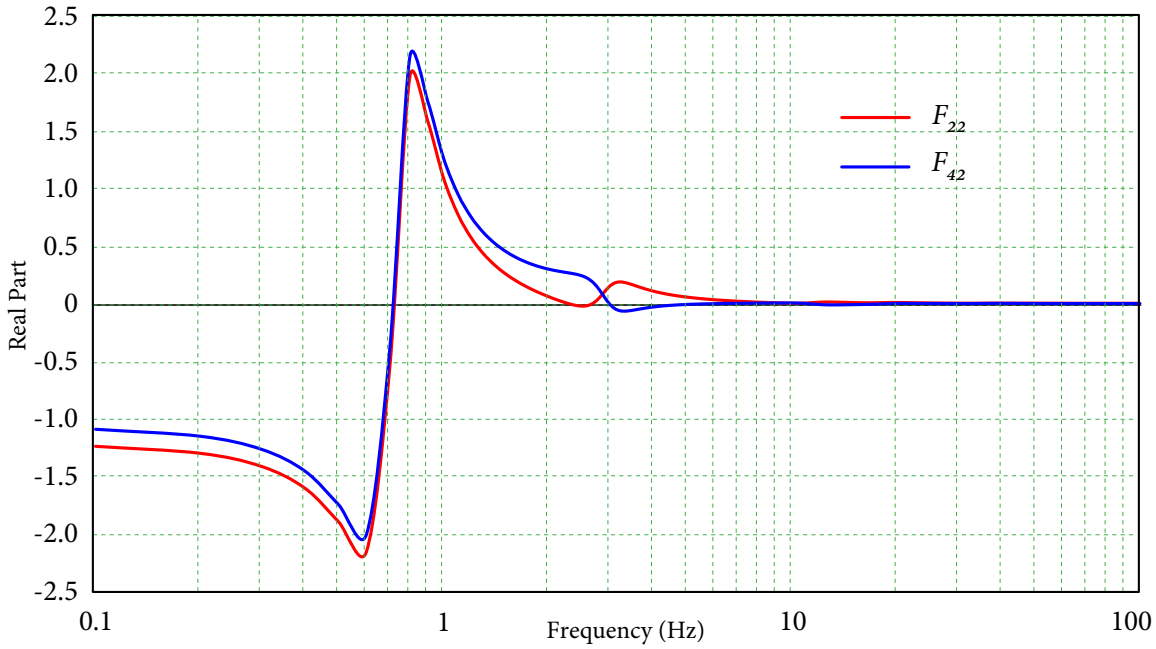


Figure 4.27 Real part of elements F_{24} and F_{44} for the dynamic flexibility matrix

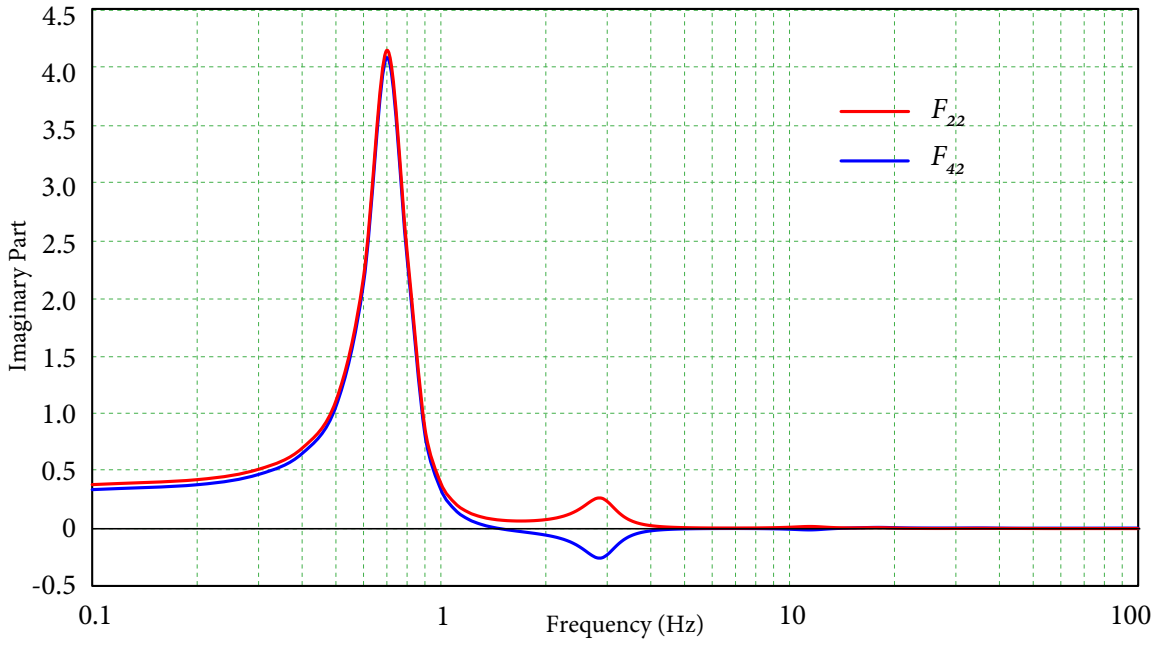


Figure 4.28 Imaginary part of elements F_{24} and F_{44} for the dynamic flexibility matrix

Different from structural dynamics, where the solution of the equation of motion is a second-order linear differential equation primarily solved using matrix notation and algebra, the solutions of the equation of motion for elastodynamic problems in soil often involve complex partial differential equations, integral transforms with complex functions, and other intricate functions such as Bessel and Hankel functions. Furthermore, most interpretations of these solutions are more mathematical than physical and intuitive.

For the analysis of critical structures such as SSCs in nuclear power plants or SMRs, a flexible foundation can be represented by m nodes. If the foundation is rigid, m is equal to 1. For each node, there are 3 translational and 3 rotational degrees of freedom. Hence, the soil stiffness is a $6m \times 6m$ matrix. The element S_{ji} in dynamic stiffness matrix is the amplitude of the reaction force at node j when the displacement at node i is forced to be equal to $e^{i\omega t}$ as shown in Figure 4.29. ω is the excitation frequency, and t is the time. Thus dynamic soil stiffness is frequency−dependent $6m \times 6m$ matrices.

One of the fundamental problems in the analysis of the dynamic stiffness of soils is the case of an elastic half-space subjected to a time-dependent load at its surface. The load can be sinusoidally fluctuating with time or applied as a short-duration pulse and then remain constant. For the case of a concentrated pulse load, solutions have been provided by Lamb (1904), Pekeris (1955), and De Hoop (1960). However, these solutions are mathematically complex.

To simplify the approach, we approximate the elastic problem by disregarding the rotational displacements and considering only horizontal and vertical displacements. This approximation, known as confined elasticity, was first suggested by Westergaard (1938) for the case of vertical displacements only.

In the previous sections, it has been demonstrated that the numerical method yields highly accurate results for elastostatic problems in the case of both lumped and consistent mass systems. In this section, we extend the method to problems of elastodynamics in soil spaces. The derived analytical solutions in simple scenarios will be used as reference for evaluating the correctness of the numerical approach.

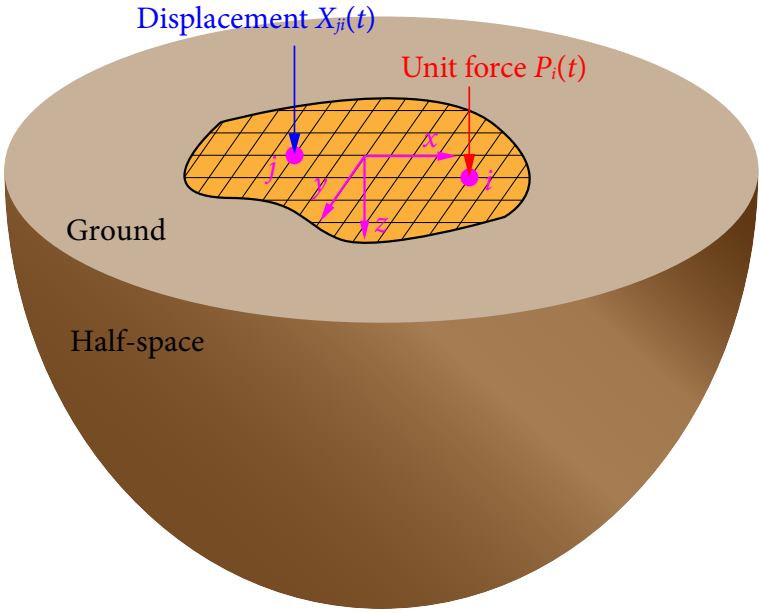


Figure 4.29 Definition of dynamic soil stiffness

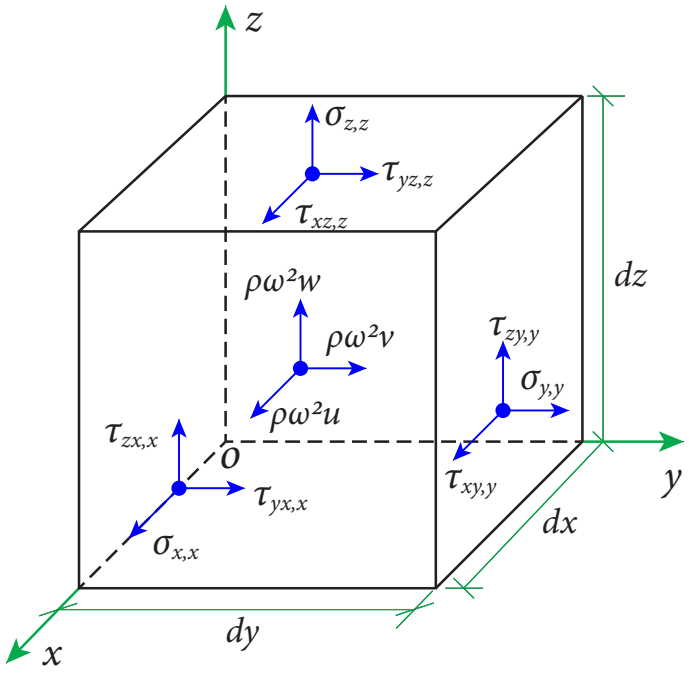


Figure 4.30 Infinitesimal cubes in harmonic motion

4.4.2 Generic Derivation in 3D Soil

To accurately capture the soil-structure interaction and derive the dynamic stiffness matrix of soils, it is crucial to understand the fundamental elastodynamic equations governing the soil system. Considering an infinitesimal cube of soil subjected to a harmonic loading with frequency ω, as depicted in Figure 4.30.

The dynamic equilibrium equations for this infinitesimal soil element can be derived by considering the balance of forces acting on the cube in each direction. These equations will involve the stress components, body forces, and inertial terms, all of which are functions of the spatial coordinates and time. The stress-strain relationships for the soil material, along with the compatibility equations, are then used to express the equilibrium equations in terms of displacements. If there are no other body forces exerted, the 3-dimensional dynamic equilibrium equations in Cartesian coordinates can be expressed as,

$$\begin{aligned}
\sigma_{x,x}(x,y,z) + \tau_{xy,y}(x,y,z) + \tau_{xz,z}(x,y,z) &= -\rho\omega^2 u(x,y,z) \\
\tau_{yx,x}(x,y,z) + \sigma_{y,y}(x,y,z) + \tau_{yz,z}(x,y,z) &= -\rho\omega^2 v(x,y,z) \\
\tau_{zx,x}(x,y,z) + \tau_{zy,y}(x,y,z) + \sigma_{z,z}(x,y,z) &= -\rho\omega^2 w(x,y,z)
\end{aligned} \tag{4.4.1}$$

in which, σ and τ denote the amplitude of normal and shear stresses. The first subscript denotes the direction of the stress component. The second one denotes the direction of the infinitesimal area's normal on which the stress component acts. The comma denotes a partial derivative with respect to the subscript following it. ρ represents the mass density. Displacements u, v, and w are in $x-$, $y-$, and $z-$direction, respectively. All amplitudes are a function of x, y, and z.

The constitutive equation, or Hooke's law, is specified as

$$\begin{aligned}
\epsilon_x &= \frac{1}{E}\left[\sigma_x - \nu(\sigma_y + \sigma_z)\right] \\
\epsilon_y &= \frac{1}{E}\left[\sigma_y - \nu(\sigma_z + \sigma_x)\right] \\
\epsilon_z &= \frac{1}{E}\left[\sigma_z - \nu(\sigma_x + \sigma_y)\right] \\
\gamma_{xy} &= \frac{\tau_{xy}}{G},
\end{aligned}$$

$$\begin{aligned} \gamma_{yz} &= \frac{\tau_{yz}}{G}, \\ \gamma_{zx} &= \frac{\tau_{zx}}{G}. \end{aligned} \tag{4.4.2}$$

in which, G is the shear modulus, which can be expressed as a function of Young's modulus of elasticity E and Poisson's ratio ν:

$$G = \frac{E}{2\,(1+\nu)} \tag{4.4.3}$$

The stress amplitudes in the above equation can be written in terms of strain amplitudes as,

$$\begin{aligned} \sigma_x &= (2G+\lambda)\,\epsilon_x + \lambda\,(\epsilon_y+\epsilon_z), \\ \sigma_y &= (2G+\lambda)\,\epsilon_y + \lambda\,(\epsilon_z+\epsilon_x), \\ \sigma_z &= (2G+\lambda)\,\epsilon_z + \lambda\,(\epsilon_x+\epsilon_y), \\ \tau_{xy} &= G\,\gamma_{xy}, \\ \tau_{yz} &= G\,\gamma_{yz}, \\ \tau_{zx} &= G\,\gamma_{zx}. \end{aligned} \tag{4.4.4}$$

in which, λ is the Lamé constant, can be expressed as

$$\lambda = \frac{\nu E}{(1+\nu)(1-2\nu)}. \tag{4.4.5}$$

The strain-displacement equations are formulated as

$$\begin{aligned} \gamma_{xy} = \gamma_{yx} &= u_{,y}(x,y,z) + v_{,x}(x,y,z)\,, \\ \gamma_{yz} = \gamma_{zy} &= v_{,z}(x,y,z) + w_{,y}(x,y,z)\,, \\ \gamma_{zx} = \gamma_{xz} &= w_{,x}(x,y,z) + u_{,z}(x,y,z)\,, \\ \epsilon_x &= u_{,x}(x,y,z)\,, \\ \epsilon_y &= v_{,y}(x,y,z)\,, \\ \epsilon_z &= w_{,z}(x,y,z)\,. \end{aligned} \tag{4.4.6}$$

The component amplitudes of the normal and shear strains are denoted by ϵ and γ , respectively. Substituting the constitutive equations (4.4.2) and strain-displacement equations (4.4.6) into the dynamic equilibrium equations (4.4.1) leads to

$$\begin{aligned}
(2G+\lambda)\,u_{,xx} &+\lambda\,(v_{,yx}+w_{,zx}) &+G(u_{,yy}+v_{,xy}+u_{,zz}+w_{,xz}) &= -\rho\omega^2 u,\\
(2G+\lambda)\,v_{,yy} &+\lambda\,(u_{,xy}+w_{,zy}) &+G(v_{,xx}+u_{,yx}+v_{,zz}+w_{,yz}) &= -\rho\omega^2 v,\\
(2G+\lambda)\,w_{,zz} &+\lambda\,(u_{,zx}+v_{,yz}) &+G(w_{,xx}+u_{,zx}+w_{,yy}+v_{,yz}) &= -\rho\omega^2 w
\end{aligned} \tag{4.4.7}$$

Rearrange equation (4.4.7) yields,

$$\begin{aligned}
G\,\nabla^2 u &+(\lambda+G)\,(u_{,xx}+v_{,yx}+w_{,zx}) &= -\rho\omega^2 u,\\
G\,\nabla^2 v &+(\lambda+G)\,(u_{,xy}+v_{,yy}+w_{,zy}) &= -\rho\omega^2 v,\\
G\,\nabla^2 w &+(\lambda+G)\,(u_{,xz}+v_{,yz}+w_{,zz}) &= -\rho\omega^2 w.
\end{aligned} \tag{4.4.8}$$

The equation above can be re-written in the following tensor form,

$$G\nabla^2\mathbf{u}+(\lambda+G)\nabla\nabla\cdot\mathbf{u}=-\rho\omega^2\mathbf{u}, \tag{4.4.9}$$

where $\mathbf{u}$ is the vector of total displacement, $\mathbf{u}=[u,\,v,\,w]^T$. $\nabla=\mathbf{i}\dfrac{\partial}{\partial x}+\mathbf{j}\dfrac{\partial}{\partial y}+\mathbf{k}\dfrac{\partial}{\partial z}$, is the gradient; $\nabla^2=\dfrac{\partial^2}{\partial x^2}+\dfrac{\partial^2}{\partial y^2}+\dfrac{\partial^2}{\partial z^2}$, is the Laplacian operator.

These are the coupled equations of motion for harmonic excitation expressed in displacement amplitudes. In order to decouple the displacements and to identify the different types of waves, an arbitrary displacement can be expressed as volumetric strain with amplitude $\{\mathbf{\Phi}\}$ and the rotational-strain vector $\{\mathbf{\Psi}\}$ with amplitudes $\{\psi_x\}$, $\{\psi_y\}$, and $\{\psi_z\}$, i.e.,

$$\mathbf{u}=\nabla\mathbf{\Phi}+\nabla\times\mathbf{\Psi}, \tag{4.4.10}$$

in which,

$$\begin{aligned}
\nabla\mathbf{\Phi} &= \mathbf{i}\,\frac{\partial\Phi}{\partial x}+\mathbf{j}\,\frac{\partial\Phi}{\partial y}+\mathbf{k}\,\frac{\partial\Phi}{\partial z}\\
&= \mathbf{i}\,\phi_{,x}+\mathbf{j}\,\phi_{,y}+\mathbf{k}\,\phi_{,z}\,,
\end{aligned} \tag{4.4.11}$$

and

$$\begin{aligned}\nabla \times \boldsymbol{\Psi} &= \begin{vmatrix} \mathbf{i} & \mathbf{j} & \mathbf{k} \\ \dfrac{\partial}{\partial x} & \dfrac{\partial}{\partial y} & \dfrac{\partial}{\partial z} \\ \psi_x & \psi_y & \psi_z \end{vmatrix} \\ &= \mathbf{i}\left(\psi_{z,y} - \psi_{y,z}\right) + \mathbf{j}\left(\psi_{x,z} - \psi_{z,x}\right) + \mathbf{k}\left(\psi_{y,x} - \psi_{x,y}\right).\end{aligned} \tag{4.4.12}$$

Therefore, the displacement in x, y, and z are,

$$\begin{aligned} u &= \phi_{,x} + \psi_{z,y} - \psi_{y,z}, \\ v &= -\psi_{z,x} + \phi_{,y} + \psi_{x,z}, \\ w &= \psi_{y,x} - \psi_{x,y} + \phi_{,z}. \end{aligned} \tag{4.4.13}$$

The equation above yields the dilatation

$$\frac{\partial u}{\partial x} + \frac{\partial v}{\partial y} + \frac{\partial w}{\partial z} = \phi_{,xx} + \phi_{,yy} + \phi_{,zz} = \nabla^2 \boldsymbol{\Phi}, \tag{4.4.14}$$

and rotation

$$\boldsymbol{\Psi}(x,y,z) = \begin{Bmatrix} \psi_x \\ \psi_y \\ \psi_z \end{Bmatrix} = \frac{1}{2}\begin{Bmatrix} \psi_{z,y} - \psi_{y,z} \\ \psi_{x,z} - \psi_{z,x} \\ \psi_{y,x} - \psi_{y,y} \end{Bmatrix}. \tag{4.4.15}$$

Knowing that the divergence of curl is 0. Therefore,

$$\begin{aligned}\nabla\nabla \times \boldsymbol{\Psi} &= \frac{\partial \psi_x}{\partial x} + \frac{\partial \psi_y}{\partial y} + \frac{\partial \psi_z}{\partial z} \\ &= \psi_{x,x} + \psi_{y,y} + \psi_{z,z} \\ &= \psi_{z,yx} - \psi_{y,zx} + \psi_{x,zy} - \psi_{z,xy} + \psi_{y,xz} - \psi_{x,yz} \\ &= 0\end{aligned} \tag{4.4.16}$$

Thus equation (4.4.8) can be rewritten as

$$\begin{aligned}
(2G+\lambda)\,\phi_{,x} + 2G\,(\,\psi_{y,z} - \,\psi_{z,y}) &= -\rho\omega^2 u,\\
(2G+\lambda)\,\phi_{,y} + 2G\,(\,\psi_{z,x} - \,\psi_{x,z}) &= -\rho\omega^2 v,\\
(2G+\lambda)\,\phi_{,z} + 2G\,(\,\psi_{x,y} - \,\psi_{y,x}) &= -\rho\omega^2 w.
\end{aligned} \tag{4.4.17}$$

The material damping occurring in a soil system involves frictional loss of energy or linear hysteretic damping. The effect of material damping, which may differ for various types of waves, is assumed to be the same. This frequency-independent property can be incorporated by replacing the elastic material constants with the corresponding complex ones. Complex shear modulus G^* and Lamé constant λ^* can be expressed as

$$\begin{aligned}
G^* &= (1+\mathrm{i}\,2\zeta)\,G,\\
\lambda^* &= (1+\mathrm{i}\,2\zeta)\,\lambda
\end{aligned} \tag{4.4.18}$$

where ζ is the damping coefficient. Replacing G and λ by G^* and λ^* in equation (4.4.17) leads to,

$$\begin{aligned}
(2G^*+\lambda^*)\,\phi_{,x} + 2G^*\,(\,\psi_{y,z} - \,\psi_{z,y}) &= -\rho\omega^2 u,\\
(2G^*+\lambda^*)\,\phi_{,y} + 2G^*\,(\,\psi_{z,x} - \,\psi_{x,z}) &= -\rho\omega^2 v,\\
(2G^*+\lambda^*)\,\phi_{,z} + 2G^*\,(\,\psi_{x,y} - \,\psi_{y,x}) &= -\rho\omega^2 w.
\end{aligned} \tag{4.4.19}$$

Translational Strain

Eliminating the rotational strains by differentiating equation (4.4.19) with respect to x, y, and z, respectively, and then adding the three equations results in

$$\begin{aligned}
(2G^*+\lambda^*)\,(\phi_{,xx} + \phi_{,yy} + \phi_{,zz}) &= -\rho\omega^2\,\phi,\\
\Longrightarrow \qquad \nabla^2\boldsymbol{\Phi} &= -\frac{\omega^2}{c_p^2}\,\boldsymbol{\Phi}.
\end{aligned} \tag{4.4.20}$$

where $c_p^2 = \dfrac{2G^*+\lambda^*}{\rho}$, is the dilatational wave velocity.

Rotational strain

Eliminating the volumetric strain by differentiating equation (4.4.19 − 2) and (4.4.19 − 3) with respect to z, y, respectively, and then subtracting these two expressions. Noting that the derivative of equation (4.4.16) with respect to x also vanished leads to

$$G^* \left(\psi_{x,xx} + \psi_{x,yy} + \psi_{x,zz}\right) = \frac{1}{2}\rho\omega^2(w_{,y} - v_{,z}) = -\rho\omega^2\psi_x \,. \tag{4.4.21}$$

By analogous,

$$\begin{aligned} G^* \left(\psi_{y,xx} + \psi_{y,yy} + \psi_{y,zz}\right) &= -\rho\omega^2\psi_y \,, \\ G^* \left(\psi_{z,xx} + \psi_{z,yy} + \psi_{z,zz}\right) &= -\rho\omega^2\psi_z \,. \end{aligned} \tag{4.4.22}$$

Equations (4.4.21) and (4.4.22) can be rewritten as

$$\nabla^2\boldsymbol{\Psi} = -\frac{\omega^2}{c_s^2}\,\boldsymbol{\Psi} \,, \tag{4.4.23}$$

where, $c_s^2 = \dfrac{G^*}{\rho}$, is the shear-wave velocity.

Therefore, for harmonic excitation, the equations of motion are specified in Equations (4.4.20) and (4.4.23) with the unknown amplitudes of the volumetric strain $\{\boldsymbol{\Phi}\}$ and the rotational strain vector $\{\boldsymbol{\Psi}\}$, respectively. These wave equations are linear partial differential equations of second order. The particular solutions to Equations (4.4.20) and (4.4.23) are the steady-state displacement response under dynamic excitations.

4.4.3 Numerical Simulation for Elastodynamic 3D Half-Space Soil

Having derived the analytical solution for the displacement in an elastic half-space subjected to the dynamic harmonic load, the numerical simulation analysis is performed. The first step is to establish a three-dimensional model of a half-space soil, followed by the applications of dynamic normal and parallel loads to calculate the displacements at the ground of the soil.

Modelling

A 3D finite element model of the half-space elastic soil body is created using ANSYS. The model consists of a finite element mesh with a radius of 20 m from the origin, in which a

cuboid with an edge of 10 m in the ground dimensions, and a depth 8 m is of interest, as shown in Figure 4.31. The rest of the space is modelled to consider the far-field domain.

The finite element mesh is generated using 3D 8-Node Structural Solid (8 nodes in 3D space). A mesh convergence study is conducted to ensure that the results are independent of the mesh size.

The soil material properties are defined as follows: Young's modulus: $E = 200$ MPa; Poisson's ratio: $\nu = 0.30$; density: $\rho = 2500$ kg/m^3; damping ratio: $\zeta = 5\,\%$. The input harmonic loading is given by: $P = 10000 \sin \omega t$, where ω varies from 0 to 100 rad/s, with a total of 1000 equally spaced frequency steps.

Boundary Conditions and Simulation

The bottom and lateral surface of the model ($R = \sqrt{x^2 + y^2 + z^2} = 20$ m) are modelled using infinite elements or dashpots to simulate the far-field domain and prevent wave reflections. The top surface of the model ($z = 0$) is free to deform.

The harmonic dynamic load is applied at $x = 0$, $y = 0$, $z = 0$. It is applied at this point in distinct directions, i.e., dynamic normal load (P_z), and dynamic parallel load (P_r, $r = \sqrt{x^2 + y^2}$), respectively.

The dynamic analysis is performed using the Full Solution Method in ANSYS. This direct method calculates the complete response at each frequency step based on the complex matrix equation 4.1.1. It provides the comprehensive complex response at each frequency, handling non-symmetric matrices that arise from asymmetric boundary conditions or the use of damping elements. This method captures the effects of frequency-dependent material properties, such as viscoelastic behaviour or frequency-dependent damping, and accurately reflects the response at each frequency step. It includes localized effects or resonances, ensuring detailed and precise analysis of the dynamic behavior of the system.

Results of Analysis

To obtain the dynamic flexibility matrix of the soil, it is essential to evaluate the displacement response at the desired locations. The dynamic loads are applied in normal (P_z) and parallel directions (P_y in this case) at the origin point of the soil body ($x = y = z = 0$) with the

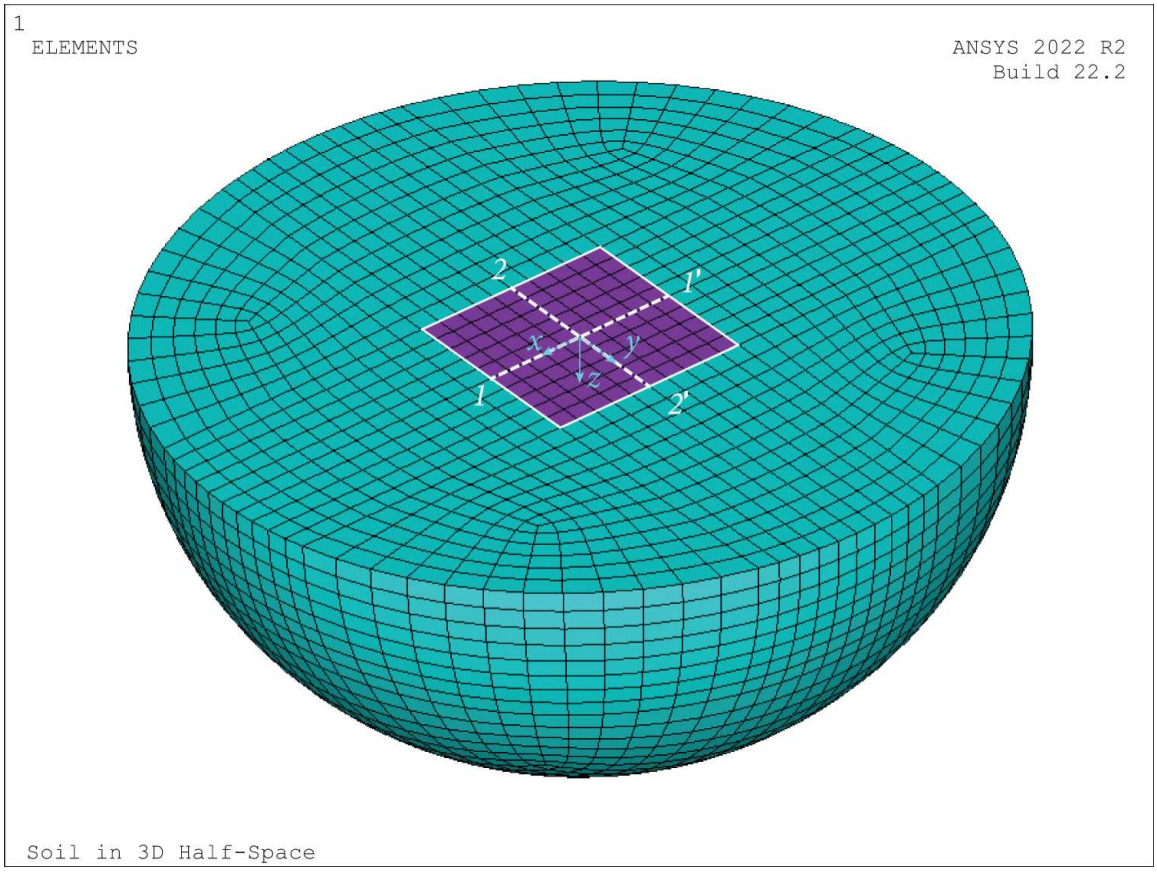


Figure 4.31 Model of soil in 3D half-space

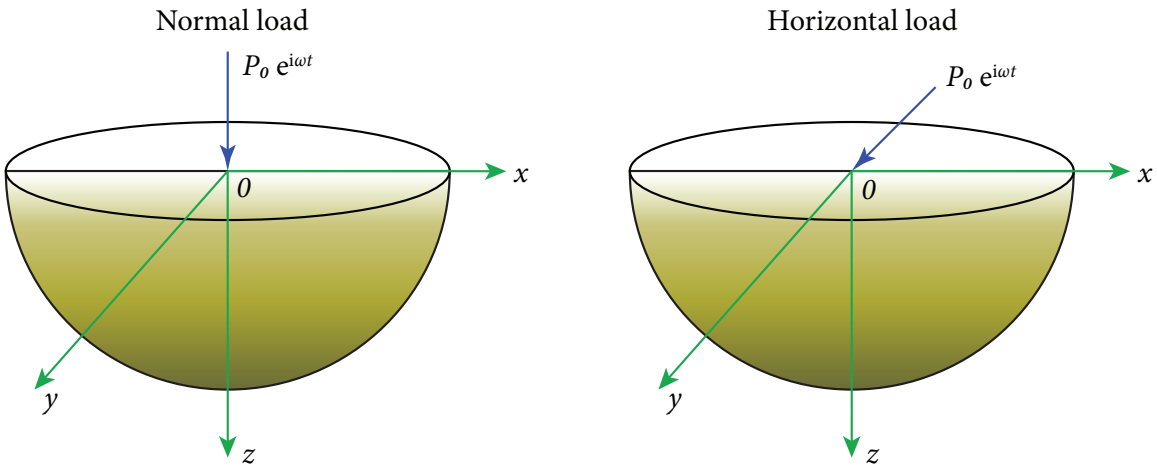


Figure 4.32 Normal and horizontal loads on the ground of 3D half-space

specified amplitude and frequency range in the above section, as shown in Figure 4.32. Numerical results of the amplitude and phase lag are obtained for the lines 1-1′ and 2-2′.

Dynamic Normal Load

(1) Amplitudes and Phase Lags

The amplitudes and phase lags in $x-$, $y-$, and $z-$ directions are calculated when the dynamic load is applied normally. Figures 4.33 to 4.38, and Figures 4.39 to 4.44 show the results for profiles 1-1′ and 2-2′, respectively.

(2) Real and Imaginary Parts

The real and imaginary parts are calculated based on the amplitudes and phase lags. Figures 4.45 to 4.50 and Figures 4.51 to 4.56 show the results for profiles 1-1′ and 2-2′, respectively.

Dynamic Horizontal Load

(1) Amplitudes and Phase Lags

The amplitudes and phase lags in $x-$, $y-$, and $z-$ directions are calculated when the dynamic load is applied horizontally. Figures 4.57 to 4.62 and Figures 4.63 to 4.68 show the results for profiles 1-1′ and 2-2′, respectively.

(2) Real and Imaginary Parts The real and imaginary parts are calculated based on the amplitudes and phase lags. Figures 4.69 to 4.74 and Figures 4.75 to 4.80 show the results for profiles 1-1′ and 2-2′, respectively.

The obtained results provide a comprehensive understanding of the soil's dynamic response under normal and horizontal harmonic loading. The amplitudes and phase lags characterize the frequency-dependent behavior of the soil, while the real and imaginary parts are essential for constructing the dynamic flexibility matrix.

By analyzing the results along the selected profiles (1-1′ and 2-2′), the spatial variation of response along the specified profiles can be assessed, providing valuable insights into the soil-structure interaction. The presented figures offer a clear visualization of the soil's dynamic behaviour, enabling researchers and engineers to make informed decisions in the design and analysis of structures considering soil-structure interaction effects.

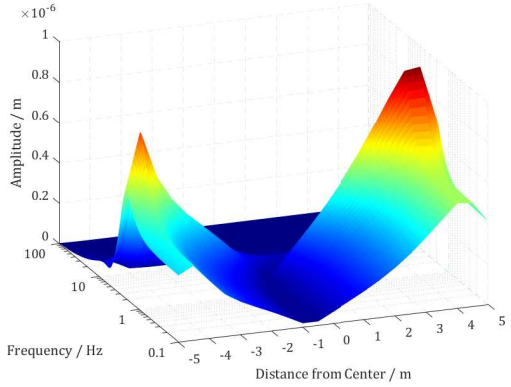


Figure 4.33 X Amplitude in 1-1′ under dynamic normal load

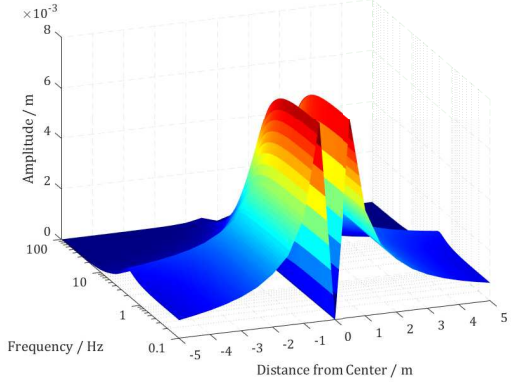


Figure 4.34 Y Amplitude in 1-1′ under dynamic normal load

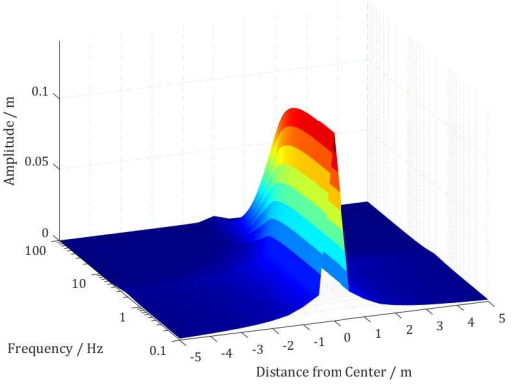


Figure 4.35 Z Amplitude in 1-1′ under dynamic normal load

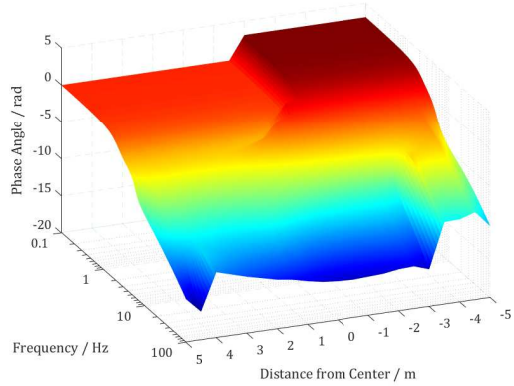


Figure 4.36 Phase lag in X direction in 1-1′ under dynamic normal load

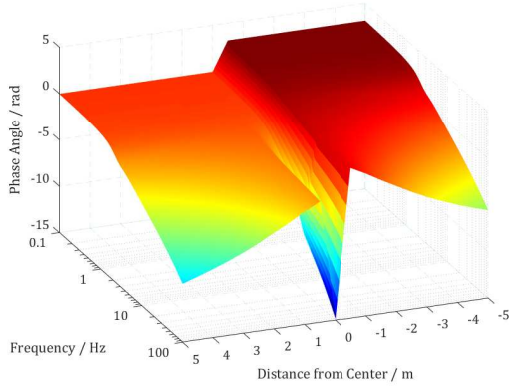


Figure 4.37 Phase lag in Y direction in 1-1′ under dynamic normal load

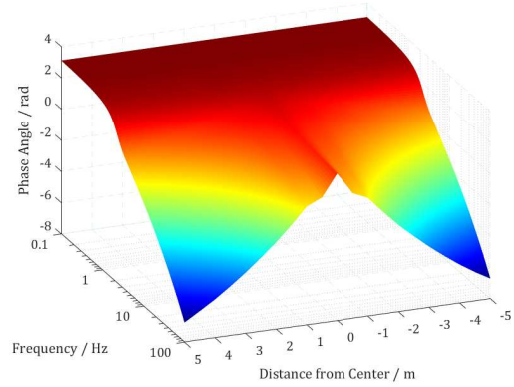


Figure 4.38 Phase lag in Z direction in 1-1′ under dynamic normal load

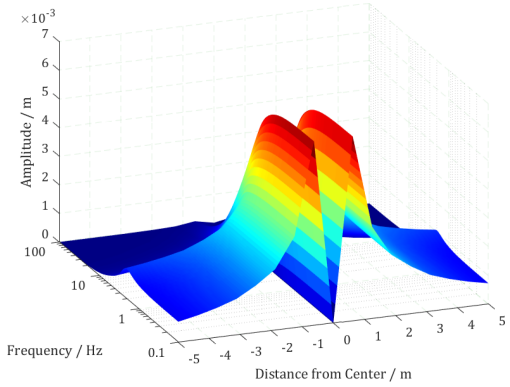


Figure 4.39 X Amplitude in 2-2′ under dynamic normal load

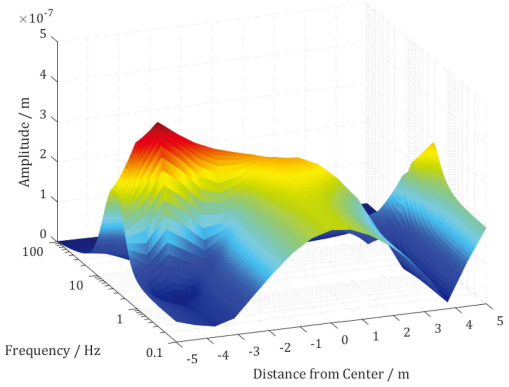


Figure 4.40 Y Amplitude in 2-2′ under dynamic normal load

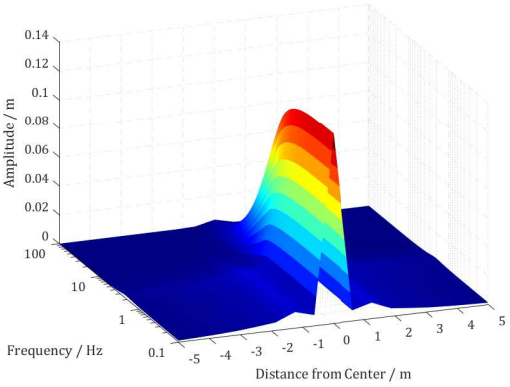


Figure 4.41 Z Amplitude in 2-2′ under dynamic normal load

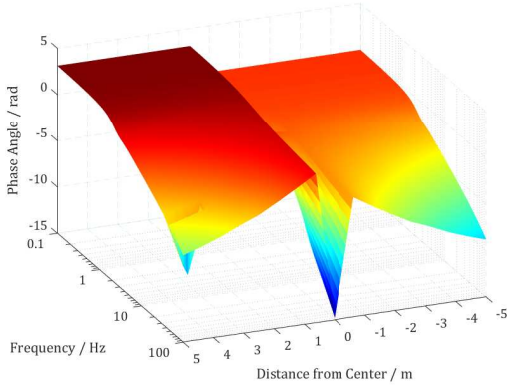


Figure 4.42 Phase lag in X direction in 2-2′ under dynamic normal load

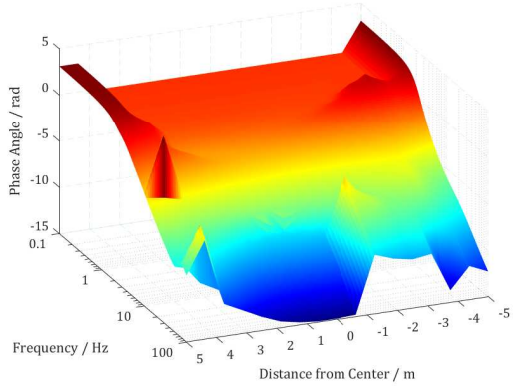


Figure 4.43 Phase lag in Y direction in 2-2′ under dynamic normal load

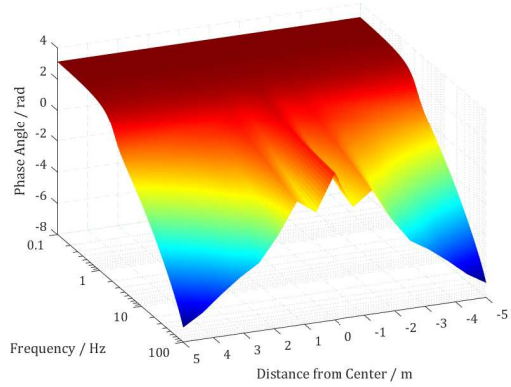


Figure 4.44 Phase lag in Z direction in 2-2′ under dynamic normal load

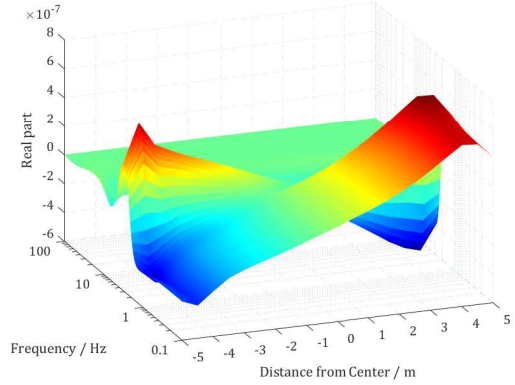


Figure 4.45 Real part in X direction in 1-1′ under dynamic normal load

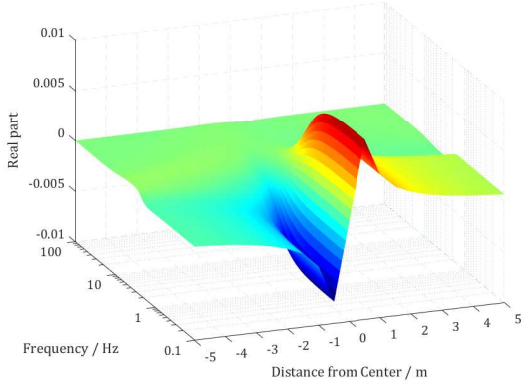


Figure 4.46 Real part in Y direction in 1-1′ under dynamic normal load

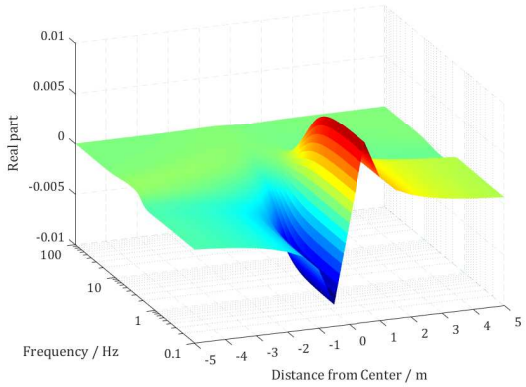


Figure 4.47 Real part in Y direction in 1-1′ under dynamic normal load

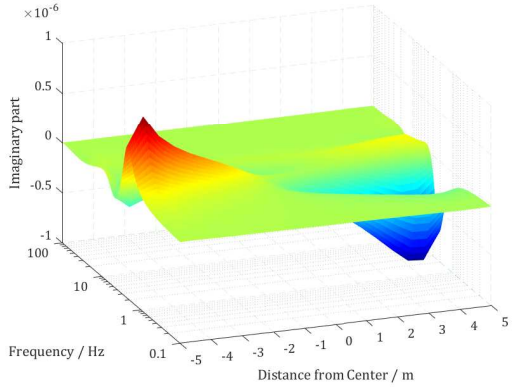


Figure 4.48 Imaginary part in X direction in 1-1′ under dynamic normal load

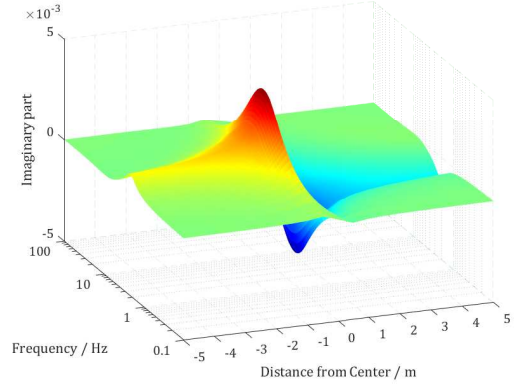


Figure 4.49 Imaginary part in Y direction in 1-1′ under dynamic normal load

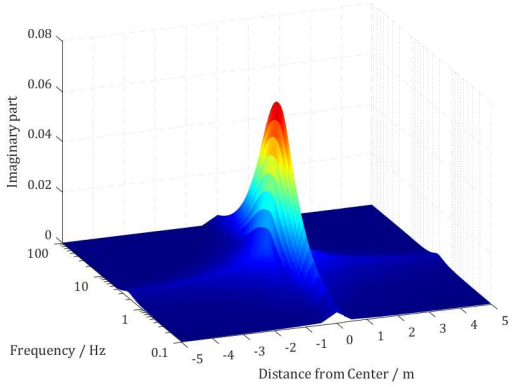


Figure 4.50 Imaginary part in Z direction in 1-1′ under dynamic normal load

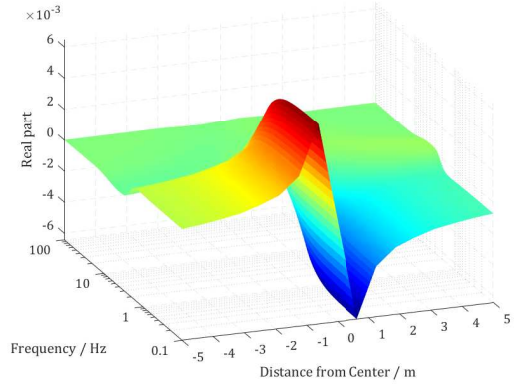


Figure 4.51 Real part in X direction in 2-2′ under dynamic normal load

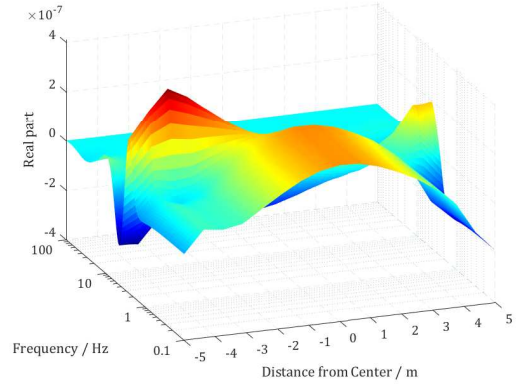


Figure 4.52 Real part in Y direction in 2-2′ under dynamic normal load

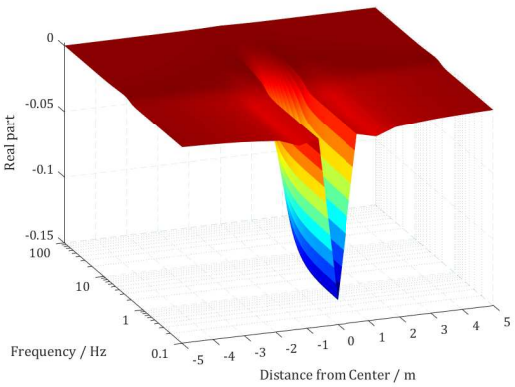


Figure 4.53 Real part in Z direction in 2-2′ under dynamic normal load

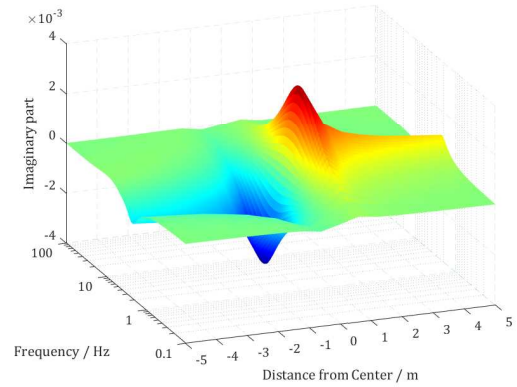


Figure 4.54 Imaginary part in X direction in 2-2′ under dynamic normal load

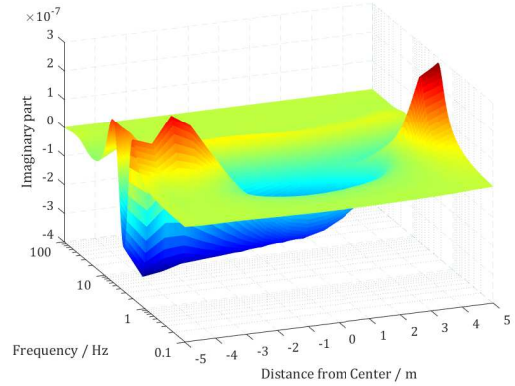


Figure 4.55 Imaginary part in Y direction in 2-2′ under dynamic normal load

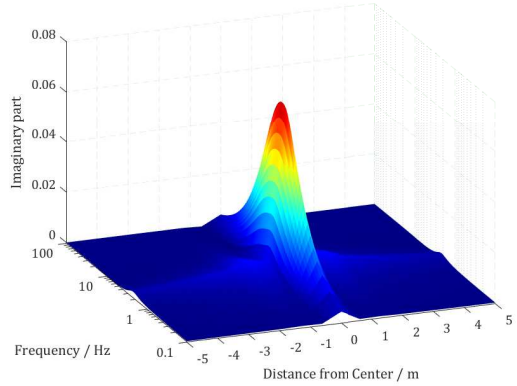


Figure 4.56 Imaginary part in Z direction in 2-2′ under dynamic normal load

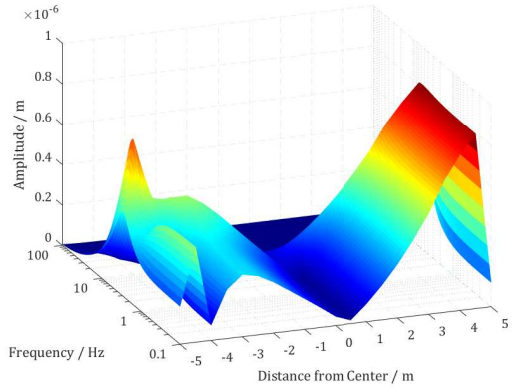


Figure 4.57 X Amplitude in 1-1′ under dynamic horizontal load

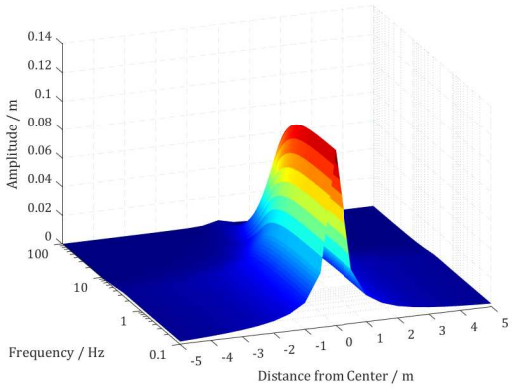


Figure 4.58 Y Amplitude in 1-1′ under dynamic horizontal load

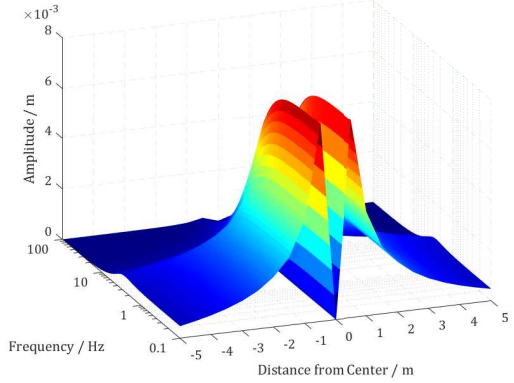


Figure 4.59 Z Amplitude in 1-1′ under dynamic horizontal load

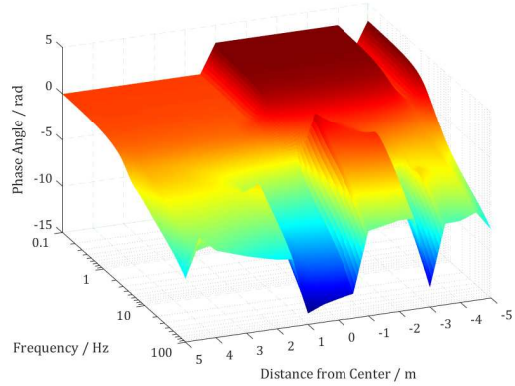


Figure 4.60 Phase lag in X direction in 1-1′ under dynamic horizontal load

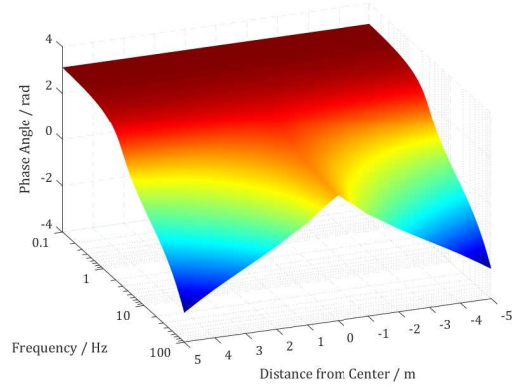


Figure 4.61 Phase lag in Y direction in 1-1′ under dynamic horizontal load

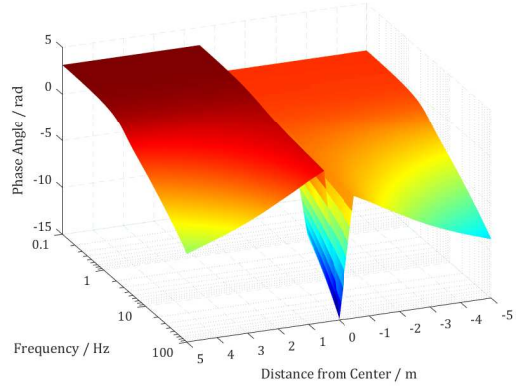


Figure 4.62 Phase lag in Z direction in 1-1′ under dynamic horizontal load

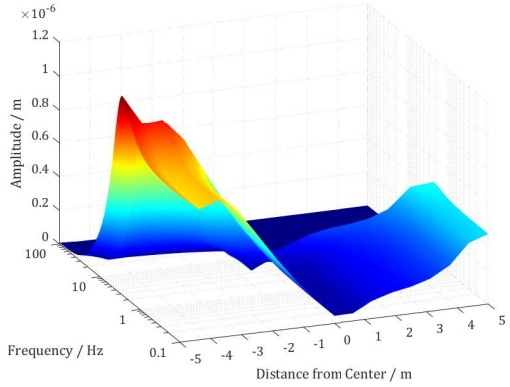


Figure 4.63 X Amplitude in 2-2′ under dynamic horizontal load

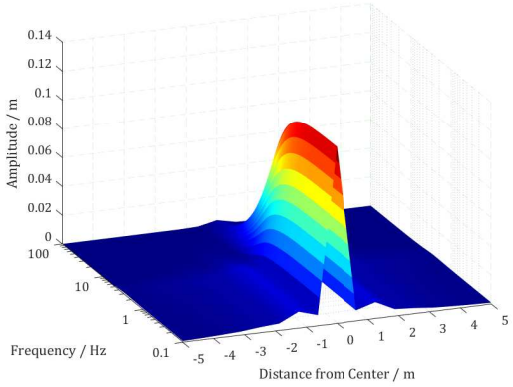


Figure 4.64 Y Amplitude in 2-2′ under dynamic horizontal load

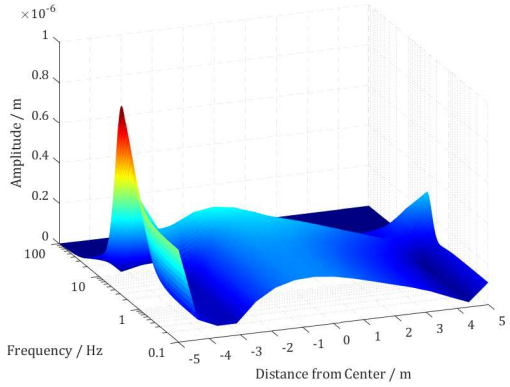


Figure 4.65 Z Amplitude in 2-2′ under dynamic horizontal load

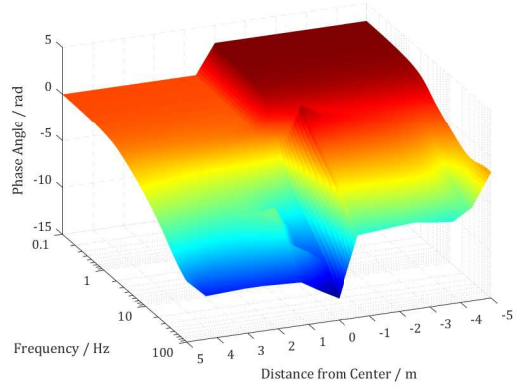


Figure 4.66 Phase lag in X direction in 2-2′ under dynamic horizontal load

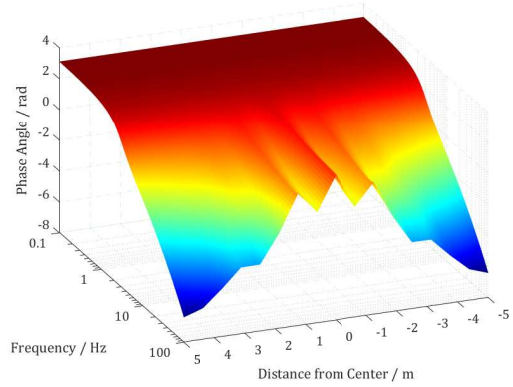


Figure 4.67 Phase lag in Y direction in 2-2′ under dynamic horizontal load

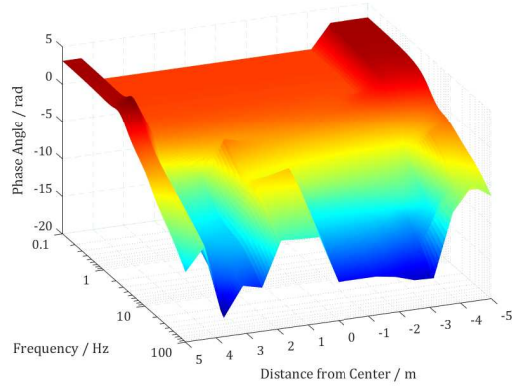


Figure 4.68 Phase lag in Z direction in 2-2′ under dynamic horizontal load

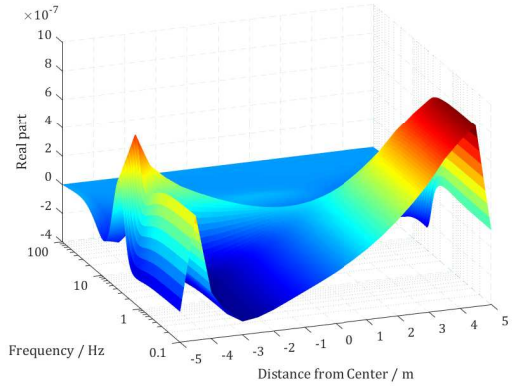


Figure 4.69 Real part in X direction in 1-1′ under dynamic horizontal load

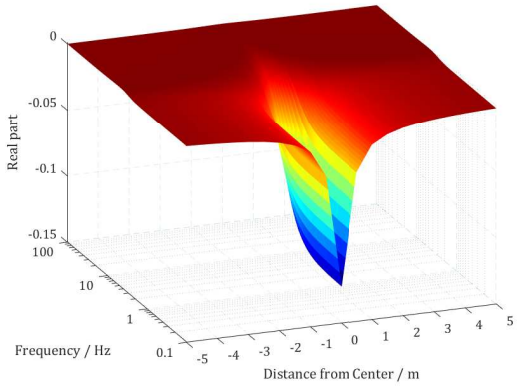


Figure 4.70 Real part in Y direction in 1-1′ under dynamic horizontal load

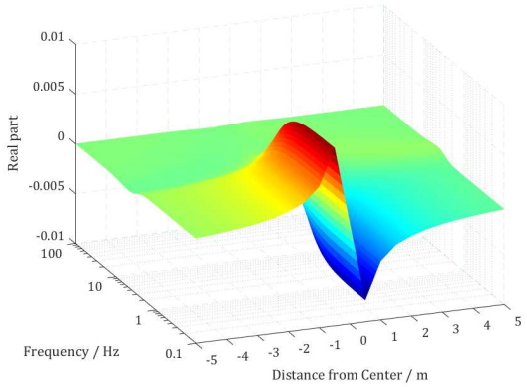


Figure 4.71 Real part in Z direction in 1-1′ under dynamic horizontal load

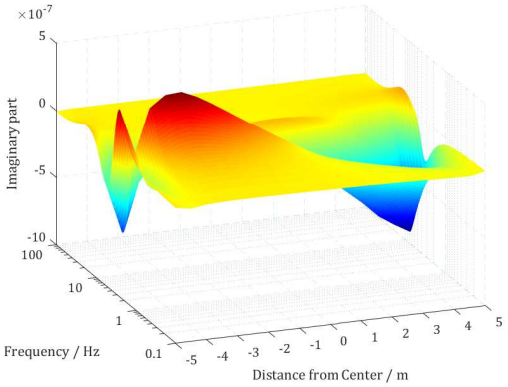


Figure 4.72 Imaginary part in X direction in 1-1′ under dynamic horizontal load

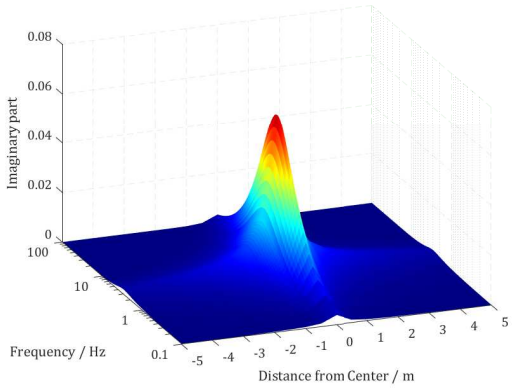


Figure 4.73 Imaginary part in Y direction in 1-1′ under dynamic horizontal load

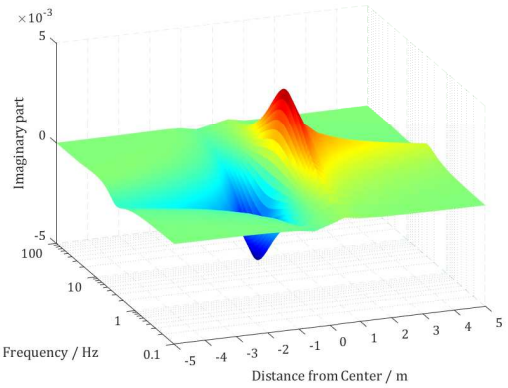


Figure 4.74 Imaginary part in Z direction in 1-1′ under dynamic horizontal load

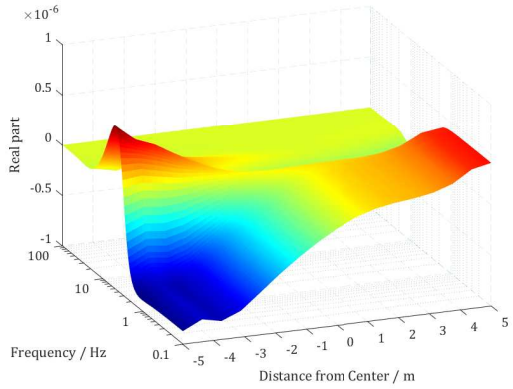


Figure 4.75 Real part in X direction in 2-2′ under dynamic horizontal load

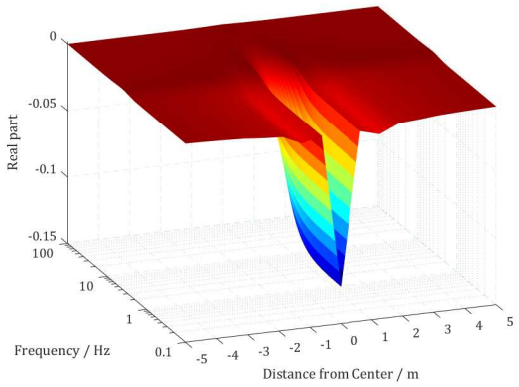


Figure 4.76 Real part in Y direction in 2-2′ under dynamic horizontal load

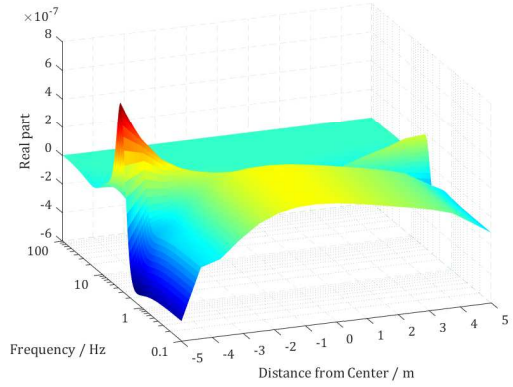


Figure 4.77 Real part in Z direction in 2-2′ under dynamic horizontal load

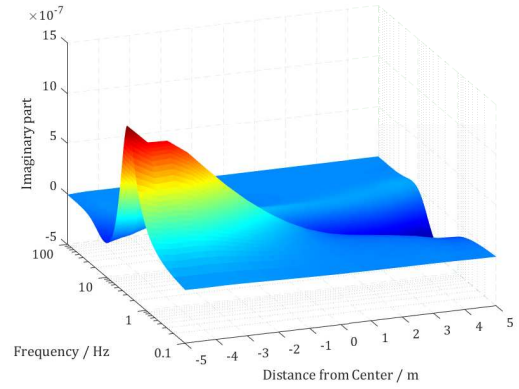


Figure 4.78 Imaginary part in X direction in 2-2′ under dynamic horizontal load

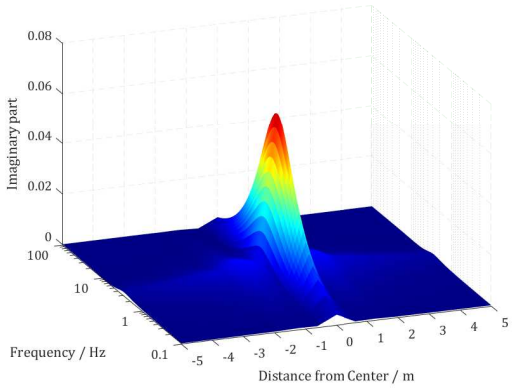


Figure 4.79 Imaginary part in Y direction in 2-2′ under dynamic horizontal load

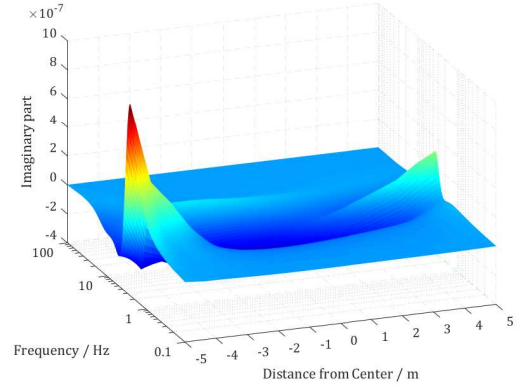


Figure 4.80 Imaginary part in Z direction in 2-2′ under dynamic horizontal load

4.4.4 Validation Against Classical Solutions ($\omega = 0$)

To verify the numerical results, analytical solutions for normal and horizontal loads with frequencies equal to 0 are compared with the outcomes from the above simulation.

Normal Load

When the load is applied normally to the ground surface and $\omega = 0$, the load becomes static. In this case, the solution to Equations (4.4.20) and (4.4.23) are given by:

$$\begin{aligned} u &= \frac{P}{4\pi GR}\left[\frac{xz}{R^2} - \frac{(1-2\nu)x}{R+z}\right], \\ v &= \frac{P}{4\pi GR}\left[\frac{yz}{R^2} - \frac{(1-2\nu)y}{R+z}\right], \\ w &= \frac{P}{4\pi GR}\left[\frac{z^2}{R^2} - (1-\nu)\right], \end{aligned} \tag{4.4.24}$$

where P is the applied load, G is the shear modulus, ν is the Poisson's ratio, and $R = \sqrt{x^2+y^2+z^2}$ is the distance from the load application point.

The numerical results obtained from the simulation are compared with the solution given by Equation (4.4.24), as shown in Figure 4.81 and Figure 4.82.

As can be seen from the result, the numerical results agree well with the classical solution, indicating the accuracy of the numerical simulation in capturing the response of the soil under normal loading conditions.

Horizontal Load

When the load is applied normally to the ground surface and $\omega = 0$, the load becomes static. In this case, the solution to Equations (4.4.20) and (4.4.23) are given by:

$$\begin{aligned} u &= \frac{P}{4\pi GR}\left[1 + \frac{x^2}{R^2} + \frac{(1-2\nu)R}{R+z} - \frac{(1-2\nu)x^2}{(R+z)^2}\right], \\ v &= \frac{P}{4\pi GR}\left[\frac{xy}{R^2} - \frac{(1-2\nu)xy}{(R+z)^2}\right], \\ w &= \frac{P}{4\pi GR}\left[\frac{xz}{R^2} + \frac{(1-2\nu)x}{R+z}\right]. \end{aligned} \tag{4.4.25}$$

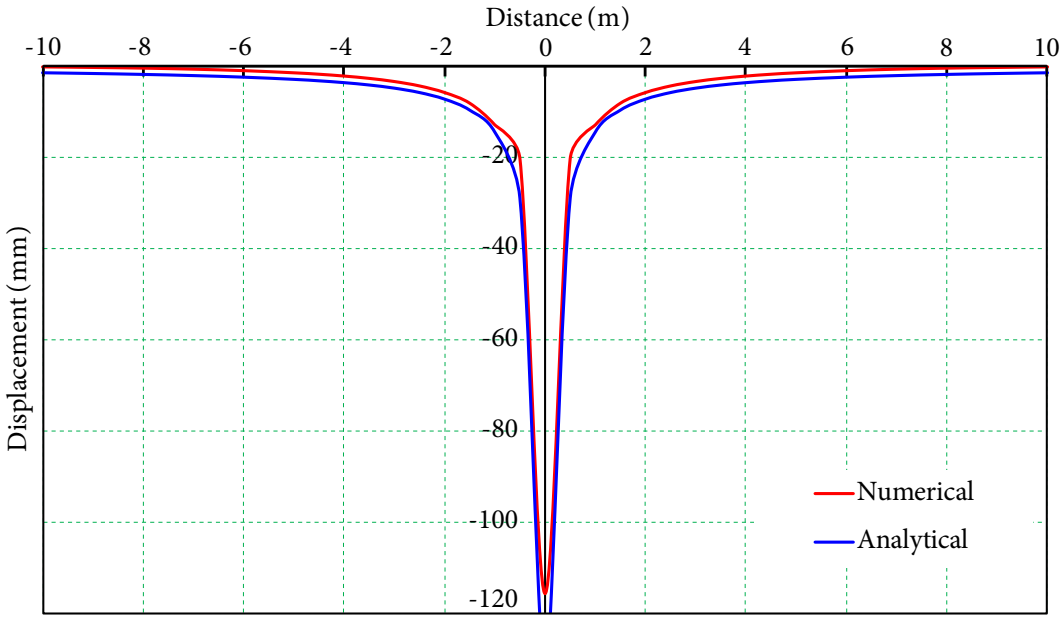


Figure 4.81 Comparison of vertical displacement in 1-1′ under dynamic normal load with $\omega = 0$

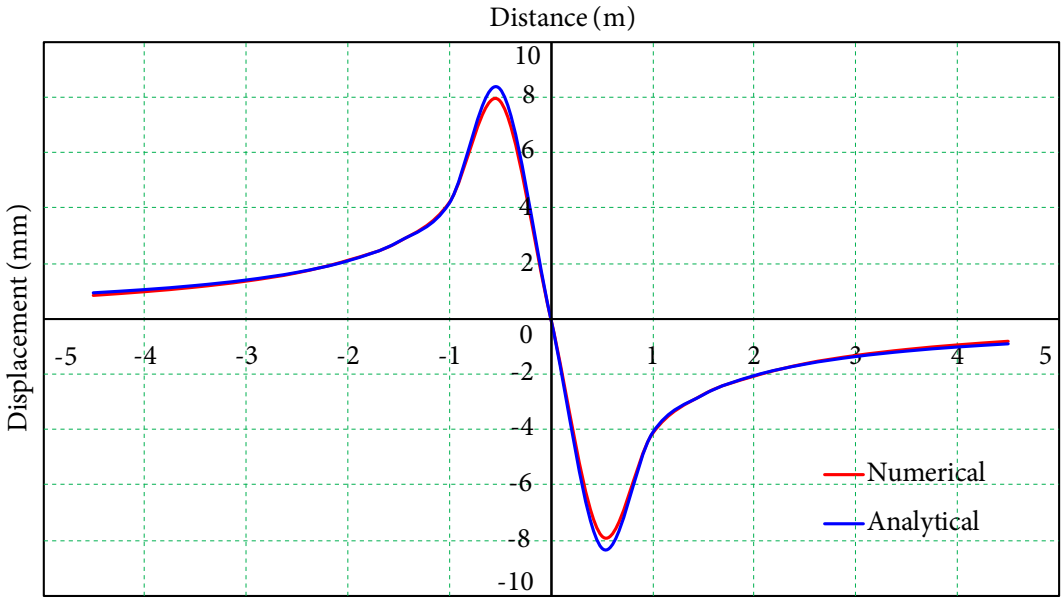


Figure 4.82 Comparison of horizontal displacement in 1-1′ under dynamic normal load with $\omega = 0$

The numerical results obtained from the simulation are compared with the solution given by Equation (4.4.25), as shown in Figure 4.83 and Figure 4.84. As can be seen from the result, the numerical results agree well with the classical solution, indicating the accuracy of the numerical simulation in capturing the response of the soil under horizontal loading conditions.

The numerical results from the simulation are compared with classical solutions for both normal and horizontal loads. The strong agreement between the two validates the accuracy of the numerical model in capturing soil displacement response. This successful validation demonstrates the method's capability in accurately modelling soil response, making it reliable for developing dynamic stiffness matrices for SSI problems.

4.4.5 Validation Against Analytical Solutions ($\omega \neq 0$)

To further establish the robustness and accuracy of our approach, the validation to dynamic loading scenarios is extended. This section presents a comprehensive comparison between our numerical results and analytical solutions for cases where the frequency of the dynamic load varies from 0 to 100 Hz. By evaluating the dynamic stiffness matrix across this frequency range, we aim to demonstrate the validity of our method for a broad spectrum of soil behaviour in the SSI problems.

In this investigation, the dynamic behaviour of the soil under vertical harmonic excitation applied at the origin point is focused. Specifically, the variation of the vertical component of the dynamic stiffness matrix at this location across the aforementioned frequency range is examined. The numerical results obtained from our proposed method are compared to the analytical solutions calculated using the methodology presented in Luco and Wong (1986), as shown in Figure 4.85. The result shows a great agreement with the analytical solution.

4.5 Dynamic Soil Stiffness for A Three-Layer Soil Foundation

An underlying soil site consists of 3 infinite soil layers resting on a homogeneous half-space. The unit weight γ, Poisson's ratio ν, damping ratio ζ, thickness of the top layers H, and shear-wave velocity V_s are shown in Figure 4.86. The result is also obtained by ACS SASSI.

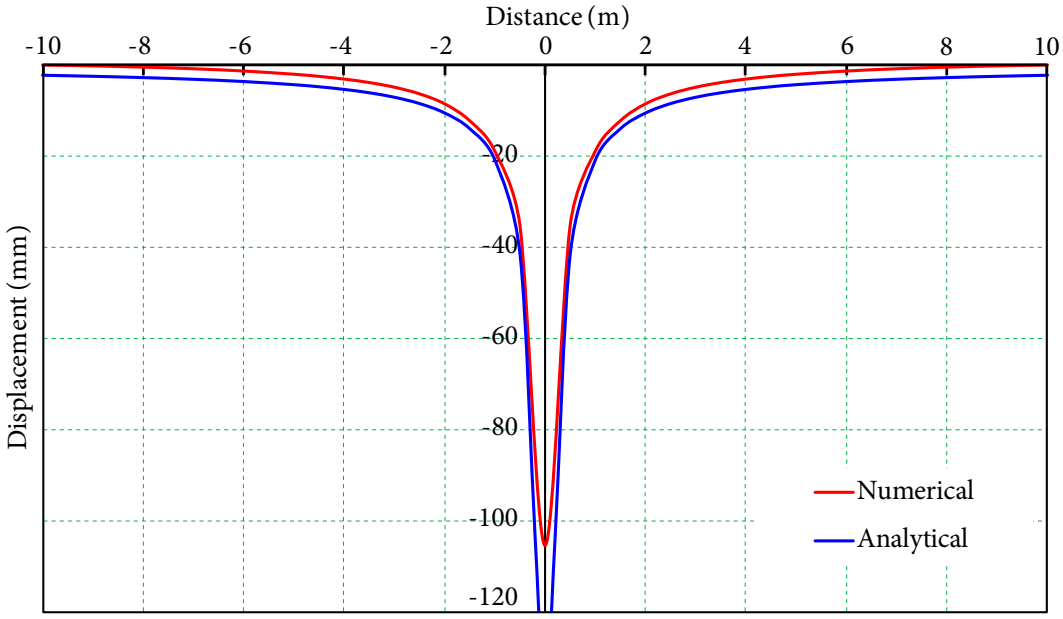


Figure 4.83 Comparison of vertical displacement in 1-1′ under dynamic horizontal load with $\omega = 0$

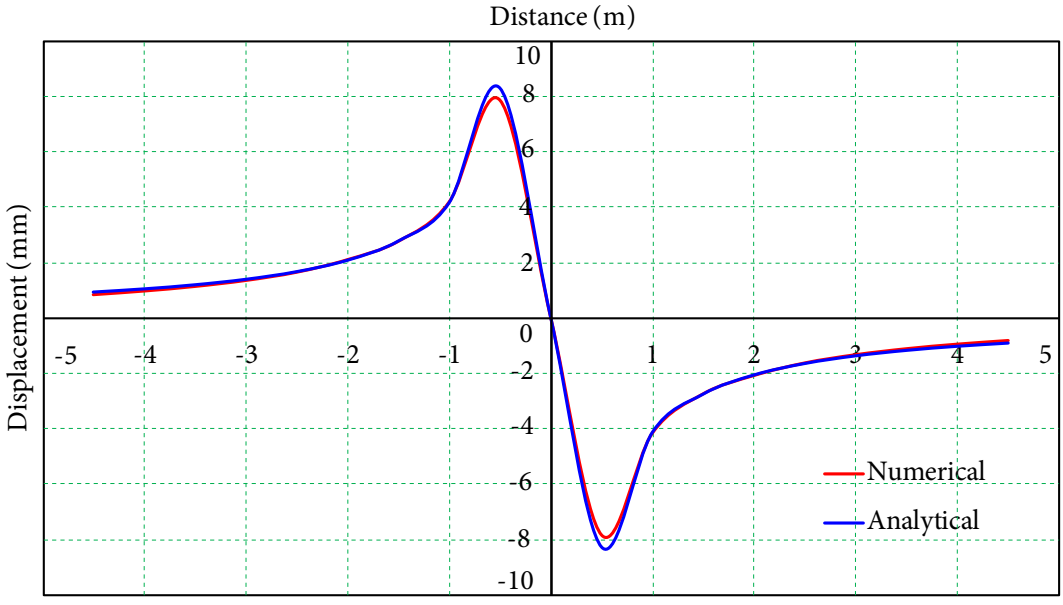


Figure 4.84 Comparison of horizontal displacement in 1-1′ under dynamic horizontal load with $\omega = 0$

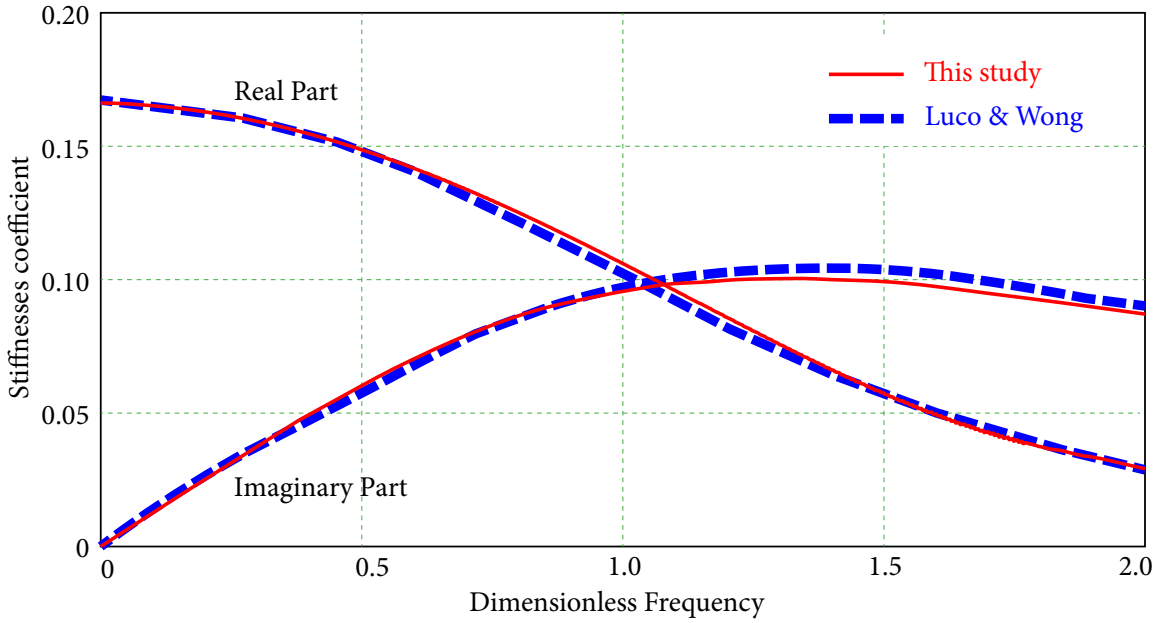


Figure 4.85 Dynamic soil stiffness of the half-space soil

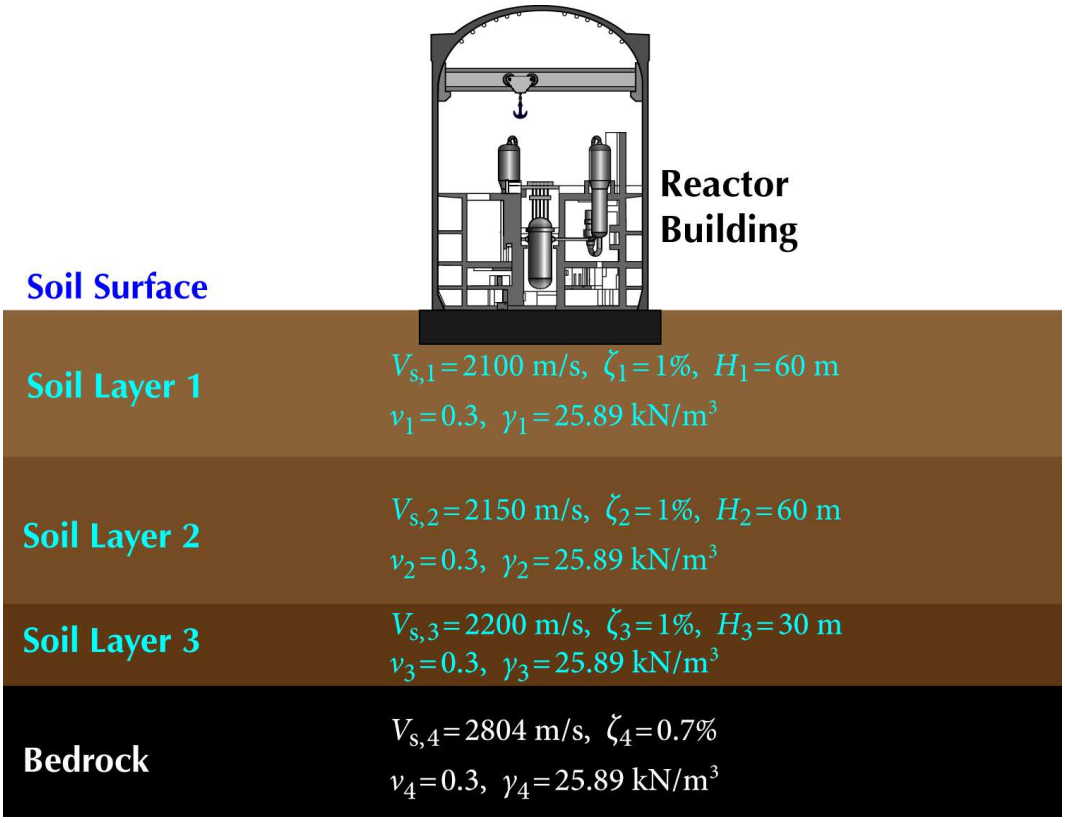


Figure 4.86 The three-layered soils and their properties

By employing the proposed method, the dynamic soil stiffness matrix is calculated, which can then be utilized for conducting SSI analysis. This dynamic soil stiffness matrix is extracted from the analysis using ACS SASSI and Zhou's method(2019), which applies the Boundary Element Method (BEM) based on Green's function.

The results, presented in Figure 4.87, demonstrate that the dynamic soil stiffness matrix obtained through the proposed method closely aligns with both the ACS SASSI solution and the BEM based on Green's function. The agreement is particularly strong with the results from Zhou's approach.

Because there are analytical results available for elastodynamic 3D half-space soil as presented in Section 4.4.3, to further ensure the correctness and accuracy of the proposed method, a 3D half-space with the properties of soil layer 1 is considered. The results are shown in Figure 4.87, which indicate that the dynamic soil stiffness matrices for the 3-layer soil and the 3D half-space with the properties of soil layer 1 are close. This is attributed to the significant thickness of the first soil layer, suggesting that the underlying relatively stiffer soil layers have minor effect on the dynamic stiffness matrix of the ground soil. The results also demonstrate the excellent accuracy of the proposed method.

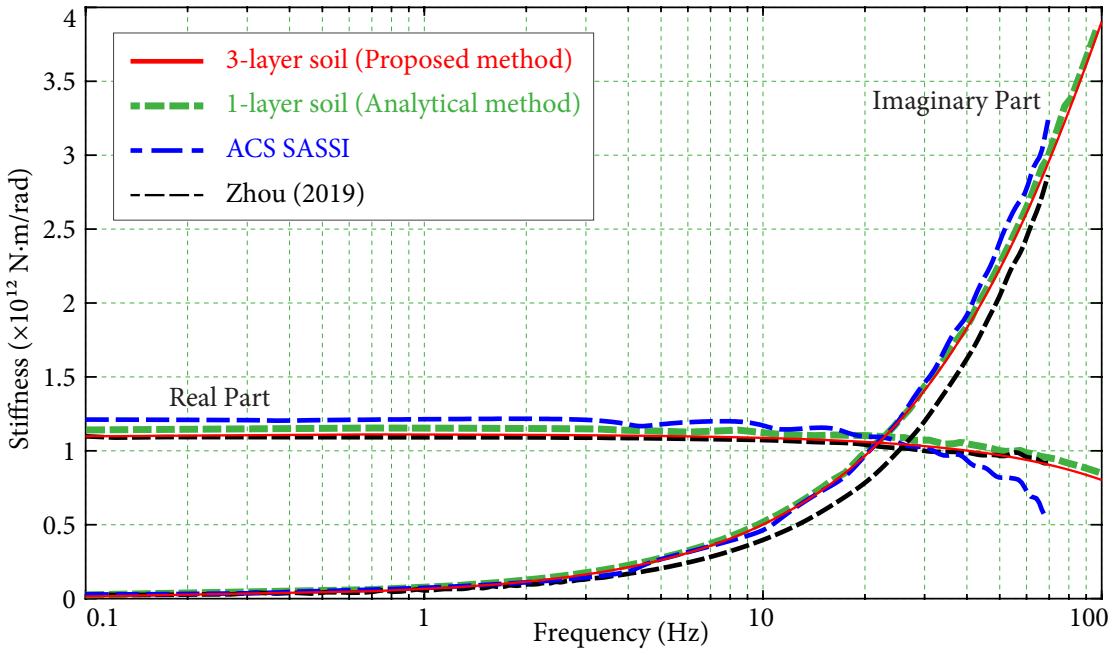


Figure 4.87 Comparison of the dynamic soil stiffness matrices by different approach

4.6 Summary

This chapter systematically explores the derivation, evaluation, and validation of dynamic stiffness matrices, providing a critical foundation for seismic analysis considering SSI.

(1) Theoretical Foundation and Methodology: The chapter begins by rigorously deriving the relationship between dynamic stiffness and dynamic flexibility matrices from basic definitions. Through mathematical proof, it demonstrates that the dynamic stiffness matrix can be obtained by inverting the unitized dynamic flexibility matrix. This theoretical foundation provides a solid mathematical basis for the subsequent numerical methods and establishes a clear procedure for practical applications.

(2) Validation Using Lumped-Mass Systems: For a 3-DOF lumped-mass system, the chapter combines theoretical derivation and numerical calculation to validate the inverse relationship between dynamic stiffness and flexibility matrices. Notably, it introduces a novel approach of applying sinusoidal excitation and analyzing the steady-state response's amplitude and phase lag to calculate the real and imaginary parts of the dynamic response. This method offers a viable numerical approach for dynamic analysis of complex systems.

(3) Extension to Continuous-Mass Systems: The methodology is extended to continuous-mass systems, exemplified by a simply supported beam. By comparing theoretical solutions with numerical simulation results, the chapter further validates the effectiveness of the amplitude and phase lag extraction method. This extension demonstrates the method's applicability and accuracy in handling more complex structural dynamics problems, bridging the gap between simplified models and real-world structures.

(4) Application to 3D Half-Space Soil Models: In a significant step towards practical engineering problems, the chapter applies the developed method to a three-dimensional half-space soil model. By analyzing the variation of dynamic flexibility matrices for nodes along study profiles under different loading directions, and comparing results in specific cases with classical analytical solutions, the chapter verifies the accuracy of the numerical method. This application provides a reliable analytical tool for studying the dynamic stiffness matrices of foundations for the nuclear facilities.

(5) Progressive Validation Approach: The chapter employs a progressive validation strategy, starting from simple systems and gradually moving to more complex ones. This approach not only ensures the reliability of the method at each step but also provides insights into the method's applicability across different levels of complexity in structural systems.

(6) Computational Efficiency: While not explicitly stated, the numerical approach in this chapter potentially offers significant computational advantages over traditional complicated mathematical method, especially for complex soil-structure interaction problems. This efficiency could be crucial for practical applications in the design and analysis of nuclear facilities.

Overall, this chapter establishes a robust and versatile method for evaluating dynamic stiffness matrices across a spectrum of systems, from simple to complex. The method's theoretical rigor, combined with its demonstrated accuracy in numerical applications, makes it a valuable tool for seismic analysis and design of nuclear power plant structures. Particularly in addressing complex soil-structure interaction problems, the approach developed in this chapter provides a promising avenue for enhancing the precision and efficiency of seismic analysis for nuclear facilities. This work lays a solid foundation for future research in the dynamic analysis of SMRs.

C H A P T E R 5

Generating FRS of Structures under Multi-support Excitations Considering SSI

This chapter focuses on generating FRS for containment structures in NPPs subjected to multiple earthquake excitations, while accounting for SSI effects. The structures are assumed to be supported on a flexible foundation overlying layered soil. The dynamic interaction between the structure and the soil is explicitly considered to enable an accurate representation of the system's seismic response. The chapter begins by evaluating dynamic soil stiffness matrix of the underlying soil, then generating FRS for a reactor building model with multiple supports. A parametric study is then conducted to investigate the influence of soil and structural stiffness on the FRS.

5.1 Model of Structure

The reactor building consists of a cylindrical containment and an internal structure, both of which are supported by a circular base slab (radius 19.8m and thickness 3 m), as illustrated in Figure 5.1. The superstructure of the finite element model of the reactor building is modelled as a lumped-parameter system, which can characterize the most significant

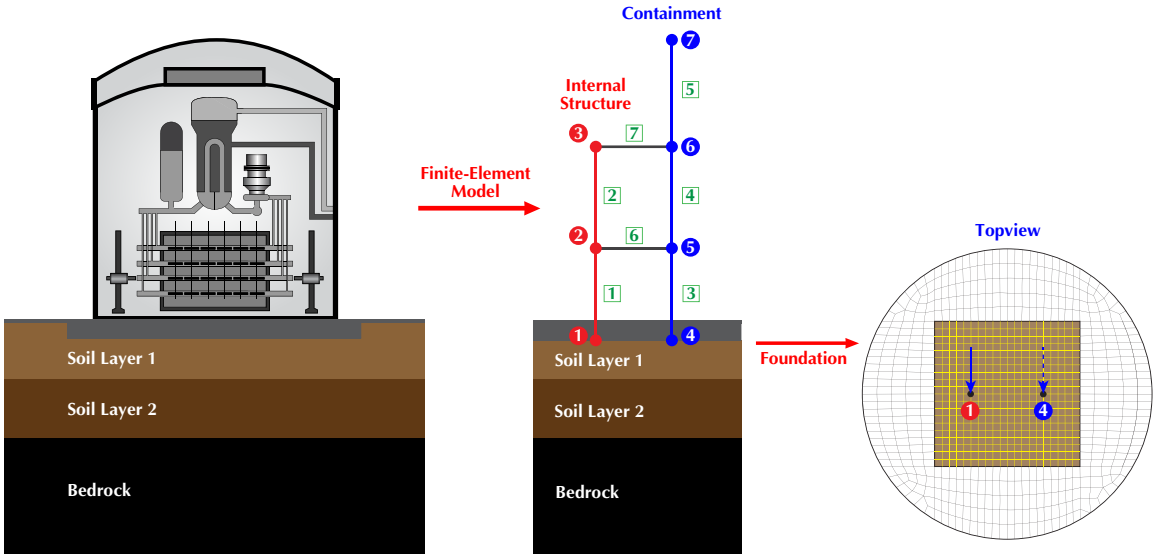


Figure 5.1 Sketch of structure and soil model for generating FRS

dynamic properties of the structure. The building is represented as a MDOF lumped-mass system:

- Nodes ①∼③ represent the internal structure.
- Nodes ④∼⑦ represent the containment.
- The internal structure and the containment connect to the foundation at Nodes ① and ④, respectively.
- Beam elements 1∼2 link internal structure masses.
- Beam elements 3∼5 link containment masses.
- The internal structure and the containment are coupled through coupling elements 6 and 7.

The finite element model information is described in Tables 5.1 and 5.2. A modal analysis is performed for the flexible-base reactor building model. Basic modal information, including natural frequencies of the internal structure, the containment, and the total system are analyzed. Modal information of the significant modes at each node are listed in Table 5.3, and the modal damping ratio of the structure is 5%.

Table 5.1 Nodal information of reactor building model

Node	Elevation (m)	Mass ($\times 10^6$ kg)	Moment of Inertia ($\times 10^6\,\mathrm{kg}\cdot\mathrm{m}^2$)	
			$I_{xx} = I_{yy}$	I_{zz}
1	-5	20	20000	20000
2	15	12	12000	12000
3	35	5.5	550	550
4	-5	20	20000	20000
5	15	5	500	5000
6	35	5	500	5000
7	55	6	600	6000

Table 5.2 Beam Element Properties of reactor building model

Beam Section	Area (m^2)	Shear Area (m^2)	Second Area Moment (m^4)
1	150	8800	15000
2	150	8800	15000
3	100	16000	16000
4	100	16000	16000
5	100	16000	16000
6	5	30	100
7	5	30	100

Table 5.3 Natural frequencies of reactor building model

Mode	Internal Structure	Containment	The System
1	5.52	4.44	4.60
2	5.52	4.44	4.84
3	5.79	5.09	5.12
4	12.66	14.30	5.76
5	12.66	14.30	5.94
6	18.83	14.36	7.37
7	18.83	14.40	12.78
8	21.14	20.55	13.16
9	24.57	24.27	14.37
10	34.05	24.27	14.51
11	34.05	29.32	14.56
12	41.72	29.32	16.72
13		40.62	18.94
14		54.70	19.52
15		54.70	20.57
16		58.12	21.28
17		74.28	24.42
18		74.28	24.75
19			25.69
20			29.35
21			29.46
22			34.13
23			34.25
24			40.70
25			41.79
26			54.74
27			54.77
28			58.18
29			74.32
30			74.34

Table 5.4 Properties of soils for each layer

Layer	V_s / m/s	ζ	H /m	ν	γ /kN/m^3
Soil Layer 1	2000	1.0%	20	0.3	25.89
Soil Layer 2	2400	1.0%	20	0.3	25.89
Bedrock	2804	0.7%	80	0.3	25.89

5.2 Model of Soil

Modelling and Parameters

In order to compute the soil impedance for SSI analysis, the base slab, which considered as flexible foundation, is discretized into solid elements, and two lumped masses that connects to the base of the superstructure are assigned at the foundation.

The soil medium is modelled as two infinite soil layers resting on a homogeneous bedrock. Each soil layer has a property as listed in Table 5.4. The Young's modulus E for each layer is calculated by

$$E = 2G\,(1+\nu), \qquad G = \rho\, V_s^2. \tag{5.2.1}$$

The Young's modulus for each layer is, $E_1 = 2.74 \times 10^7$ kPa, $E_2 = 3.95 \times 10^7$ kPa, $E_3 = 5.40 \times 10^7$ kPa.

Note that even though there are only three sets of soil properties, it is still necessary to divide the soil into a number of thinner layers, because the thickness of a layer should not exceed one-fifth of the wave length. The finite element model of the underlying soil system is modelled in ANSYS and presented in Figure 5.2. The soil model is discretized using a graded mesh. The mesh is refined in the central region of interest, where the soil-structure interaction is most significantly affected. This finer mesh allows for a more accurate capture of the stress and displacement gradients near the structure. Away from the structure, the mesh gradually becomes coarser to reduce computational expense without significantly compromising accuracy. The mesh comprises 38766 nodes and 35711 elements.

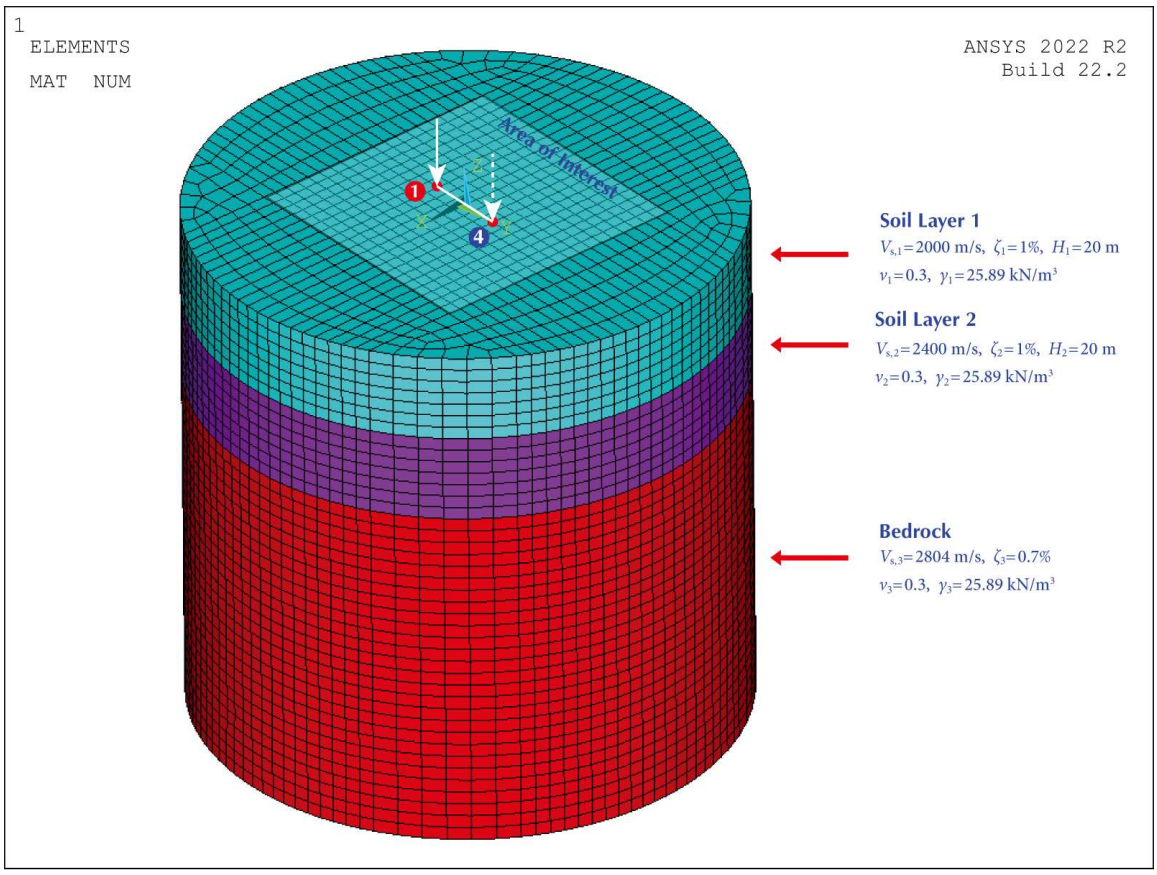


Figure 5.2 Numerical model for generating dynamic soil stiffness matrix

Dynamic Response of Nodes

To determine the dynamic response of the soil model, dynamic sinusoidal forces are applied at Node 1 and Node 4 separately, and the resulting displacements at both nodes in the $x-$, $y-$, and $z-$ directions are calculated. When a unit force is applied at Node 1, the amplitudes and phase lags of the displacements at Node 1 and Node 4 are computed, as illustrated from Figure C.1 to C.18. Similarly, when a unit force is applied at Node 4, the amplitudes and phase lags of the displacements at Node 1 and Node 4 are determined, as shown from Figure C.19 to C.36.

The real and imaginary parts of the displacements are thus calculated through the amplitudes and phase lags in the corresponding conditions. The real and imaginary parts for the load applied at Node 1 are shown from Figure 5.3 to 5.20, and Figure 5.21 to 5.38 show

the real and imaginary parts for the load applied at Node 4. The result can be an input as dynamic soil stiffness matrix for generating FRS of structures considering SSI.

5.3 Foundation Input Response Spectra (FIRS)

For the purpose of illustration, USNRC R.G. 1.60 response spectra (USNRC, 2014) are assumed as the FIRS obtained from a site response analysis. The PGA are anchored at $0.3g$ and $0.2g$ for the horizontal and vertical directions, respectively. 30 sets of tridirectional compatible time-histories generated in Section 3.4 are used for performing time-history analyses to provide the benchmark FRS. To further investigate the impact of seismic excitation characteristics on the response of the structure, two distinct FIRS input cases are considered: (1) fully correlated seismic excitations, and (2) fully independent seismic excitations, at the supports of Nodes 1 and 4. These cases represent the extreme scenarios of spatial variability in the seismic input motion.

Case of Fully Correlated Excitation

When the supports of a structure are closely spaced, the seismic excitations at these locations may be highly correlated due to their proximity. In such cases, it is reasonable to assume that the input motions are essentially identical, particularly for structures with small footprints. In this case, the input time histories at the two supports, i.e., Nodes 1 and 4, are identical in both the horizontal directions and vertical direction, as illustrated in Figure 5.39-(a).

Case of Fully Independent Excitation

The assumption of fully independent support excitations is relevant for certain situations in nuclear power plants. For instance, consider a main steam line that is supported at multiple locations, some on the reactor building and others on adjacent structures. In this case, the seismic input motions at the supports may be significantly different due to the spatial variability of the ground motion and the distinct dynamic characteristics of the supporting structures. In this case, the input time histories in the direction of two supports, i.e., Nodes 1 and 4, are totally distinct in their horizontal directions and vertical direction, as illustrated in Figure 5.39-(b).

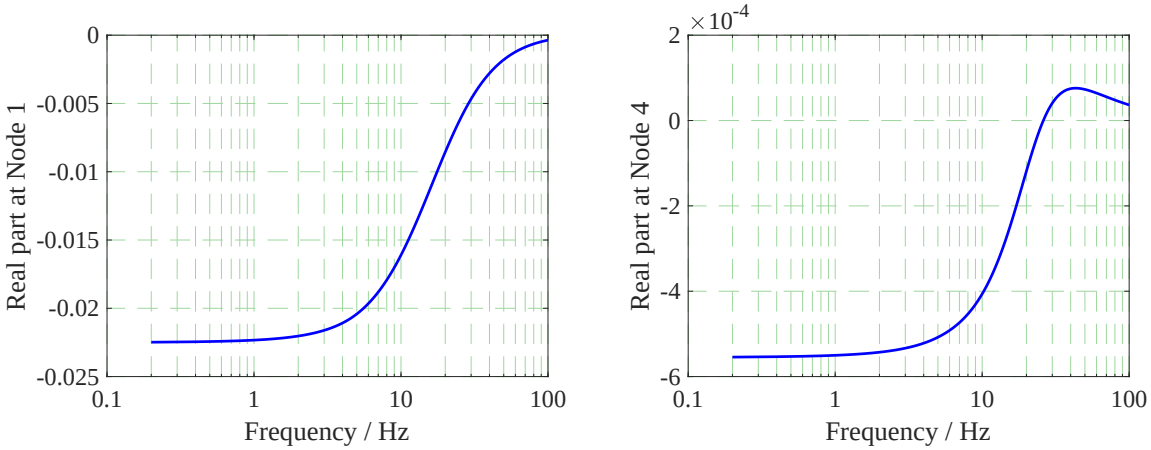


Figure 5.3 Real part in X direction under harmonic load at Node 1 in X direction

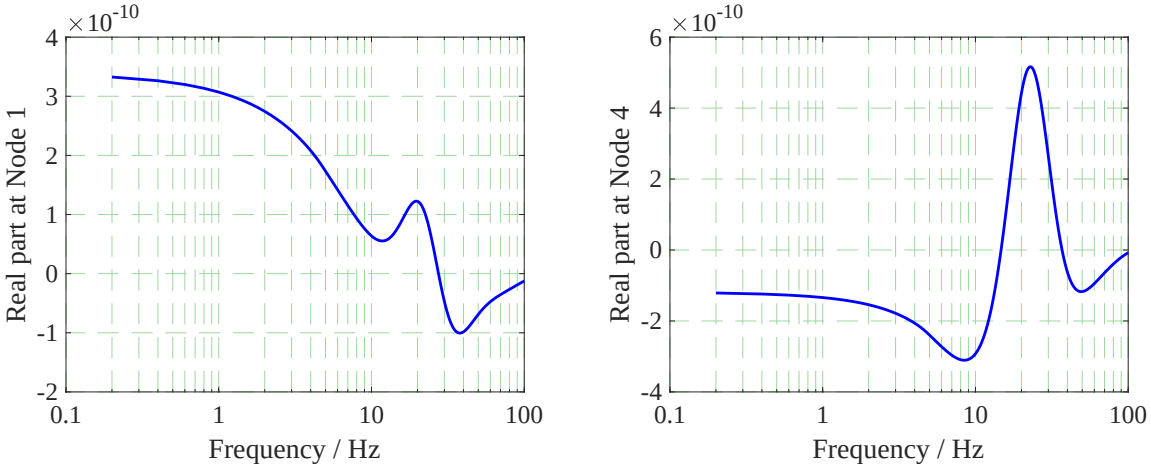


Figure 5.4 Real part in Y direction under harmonic load at Node 1 in X direction

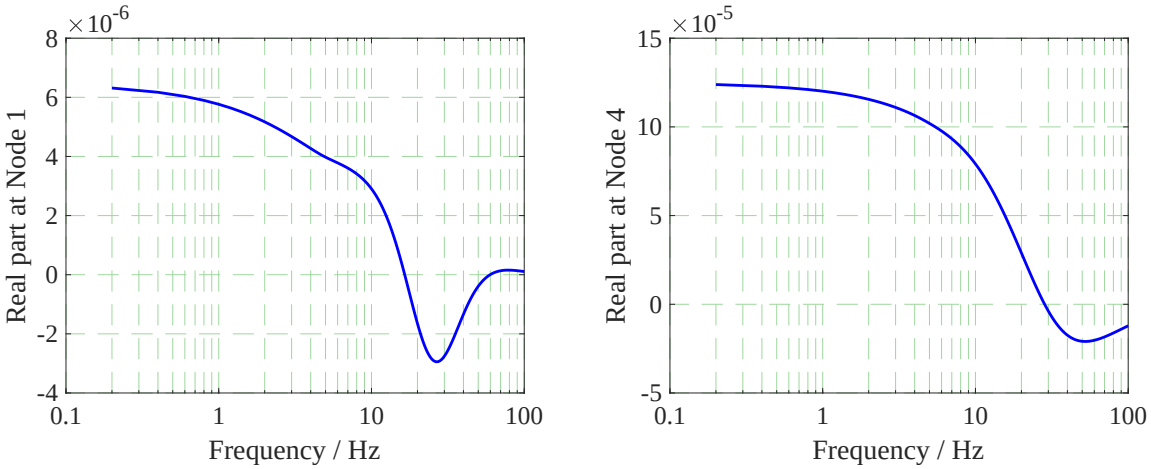


Figure 5.5 Real part in Z direction under harmonic load at Node 1 in X direction

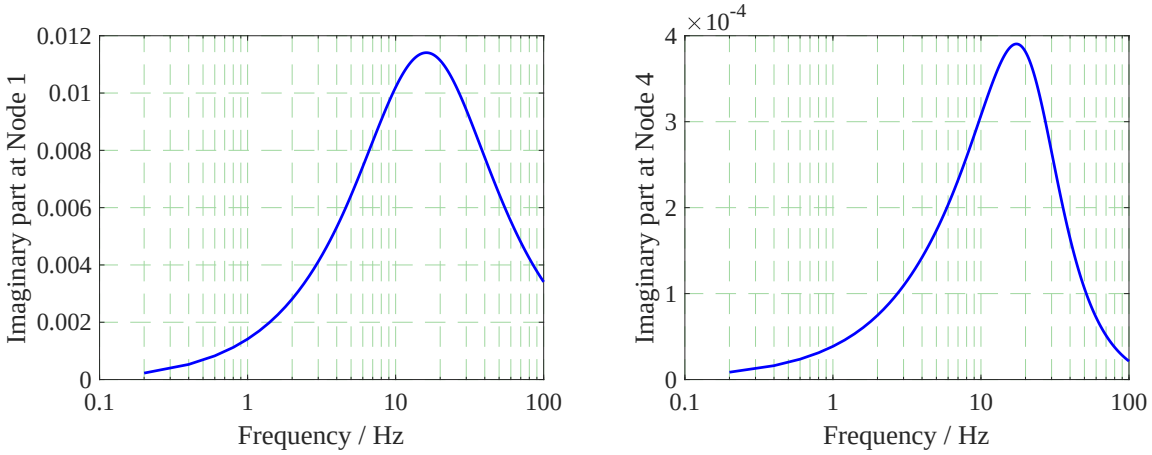


Figure 5.6 Imaginary part in X direction under harmonic load at Node 1 in X direction

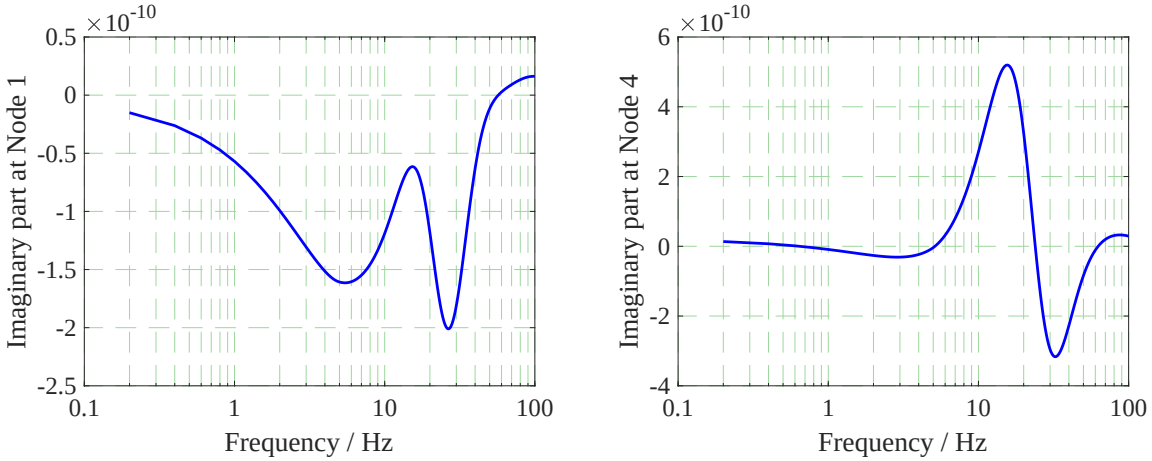


Figure 5.7 Imaginary part in Y direction under harmonic load at Node 1 in X direction

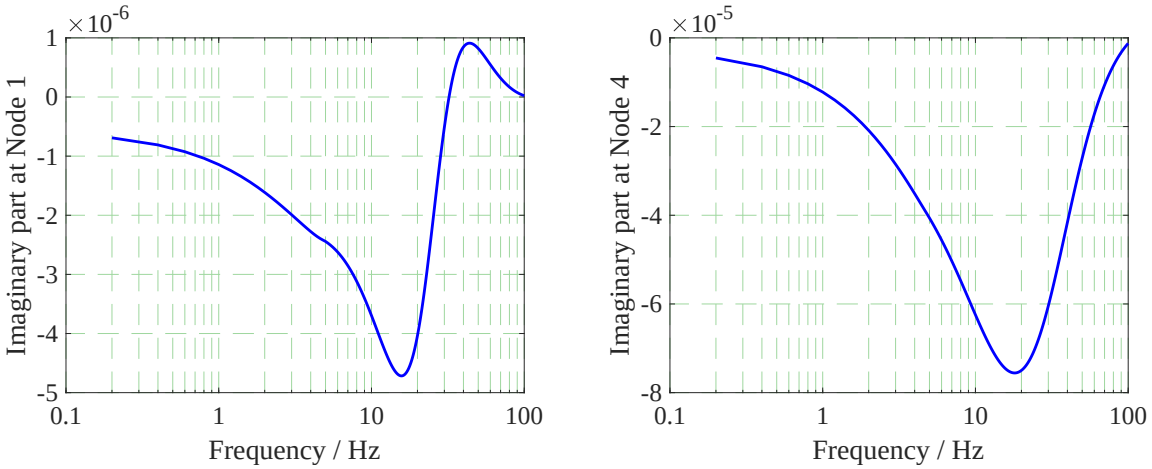


Figure 5.8 Imaginary part in Z direction under harmonic load at Node 1 in X direction

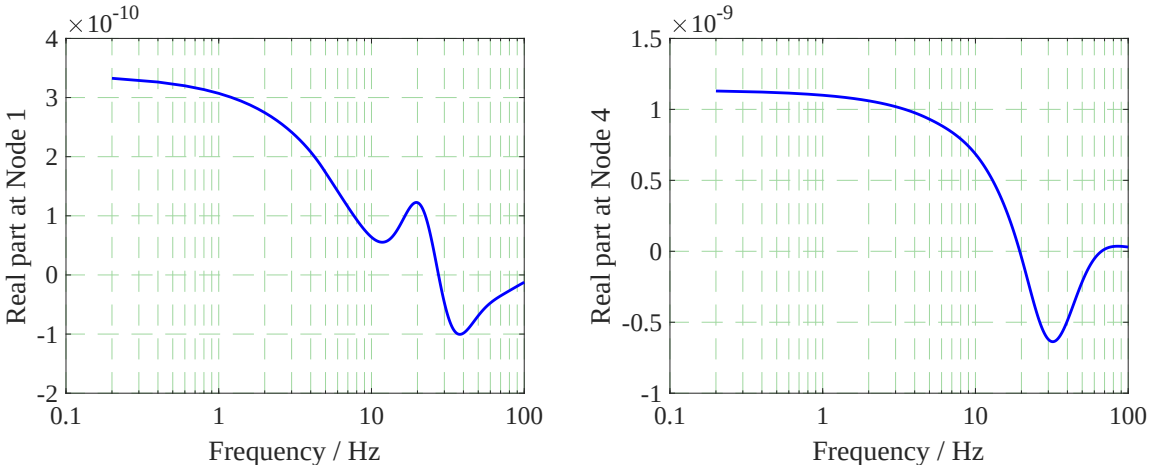


Figure 5.9 Real part in X direction under harmonic load at Node 1 in Y direction

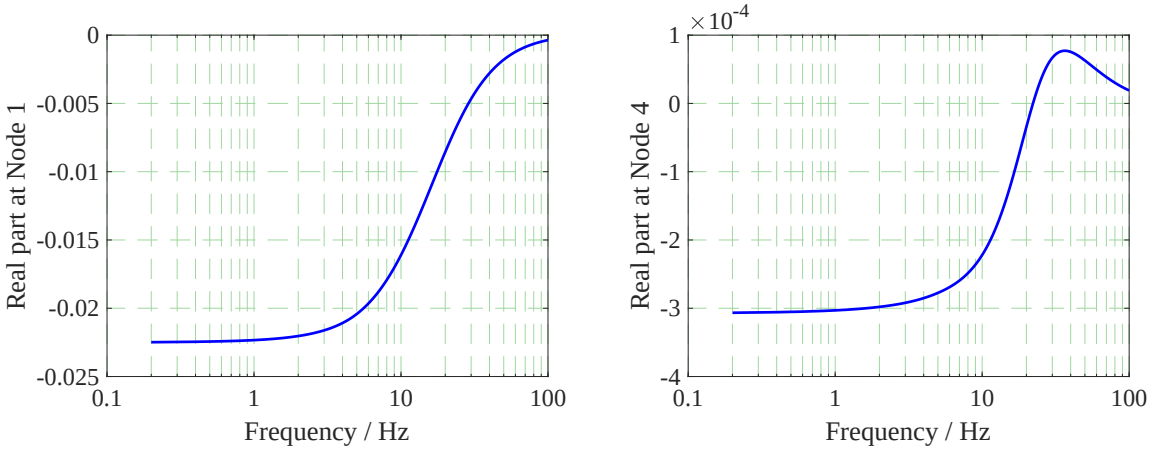


Figure 5.10 Real part in Y direction under harmonic load at Node 1 in Y direction

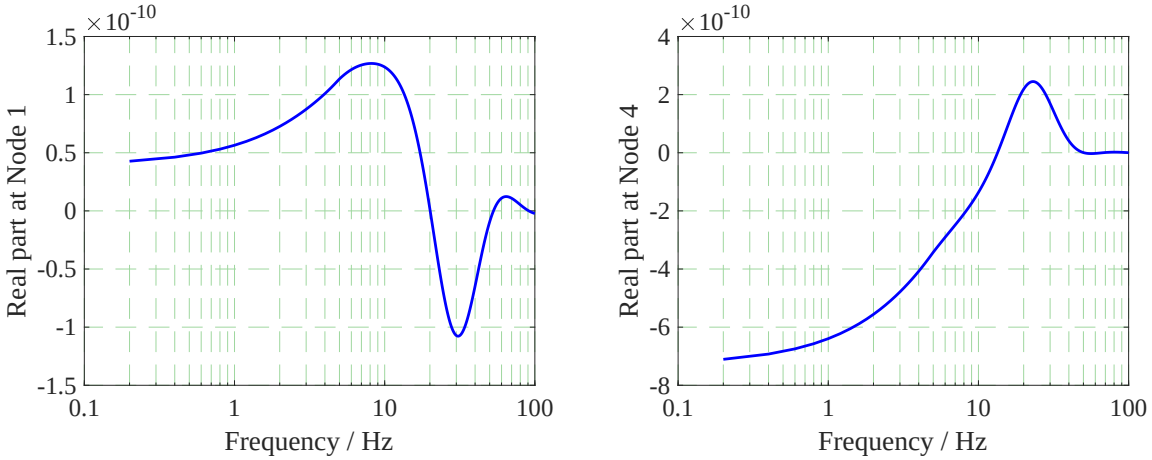


Figure 5.11 Real part in Z direction under harmonic load at Node 1 in Y direction

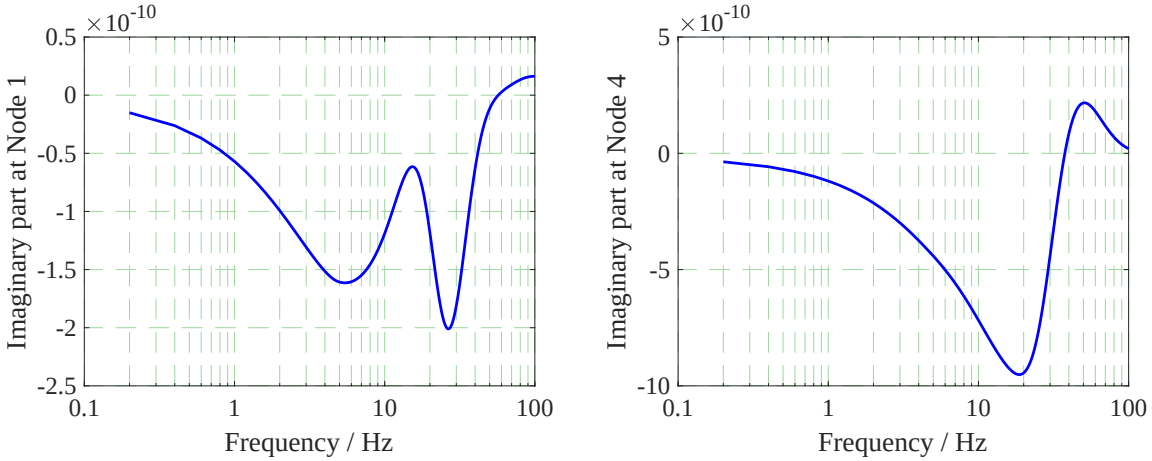


Figure 5.12 Imaginary part in X direction under harmonic load at Node 1 in Y direction

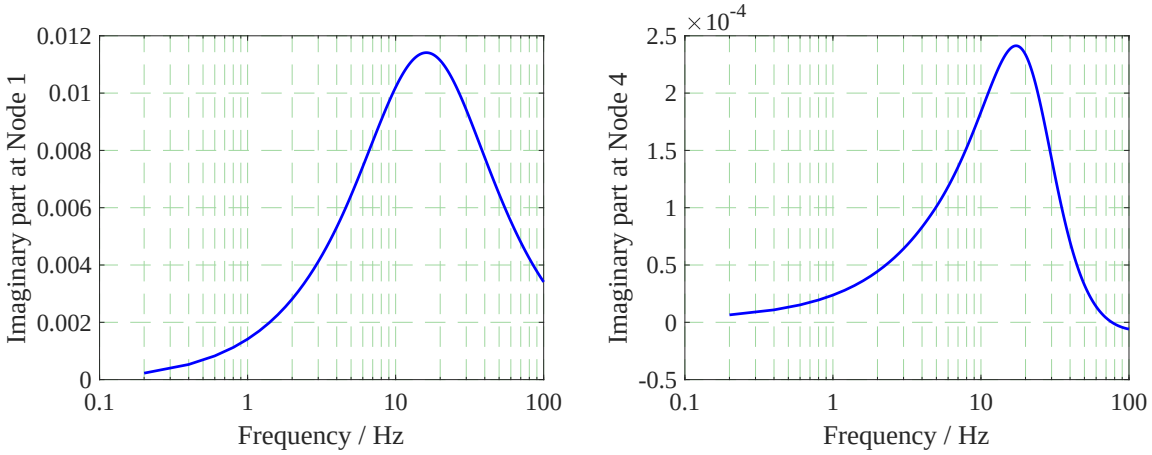


Figure 5.13 Imaginary part in Y direction under harmonic load at Node 1 in Y direction

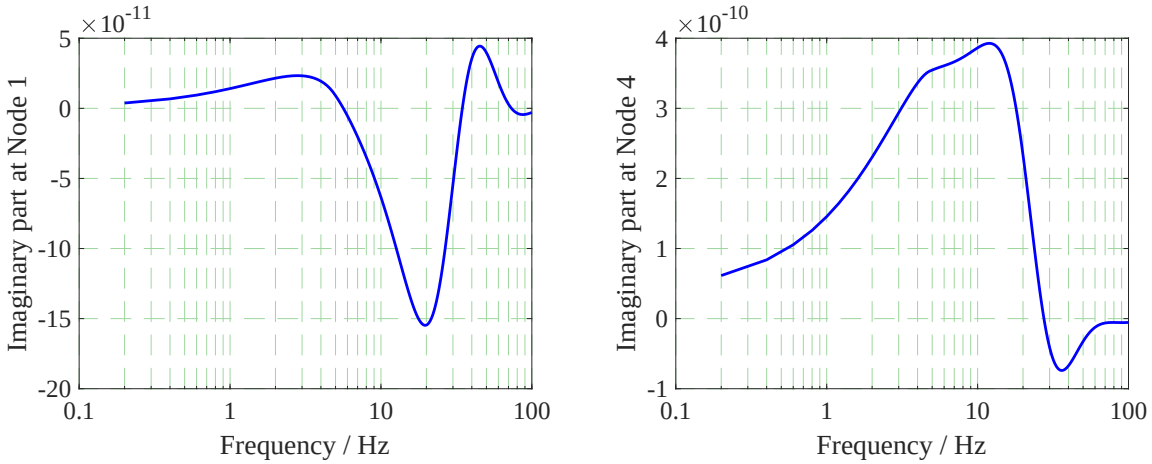


Figure 5.14 Imaginary part in Z direction under harmonic load at Node 1 in Y direction

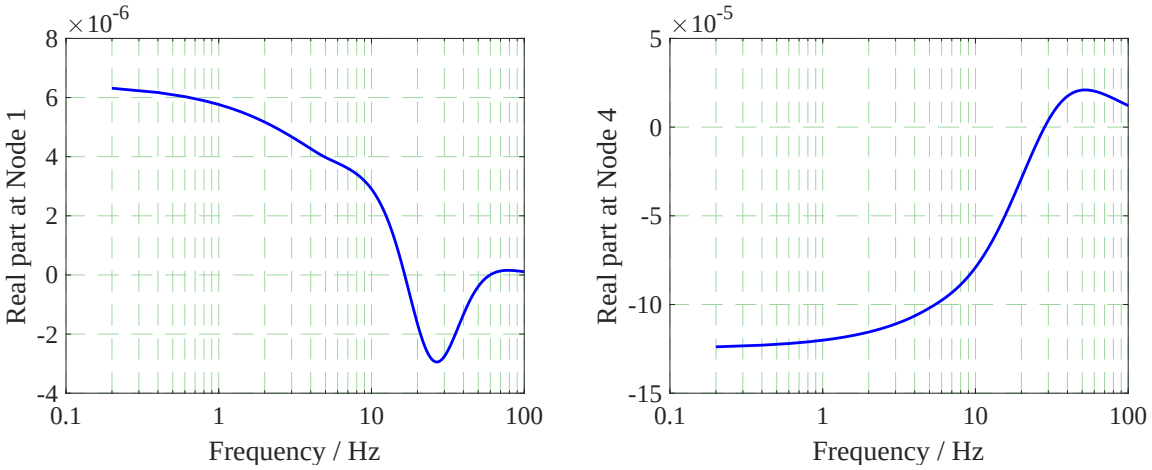


Figure 5.15 Real part in X direction under harmonic load at Node 1 in Z direction

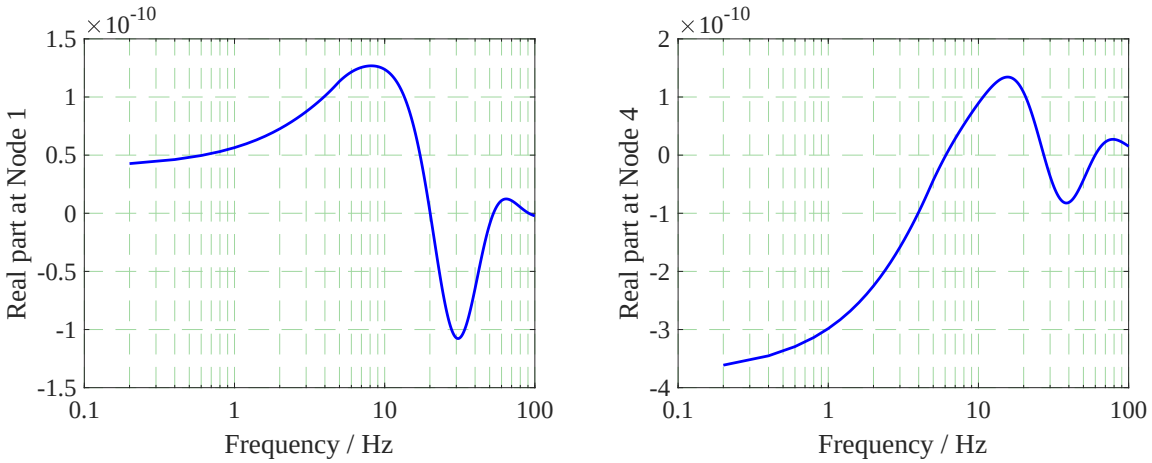


Figure 5.16 Real part in Y direction under harmonic load at Node 1 in Z direction

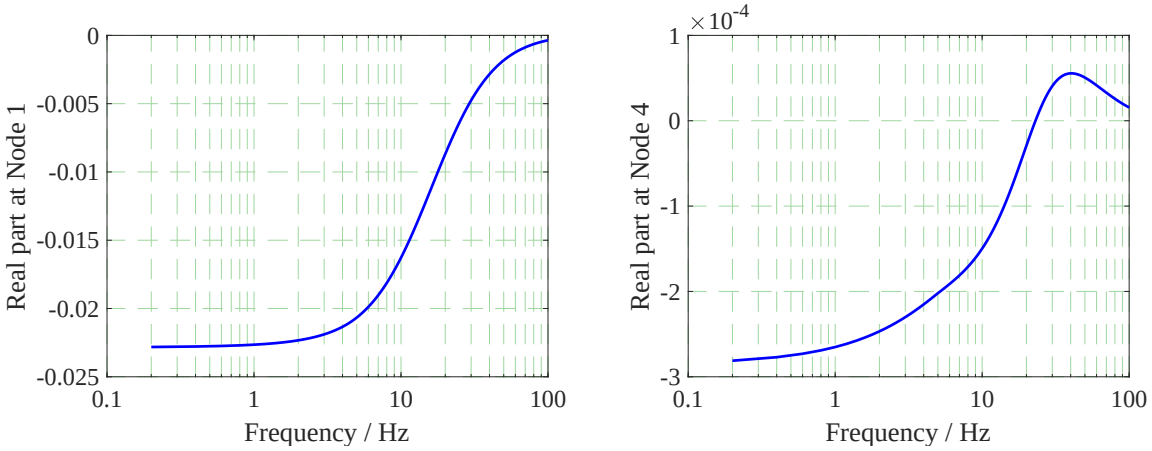


Figure 5.17 Real part in Z direction under harmonic load at Node 1 in Z direction

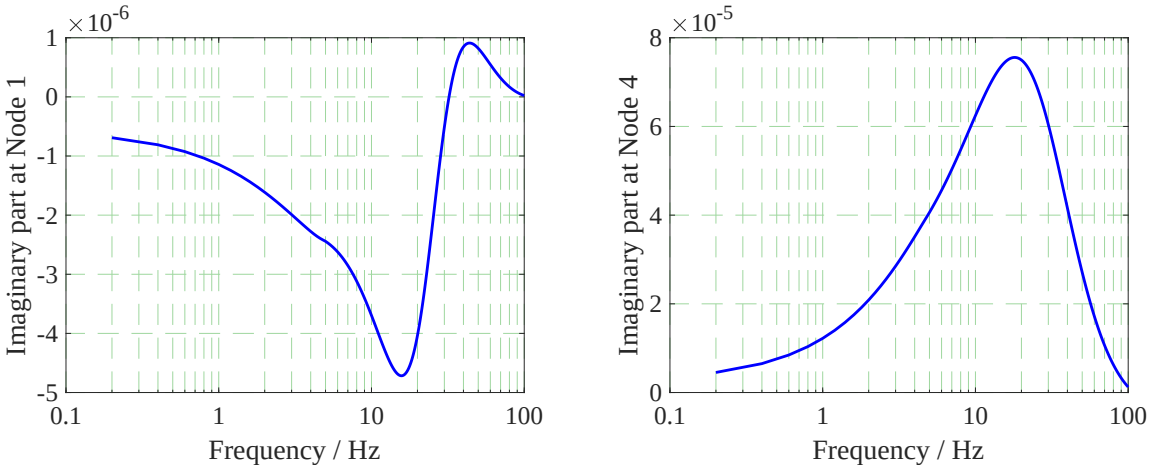


Figure 5.18 Imaginary part in X direction under harmonic load at Node 1 in Z direction

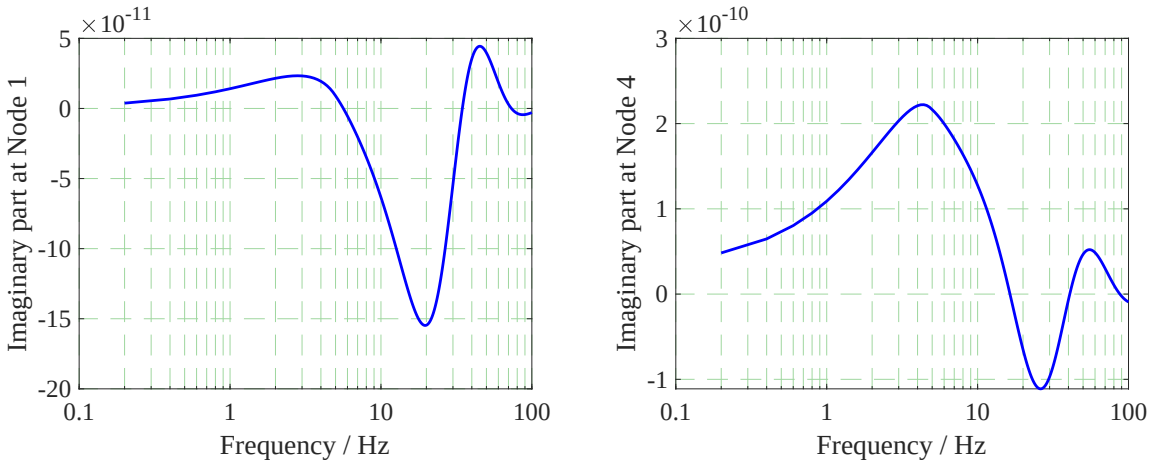


Figure 5.19 Imaginary part in Y direction under harmonic load at Node 1 in Z direction

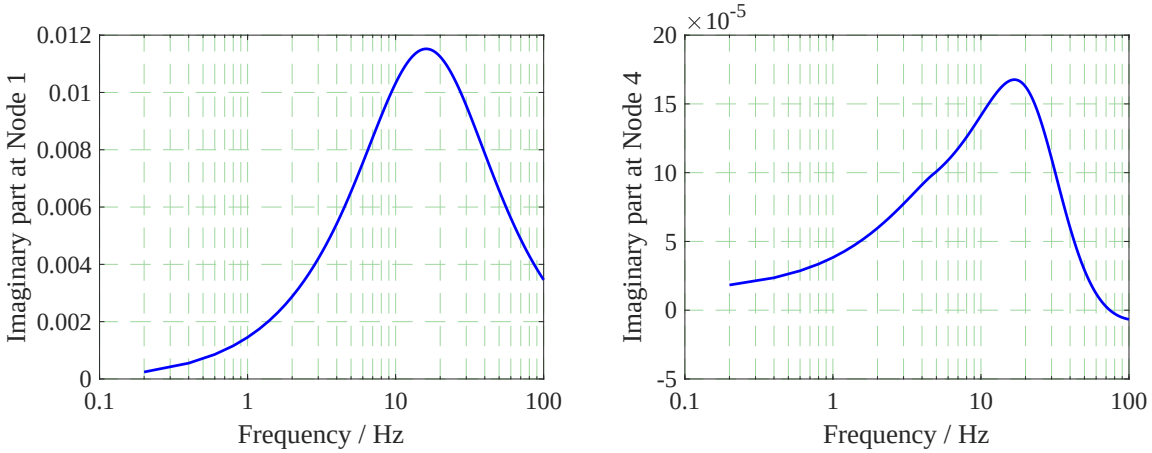


Figure 5.20 Imaginary part in Z direction under harmonic load at Node 1 in Z direction

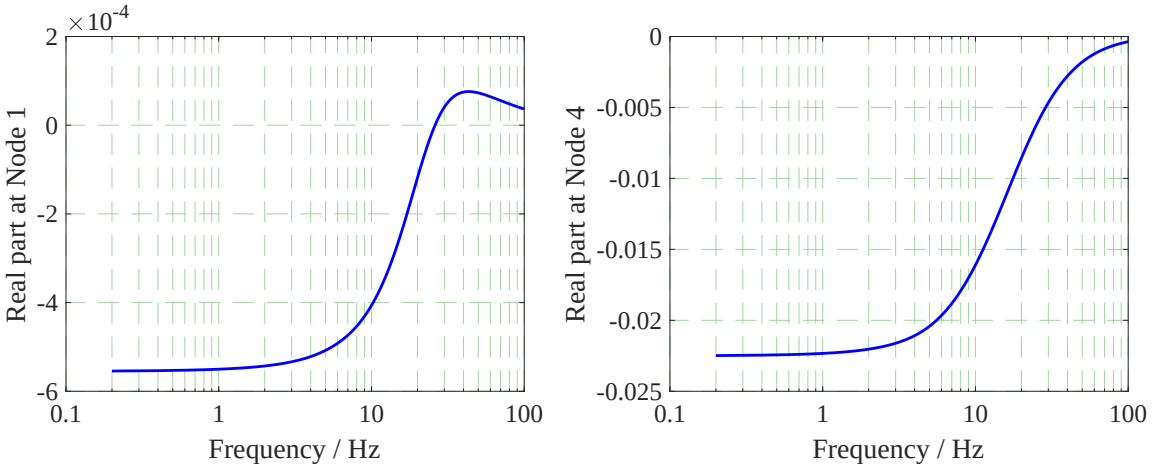


Figure 5.21 Real part in X direction under harmonic load at Node 4 in X direction

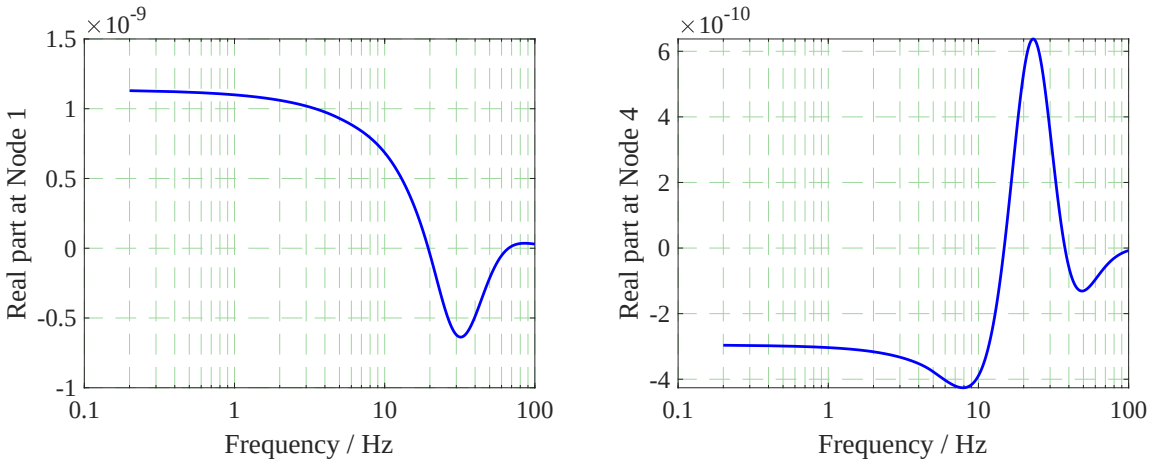


Figure 5.22 Real part in Y direction under harmonic load at Node 4 in X direction

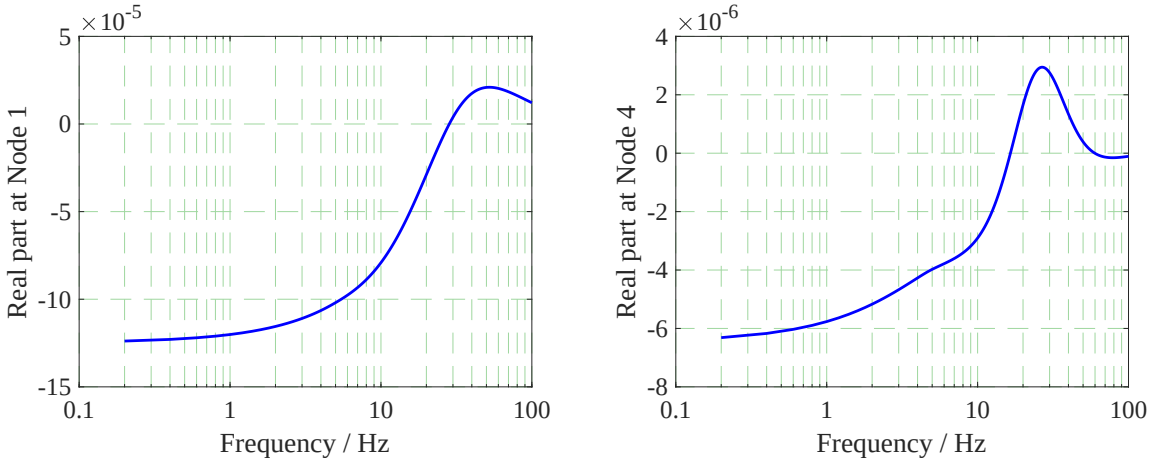


Figure 5.23 Real part in Z direction under harmonic load at Node 4 in X direction

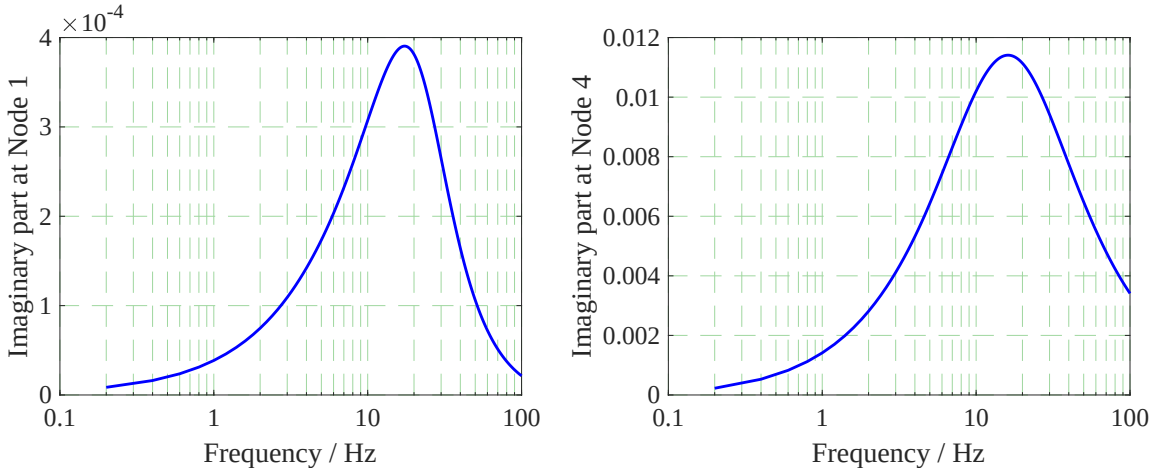


Figure 5.24 Imaginary part in X direction under harmonic load at Node 4 in X direction

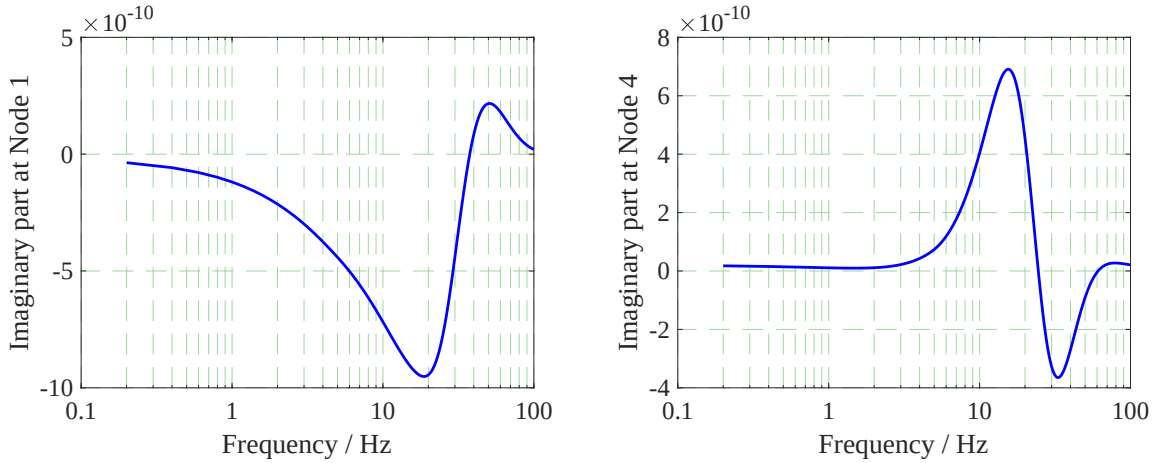


Figure 5.25 Imaginary part in Y direction under harmonic load at Node 4 in X direction

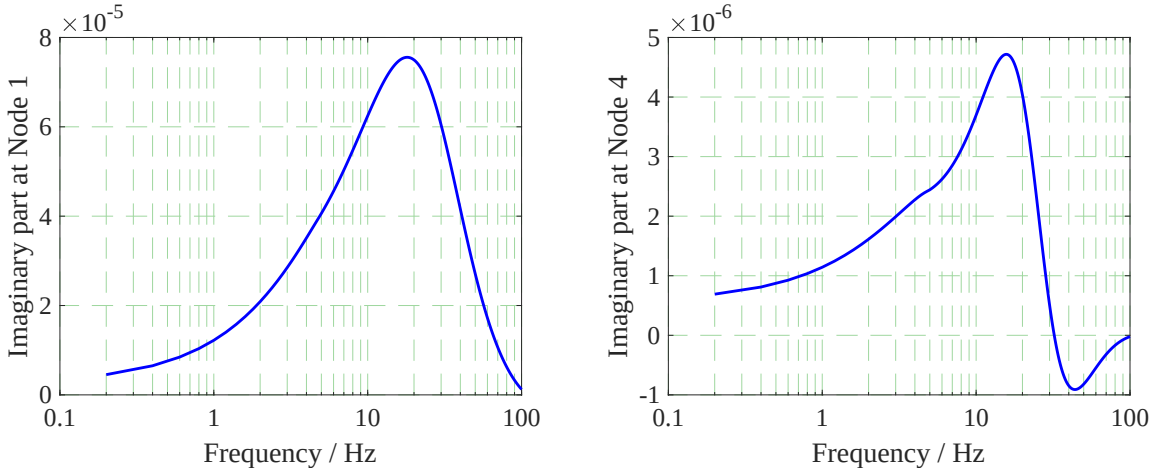


Figure 5.26 Imaginary part in Z direction under harmonic load at Node 4 in X direction

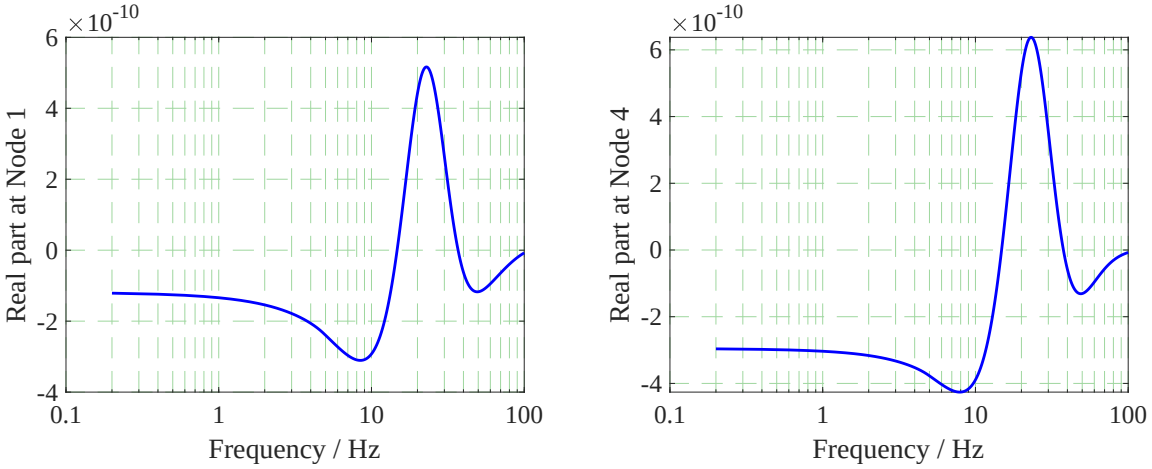


Figure 5.27 Real part in X direction under harmonic load at Node 4 in Y direction

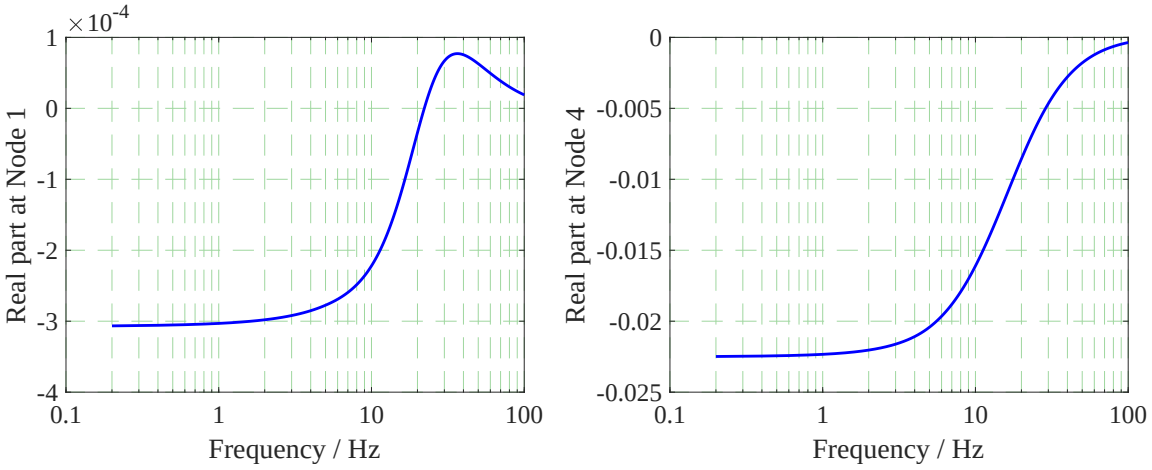


Figure 5.28 Real part in Y direction under harmonic load at Node 4 in Y direction

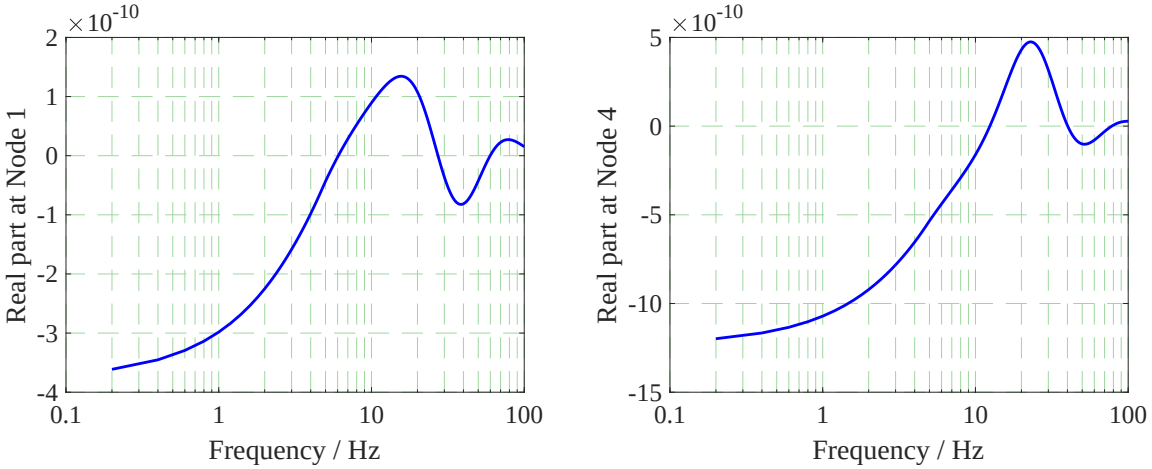


Figure 5.29 Real part in Z direction under harmonic load at Node 4 in Y direction

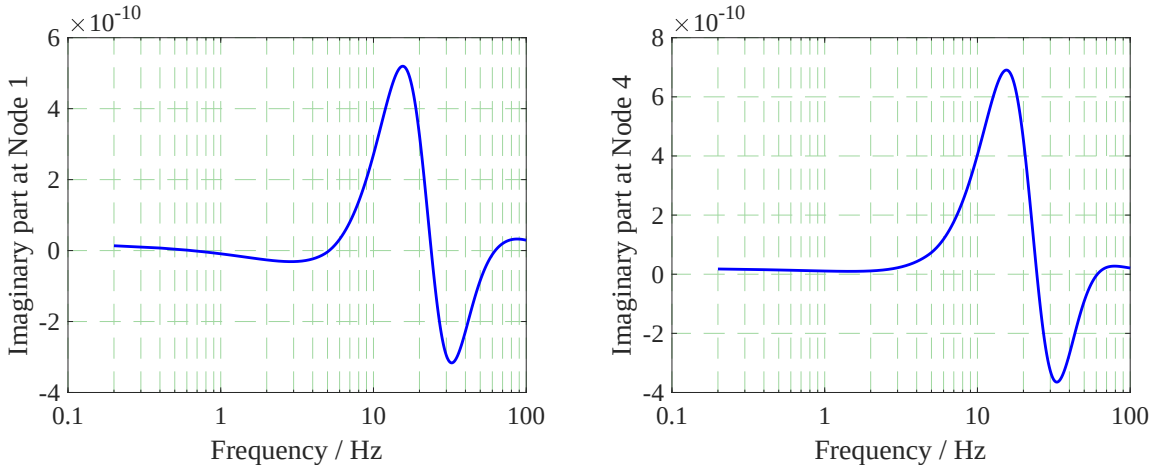


Figure 5.30 Imaginary part in X direction under harmonic load at Node 4 in Y direction

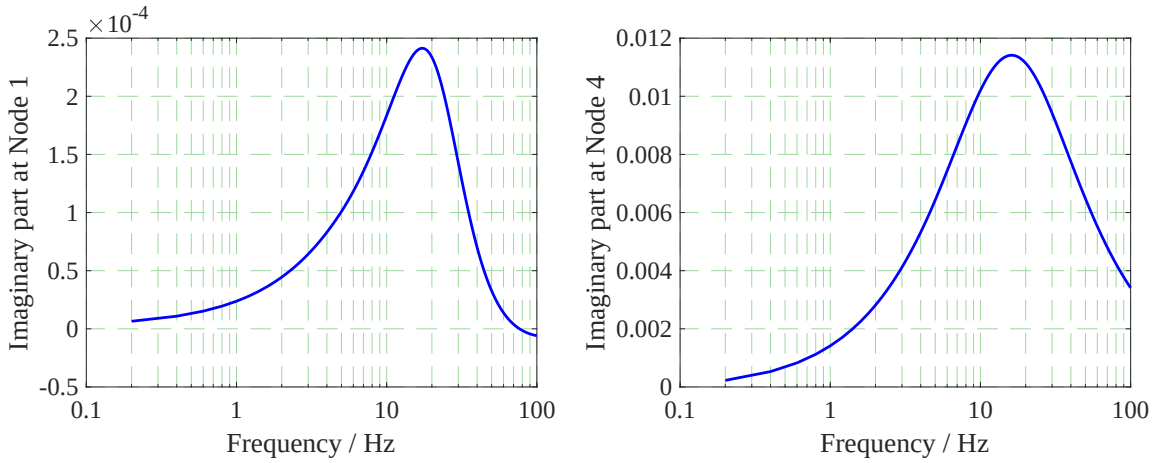


Figure 5.31 Imaginary part in Y direction under harmonic load at Node 4 in Y direction

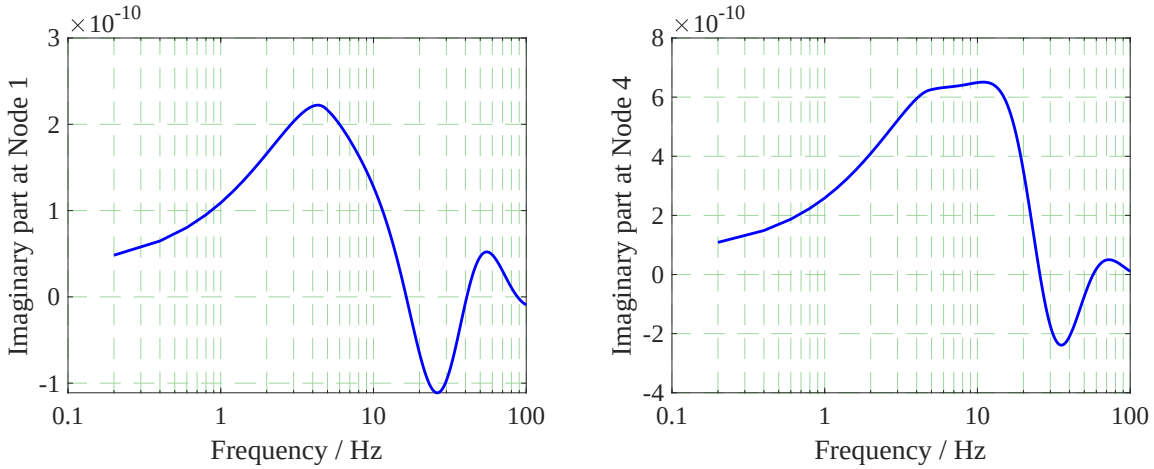


Figure 5.32 Imaginary part in Z direction under harmonic load at Node 4 in Y direction

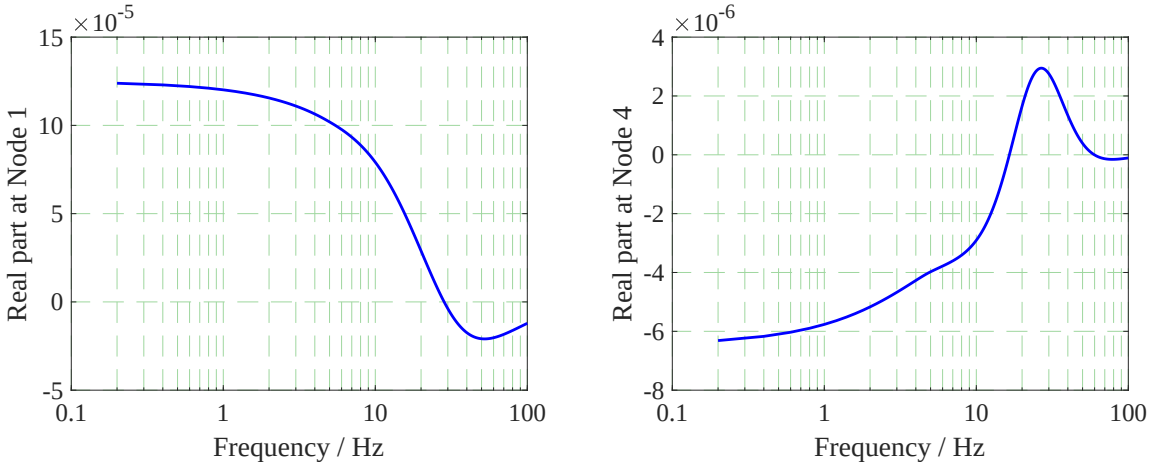


Figure 5.33 Real part in X direction under harmonic load at Node 4 in Z direction

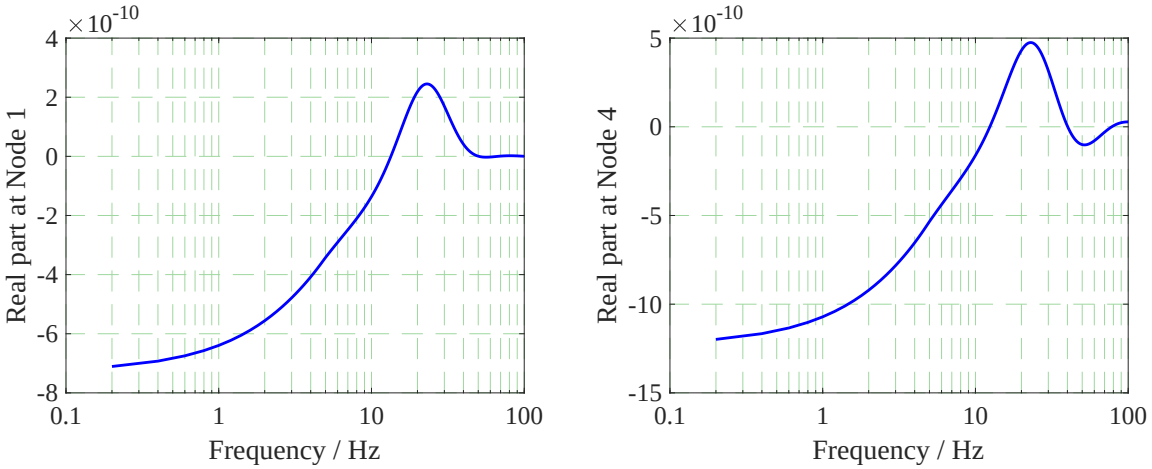


Figure 5.34 Real part in Y direction under harmonic load at Node 4 in Z direction

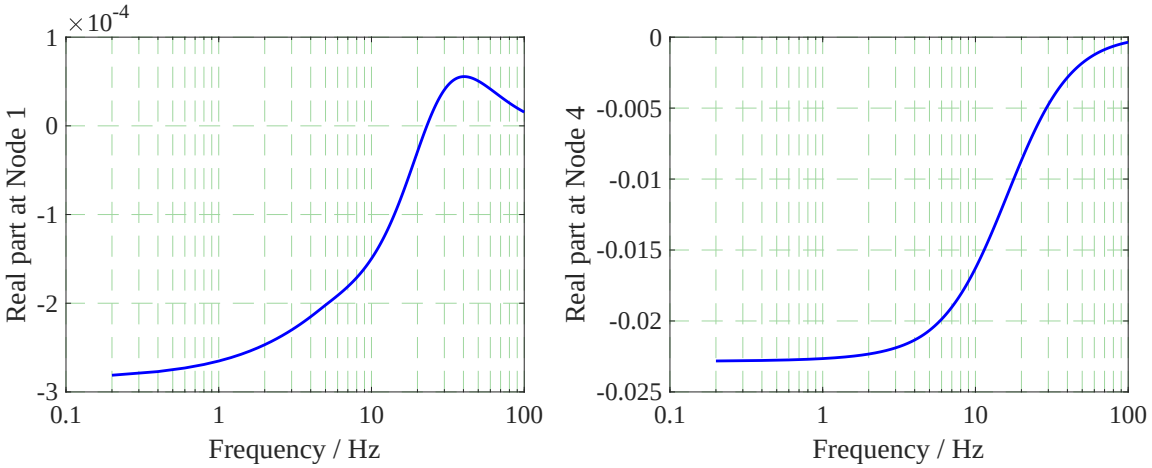


Figure 5.35 Real part in Z direction under harmonic load at Node 4 in Z direction

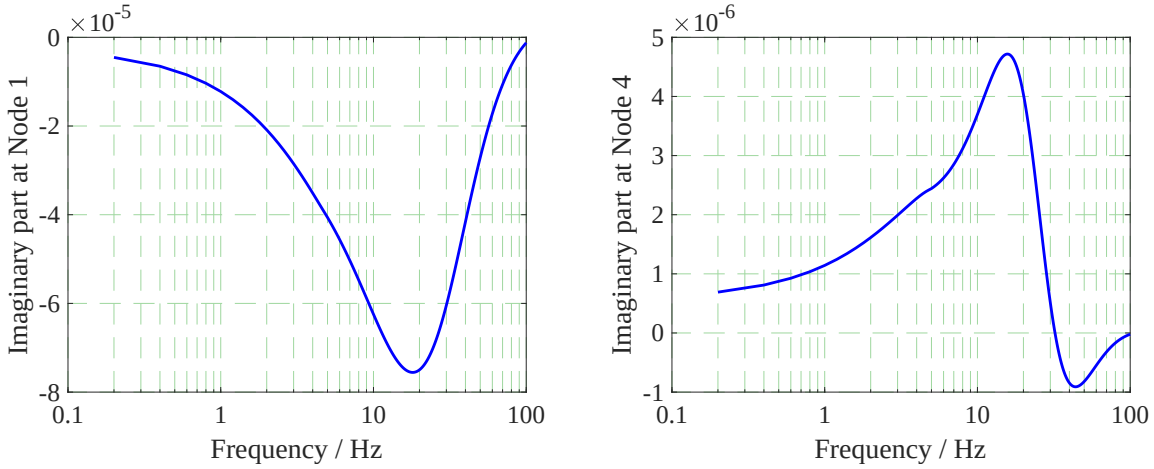


Figure 5.36 Imaginary part in X direction under harmonic load at Node 4 in Z direction

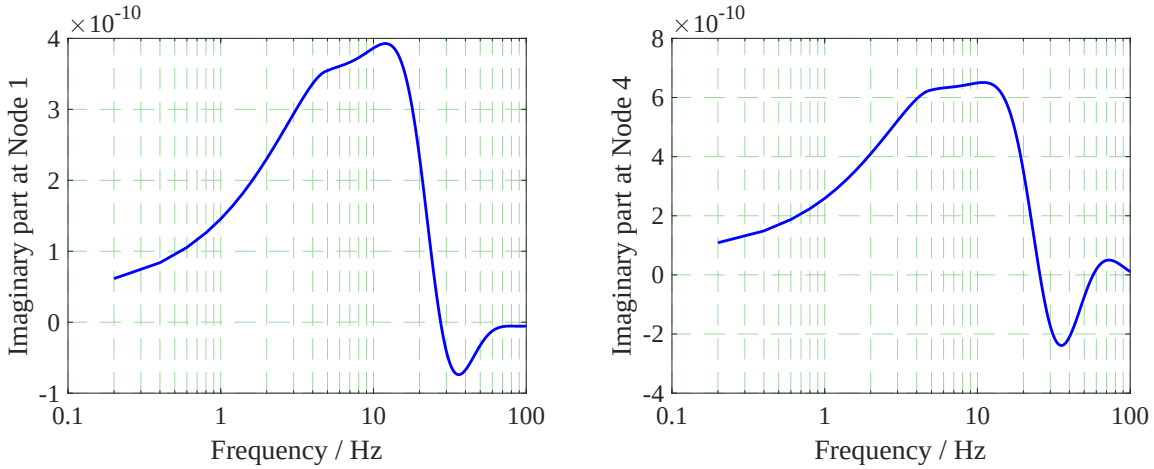


Figure 5.37 Imaginary part in Y direction under harmonic load at Node 4 in Z direction

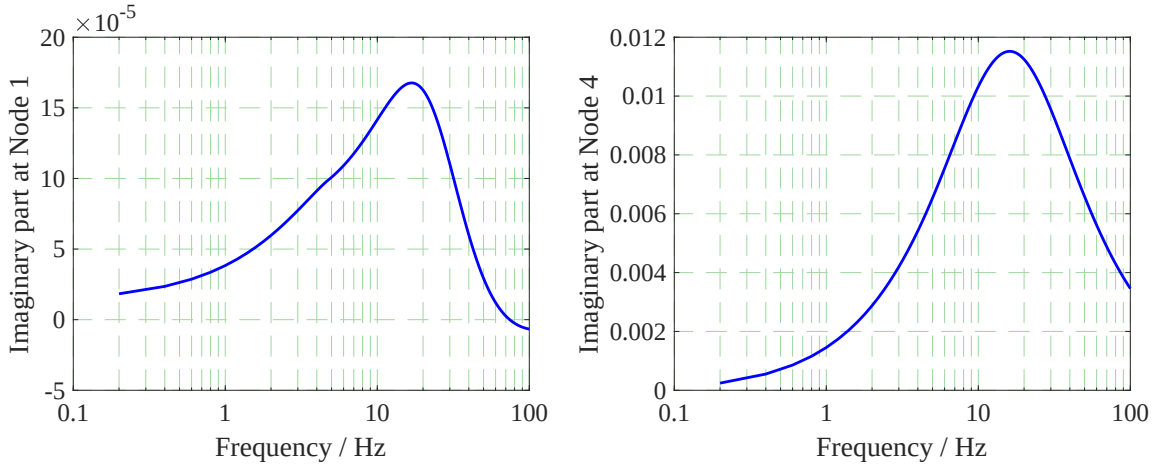


Figure 5.38 Imaginary part in Z direction under harmonic load at Node 4 in Z direction

5.4 Development of Floor Response Spectra (FRS)

5.4.1 Dynamic Influence Matrix

Following Step 4 in the procedure in Section 2.2.4, the mass matrix and earthquake influence matrix can be readily determined from the information in Table 5.3. The dimensionless transfer matrix of the $\mathbf{S}^{\mathrm{MS}}$ is calculated for different values of ω, varying from 0.2π to 200π, with an increment of 0.1. Each element in matrix $\mathbf{S}^{\mathrm{MS}}$ is complex and can be regarded as a transfer function. The modulus of the elements corresponding to the translational DOF versus frequency are plotted in Figure 5.40 for all the structural nodes. It can be observed that the modulus of the transfer functions peak at the frequencies of the significant modes.

5.4.2 Case of Fully Correlated Excitation

FLIRS Transfer Matrix and Modification Factor

Similar to dynamic influence matrix $\mathbf{S}^{\mathrm{MS}}$, FLIRS transfer matrix $\mathcal{T}$ and FLIRS modification factor $\mathcal{R}$ are also evaluated for the circular frequency range from 0.2π to 200π, shown in Figures 5.41 and 5.42, respectively. It is found that unlike $\mathbf{S}^{\mathrm{MS}}$, which peaks at the natural frequencies of the decoupled structure, the peaks of $\mathcal{T}$ and $\mathcal{R}$ are located near the natural frequencies of the coupled structural system, whereas two valleys located at the natural frequencies of the superstructure are identified. This is because dynamic influence matrix $\mathbf{S}^{\mathrm{MS}}$ reflects the influence of base motion on superstructure; or in other words, $\mathbf{S}^{\mathrm{MS}}$ is only determined by the structural information of the decoupled structure as can be seen in equation (2.2.11). On the other hand, superstructure as well as soil properties are both considered in obtaining FLIRS transfer matrix $\mathcal{T}$ and FLIRS modification factor $\mathcal{R}$.

The valleys in $\mathcal{T}$ and $\mathcal{R}$ can be interpreted as a result of the absorption of vibration. It means that the soil in a coupled soil-structure system may play the same role as vibration absorber, in which the energy of excitation is absorbed at certain frequencies, i.e., natural frequencies of the decoupled model.

Furthermore, the result of the modification factor given in Figure 5.42 shows that the FIRS is mainly modified within the frequency range 1 Hz to 33 Hz. This is because earthquake excitations with low frequency do not have much influence on seismic vibration

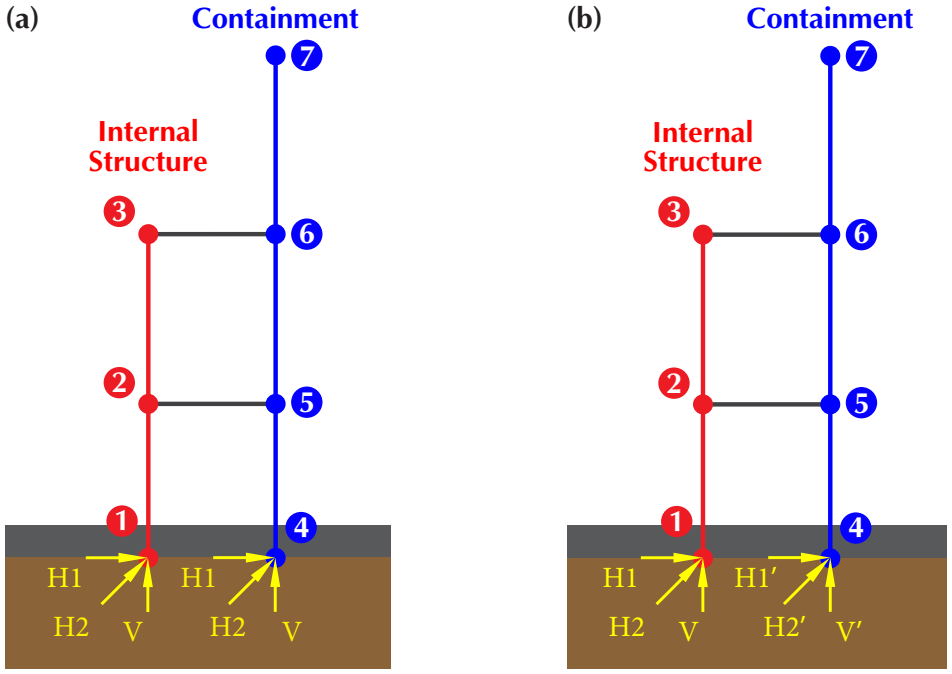


Figure 5.39 Seismic excitation cases of fully correlated and independent

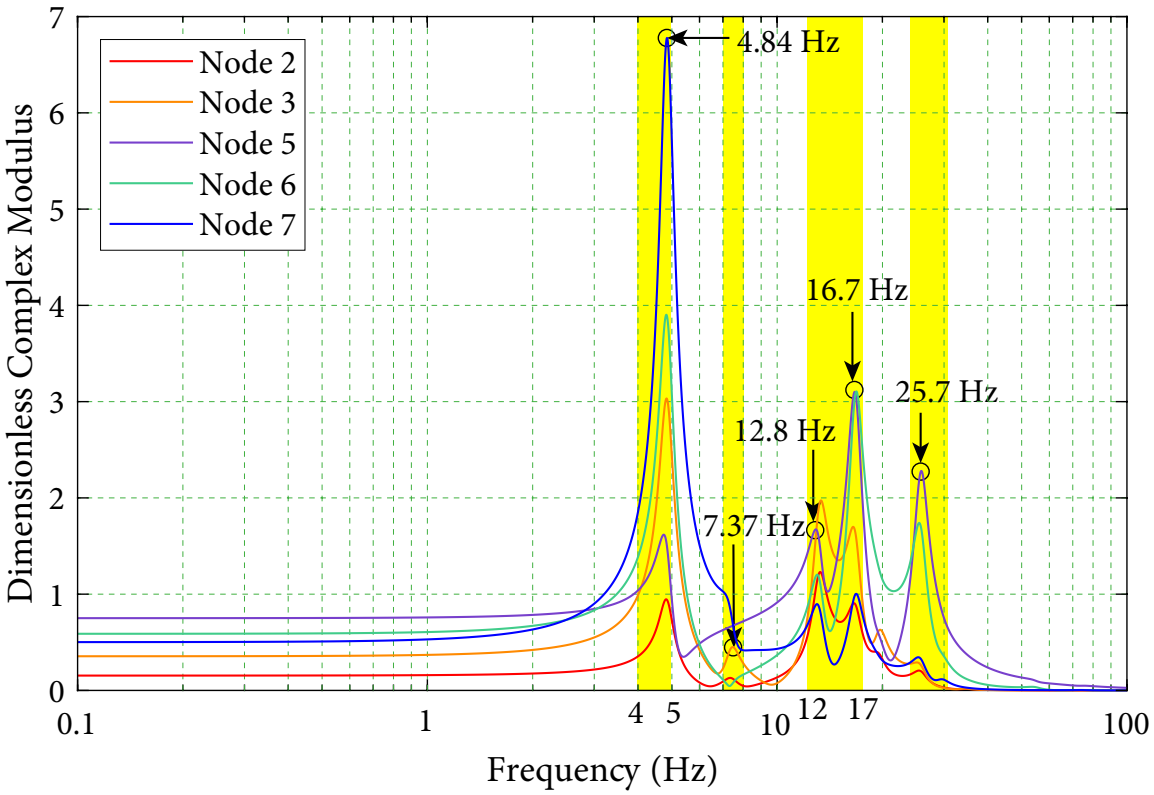


Figure 5.40 Modulus of the dynamic influence matrix for superstructure nodes.

of this system, while a structure can be regarded as rigid when the natural frequencies exceed 33 Hz. Therefore, the modification factor in these frequency ranges is approximately 1. One more observation made from Figure 5.42 suggests that earthquake excitations at the dominant frequencies of either coupled or uncoupled system are changed more significantly comparing with other frequencies when SSI effect is considered. Therefore, one has to pay more attention to the dominant frequencies of both coupled and uncoupled systems in engineering practice.

Development of FLIRS

FLIRS is determined through FIRS by multiplying the modification factor, $\mathcal{R}$. Since the FLIRS is verified to be accurate in Section 3.4.2, it is essential to analyze the FLIRS at both supports of the structure, ensuring a more comprehensive understanding of how the FIRS is modified by the soil-structure interaction in the flexible foundation under the circumstance of fully independent seismic input.

Figure 5.43 shows the tri-directional FLIRS for both supports Nodes 1 and 4. As can be seen from Figure 5.43 that FLIRS generated by the proposed method are modified significantly in the horizontal directions within the frequency range 1 Hz to 33 Hz, while the FLIRS is consistent with the input FIRS in the vertical direction. The modified input FLIRS has a significant valley near the dominant frequency of the superstructure (i.e., frequency range between 3 Hz to 8 Hz). The frequency range is the dominant frequency of the decoupled internal structure and containment, as well as the whole structure system. This suggests that the soil in the coupled soil-structure system acts as a vibration absorber that the power of earthquake excitation near the most dominant natural frequency of the superstructure is absorbed to some extent. On the other hand, the peak located near 4.40 Hz of FLIRS indicates that the energy of seismic excitation near the natural frequency of the decoupled model is shifted to lower frequency due to the presence of soil, which could result in a larger FRS around this frequency.

The obtained FLIRS is input to the model to generate FRS, which are calculated at 200 frequencies including the natural frequencies of the structure using the direct spectra-to-

spectra method. In this procedure, either the method developed in Chapter 2 or the method by Jiang (2016) can be applied because the superstructure has only one input.

FRS at Containment Nodes

FRS at Nodes 5, 6 and 7 obtained by the direct method are plotted along with those generated by the 30 sets of time history analyses from Figures 5.44 to 5.52.

FRS at Internal Structural Nodes

FRS at Node 2 and 3 obtained by the direct method is plotted along with those generated by the 30 sets of time history analyses in Figures 5.53 and 5.58.

5.4.3 Discussion for the FRS with fully correlated excitation

FRS obtained by the direct method and the mean FRS of the time history analyses, which is regarded as the "benchmark" FRS, are shown in black solid lines and red dash lines, respectively. The difference between two approaches are listed in Table 5.5.

Based on the data shown in the table, the following observations can be made regarding the comparison between the Direct Method (DM) and Time History (TH) results:

- The FRS obtained from the direct method agrees well with the "benchmark" FRS over the entire frequency range,. This agreement validates the accuracy and reliability of the direct method in generating FRS for the structure under consideration.
- The individual FRS obtained by the time history method exhibits large variability. A single set of time history analysis can lead to a maximum 77.4% overestimation or 49.8% underestimation of FRS peak depending on the input acceleration time history used.
- For all nodes, the errors in the horizontal directions (H1 and H2) are consistently small, with all values below 5% , which are well within the range of acceptable errors. This indicates that the direct method performs exceptionally well in capturing the horizontal response of the structure.
- In the vertical direction (V), the errors between the direct method and time history method results are relatively larger compared to the horizontal directions. Considering the vertical response is more sensitive to the high-frequency content of the seismic input

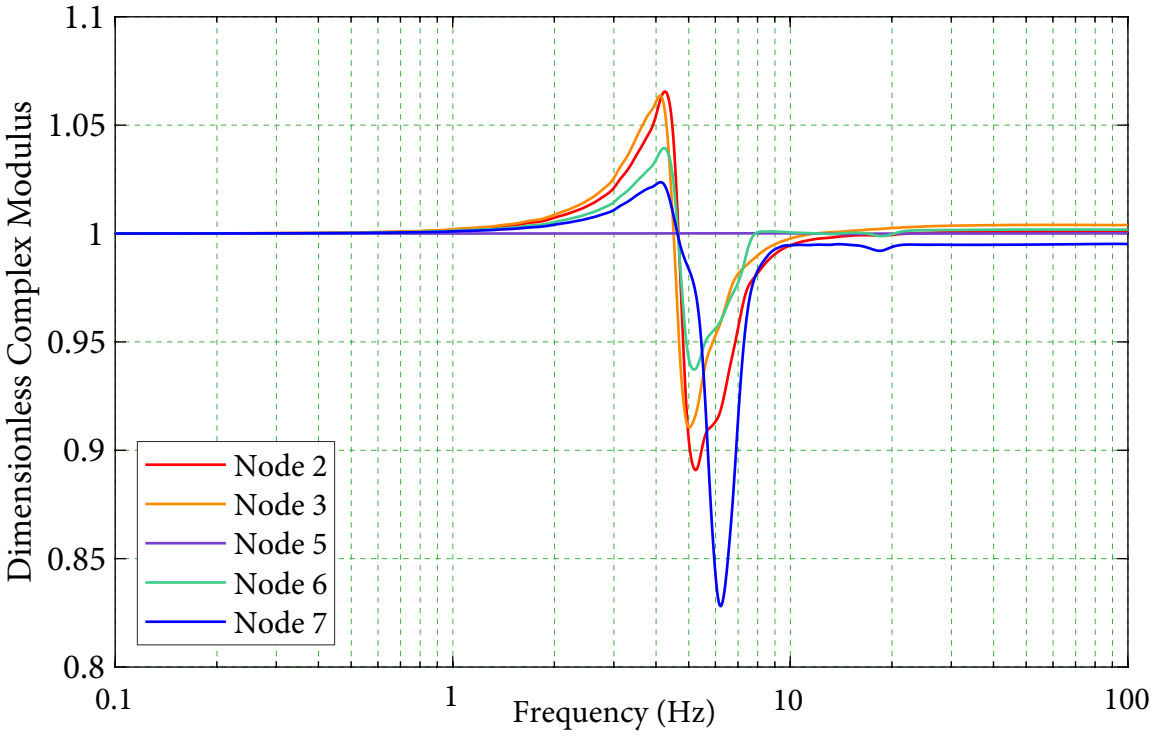


Figure 5.41 Modulus of FLIRS transfer matrix.

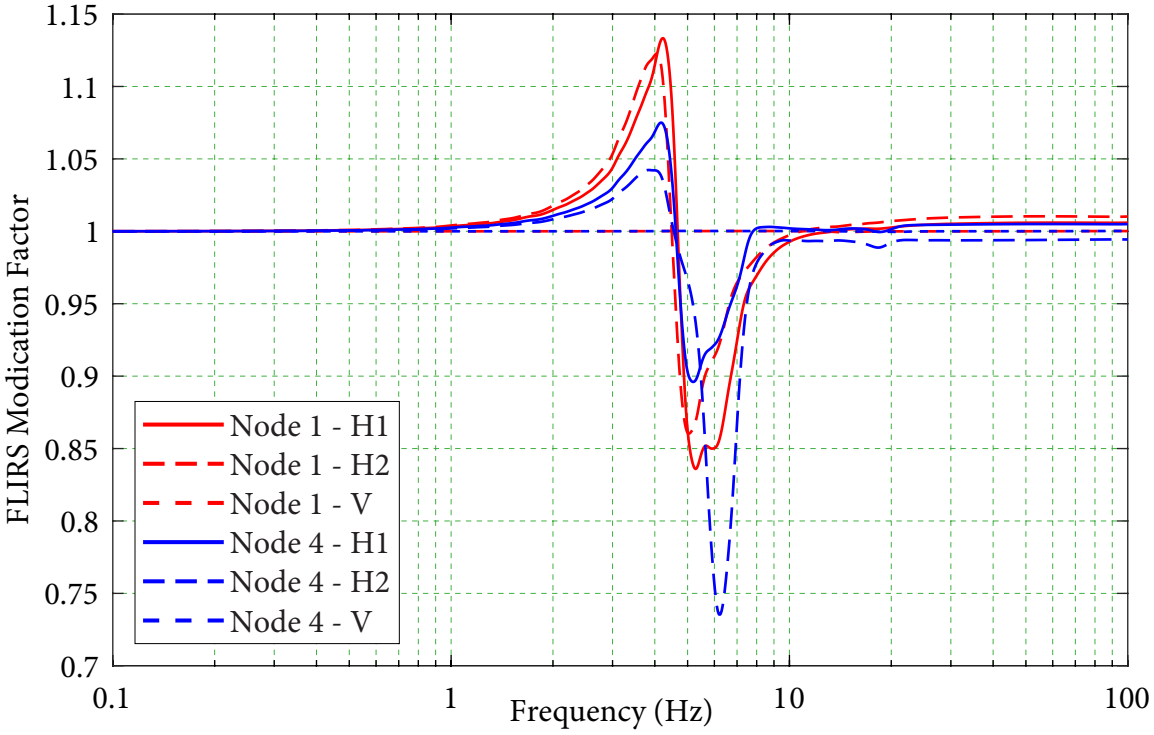


Figure 5.42 FLIRS modification factor for fully correlated case.

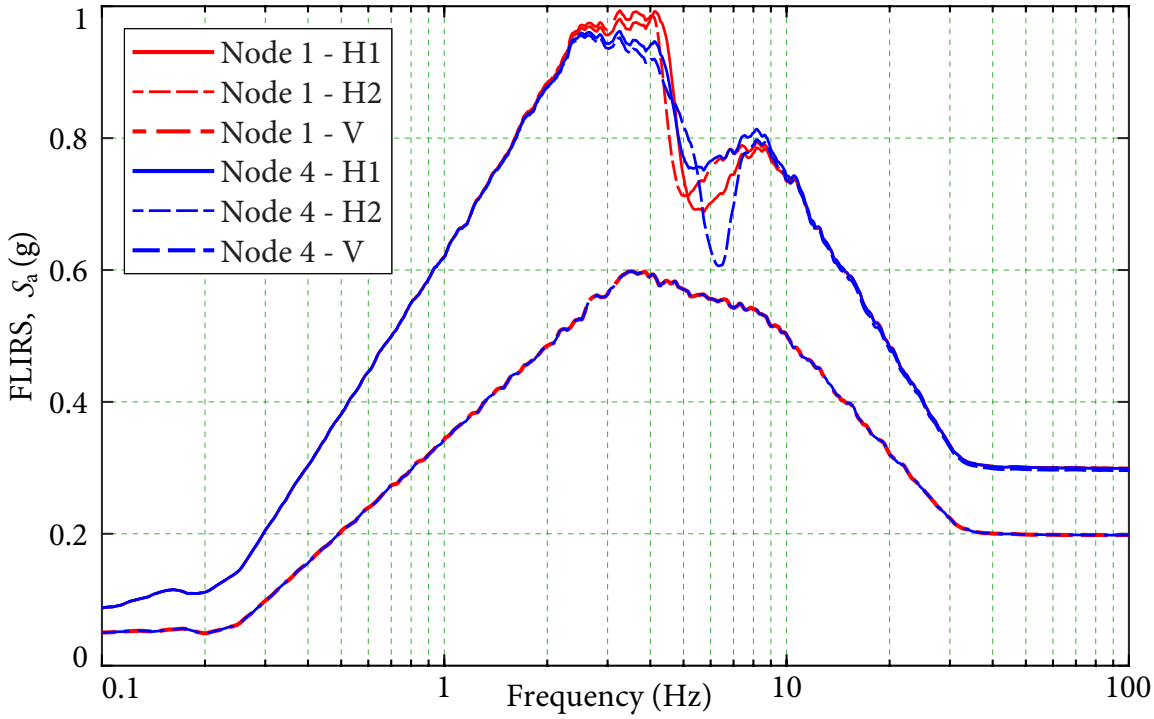


Figure 5.43 FLIRS by direct method in the fully correlated excitation case.

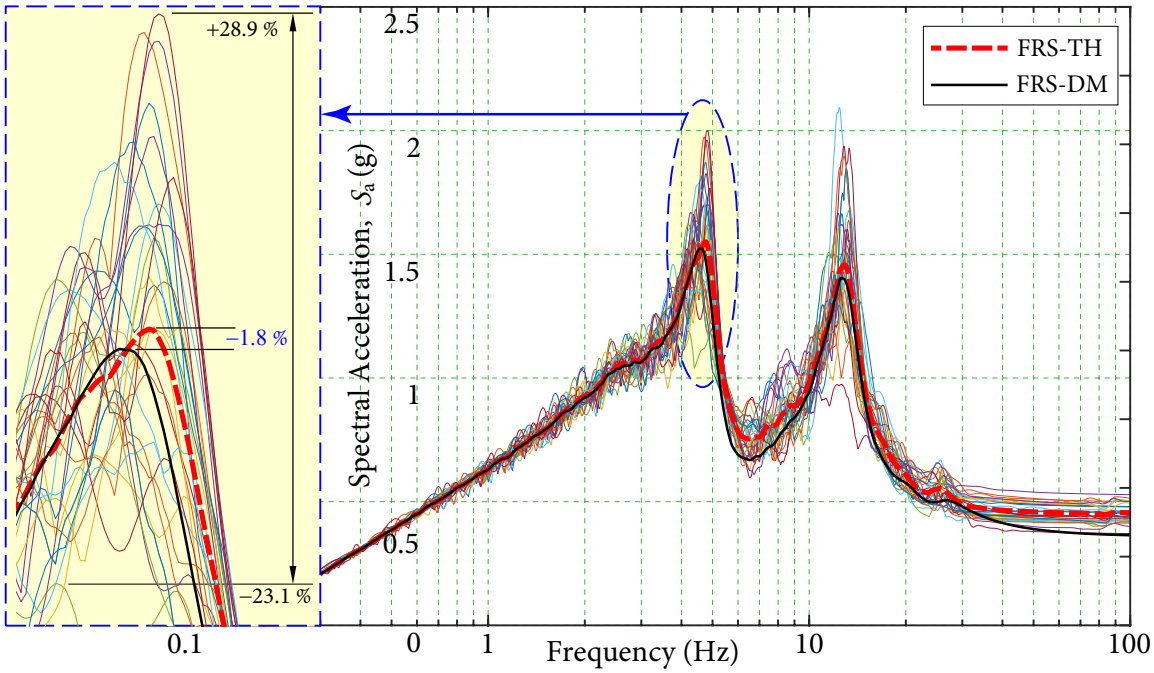


Figure 5.44 FRS in H1 direction at Node 5 in the fully correlated excitation case.

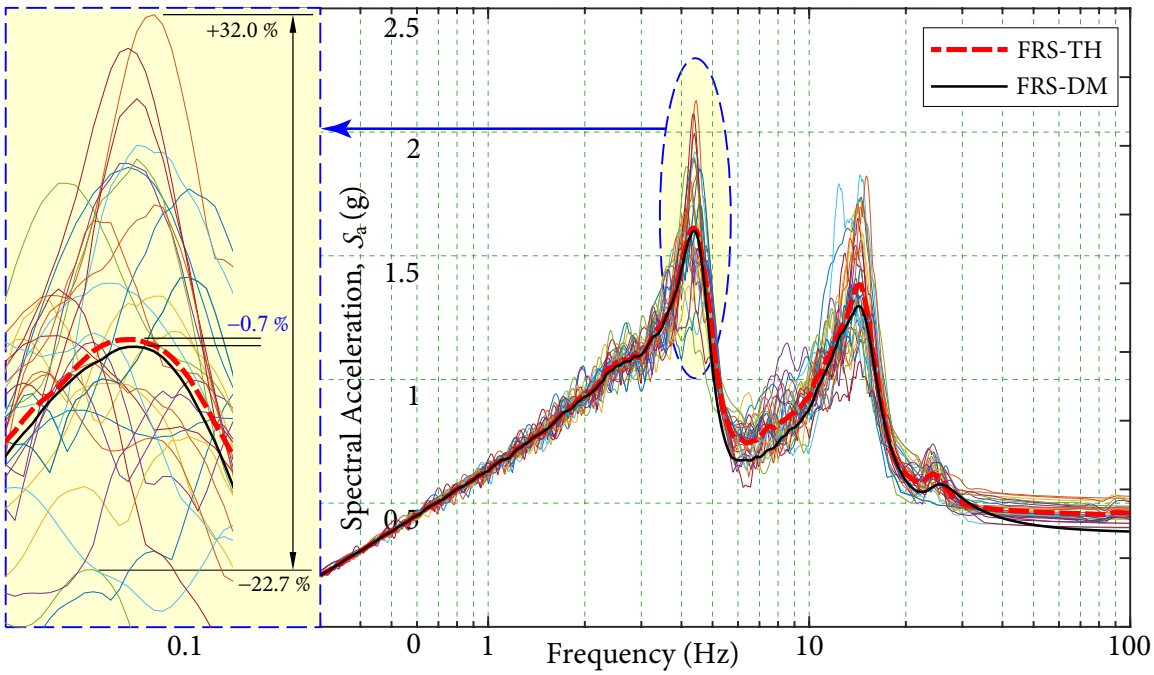


Figure 5.45 FRS in H2 direction at Node 5 in the fully correlated excitation case.

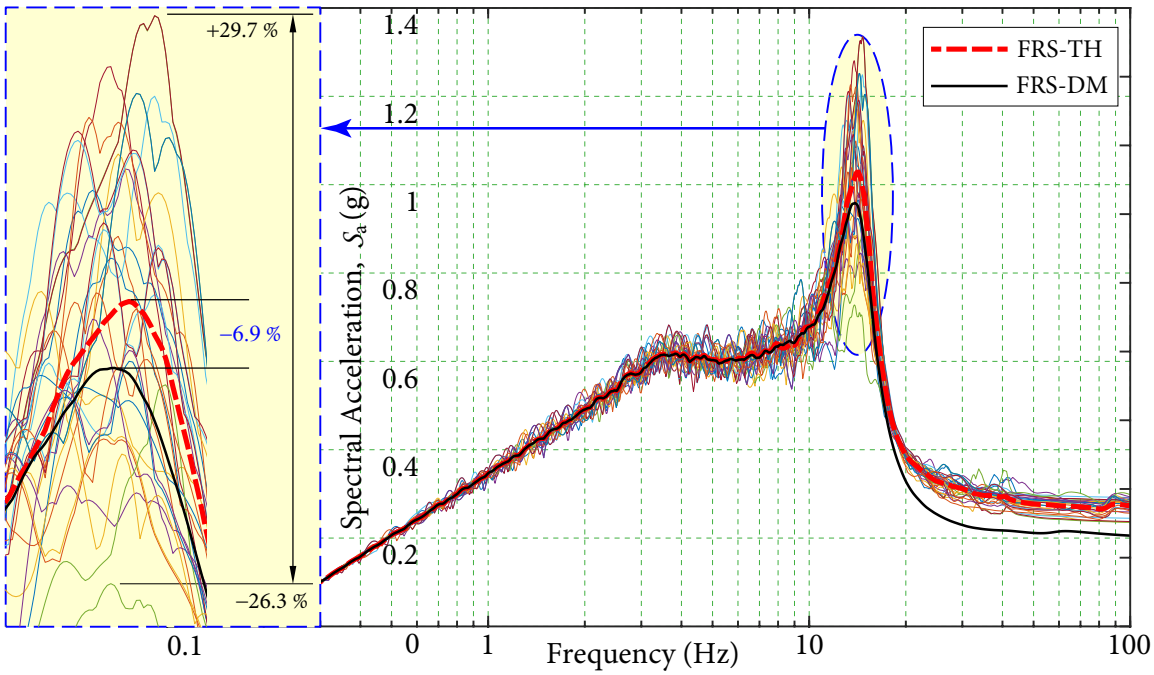


Figure 5.46 FRS in V direction at Node 5 in the fully correlated excitation case.

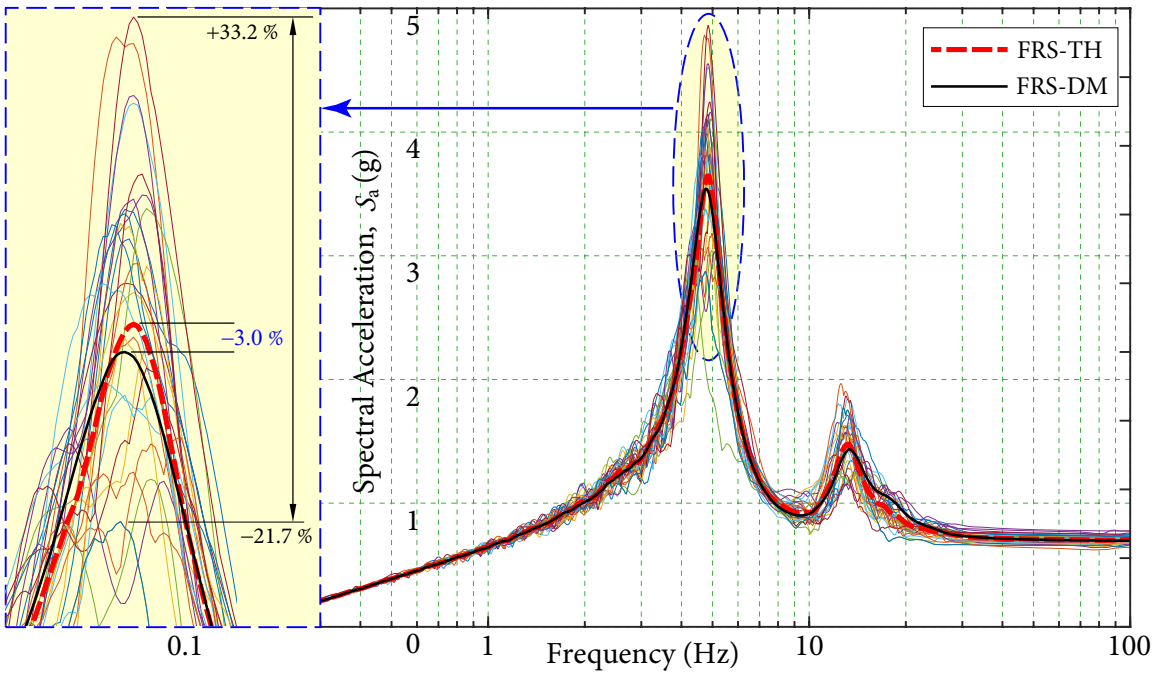


Figure 5.47 FRS in H1 direction at Node 6 in the fully correlated excitation case.

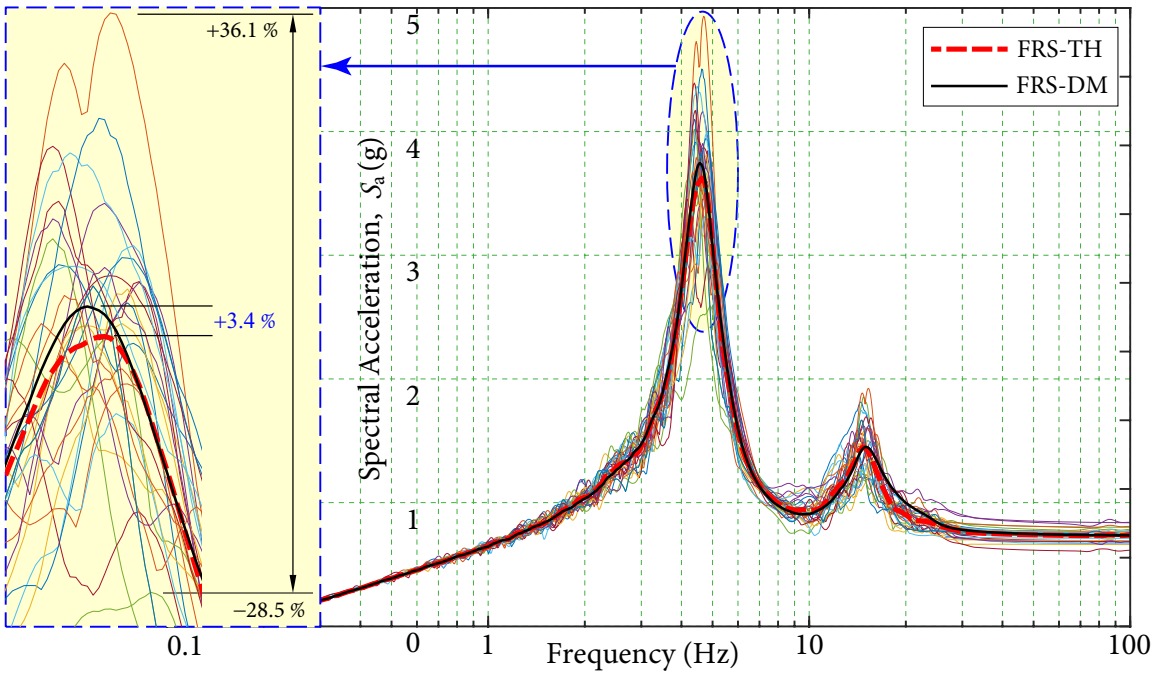


Figure 5.48 FRS in H2 direction at Node 6 in the fully correlated excitation case.

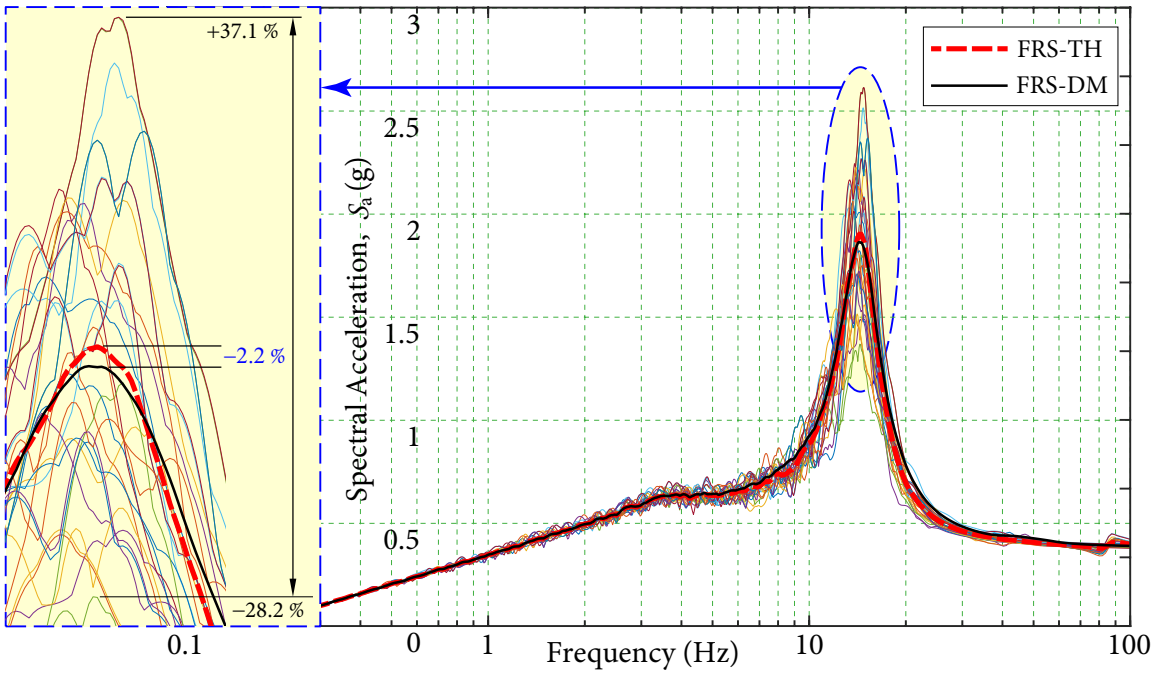


Figure 5.49 FRS in V direction at Node 6 in the fully correlated excitation case.

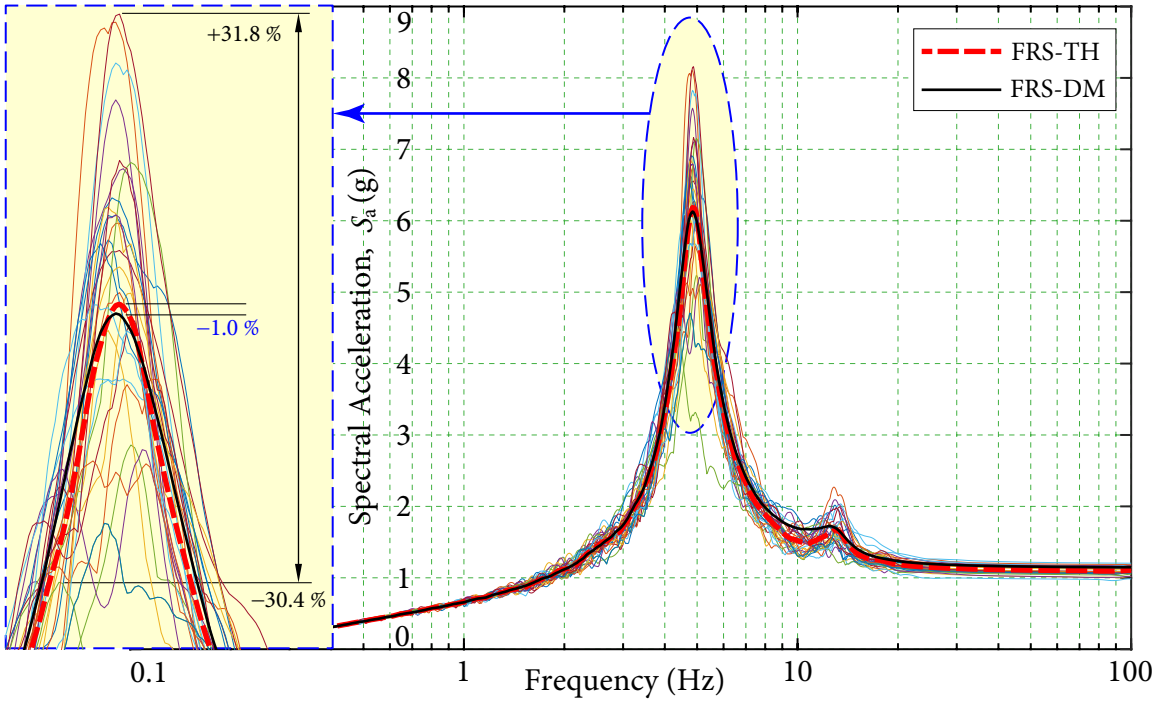


Figure 5.50 FRS in H1 direction at Node 7 in the fully correlated excitation case.

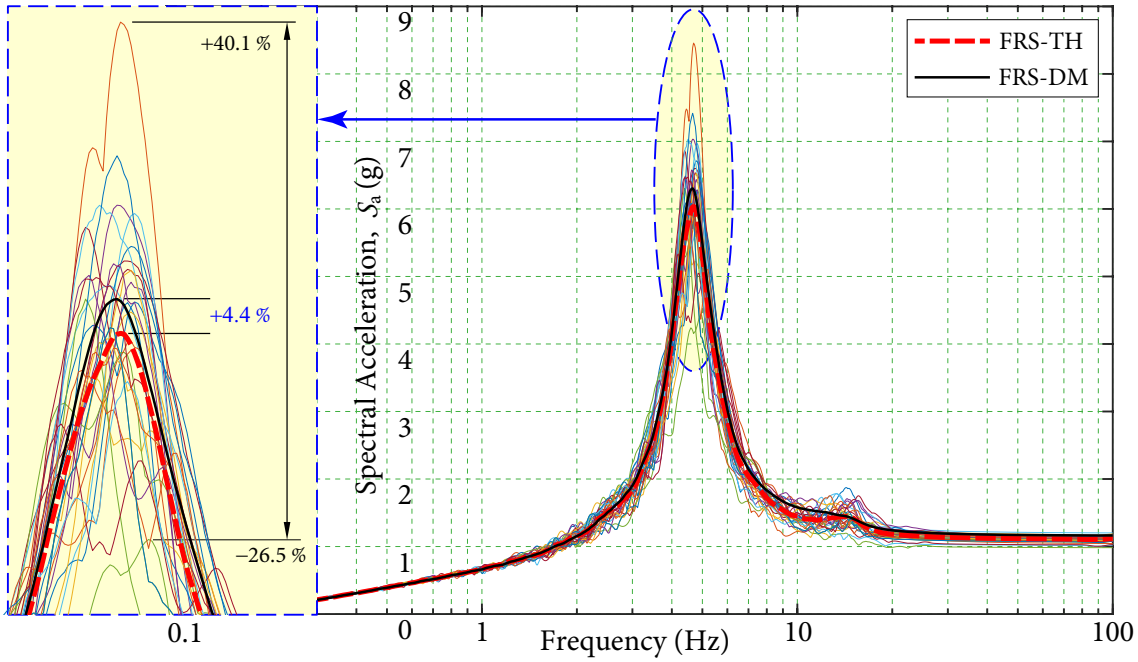


Figure 5.51 FRS in H2 direction at Node 7 in the fully correlated excitation case.

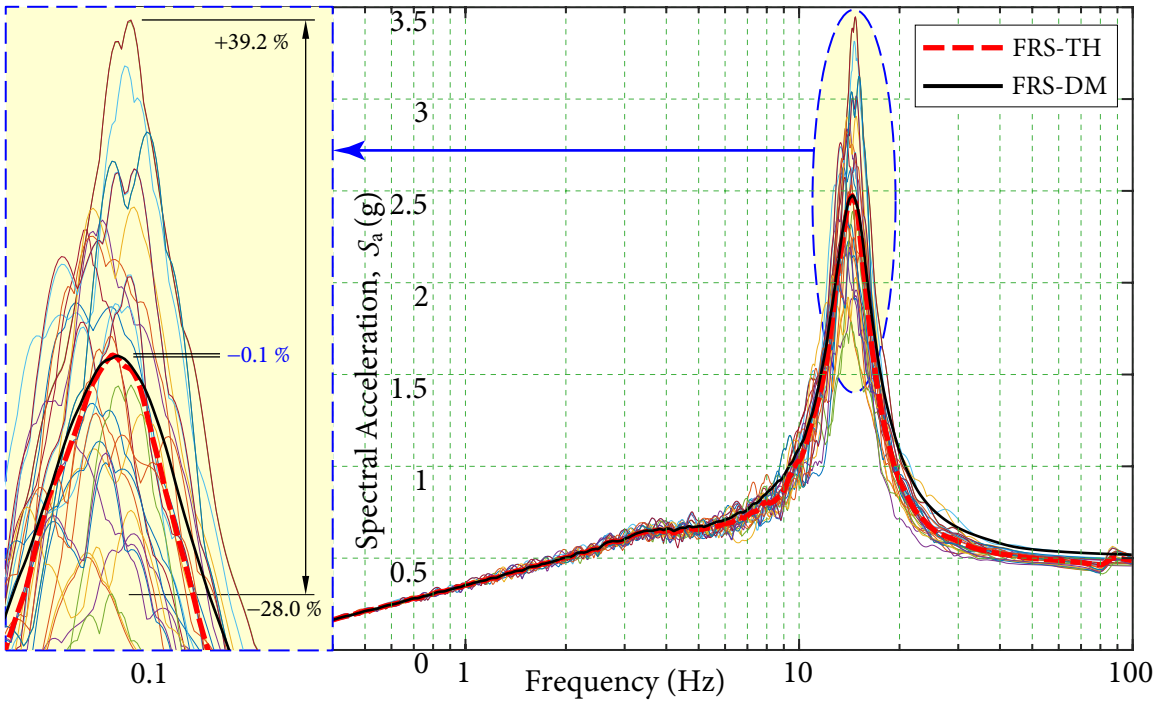


Figure 5.52 FRS in V direction at Node 7 in the fully correlated excitation case.

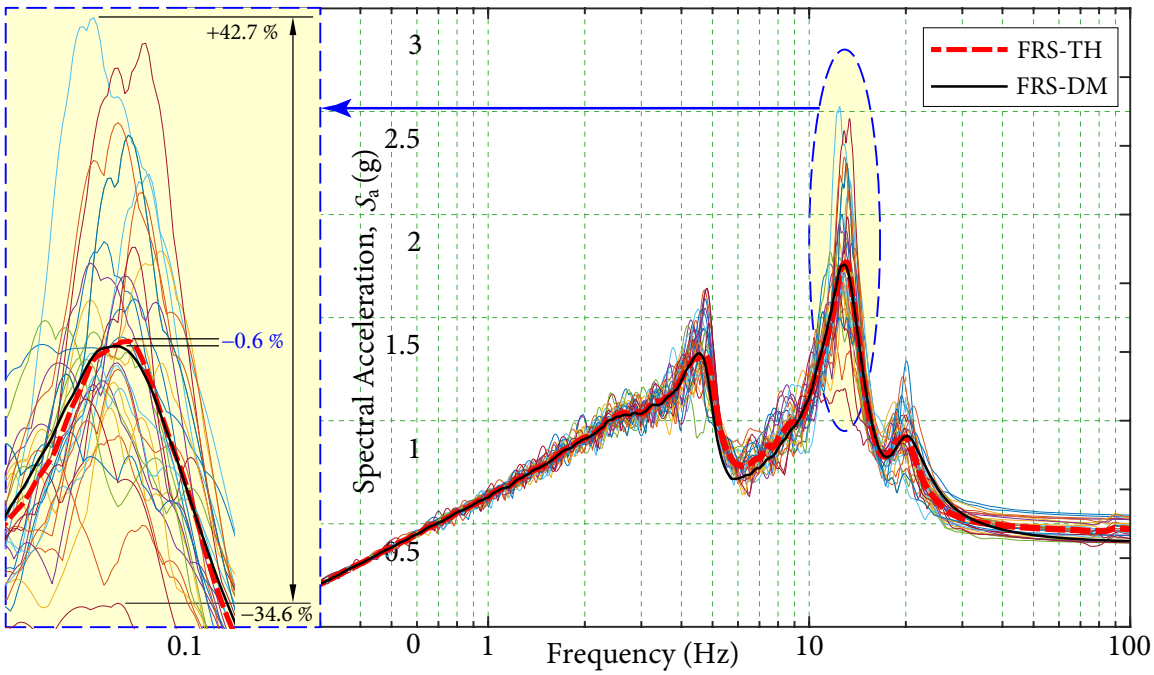


Figure 5.53 FRS in H1 direction at Node 2 in the fully correlated excitation case.

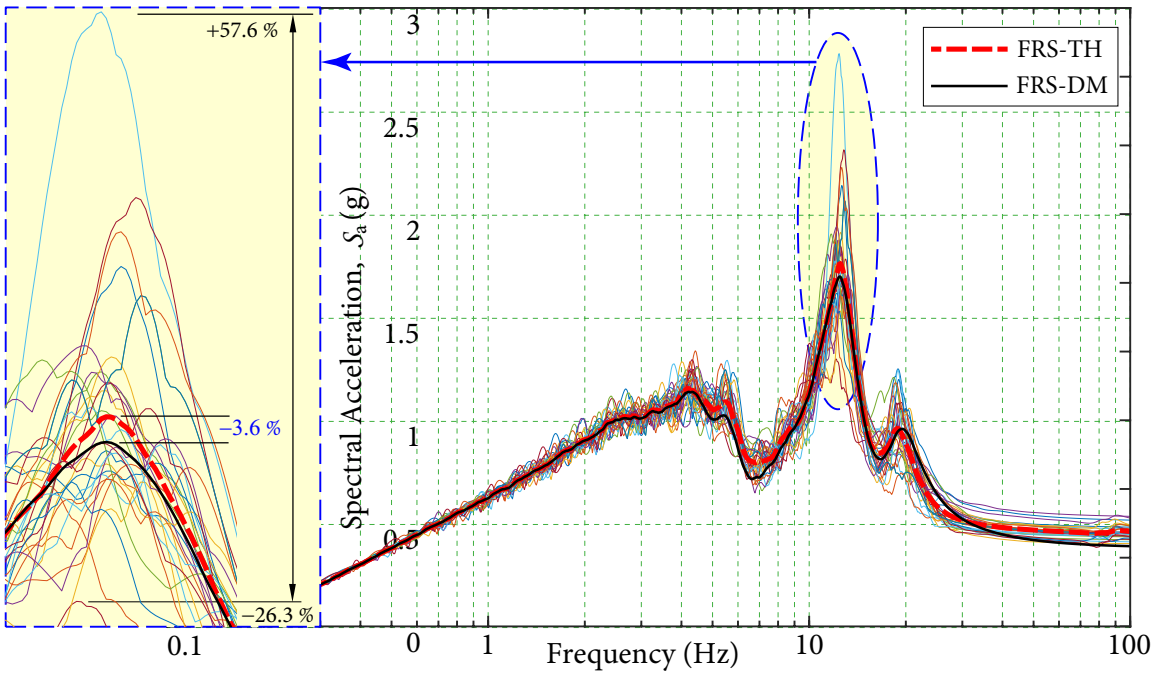


Figure 5.54 FRS in H2 direction at Node 2 in the fully correlated excitation case.

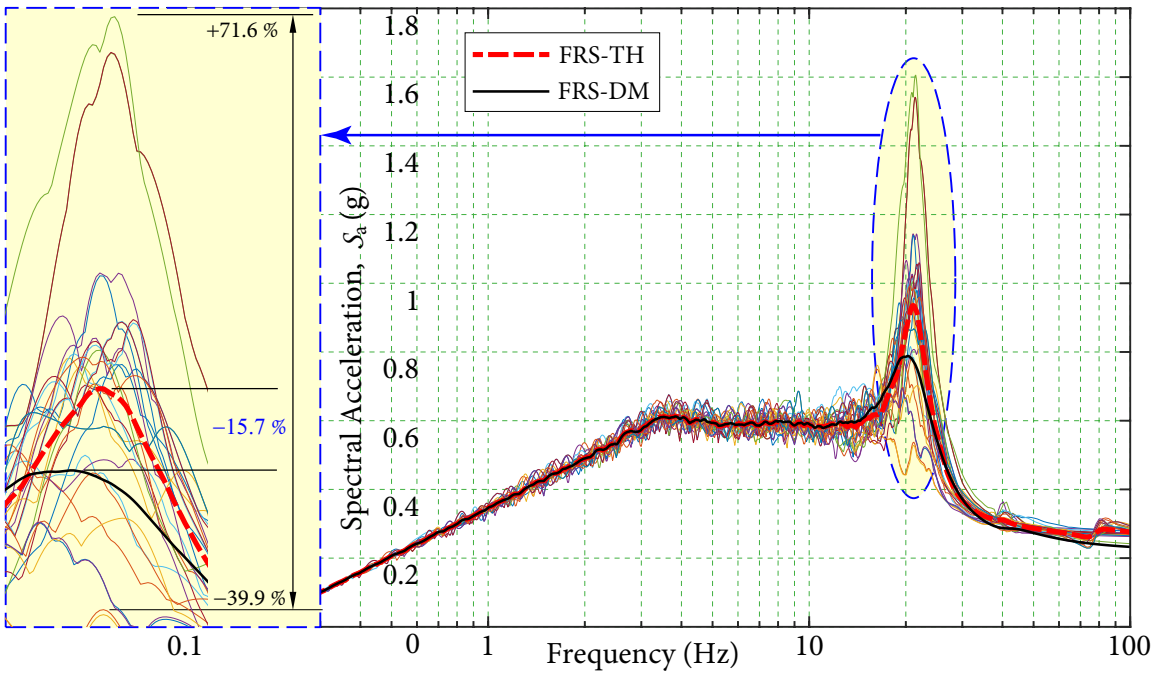


Figure 5.55 FRS in V direction at Node 2 in the fully correlated excitation case.

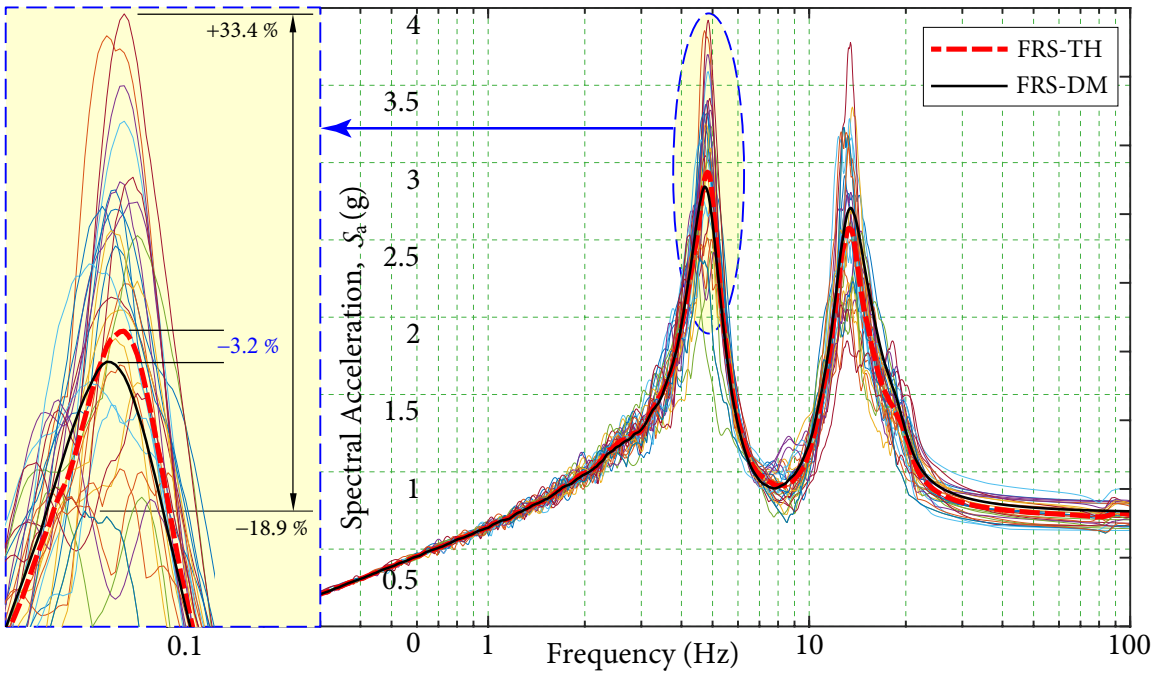


Figure 5.56 FRS in H1 direction at Node 3 in the fully correlated excitation case.

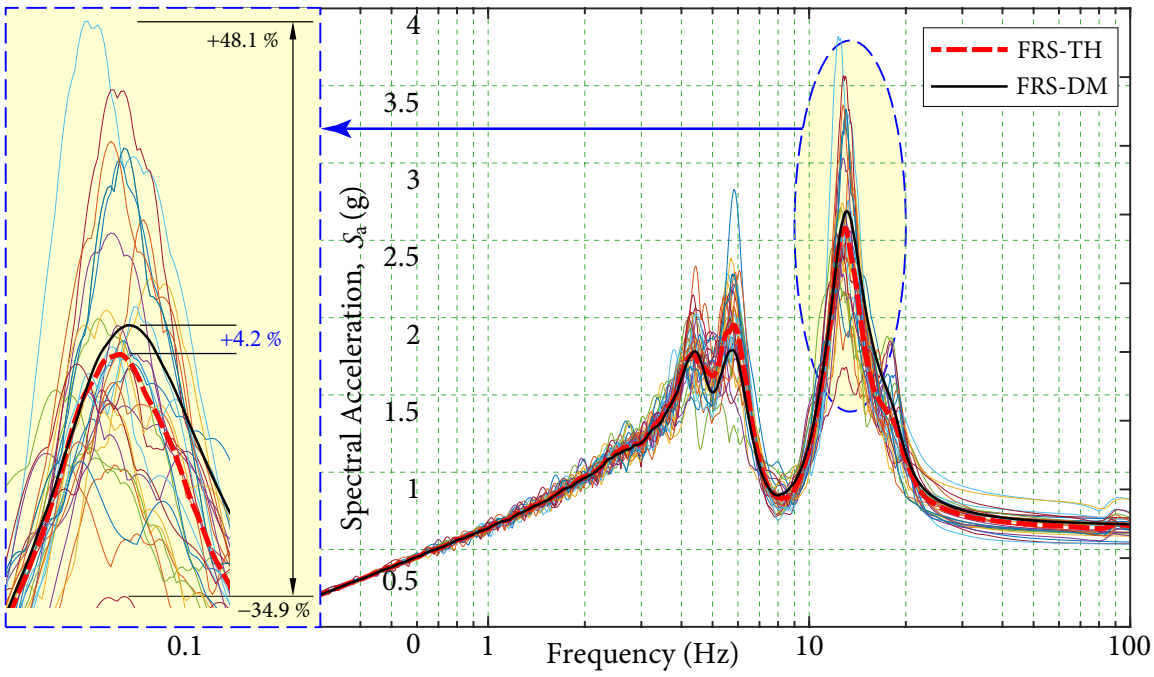


Figure 5.57 FRS in H2 direction at Node 3 in the fully correlated excitation case.

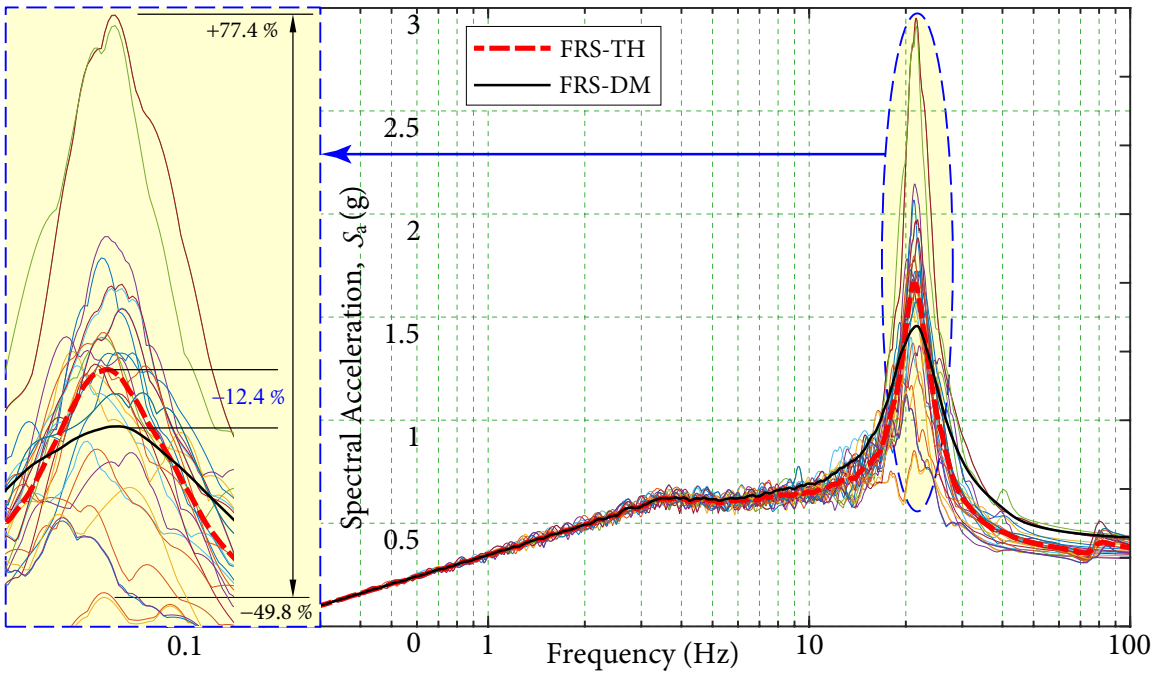


Figure 5.58 FRS in V direction at Node 3 in the fully correlated excitation case.

motion, the spectrum in the high-frequent tRSmay in a loss of some information, leading to larger errors in the vertical FRS.

In summary, the direct method demonstrates excellent agreement with the time history method in the horizontal directions, with errors consistently below 5%. However, the vertical FRS obtained from the direct method exhibits a relative larger errors compared to the time history results, possibly due to the limitations of the tRSapproach in capturing the complex vertical response of the soil-structure system. Further research is needed to improve the accuracy of the tRS.

Table 5.5 FRS differences between time history and direct method for the fully correlated case

Direction	Node	FRS_TH	TH_Max	Error_Max	TH_Min	Error_Min	FRS_DM	FRS_Error
H1	2	1.768	2.524	42.70%	1.156	-34.60%	1.757	-0.60%
H1	3	2.939	3.921	33.40%	2.382	-18.90%	2.844	-3.20%
H1	5	1.552	2.000	28.90%	1.193	-23.10%	1.524	-1.80%
H1	6	3.652	4.862	33.20%	2.860	-21.70%	3.542	-3.00%
H1	7	6.191	8.157	31.80%	4.306	-30.40%	6.128	-1.00%
H2	2	1.767	2.784	57.60%	1.303	-26.30%	1.703	-3.60%
H2	3	2.580	3.820	48.10%	1.679	-34.90%	2.688	4.20%
H2	5	1.612	2.128	32.00%	1.247	-22.70%	1.600	-0.70%
H2	6	3.623	4.931	36.10%	2.590	-28.50%	3.745	3.40%
H2	7	6.038	8.456	40.10%	4.436	-26.50%	6.304	4.40%
V	2	0.936	1.606	71.60%	0.562	-39.90%	0.788	-15.70%
V	3	1.663	2.950	77.40%	0.835	-49.80%	1.456	-12.40%
V	5	1.029	1.335	29.70%	0.759	-26.30%	0.958	-6.90%
V	6	1.906	2.614	37.10%	1.369	-28.20%	1.864	-2.20%
V	7	2.474	3.445	39.20%	1.782	-28.00%	2.472	-0.10%

5.4.4 Case of Fully Independent Excitation

FLIRS Transfer Matrix and Modification Factor

Analogous to the case of fully correlated excitations, FLIRS transfer matrix $\mathcal{T}$ and FLIRS modification factor $\mathcal{R}$ are shown in 5.59. It is found that the peaks of $\mathcal{T}$ and $\mathcal{R}$ are also located near the natural frequencies of the coupled structural system, whereas the valleys located at the natural frequencies of the superstructure are identified. This is because superstructure and soil properties are both considered in obtaining FLIRS transfer matrix $\mathcal{T}$ and FLIRS modification factor $\mathcal{R}$.

The valleys in $\mathcal{T}$ and $\mathcal{R}$ can be interpreted as a result of the absorption of vibration. It means that the soil in a coupled soil-structure system may play the same role as vibration absorber, in which the energy of excitation is absorbed at certain frequencies, i.e., natural frequencies of the decoupled model.

Furthermore, the result of the modification factor given in Figure 5.59 shows that the FIRS is mainly modified within the frequency range 1 Hz to 33 Hz. This is because earthquake excitations with low frequency do not have much influence on seismic vibration of this system, while a structure can be regarded as rigid when the natural frequencies exceed 33 Hz. Therefore, the modification factor in these frequency ranges is approximately 1. One more observation made from Figure 5.59 suggests that earthquake excitations at the dominant frequencies of either coupled or uncoupled system are changed more significantly comparing with other frequencies when SSI effect is considered. Therefore, one has to pay more attention to the dominant frequencies of both coupled and uncoupled systems in engineering practice.

Development of FLIRS

Analogous to the case of fully correlated, FLIRS is determined through FIRS by multiplying the modification factor, $\mathcal{R}$. Since the FLIRS is verified to be accurate in Section 3.4.2, it is essential to analyze the FLIRS at both supports of the structure, ensuring a more comprehensive understanding of how the FIRS is modified by the soil-structure interaction in the flexible foundation under the circumstance of fully independent seismic input.

Figure 5.60 shows the tri-directional FLIRS for both supports Nodes 1 and 4. As can be seen from Figure 5.60 that FLIRS generated by the proposed method are modified significantly in the horizontal directions within the frequency range 1 Hz to 33 Hz, while the FLIRS is consistent with the input FIRS in the vertical direction. The modified input FLIRS has a significant valley near the dominant frequency of the superstructure (i.e., frequency range between 3 Hz to 8 Hz). The frequency range is the dominant frequency of the decoupled internal structure and containment, as well as the whole structure system. This suggests that the soil in the coupled soil-structure system acts as a vibration absorber that the power of earthquake excitation near the most dominant natural frequency of the superstructure is absorbed to some extent. On the other hand, the peak located near 4.40 Hz of FLIRS indicates that the energy of seismic excitation near the natural frequency of the decoupled model is shifted to lower frequency due to the presence of soil, which could result in a larger FRS around this frequency.

The obtained FLIRS is input to the model to generate FRS, which are calculated at 200 frequencies including the natural frequencies of the structure using the direct spectra-to-spectra method. In this procedure, either the method developed in Chapter 2 or the method by Jiang (2016) can be applied because the superstructure has only one input.

FRS at Containment Nodes

FRS at Nodes 5 and 6 and 7 obtained by the direct method are plotted along with those generated by the 30 sets of time history analyses from Figures 5.61 to 5.69.

FRS at Internal Structural Nodes

FRS at Node 2 and 3 obtained by the direct method is plotted along with those generated by the 30 sets of time history analyses in Figures 5.70 and 5.75.

5.4.5 Discussion for the FRS with Fully Independent Excitation

FRS obtained by the direct method and the mean FRS of the time history analyses, which is regarded as the "benchmark" FRS, are shown in black solid lines and red dash lines, respectively. The difference between two approaches are listed in Table 5.5.

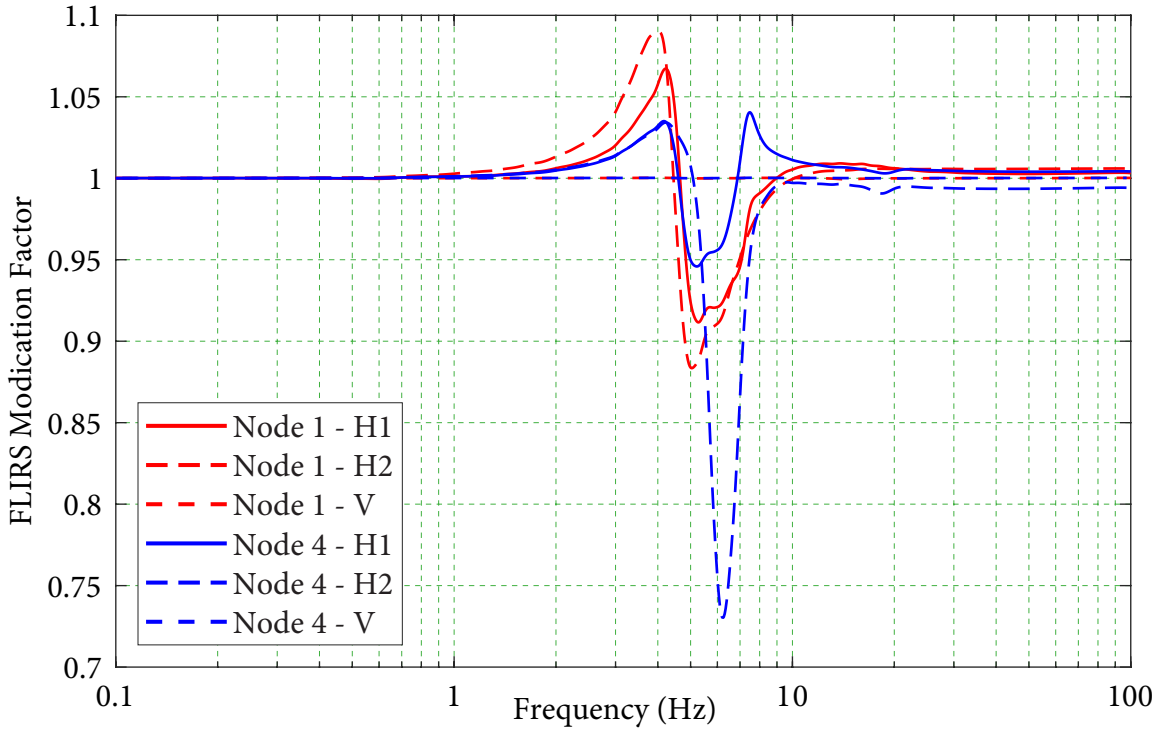


Figure 5.59 FLIRS modification factor for fully independent case.

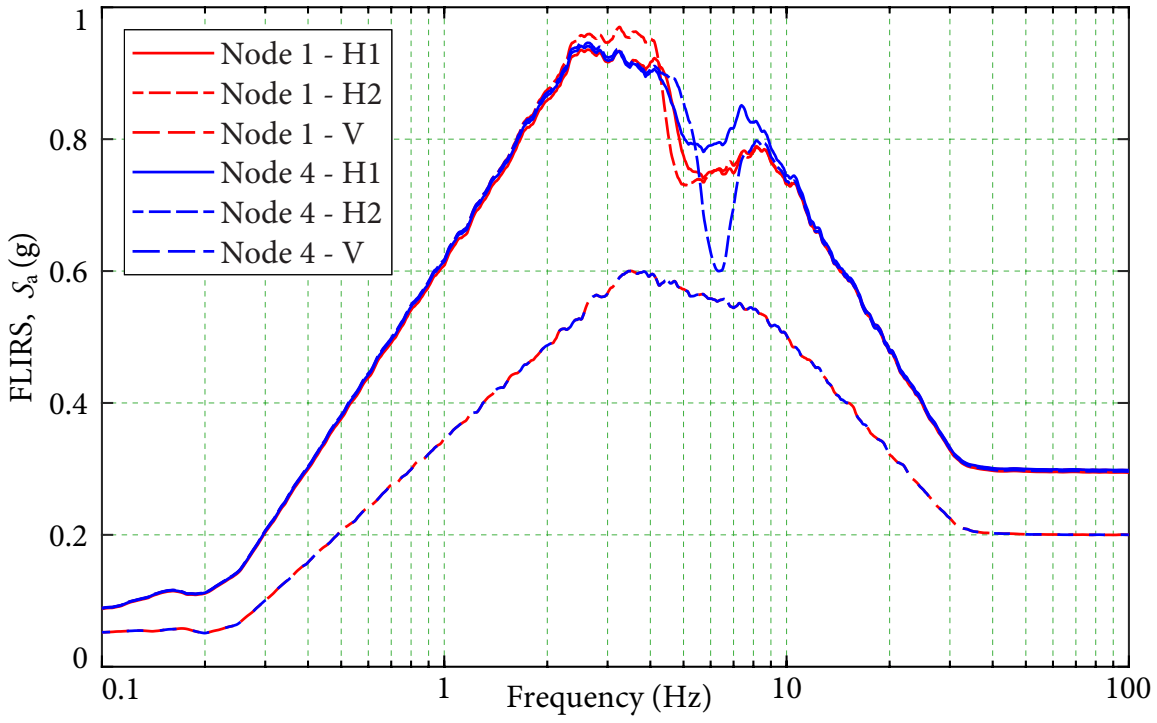


Figure 5.60 FLIRS by direct method in the fully independent excitation case.

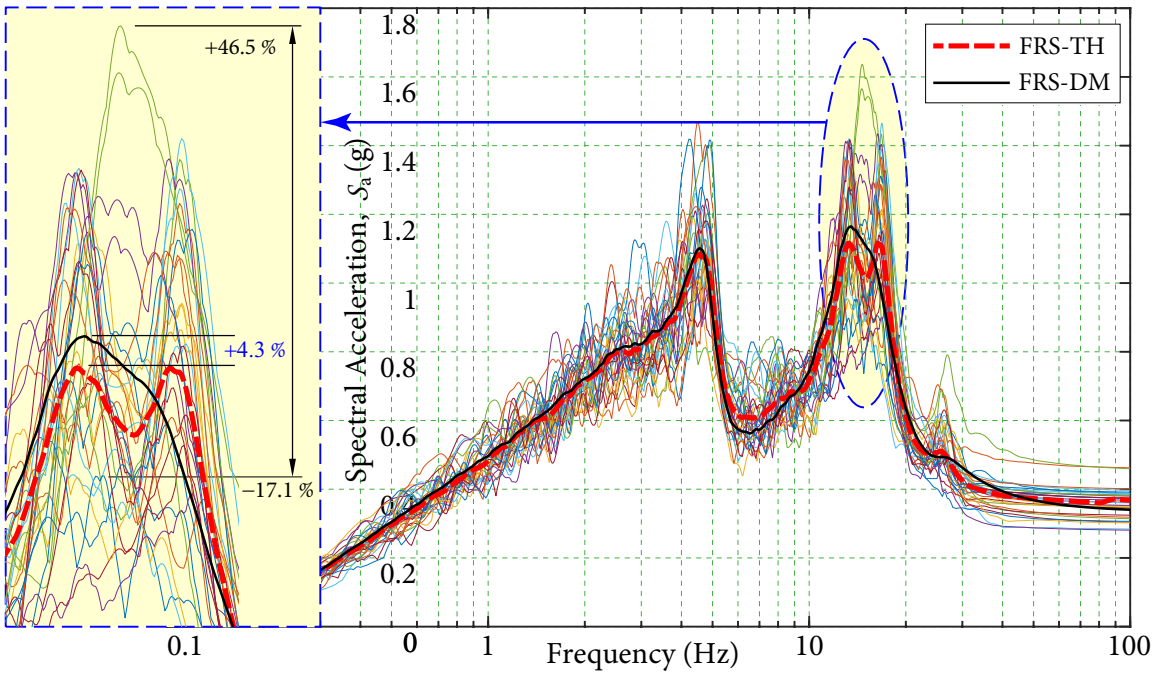


Figure 5.61 FRS in H1 direction at Node 5 in the fully independent excitation case.

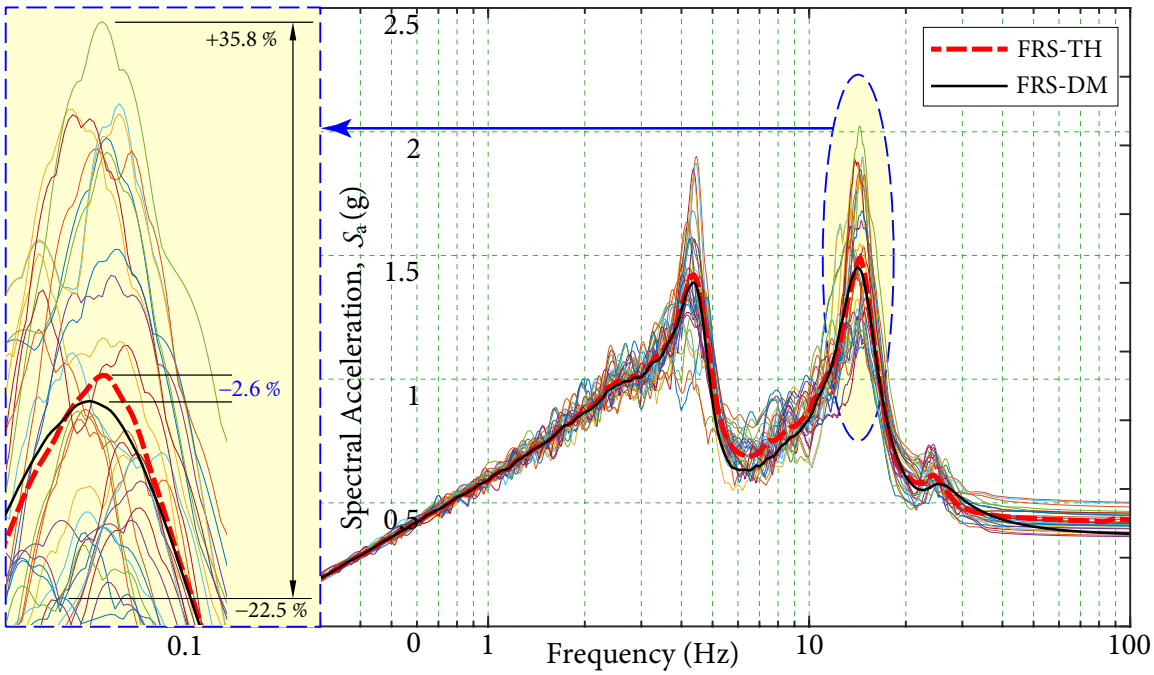


Figure 5.62 FRS in H2 direction at Node 5 in the fully independent excitation case.

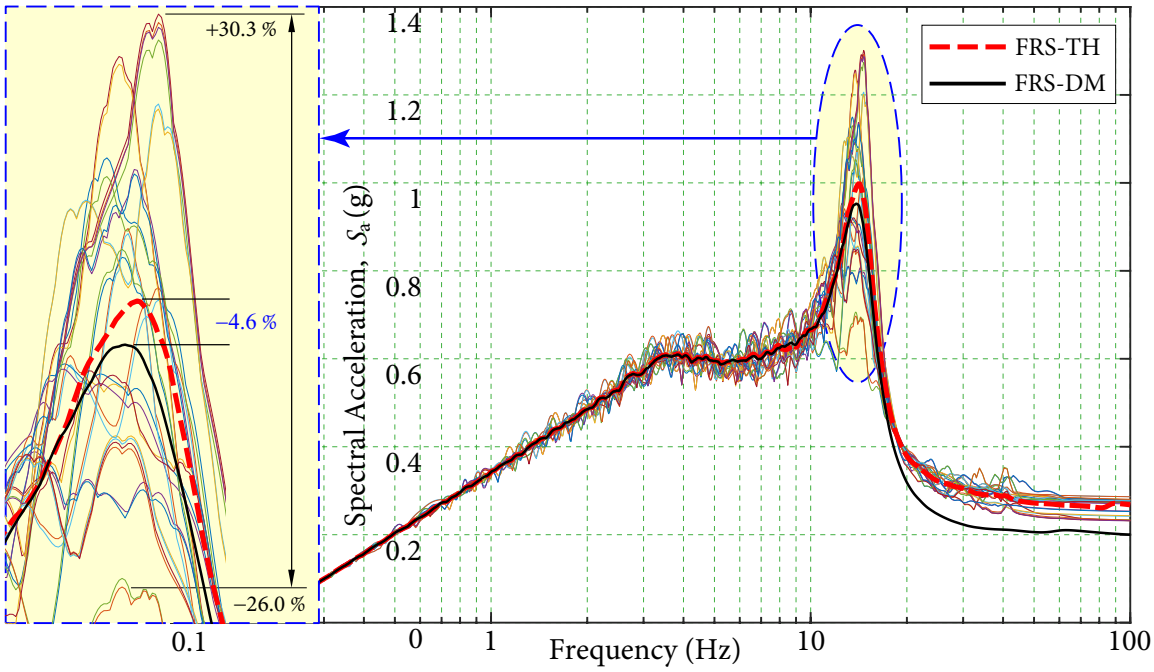


Figure 5.63 FRS in V direction at Node 5 in the fully independent excitation case.

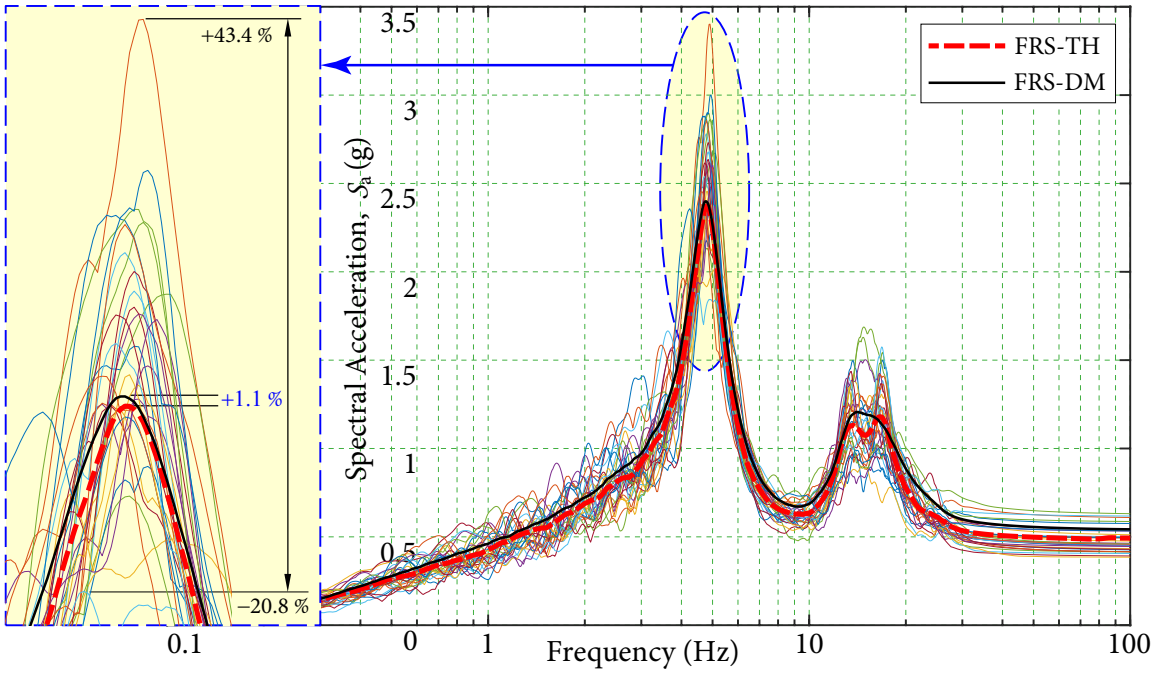


Figure 5.64 FRS in H1 direction at Node 6 in the fully independent excitation case.

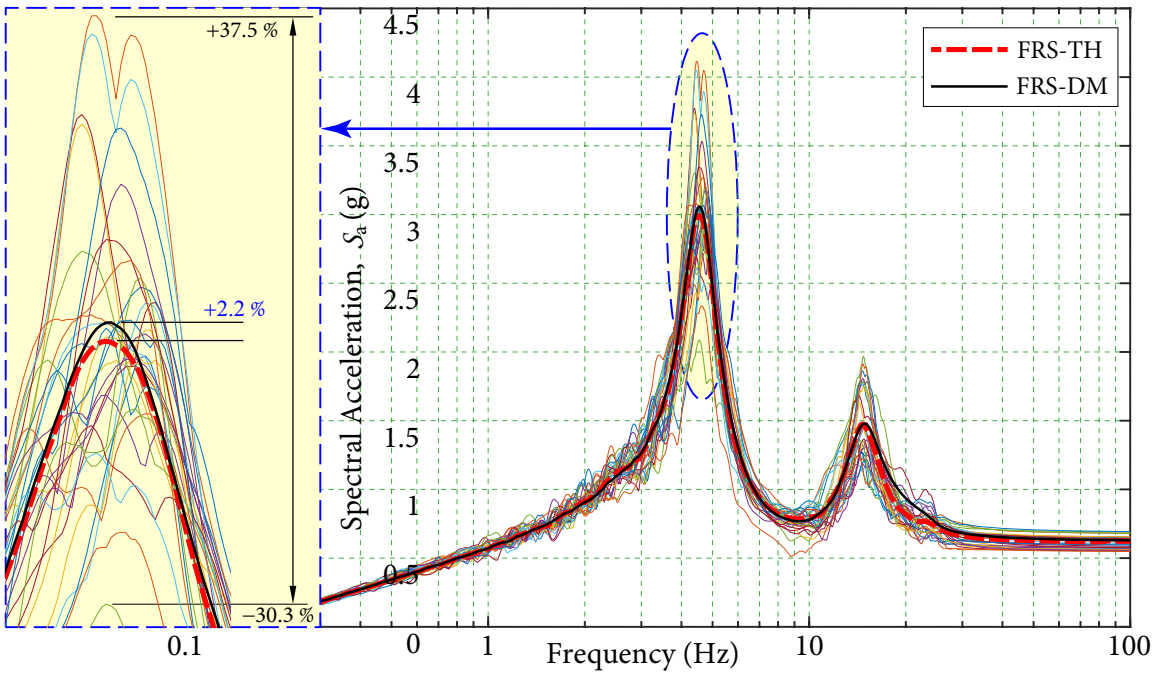


Figure 5.65 FRS in H2 direction at Node 6 in the fully independent excitation case.

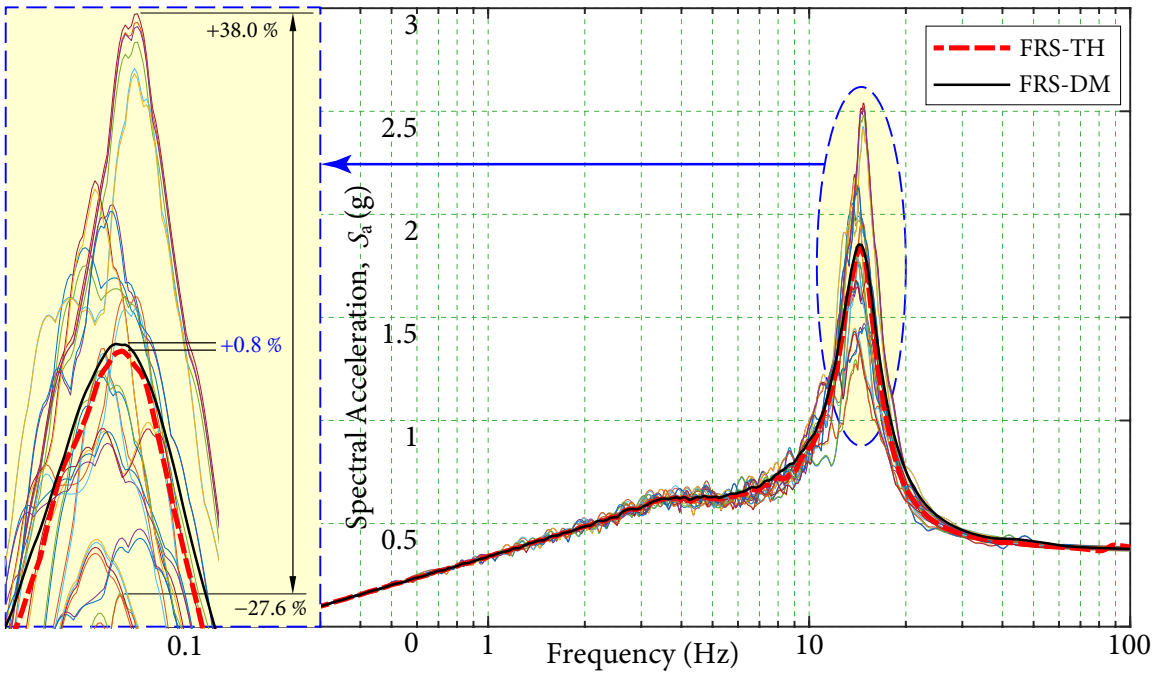


Figure 5.66 FRS in V direction at Node 6 in the fully independent excitation case.

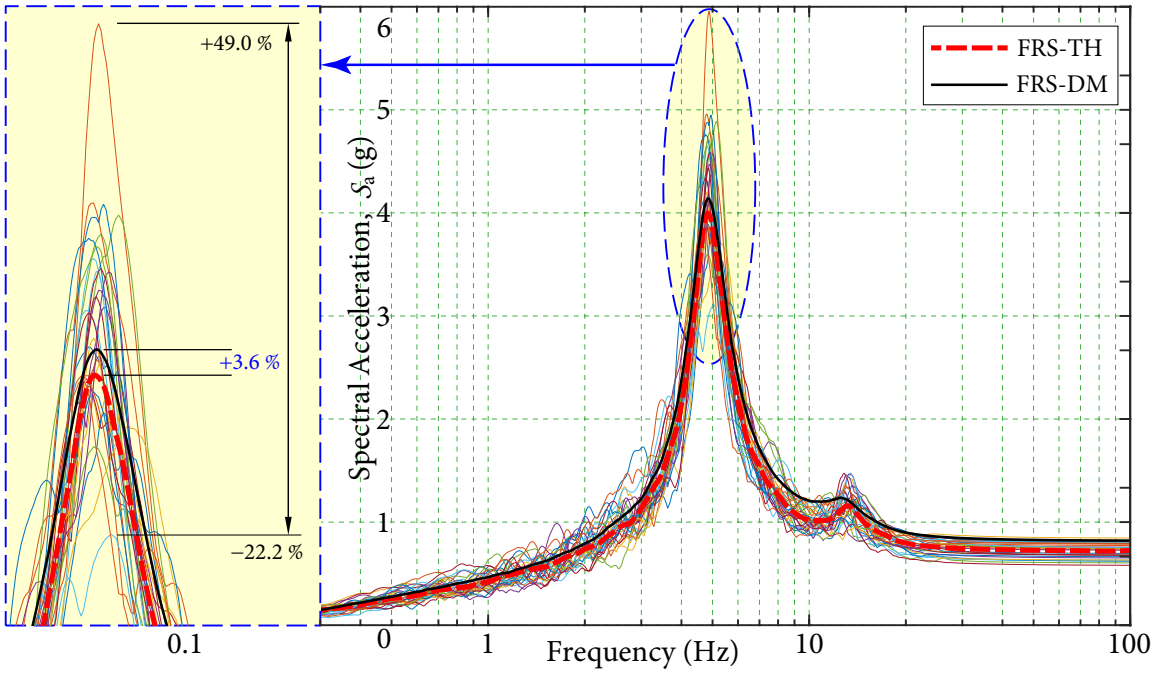


Figure 5.67 FRS in H1 direction at Node 7 in the fully independent excitation case.

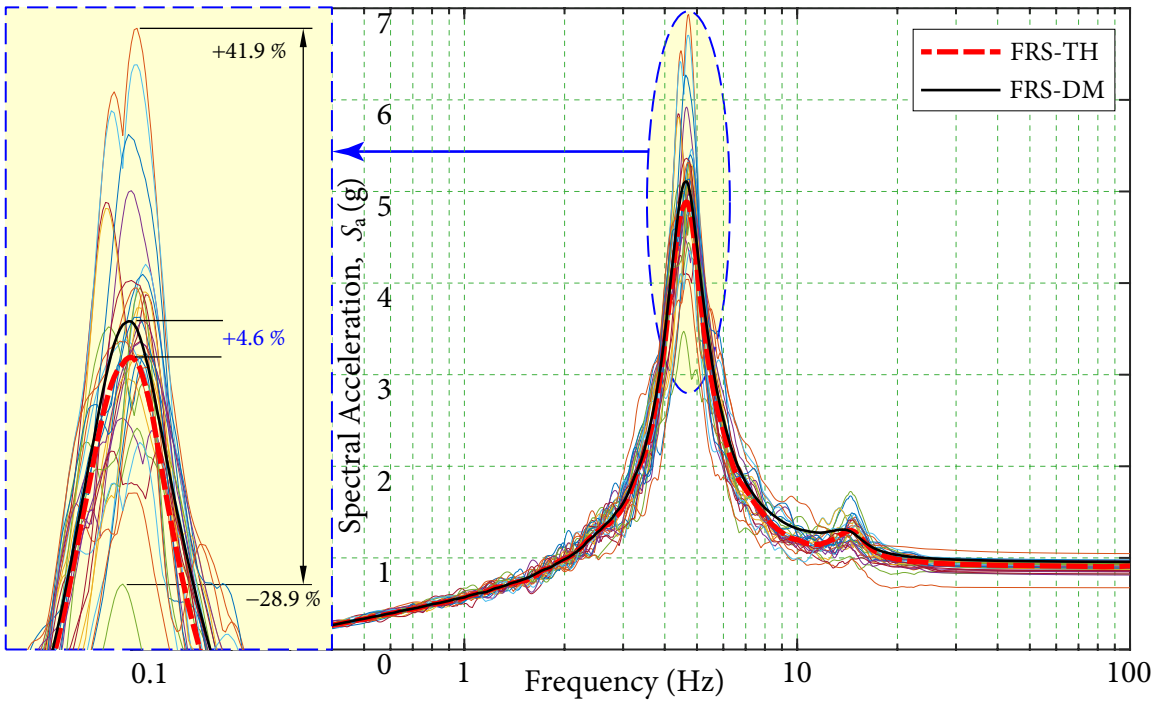


Figure 5.68 FRS in H2 direction at Node 7 in the fully independent excitation case.

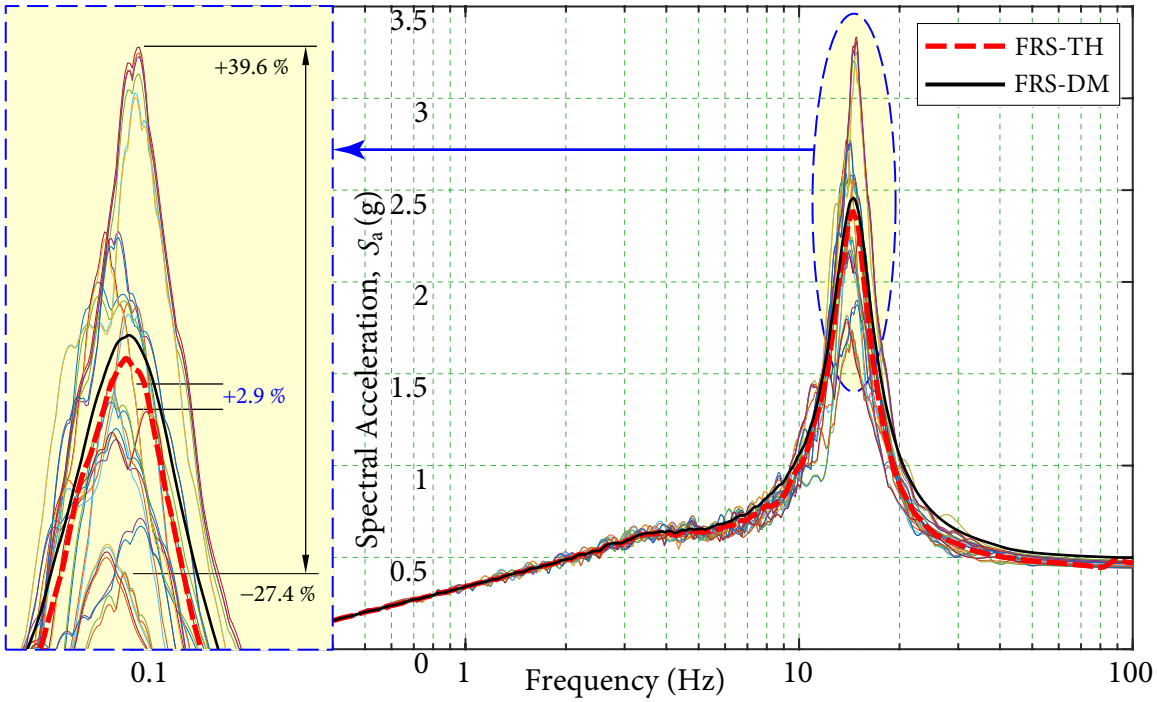


Figure 5.69 FRS in V direction at Node 7 in the fully independent excitation case.

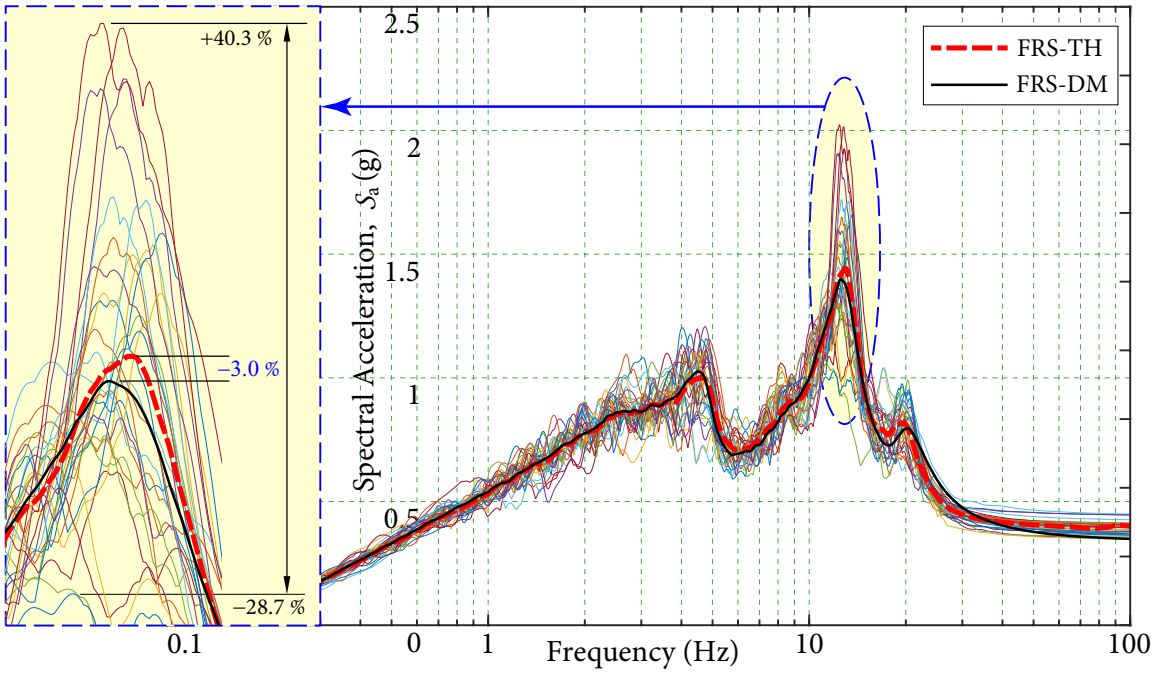


Figure 5.70 FRS in H1 direction at Node 2 in the fully independent excitation case.

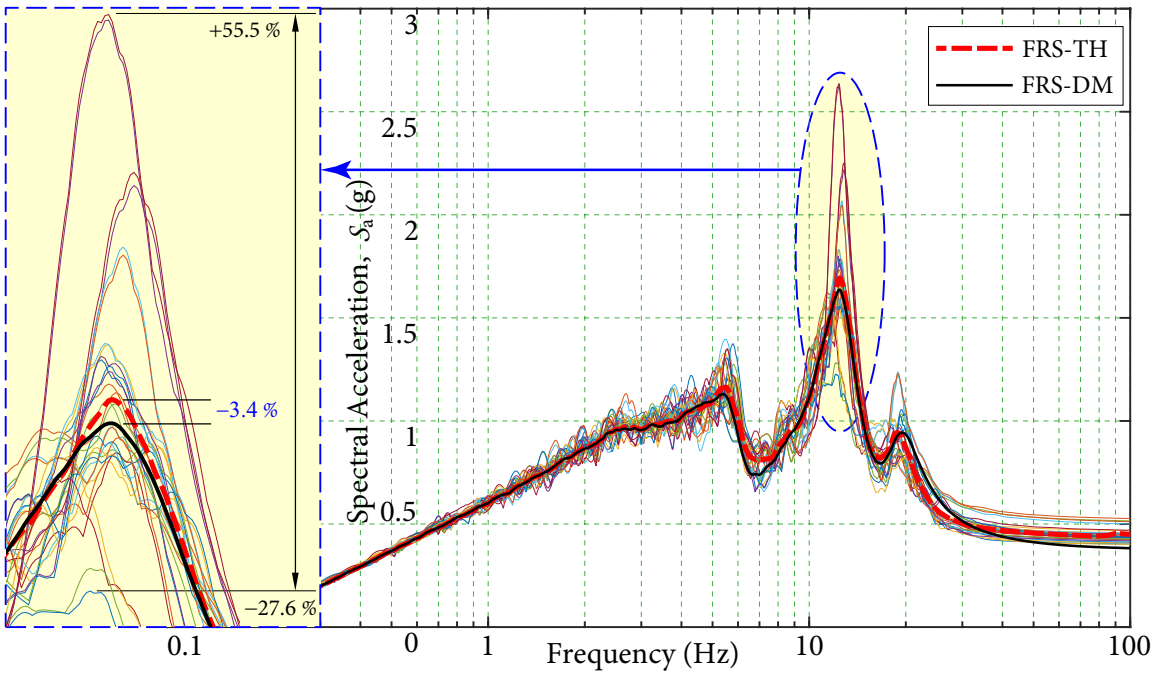


Figure 5.71 FRS in H2 direction at Node 2 in the fully independent excitation case.

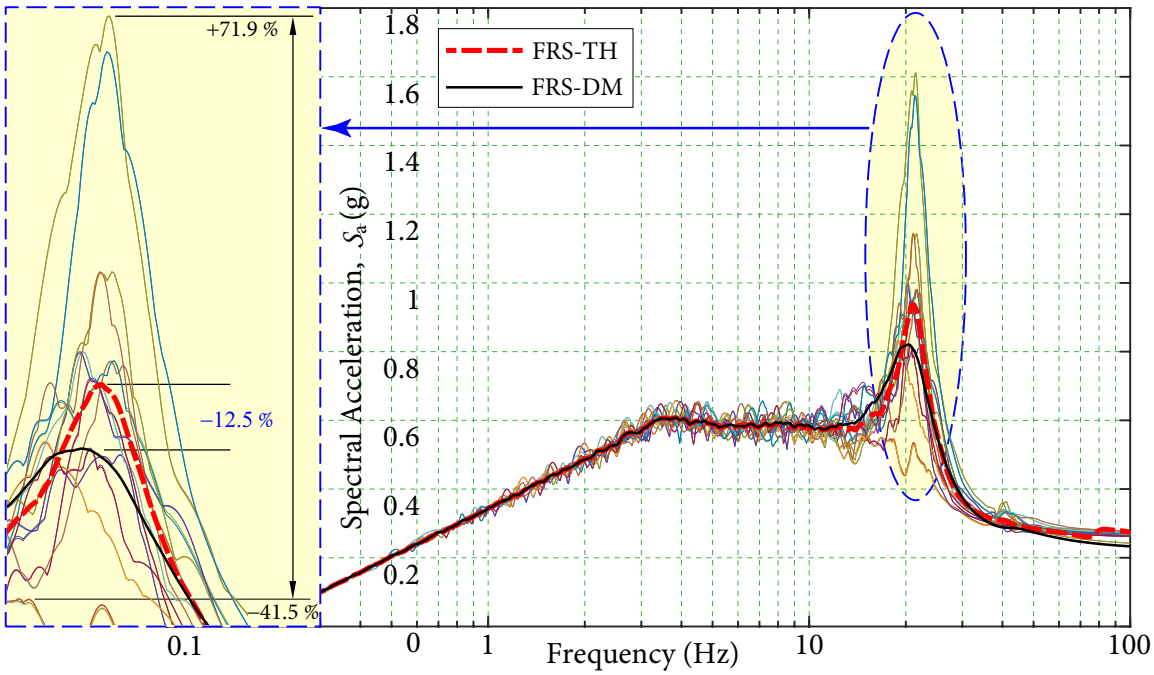


Figure 5.72 FRS in V direction at Node 2 in the fully independent excitation case.

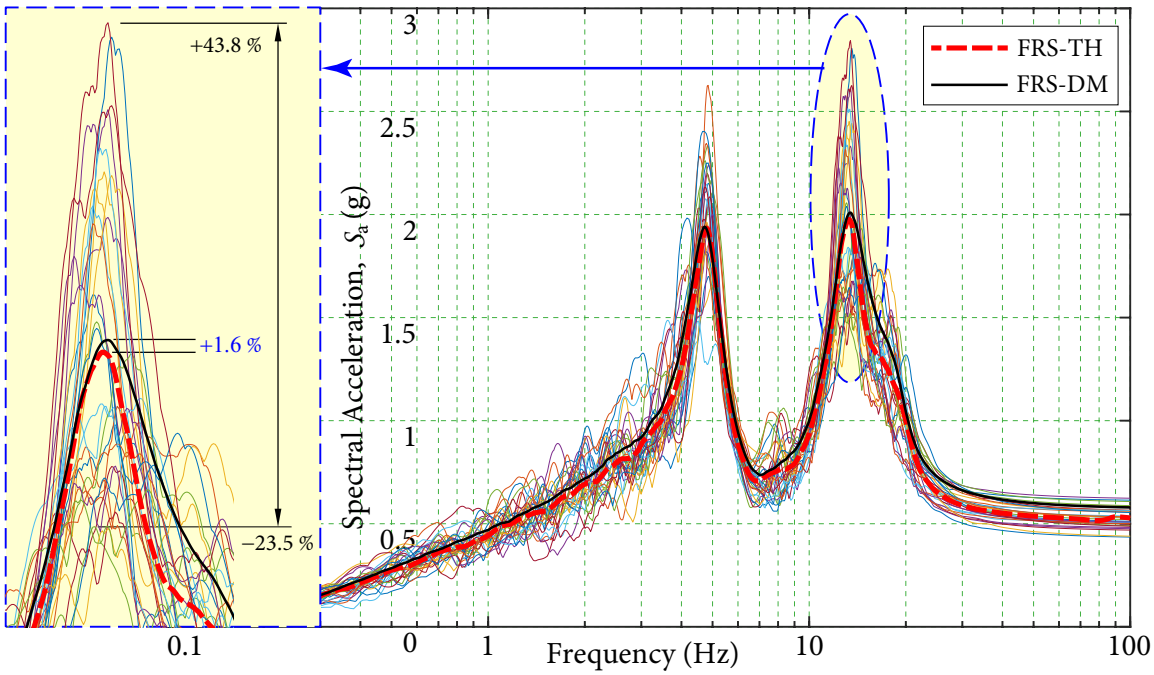


Figure 5.73 FRS in H1 direction at Node 3 in the fully independent excitation case.

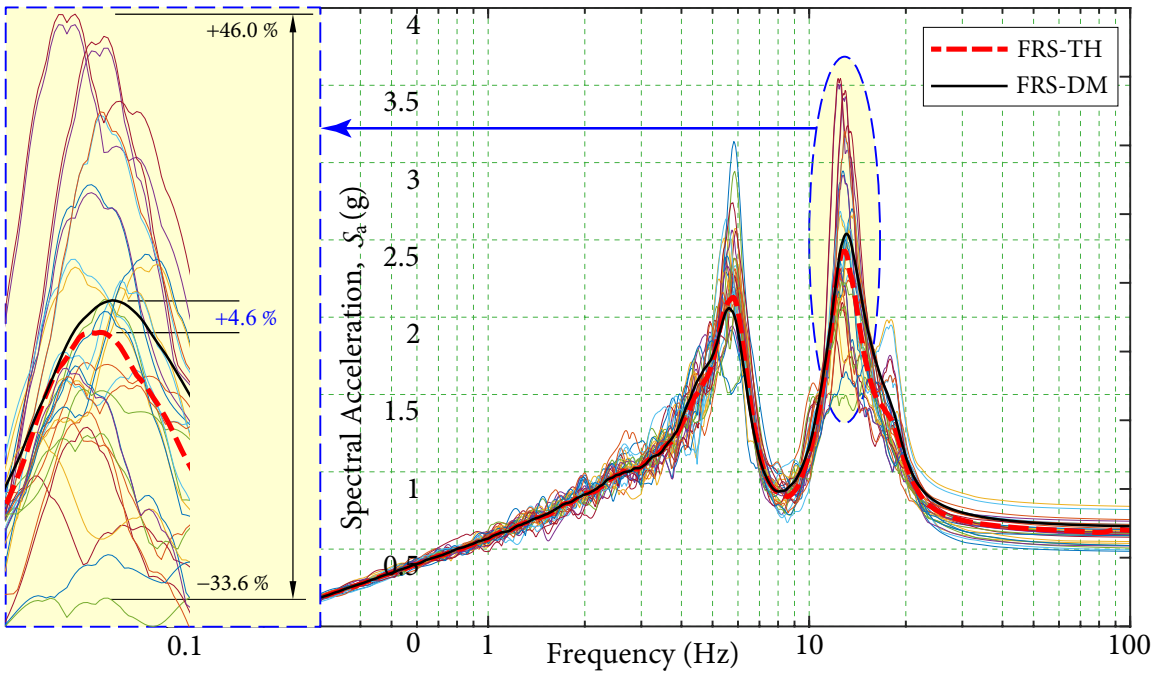


Figure 5.74 FRS in H2 direction at Node 3 in the fully independent excitation case.

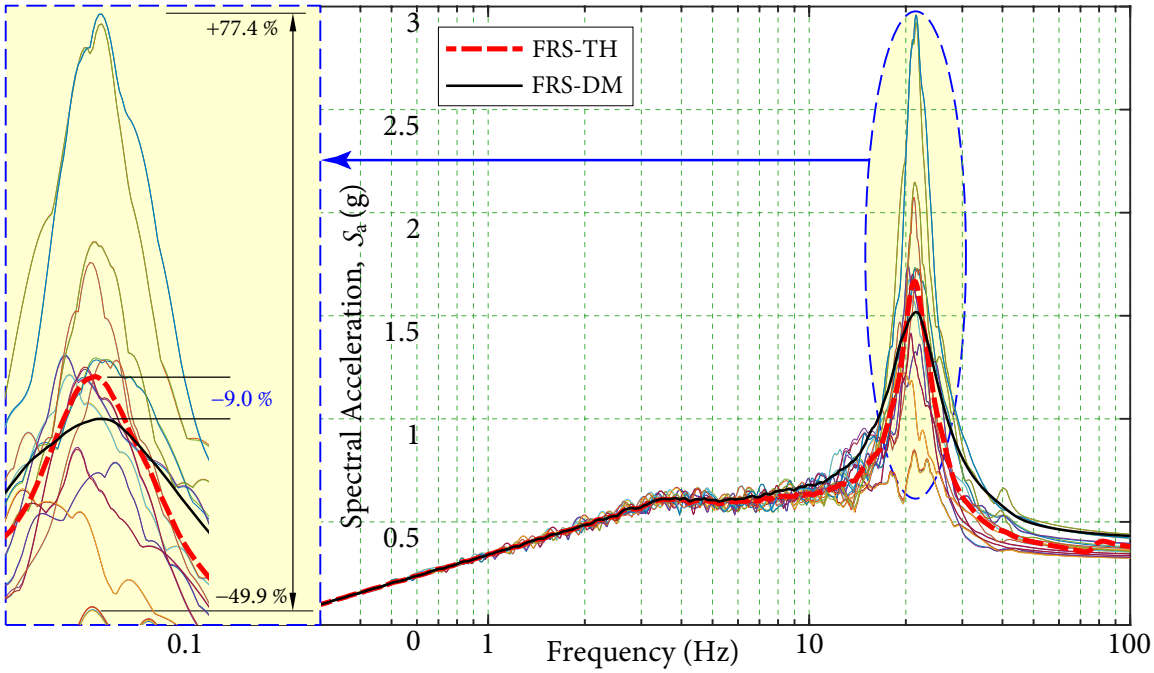


Figure 5.75 FRS in the V direction at Node 3 in the fully independent excitation case.

Based on the data shown in the table, the following observations can be made regarding the comparison between the Direct Method (DM) and Time History (TH) results:

- The FRS obtained from the direct method agrees well with the "benchmark" FRS over the entire frequency range. This agreement validates the accuracy and reliability of the direct method in generating FRS for the structure under consideration.
- The individual FRS obtained by the time history method exhibits large variability. A single set of time history analysis can lead to a maximum 77.4% overestimation or 49.8% underestimation of FRS peak depending on the input acceleration time history used.
- For all nodes, the errors in the horizontal directions (H1 and H2) are consistently small, with all values below 5% , which are well within the range of acceptable errors. This indicates that the direct method performs exceptionally well in capturing the horizontal response of the structure.
- In the vertical direction (V), the errors between the direct method and time history method results are remarkably small, except the two points in the lower elevation. The relatively larger discrepancies can be accounted for by the subsequent reason: the vertical

response is more sensitive to the high-frequency content of the seismic input motion. The spectrum in the high-frequent tRSmay in a loss of some information, leading to larger errors in the vertical FRS.

In summary, the direct method demonstrates excellent concordance with the time history method, with errors consistently remaining below 5%. Some relatively larger discrepancies observed at lower elevation nodes of the structure in the vertical direction may be attributed to the absence of some information in vertical tRS. Further research is required to address and mitigate these issues.

Table 5.6 FRS differences between time history and direct method for the fully independent case

Direction	Node	FRS_TH	TH_Max	Error_Max	TH_Min	Error_Min	FRS_DM	FRS_Error
H1	2	1.441	2.023	40.30%	1.027	-28.70%	1.399	-3.00%
H1	3	1.977	2.844	43.80%	1.513	-23.50%	2.009	1.60%
H1	5	1.117	1.637	46.50%	0.926	-17.10%	1.165	4.30%
H1	6	2.373	3.402	43.40%	1.880	-20.80%	2.399	1.10%
H1	7	3.997	5.956	49.00%	3.109	-22.20%	4.141	3.60%
H2	2	1.695	2.636	55.50%	1.227	-27.60%	1.637	-3.40%
H2	3	2.428	3.544	46.00%	1.612	-33.60%	2.540	4.60%
H2	5	1.490	2.024	35.80%	1.155	-22.50%	1.452	-2.60%
H2	6	2.993	4.115	37.50%	2.087	-30.30%	3.058	2.20%
H2	7	4.885	6.932	41.90%	3.474	-28.90%	5.109	4.60%
V	2	0.938	1.612	71.90%	0.548	-41.50%	0.821	-12.50%
V	3	1.668	2.959	77.40%	0.835	-49.90%	1.517	-9.00%
V	5	0.999	1.301	30.30%	0.739	-26.00%	0.953	-4.60%
V	6	1.840	2.540	38.00%	1.332	-27.60%	1.854	0.80%
V	7	2.387	3.333	39.60%	1.732	-27.40%	2.457	2.90%

5.5 FRS Differences Between Fully Correlated and Independent Cases

The FRS for the superstructural nodes under fully correlated and independent excitations are shown in Figures 5.76 to 5.80. Analysis of these results reveals the following characteristics:

(1). The FRS values for the fully correlated case are generally higher than those for the fully independent case, particularly near the first dominant natural frequencies.

(2). The differences in the FRS between the two cases become less significant at the nodes with higher elevation. For instance, FRS at Node 7 shows less difference compared to the other nodes.

(3). Soil-structure interaction (SSI) effects are more pronounced in the fully correlated case, causing a shift in the FRS of the structure towards first dominant natural frequencies. The frequency shift is more remarkable at Nodes 2 and 5 than at Nodes 3 and 6, respectively, indicating that the shift is more evident at nodes closer to the soil-structure interface.

These differences in the FRS can be attributed to the contrasting effects of fully correlated versus independent seismic excitations on the structural response. Under fully correlated excitations, all support nodes of the structure are subjected to identical ground motion, leading to a synchronous response, and resulting in higher peak accelerations, particularly near the first dominant natural frequencies. In contrast, independent excitations applied at each support point leads to a more randomized and less coherent response across the structure. Consequently, the peak accelerations are lower as the modal responses are not additive, and due to the cancellation effects of uncorrelated motions.

The fully correlated seismic excitations lead to higher FRS compared to independent excitations, especially at lower elevations of the structure where the modal responses are more significant. These findings underscore the importance of considering the spatial correlation of seismic inputs in the response analysis and design of structures, particularly for critical facilities like nuclear power plants where a realistic assessment of the structural demands is crucial for safety and reliability.

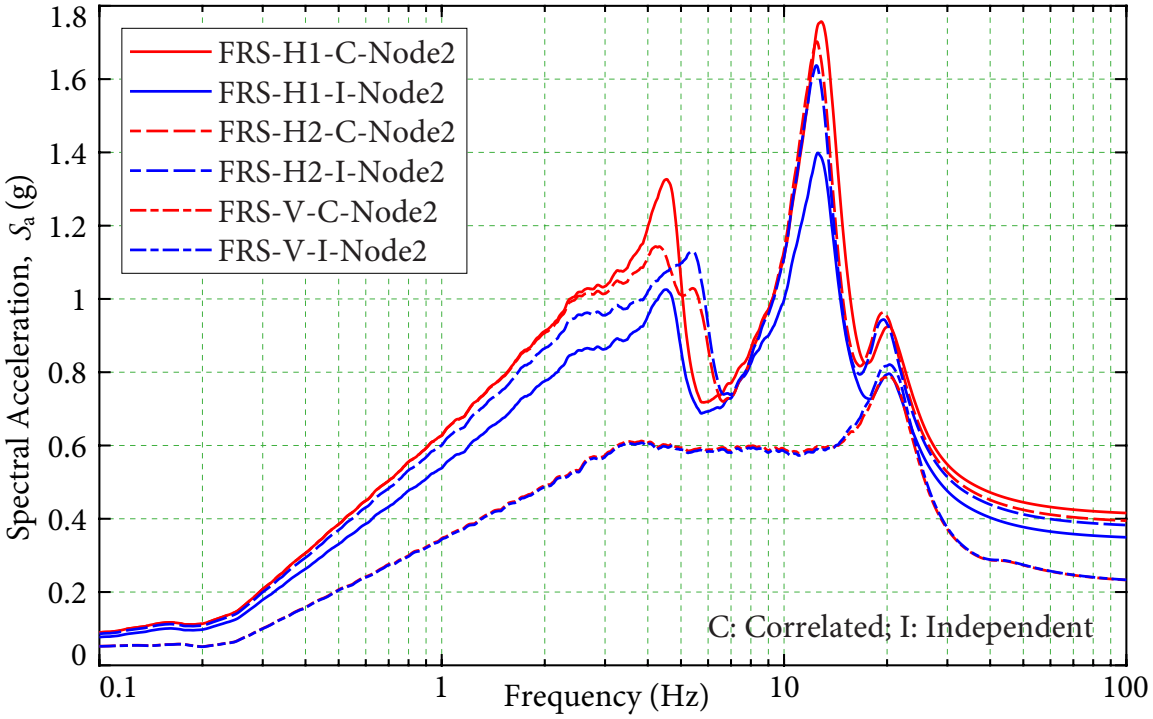


Figure 5.76 FRS-DM at Node 2 in fully correlated and independent excitation cases.

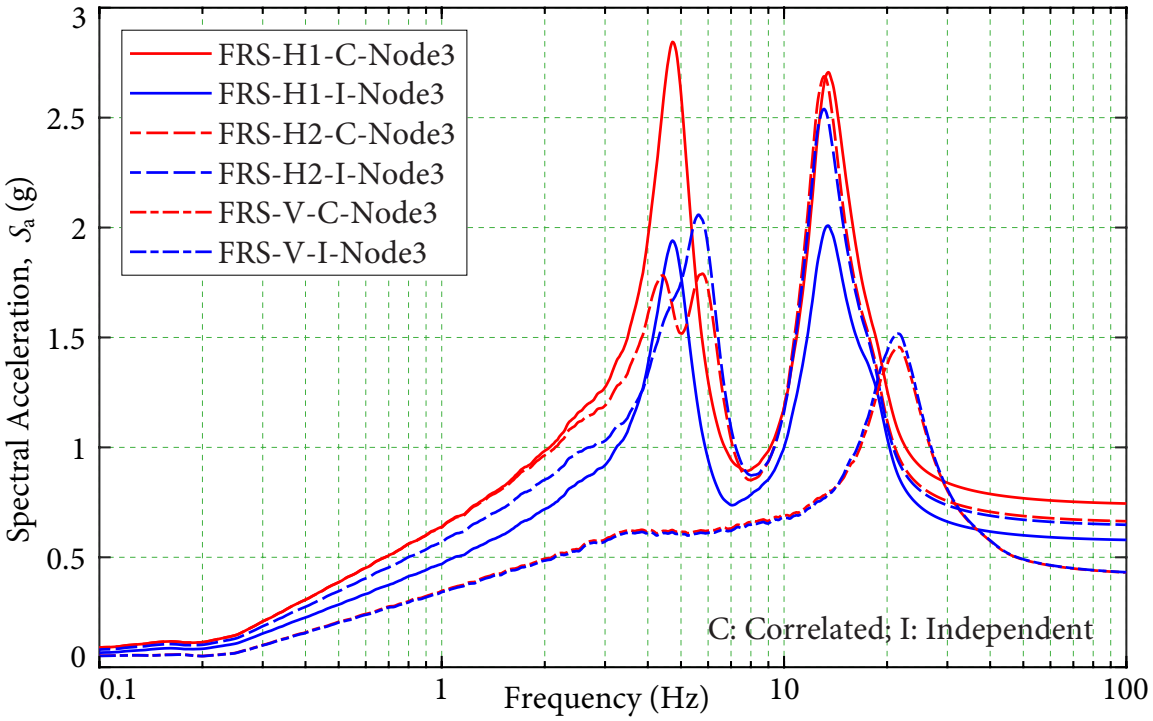


Figure 5.77 FRS-DM at Node 3 in fully correlated and independent excitation cases.

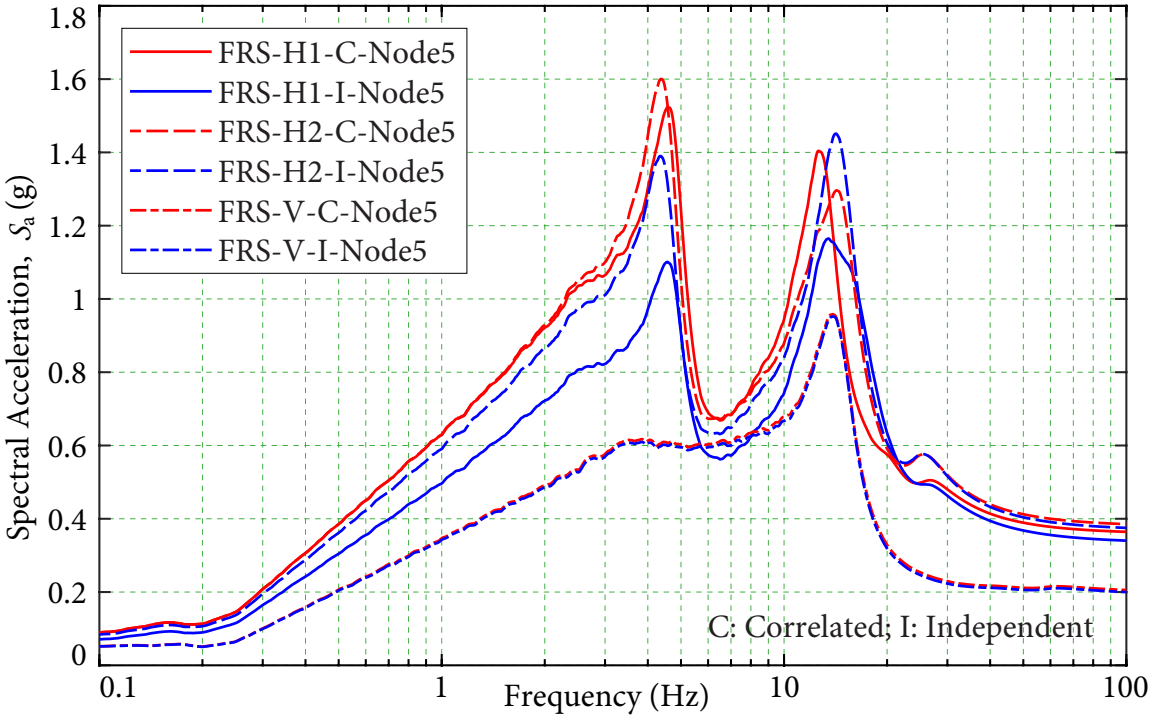


Figure 5.78 FRS-DM at Node 5 in fully correlated and independent excitation cases.

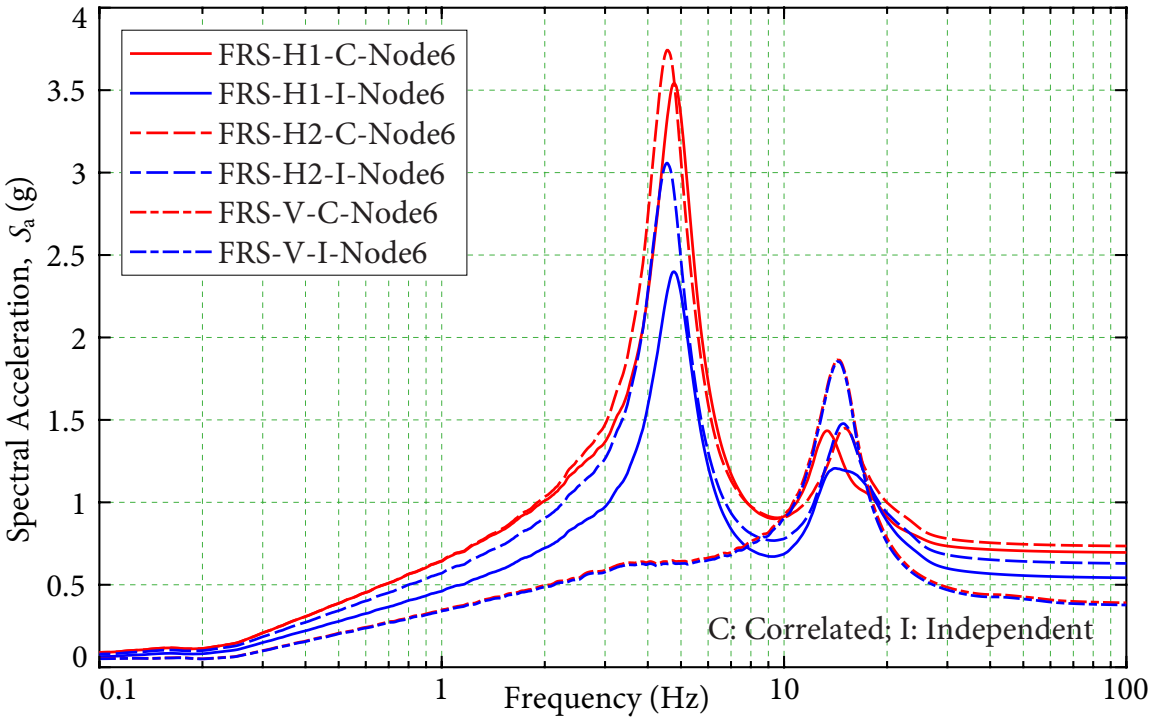


Figure 5.79 FRS-DM at Node 6 in fully correlated and independent excitation cases.

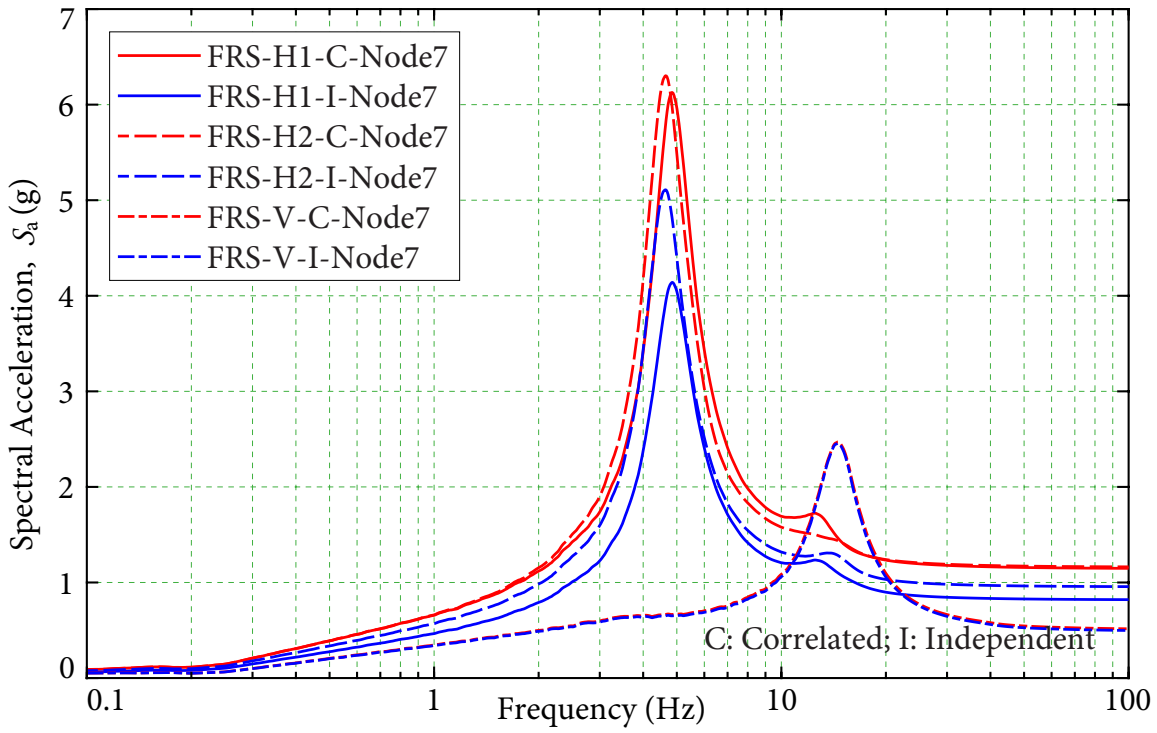


Figure 5.80 FRS-DM at Node 7 in fully correlated and independent excitation cases.

5.6 Influence of Site Conditions on FRS

The seismic response of structures, including NPPs and SMRs, is significantly influenced by the characteristics of the underlying soil. The importance of considering site-specific soil properties in seismic analysis and design has been recognized by various standards and guidelines, such as ASCE 7-10 (2010), which categorizes site conditions into several classes based on the properties of the soil strata. These site classes correspond to different soil profiles, ranging from hard rock to soft clay, and are characterized by their shear wave velocity, standard penetration resistance, and undrained shear strength.

The characteristics of the soil at an NPP site play a crucial role in determining the seismic response of the structure and the resulting FRS. The soil properties affect the amplitude, frequency content, and duration of the seismic ground motion that propagates through the soil layers and reaches the foundation of the structure. The soil-structure interaction (SSI) effects, which involve the dynamic coupling between the structure and the soil, are

highly dependent on the soil properties. Softer soils, with lower shear wave velocities and stiffness, tend to amplify the low-frequency components of the ground motion and increase the overall seismic demand on the structure. On the other hand, stiffer soils or rock sites may result in higher-frequency ground motions and reduced SSI effects.

Considering the critical safety requirements of NPPs, it is essential to accurately account for the site-specific soil characteristics in the seismic analysis and design process. Failure to properly consider the soil properties may lead to an underestimation or overestimation of the seismic demand on the structure and the equipment housed within it, potentially compromising the safety and functionality of the NPP during and after a seismic event.

5.6.1 Key Soil Parameters in This Study

A parametric study with related to the influence of site conditions on the FRS of NPP structures is conducted considering different site classes as per ASCE 7-10 (2010). The standard classifies sites mainly by considering shear wave velocity (V_s), (1) Site Class A: Hard rock with an average shear wave velocity (V_s) greater than 1500 m/s. (2) Site Class B: Rock with an average V_s between 760 m/s and 1500 m/s. (3) Site Class C: Very dense soil and soft rock with an average V_s between 360 m/s and 760 m/s. (4) Site Class D: Stiff soil with an average V_s between 180 m/s and 360 m/s. (5) Site Class E: Soft clay soil with an average V_s less than 180 m/s. (6) Site Class F: Soils vulnerable to potential failure or collapse under seismic loading, such as liquefiable soils, quick and highly sensitive clays, and collapsible weakly cemented soils.

The shear wave velocity is a measure of the soil stiffness and is directly related to the shear modulus of the soil. It controls the propagation speed of seismic waves through the soil layers and influences the frequency content of the ground motion. The selected shear wave velocity V_s , unit weight γ , and Poisson's ratio ν for certain sites are listed in Table 5.7. The parameters are based on typical values encountered in geotechnical engineering practice. It is important to note that the actual values of the parameters may vary depending on factors such as the specific soil type, confining pressure, and strain levels. The dynamic soil stiffness matrices for each type of site are obtained through the method proposed in 4.1.

Table 5.7 Selected soil parameters for different sites

Case	Site Class	Soil Type	V_s / m/s	γ / kN/m^3	ν	E / MPa
A	A	Hard Rock	2000	28.50	0.26	2.93×10^3
B	B	Regular Rock	1000	27.50	0.27	7120
C	C	Dense Clay or Soft Rock	600	26.20	0.28	2461
D	D	Stiff Soil	300	24.50	0.30	584

5.6.2 FRS for Soil in Different Sites

A parametric study is performed in this section to investigate the influence of soil in different sites on FRS for multi-supported structures. The input FIRS are 30 sets of R.G. 1.60, and the properties of the soils in each case are shown in Table 5.7.

Soil Case A

The FRS in H1 direction at superstructural nodes 7 for soil case A under seismic excitations of fully correlated cases is shown in Figure 5.81. The FRS for nodes 2, 3, 5, 6, are shown in Appendix D.

Soil Case B

The FRS in H1 direction at superstructural nodes 7 for soil case B under seismic excitations of fully correlated cases is shown in Figure 5.82. The FRS for nodes 2, 3, 5, 6, are shown in Appendix D.

Soil Case C

The FRS in H1 direction at superstructural nodes 7 for soil case A under seismic excitations of fully correlated cases is shown in Figure 5.83. The FRS for nodes 2, 3, 5, 6, are shown in Appendix D.

Soil Case D

The FRS in H1 direction at superstructural nodes 7 for soil case A under seismic excitations of fully correlated cases is shown in Figure 5.84. The FRS for nodes 2, 3, 5, 6, are shown in Appendix D.

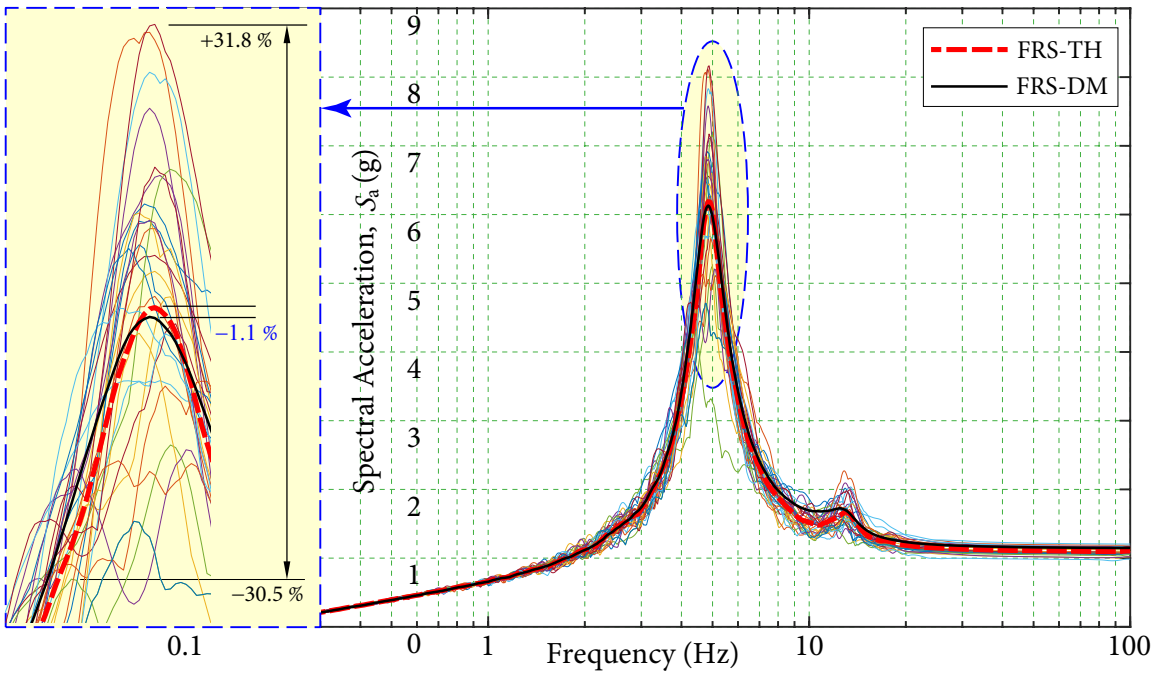


Figure 5.81 FRS in H1 direction at Node 7 for soil case A (correlated).

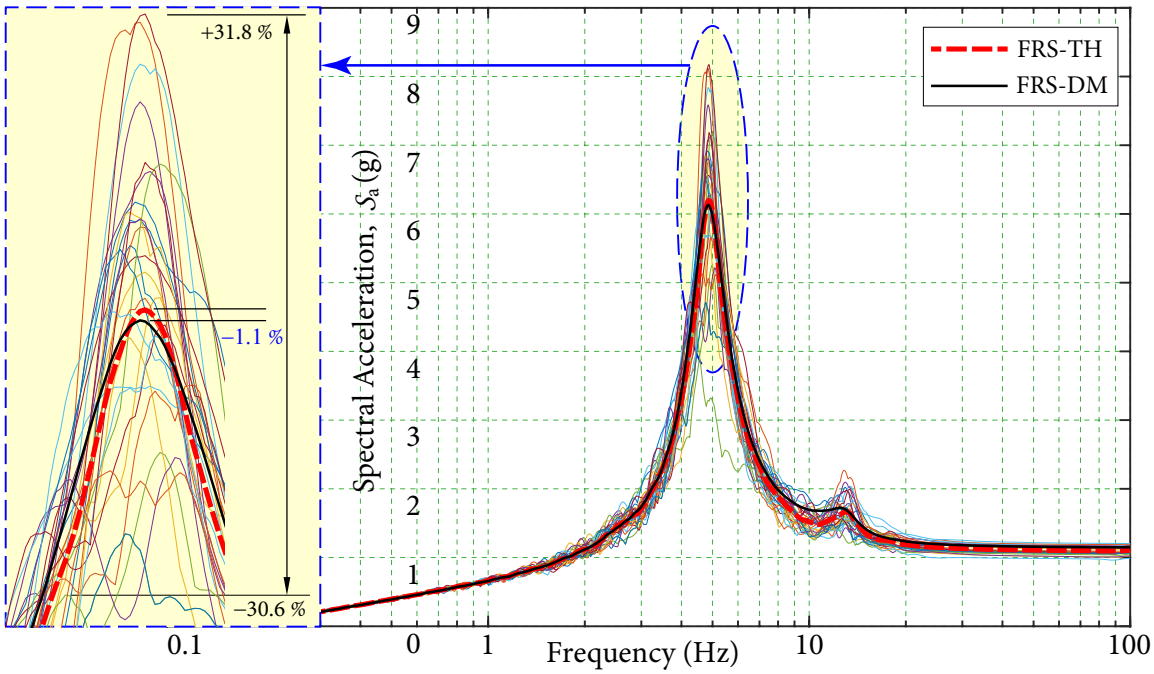


Figure 5.82 FRS in H1 direction at Node 7 for soil case B (correlated).

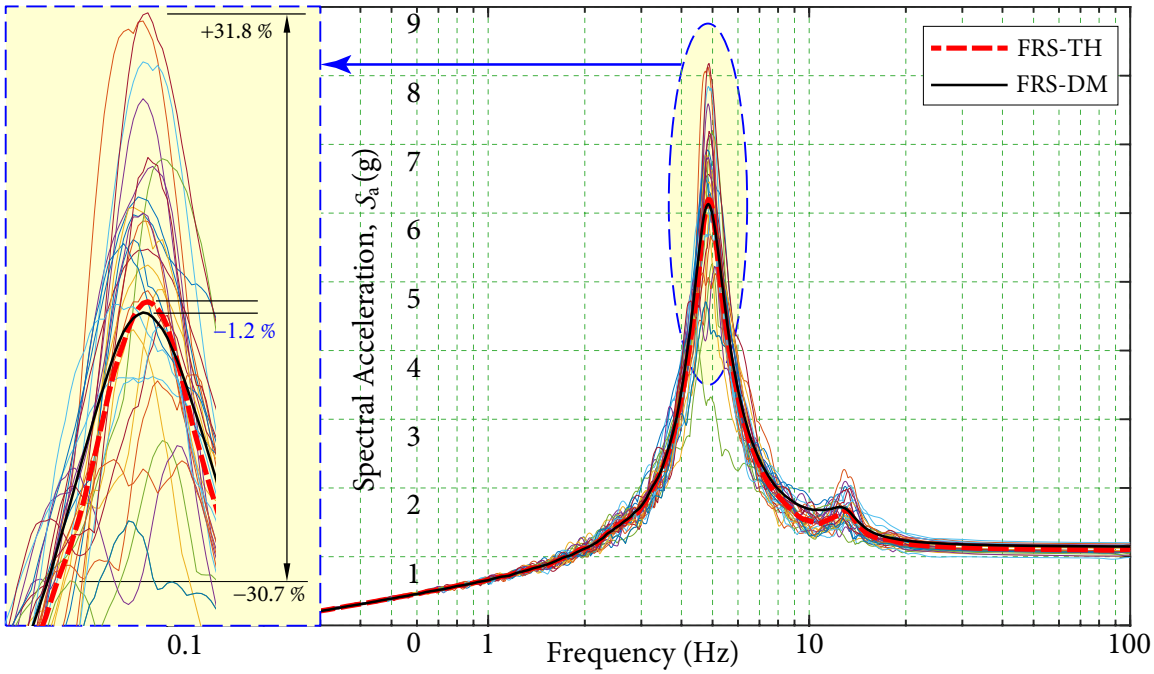


Figure 5.83 FRS in H1 direction at Node 7 for soil case C (correlated).

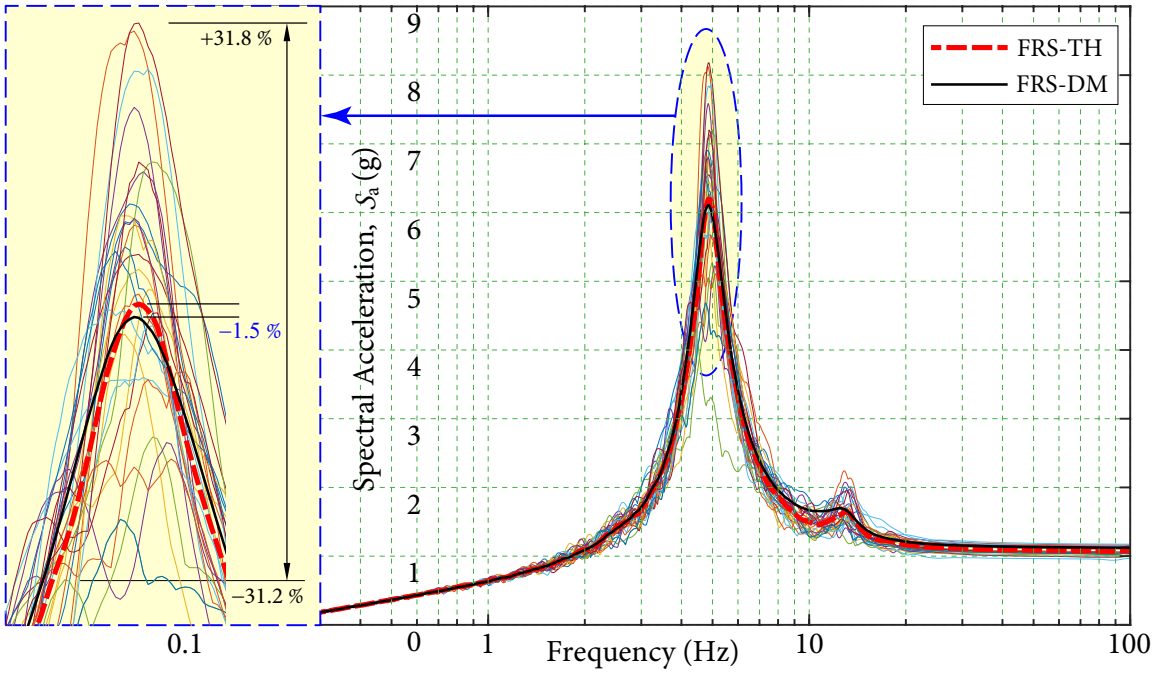


Figure 5.84 FRS in H1 direction at Node 7 for soil case D (correlated).

5.6.3 Discussion

The comparison of FRS between the Time History method and Direct Method for all four site cases are illustrated graphically. FRS differences are visually depicted for sites A, B, C, and D. The graphical analysis indicates that the FRS obtained from the direct method closely aligns with the "benchmark" FRS across a broad frequency range for all the sites, suggesting that the proposed direct method is applicable and yields reliable results for these soil sites.

However, some large deviations are observed in the FRS comparison for site D. As discussed earlier, these discrepancies can primarily be attributed to the need for refining tRS. Nonetheless, it is essential to note that all nuclear power facilities must be constructed on rigid materials, indicating that the proposed direct method performs exceptionally well in the dynamic response analysis of nuclear facilities.

5.7 Influence of Coupling Element Stiffness on FRS

The dynamic interaction between internal structures and containment in nuclear facilities plays a crucial role in their overall seismic response. This section investigates the influence of coupling element stiffness on FRS, focusing on the horizontal beams (elements 6 and 7 in Figure 5.1) that link these components. Despite their significance, these elements are often simplified or overlooked in preliminary analyses, potentially leading to inaccuracies in FRS generation and subsequent equipment qualification.

This study employs a parametric approach, systematically varying the stiffness of beams 6 and 7 to quantify their impact on FRS. The analysis utilizes the direct method, enabling rigorous comparison across different stiffness configurations.

5.7.1 Stiffness Variation of Coupling Elements

Three distinct stiffness cases were considered: "Small", "Medium", and "Large", as listed in Table 5.8. This range allows examination of scenarios from highly flexible to rigid coupling connections between internal structure and containment. This approach enables

understanding of how coupling element stiffness interacts with different seismic input characteristics to influence FRS.

5.7.2 FRS Results and Analysis

FRS were evaluated for superstructural nodes 2, 3, 5, 6, and 7 in all three directions, under both fully correlated and fully independent excitations. For conciseness, the analysis focuses on H1 direction, as other directions exhibit similar characteristics.

Fully Correlated Case

FRS for internal structure nodes 2, 3 are presented in Figures 5.85-5.86, while those for containment nodes 5, 6, and 7 are shown in Figures 5.87-5.89.

Internal Structure Nodes

The analysis reveals that the peak amplitude at the first dominant frequency increases with the stiffness of the coupling elements. Specifically, the highest stiffness results in the highest peak, while the lowest stiffness results in a slightly lower peak. Interestingly, the intermediate stiffness scenario shows the lowest peak at the first dominant frequency. This suggests that an optimal range of stiffness exists that minimizes the FRS, indicating that neither extreme stiffness nor maximum flexibility is ideal.

Conversely, the second dominant frequency displays an inverse trend. The highest stiffness results in the lowest peak amplitude, while the intermediate stiffness leads to the highest peak. This inverse relationship indicates that energy is primarily concentrated in the first mode when stiffness is highest, shifting to the second mode as stiffness decreases.

Containment Nodes

Table 5.8 Stiffness variation cases for coupling elements

Case	1	2	3
Description of Stiffness	Small	Medium	Large
E / N/m^2	4.00×10^5	4.00×10^8	4.00×10^{10}
k / kN/m	2.67×10^3	2.35×10^7	8.00×10^{10}

The variation of peaks at the first dominant frequency are opposite to that of the internal structure node. The increased stiffness in the coupling elements transfers more energy to the internal nodes at the first dominant frequency, resulting in higher peaks. Simultaneously, the external nodes exhibit reduced peaks at the first dominant frequency and increased peaks at the second dominant frequency. This indicates a transfer of seismic energy from the internal to external linked nodes (2 and 5, 3 and 6) with increasing stiffness.

Node 7, in particular, exhibits a unique behavior. The effectiveness of stiffness in reducing the FRS peak is less pronounced for this node. However, when the stiffness is at its maximum, a noticeable frequency shift occurs at the peak. This shift can be attributed to an increase in the structure's natural frequency due to the enhanced stiffness. The increase in natural frequency indicates that the structure becomes stiffer, thus altering its dynamic characteristics and the way it responds to seismic excitation.

Fully Independent Case

Similarly, FRS for internal structure nodes 2, 3 and containment nodes 5, 6, 7 under independent excitations are illustrated in Figures 5.90-5.91 and Figures 5.92-5.94, respectively.

- **Internal Structure Nodes**

The FRS reveals a similar pattern as correlated case based on the stiffness of coupling elements. The peak amplitudes at first dominant frequency show less sensitivity to stiffness changes, while the peak variation at second dominant frequency exhibits a larger decrease in the amplitude. These observations suggest that independent excitation tends to mitigate the effects of coupling element stiffness on the internal structure's response, particularly at higher frequencies.

- **Containment Nodes**

Different from the correlated case, where peaks of internal nodes increased as peaks of external nodes decreased with varying stiffness, the independent excitation scenario exhibits a more synchronized response. FRS peaks for both internal and external nodes tend to increase or decrease together across different stiffness cases. This pattern is particularly evident in the nodes with lower elevation.

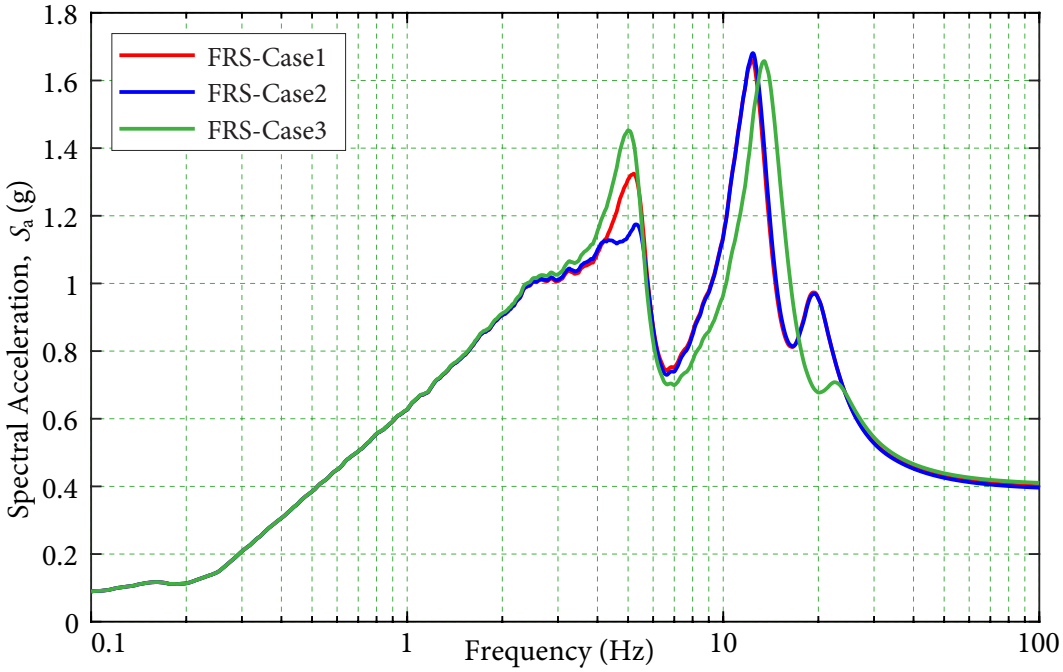


Figure 5.85 FRS for internal node in H1 direction for fully correlated case (Node 2).

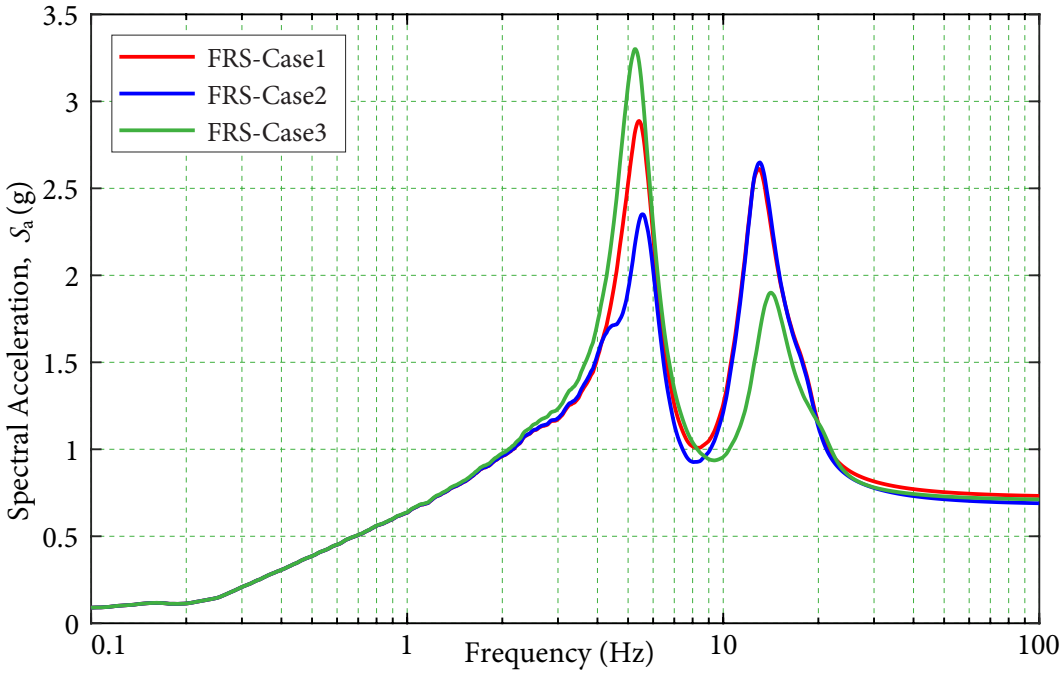


Figure 5.86 FRS for internal node in H1 direction for fully correlated case (Node 3).

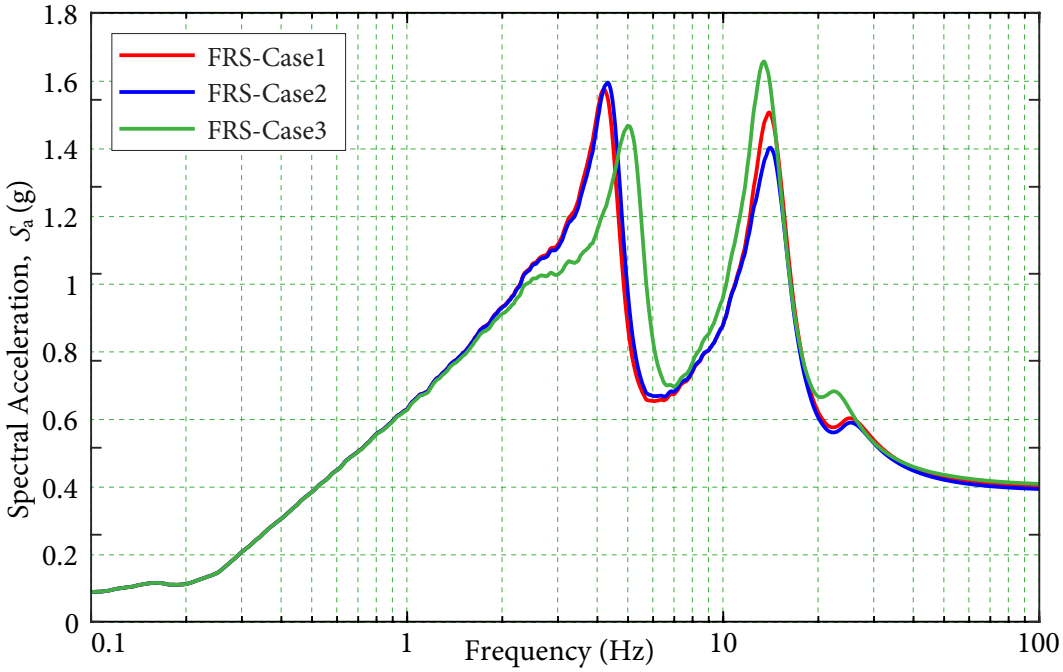


Figure 5.87 FRS for containment node in H1 direction for fully correlated case (Node 5).

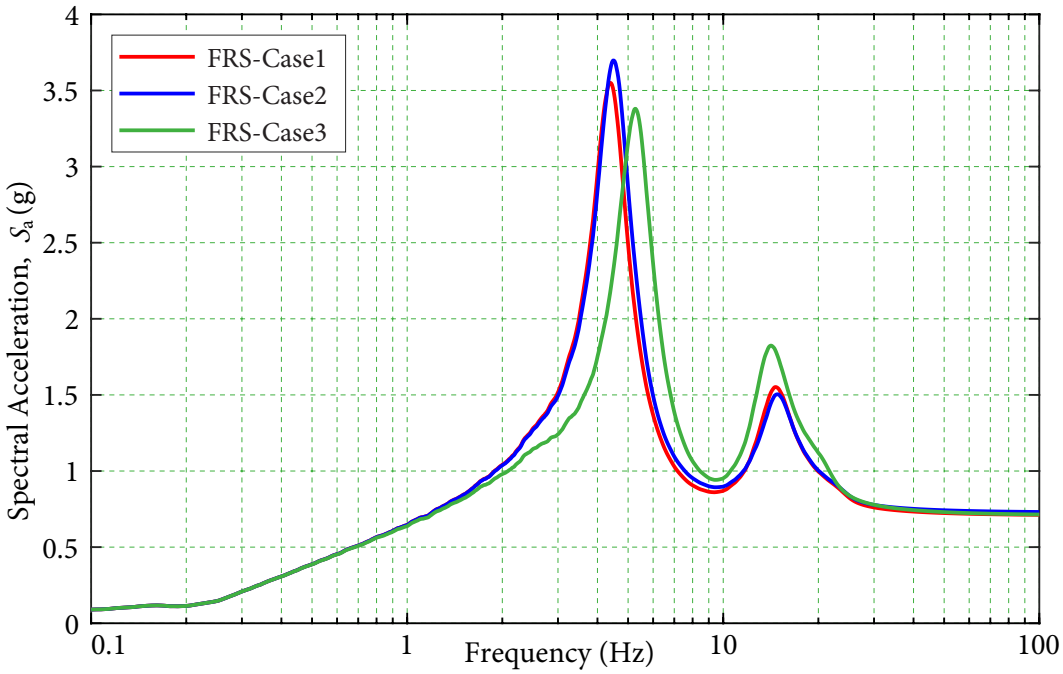


Figure 5.88 FRS for containment node in H1 direction for fully correlated case (Node 6).

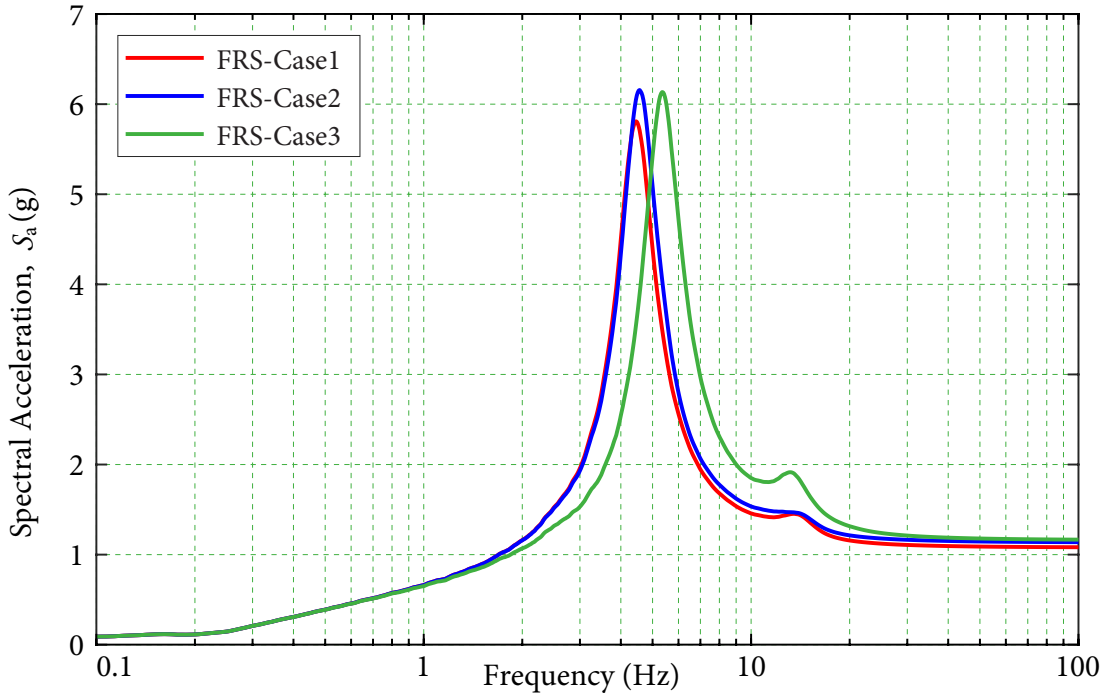


Figure 5.89 FRS for containment node in H1 direction for fully correlated case (Node 7).

That is because, (1) the independent excitations appear to diminish the coupling effect between the internal structure and containment. This reduction in coupling means that energy is not as readily transferred between these components, leading to more independent responses. (2) The independent excitation at each support point may cause local responses to dominate over the global structural response. As for Node 7, the FRS behaviour shows similarities to the correlated case.

Furthermore, as can be observed from the results, the overall amplitude of FRS in the independent case is lower than that of correlated case. This is similar to the previous observations.

5.7.3 Discussion

The observed phenomena can be explained in the following perspectives,

(1) Modal Energy Distribution: Stiffness variations alter the participation factors of different modes. Higher stiffness enhances the contribution of the first mode for internal nodes, the modal characteristics and frequency responses thus been changed.

(2) Structural Coupling Effects: The inverse relationship between internal and external node responses suggests that increased stiffness facilitates energy transfer from the containment to the internal structure, particularly at the first dominant frequency.

(3) Optimal Stiffness Range: An optimal stiffness range is exists for minimizing FRS peaks. It suggests that carefully tuned coupling element stiffness can create beneficial interaction between the internal structure and containment, potentially leading to energy redistribution that reduces peak responses.

5.8 Summary

This chapter presents a thorough analysis for generating FRS for structures in the nuclear industry, considering multi-support seismic excitations and SSI effects. The study utilizes the direct method for FRS generation, comparing it with traditional time history analyses for validation and efficiency evaluation.

The dynamic soil stiffness matrix is evaluated using the inverse of the unitized dynamic flexibility matrix method proposed in Chapter 4. This approach significantly reduces dependence on specialized commercial software like ACS SASSI, allowing the use of any FEM tool for dynamic soil stiffness matrix analysis. This flexibility enhances the accessibility and efficiency of SSI analysis in nuclear facility design, offering a more versatile solution for seismic response evaluation.

Two seismic input scenarios, fully correlated and fully independent excitations at multiple support points, are explored. The direct method shows excellent agreement with "benchmark" time history results, particularly in horizontal directions, with errors consistently below 5% . Discrepancies in the vertical direction can attributed to limitations in the tRS, which has to be further refined.

A parametric study across different soil classes per ASCE 7-10 standards is conducted to investigate the influence of site conditions on FRS. The method demonstrates robust performance across various soil conditions.

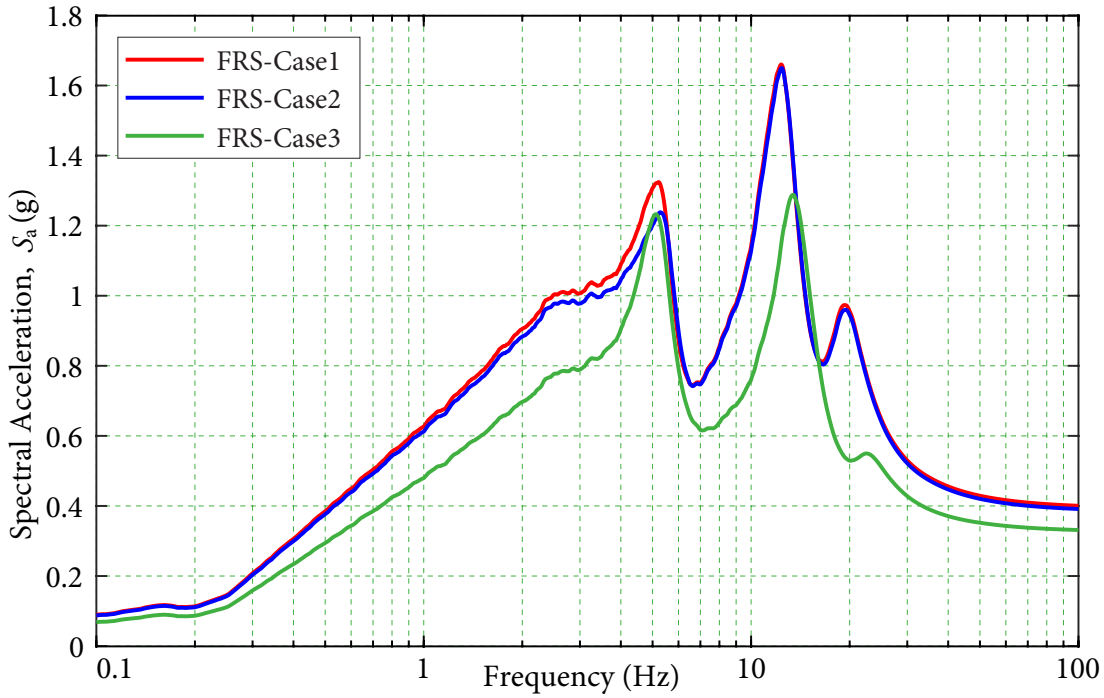


Figure 5.90 FRS for internal node 2 in H1 direction for fully independent case.

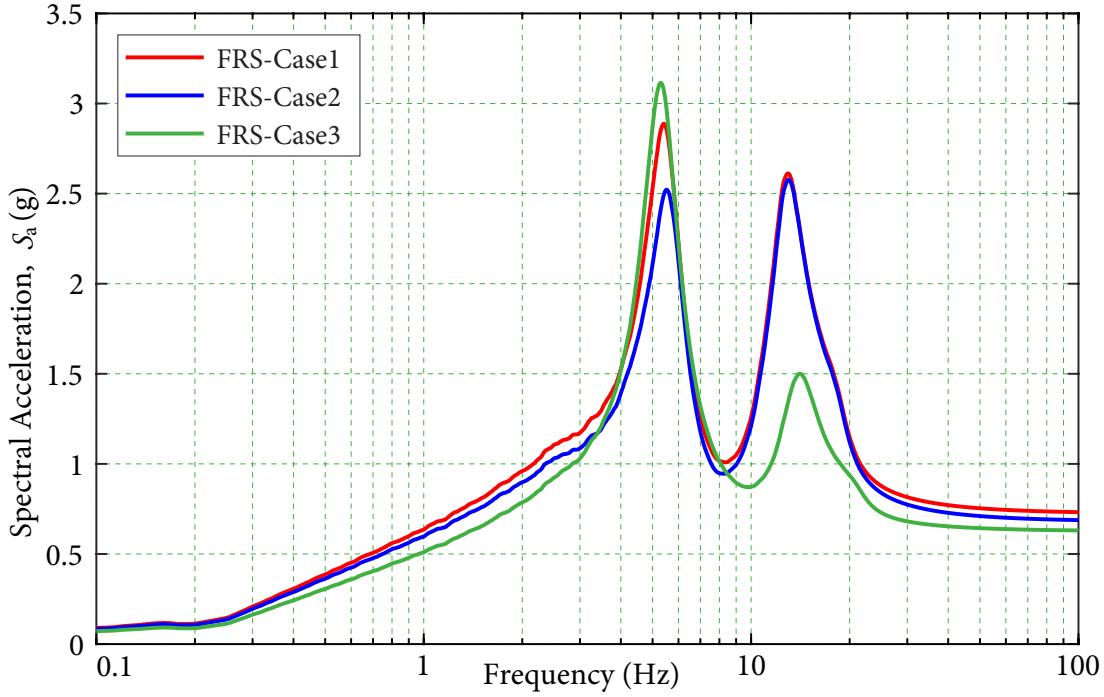


Figure 5.91 FRS for internal node 3 in H1 direction for fully independent case.

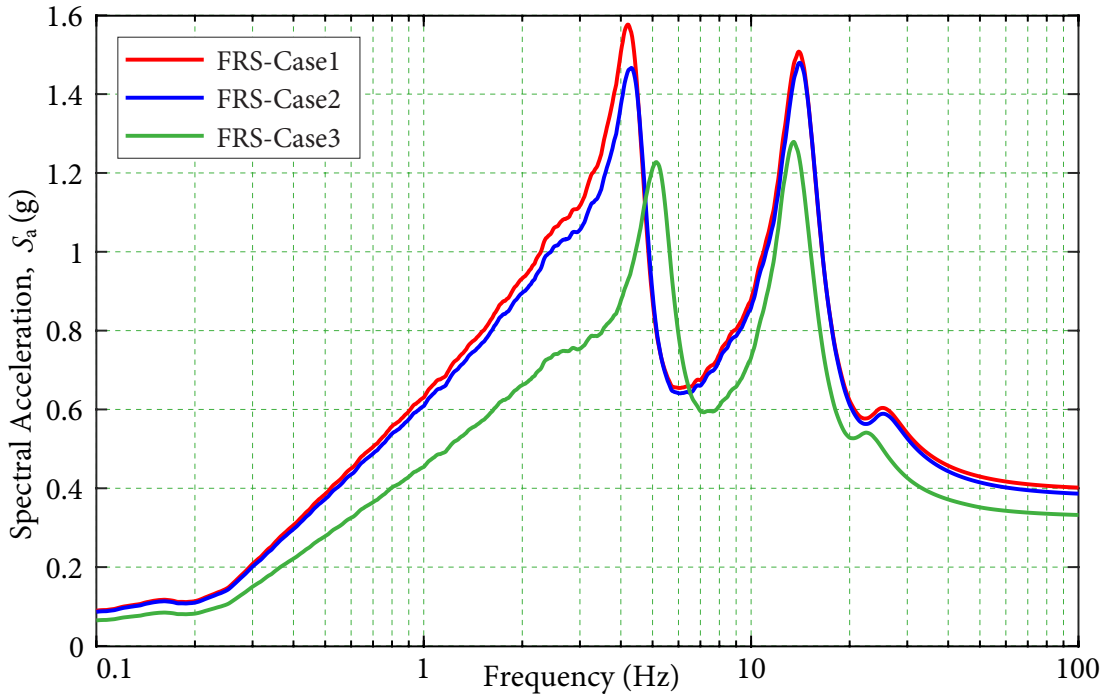


Figure 5.92 FRS for containment node 5 in H1 direction for fully independent case.

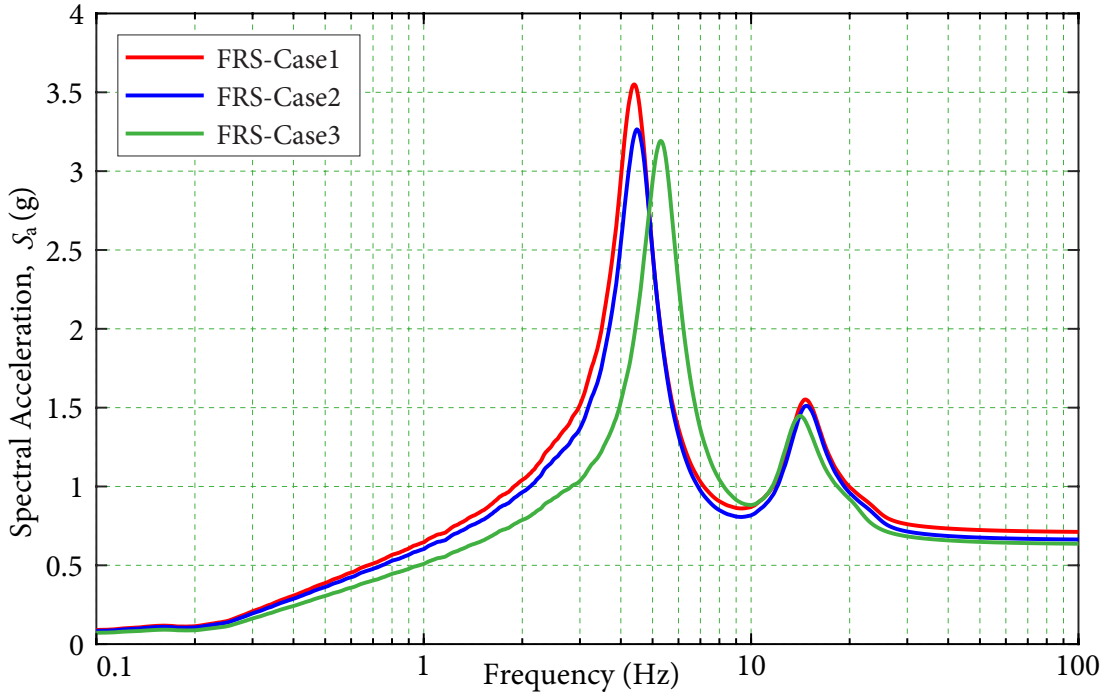


Figure 5.93 FRS for containment node 6 in H1 direction for fully independent case.

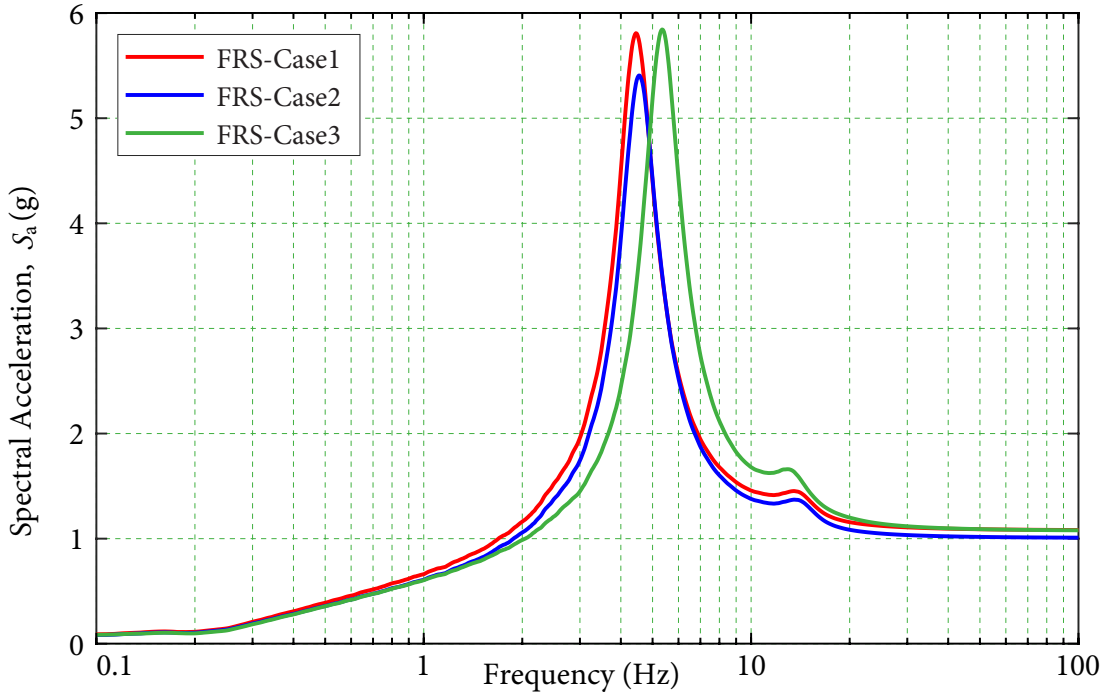


Figure 5.94 FRS for containment node 7 in H1 direction for fully correlated case.

The impact of coupling element stiffness on FRS is also examined, providing insights into optimal stiffness ranges for minimizing FRS peaks and highlighting complex energy transfer mechanisms between structural components.

These achievements demonstrate that the proposed direct method for structures with multiple supports considering SSI is robust and reliable, particularly applicable for structures with complex foundation systems, such as SMRs.

C H A P T E R 6

Conclusions and Future Research

Floor Response Spectrum (FRS) is critical in seismic analysis and design of secondary systems in nuclear power facilities. Generation of FRS for structures with multiple support excitations considering soil-structure interaction (SSI) is paramount for NPPs, especially for the emerging SMRs. The objective of this study is to develop an approach to address SSI effect with flexible foundations and seismic input at multiple points in the generation of FRS. FRS is developed after considering SSI effect accurately and efficiently in this study. Some contributions for this purpose have been accomplished in this study, and are summarized as follows.

6.1 Direct Spectra-to-Spectra Method for Generating Floor Response Spectra

A direct spectra-to-spectra method is developed for generating FRS of multi-supported structures. "Direct" means Ground Response Spectrum (GRS) is used as seismic input directly without generating any intermediate input, such as artificial spectrum-compatible time histories. Only the information used in conventional response spectrum analysis, such as the input ground motions GRS and the basic modal information, is needed in the proposed method. Some remarkable features and advantages of the proposed direct spectra-to-spectra method are summarized as follows:

- The direct method gives accurate FRS for structures with multiple supports; FRS obtained by this method agree extremely well with the "benchmark" results obtained from a large number of time history analyses. Particularly, the direct method can deal with the resonance cases, corresponding to FRS peaks, properly, which has not been satisfactorily solved in previous direct spectrum-to-spectrum methods. It is shown that FRS obtained by a single time history method has large variabilities. Therefore, if a single or a small number of time history analyses are performed to generate FRS, the result is not reliable, while it is very computationally expensive to perform a large number of time history analyses. The proposed method can avoid the deficiencies of the time history method.
- By using the concept of tRS, the direct method can give full probabilistic descriptions at FRS peaks, which can satisfy various seismic design and assessment requirements for SSCs with different safety margins.
- The direct method is analytically formulated and it is convenient to implement in any programming software such as MATLAB. Furthermore, the direct method is highly efficient because it only has to run analysis once. On the contrary, much more computational efforts are required in the application of the time history method to obtain a reliable result.

6.2 Generating FRS Considering Soil-Structure Interaction

The effect of soil-structure interaction (SSI) has great influence on the seismic behaviour of primary structures and supported secondary systems. A methodology is developed to generate FRS for multi-supported structures considering SSI effect, using the substructure method and the proposed direct spectra-to-spectra method. Some remarkable features and advantages of the proposed method are summarized as follows:

- A method of determining FLIRS modification factors for the Foundation Input Response Spectra (FIRS), which is obtained from a free-field site response analysis, is developed to integrate the SSI effect. The modified FIRS, called Foundation Level

Input Response Spectra (FLIRS), are input to the decoupled model to generate FRS using the direct spectra-to-spectra method.

- FLIRS can be generated directly by multiplying FIRS by the FLIRS modification factor. The FLIRS modification factor is derived based on the transfer function, and is given implicitly depend on the structural information and the soil properties. It has been proved that FRS of the decoupled structure using FLIRS is theoretically equivalent to that generated by the combined soil-structure system using FIRS.
- The proposed method considering SSI is demonstrated using a numerical example. FRS obtained by the proposed method agree well with "benchmark" results obtained from a large number of time history analyses.
- Performing a large number of time history analyses can be avoided in the whole process, from which the computational cost has been considerably reduced. More importantly, the variabilities in the time history method are eliminated by applying the proposed method. A reanalysis of the entire soil-structure system can be avoided when the properties of the superstructure or soil are changed; thus the efficiency of the proposed method is further improved. Furthermore, instead of evaluating the inverse of a $6N \times 6N$ matrix, only the inverse of a $6M \times 6M$ matrix is required, in which N and M are the number of the nodes of the structure and the foundation, respectively. Because the number of supports is generally much less than the number of structural nodes, the numerical difficulties of a large-scale system can be avoided.
- It is found that the consideration of SSI may either increase or reduce the seismic responses depending on soil conditions. Besides of the modification of the magnitude of FRS due to the presence of soil, the shifting of FRS peaks also deserves much attention in engineering practice. Neglecting this effect could lead to nonconservative results around the frequencies of the combined soil-structure system.

6.3 Evaluation of Dynamic Soil Stiffness Matrices

A comprehensive methodology is developed for the derivation, evaluation, and validation of dynamic stiffness matrices, providing a critical foundation for seismic analysis considering SSI. The key features and conclusions are summarized as follows:

- A rigorous theoretical foundation is established, demonstrating that the dynamic stiffness matrix can be obtained by inverting the unitized dynamic flexibility matrix. This provides a solid mathematical basis for subsequent numerical methods and establishes a clear procedure for practical applications.
- A novel approach is introduced for applying sinusoidal excitation and analyzing the steady-state response's amplitude and phase lag to calculate the real and imaginary parts of the dynamic response. This method is validated using both lumped-mass and continuous-mass systems, offering a viable numerical approach for dynamic analysis of complex systems.
- The methodology is successfully extended to 3D half-space soil models, a significant step towards practical engineering problems. By analyzing the variation of dynamic flexibility matrices for nodes along study profiles under different loading directions, and comparing results with classical analytical solutions, the accuracy of the numerical method is verified.
- A progressive validation strategy is employed, starting from simple systems and gradually moving to more complex ones. This approach ensures the reliability of the method at each step and provides insights into its applicability across different levels of complexity in structural systems.
- The numerical approach potentially offers significant computational advantages over traditional complicated mathematical methods, especially for complex soil-structure interaction problems. This efficiency is crucial for practical applications in the design and analysis of nuclear facilities.
- The theoretical rigorous of the method, combined with its demonstrated accuracy in numerical applications, makes it a valuable approach for seismic analysis and design

of nuclear power plant structures, particularly in addressing complex soil-structure interaction problems in SMRs. Moreover, this approach effectively eliminates the need for specialized software like ACS SASSI, enabling the calculation of dynamic soil stiffness matrices using general-purpose finite element software. This feature not only enhances the method's accessibility and flexibility but also potentially reduces costs and learning curves associated with specialized software in the nuclear industry.

6.4 Application to Multi-Support Excitations and SSI Effects

The developed methodology is applied to generate FRS for structures in the nuclear industry, accounting for multi-support seismic excitations and SSI effects. The key findings and advantages are as follows:

- The direct method shows excellent agreement with "benchmark" time history results, particularly in horizontal directions, with errors consistently below 5% . This demonstrates the accuracy and reliability of the proposed direct method for practical applications.
- Two seismic input scenarios, fully correlated and fully independent excitations at multiple support points, are successfully explored, showcasing versatility of the proposed direct method in handling different seismic input conditions.
- A parametric study across different soil classes per ASCE 7-10 standards reveals the robust performance of the proposed direct method across various soil conditions, with some limitations noted for very soft soils. This provides valuable insights into the influence of site conditions on FRS.
- The impact of connecting element stiffness on FRS is examined, providing insights into optimal stiffness ranges for minimizing FRS peaks and highlighting complex energy transfer mechanisms between structural components.
- The ability to handle multi-support excitations and SSI effects simultaneously represents a significant advancement in the field of seismic analysis for nuclear structures, particularly for SMRs with complex foundation configurations.

6.5 Future Research

Based on the findings and contributions of this study, several promising directions for future research have been identified:

- Refinement of tRS Approach

  Statistical expressions of ttRS will be investigated. ttRS represents the maximum response of an oscillator mounted on an identical oscillator supported by another identical one. This development aims to enhance the accuracy of the tRS approach, particularly for vertical response predictions where current methods show limitations. Once ttRS has been obtained, a new direct method for generating TRS will be developed, allowing for the direct generation of TRS from GRS. This will simplify the current procedures for generating TRS using F-tRS or tRS as the intermediate outputs, such as FRS, are not required. Furthermore, the minor error in TRS obtained using the approximation on F-tRS can be further avoided.

- Application to SMR Case Studies

  While the developed methods are already applicable to deeply embedded Small Modular Reactors (SMRs), future research will focus on implementing these methodologies in specific SMR case studies. This practical application will provide valuable insights into the method's performance in real-world SMR scenarios and may reveal areas for further refinement or adaptation to the unique characteristics of SMR designs.

- Development of User-Friendly Software Tools

  To facilitate the adoption of these advanced methods in practice, future work could focus on developing user-friendly software tools that implement the proposed methodologies. These tools could streamline the process of generating FRS and performing SSI analysis for nuclear facility design.

Bibliography

Abrahamson, N.A., Schneider, J.F., and Stepp, J.C., 1991. Empirical spatial coherency functions for application to soil-structre interaction analysis. *Earthquake Spectra*, **7**: 1–28.

An, Y., Jiang, Y., and Ly, B., 2013. Direct generation of RRS from FRS. In *Proceedings of the 22nd International Conference on Structural Mechanics in Reactor Technology*.

ASCE, 1998. *Seismic Analysis of Safety-Related Nuclear Structures and Commentary*, **ASCE 4-98**. American Society of Civil Engineers (ASCE).

ASCE, 2005. *Seismic Design Criteria for Structures, Systems, and Components in Nuclear Facilities*, **ASCE/SEI 43-05**. Structural Engineering Institute, American Society of Civil Engineers (ASCE).

ASCE, 2010. *Minimum Design Loads for Buildings and Other Structures*, **ASCE/SEI 7-10**. American Society of Civil Engineers, Reston, Virginia.

Asfura, A. and Kiureghian, A.D., 1986. Floor response spectrum method for seismic analysis of multiply supported secondary systems. *Earthquake Engineering and Structural Dynamics*, **14**(2): 245–265.

Bielak, J. and Christiano, P., 1984. On the effective seismic input for non-linear soil-structure interaction systems. *Earthquake Engineering and Structural Dynamics*, **12**: 107–119.

Biggs, J.M. and Roesset, J.M., 1970. Seismic analysis of equipment mounted on a massive structure. *Seismic Design for Nuclear Power Plants*, 319–343.

Burdisso, R.A. and Singh, M.P., 1987. Multiply supported secondary systems part i: Response spectrum analysis. *Earthquake Engineering and Structural Dynamics*, **15**(1): 53–72.

Ceballos, M.A. and Prato, C.A., 2012. Half-space dynamic stiffness models compatible with the thin layer formulation for use in response analysis of soil profiles. In *Nondestructive Testing of Materials and Structures*, **6** of *RILEM Bookseries*, 745–750. Springer Netherlands, Dordrecht.

Chaudhuri, S. R. and Gupta, V.K., 2003. Mode acceleration approach for generation of floor spectra including soil-structure interaction. *ISET Journal of Earthquake Technology*, **40**(434): 99–115.

Chen, Y. and Soong, T.T., 1988. Seismic response of secondary systems. *Engineering Structures*, **10**(4): 218–228.

Chopra, A.K., 2012. *Dynamics of Structures — Theory and Applications to Earthquake Engineering*. Prentice Hall, fourth edition.

Collino, F., 1993. High order absorbing boundary conditions for wave propagation models. straight line boundaries and corner cases. *Proceedings of the Second International Conferenceon Mathematical and Numerical Aspects of Wave Propagation*, p. 161–171.

CSA, 2020. *Design Procedures for Seismic Qualification of Nuclear Power Plants*, **CSA N289.3-20**. Canadian Standard Association (CSA), Toronto.

Der Kiureghian, A., 1996. A coherency model for spatially varying ground motions. *Earthquake Enginnering and Structural Dynamics*, **25**(1): 99–111.

Dominguez, J., 1993. *Boundary elements in dynamics*. International series on computational engineering. Computational Mechanics Publications, Southampton.

Duff, C.G., 1975. Simplified method for development of earthquake ground and floor response spectra for nuclear power plant design. Technical report, Atomic Energy of Canada Ltd., Ontario.

Gazetas, George, 1991. Formulas and charts for impedances of surface and embedded foundations. *Journal of geotechnical engineering*, **117**(9): 1363–1381.

Ghiocel, D.M., 2015. ACS **SASSI**, **3.0**. GP Technologies, Inc.

Guner, Tugberk, Bursi, Oreste S., and Erlicher, Silvano, 2022. Optimization and performance of metafoundations for seismic isolation of small modular reactors. *Computer-Aided Civil and Infrastructure Engineering*, 1–25.

Gutierrez, J.A. and Chopra, A.K., 1978. A substructure method for earthquake analysis of structures including structure-soil interaction. *Earthquake Engineering and Structural Dynamics*, **6**(1): 51–69.

Higdon, R. L., 1991. Absorbing boundary conditions for elastic waves. *Geophysics*, **56**(2): 231–241.

Igusa, T. and Kiureghian, A.D., 1985. Dynamic characterization of two-degree-of-freedom equipment-structure systems. *Journal of Engineering Mechanics*, **111**(1): 1–19.

Jeanpierre, F. and Livolant, M., 1977. Direct calculation of floor response spectra from the fourier transform of ground movement-application to the superphenix fast reactor project. *Nuclear Engineering and Design*, **41**(1): 45–51.

Jiang, W., Li, B., Xie, W-C., and Pandey, M.D., 2015. Generate floor response spectra: Part 1. direct spectra-to-spectra method. *Nuclear Engineering and Design*, **293**: 525–546.

Jiang, W., Zhou, Y., Xie, W.-C., and Pandey, M. D., 2022. Direct method for generating floor response spectra considering soil-structure interaction. *Journal of Earthquake Engineering*, **26**(10): 4956–4976.

Jiang, W., 2016. *Direct Method of Generating Floor Response Spectra*. PhD thesis, University of Waterloo.

Kapur, K.K. and Shao, L.C., 1970. Generation of seismic floor response spectra for equipment design. *Seismic Design for Nuclear Power Plants*, **1**: 29–71.

Kennedy, R. P., Short, S. A., and Newmark, N. M., 1981. The response of a nuclear power plant to near-field moderate magnitude earthquakes. In *Transactions of the 6th International Conference on Structural Mechanics in Reactor Technology, Palais des Congres*. Co. for the Commission of the European Communities: Paris, France.

Kim, Doo-Kie and Yun, Chung-Bang, 2000. Time-domain soil-structure interaction analysis in two-dimensional medium based on analytical frequency-dependent infinite elements. *International journal for numerical methods in engineering*, **47**(7): 1241–1261.

Kiureghian, A.D., Sackman, J.L., and Nour-Omid, B., 1983. Dynamic analysis of light equipment in structures: Response to stochastic input. *Journal of Engineering Mechanics*, **109**(1): 90–110.

Liao, Z. P. and Wong, H. L., 1984. A transmitting boundary for the numerical simulation of elastic wave propagation. *Soil Dynamics And Earthquake Engineering*, **3**(3): 174–183.

Lin, Y.K., 1967. *Probabilistic theory of structural dynamics*. McGraw-Hill, N.

Li, B., Jiang, W., Xie, W-C., and Pandey, M.D., 2015. Generate floor response spectra: Part 2. response spectra for equipment-structure resonance. *Nuclear Engineering and Design*, **293**: 547–560.

Lou, M., Wang, H., Chen, X., and Zhai, Y., 2011. Structure-soil-structure interaction: Literature review. *Soil dynamics and earthquake engineering*, **31**(12): 1724–1731.

Luco, J.E. and Wong, H.L., 1986. Response of a rigid foundation to a spatially random ground motion. *Earthquake Engineering and Structural Dynamics*, **14**: 891–908.

Lysmer, J., , Tabatabaie-Raissi, M., Tajirian, F., Vahdani, S., and Ostadan, F., 1983. **SASSI**. *System for Analysis of Soil Structure Interaction*. UC Berkeley, Department of Civil Engineering, Berkeley, CA.

Molina-Villegas, Juan Camilo, Ballesteros Ortega, Jorge Eliecer, and Ruiz Cardona, David, 2022. Formulation of the greenâŁ™s functions stiffness method for eulerâŁ“bernoulli beams on elastic winkler foundation with semi-rigid connections. *Engineering structures*, **266**: 114616–.

Morici, Michele, Minnucci, Lucia, Carbonari, Sandro, Dezi, Francesca, and Leoni, Graziano, 2019. Simple formulas for estimating a lumped parameter model to reproduce impedances of end-bearing pile foundations. *Soil dynamics and earthquake engineering*, **121**: 341–355.

Ni, S-H., Xie, W-C., and Pandey, M. D., 2011. Tri-directional spectrum-compatible earthquake time-histories for nuclear energy facilities. *Nuclear Engineering and Design*, **241**(8): 2732–2743.

Ni, S-H., Xie, W-C., and Pandey, M. D., 2013. Generation of spectrum-compatible earthquake ground motions considering intrinsic spectral variability using Hilbert-Huang transform. *Structural Safety*, **42**: 45–53.

Pedraza, J. Morales, 2017. *Small Modular Reactors for Electricity Generation*. Springer International Publishing.

Peters, K.A., Schmitz, D., and Wagner, U., 1977. Determination of floor response spectra on the basis of the response spectrum method. *Nuclear Engineering and Design*, **44**(2): 255–262.

Raychowdhury, P. and Ray-Chaudhuri, S., 2015. Seismic response of nonstructural components supported by a 4-story smrf: Effect of nonlinear soil-structure interaction. *Structures*, **3**: 200–210.

Scanlan, R.H., 1974. Earthquake time histories and response spectra. *Journal of the Engineering Mechanics Division*, **100**(4): 635–655.

Singh, M.P. and Sharma, A.M., 1985. Seismic floor spectra by mode acceleration approach. *Journal of Engineering Mechanics*, **111**(11): 1402–1419.

Singh, M.P., 1975. Generation of seismic floor spectra. *Journal of the Engineering Mechanics Division*, **101**(5): 593–607.

Singh, M.P., 1980. Seismic design input for secondary systems. *Journal of the Structural Division*, **106**(2): 505–517.

Singh, M.P., 1988. Seismic design of secondary systems. *Probabilistic Engineering Mechanics*, **3**(3): 151–158.

USNRC, 1973. *Design Response Spectra for Seismic Design of Nuclear Power Plants*, **R.G. 1.60**. U.S. Atomic Energy Commission.

Verruijt, Arnold, 2017. Boussinesq. In *An Introduction to Soil Mechanics*, **30** of *Theory and Applications of Transport in Porous Media*, 219–224. Springer International Publishing AG, Switzerland.

Villaverde, R., 1997. Seismic design of secondary structures: state of the art. *Journal of Structural Engineering*, **123**(8): 1011–1019.

Villaverde, R., 2009. *Fundamental Concept of Earthquake Engineering*. CRC Press, New York.

Waas, G., Riggs, H.R., and Werkle, H., 1985. Displacement solutions for dynamic loads in transversely–isotropic stratified media. *International journal of rock mechanics and mining sciences and geomechanics abstracts*, **22**(5): 155–160.

Wang, J., August 7-12 2005. Influence of different boundary conditions on analysis of ssi. In *18th International Conference on Structural Mechanics in Reactor Technology*. Beijing, China.

Wang, R., Xie, W.-C., and Pandey, M. D., 2022a. Generation of Floor and Tertiary Response Spectra of Structures Under Seismic Excitations at Multiple Supports. *Earthquake Engineering and Structural Dynamics*, **51**(4): 853–874.

Wang, R., Xie, W.-C., and Pandey, M. D., 2022b. Generation of floor response spectra of structures under seismic excitations at multiple supports. *Nuclear Engineering and Design*, **51**(4): 111527:1–14.

Wang, R., 2023. *Direct Method of Generating Floor Response Spectra for Structures under Earthquake Excitations at Multiple Supports*. PhD thesis, University of Waterloo.

Wolf, John P., 1994. *Foundation vibration analysis using simple physical models*. PTR Prentice Hall, Englewood Cliffs, NJ.

Wolf, J.P., 1985a. *Dynamic Soil Structure Interaction*. Prentice Hall.

Wolf, J.P., 1987. *Soil-Structure-Interaction Analysis in Time Domain*. Structural Mechanics in Reactor Technology.

Wolf, J. P., 1985b. *Dynamic Soil-Structure Interaction*. Prentice-Hall, New Jersey, USA.

World Nuclear Association, 2021. World Nuclear Performance Report 2021, Report No. 2021/003. Technical report, World Nuclear Association.

Xie, Wei-Chau, Ni, Shun-Hao, Liu, Wei, and Jiang, Wei, 2019. *Seismic Risk Analysis of Nuclear Power Plants*. Cambridge University Press.

Xie, W.-C., 2010. *Differential Equations for Engineers*. Cambridge University Press, New York, USA.

Yasui, Y., Yoshihara, J., Takeda, T., and Miyamoto, A., 1993. Direct generation method for floor response spectra. *Proceedings of the 12th International Conference on Structural Mechanics in Reactor Technology*, **13**(4): 367–372.

Zhang, C. and Jiang, N., 2017. Effects of equipment-structure-soil interaction on seismic response of equipment and structure via real-time dynamic substructuring shaking table testing. *Shock and Vibration*, **2017**: 1–13.

Zhang, D.-Y., Xie, W.-C., and Pandey, M. D., 2012. Synthesis of spatially correlated ground motions at varying sites based on vector-valued seismic hazard deaggregation. *Soil Dynamics and Earthquake Engineering*, **41**: 1–13.

Zhou, Y., 2019. *Direct Method for Floor Response Spectra Considering Soil-Structure Interaction*. PhD thesis, University of Waterloo.

APPENDIX A

Classification of Soil Sites

The stiffness of foundation is the amount of force required to produce an unit deformation at the foundation level. It is a measure of the resistance of the foundation to the unit deflection. ASCE 4-98 (1998) suggests that SSI should be considered if the supporting soil is not rock or rock-like soil. The provision put forward that the underlying soil can be represented by generalized soil spring, which equivalent spring constant can be evaluated in the following manner if the base shape is circular.

$$\text{Horizontal}: \ k_{sx} = \frac{32(1-\mu)GR}{7-8\mu} \qquad \text{Vertical}: \ k_{sz} = \frac{4GR}{1-\mu}$$

where G is shear modulus, μ is the Poisson's ratio of soil, R is the radius.

To evaluate the stiffness range of underlying soil, a representative type of soil was selected for each site class. These include different clays to represent soft, medium, and dense or stiff soils; while soft sandstone, medium basalt, and granite were used to represent soft, medium, and hard rocks, respectively. Two shear wave velocities were selected as the lower and upper bounds. To ensure a reasonable estimation of the bounds of stiffness, equivalent minimum and maximum radii of 3 m and 30 m were set to evaluate the range of k_s for each site category. Table A.1 lists the relevant parameters and results. The range of stiffnesses for soils in different site classes was thus estimated, as presented in Table A.2.

Table A.1 Evaluation of soil stiffnesses for different site classes

Site Class	Soil	Type	Bound	V_s (m/s)	μ	E (MPa)	G (MPa)	R=3 m		R=30 m	
								k_H (kN/m)	k_V (kN/m)	k_H (kN/m)	k_V (kN/m)
E	Soft Clay	soft soil	LB	30	0.49	0.4	134.23	2.13×10^3	3.16×10^3	2.13×10^4	3.16×10^4
			UB	120	0.42	5	1760.56	2.67×10^4	3.64×10^4	2.67×10^5	3.64×10^5
D	Medium Clay	stiff soil	LB	150	0.46	6	2054.79	3.20×10^4	4.57×10^4	3.20×10^5	4.57×10^5
			UB	300	0.38	1.80×10^4	6521.74	9.66×10^4	1.26×10^5	9.66×10^5	1.26×10^6
C	Dense Clay	very dense soil	LB	350	0.39	2.00×10^4	7194.24	1.07×10^5	1.42×10^5	1.07×10^6	1.42×10^6
	Soft sandstone	and soft rock	UB	700	0.33	9.00×10^4	33834.59	4.86×10^5	6.06×10^5	4.86×10^6	6.06×10^6
B	Medium Basalt	rock	LB	800	0.34	1.00×10^5	37313.43	5.39×10^5	6.78×10^5	5.39×10^6	6.78×10^6
			UB	1500	0.29	2.00×10^5	77519.38	1.09×10^6	1.31×10^6	1.09×10^7	1.31×10^7
A	Granite	hard rock	LB	1600	0.3	1.00×10^6	384615.38	5.43×10^6	6.59×10^6	5.43×10^7	6.59×10^7
			UB	3000	0.25	2.00×10^8	80000000	1.10×10^9	1.28×10^9	1.10×10^{10}	1.28×10^{10}

Table A.2 Estimated lower and upper bound of soil stiffnesses for different site classes

Site class	E		D		C		B		A	
Bound	LB	UB	LB	UB	LB	UB	LB	UB	LB	UB
k_s (kN/m)	2×10^3	4×10^5	3×10^4	2×10^6	1×10^5	6×10^6	5×10^5	2×10^7	5×10^6	2×10^{10}

APPENDIX B

Results of FLIRS and FRS

FLIRS were generated for the structure in Figure 3.1 using general formulation for the coupled soil-structure model. The corresponding FRS at m_B were obtained through time history analysis. Except for the case of the softest soil (k_s=8 × 10^4 kN/m), Figures B.1 to B.3 present the FLIRS in the coupled model and the corresponding FRS in the fixed-base model for all other cases. Figures B.4 to B.6 display the comparison of FRS at Node 1, and Figures B.7 to B.9 show the comparison of FRS at Node 2 for all the soil cases.

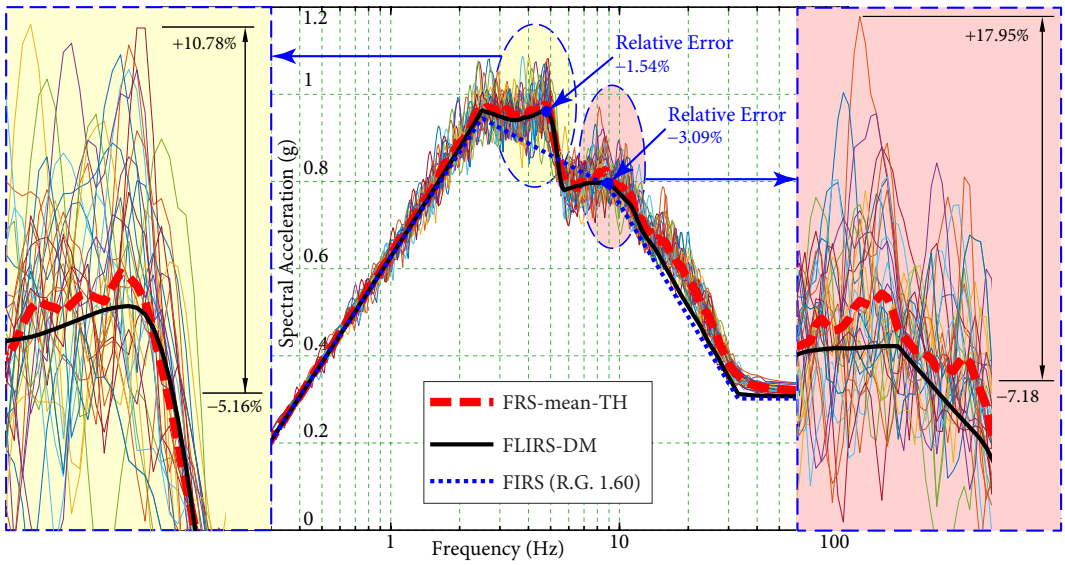
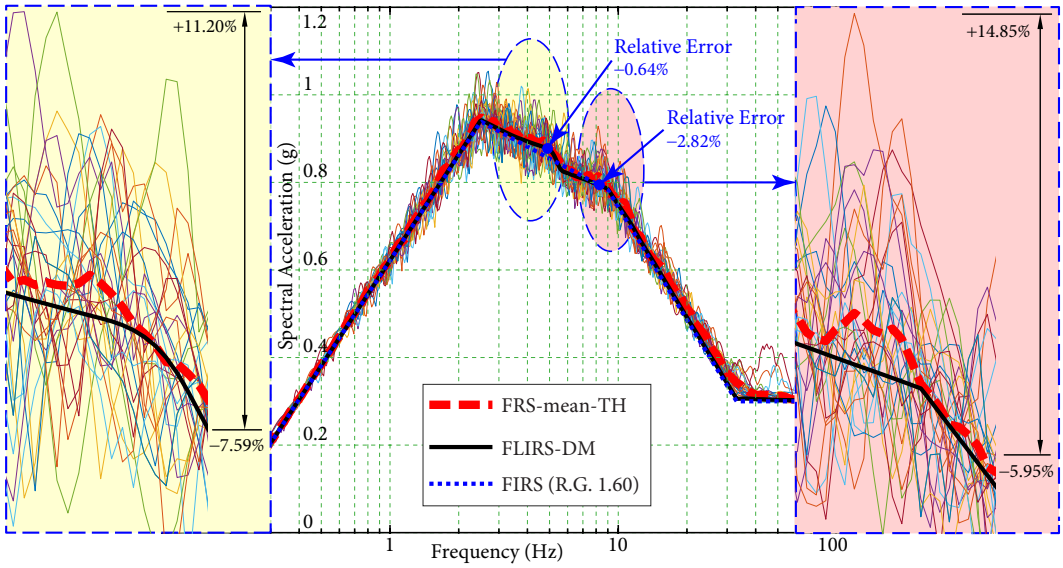
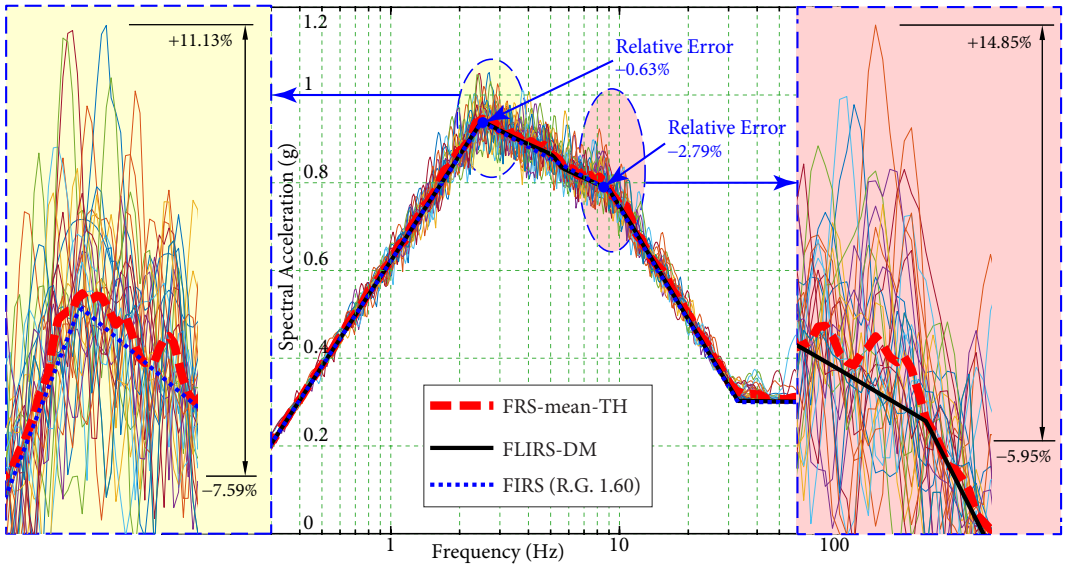


Figure B.1 Comparison of FLIRS and the corresponding FRS from time history analyses (site D, k_s=1 × 10^5 kN/m)

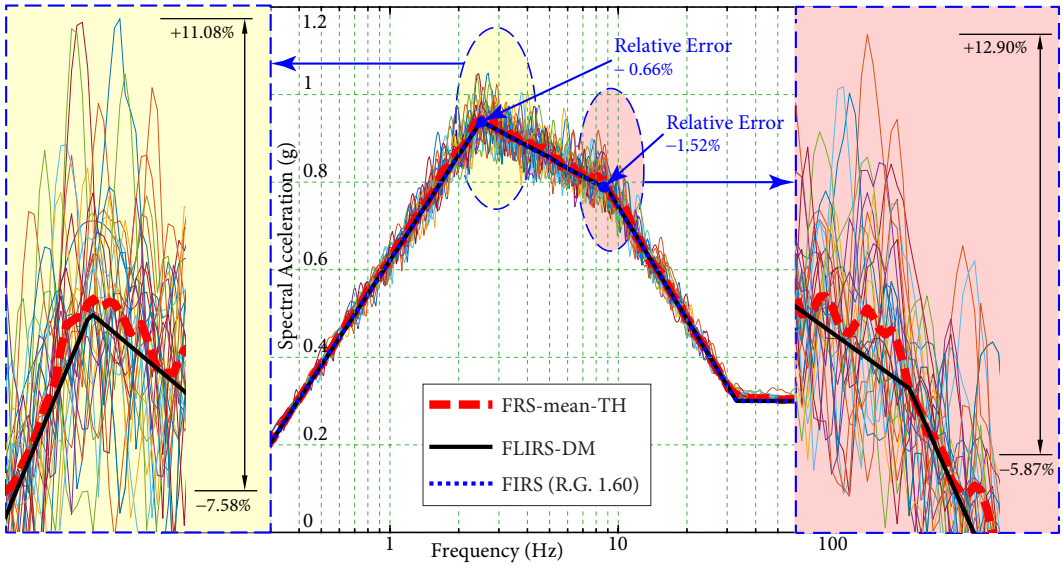


(a) FLIRS in stiff soil of site C (k_s=5 × 10^5 kN/m)



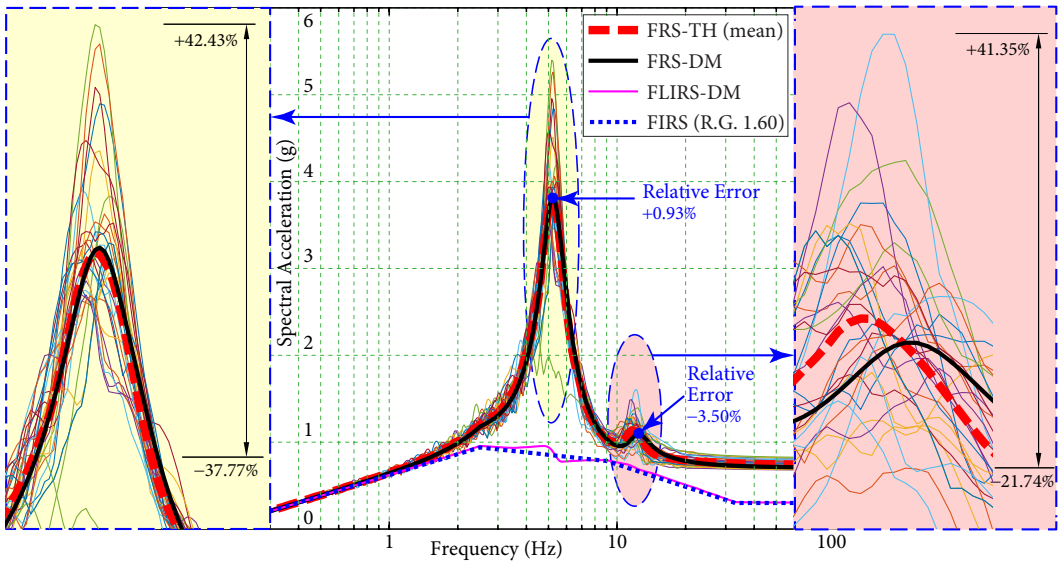
(b) FLIRS in soft rock of site C (k_s=1 × 10^6 kN/m)

Figure B.2 Comparison of FLIRS and the corresponding FRS from time history analyses (site C)



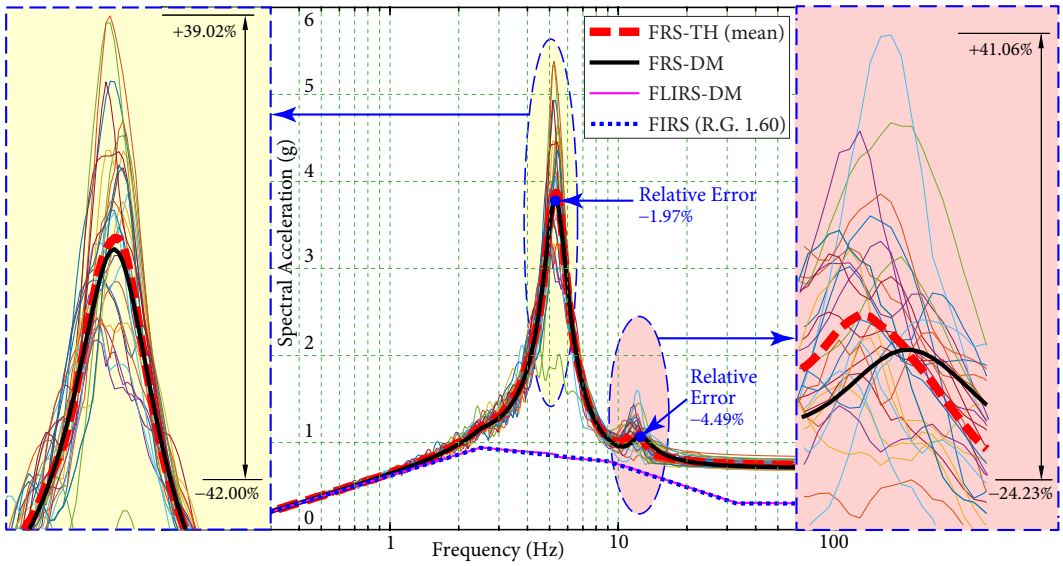
(a) FLIRS in medium hard rock of site B (k_s=5 × 10^6 kN/m)

Figure B.3 Comparison of FLIRS and the corresponding FRS from time history analyses (site B)

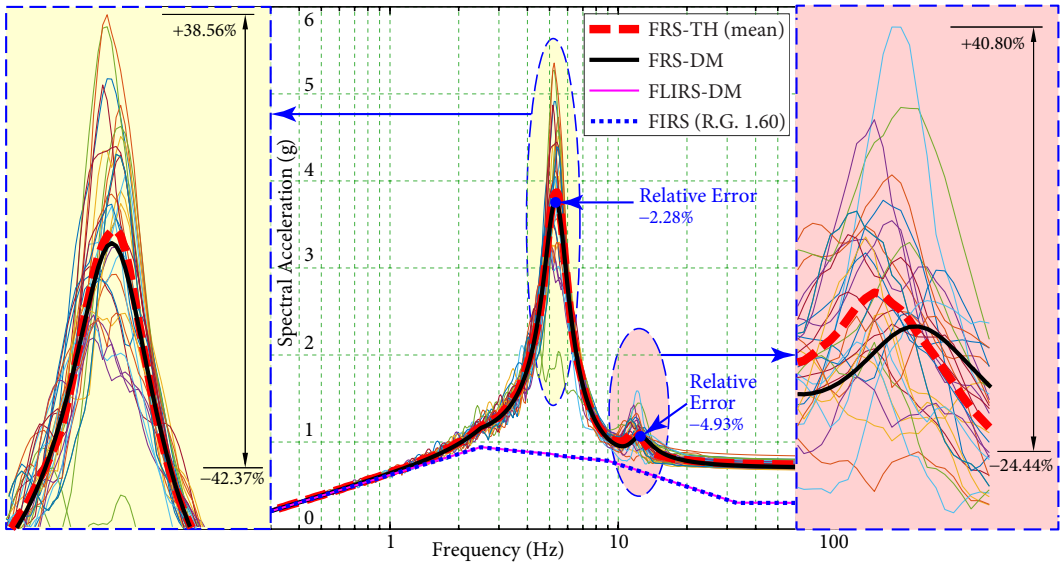


(a) FRS in harder soil of site D (k_s=1 × 10^5 kN/m)

Figure B.4 Comparison of FRS for Node 1 (site D)

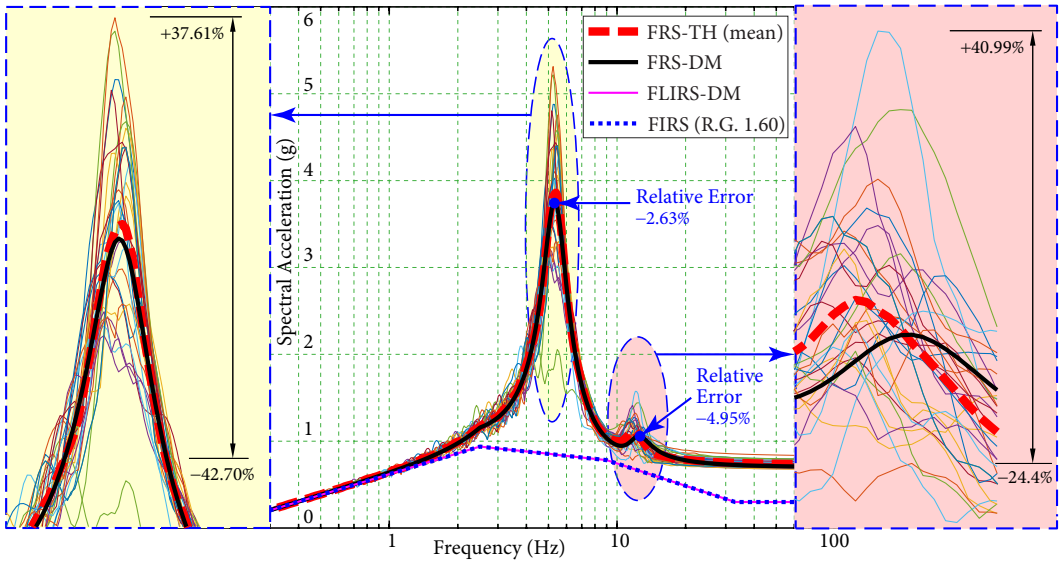


(a) FRS in stiff soil of site C (k_s=5 × 10^5 kN/m)



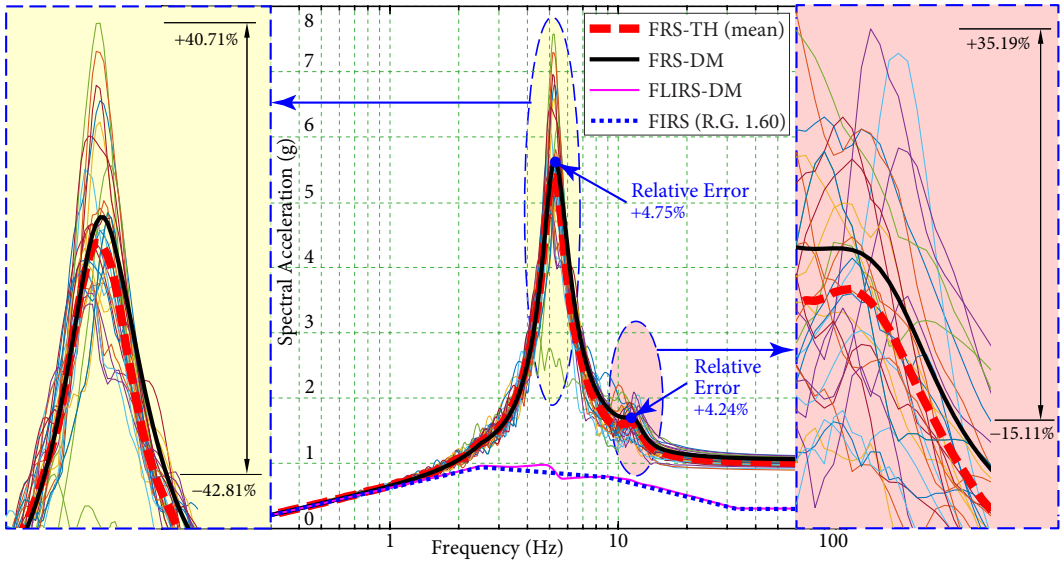
(b) FRS in soft rock of site C (k_s=1 × 10^6 kN/m)

Figure B.5 Comparison of FRS for Node 1 (site C)



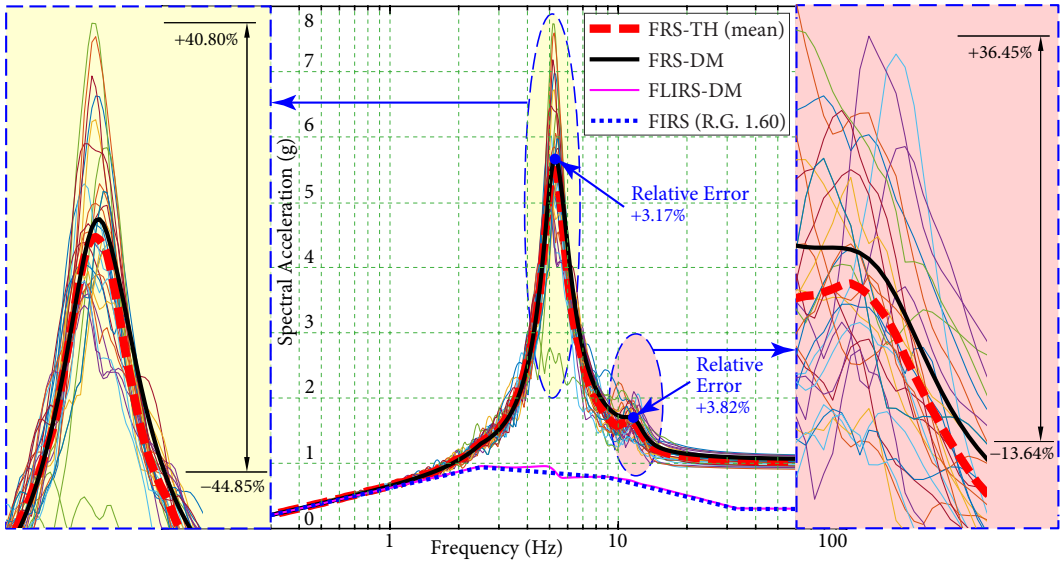
(a) FRS in medium hard rock of site B (k_s=5 × 10^6 kN/m)

Figure B.6 Comparison of FRS for Node 1 (site B)

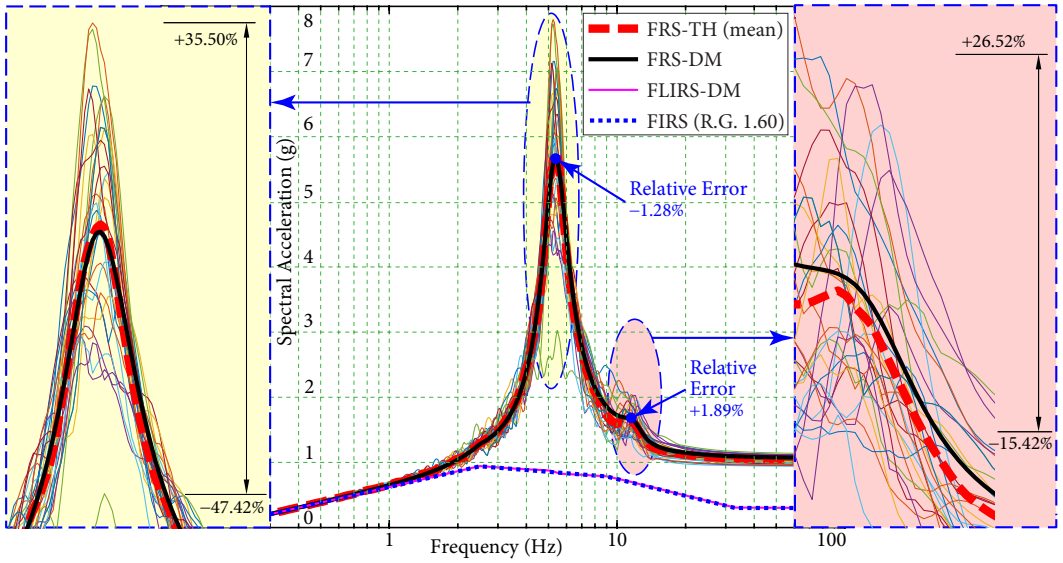


(a) FRS in medium soil of site D (k_s=8 × 10^4 kN/m)

Figure B.7 Comparison of FRS for Node 2 (medium soil of site D)

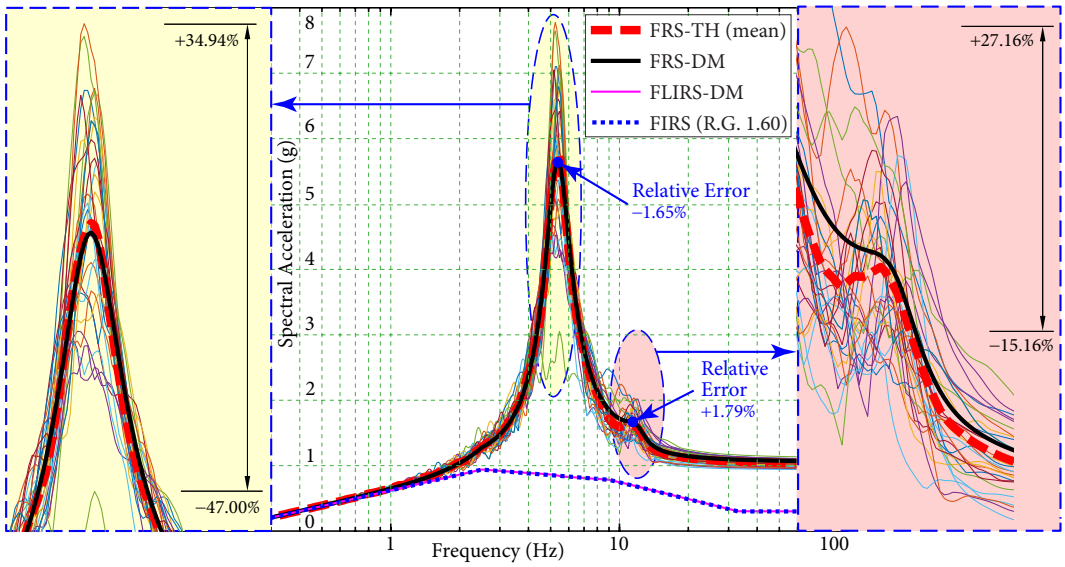


(a) FRS in harder soil of site D (k_s=1 × 10^5 kN/m)

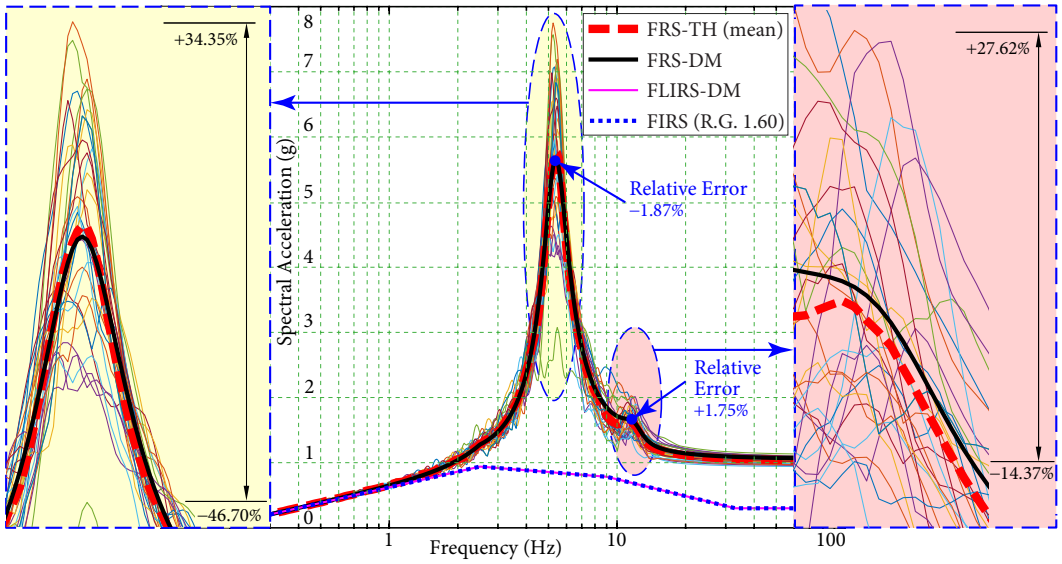


(b) FRS in stiff soil of site C (k_s=5 × 10^5 kN/m)

Figure B.8 Comparison of FRS for Node 2 (harder soil of site D, stiff soil of site C)



(a) FRS in soft rock of site C (k_s=1 × 10^6 kN/m)



(b) FRS in medium hard rock of site B (k_s=5 × 10^6 kN/m)

Figure B.9 Comparison of FRS for Node 2 (soft rock of site C, hard rock of site B)

APPENDIX C

Response of Amplitudes and Phase Lags for Nodes on Soil Cake

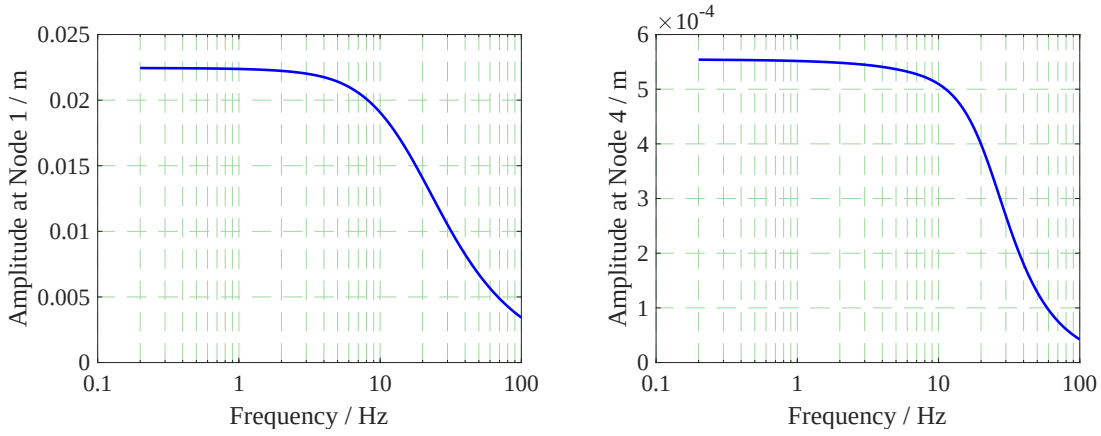


Figure C.1 Amplitude in X direction under harmonic load at Node 1 in X direction

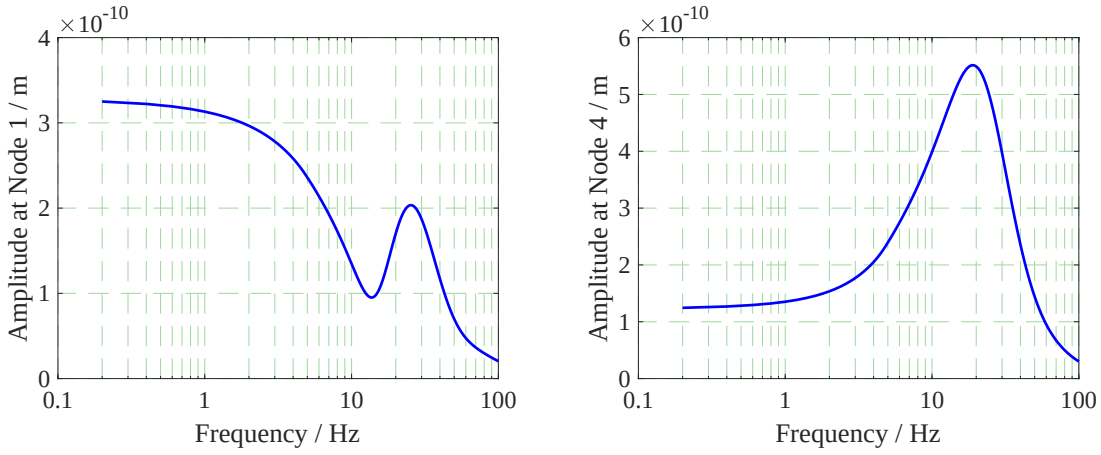


Figure C.2 Amplitude in Y direction under harmonic load at Node 1 in X direction

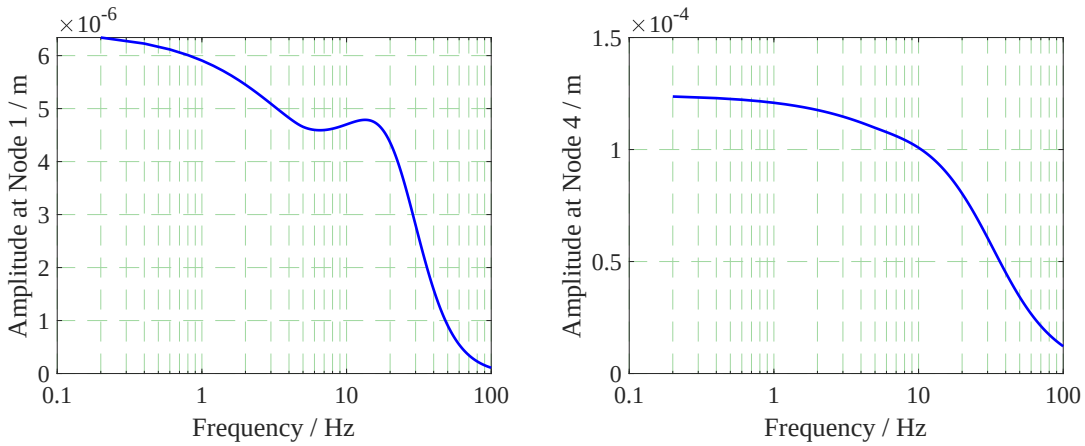


Figure C.3 Amplitude in Z direction under harmonic load at Node 1 in X direction

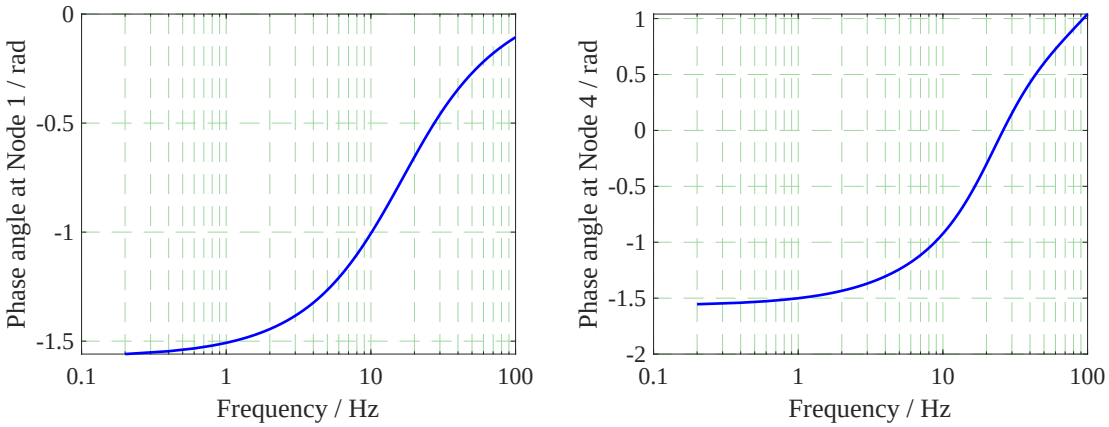


Figure C.4 Phase Angle in X direction under harmonic load at Node 1 in X direction

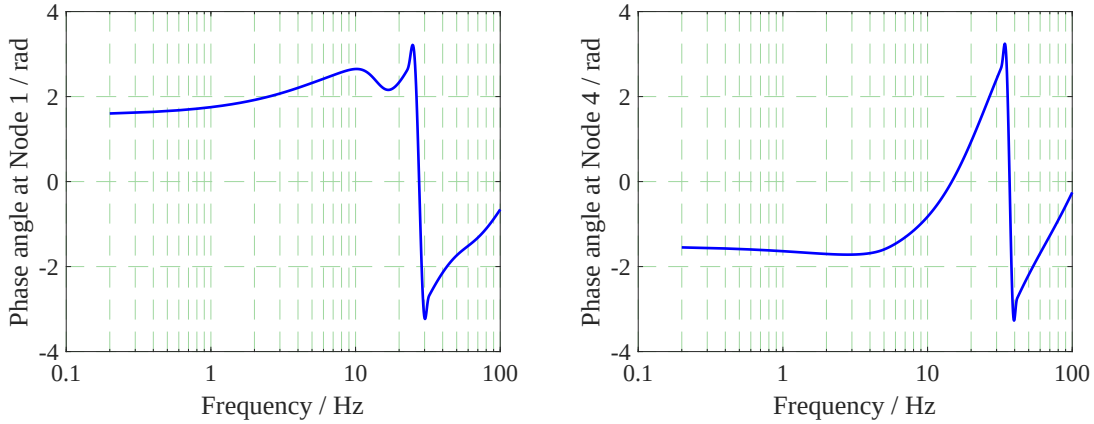


Figure C.5 Phase Angle in Y direction under harmonic load at Node 1 in X direction

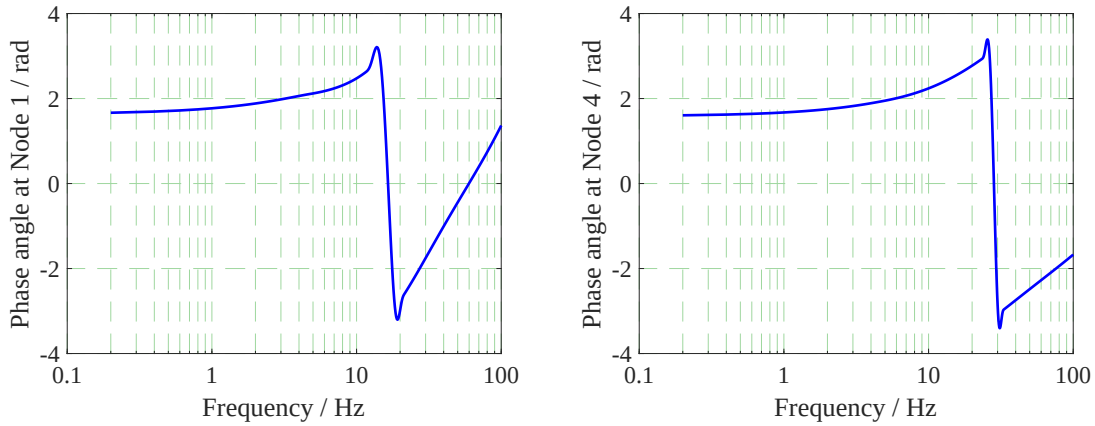


Figure C.6 Phase Angle in Z direction under harmonic load at Node 1 in X direction

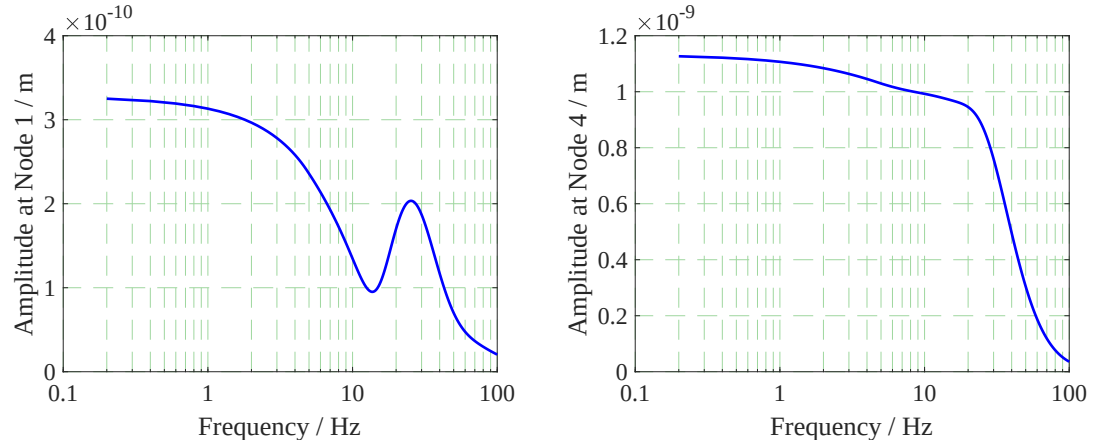


Figure C.7 Amplitude in X direction under harmonic load at Node 1 in Y direction

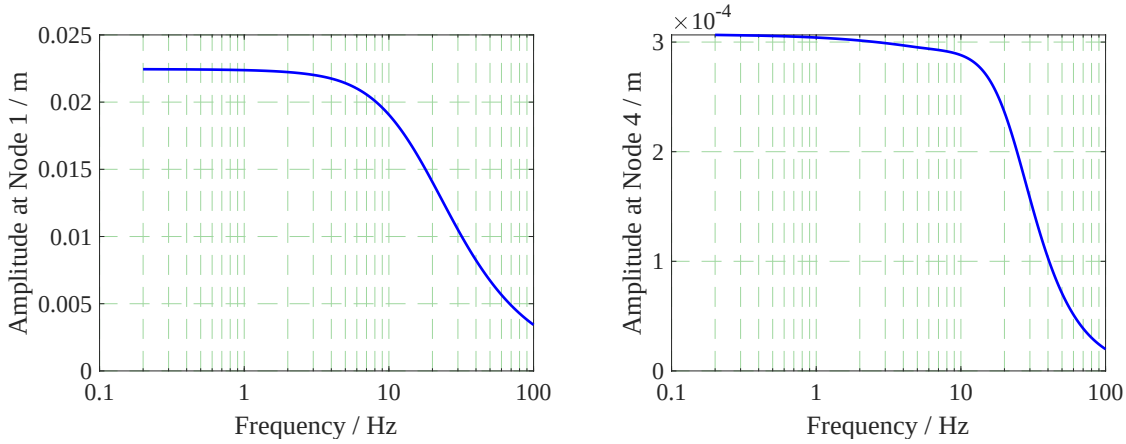


Figure C.8 Amplitude in Y direction under harmonic load at Node 1 in Y direction

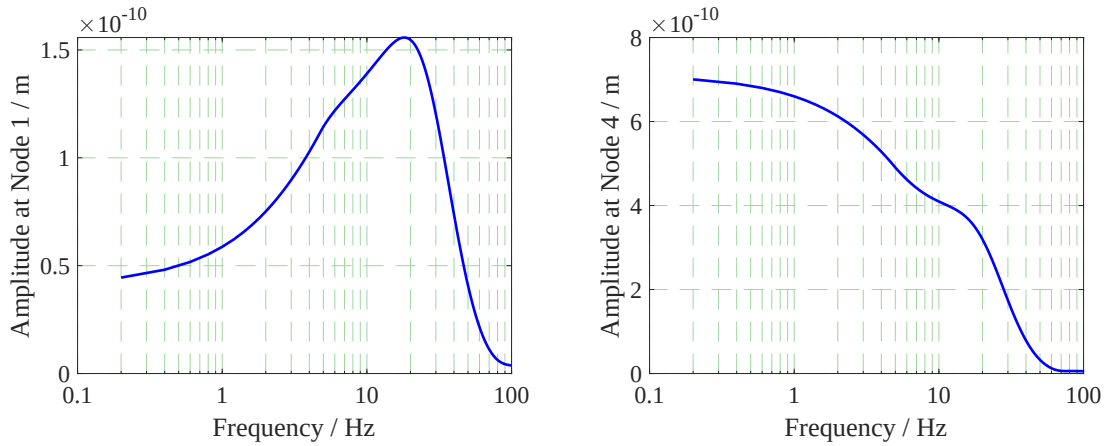


Figure C.9 Amplitude in Z direction under harmonic load at Node 1 in Y direction

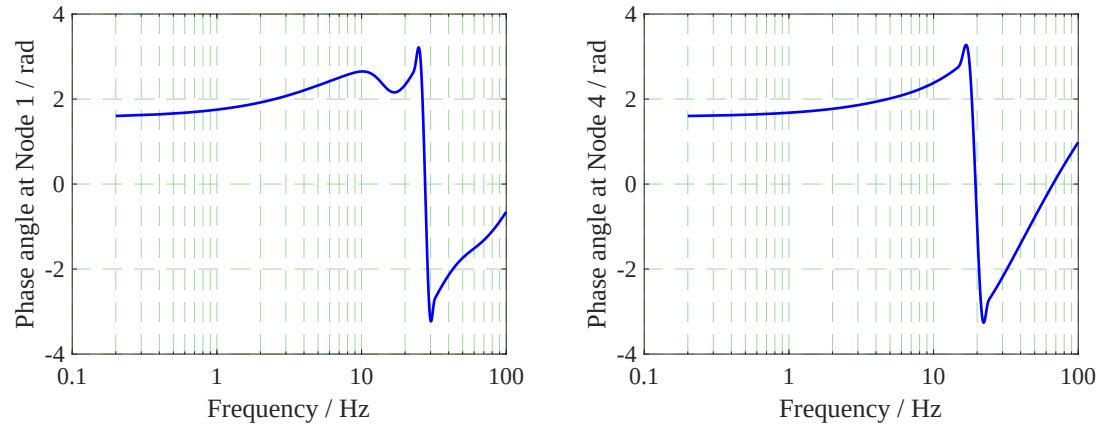


Figure C.10 Phase Angle in X direction under harmonic load at Node 1 in Y direction

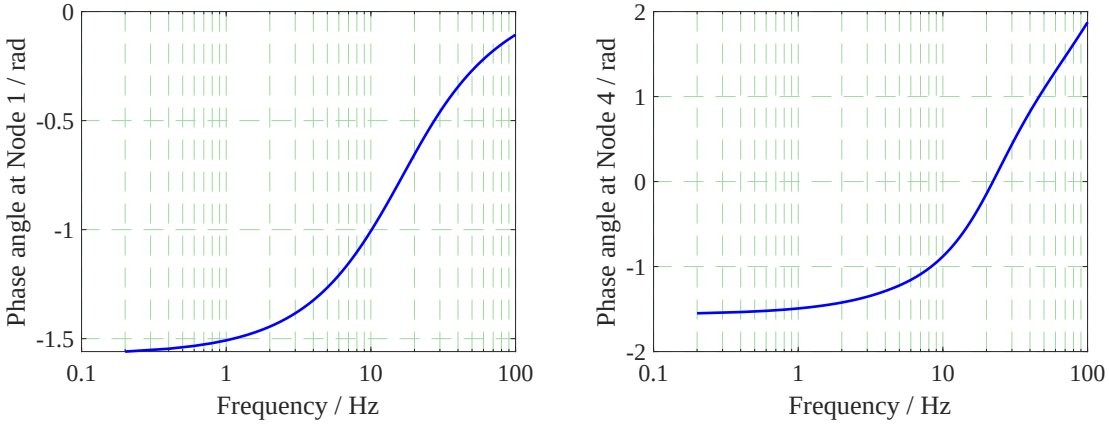


Figure C.11 Phase Angle in Y direction under harmonic load at Node 1 in Y direction

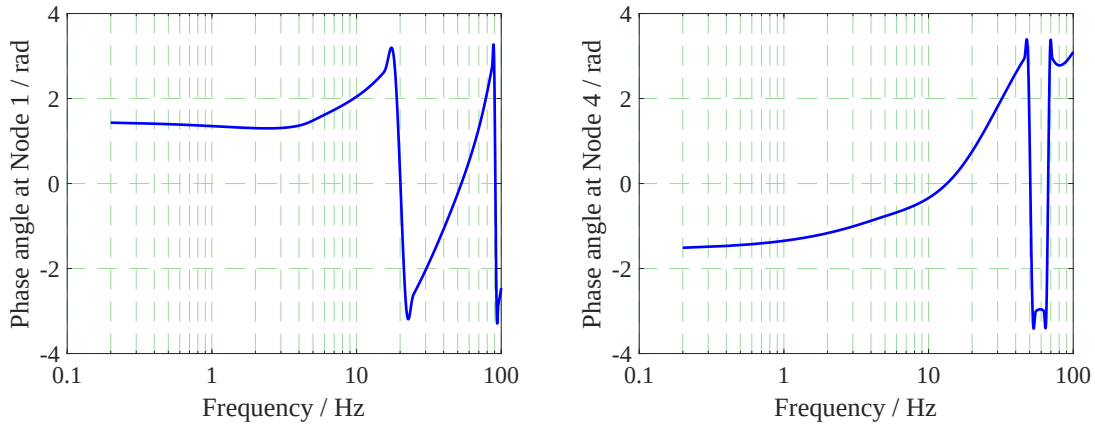


Figure C.12 Phase Angle in Z direction under harmonic load at Node 1 in Y direction

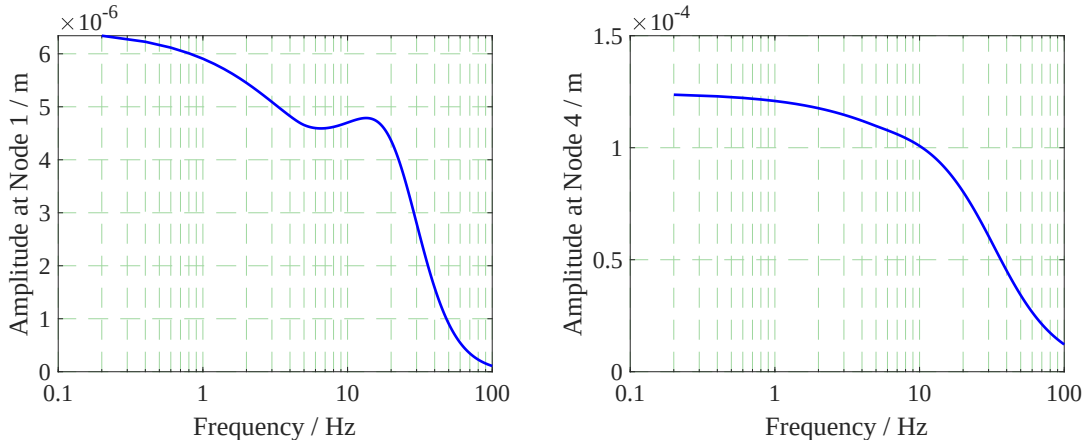


Figure C.13 Amplitude in X direction under harmonic load at Node 1 in Z direction

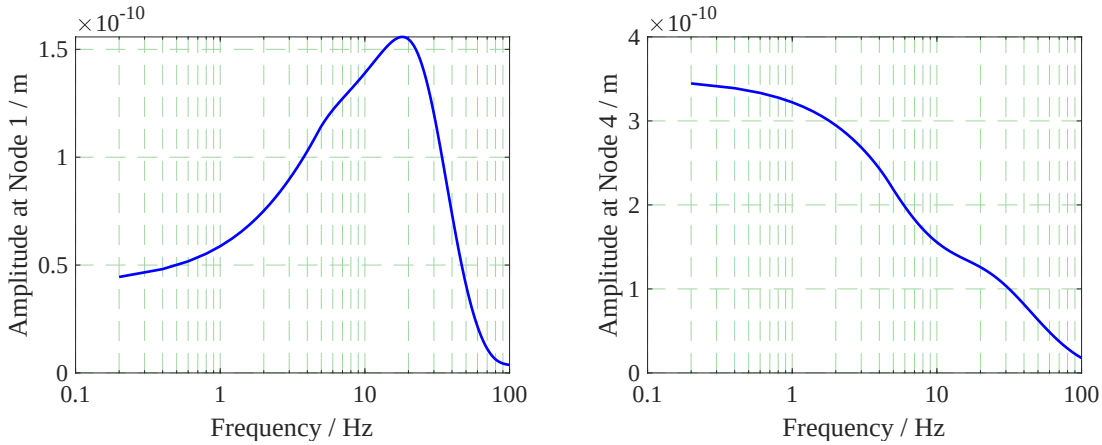


Figure C.14 Amplitude in Y direction under harmonic load at Node 1 in Z direction

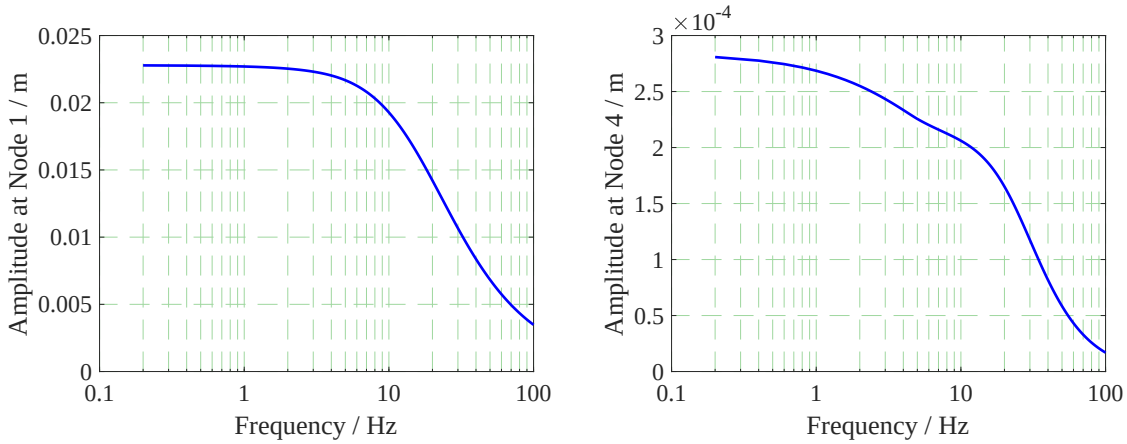


Figure C.15 Amplitude in Z direction under harmonic load at Node 1 in Z direction

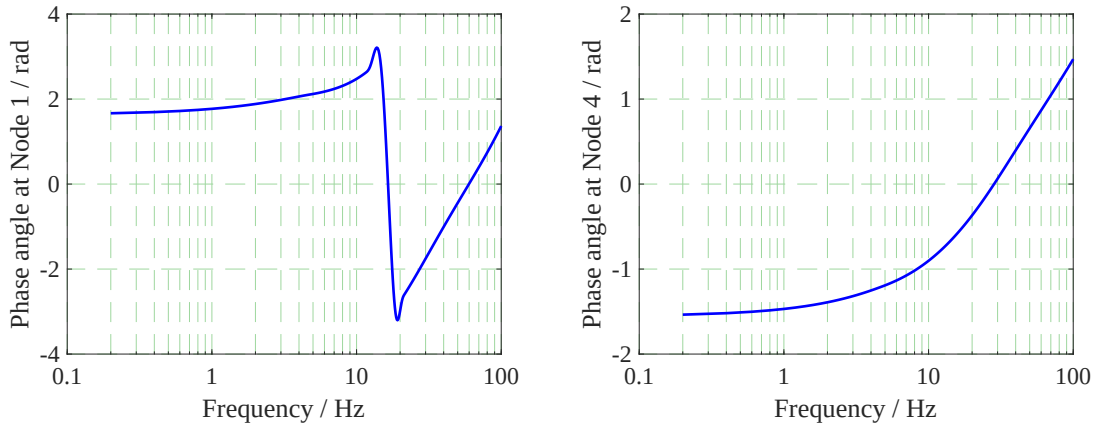


Figure C.16 Phase Angle in X direction under harmonic load at Node 1 in Z direction

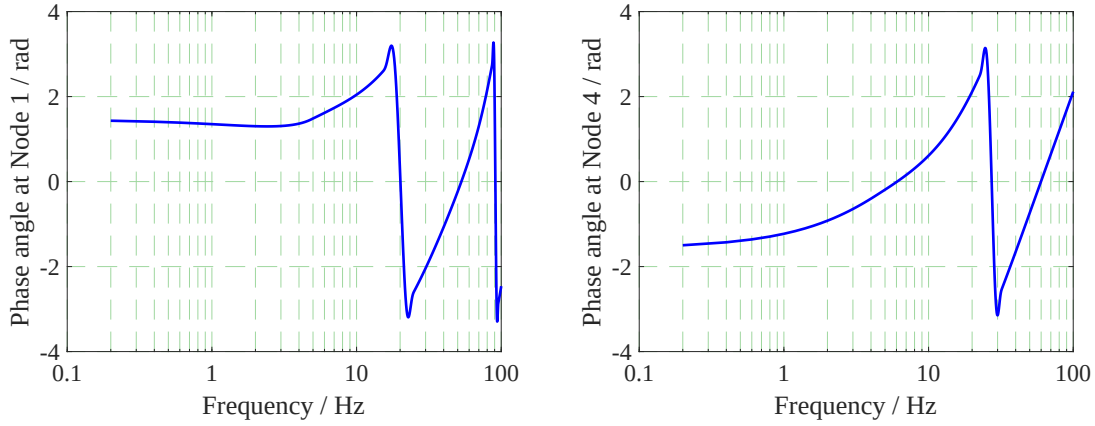


Figure C.17 Phase Angle in Y direction under harmonic load at Node 1 in Z direction

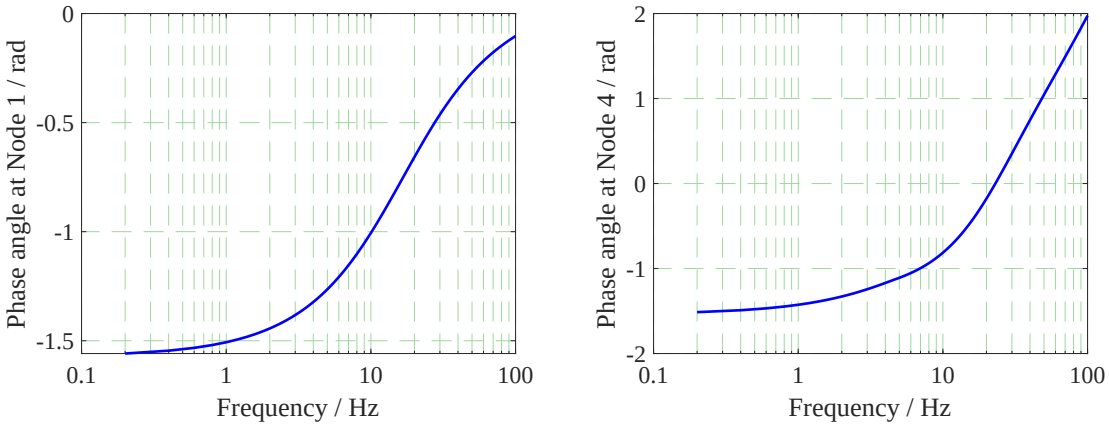


Figure C.18 Phase Angle in Z direction under harmonic load at Node 1 in Z direction

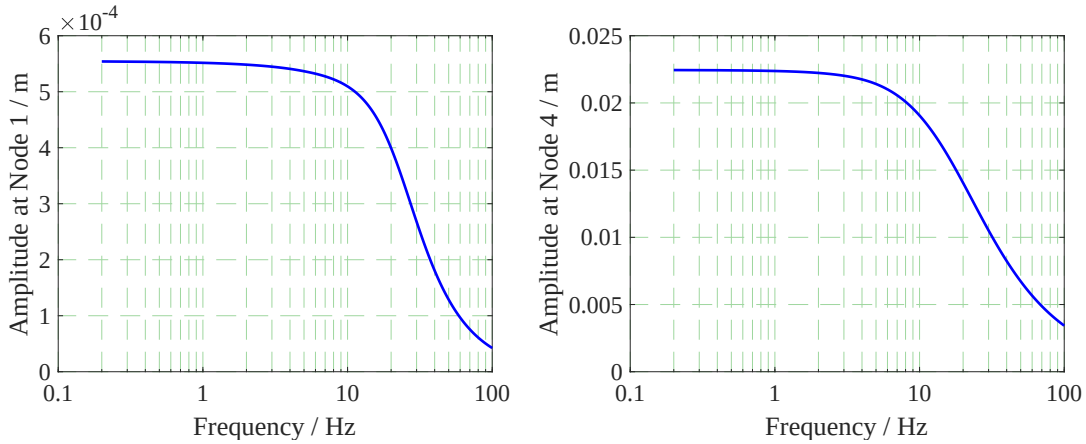


Figure C.19 Amplitude in X direction under harmonic load at Node 4 in X direction

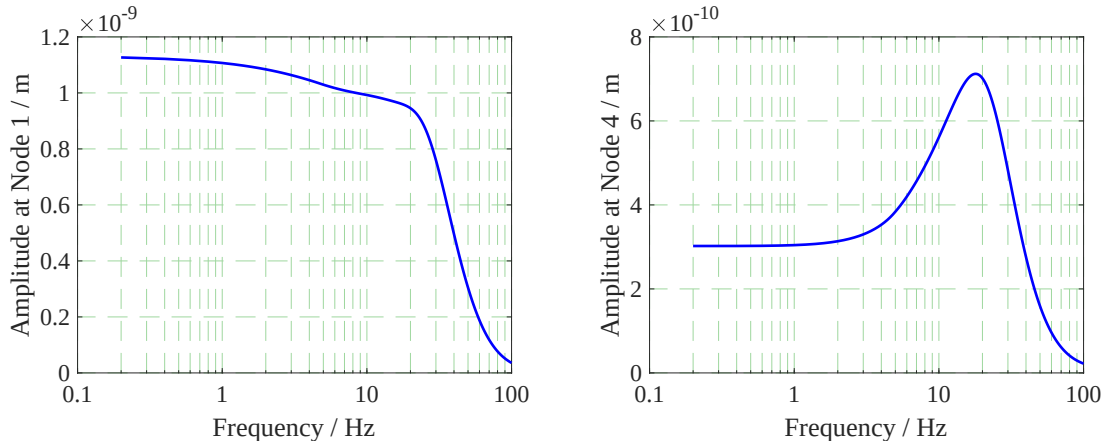


Figure C.20 Amplitude in Y direction under harmonic load at Node 4 in X direction

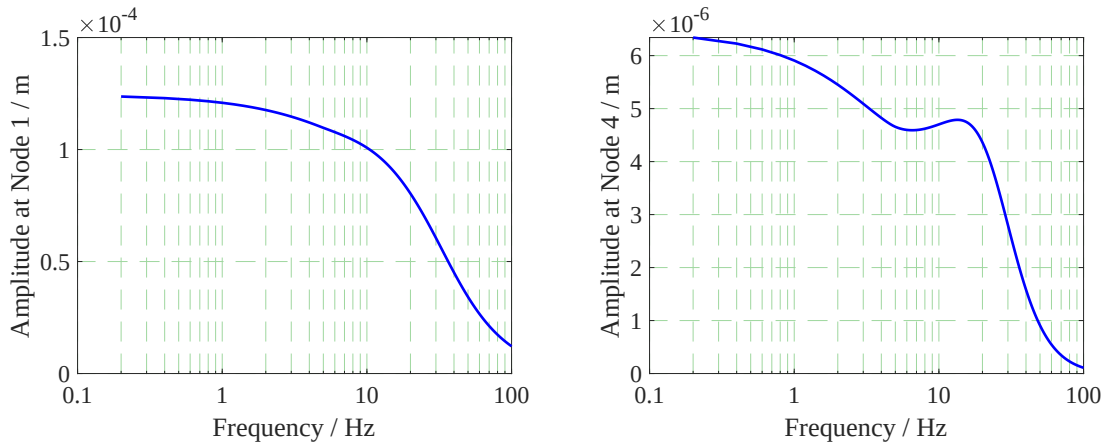


Figure C.21 Amplitude in Z direction under harmonic load at Node 4 in X direction

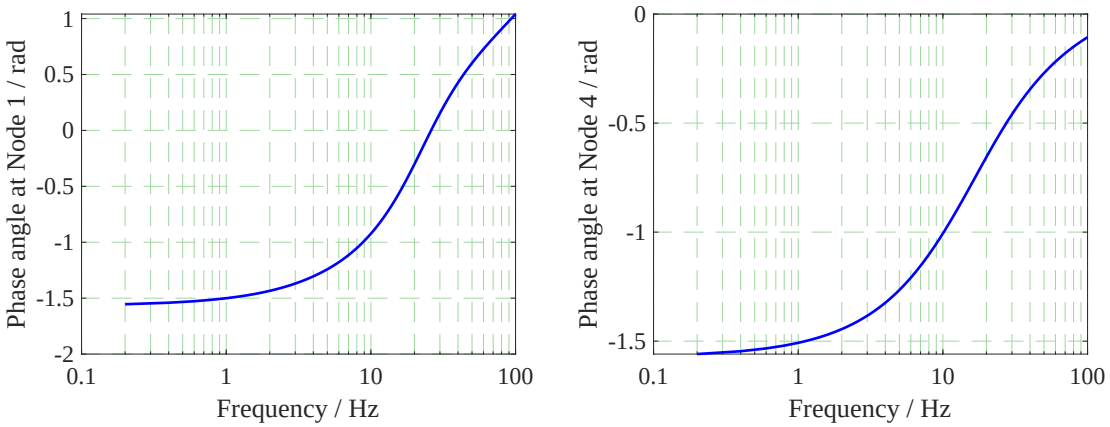


Figure C.22 Phase Angle in X direction under harmonic load at Node 4 in X direction

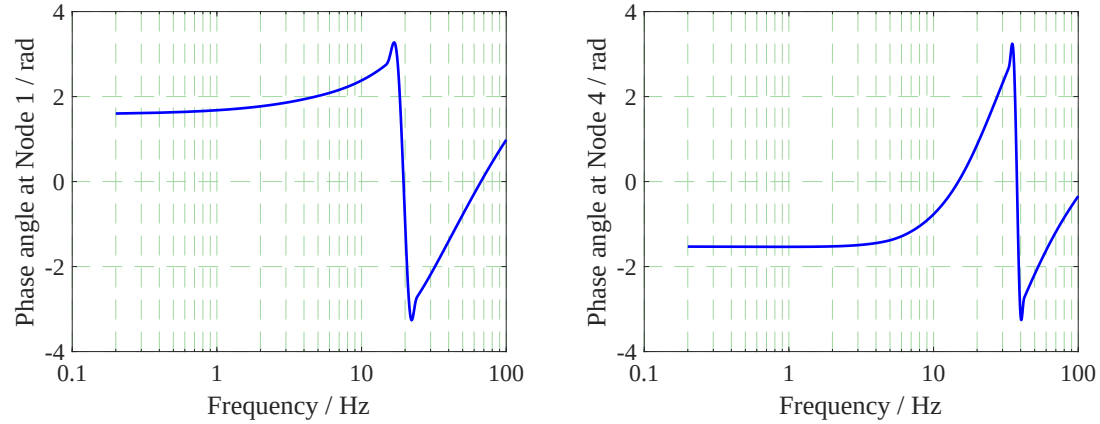


Figure C.23 Phase Angle in Y direction under harmonic load at Node 4 in X direction

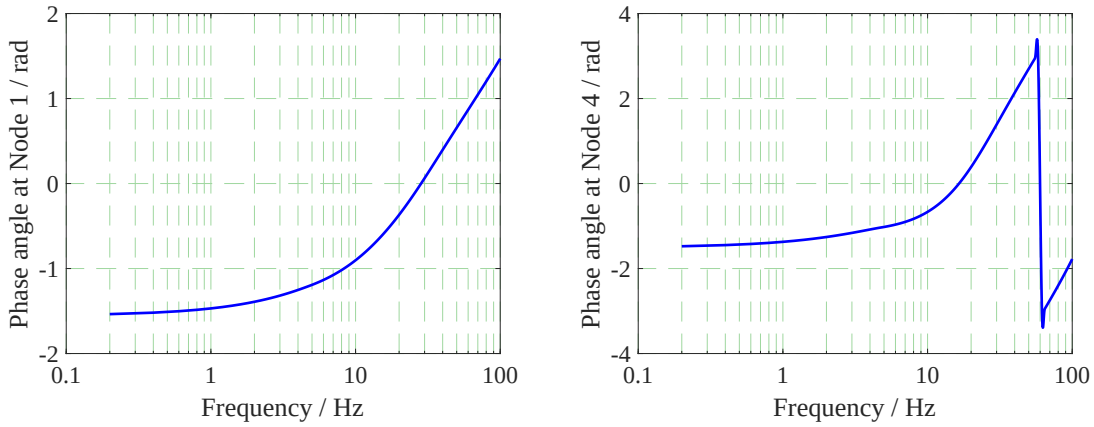


Figure C.24 Phase Angle in Z direction under harmonic load at Node 4 in X direction

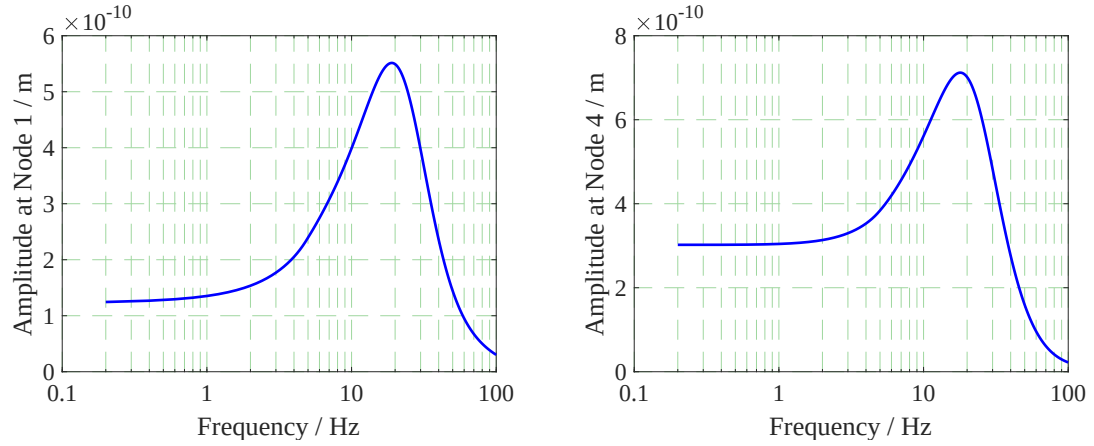


Figure C.25 Amplitude in X direction under harmonic load at Node 4 in Y direction

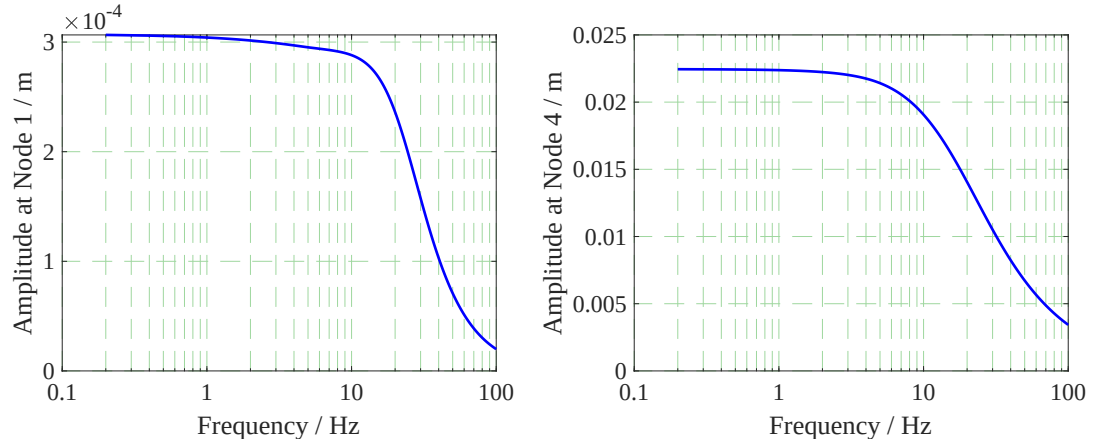


Figure C.26 Amplitude in Y direction under harmonic load at Node 4 in Y direction

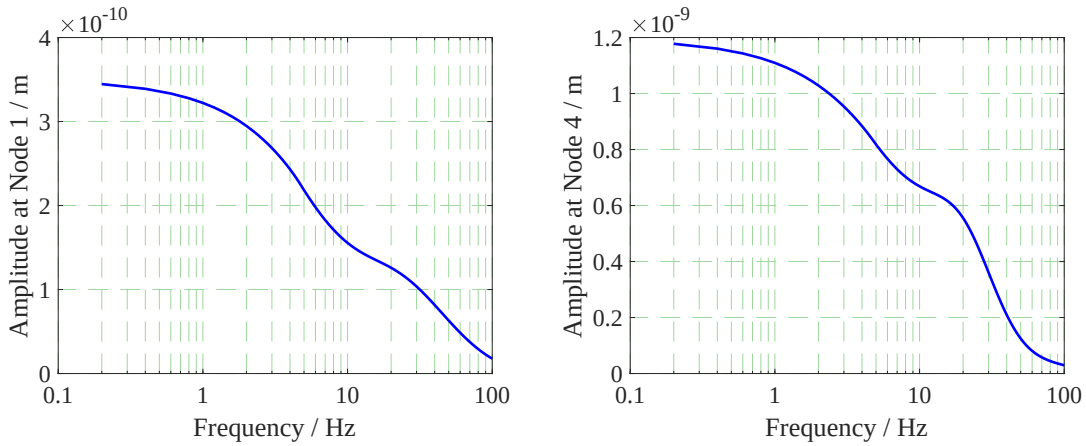


Figure C.27 Amplitude in Z direction under harmonic load at Node 4 in Y direction

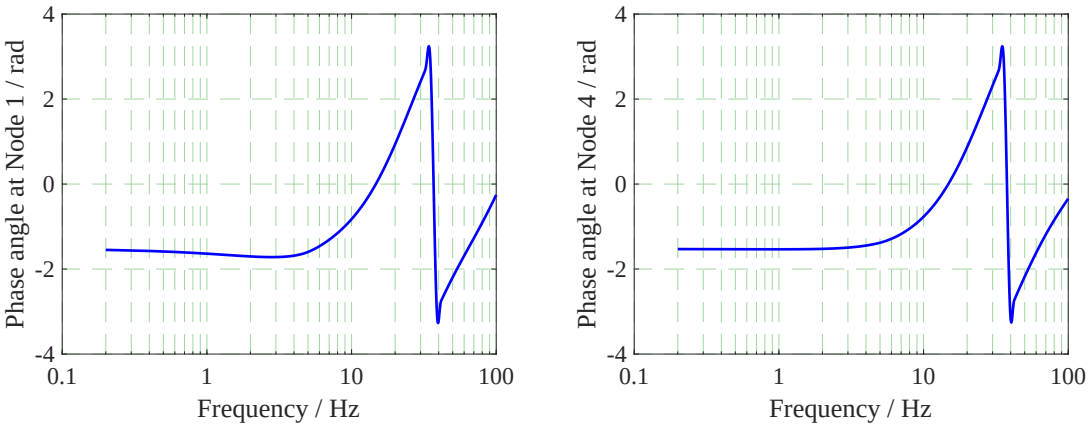


Figure C.28 Phase Angle in X direction under harmonic load at Node 4 in Y direction

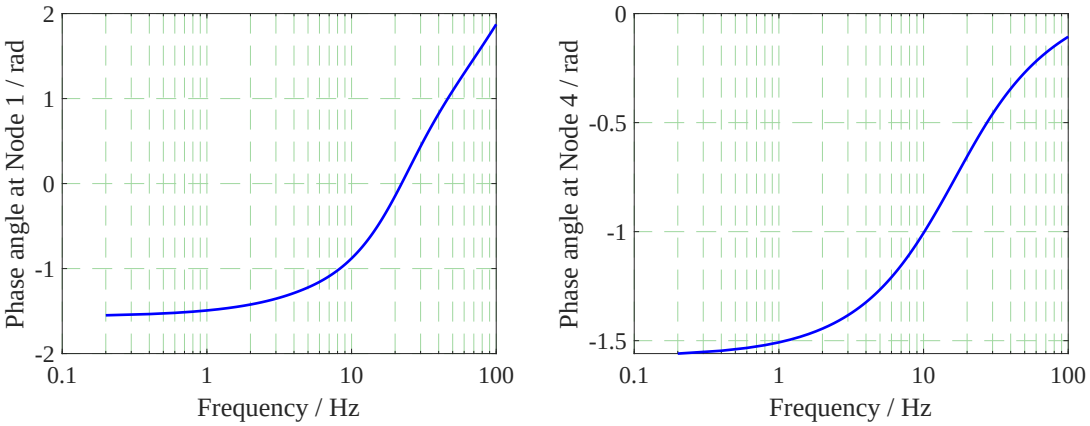


Figure C.29 Phase Angle in Y direction under harmonic load at Node 4 in Y direction

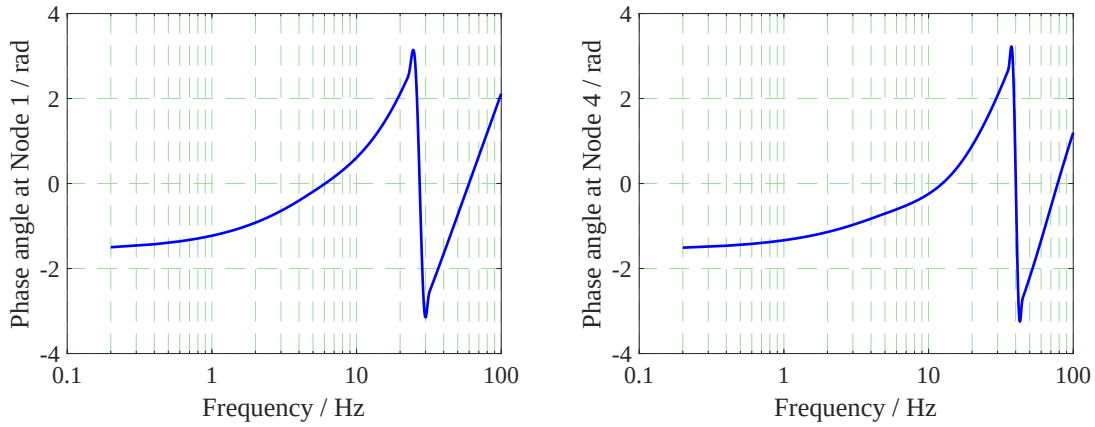


Figure C.30 Phase Angle in Z direction under harmonic load at Node 4 in Y direction

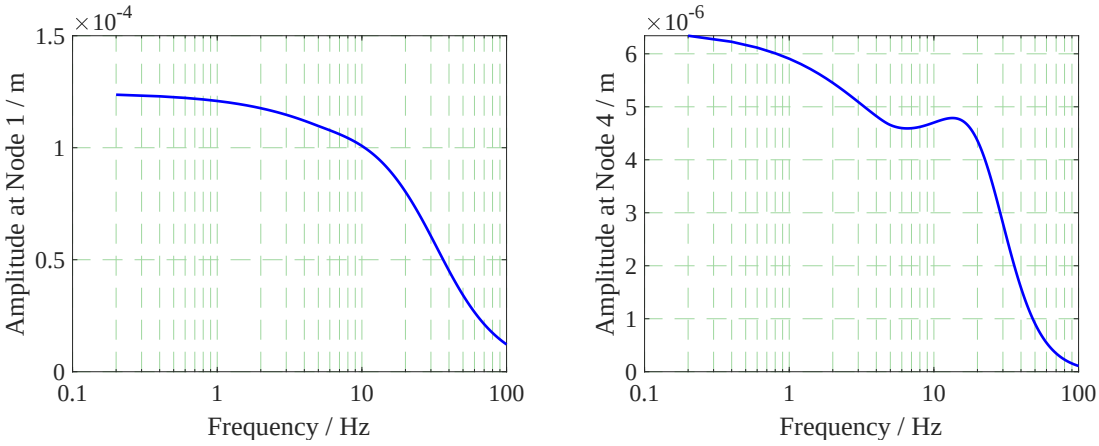


Figure C.31 Amplitude in X direction under harmonic load at Node 4 in Z direction

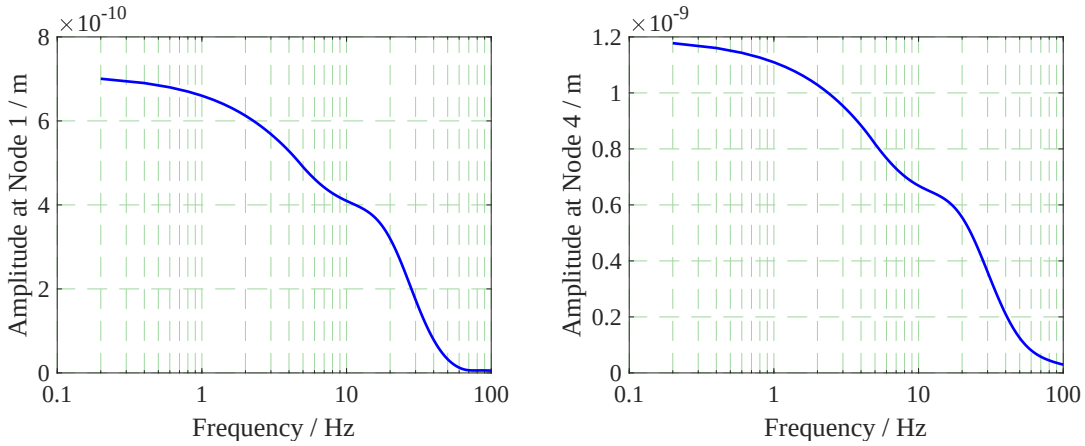


Figure C.32 Amplitude in Y direction under harmonic load at Node 4 in Z direction

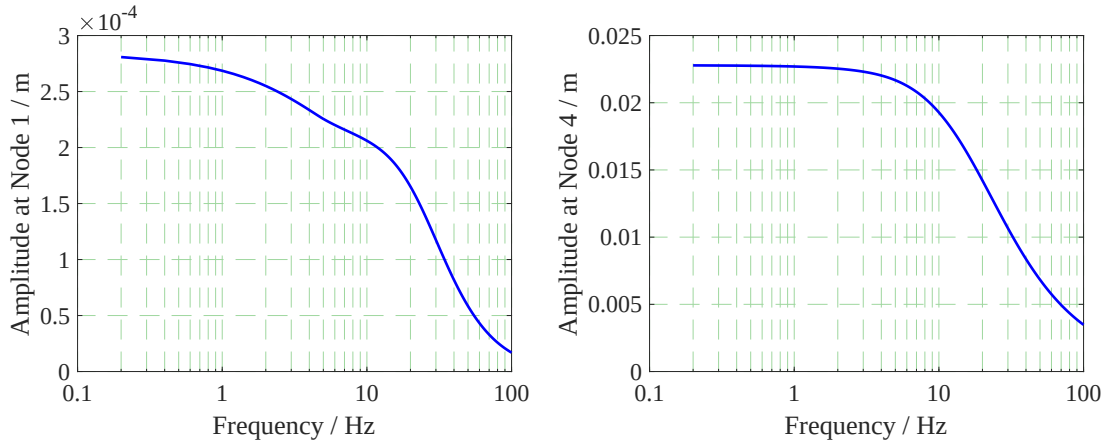


Figure C.33 Amplitude in Z direction under harmonic load at Node 4 in Z direction

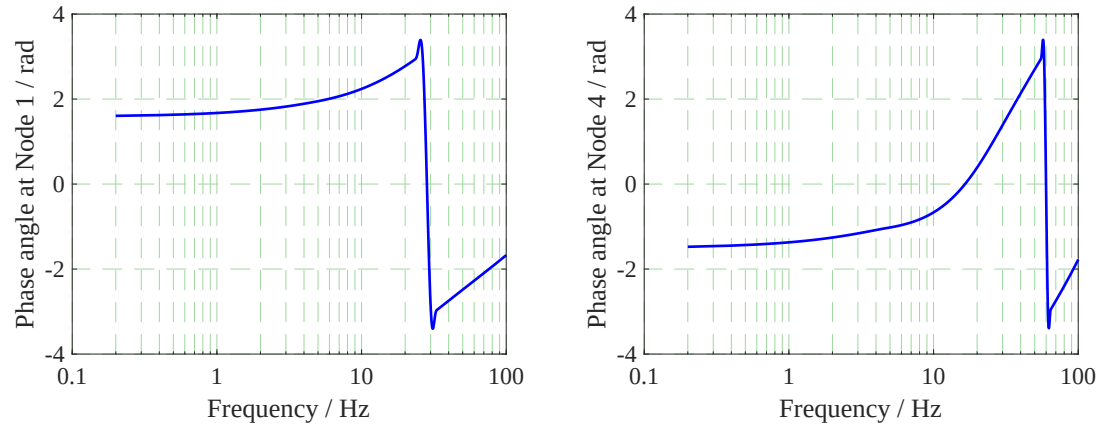


Figure C.34 Phase Angle in X direction under harmonic load at Node 4 in Z direction

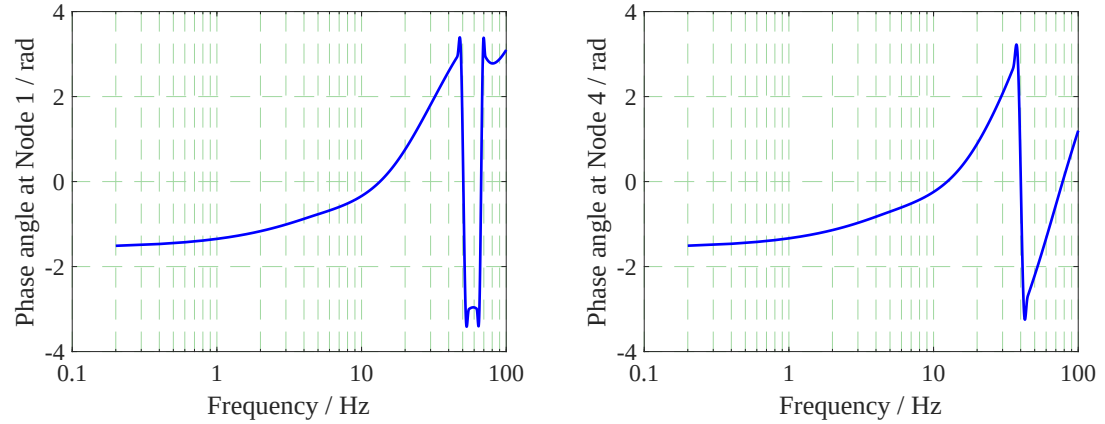


Figure C.35 Phase Angle in Y direction under harmonic load at Node 4 in Z direction

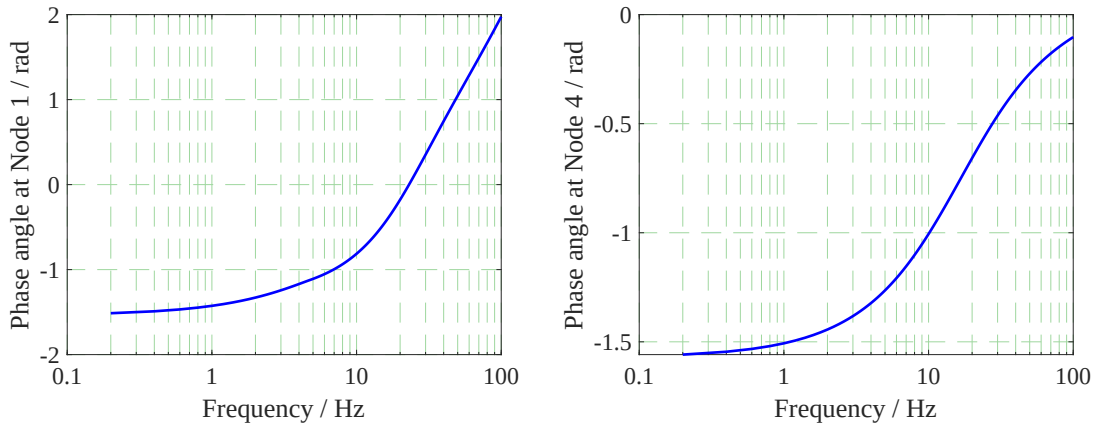


Figure C.36 Phase Angle in Z direction under harmonic load at Node 4 in Z direction

APPENDIX D

FRS for Different Site Classes

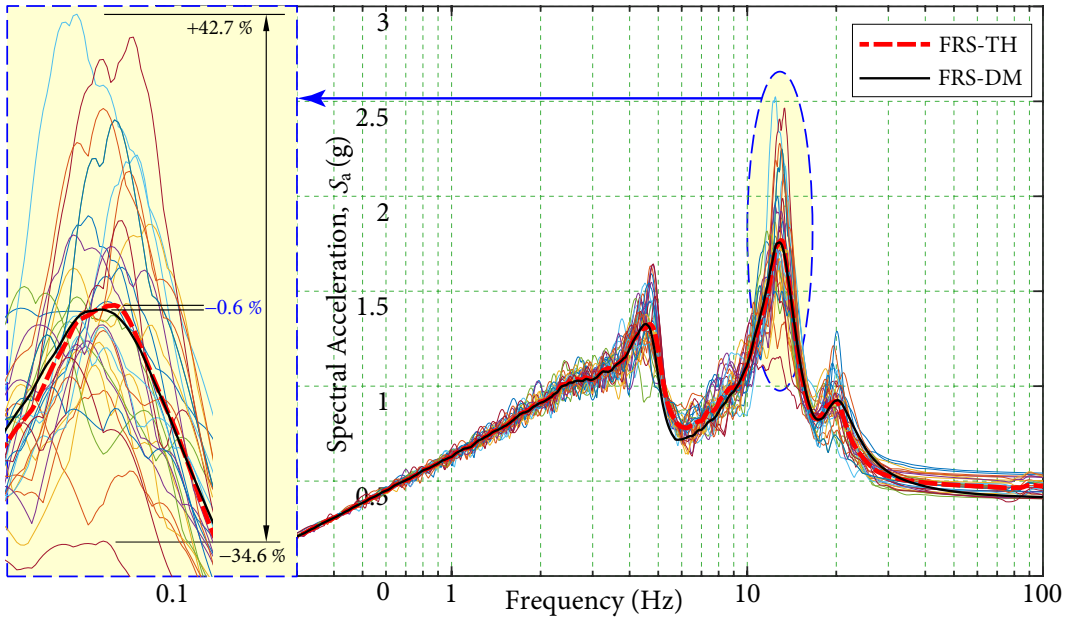


Figure D.1 FRS in H1 direction at Node 2 for soil case A (correlated).

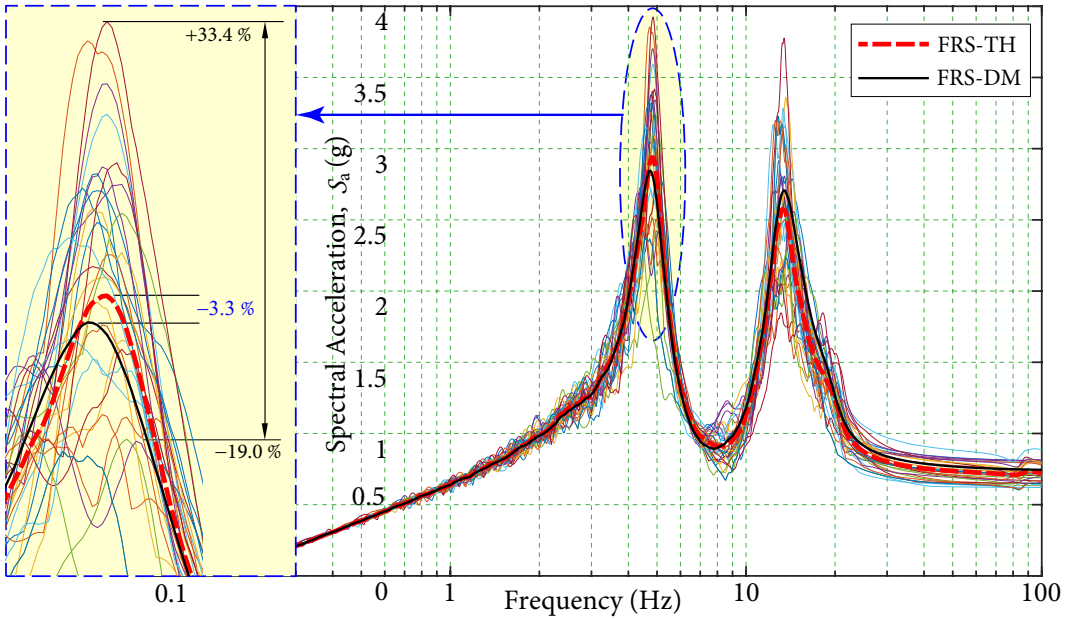


Figure D.2 FRS in H1 direction at Node 3 for soil case A (correlated).

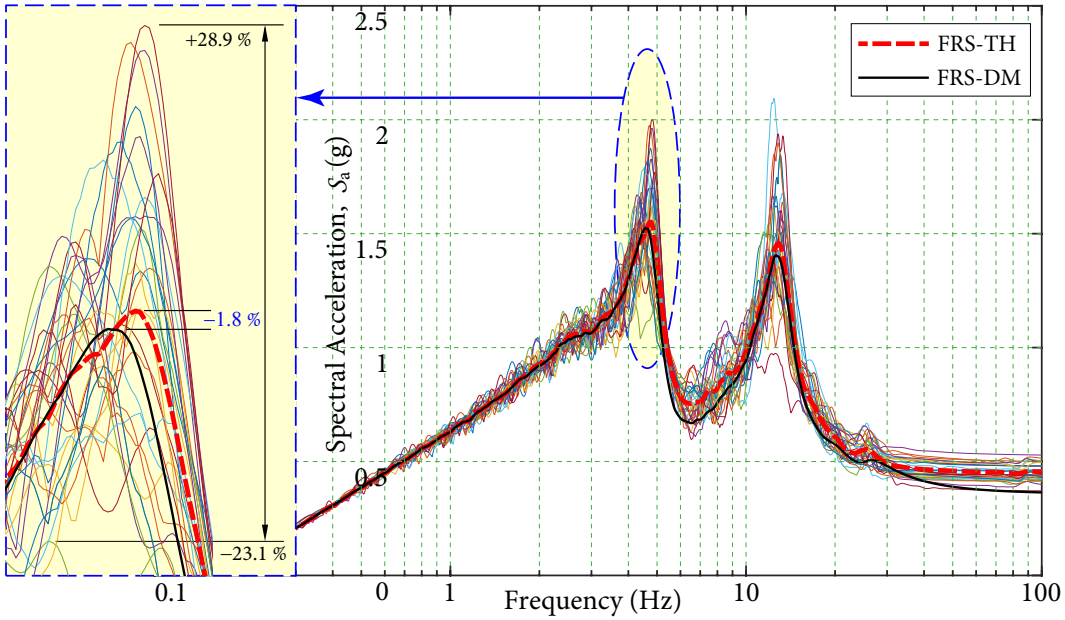


Figure D.3 FRS in H1 direction at Node 5 for soil case A (correlated).

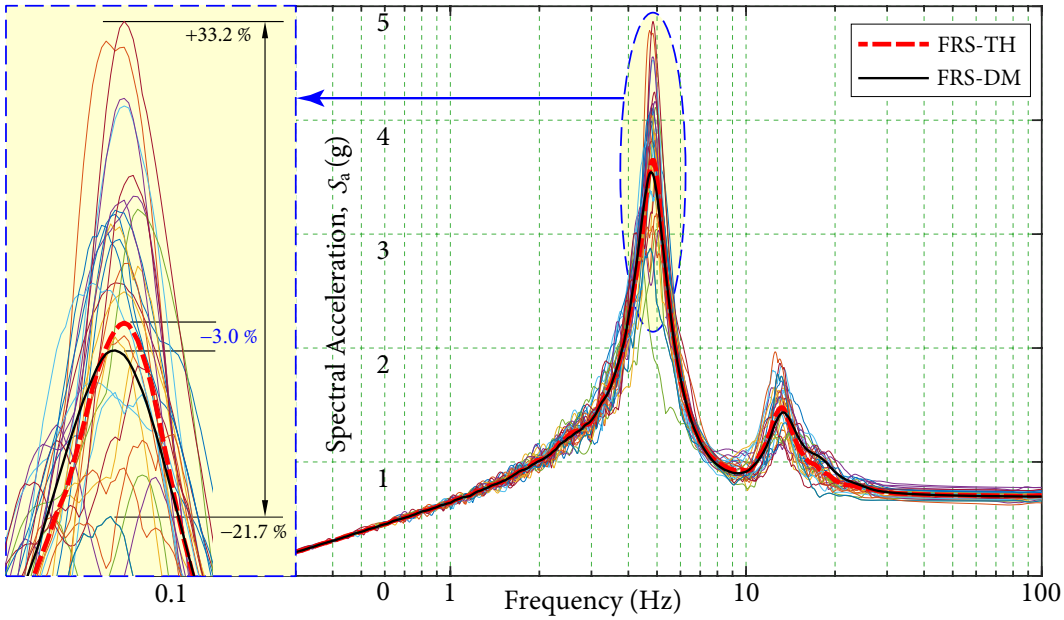


Figure D.4 FRS in H1 direction at Node 6 for soil case A (correlated).

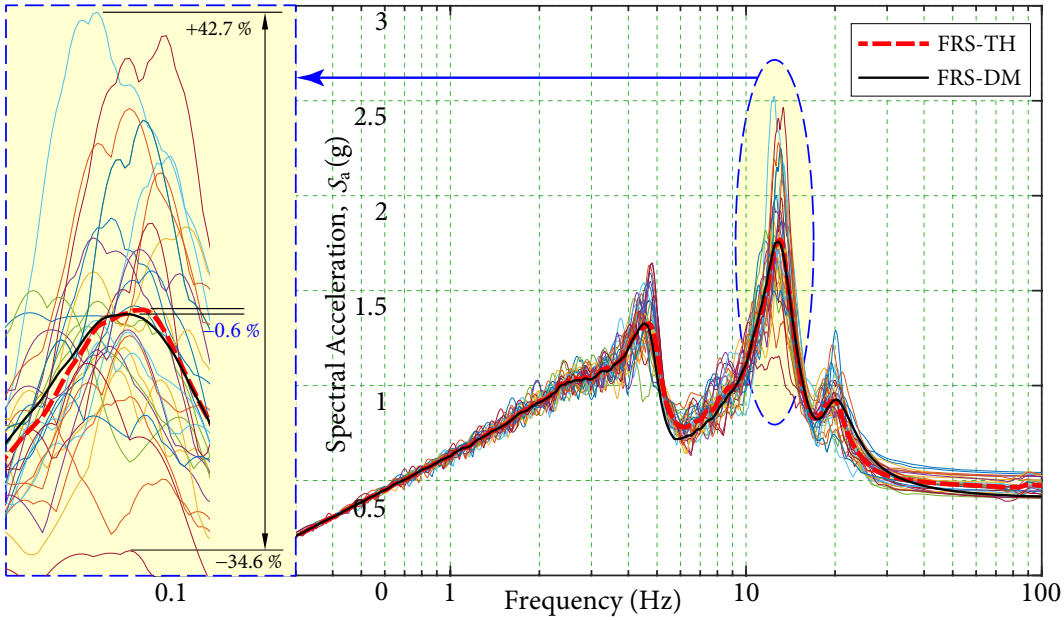


Figure D.5 FRS in H1 direction at Node 2 for soil case B (correlated).

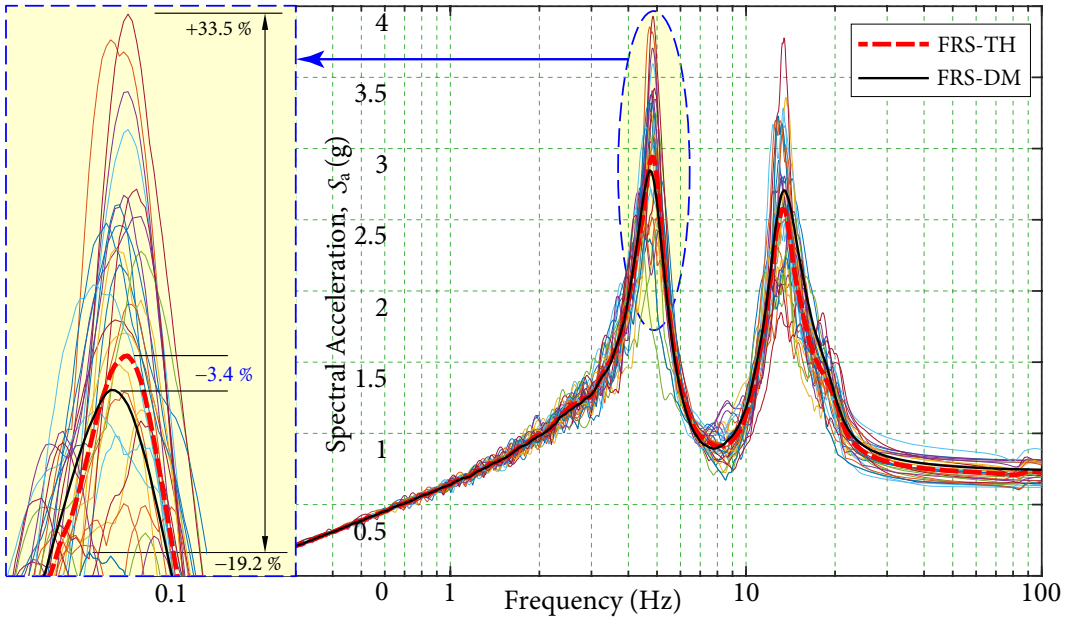


Figure D.6 FRS in H1 direction at Node 3 for soil case B (correlated).

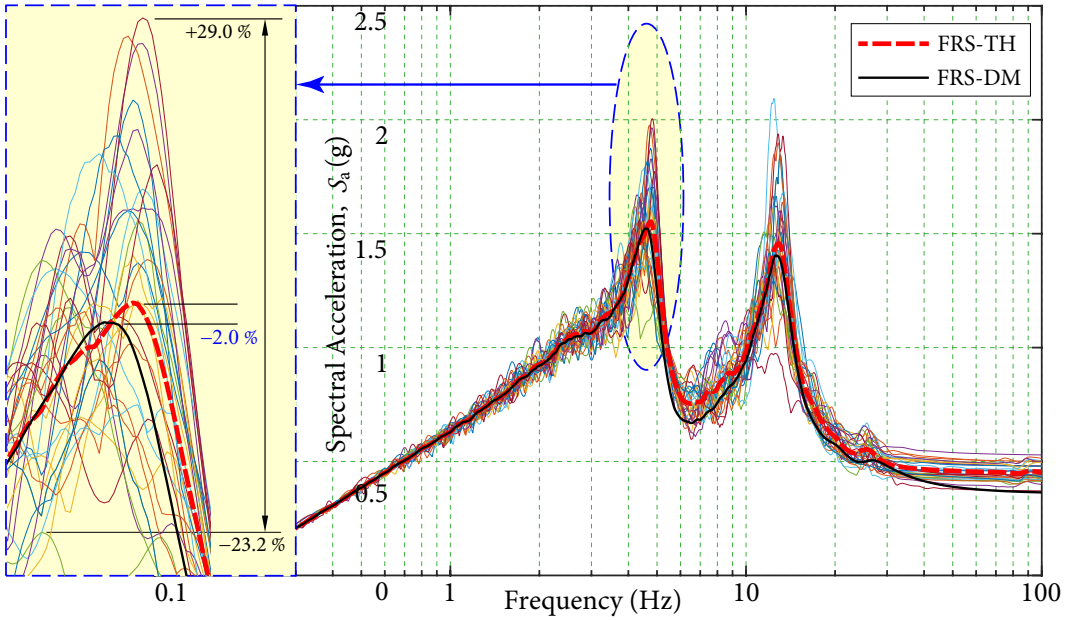


Figure D.7 FRS in H1 direction at Node 5 for soil case B (correlated).

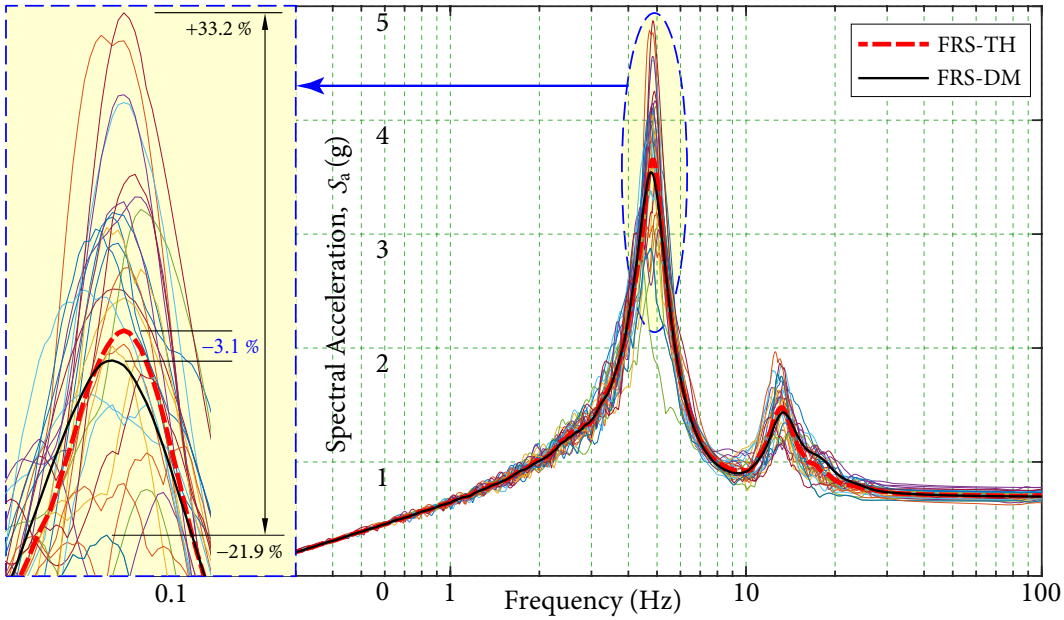


Figure D.8 FRS in H1 direction at Node 6 for soil case B (correlated).

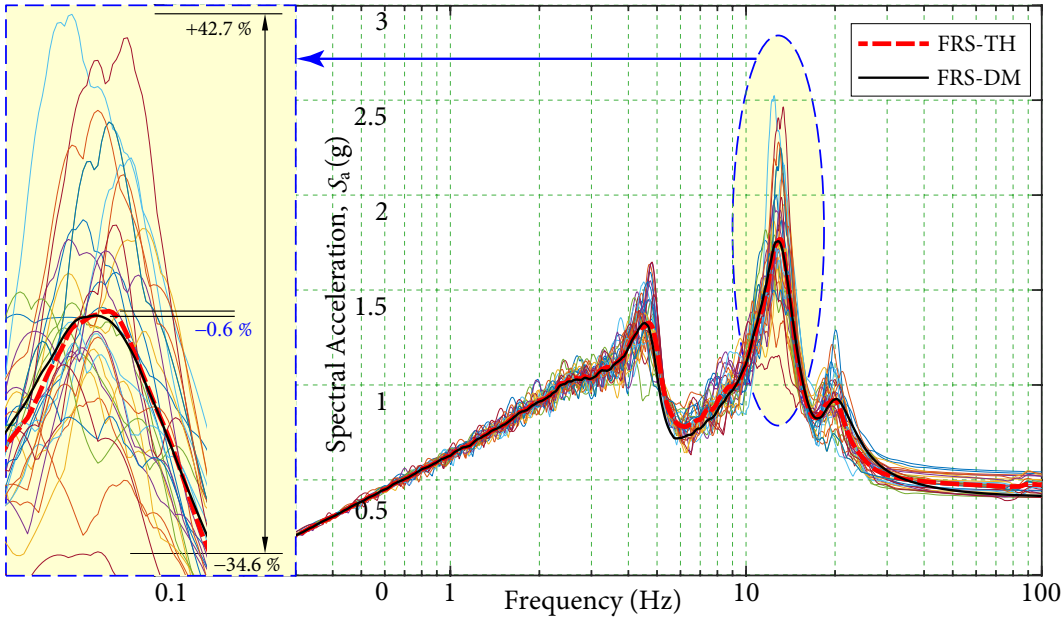


Figure D.9 FRS in H1 direction at Node 2 for soil case C (correlated).

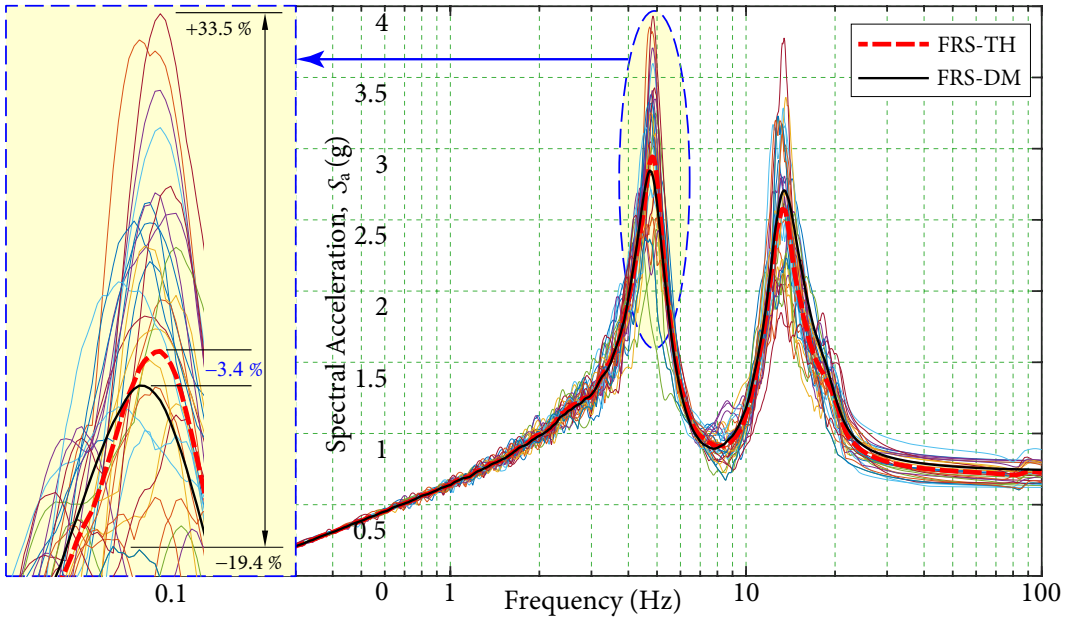


Figure D.10 FRS in H1 direction at Node 3 for soil case C (correlated).

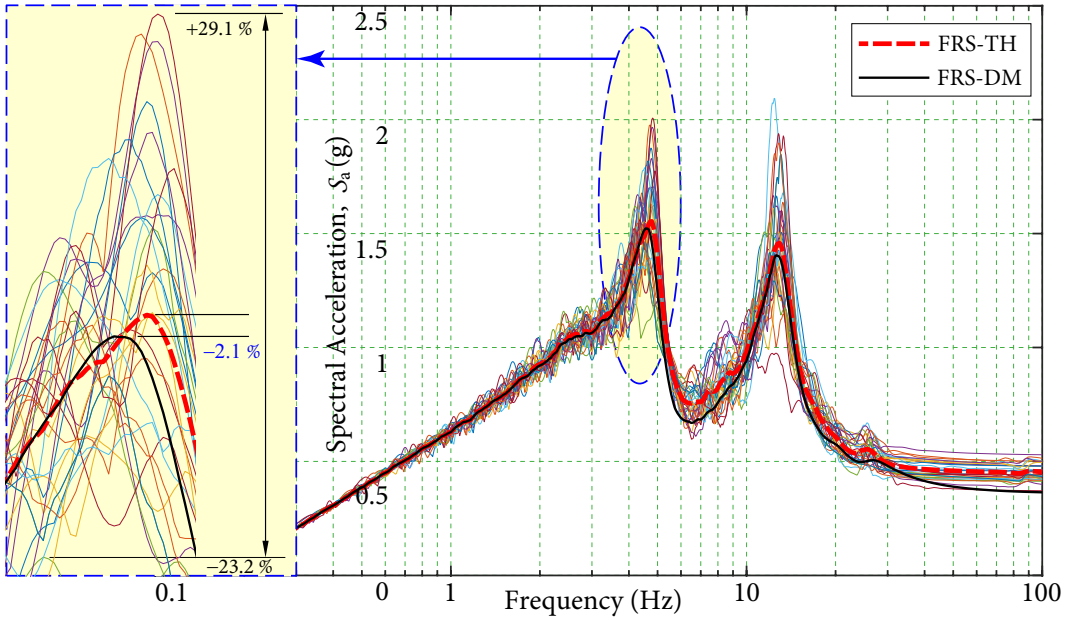


Figure D.11 FRS in H1 direction at Node 5 for soil case C (correlated).

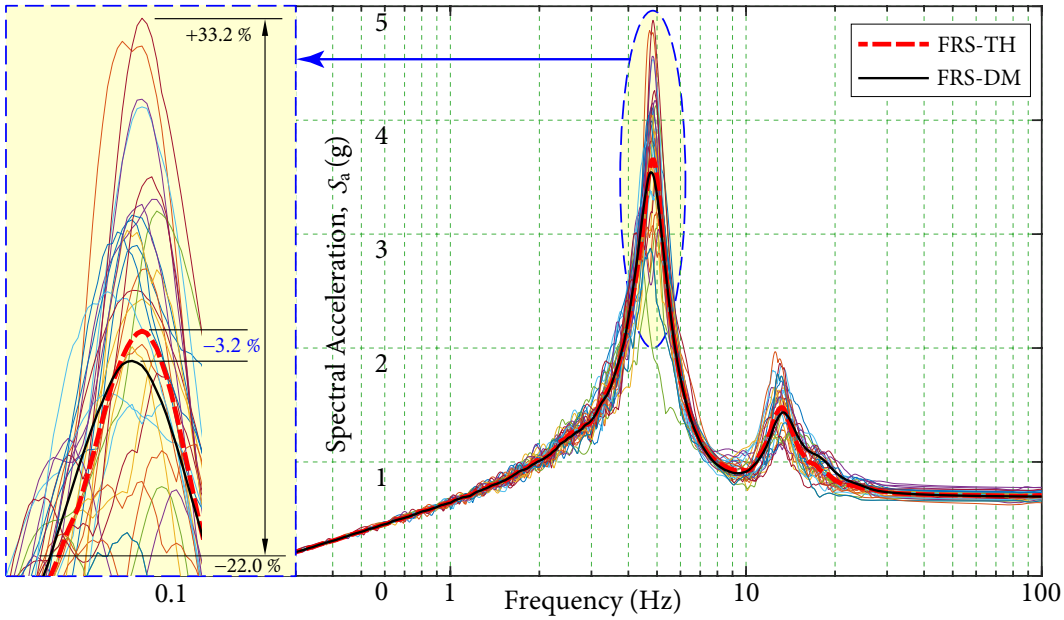


Figure D.12 FRS in H1 direction at Node 6 for soil case C (correlated).

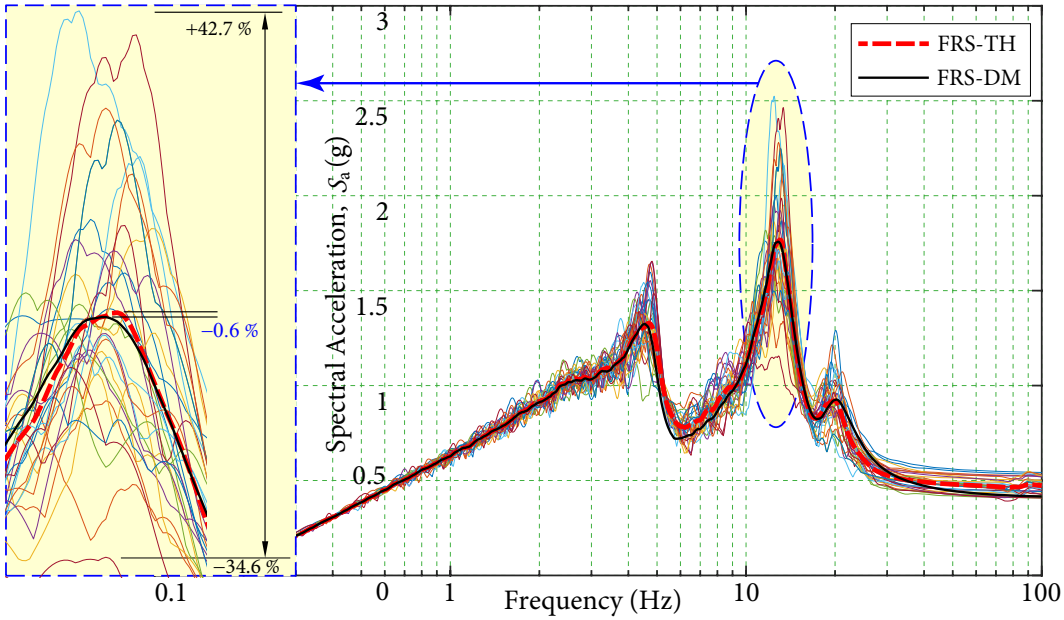


Figure D.13 FRS in H1 direction at Node 2 for soil case D (correlated).

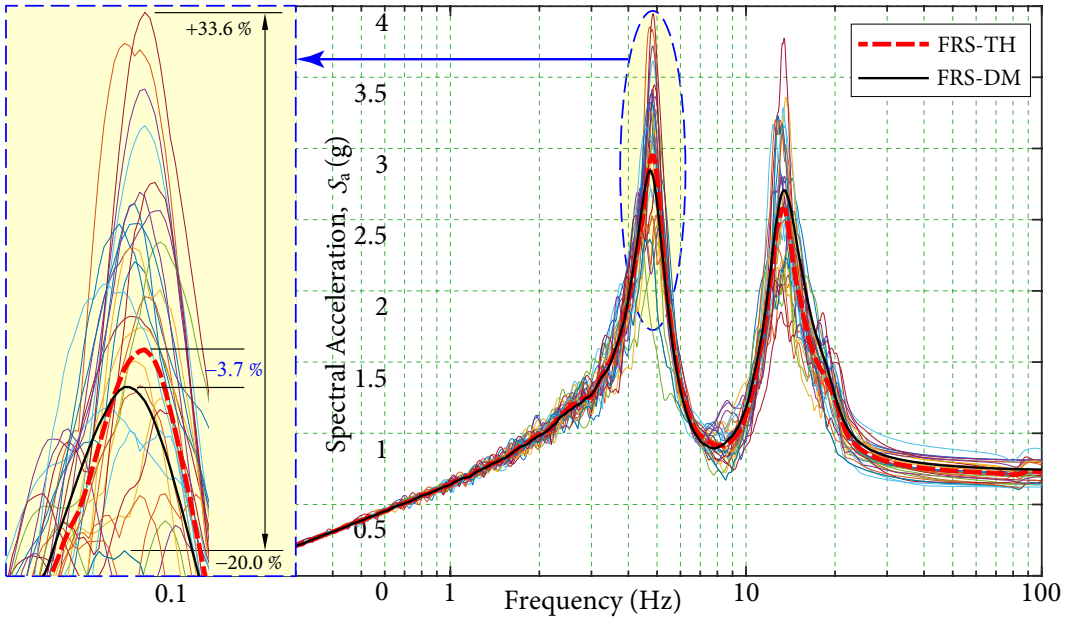


Figure D.14 FRS in H1 direction at Node 3 for soil case D (correlated).

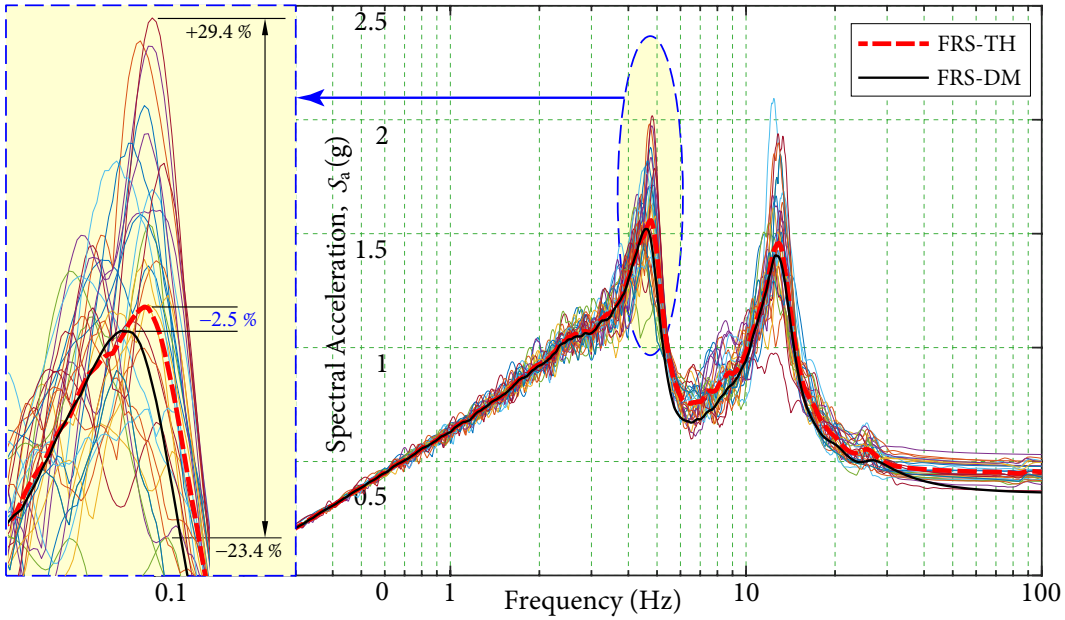


Figure D.15 FRS in H1 direction at Node 5 for soil case D (correlated).

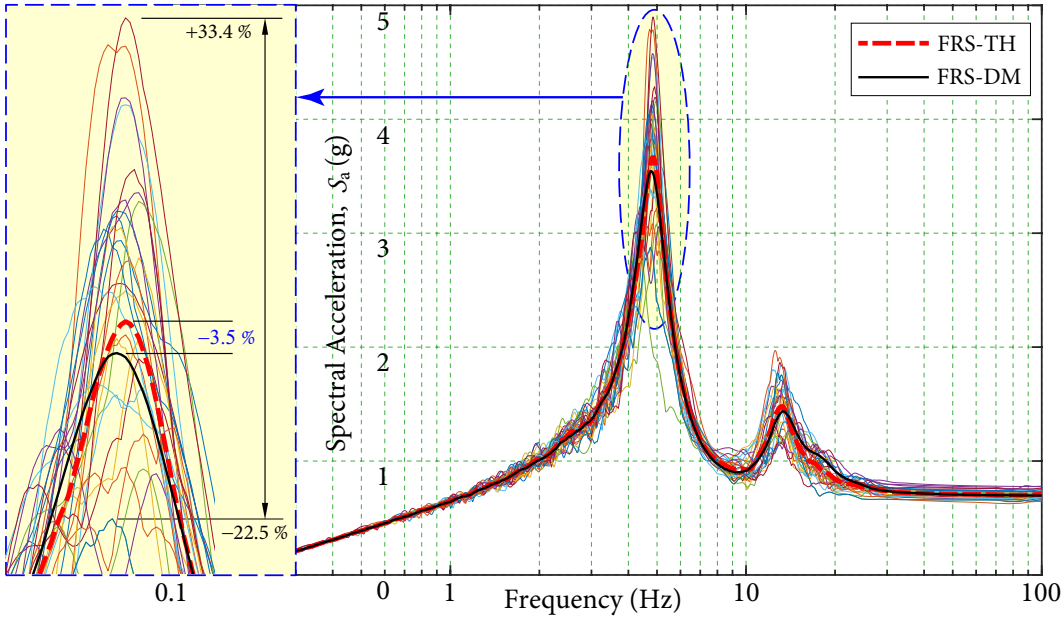


Figure D.16 FRS in H1 direction at Node 6 for soil case D (correlated).